TARGETING NATURAL SUPERSYMMETRY WITH TOP QUARKS

T. Christian Herwig

A DISSERTATION

in

Physics and Astronomy

Presented to the Faculties of The University of Pennsylvania

in Partial Fulfillment of the Requirements for the Degree of Doctor of Philosophy

2019

Elliot Lipeles, Associate Professor, Physics

Supervisor of Dissertation

Joshua Klein, Edmund J. and Louise W. Kahn Professor, Physics

Graduate Group Chairperson

Dissertation Committee

Justin Khoury, Professor, Physics

Joseph Kroll, Professor, Physics

Evelyn Thomson, Associate Professor, Physics

Burt Ovrut, Professor, Physics

Elliot Lipeles, Associate Professor, Physics

TARGETING NATURAL SUPERSYMMETRY WITH TOP QUARKS

COPYRIGHT
2019
T. Christian Herwig

To my parents.

Acknowledgements

First, I'd like to thank Brig Williams, Joe Kroll, Evelyn Thomson, and Elliot Lipeles for cultivating the environment of the Penn ATLAS group. It has been a tremendously enjoyable place to work, and full of broad and exciting research opportunities. This does not come "for free" and it is thanks to the hard work and attention from them, along with past generations of students and postdocs, that there exists such a unique setting where students can thrive.

I am extremely grateful to Elliot for his advising and mentorship to me throughout graduate school. His meticulous thoughtfulness, passion for digging into the details of an idea, and fervor for experimentation (not to mention his appreciation of coffee and practical jokes!) were beyond anything I could have hoped to have in a mentor. I thank him for guiding me through one interesting project after another, for always being eager to teach and discuss new ideas, and for preparing me to become an independent researcher. He is an excellent person and a model physicist from whom I feel incredibly lucky to have learned over the past five years.

I am also very grateful to Joe for his guidance throughout my PhD, and am especially happy to have had the opportunity to work together through the stop one-lepton analysis. Thank you for encouraging me to be precise and thoughtful, and for your generous advice and perspective.

I had the pleasure of working with many excellent physicists on various trigger topics (Steven Schramm, Andy Pilkington, Peter Sherwood, Mark Sutton, Anna Sfyrla, John Alison, Joana Machado Miguens), stop searches (Keisuke Yoshihara, Javier Montejo Berlingen, Sophie Pataraia, Jan Küchler, Daniela Boerner, Johanna Gramling, Kouta Onogi, Tomohiro Yamazaki), top measurements (Ben Nachman, Till Eifert, Dominic Hirschbühl), and $B-L$ SUSY (Burt Ovrut, Sebastian Dumitru), all of whom I owe much credit for the work described in this dissertation.

In particular, I'd like to thank three of these people who go above and beyond, and who were instrumental in shaping my graduate education. John, you challenge me to ask 'why' more often and to focus on answering the most important questions. Keisuke, you taught me every technical aspect of performing a careful analysis and the fruits that true dedication can produce. Ben, every conversation with you leaves me more inspired and excited than before to be a physicist. My ideal day at work would finish with at least two of us going for a beer together!

I've been very lucky to have an excellent group of other physicists as friends from my first days at Penn. Saul and Ashley, thank you for all of the dinners, games, jokes and everything else that made the Sansom house such a magical place. Thanks to all the older ATLAS students (and in particular the "second-years" Bijan, Bill, Joey, Khilesh, Leigh, and Will) for inviting Alpgen Jimmy out for Dim Sum and doughnuts, and pulling me into the group head-first from Day 1. Elodie, I'm so glad that we went through this whole experience together from the very beginning, and thank you for always wanting to know how I was doing. ('Sup Elodie!) Ben, thank you for greeting all of my inanities with a smile, for your patience, and for embracing Team Elliot. Thanks to all of the Penn group for the many memorable lunchtime conversations. Khilesh, thanks for running a top-notch coffee club, for having such a cheap yet high-quality brew, and for your liberal credit policy. Thanks for being a true friend.

Thanks to my family for encouraging me to be creative and scientific from the beginning, and for their encouragement in all that I've done. Rachel, thank you for all of your love, through this PhD and beyond.

ABSTRACT

TARGETING NATURAL SUPERSYMMETRY WITH TOP QUARKS

T. Christian Herwig

E. Lipeles

This thesis describes a search for natural supersymmetry via the production of light top squarks (*stops*) with the ATLAS experiment, using 13 TeV proton-proton collision data delivered by the Large Hadron Collider. A range of models is considered where the stop may decay to top quarks, b jets, and a variety of other supersymmetric particles. Stop masses as large as 950 GeV are excluded at 95% confidence level when decaying to a top quark and massless lightest supersymmetric particle (LSP). In scenarios where the LSP is a Higgsino, exclusions vary from 600 to 900 GeV depending on the relative stop branching fractions and Higgsino mass splitting. The impact of precision top-quark measurements on future searches is also discussed, including a measurement of quantum interference in top-quark production and measurement of the top-quark width. A differential mass distribution is measured in events with two charged leptons and two b-tagged jets that is sensitive to the interference property. The measurement is unfolded to particle level and the data are compared to state-of-the-art Monte Carlo predictions, which are found to describe the data well. A new technique is proposed to utilize this dataset to extract a value of the top-quark width, inspired by recent efforts to measure the Higgs boson width using off-shell decays. A value of $1.28 \pm 0.27(\text{exp.}) \pm 0.15(\text{theory})$ GeV is extracted from the ATLAS data, in good agreement with the standard model prediction. Finally, a new hardware tracking system is described for use in the upgraded ATLAS Trigger system for the high-luminosity run of the LHC.

Contents

List of Tables

List of Figures

List of Common Abbreviations

$B-L$ **MSSM** $B-L$ Minimal Supersymmetric extension of the Standard Model. xiv, xviii, xix, xxvii, 25, 26, 226, 228, 230, 232, 235, 236, 241, 242, 244–246, 249, 250, 252, 253

2HDM two-Higgs doublet model. 205

4FS four-flavor scheme. 158, 194

5FS five-flavor scheme. 158

AM associative memory. 61, 63, 64, 69, 70, 74, 80, 81

AMTP Associative Memory Track Processor. 80, 81

ASIC application-specific integrated circuit. 61, 81

ATCA Advanced Telecommunications Computing Architecture. 80

BCID bunch-crossing identifier. 39

BDT boosted decision tree. 50, 51

BSM beyond the Standard Model. 1, 2, 16, 17, 22, 91, 92, 105, 114, 139, 142, 143, 159, 160, 204, 207, 218, 223, 224, 226, 246

BW Breit-Wigner distribution. 158, 205, 207

CDF Collider Detector at Fermilab. 57, 68

CMM Common Merger Module. 40

CoM center-of-mass. 28

CP Cluster Processor. 39

CPU central processing unit. 38, 40

CR control region. xii, xvi, 90, 91, 117–123, 125–128, 132, 133, 139, 141–144, 164–169, 171, 172

CSC Cathode-Strip Chamber. 36, 37

CTP Central Trigger Processor. 39

DC don't care. 63, 64, 70–73, 79

DIS deep inelastic scattering. 9

DM dark matter. 14, 15, 25, 153, 226

DO Data Organizer. 81

DR diagram removal. xvi, xvii, 93, 138, 158, 159, 173, 179–186, 194, 201–203, 224

DS diagram subtraction. xvi, xvii, 93, 138, 158, 159, 173, 179–186, 194, 201–203, 224

EF Event Filter. 56, 57, 61, 62, 67, 80, 81

EM electromagnetic. 39, 44, 46, 49, 51, 60

EMEC Electromagnetic Endcap Calorimeter. 34

FCal Forward Calorimeter. 36

FELIX Front-End Link Exchange. 62, 80

FPGA field programmable gate array. 57, 61, 80, 81

FSR final-state radiation. 52

FTK Fast Tracker. 38, 57, 68

gHTT Global Hardware Tracking for the Trigger. 62, 69, 76, 79, 80

GRL Good Runs List. 99

GSC Global Sequential Correction. 42, 43, 49

GSF Gaussian sum filter. 46

HEC Hadronic Endcap Calorimeter. 36

HL-LHC High-Luminosity run of the Large Hadron Collider. xiv, xxvi, 41, 53–56, 59, 63, 225, 226

HLT High-Level Trigger. 37–45, 56, 100, 162

HTT Hardware Tracking for the Trigger. 57, 59–65, 67–69, 78, 80–82

HTTIF HTT Interface. 80, 81

HW hit warrior. 67, 72

IBL Insertable *B*-Layer. 32

ID Inner Detector. 30, 32, 40, 41, 43, 44, 46, 48, 62, 77, 78

IP interaction point. 28–33, 36

IQR inter-quartile range. 190

IR infrared. 5

ISR initial-state radiation. 124, 130

ITk Inner Tracker. xv, 62, 64, 67, 69, 74, 75, 80

JEP Jet/Energy-sum Processor. 39, 40

JER jet energy resolution. 59, 196

JES jet energy scale. 49, 136, 196

JVF jet vertex fraction. 50, 59

JVT jet vertex tagger. 50

L0 Trigger Level-0 Trigger. 56, 57, 59, 61, 62

L1 Calo Level-1 Calorimeter Trigger. 39

L1 Muon Level-1 Muon Trigger. 39, 40

L1 Topo Level-1 Topological Trigger. 38

L1 Track Level-1 Track Trigger. 60–62, 78, 81

L1 Trigger Level-1 Trigger. 37–42, 45, 56, 57, 62, 81, 82, 162

LAr liquid argon. 33–36, 39

LC Local Hadronic Calibration. 44, 51

LHC Large Hadron Collider. xiv, xxvi, xxvii, 1, 2, 7–15, 22, 23, 25, 28–30, 37, 41, 53, 54, 84, 85, 99, 105, 112, 155, 157–159, 203, 207, 222–226, 228, 236

LINAC 2 Linear Accelerator 2. 28

LL leading logarithm. 13

LO leading order. 9, 13, 93–95, 138, 155, 156, 158, 160, 201, 203, 209, 210

LSP lightest supersymmetric particle. xii, xiv–xvi, xviii, xxvii, 18, 22, 25–27, 55, 85–88, 95, 96, 98, 99, 105, 112, 114, 117, 123, 124, 129, 130, 147, 149–154, 222, 225–231, 236–238, 240–242, 249, 250, 253

MC Monte Carlo. xiii, xv–xvii, xxvii, 12–14, 46, 47, 49, 51, 90–92, 115–117, 121, 123, 126, 127, 135–137, 141, 142, 157, 162, 164–168, 170–172, 176, 181, 182, 186–190, 192–194, 196, 197, 201, 202, 204, 210, 223, 224

MDT Monitored Drift Tube chamber. 36, 37, 41, 47

ME matrix element. 7, 9, 12–14, 92, 96, 138, 156–158, 193

MS Muon Spectrometer. 30, 36, 37, 40, 41, 47, 48, 60

MSSM Minimal Supersymmetric extension of the Standard Model. xii, 17, 19, 20, 22, 23, 25, 84, 228, 241

mSUGRA minimal Supergravity. 22, 23

nDOF number of degrees of freedom. xv, 72

NF normalization factor. 141, 165–167, 172, 188, 196

NLL next-to-leading logarithm. 95, 241, 246

NLO next-to-leading order. 9, 12–14, 92–95, 137, 138, 155–159, 193, 199, 200, 203, 205, 209, 210, 223, 224, 241, 246

NLSP next-to-lightest supersymmetric particle. xv, xvi, 87, 95, 112, 151, 153, 241

nMCM new Multi-Chip Module L1 Calo Pre-Processor. 39

NNLL next-to-next-to-leading logarithm. 155

NNLO next-to-next-to-leading order. 13, 92, 155, 205

NP nuisance parameter. 136, 137, 140, 141

NWA narrow width approximation. 92, 206, 221

OS opposite-sign. xiii, xvi, 166–168

P2012 Perugia 2012. 92

PCB printed circuit board. 34

PDF parton distribution function. xiv, xvii, 9, 10, 13, 93–95, 138, 140, 156, 194, 199, 202, 209, 212, 213

pdf probability density function. 140, 155

pMSSM phenomenological MSSM. xii, xv, xvi, 23, 24, 96, 98, 99, 123, 129, 147, 150–154

PMT photomultiplier tube. 35

PRM Pattern Recognition Mezzanine. 80

PS parton shower. 13, 157–159, 199, 200, 209, 223, 224

PSB Proton Synchrotron Booster. 28, 29

PU pile-up. 35, 38, 42, 44, 49, 50, 59, 68, 137

PV primary vertex. 51

QCD Quantum Chromodynamics. xiv, 6, 20, 42, 48, 93, 94, 209

QFT Quantum Field Theory. 4, 5

RF radio-frequency. 28

RG renormalization group. xxvii, 5, 25, 228, 230

rHTT Regional Hardware Tracking for the Trigger. 62, 81

RMS root mean square. 48, 69, 138, 213

ROD Read-Out Driver. 38

ROI region of interest. xv, 39–43, 59, 60, 62, 68, 81, 82

ROS Read-Out System. 38, 40

RPC Resistive Plate Chamber. 36, 37, 40

RPV R-parity violation. 25, 26, 227–229, 232, 233, 236, 241, 242, 245, 246

RTM Rear Transition Module. 80

SCT Semiconductor Tracker. 32, 44

SFOS same-flavor, opposite-sign. 162, 243, 251

SM Standard Model. xii–xiv, xvi, 1, 3, 5, 7, 8, 14–21, 24–27, 41, 53–55, 84–86, 88, 90–92, 105, 116–120, 125, 128, 130–134, 137, 139, 141–143, 149, 157, 166, 173, 174, 204, 205, 207, 211, 220, 229, 232, 233, 237, 240

SPS Super Proton Synchrotron. 29

SR signal region. xii, xiii, xv, xvi, 90–92, 112, 114, 117–134, 138–144, 147, 153, 154, 162–169, 171, 172, 179–183, 188, 191, 192

SS super-strip. 62–64, 69, 70, 79

SS same-sign. xiii, xvi, 166–168

SSID super-strip identifier. 63, 64, 69, 70, 80, 81

SSTP Second-Stage Track Processor. 80, 81

SUSY Supersymmetry. xiii–xv, xviii, xxvi, xxvii, 1, 18–27, 54–57, 84–86, 90, 95, 123, 130, 159, 190, 205, 222, 224–228, 236, 237, 240–245, 251, 253

SV secondary vertex. 50

SVD singular value decomposition. xvii, 177, 179, 182

SVT Silicon Vertex Tracker. 57, 68

TDAQ Trigger and Data Acquisition. xiv, 37, 56, 58, 61, 69, 81, 83

TDR Technical Design Report. xv, 53, 69, 74, 75, 83

TF transfer factor. 167, 196

TFM Track-Fitting Mezzanine. 80, 81

TGC Thin Gap Chamber. 36, 37, 40

ToF time of flight. 85

ToT time over threshold. 32

TP Track Processor. 80

TR transition radiation. 33

TRT Transition Radiation Tracker. 32, 33, 45, 46

TSP thin-strip pattern. 63, 64, 69–72

UV ultraviolet. 5, 22, 25

VBF vector boson fusion. 208

VEV vacuum expectation value. 7, 8, 25, 54, 84, 228, 229

VLQ vector-like quark. 205

VR validation region. xii, 91, 117–121, 126–128, 132–134, 141, 144

WC wildcard. xii, 63, 64, 70–74

WIMP weakly-interacting massive particle. 15, 18

WP working point. 51, 171

Preface

In fall 2014 I began my PhD by joining the ATLAS group at the University of Pennsylvania. Previously, I was an undergraduate at the University of Chicago, where Argonne Scientist Sasha Paramonov, and Professors Jim Pilcher and Carlos Wagner first introduced me to the Higgs boson, Supersymmetry (SUSY), and how we might discover them at the Large Hadron Collider (LHC).

My first project at Penn was to join Professor Elliot Lipeles' effort to design a hardware-based track-finding system for the trigger during the High-Luminosity run of the Large Hadron Collider (HL-LHC). Initially, I designed algorithms utilizing the new tracking information to more efficiently identify multi-jet signatures, leading towards the Phase-II Upgrade Scoping Document [5]. These triggers would improve our ability to probe the Higgs self-coupling through di-Higgs production in both the $b\bar{b}b\bar{b}$ and $b\bar{b}\tau^+\tau^-$ final states.

In 2015 I began qualifying as an ATLAS author, improving the current (Run 2) software jet trigger. Here I used charged particle track information to improve the jet energy calibrations. Reduced energy resolution leads to a sharper "turn-on" of the trigger so that a larger fraction of events are recorded where the trigger is fully efficient. This was made possible by reorganizing the jet and b tagging software trigger to take advantage of common track inputs. The new energy corrections improved trigger performance and became standard for Run 2 data collection after commissioning in 2016. I traveled to Chicago for the ICHEP 2016 conference to present these results for the first time, along with my measurements of the trigger performance in early 2016 [6].

Around this time I joined Professor Joe Kroll and Postdoctoral Associate Keisuke Yoshihara at Penn in a search for supersymmetric top-quark partners (*stops*), using events with one charged lepton and a large transverse momentum (p_{T}) imbalance. This was an exciting time to search for stops as the 2016 data would improve the experiment's sensitivity by several hundreds of GeV in stop mass. I began by optimizing searches for stop decays to charginos and working to estimate theoretical uncertainties for top-quark processes. That spring I moved to CERN to work closely with my collaborators, as well as to more effectively serve the jet trigger group. Later, I focused on developing the analysis' sensitivity to stop signals with low-p_{T} leptons – a signature of "natural SUSY" with light Higgsinos. With K. Yoshihara, I surveyed the space of various SUSY parameters and developed the set of benchmark models to be used by all third-generation SUSY searches on ATLAS. Though we observed an exciting (3.3σ) excess in the early 2016 data it did not persist in the full data-set, and the analysis instead set strong limits on the possibility of light top squarks [7].

My studies of top-quark theory systematics lead to a new project, motivated to better understand the interference between top-quark pair production and single top production, which led to a dominant uncertainty for the stop analysis. With LBNL Chamberlain Fellow Ben Nachman and CERN Scientist Till Eifert I developed a new measurement to constrain this effect with data [8]. Working in a small, experienced team allowed me to conduct nearly all aspects of the analysis. I learned much, from the nuances of unfolding techniques to the details of Monte Carlo (MC) calculations of top-quark processes. Following this publication, B. Nachman and I realized that the measurement should also have sensitivity to the top-quark width. With Universität Zürich Postdoctoral Associate Tomáš Ježo, we published the technique alongside a reinterpretation of the ATLAS measurement [9].

After returning to Penn in the winter of 2017 I rejoined the hardware track trigger effort with Prof. Lipeles in wide-ranging work that involved writing software to simulate the system, designing and implementing new algorithms, and estimating performance and data-flow metrics to inform the overall system design. This led towards the Phase-II Trigger upgrade Technical Design Report [10], and continued with studies towards the initial hardware prototype.

Finally, I joined Penn theorists Professor Burt Ovrut and PhD student Sebastian Dumitru in phenomenological studies of the $B-L$ Minimal Supersymmetric extension of the Standard Model ($B-L$ MSSM) [11]. We investigated scenarios where the *Bino* of SUSY (partner of the photon/Z admixture) is the lightest supersymmetric particle (LSP), favored by the renormalization group (RG) flow of the soft SUSY masses from high scales. In particular I contributed calculations for low-mass Binos, where R-parity violating decays via virtual gauge bosons lead to long-lived particle decays. This collaboration with members of the physics deparment at Penn outside of the ATLAS group expanded my views of SUSY at the LHC and how one should go about finding it!

T. Christian Herwig
Philadelphia, July 2019

CHAPTER 1

Introduction

The top quark is the most massive fundamental particle known to exist. Despite being discovered nearly 25 years ago, it continues to provide one of the most fertile testing grounds for the Standard Model (SM) of particle physics and a promising means to access new physics, beyond the SM. In some aspects, the top quark is not a novelty; it is apparently the final element of the intensely-scrutinized quark sector and interacts in a similar manner to its less-massive counterparts. However, the simple feature that is is forty times more massive than any other quark leads to an associated phenomenology that is completely unique.

The observation of the Higgs boson in 2012 at the LHC gave the first strong indication of the mechanism by which masses are generated for the particles of the SM. The particle is now an object of intense study, with theoretical considerations strongly suggesting that further new physics should be associated with this newly-observed scalar. However, the Higgs discovery affirms the special role of the top quark –the SM particle with the strongest coupling to the new state– and suggests that new physics associated with the Higgs may be intimately connected with the top quark. The Naturalness paradigm is one manifestation of this argument, intimately connecting the scalar nature of the new boson with the presence of new beyond the Standard Model (BSM) partners of the top quark.

This dissertation is structured as follows. Chapter 2 introduces the necessary theoretical framework for the remainder of the document, focusing on the foundational properties of the SM. Calculational tools used to obtain predictions for collider experiments are also discussed. The chapter concludes with a discussion of the SM's shortcomings and hints of how the theory may be extended. Chapter 3 presents SUSY as a possible extension of the SM and introduces the most common frameworks used by collider searches to search for and interpret results of searches for supersymmetric phenomena. The experimental tools used to conduct analyses of proton-proton collisions are described in Chapter 4. This includes discussion of the LHC, the ATLAS detector, and the techniques used to reconstruct signatures of particle interactions with the measurement apparatus. Following the description of the current experiment, Chapter 5 digresses to discuss a hardware-based tracking system, designed as an upgrade to the trigger system needed for future high-luminosity data-taking campaigns. Chapter 6 describes a search for supersymmetric partners of the top quark, using proton-proton collision data collected in 2015 and 2016. A follow-up measurement of SM top-quark production, sensitive to interference between singly- and doubly-resonant diagrams is described in Chapter 7. In Chapter 8, a new technique is presented to measure the top-quark width using off-shell production. The data presented in Chapter 7 are recast using this method, providing a new constraint on the width. Further avenues to probe BSM physics with similar techniques are also discussed.

Chapter 2

Theoretical Background: The Standard Model

The domain of particle physics is to describe nature at the smallest observable scales, governed by the principles of quantum mechanics and special relativity. Experimental observations are interpreted in the context of the Standard Model (SM), a quantum field theory with specific gauge structure and matter content. The theory describes the electromagnetic, weak, and strong forces, and the quantum matter fields that interact according to them. Particles are localized quantizations of these fields with definite energy-momentum, spin, and charges under each of the SM symmetries. The structure and parameters of the theory are encoded in a Lagrangian density $\mathcal{L}_{\mathrm{SM}}$, from which experimentally-measurable predictions may be calculated. This chapter will describe the structure of the SM, how collider observables are calculated using it, and some known limitations of the model.

2.1 The Framework

Particle physics experiments are conducted by observing particle interactions. In fixed-target or colliding-beam experiments, $2 \to n$ interactions are generally studied, where incoming particles may simply scatter or undergo more complicated processes where (potentially many) new particles are produced. Other experiments study the decays of unstable particles, proceeding via $1 \to n$ reactions. A useful theory of particle physics must thus describe both the "matter content" of scattering and decaying particles in the theory, as well as the allowed interactions that dictate how these processes occur.

Particles

The basic element of a Quantum Field Theory (QFT) is the quantum field: a wave-function $\psi(x)$, taking some complex value for every point x in four-dimensional spacetime. The dynamics of these fields are governed by a Lagrangian density $\mathcal{L}$ with contributions from kinetic and potential energy terms. By demanding that the Lagrangian respect a set of general symmetry principles, a highly constrained, but rich structure must be accepted. To be consistent with relativity, the theory must obey the symmetries of the Poincarè group: Lagrangian terms must be invariant under translation, rotation, and boost symmetries. Conservation of momentum follows from translation invariance, so physical states may be labeled by their momentum. This is true because the generator of translations is the momentum operator P, which commutes with the Hamiltonian. The conserved quantities emerging from Lorentz invariance are obtained by finding the representations of the *little group* of Wigner [12]: transformations which leave the momentum of a state invariant. For massive particles, this is the three-dimensional rotation group SO(3), whose irreducible representations have dimensions $2j+1$ corresponding to spin $j = 0, \frac{1}{2}, 1, \ldots$ and so on. For massless particles, the little group is given by the isometries of the 2-dimensional Euclidean plane ISO(2), which factorizes into rotational and translational components. Rotations give rise to two helicity states, regardless of spin and similar to the massive case. The translational invariance leads to electromagnetic gauge freedom.

Gauge symmetry

The simplest Lagrangian density, for a free scalar ψ with mass m, may be written

$$\mathcal{L}_{\text{free}} = \partial^2\psi + m^2\phi^2, \tag{2.1}$$

where ψ may collect multiple degrees of freedom. In gauge theories, the observables derived from the Lagrangian are demanded to remain invariant under the action of a gauge symmetry group. Writing ψ in the k-dimensional representation of the n-dimensional group G, this corresponds to the set of unitary transformations $\psi \to U(x)\psi$ with $U = \exp(i\alpha^a(x)t^a)$. Here t^a are the n generators of G acting on the k-plet ψ with magnitudes parameterized by the local (gauge) family of functions α. Because $\partial_\mu\psi$ does not respect this symmetry, connection fields A^a_μ are introduced to compensate for the change in local symmetry transformations. The covariant derivative $D_\mu = \partial_\mu - igA^a_\mu t^a$ is the gauge-invariant form of the original kinetic energy term for the matter field ψ, where g is an arbitrary constant. However, kinetic terms for the new gauge fields A^a_μ are now also required, obtained from the commutator of the covariant derivative $[D_\mu, D_\nu] = -igF^a_{\mu\nu}$, which gives $F^a_{\mu\nu} = \partial_\mu a^a_\nu - \partial_\nu a^a_\mu + gf^{abc}A^b_\mu A^c_\nu$. Here f^{abc} are the structure constants of G in the chosen representation defined by $[t^a, t^b] = if^{abc}t^c$. The field strength tensor may be used to construct a kinetic term $(F^a_{\mu\nu})^2$ for the fields A^a_μ, completing the gauge-symmetric Lagrangian.

The electromagnetic force realizes the simplest case, where the symmetry is given by the Abelian group U(1). In this theory, the two spin-one degrees of freedom naïvely cannot be represented as a vector field, without accounting for the additional degrees of freedom afforded by the vector. Gauge invariance solves this dilemma, dictating the necessary additional constraints on the photon field A_μ. On the other hand, the first construction of a non-Abelian gauge theory is that of the special unitary group SU(n) of n-dimensional linear transformations, due to Yang and Mills [13]. These account for the gauge groups of the SM associated with the strong and weak forces.

Renormalization

The presence of ultraviolet (UV) divergences in QFTs describing the SM are inescapable features of the theory that can be addressed through a renormalization scheme. Computations involving virtual particles lead to integrals over arbitrarily high-momentum degrees of freedom that must be regulated. A modern viewpoint takes the parameters of the theory measured at some reference scale (the *renormalization scale* μ_R) to be fundamental, as opposed to the "bare" terms present in the Lagrangian. This method was formalized by Kenneth Wilson [14] through the development of the RG. In this approach, the integration over high-momentum degrees of freedom corresponds to an RG 'flow' of the parameters of an effective Lagrangian, with the free field representing a fixed-point. Lagrangian terms may be classified as relevant or irrelevant operators depending on whether they become larger in magnitude during this procedure or smaller, converging to the original free theory. These correspond to terms with couplings of positive and negative mass dimension, respectively. Interactions with mass dimension of exactly four have dimensionless coupling constants that "run" or flow in a non-trivial way. The evolution of couplings and field strengths in this manner is described by the β and γ functions of the Callan-Symanzik Equation [15, 16].

For non-Abelian theories, the β function describing the evolution of the gauge coupling is negative so that at large momenta the coupling tends toward zero. This is the phenomenon of *asymptotic freedom*, realized in the SM by the strong force. Conversely, the coupling grows large in the infrared (IR), with Λ_{QCD} defined as the scale at which the coupling, properly normalized becomes unity. Near this scale the theory becomes non-perturbative, necessitating an different suite of techniques

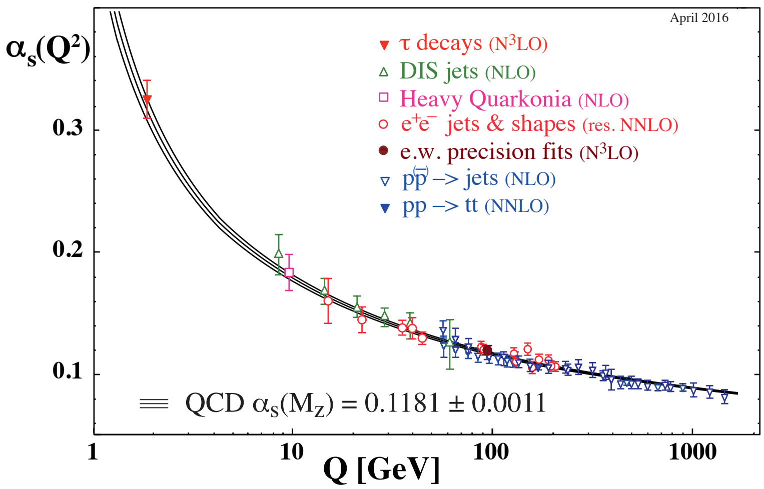

Figure 2.1: The running of the strong coupling constant is shown across several decades of momenta. The scaling predicted by QCD theory is shown compared to experimental measurements in a variety of energy regimes and physical processes. Figure is reproduced from Ref. [1].

to understand Quantum Chromodynamics (QCD) in this regime. The scaling behavior of α_S across a several decades of momenta predicted by QCD is shown in Figure 2.1 alongside a number of experimental measurements at varying scales.

Interactions

The most basic quantity needed to calculate interaction rates is the two-point correlation function $\langle 0|\psi(y)\psi(x)|0\rangle$, giving the probability for a particle to travel from x to y. The state $|0\rangle$ denotes the vacuum of the theory. Correlation functions are efficiently obtained from the Lagrangian in Feynman's path integral formalism from the generating functional:

$$Z[J] = \int \mathcal{D}\psi \ \exp\left[i \int d^4x(\mathcal{L} + J(x)\psi(x))\right]. \tag{2.2}$$

This may be differentiated n times to obtain the n-point function, with $n = 2$ given by

$$\langle 0|\psi(y)\psi(x)|0\rangle = \frac{1}{Z[J=0]}\left[\left(-i\frac{\delta}{\delta J(x)}\right)\left(-i\frac{\delta}{\delta J(y)}\right) Z[J]\right]_{J=0}. \tag{2.3}$$

The probability for a scattering process where "in" states $\mathcal{A}$ and $\mathcal{B}$ are prepared, interact, and lead to "out" states $1, 2, \ldots, n$ at a much later time is given by

$$|_{\text{out}}\langle\psi_1, \ldots, \psi_n|\psi_\mathcal{A}, \psi_\mathcal{B}\rangle_{\text{in}}|^2 = |\langle\psi_1, \ldots, \psi_n|S|\psi_\mathcal{A}, \psi_\mathcal{B}\rangle|^2, \tag{2.4}$$

where S (the "S-matrix") is the unitary operator relating the corresponding equal-time states. This can be composed into interacting and non-interacting parts $S = 1 + iT$ for physical states, with the interesting physics encoded in the matrix element $\mathcal{M}$ defined by

$$\langle \psi_1, \ldots, \psi_n | iT | \psi_\mathcal{A}, \psi_\mathcal{B} \rangle = (2\pi)^4 \delta^{(4)}(k_\mathcal{A} + k_\mathcal{B} - \sum_{f=1}^{n} p_f) \mathcal{M}(k_\mathcal{A}, k_\mathcal{A}, p_f), \tag{2.5}$$

where momentum conservation terms have been factored out. Matrix elements immediately allow one to calculate decays rates for $1 \to n$ processes

$$d\Gamma(\mathcal{A} \to 1, \ldots) = \frac{1}{m_\mathcal{A}} \left(\prod_{f=1,\ldots} \frac{d^3 p_f}{(2\pi)^3} \frac{1}{2E_f} \right) |\mathcal{M}|^2 \tag{2.6}$$

and cross sections for $2 \to n$ processes

$$d\sigma(\mathcal{A}, \mathcal{B} \to 1, \ldots) = \frac{1}{4E_\mathcal{A} E_\mathcal{B} |v_\mathcal{A} - v_\mathcal{B}|} \left(\prod_{f=1,\ldots} \frac{d^3 p_f}{(2\pi)^3} \frac{1}{2E_f} \right) |\mathcal{M}|^2. \tag{2.7}$$

While exact expressions for matrix elements (MEs) are generally not easily calculable, weakly-coupled theories admit the use of perturbative techniques. Here the full process may be organized through the use of Feynman diagrams, each representing a contribution proportional to some fixed power of the relevant coupling constant. For calculations of LHC interactions stemming from the SM gauge groups, perturbation theory is a powerful tool with a wide range of applicability to be discussed further in the following sections.

2.2 The Standard Model

The gauge structure of the SM is given by the product of symmetry groups U(1) × SU(2) × SU(3). This leads to gauge fields associated with each symmetry: B denotes the U(1) field quanta, W^a the triplet associated with SU(2), and G^a the eight gluons in correspondence with the generators of SU(3). However, the Lagrangian described in the previous section did not include particle masses, which do not respect gauge-invariance.

Particle masses are incorporated via the Higgs mechanism [17–20], which augments the electroweak sector with an additional complex scalar SU(2) doublet ϕ with Lagrangian

$$\mathcal{L} = (D_\mu \phi)^2 - m^2 \phi^2 - \frac{\lambda}{4} \phi^4 \tag{2.8}$$

In the case where the m^2 parameter is negative, ϕ acquires a vacuum expectation value (VEV) and the field may be written $\phi = \binom{0}{v+h}$, re-expressed about the new perturbative minimum v as h.

Obscuring the rotational symmetry of the initial Lagrangian, it may be expressed in terms of the physical Higgs state as

$$\mathcal{L}_{\text{broken}} = (D_\mu \phi)^2 + \frac{1}{2}m_h^2 h^2 + \sqrt{\frac{\lambda}{2}} m_h h^3 + \frac{1}{4}\lambda h^4, \tag{2.9}$$

where the Higgs boson mass has been substituted. The remaining three degrees of freedom of the SU(2) doublet give rise to Goldstone bosons, which are observed in the physical theory as SU(2) gauge boson masses. After electroweak symmetry breaking, the neutral components of the B and W^0 mix to produce the massless photon γ as well as the massive Z^0 boson. The masses of the Z^0 and $W^\pm$ bosons are proportional to the Higgs VEV, with constants of proportionality given by the SU(2) gauge coupling and electroweak mixing angle.

The fermionic content of the SM consists of quarks, which are charged under the SU(3) color force, and the leptons, which are not. The left-handed quarks are arranged into SU(2) doublets consisting of an up- and down-type component with electromagnetic charges +2/3 and -1/3, respectively. The right-handed quarks are SU(2) singlets, but are otherwise identical. There is also a left-handed SU(2) lepton doublet, with charged ("electron"-type) and neutral ("neutrino"-type) components. The charged leptons have right-handed, SU(2) singlet partners, while the neutral leptons do not. If present in the theory, right-handed neutrinos would be singlets under all SM gauge groups.

The Higgs mechanism also provides fermion masses through Yukawa interactions of the form

$$\mathcal{L}_{\text{Yukawa}} = -\lambda_\psi(\bar{\psi}_L \phi \psi_R + \psi_L \phi \bar{\psi}_R) \tag{2.10}$$

$$\rightarrow -\frac{\lambda_\psi v}{2}(\bar{\psi}_L \psi_R + \psi_L \bar{\psi}_R) \tag{2.11}$$

that mixes left- and right-handed states and leads to a mass term $\lambda_\psi v/2$ proportional to the Yukawa coupling and Higgs VEV. Thus, the only dimensionful parameter in the SM is the Higgs boson VEV, with fermion masses all originating from their distinct Yukawa couplings and vector boson masses set by the gauge couplings.

2.3 Calculations for Colliders

The elegant gauge structure of the SM may seem deceptively simple, given the diverse landscape of phenomena that arises from its structure. This complexity is realized in SM calculations of collider phenomena, which may require descriptions of all forces across a variety of scales. While the LHC accelerates beams of protons, the particles which take place in the high-energy interactions are instead their quark and gluon constituents. The master equation describing cross sections of pp

collision processes is

$$\sigma(pp \to X) = \int_0^1 dx_1 \int_0^1 dx_2 \sum_a \sum_b f_a(x_1) f_b(x_2) \sigma(ab \to X). \tag{2.12}$$

Here, $f_a(x)$ is the parton distribution function (PDF), which gives the probability to find a parton $a = g, u, \bar{u}, d \ldots$ with a fraction x of the original proton's momentum. Tis effectively decouples the non-perturbative physics within the proton from the large-Q^2 calculation of parton interactions using the perturbative machinery of Feynman diagrams discussed in Sec. 2.1. However, the picture becomes further complicated when considering the possible outcomes of the $ab \to X$ reaction, which will necessarily include final states with (color-charged) partons. The evolution of high-energy partons to showers of low energy hadrons must also be accurately described to produce precise calculations of LHC processes.

Parton distribution functions

The PDFs f_a introduced above parameterize the probability to extract a parton of species a from the proton. This depends on the fraction x of the momentum of the initial proton carried off by the outgoing parton, and also weakly on the scale Q^2 of the hard process. The logarithmic dependence of f_a on the scale choice is parameterized by the DGLAP equations [21–23]. These describe the evolution of the parton splitting functions $P_{ab}(z, \alpha_S)$, which give the probabilities to find a parton of species a within one of species b, with a fraction z of the initial parton momentum. This dependence can thus be calculated perturbatively as a power series in $\alpha_S(Q^2)$, leading to leading order (LO) and next-to-leading order (NLO) PDFs, to match the accuracy of the calculation of the partonic matrix element $\sigma(ab \to X)$. In practice, the effect of higher-order corrections to Equation 2.12 due to the PDF dependence is larger than the ME, so that it is generally recommended to take advantage of higher-order determinations of the PDF even if the corresponding ME calculation is not available.

On the other hand, the variation of each PDF with x cannot be calculated with perturbative techniques and must be obtained directly from experimental data. The low-x region is covered by electron-proton collision measurements at HERA, with fixed-target experiments measuring deep inelastic scattering (DIS) and Drell-Yan production contribute at larger x. Collider measurements from the Tevatron and LHC also provide constraints, giving the largest impact on the gluon PDF at high x. The coverage of the $x - Q^2$ plane by measurements included in a modern fit by the NNPDF Collaboration [24] is shown in Figure 2.2. Similar fits are provided by other collaborations, such as CTEQ [25] and MSTW [26], with varying fit techniques and assumptions. The reader is referred to the specific combination papers for references to the particular data sets used in each of the fits.

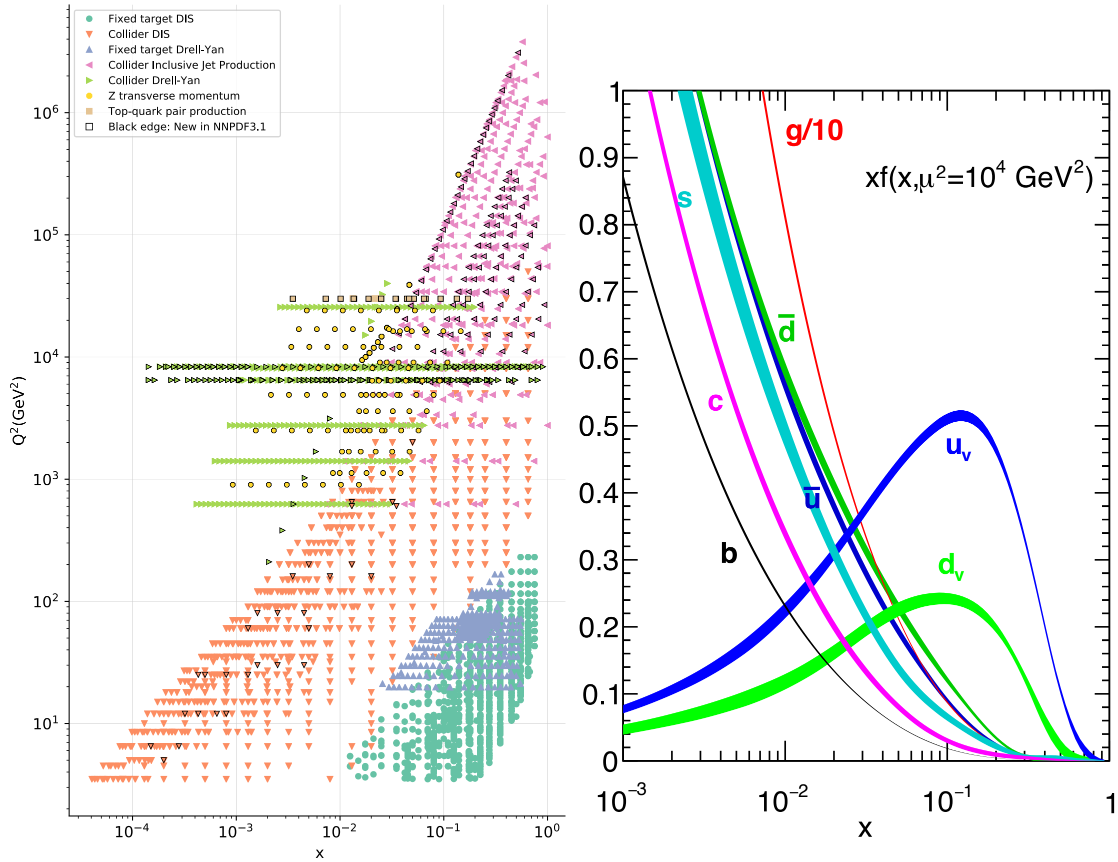

Figure 2.2: At left, the coverage of the $x - Q^2$ plane by the experimental data sets used in the `NNPDF3.1_nnlo` PDF set is shown. At right, the resulting values of the PDF $xf_a(x)$ are shown for $Q^2 = 10^4\,\text{GeV}^2$. Figures are reproduced from Ref. [24].

The vast experimental data sets available call for a complex fitting mechanism that may be used to derive a unified model of the PDFs across a wide range of phase space. The basic model is a fit of the form $f(x) = c_0 x^{c_1}(1-x)^{c_2} \cdot F(c_3, \ldots)$ with separate power-law coefficients c_1 and c_2 capturing the asymptotic behavior at low- and high-x and an empirically-determined smooth function F chosen to enhance the quality of the fit. Uncertainties on each of the fitted parameters are obtained and reduced to a set of eigenvectors encapsulating the most significant variations. In this manner, LHC analyses making use of PDF inputs may be repeated with eigen-varied sets to capture the effect of the fit uncertainty on the analysis. Finally, each PDF set is generally defined with a reference value of α_S set at the Z boson mass. Extractions of the fit parameters under varied values of the strong coupling constant may also be propagated into an uncertainty on the resulting PDF set.

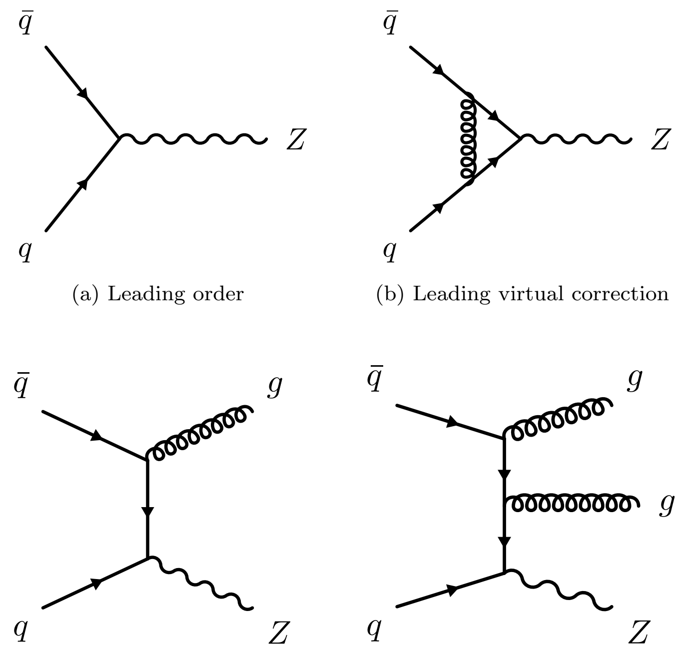

(a) Leading order (b) Leading virtual correction

(c) Leading real correction (d) Next-to-leading real correction

Figure 2.3: A collection of Feynman diagrams for the $Z+$ jets process, initiated by quark-anti-quark fusion. At top left, the leading order diagram is shown, which is independent of the strong coupling constant. At top right, the leading virtual correction is shown, modifying the $q\bar{q}Z$ vertex, proportional to α_S^2. At bottom left example (right) diagrams corresponding to (next-to-)leading real emissions are shown, proportional to α_S (α_S^2).

Perturbative expansions

At energy scales much larger than Λ_{QCD}, the strong coupling constant is sufficiently small to enable precise perturbative calculations of LHC processes. This enables the machinery of Feynman diagrams to be used, with several example representations shown in Figure 2.3 for the Z+jets process. At zero-th order, the Z is produced without any jets and thus had no momentum in the direction transverse to the collision axis. Higher-order calculations include additional real emissions (Figures 2.3c and 2.3d) as well as virtual corrections, canceling infrared and colinear divergences at each order in α_S. While higher order terms in α_S generally yield the most important corrections, higher-order electroweak corrections can also become necessary for very precise measurements.

The value of α_S included in these perturbative calculations must be defined at a fixed scale μ_R. In an all-orders calculation the dependence of the final result on μ_R would vanish, but including only the first k terms in the expansion leaves a dependence of order α_S^{k+1}. While one often can choose μ_R equal to the natural scale of the hard process (e.g. m_Z in $Z+$jets production) the choice is subjective and can be ambiguous (one might reasonably replace $m_Z \to \sqrt{m_Z^2 + p_{\mathrm{T}}^2}$). Variations in the choice of this scale, often by a factor of two in each direction, are traditionally used to parameterize the uncertainty due to missing higher-order terms in the calculation, and are indeed reduced as additional terms in the calculation are included. However, it should be cautioned that historically the uncertainty bands from such scale variations have often failed to cover the true higher-order cross section once its calculation has been completed. As such, these uncertainties should be interpreted with care and require dedicated study when important for an experimental measurement.

For the simplest processes, the relevant MEs can be calculated analytically. However, the advent of automated calculational tools (such as `Madgraph`) has improved the ability to easily perform numeric calculation for a large range of processes. This also presents the opportunity to generate simulated 'events' which, when integrated over, may be used to estimate observables based on the kinematic configuration of the outgoing participants in the hard process. Similar automatic calculations of NLO processes have also recently become possible [27].

Parton Evolution

The high-energy processes calculated at fixed order in α_{S} do not generally allow for useful comparisons with LHC data, as the bare partons of Figure 2.3d, for example, are never observed. Due to the confining property of the strong force, quarks and gluons iteratively fragment (according to the splitting functions $P_{ab}(z, \alpha_{\mathrm{S}})$ referenced above) before hadronizing into ultimate color-neutral observed particles. Parton shower MC programs provide a useful description of this regime, relating the high-energy partons described by the ME calculation to a collection of low-energy partons near Λ_{QCD}. This is done by considering Sudakov suppression factors, which give the probability for a high-energy parton to evolve to a lower scale without some fixed-energy gluon emission. For in-going partons, this allows the relation of the hard-scale to the lower cutoff scale through products of Sudakovs and the parton distribution functions. Splitting of the outgoing partons is considered according to an evolution variable (with transverse momentum $k_\perp$- and angular-ordered showers most commonly used, namely by the `PYTHIA` [28, 29] and `HERWIG` [30] shower programs, respectively) that is randomly selected along with the relative fraction of energy, angular separation of the products, and species of the daughter partons. Once all partons have reached a scale near Λ_{QCD} a universal hadronization model groups the particles into ultimate, color-neutral states. As these describe non-perturbative physics, heuristic models must be tuned with experimental data to reproduce observed phenomena. By design, parton shower calculations are accurate to leading logarithm (LL), as colinear contributions are resummed to all orders, leading to n-leg corrections of the form $\alpha_S^n \log^n(Q^2/\Lambda_{QCD})$.

The transition between phase space described by perturbative calculations and by the PDFs is set by the *factorization scale* μ_f. This is the scale discussed above that explicitly enters the PDF in the factorization equation (2.12) as well as defining a cutoff for the integration of the ME. The value of μ_f is typically set in the same manner as μ_R, at some scale inherent to the process under study. Variations about the central value are used to assess an uncertainty accounting for missing higher-order terms in the calculation.

Combined Techniques

At the LHC, the proton-proton initial state and relatively high probabilities for the emission of additional colored particles make higher-order calculations a necessity. At present, cross sections for physical processes of interest have generally all been calculated at full NLO, with the inclusive cross section for some benchmark processes calculated to next-to-next-to-leading order (NNLO) or higher (W/Z+jets [31,32] and $t\bar{t}$ [33]). Dedicated calculations of differential distributions at higher orders have been accomplished, such as the p_T spectrum of the recently-discovered Higgs boson [31,34,35]. Arbitrary observables may be calculated for most processes at NLO with the use of automated MC techniques.

LO matrix element calculations may be combined with a parton shower (PS) to produce particle-level predictions of collider events. However, achieving improved accuracy introduces a series of new challenges, stemming from the division of the phase-space to be calculated between the PS and ME calculations of various orders. LO+PS calculations can be improved by separately performing LO calculations for multiple emissions, each corresponding to the hard process in association with $1, \ldots, N$ jets. These calculations may then be *merged* together so that the most accurate calculation is used in each region of phase space. A variety of methods exist for doing so (MLM [36], CKKW [37], CKKW-L [38]), with the general idea being that the ME calculations are combined according to their respective cross sections and used to populate only the non-colinear regime (omitting configurations where two partons have virtuality $Q^2_{\text{hard}} < Q^2_{\text{cut}}$). The parton shower may then be used to re-weight the value of α_S used in hard process (accounting for evolution), reject events failing a Sudakov criterion, and shower the remaining configurations. The choice of cutoff scale Q^2_{cut} is often set near

20 GeV for typical LHC processes and may be reconfigured to assess the corresponding uncertainties related to this selection in a similar manner to μ_R and μ_f.

A similar problem is encountered with NLO ME calculations, where care must be taken to properly treat the overlapping phase space between the parton shower and real emissions. The `MC@NLO` subtraction scheme [39] presents one possible solution to the problem of canceling divergences from real and virtual corrections, where MC subtraction terms are crafted to remove the diverging phase-space from the calculation. This is done in an approximate manner, with the re-shuffled momenta from the parton shower MC utilized everywhere in the calculation. This scheme has been implemented in numerous MC programs (e.g. `Madgraph5_aMC@NLO` and `SHERPA` [40]) along with a variation that avoids the production of negative-weight events by never using the parton shower to generate leading emissions (`POWHEG` [41]).

For calculations where decays of intermediate particles are treated in the ME calculation, this NLO interface with the parton shower can become problematic. This is because the momentum-shuffled kinematic configuration necessitated by the subtraction terms need not preserve the resonance history. This can be particularly important for unstable, colored resonances (i.e. the top quark), and is addressed in a recent improvement to the `POWHEG BOX` framework for automatic calculation of NLO processes (`POWHEG BOX RES`) [42].

2.4 Problems with the Standard Model

For all of its predictive power and successful validation against experimental data, the SM is not without problems. The theory cannot account for a number of important findings, such as the observation that luminous matter (made of electromagnetically interacting particles) accounts for only about 20% of the observed matter in the universe. The remaining "dark matter" is not explained by the SM, suggesting that some improvement to the theory is needed. Neutrino masses, proven to be non-zero by observations of flavor oscillations are also not included in the SM. Finally, the SM is clearly incomplete, as it does not incorporate a quantum description of the fourth fundamental force: gravity.

Dark Matter

The earliest evidence for dark matter (DM) comes from the observation that the rotation of objects within galaxies proceeds more quickly than expected from the luminous matter distributions at their center. The near-constant velocities at large radii could be explained by an additional, diffuse matter component that forms a 'halo' about the galaxies, affecting the trajectories of objects in orbit. Further evidence comes from the observation of very old galaxies, whose formation is predicated on the presence of an additional matter component that would lead to earlier structure formation in the early universe than would otherwise occur. Observations of colliding clusters of galaxies (most famously the "Bullet Cluster") present further evidence of the additional matter component, as the luminous and total matter populations may be separately inferred by a combination of x-ray and weak gravitational lensing measurements. While the visible matter of each cluster violently interacted and slowed, the total matter population of each system proceeded on a minimally-disturbed trajectory.

The current picture of the SM plus gravity presents no satisfying dark matter candidate. At first consideration the SM neutrinos are an attractive candidate, but their masses are much too small to satisfy the measured DM density. Primordial black holes (with comparatively light masses due to their formation in the very early universe) have also gained attention as a candidate that requires no additional particle content to supplement the SM [43–45]. However, the space of allowed black hole masses is tightly constrained by existing astrophysical measurements, with little to none remaining if the relic density is to be satisfied [46].

The space of non-SM particle DM candidates is extraordinarily large, encompassing a wide range of particle masses and interaction strengths. Theories range from minimal additions to the SM (such as axions [47, 48]) to entirely new sectors of particles and interactions. The weakly-interacting massive particle (WIMP) miracle provides one of the oldest and most compelling motivations to search for a particle DM candidate at the LHC. This is the observation that a new particle with weak-scale mass and weak coupling constant reproduces the correct DM relic density. Under the assumption that the DM particles are initially in thermal equilibrium with the SM particles, the WIMP freeze-out would occur when the SM-DM interaction rate becomes smaller than the expansion rate of the universe. This motivates searches for new weakly-interacting particles in the mass range probed by the LHC.

The Hierarchy Problem

The term in the SM Lagrangian corresponding to a particle's mass is computed from its two-point correlation function. The Higgs boson has a tree-level contribution from its own bare mass parameter $m_{h\ (\mathrm{tree})}$, in addition to loop corrections δm_h^2 entering due to its interactions with the other SM particles

$$m^2_{h\text{ (physical)}} = m^2_{h\text{ (tree)}} + \delta m^2_h. \tag{2.13}$$

Together these contributions must reproduce the observed Higgs boson mass $m^2_{h\text{ (physical)}}$. At one loop, the largest corrections are due to top quark-, W boson-, and Higgs self-interactions. Choosing a regularization scheme where the SM theory is assumed valid up to some cutoff scale $\Lambda \gg v_h$, the largest correction to the Higgs mass, due to the top quark, is

$$\delta m^2_h = -\frac{3}{8\pi^2} y_t^2 \Lambda^2 \sim -2 \left(\frac{\Lambda}{\text{TeV}}\right)^2 (125\text{ GeV})^2. \tag{2.14}$$

Neglecting sub-dominant corrections, this term must balance the bare mass in order to obtain the physical Higgs mass of 125 GeV. If the scale where new physics must be considered is just beyond the reach of the LHC (Λ =10 TeV) the bare mass must cancel the large correction to one part in 200. This can be seen by substituting into Equation 2.13, which becomes

$$(125\text{ GeV})^2 = m^2_{h\text{ (tree)}} - 200 \cdot (125\text{ GeV})^2 \tag{2.15}$$

$$\Rightarrow m^2_{h\text{ (tree)}} = (200+1)(125\text{ GeV})^2. \tag{2.16}$$

For a Planck scale ($\sim 10^{16}$ TeV) cutoff, the cancellation becomes one part in 10^{32}.

This sensitivity of the Higgs mass to large quantum corrections from to new degrees of freedom in the theory leads to the *hierarchy problem*. The options presented by this puzzle are that either (a) there is new physics (NP) that modifies this picture not much heavier than the electroweak scale, or (b) $\lambda_{\text{NP}}/m_h \gg 1$ but there exists some *unnatural* correlation between the physics at these far-separated scales, producing a cancellation that allows for light scalar masses.

Hints of new scales?

Confronted with the deficiencies of the SM, one must consider what other clues exist as to the nature of BSM extensions. While the SM delivers precisely-measured predictions at mass scales up to several TeV, certainly it must break down below the gravitational scale $M_{\text{Planck}} \sim 10^{19}$ GeV.

It is possible that the observed neutrino mass differences provide another indication, under the supposition that they are generated from a seesaw mechanism. In such a scenario, the neutrino sector contains large Majorana masses M_{maj} as well as electroweak-scale Dirac masses, giving rise to states of mass M_{maj} and $O(m_Z^2/M_{\text{maj}})$. For eV-mass neutrinos, this indicates $M_{\text{maj}} \sim 10^{11}$ GeV.

Finally, the running of the SM gauge couplings causes them to evolve in a common direction at very large energies. The unification of all three couplings is not exact in the SM, with α_{EM} and g_2

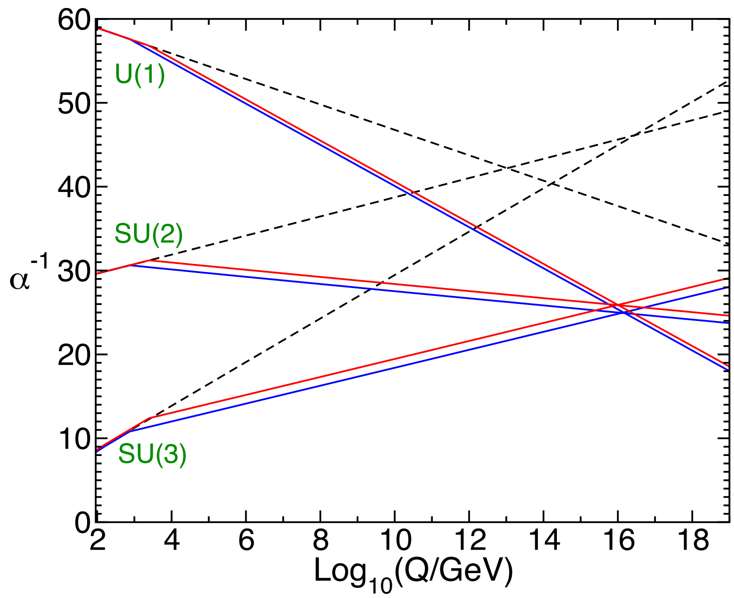

Figure 2.4: The value of the three gauge couplings of the SM as a function of the energy scale. The running is shown with SM (dashed lines) and supersymmetric (solid lines) scenarios in the Minimal Supersymmetric extension of the Standard Model (MSSM), with blue and red variations indicating different choices of common sparticle mass scale.

meeting at $\sim 10^{12}$ GeV and subsequently diverging before α_{S} becomes sufficiently feeble. Adding additional fields to the SM at relatively low energies can alter the RG trajectories so that all three couplings become equal at a common *unification scale*. Such behavior would naturally fall out of a larger theory where the more fundamental symmetry group is broken into the observed SM factors. The SM scenario is shown in Figure 2.4, as well as modifications induced by a BSM extension with TeV-scale supersymmetric particles.

Chapter 3

Supersymmetry

3.1 Structure of the theory

Supersymmetry (SUSY) is a proposed symmetry of space-time relating fermions and bosons to one another. It hypothesizes that each of the observed SM particles belongs to a super-multiplet, transforming under the symmetry along with a (yet-unobserved) super-partner particle. Thus *sparticle* partners are predicted for each of the existing SM particles, with masses set by SUSY-breaking parameters.

Supersymmetric theories are attractive candidates to extend the SM for three main reasons. First, they offer the possibility of a natural dark matter candidate. In models where R-parity is conserved, the LSP is a stable particle, forbidden to decay back to any SM particle. An LSP with mass near the electroweak scale could present an excellent WIMP candidate, compatible with the observed dark matter relic abundance. Second, the quadratic divergence of the Higgs mass described in Section 2.4 is canceled by opposing contributions from the new super-partner particles. In particular, the largest SM correction, proportional to the top-quark Yukawa, is canceled by that of the supersymmetric partner of the top quark: the top squark or 'stop'. Finally, the additional "light" particle content modifies the β-functions of the SM gauge couplings in such a manner that the unification is achieved, near 10^{16} GeV.

Formally, supersymmetric theories can be obtained by embedding the SM Lagrangian into super-space, parameterized by the usual spacetime coordinate x^μ in addition to complex anti-commuting spinors θ^α and $\theta^\dagger_{\dot\alpha}$. One may define new differential operators D_α including these Grassman coordinates that are SUSY covariant, and in doing so find that SUSY transformations are equivalent to translations in super-space. Standard fields $\phi(x^\mu)$ are upgraded to super-fields $\Phi(x^\mu, \theta^\alpha, \theta^\dagger_{\dot\alpha})$, with both chiral and vector super-fields necessary to encapsulate the particle content of the SM. This can be seen by expanding super-fields in the Grassman coordinate, which leads to an (exactly) finite series of terms due to the anti-commuting property of these variables. Imposing the condition $D_\alpha \Phi = 0$ leads to the constraints among the superfield components resulting in four degrees of freedom for Φ, corresponding to a complex scalar and two-component fermion. These can be associated with a SM fermion and a new scalar partner, for example the top quark and the stop. Imposing instead the vector criterion $V = V^*$ leads to a field with vector boson and fermion components, for example the SM B^μ field and Bino neutralino. Finally the machinery of SM gauge symmetries can be extended to super-fields in a natural way, with vector super-fields corresponding to each generator of the gauge groups and field strength tensors similarly defined. From these ingredients, one can build SUSY-invariant Lagrangians, extending the SM.

3.2 The Minimal Supersymmetric Standard Model

The Minimal Supersymmetric extension of the Standard Model (MSSM) is obtained by elevating the SM matter and gauge fields to super-fields and extending the Higgs mechanism. As hinted at in the previous section, the gives a pair of super-partner bosons corresponding to each of the SM quarks and leptons (*squarks* and *sleptons*). The gauge vector fields are similarly extended to include fermion *gauginos* inheriting similar gauge interactions as the SM bosons. The Higgs SU(2) doublet of the SM must however be extended to a Higgs sector, including both “up-type” and “down-type” complex scalar pairs. This is because the naïve addition to the MSSM Lagrangian involving a single Higgs superfield and its complex conjugate does not respect supersymmetry, so that separate fields are required to give masses to the up- and down-type particles. Table 3.1 summarizes the resulting super-field content of the MSSM.

The Lagrangian of the MSSM consists of a Higgs super-potential added to the chiral and vector field kinematic terms. The super-potential consists of Yukawa couplings to the quarks and leptons as well as the “mu term” responsible for electroweak symmetry breaking

$$\mathcal{W} = \bar{u} y_u Q H_u - \bar{d} y_d Q H_d - \bar{e} y_e L H_d + \mu H_u H_d, \tag{3.1}$$

where super-fields X^S are written X and all suppressed indices are summed over. Here Yukawa couplings are represented as matrices in generation-space so that information on particle masses as well as mixing matrices (i.e. CKM) are encoded. In addition to providing particle masses, these terms are responsible for mediating the $t\bar{t}h$ interaction, stop decays via the $t\tilde{t}\tilde{h}$ vertex, and stop self-interactions. Each process is governed by the universal top Yukawa coupling, a fact critical to the cancellations providing the SUSY solution of the hierarchy problem.

Each Higgs doublet separately attains a vacuum expectation value, denoted v_u and v_d, which are usually re-expressed as the ratio of the two values $\tan\beta = v_u/v_d$ constrained by the measured value of $v_{\mathrm{SM}}^2 = v_u^2 + v_d^2$. Similar to the SM case, the Goldstone degrees of freedom give rise to gauge boson masses with those remaining leading to physical Higgs bosons. However, the two complex SU(2) doublets correspond to eight degrees of freedom, leading to five new massive scalar bosons. These are two charged Higgs $H^{\pm}$, two scalars h^0 and H^0 (with h^0 the lighter of the two, most often assumed to be the SM Higgs boson), and a pseudoscalar A^0. The relation between the parameters of the Lagrangian and the physical masses may be found in Ref [49].

The remaining interactions added to the theory by enforcing SUSY are each proportional to the SM gauge couplings. For example, gluinos may be directly produced via the $gg\tilde{g}\tilde{g}$ coupling arising from kinetic QCD terms. Color factors associated with such vertices lead to large $pp \to \tilde{g}\tilde{g}^*$[1] cross sections, making these sparticles early targets of new, record-energy particle colliders. Kinetic terms for the chiral quark multiplets lead to $t\tilde{t}\tilde{g}$ vertices (and similar) allowing gluinos to decay. The structure of the interactions of the electroweak bosons and their superpartners is similar, with

Table 3.1: The super-field content of the MSSM. All but generational indices are suppressed.

Type	Super-field	Particle content	Sparticle content
Chiral	Q_i^S	LH up-, down-type quarks (e.g. t_L, b_L)	LH up-, down-type squarks (e.g. $\tilde{t}_L, \tilde{b}_L$)
	u_i^S	RH up-type quarks (e.g. t_R)	RH up-type squarks (e.g. $\tilde{t}_R$)
	d_i^S	RH down-type quarks (e.g. b_R)	RH down-type squarks (e.g. $\tilde{b}_R$)
	L_i^S	LH charged and neutral leptons (e.g. τ_L, ν_L^τ)	LH charged and neutral sleptons (e.g. $\tilde{\tau}_L, \tilde{\nu}_L^\tau$)
	e_i^S	RH charged leptons (e.g. τ_R)	RH charged sleptons (e.g. $\tilde{\tau}_R$)
	H_u^S	Charged, neutral up-type Higgs (h_u^0, h_u^+)	Charged, neutral up-type Higgsinos $(\tilde{h}_u^0, \tilde{h}_u^+)$
	H_d^S	Charged, neutral down-type Higgs (h_d^0, h_d^-)	Charged, neutral down-type Higgsinos $(\tilde{h}_d^0, \tilde{h}_d^-)$
Vector	g^S	Gluons g	Gluinos $\tilde{g}$
	W^S	W bosons W^0, $W^{\pm}$	Winos $\tilde{W}^0$, $\tilde{W}^{\pm}$
	B^S	B boson B^0	Bino $\tilde{B}^0$

[1] In this document SUSY anti-particles will be denoted $\tilde{s}^*$ in place of the usual $\bar{\tilde{s}}$ convention to achieve more compact notation.

the complete set obtained from the SM gauge vertices, exchanging pairs of SM particles with their supersymmetric partners.

However, as SUSY is apparently not perfectly realized in nature, the completely supersymmetric Lagrangian must be augmented by SUSY-breaking terms. In order to not re-introduce similar problems to the ones that we have previously advertised SUSY as solving, only a subset of terms are considered, which break SUSY *softly* (do not introduce new quadratic divergences). The possible soft breaking terms include gaugino and scalar mass terms as well as (dimensionful) scalar trilinear self-couplings. Such soft-breaking parameters cannot be too close to the electroweak scale in order to evade experimental limits from a wide array of sparticle searches. However, pushing the the soft masses to too high a scale would produce a new hierarchy problem (the addition of soft stop mass produces a correction $\delta m_h^2 \sim y_t^2 m_{\tilde{t}}^2$), motivating soft masses not far beyond the TeV-scale.

With the introduction of soft masses, the spectra of physical sparticle masses becomes more complicated, with the dependence on various parameters of the theory encoded in the mass matrices. In the case of top squarks, the is given by [50]:

$$M_{\tilde{t}} = \begin{pmatrix} m_{\tilde{t}_L}^2 + m_t^2 + \left(\frac{1}{2} - \frac{2}{3}\sin\theta_W^2\right) m_Z^2 \cos 2\beta & m_t(A_t - \mu/\tan\beta) \\ m_t(A_t - \mu/\tan\beta) & m_{\tilde{t}_R}^2 + m_t^2 + \frac{2}{3}\sin\theta_W^2 m_Z^2 \cos 2\beta \end{pmatrix} \tag{3.2}$$

in the basis of chiral states. Here $m_{\tilde{t}_L}$ and $m_{\tilde{t}_R}$ are the soft masses and A_t is the stop trilinear coupling. Similar relations hold for the remaining fermions and can be simplified by neglecting first- and second-generation Yukawa couplings.

The case of neutralinos and charginos (often *electroweakinos*) is similarly complex, with mixing among each of the Bino, Wino, and Higgsino states. The neutralino mass matrix is

$$M_{\chi^0} = \begin{pmatrix} M_1 & 0 & -\cos\beta\sin\theta_W m_Z & \sin\beta\sin\theta_W m_Z \\ 0 & M_2 & \cos\beta\cos\theta_W m_Z & -\sin\beta\cos\theta_W m_Z \\ -\cos\beta\sin\theta_W m_Z & \cos\beta\cos\theta_W m_Z & 0 & -\mu \\ \sin\beta\sin\theta_W m_Z & -\sin\beta\cos\theta_W m_Z & -\mu & 0 \end{pmatrix} \tag{3.3}$$

and the chargino matrix is more easily diagonalized to give eigenvalues [49]

$$m_{\chi_{1,2}^\pm}^2 = \frac{1}{2}\left[|M_2|^2 + |\mu|^2 + 2m_W^2 \mp \sqrt{(|M_2|^2 + |\mu|^2 + 2m_W^2)^2 - 4|\mu M_2 - m_W^2 \sin 2\beta|^2}\right]. \tag{3.4}$$

In the decoupling limit, the neutralino mass matrix M_{χ^0} describes four mass eigenstates specified by three mass parameters. The Bino-like state and Wino-like states are controlled by M_1 and M_2, respectively, while two near-degenerate Higgsino-like states have masses near μ. In the case of a

Higgsino LSP where $m_Z \ll \mu \ll M_1, M_2$, the mass of these states may be approximated as

$$m_{\tilde{H}^0_{1,2}} = |\mu| + \frac{m_Z^2(\text{sgn}(\mu) \mp \sin 2\beta)(\mu \pm M_1 \cos^2\theta_W \pm M_2 \sin^2\theta_W)}{2(\mu \pm M_1)(\mu \pm M_2)}. \quad (3.5)$$

This leads to the interesting prediction of two new neutral states with

$$\Delta M \approx \frac{m_W^2 \tan^2\theta_W(\pm|\mu| \sin 2\beta + M_1)}{(M_1^2 - |\mu|^2)}, \quad (3.6)$$

along with an intermediate charged state (with mass given by Equation 3.4) [51].

While the MSSM provides a rich framework to understand the signatures of SUSY that one might expect to observe near the electroweak scale, in practice experimental results are not often interpreted using this model. One the one hand, the MSSM Lagrangian contains many free parameters that have already been tightly constrained by low-energy physics. For example, off-diagonal mass terms relating the first two generations could lead to appreciable $\mu \to e\gamma$ rates in the lepton sector and $K^0 - \bar{K}^0$ mixing in the quark sector. Given these bounds and the relative lack of sensitivity to the remaining phase space at high-energy colliders, it is reasonable to make simplifying assumptions when interpreting LHC results. On the other hand there is motivation to go beyond the MSSM, adding new Lagrangian terms that may result from explicit manifestations of SUSY-breaking, explain the neutrino mass hierarchy, and solve further theoretical problems. Both approaches will be explored in the following sections.

3.3 Simplifying Assumptions for Experiments

The MSSM contains such a strikingly large number of free parameters (105) that it is often useful to make simplifying assumptions which restrict the phase space to become more manageable. The strategy allows experiments to more efficiently explore the region of interesting model space predicted by the full theory, while retaining dependence on only the most important physical parameters which might impact the signature of BSM physics, at a collider for example. Of course, different sets of parameters may be relevant for different experiments and so it can still be very useful to consider the full model space when combining results across different experiments (e.g. B physics, direct DM detection experiments, and collider searches).

A classic example of a reduced version of the MSSM is minimal Supergravity (mSUGRA), in which only five free parameters describe the low-energy physics of a UV-complete theory. In this theory of gravity-mediated SUSY breaking, common mass terms are given to all scalar (m_0) and spin-1/2 ($m_{1/2}$) sparticles, as well as a common trilinear coupling A_0. The ratio of Higgs vacuum expectations values $\tan\beta$ and the sign of the Higgs mass parameter μ makeup the remaining free parameters. For a length of time leading to the development of the LHC as well as predecessor colliders, points in mSUGRA model space were used to develop benchmark scenarios for how we might discover SUSY at the next machine (see e.g. Ref. [52]). However, in current times the simplicity of mSUGRA has become its downfall. As the LHC continues to publish analyses on the wealth of data collected during Run 1 and Run 2 data-taking periods, a more broader set of models is required to fully encapsulate the diverse collider phenomena predicted by SUSY.

3.3.1 The pMSSM

To reduce the dimensionality of the full space of models allowed in the MSSM, the phenomenological MSSM (pMSSM) is defined. The pMSSM has 19 free parameters in place of 105 and is designed to retain much of the predictive breadth of the MSSM for collider physics with as few free parameters as possible. The assumptions of the pMSSM which allow for such a reduction are [53, 54]:

- *No CP violation*: a significant number of free MSSM parameters are phases which may be set to zero. New sources of CP violation are tightly constrained by measurements of the electron and neutron electric moments.
- *No flavor changing neutral currents*: requires that fermion mass matrices be largely diagonal in flavor-space.
- *First and second generation universality*: soft masses are set equal and trilinear terms are set to zero for the first two generations. Light sfermions without flavor-blind masses are constrained by $K_0 - \bar{K}_0$ mixing.

In general, the neglected terms have no significant effect on the predicted collider phenomenology, so that the pMSSM presents an excellent benchmark for LHC searches. The terms which are retained are the SUSY soft masses, third generation trilinear couplings, and the μ, m_A, and $\tan\beta$ parameters of the Higgs sector.

The set of free parameters of the pMSSM are described in Table 3.2. The left-handed third generation squark mass is sometimes also written as $m_{Q_{3L}}/m_{Q3L}$ for clarity. Physical masses are obtained by diagonalizing the mass matrices as described in Section 3.2, with the top squark matrix given by Equation 3.2. For large stop masses, the values of the sparticle mass parameters $m_{\tilde{Q}}$ and $m_{\tilde{t}_R}$ closely approximate the physical stop masses $m_{\tilde{t}_1}$ and $m_{\tilde{t}_2}$, as shown in Figure 3.1. It can also be convenient to define further combinations of the pMSSM parameters. The geometric mean of the

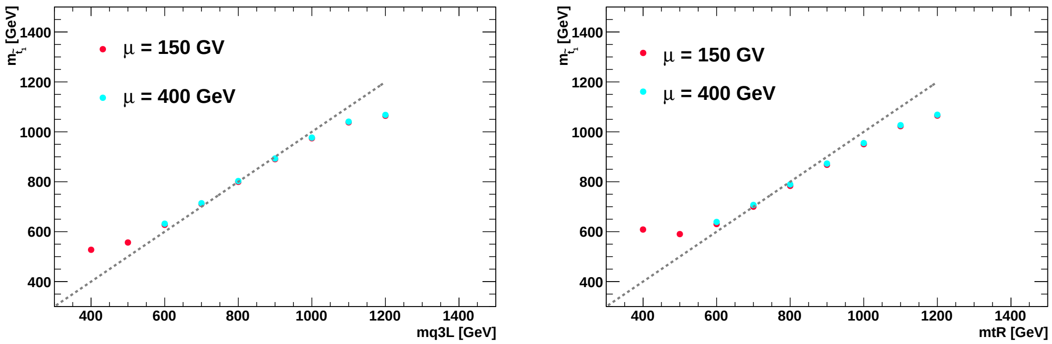

(a) (b)

Figure 3.1: At left, the correspondence is shown between the SUSY mass parameter controlling third generation, left-handed squarks $m_{\tilde{Q}}$ and the mass of the lightest stop. At right, the analogous figure is shown for the right-handed stop mass parameter $m_{\tilde{t}_R}$. In each case, the SUSY breaking scale M_S is set to 1.2 TeV and $\tan\beta = 20$ is assumed.

stop masses is written $M_S = \sqrt{m_{\tilde{t}_1} m_{\tilde{t}_2}}$ and it can be useful to identify this as the SUSY breaking scale if other sparticles are found at higher energies. Corrections to the SM Higgs mass depend on the stop mixing parameter $X_t = A_t - \mu/\tan\beta$, which appears in the off-diagonal terms of the mass matrix. Maximal $\tilde{t}_L - \tilde{t}_R$ mixing is given when $X_t/M_S \sim \sqrt{6}$ and ensures that such corrections to m_h are small.

3.4 Beyond the MSSM

There is a notable absence of several terms from the supersymmetric Lagrangian presented in Section 3.2, each of which are respect SUSY invariance. These are the couplings which violate R-parity

Table 3.2: The free parameters of the pMSSM and their definitions.

Parameter	Description
$\tan\beta$	ratio of the vacuum expectation values of the Higgs field doublets
μ	Higgs mass parameter
m_A	pseudoscalar Higgs mass
M_1, M_2, M_3	Bino, Wino, and Gluino mass parameters
$m_{\tilde{q}}, m_{\tilde{u}_R}, m_{\tilde{d}_R}$	First and second generation squark masses
$m_{\tilde{l}}, m_{\tilde{e}_R}$	First and second generation slepton masses
$m_{\tilde{Q}}, m_{\tilde{t}_R}, m_{\tilde{b}_R}$	Third generation squark masses
$m_{\tilde{L}}, m_{\tilde{\tau}_R}$	Third generation slepton masses
A_t, A_b, A_τ	Third generation trilinear couplings

$R = (-1)^{3(B-L)}$, which takes opposing values for the SM and SUSY particles. In the SM, all interactions separately conserve baryon and lepton numbers so the symmetry follows trivially. The possible new R-parity violation (RPV) terms are

$$\mathcal{L}_{\text{RPV}} = \lambda^{ijk} L_i L_j \bar{e}_k + \lambda'^{ijk} L_i Q_j \bar{d}_k + \mu^i L_i H_u + \lambda''^{ijk} \bar{u}_i \bar{d}_j \bar{d}_k, \tag{3.7}$$

the first of three of which which violate lepton number and the last of which violates baryon number. Here the explicit indices denote the fermion generation $i = 1, 2, 3$, where λ''^{ijk} in particular is constrained to be anti-symmetric in the last two indices. These terms are generally not included in the MSSM, as they can lead to unsavory phenomena. Foremost, R-parity violation in general allows the LSP to decay to lighter SM particles, spoiling its viability as a DM candidate. Second, strict limits have been placed on the product of baryon- and lepton-number violating couplings, most famously by measured lower limits on the lifetime of the proton. Despite this, a wide range of RPV models remain experimentally viable, often with mechanisms proposed to explain the why the RPV couplings should be relatively small.

3.4.1 The $B - L$ MSSM

Following the proposal of string theories as potential UV-completions of the SM, there has been interest in exploring the region of high-scale parameter space which may lead to low-energy conditions consistent with the observed particles and gauge groups. Many such varieties of string phenomenology have been considered, in attempts to map the UV theory involving many extra space-time dimensions and large gauge groups to the MSSM at low energy. The $B - L$ MSSM is such a low-energy model arising from a compactification of $E_8 \times E_8$ heterotic M-theory [55–57]. This consists of the MSSM augmented with chiral multiplets corresponding to right-handed neutrinos, with the $B - L$ symmetry gauged so that another vector multiplet is also produced. The $B - L$ symmetry is assumed to be broken at some intermediate scale when a right-handed sneutrino develops a non-zero VEV; this leads to a mass for the $B - L$ gauge boson. After electroweak symmetry breaking is invoked this also leads to VEVs for the left-handed sneutrinos. This directly leads to RPV terms, specifically those that violate lepton number conservation.

The consequences of this model for LHC-accessible physics have been investigated in a series of results. Scans of model space have been conducted where the parameters of the theory are randomly scattered around an assumed SUSY breaking scale in the range of a few TeV, and RG evolution equations used to predict the resulting physical mass spectrum. Points in model-space that lead to the correct Higgs mass, achieve electroweak symmetry breaking, and satisfy all lower bounds

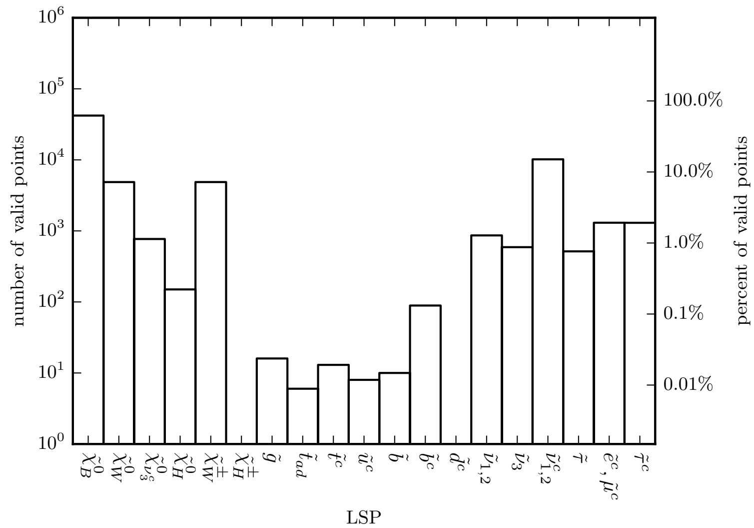

Figure 3.2: A histogram of the relative frequency of different LSPs obtained after a random scan of $B-L$ MSSM SUSY parameters as described in Ref. [58]. A large fraction of simulated models result in an LSP that is a super-partner of one of the electroweak bosons.

on sparticle and Z' masses have been analyzed to determine the distribution of possible LSPs. A representative histogram is reproduced from from Ref. [58] in Figure 3.2, demonstrating the wide range of candidates. As the RPV coupling predicted in the $B-L$ MSSM are generally small, their most significant impact is in allowing the LSP to decay to SM particles, leading to novel collider signatures.

Early searches were conducted for stop LSPs using 8 TeV and 13 TeV data [59,60]. While not the most common LSP in random scans, the large cross section and novel decay signature to charged leptons and b quarks present an attractive experimental candidate. The likelier scenario however, according to Figure 3.2, is that the LSP is one of the neutralino or chargino states. These states may decay to electroweak bosons and leptons, leading to a variety of novel decay signatures not explicitly targeted by past SUSY searches. The phenomenology of such scenarios is presented in Refs. [61] and [11], exploring the case of a Wino-like and Bino-like LSP, respectively. The latter scenario is particularly interesting, as the Bino mass is completely unconstrained by collider searches and may be arbitrarily light. This is fundamentally different than the Wino and Higgsino cases, where limits on new charged particles below ≈ 100 GeV have been established [62]. When the Bino mass is lighter than the W boson, each of the decays $\tilde{B}^0 \to W^{\pm}\ell^{\mp}$, $\tilde{B}^0 \to Z^0\nu$, and $\tilde{B}^0 \to h^0\nu$ are suppressed, as the intermediate bosons are forced off-shell. While in other cases the LSP decays proceed promptly, here the Bino can have a potentially long lifetime before its decay. This could result in a displaced vertex that may be directly reconstructed, a smoking-gun signature of new physics that is not produced by any SM process. Appendix A presents a more detailed analysis of the scenario with a Bino LSP. Appendix B explores how traditional searches for SUSY with stable LSPs may be recast to constrain models with R-parity violation, investigating the case of a Wino LSP in particular.

Chapter 4

Experimental Apparatus

4.1 The Large Hadron Collider

Protons which collide at the interaction point (IP) at the center of the ATLAS experiment are delivered by the Large Hadron Collider (LHC) [63] and supporting injector complex. The LHC was designed with an ultimate energy of 8 TeV per colliding beam, leading to a center-of-mass (CoM) collision energy of $\sqrt{s} = 14\,\text{TeV}$. Protons are grouped into discrete bunches in the injector path, so that ATLAS records events in which multiple proton-proton collisions take place, every 25 ns. Combined with the proton density and beam optics, this leads to a design luminosity for the machine of $10^{34}\,\text{cm}^{-2}\text{s}^{-1}$. As of 2018, collisions up to 13 TeV have been achieved and peak instantaneous luminosities greater than $2 \cdot 10^{34}\,\text{cm}^{-2}\text{s}^{-1}$, corresponding to an average of 60 interactions per bunch crossing.

The LHC injection chain makes extensive use of proton acceleration facilities designed for previous, lower-energy experiments. The design is comprised of multiple sub-accelerator components each with a modest dynamic range, to achieve an ultimate acceleration of 8 TeV per beam. A hydrogen source is first pulsed through an electric field to strip electrons from the nucleus, producing a jet of ions. The Linear Accelerator 2 (LINAC 2) accelerates protons to 50 MeV through a series of radio-frequency (RF) cavities over a length of 33 m. The Proton Synchrotron Booster (PSB) is the first synchrotron in the complex, receiving injections from LINAC 2 and accelerating protons up to 1.4 GeV. Pulsed bunches are added in the plane transverse to the beam propagation direction, so that the PSB step limits the transverse emittance of the ultimate beam. The Proton Synchrotron has 4x the radius of the PSB at 628 m and accelerates protons to 26 GeV. A complex system of RF cavities allows the compression, merging, and splitting of the beam to mitigate beam-spread effects.

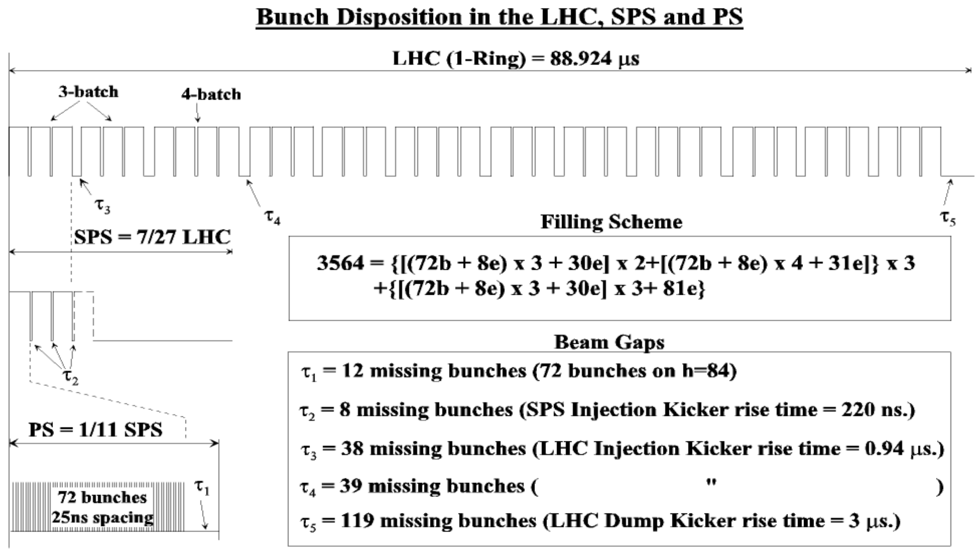

Figure 4.1: The standard filling scheme is shown with notes on the origin of the bunch structure from upstream injector systems. Figure is reproduced from Ref. [63].

The 6.9 km circumference Super Proton Synchrotron (SPS) further accelerates protons to 450 GeV before the 26.7 km LHC ring attains the final acceleration to an ultimate energy of 13 to 14 TeV.

The structure of the proton bunches delivered to the ATLAS interaction point (IP) is determined by the parameters of the upstream injectors. The LHC was designed to carry 2800 bunches per beam over the entire length of the LHC ring. These are nominally grouped into 72-bunch units corresponding to a single Proton Synchrotron fill. As four such fills populate the SPS, the LHC is predominantly filled with 288-bunch such batches. Proton Synchrotron and SPS batches are separated by empty bunches corresponding to the time required to regenerate the 'kicker' magnetic fields used to deflect and extract the beam. These effects are illustrated in Figure 4.1. More recently alternative fill schemes have been tested and utilized to push the LHC beyond its initial design luminosity. The majority of 2018 data was taken with the '8b4e' bunch scheme, where eight filled bunches are followed by four empty bunches, minimizing the splitting in the PSB to lead to lower emittance and higher luminosity.

Varying machine configurations lead to a significant change in performance over the LHC data-taking periods to date. Run 1 of the LHC ran from the inception of the machine to 2012, colliding beams up to 8 TeV and collecting a data set of nearly 25fb^{-1}. Run 2 began in 2015 with an increased energy of 6.5 TeV per beam. After the first year of running where a 3.2fb^{-1} dataset was collected, the bunch spacing was decreased from 50 to 25 ns and higher-luminosity data-taking commenced.

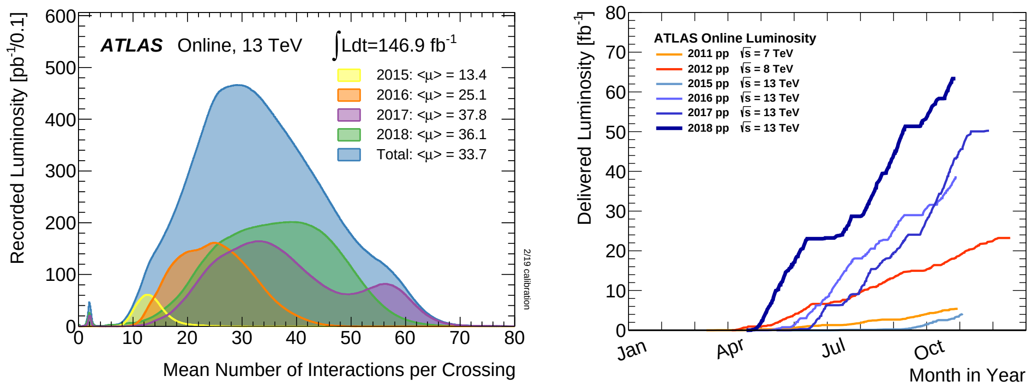

Figure 4.2: At left, the distribution of average number of interactions per bunch crossing is shown across the Run 2 data-taking period, with separate contributions shown for each year. At right, the recorded luminosity is shown as a function of time, with each year of LHC running separately overlaid.

In 2016 a sample of 36.1fb^{-1} was collected in which the peak number of interactions per bunch crossing reached 40. In the following two years, a luminosity of over $2 \cdot 10^{34}\,\mathrm{cm}^{-2}\mathrm{s}^{-1}$ was attained and a luminosity-leveling beam-separation strategy was used to maximize the size of the collected dataset while maintaining a peak collision rate near 60 interactions per crossing. This resulted in data sets of 47 and 61fb^{-1} in 2017 and 2018, respectively, leading to an ultimate Run 2 data set of nearly 150fb^{-1} collected. The distribution of the average number of interactions per bunch crossing for each year of Run 2 is shown in Figure 4.2, alongside a comparison of the integrated luminosity collected throughout each year of LHC running.

4.2 The ATLAS detector

ATLAS [64] is a multi-purpose particle detector with near-4π coverage about the proton-proton IP. It is comprised of a set of mostly-concentric sub-detector systems, each designed for different aspects of particle reconstruction. A schematic diagram is shown in Figure 4.3 outlining the major features of the apparatus. The Inner Detector (ID) is the sub-system nearest to the beamline and aims to precisely reconstruct the trajectories of charged particles inside a solenoidal magnetic field. Outside the tracking apparatus, a system of calorimeters absorbs most particles produced in collisions and provides measurements of their energies. The outermost sub-system of the central detector is the Muon Spectrometer (MS), which identifies charged particles that penetrate the calorimeters and measures their trajectories in a second, toroidal magnetic field.

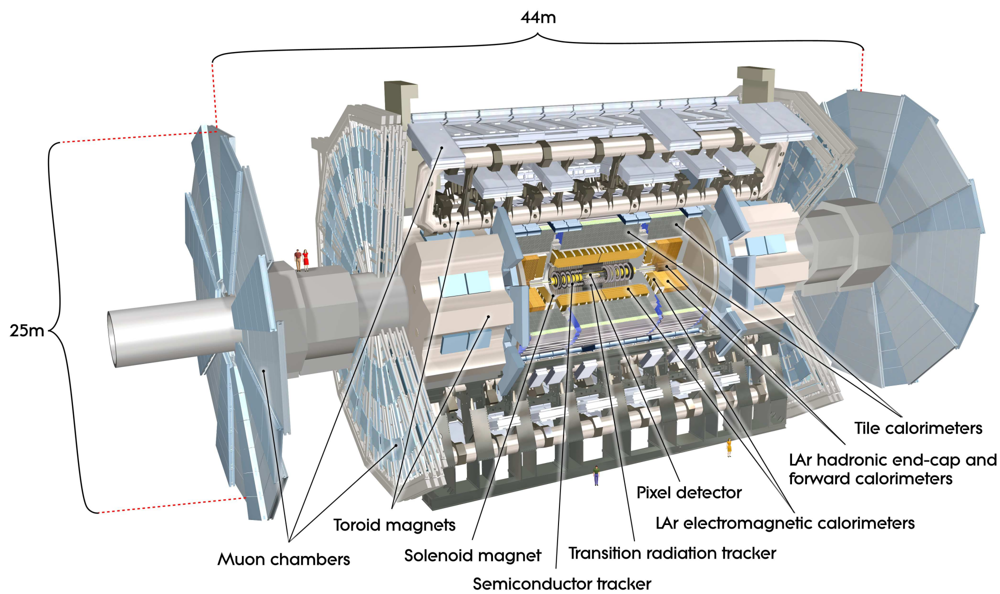

Figure 4.3: A schematic view of ATLAS, with various sub-detectors and other components indicated.

Coordinates

The ATLAS coordinate system is defined so that the z-axis is tangent to the beam-line at the IP, the x-axis points from the IP to the center of the LHC ring, and the y-axis points upward. The coordinate system is chosen to be right-handed so that Lake Geneva is located at large, positive z. Angular coordinates are often used, with radial coordinate r, azimuthal angle ϕ, and polar coordinate θ. The re-scaled pseudorapidity coordinate $\eta = -\log(\tan(\theta/2))$ is often convenient, as $\Delta\eta$ is invariant under Lorentz boosts along the z coordinate. The IP is located at $x = y = z = 0$. Due to the extension of the luminous region in z the pseudorapidity of a particle measured from its production vertex and from the IP may be significantly different, and so in the case of particle measurements a shifted coordinate system (x, y, z') may be defined where $z' = 0$ at the production vertex. In the present discussion the standard coordinate system is always used, and in cases where the choice is not clear from context the coordinate may be explicitly labeled η_{det}. Quantities X which are projected into the plane transverse to the beam are denoted X_{T}, so that $p_{\mathrm{T}} = p\sin\theta$ and $E_{\mathrm{T}} = E\sin\theta$.

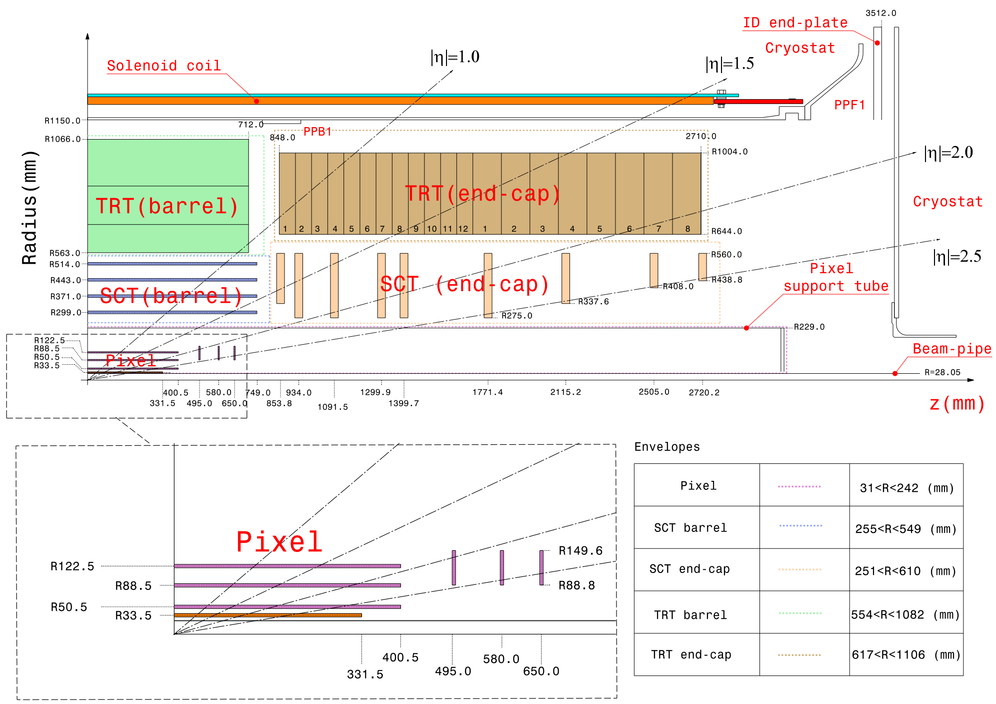

Figure 4.4: An $r - z$ view of the ID is shown, indicating the positions of the silicon pixel and Semiconductor Tracker (SCT) detectors and the Transition Radiation Tracker (TRT). The lower inset shows a magnified view of the pixel system. Figure reproduced from Ref. [67].

4.2.1 The Inner Detector

The ATLAS Inner Detector (ID) is comprised of three main sub-systems, illustrated in Figure 4.4, designed to reconstruct tracks with $|\eta| < 2.5$. The pixel detector [65, 66] is nearest to the IP and consists of four concentric cylinders of silicon sensor modules with radii ranging from 33.5 mm to 122.5 mm. In addition, three radially-extending endcap layers are present from $z = \pm 495$ mm to ± 650 mm to increase coverage of forward particles. The innermost barrel layer is the Insertable B-Layer (IBL), which extends to $|\eta| < 3.03$ and contains sensors with individual active pixel elements measuring $50\,\mu\text{m} \times 250\,\mu\text{m}$ in size $(r/\phi \times z)$, arranged in two-dimensional arrays. The remaining layers use pixels with sizes of $50\,\mu\text{m} \times 400\,\mu\text{m}$ in $(r/\phi \times z)$ in $250\,\mu\text{m}$-thick sensors. Tracks are reconstructed from measured 'hits': charge collected from particles' ionization energy as time over threshold (ToT) signals. The sub-detectors includes over 92 million pixels corresponding to about $2\,\text{m}^2$ of active silicon.

The SCT, a silicon micro-strip tracker, consists of four double-sided barrel layers ranging from $r =$ 299 mm to 514 mm and nine double-sided endcap layers from 854 mm to 2720 mm in a configuration designed to provide measurements on four layers independent of polar angle. The strips are 80 μm $\times$ 6 cm, providing finer granularity in the r/ϕ bending coordinate. Sensors are assembled into double-sided modules with a slight relative angle ($\pm 20\,\mathrm{mrad}$) allowing for measurements to be combined to form three-dimensional space-points. The sub-detector corresponds to 6.3 million channels and $63\,\mathrm{m}^2$ of silicon.

The TRT is composed of 350 thousand 4 mm diameter polyimide drift tubes interspersed with transition radiation (TR) material that provides many hits on track (36, on average) as well as electron identification capabilities. Drift tubes are filled with a gas mixture that is dominantly composed of either Xenon or Argon, which are ionized when traversed by charged particles. Photons are produced by the TR process, proportional in number to the Lorentz γ factor of the particle traversing the polypropolene/polyethylene material. Individual TRT straws are read out according to the amount of ionized charge collected, with low-threshold hits corresponding to typical tracks and high-threshold hits produced by TR photons. For the low-mass, high-γ electron, an average of 20$ of recorded hits pass the high threshold, while this figure is less than 5% for the significantly heavier pion. The outer radius of the TRT is 1 m from the IP, providing a large lever arm for track p_{T} measurements.

The entire tracking apparatus sits inside a 2 Tesla field provided by a solenoidal magnet outside the TRT, from $r = 2.46\,\mathrm{m}$ to $2.56\,\mathrm{m}$. The amount of material in the tracking volume may be characterized by the number of radiation lengths X_0 and nuclear interaction lengths λ_I traversed by an outward-traveling particle, defined as the distance over which an electron or nuclear-interacting particle's energy decreased by one e-fold ($E_{\mathrm{final}} = \frac{1}{e} E_{\mathrm{initial}}$). The number of radiation lengths (nuclear interaction lengths) traversed by a particle passing through the inner detector envelope ranges from 0.4 to 2.4 (0.2 to 0.7), varying with η_{det}. The solenoid corresponds to an additional $0.66\,X_0$ and $0.13\,\lambda_I$ for particles normal to the cylindrical surface [68].

4.2.2 Calorimeters

The ATLAS calorimeter system consists of components designed to measure the energy of electromagnetically charged and neutral particles, accessible only through their nuclear interactions. An illustration of the system is shown in Figure 4.5, with sub-systems indicated.

The electromagnetic system is comprised of sampling calorimeters with LAr as the active material [70]. The barrel LAr calorimeter ($|\eta| < 1.375$, $1.4\,\mathrm{m} < r < 2\,\mathrm{m}$) is comprised of accordion-shaped layers of lead absorbers, sandwiched between stainless-steel sheets for structural support, and in-

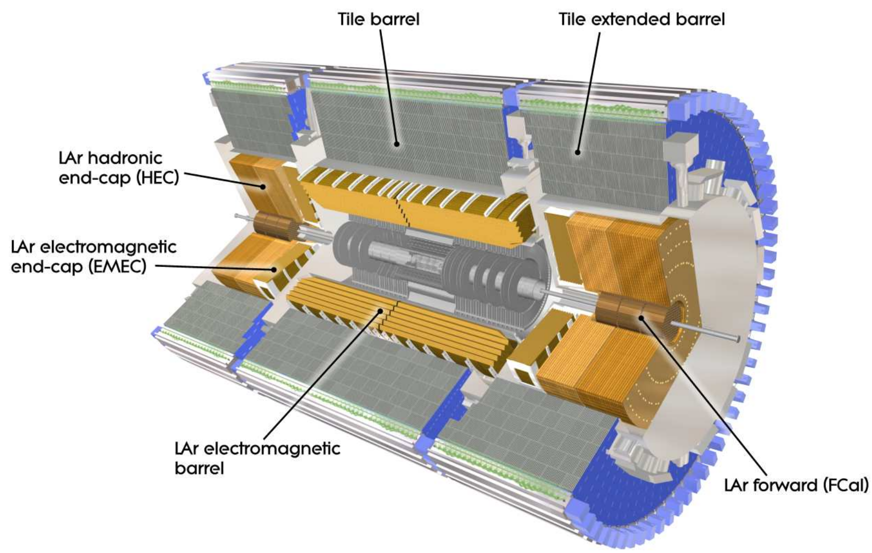

Figure 4.5: A schematic view of the ATLAS calorimetry system. The liquid argon (LAr) electromagnetic barrel and electromagnetic endcap provide coverage up to $|\eta| < 3.2$. The tile calorimeter, LAr hadronic endcap, and forward calorimeter measure hadronic interactions up to $|\eta| < 4.9$. Figure reproduced from Ref. [69].

terspersed with electrodes comprised of a printed circuit board (PCB) with three copper layers. The outer layers are held at large potential difference, while the inner layer measures the current induced by the charge drifting through the LAr via capacitive coupling. The LAr signals are further discretized by etching structures into the electrodes in the longitudinal and polar dimensions, leading to separate readout channels for each region [71]. The desired ϕ granularity for each region is obtained by ganging together the readout across accordion layers. The innermost layer ($\sim 4.3X_0$ depth) is very finely segmented in the non-bending direction $\Delta\eta \approx 0.0031$ to achieve $\gamma/\pi^0(\rightarrow \gamma\gamma)$ discrimination and precise photon pointing. The middle layer ($\sim 18X_0$) measures the majority of the electromagnetic shower with segmentation $\Delta\eta \times \Delta\phi = 0.025 \times 0.0245$. The final layer ($2X_0$) covers twice the angular area ($\Delta\eta = 0.05$) as the middle layer, and measuring the leakage of high-energy showers into the hadronic calorimeter. The accordion design allows for uniform coverage in ϕ, as well as convenient readout of all three layers at the inner (outer) radius for the innermost electrode (outer two electrodes). This geometry for the inner barrel detector is shown in Figure 4.6. The precision detection capabilities are extended by the Electromagnetic Endcap Calorimeter (EMEC) to $|\eta| < 3.2$ using the same technology. The number longitudinal segmentation is reduced to two layers in the region $2.5 < |\eta| < 3.2$. The region between the barrel and endcap calorimeters ($1.37 < |\eta| < 1.52$)

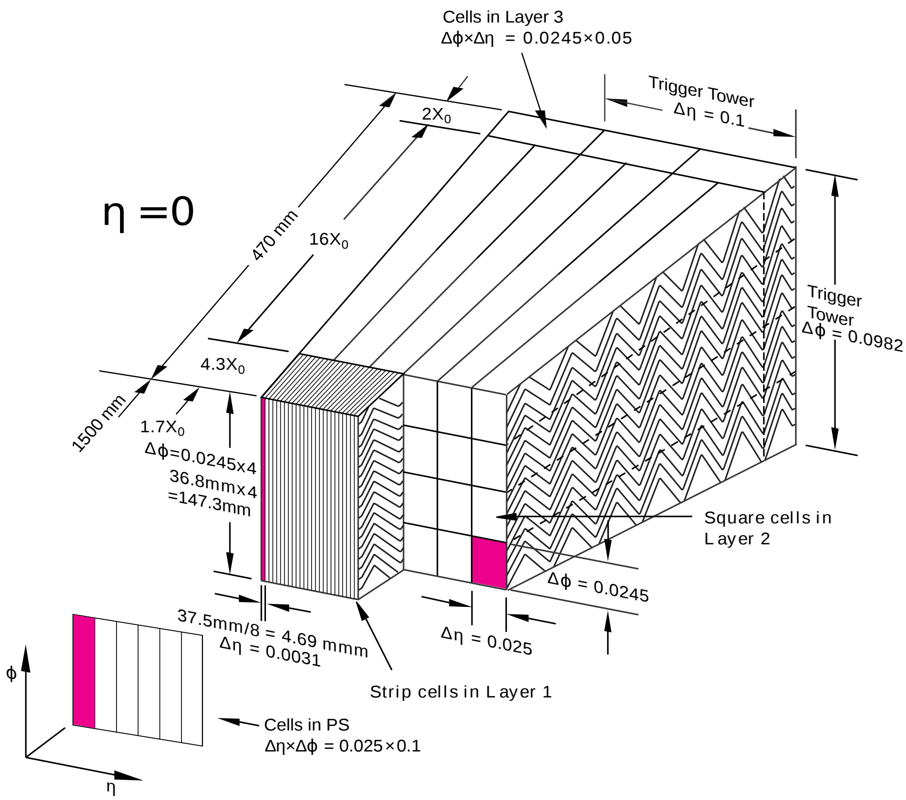

Figure 4.6: The segmentation of the three longitudinal layers of the barrel LAr calorimeter is shown. The innermost strip layers enhance $\pi^0 \to \gamma\gamma$ rejection, while the outermost layer estimates the leakage of high-energy showers into the hadronic calorimeter. Energy measurements of cells in 0.1×0.982 regions are summed to provide coarser measurements for the trigger logic. Figure reproduced from Ref. [64].

contains a relatively large fraction of inactive material. A pre-sampler is also located in a common cryostat over the region $|\eta| < |1.8$ to estimate losses to dead material traversed prior to the calorimeter [72]. Due to the peak-dip structure of the LAr signal pulse shape (see Ref [73] for example) a degree of pile-up (PU) is inherent in the technology, with signals corresponding to out-of-time PU subtracted from measurements in subsequent bunch-crossings.

The barrel tile calorimeter provides measurements of hadronically interacting particles up to $|\eta| < 1.7$, using steel absorbers and plastic scintillating tiles [74]. The detector is comprised of a series of radially-extending modules with size 0.1 in ϕ and ranges from $2.28\,\mathrm{m} < r < 4.25\,\mathrm{m}$, corresponding to $7.4\lambda_I$. Each module consists of stacks of sandwiched steel and plastic plates, mounted to an outer self-supporting girder structure, containing 'drawers' of photomultiplier tubes (PMTs) and readout electronics. Scintillation light produced in doped polystyrene tiles is transmitted through a network of wavelength-shifting optical fibers to the outer drawers, where they are shaped and digitized.

In the farther forward region, the tile calorimeter is complemented by the LAr-based Hadronic Endcap Calorimeter (HEC) and Forward Calorimeter (FCal), sharing a cryostat with the LAr barrel electromagnetic calorimeter [70, 75, 76]. The HEC uses copper absorbers and covers the region $1.5 < |\eta| < 3.2$, with granularity of 0.1×0.1 (0.2×0.2) in $\Delta\eta \times \Delta\phi$ for $|\eta| < 2.5$ ($|\eta| > 2.5$). The FCal is located approximately 4.7 m from the IP and provides calorimetry in the region $3.1 < |\eta| < 4.9$. The innermost of three layers uses copper absorber while the outer two use tungsten, with readout regions of various sizes, regular in x and y.

4.2.3 The Muon Spectrometer

The MS is composed of barrel and endcap regions embedded in a toroidal magnetic field, with a variety of charged particle sensing technologies [77]. The barrel toroid magnet consists of eight air-core, elongated coil structures encased in cryogenic vacuum vessels [78, 79]. It's cold mass operates at 4.6 K, requiring five weeks to cool the full 360-tonne assembly. The endcap toroids use a similar configurations of eight-coil arrays of NbTi/Cu winding in aluminum vacuum vessels [80]. Charged particle reconstruction for $|\eta| < 2.7$ with 10% momentum resolution for TeV muons is targeted, as well as trigger capabilities to $|\eta| < 2.4$. The barrel region is instrumented with three concentric cylindrical layers of detecting chambers, from $r = 5$ m to 10 m from the IP. Four endcap 'wheels', transverse to the beam-line, are located from $z \approx 7.4$ m to 21.5 m from the IP. Figure 4.7 displays the various components of the MS.

The MDT system is composed of layers of aluminum tubes filled with an Argon/CO_2 gas mixture and central tungsten-rhenium wire at 3 kV potential difference. Typical assemblies include two four-tube multi-layers separated by spacers (mostly $17 - 32$ cm), with $\approx 80\mu$m resolution per tube. Due to limitations on the MDT counting rate, the use of this technology is restricted to $|\eta| < 2.0$ beyond which Cathode-Strip Chambers (CSCs) are used to provide precision hit information. CSCs are multi-wire proportional chambers with signals on the wire arrays measured through cathode strips in two dimensions. The system provides two-dimensional measurements across four planes from $2.0 < |\eta| < 2.7$.

Additional systems targeting fast readout for the trigger and acceptable p_{T} resolution are interspersed with the precision chambers. The barrel includes three layers of double-sided Resistive Plate Chambers (RPCs), allowing up to six measurements in each (η, ϕ) dimension and $n-1$ trigger logic for maximal acceptance. Beyond the $|\eta| < 1.05$ covered by the RPCs, the Thin Gap Chamber

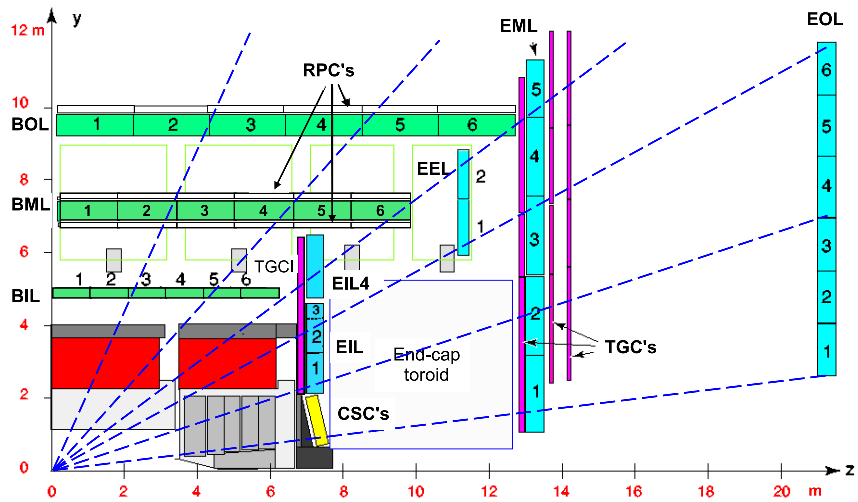

Figure 4.7: The components of the Muon Spectrometer are pictured. The precision measurement components of the Monitored Drift Tube chamber (MDT) system are shown in green (barrel) and cyan (endcap), as well as the Cathode-Strip Chamber in yellow. The Resistive Plate Chamber trigger chambers are pictured in white adjacent to the barrel Monitored Drift Tube chambers (MDTs), while the Thin Gap Chamber system is shown in purple.

(TGC) system is used (up to $|\eta| < 2.4$). TGCs operate similarly to the CSC concept, providing measurement in the second, non-bending coordinate to forward regions covered by MDTs.

4.3 Trigger and Data Acquisition

The maximum rate of collisions at the LHC is set by the bunch crossing frequency, so that consecutive collisions occur as frequently as 40 Mhz. However, due to the relatively small cross sections for the rare processes of interest (for example, the ratio of $W+$jets production to the total cross section is $\sigma_W/\sigma_{pp} \approx 2 \cdot 10^{-6}$), not all events must be recorded. The ATLAS Trigger and Data Acquisition (TDAQ) system [81, 82] is responsible for identifying interesting proton-proton collisions in real time and recording the corresponding detector outputs to permanent storage. Electronic signals containing the event data follow two paths off of the detector: the *trigger path* and the *read-out path*. The trigger path reads out partial and/or simplified event information to select events, while the read-out path transfers full-granularity readout for the subset of selected events. Figure 4.8 shows a schematic overview of the TDAQ system as configured for the 2015 data-taking period. The identification proceeds in a series of two steps, implemented in the hardware-based Level-1 Trigger (L1 Trigger) and in the downstream, software-based High-Level Trigger (HLT). For fast

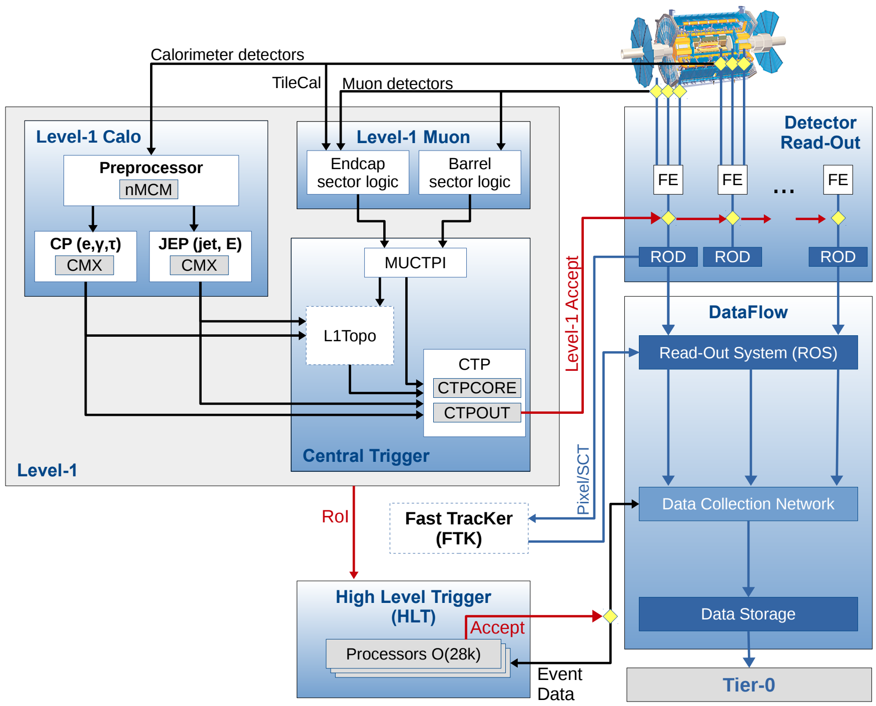

Figure 4.8: An illustration of the detector readout and trigger systems. The readout path is shown, in addition to the sub-components of the hardware-based L1 Trigger Trigger system and upstream HLT central processing unit (CPU) farm. Black arrows indicate the trigger path, red arrows the trigger decision and object outputs, while blue arrows indicate the full-event read-out path. The Level-1 Topological Trigger (L1 Topo) and Fast Tracker (FTK) were used only for commissioning studies over the 2015-2016 data-taking period. Figure is reproduced from Ref. [81].

identification, a limited set of detector information is used in the trigger decisions, according to bandwidth, latency, and processing constraints. The identification task is made more challenging by the presence of PU, simultaneous proton-proton collisions within the same bunch crossing leading to extraneous detector noise that complicates unambiguous event reconstruction. The following sections describe the L1 Trigger and HLT systems used to record the data analyzed by ATLAS.

4.3.1 The hardware-based Level-1 trigger

The L1 Trigger system considers all events in real-time, selecting events with an output rate up to 100 kHz based on information from the calorimeter and muon systems. Events are buffered on the front-end electronics while awaiting a L1 Trigger accept, after which detector-specific Read-Out Drivers (RODs) package the event data into a common format and transmit it to the Read-Out

System (ROS) to await an HLT decision. The L1 Trigger decision is made by the Central Trigger Processor (CTP) after receiving inputs from the Level-1 Calorimeter Trigger (L1 Calo) and Level-1 Muon Trigger (L1 Muon) sub-systems. The CTP checks multiplicity requirements and pre-scale factors[2] based on L1 Calo and L1 Muon outputs before issuing an accept, as well as enforcing dead-time requirements and any logic dependent on the LHC bunch-crossing identifier (BCID).

The Level-1 calorimeter trigger

The L1 Calo sub-system [83] takes inputs from the electromagnetic and hadronic calorimeters with limited granularity. Calorimeter cells are summed to form a set of 0.1×0.1 "trigger towers" for each calorimeter. In the forward region $|\eta| > 2.5$, larger cells are used. A dedicated pedestal subtraction is performed for each cell by the new Multi-Chip Module L1 Calo Pre-Processor (nMCM) auto-correlation filter. The value varies as a function of the BCID due to the non-uniform response stemming from out-of-time effects on the LAr signal pulse-shape. The corrected trigger towers are sent to the Cluster Processor (CP) and the Jet/Energy-sum Processor (JEP) systems.

The CP forms trigger objects for electrons and photons as well as for hadronic tau decays. region of interests (ROIs) are built for electromagnetic ('EM') objects by considering 2×2 regions of trigger towers (a total of 0.2×0.2 in $\eta \times \phi$) and requiring that two of the four adjacent cells have $\sum E_{\mathrm{T}}$ above some configurable threshold. Aside from requiring a narrow, high-energy deposit, isolation requirements may be enforced by requiring that either: (a) the trigger towers adjacent to the 2×2 region have low $\sum E_{\mathrm{T}}$; or, (b) that the 2×2 group of hadronic calorimeter towers behind the electromagnetic (EM) ROI has small $\sum E_{\mathrm{T}}$. Typical nomenclature for such an L1 Trigger requirement is `L1_EM20VHI`, which requires an EM calorimeter ROI with two adjacent towers having $\sum E_{\mathrm{T}} > 20\,\mathrm{GeV}$ ('EM20') and enforces electromagnetic ('I') and hadronic ('H') isolation requirements. Further, 'V' denotes that the E_{T} threshold varies with η_{det} to account for non-uniform detector response. This trigger or variants thereof were used to record single-electron events without pre-scale in 2015 and 2016.

The JEP evaluates jet signatures as well as total energy ($\sum E_{\mathrm{T}}$ over calorimeter inputs) and missing energy ($\sqrt{(\sum E_x)^2 + (\sum E_x)^2}$) triggers. Inputs are energy sums over 0.2×0.2 regions and both EM and hadronic calorimeters. Jet ROIs are built from 2×2, 3×3, or 4×4 tower regions (up to 0.8×0.8 in $\eta \times \phi$). The $E_{\mathrm{T}}^{\mathrm{miss}}$ is calculated by summing the x- and y-components of the

[2] Certain trigger items may only be used to collect a fraction of events (the inverse of the pre-scale factor) which pass the trigger requirements. This is especially useful for triggers that require low-energy objects for commissioning and background studies.

energies of all cells, with a per-tower E_{T} granularity of 1 GeV. Energies from multiple JEPs are appropriately combined to form the final $E_{\mathrm{T}}^{\mathrm{miss}}$ estimate in the Common Merger Module (CMM). The $E_{\mathrm{T}}^{\mathrm{miss}}$ threshold is configurable, with 50 GeV nominally used in the `L1_XE50` item that ran un-prescaled for much of 2015 and 2016.

The Level-1 muon trigger

The complementary L1 Muon system is dedicated to processing signals from the MS. In the barrel, coincidences are required among layers of RPCs, with coincidences in the four innermost layers used to define a search region in the outermost two layers. Coverage is incomplete in the barrel due to services near $\eta = 0$, support structures, and two elevators within the detector. In the endcap region, similar logic to the barrel is applied to TGC outputs, using an outside-in road-following strategy. Six momentum requirements are supported, divided equally among low- and high-p_{T} working points, with the higher-p_{T} items requiring hits in sub-regions of the 'roads' (extrapolated hit trajectories) defined by the low-p_{T} triggers. The lowest un-prescaled triggers in 2015 and 2016 utilized the `L1_MU20` trigger item.

4.3.2 HLT software trigger

Following a L1 Trigger accept, events are buffered in the ROS while event data is partially reconstructed in a farm of $\approx 40\,000$ CPU cores before ultimately forming a final trigger decision. The final output rate is limited to an average of ~ 1 khz, which is allocated across a range of signatures (e.g., single-lepton, multi-lepton, jets, $E_{\mathrm{T}}^{\mathrm{miss}}$, and others). HLT reconstruction is limited to the ROIs obtained from the specific L1 Trigger item accept and often corresponds to a simplified version of the offline reconstruction.

Single lepton triggers

The largest fraction of the total trigger rate (~ 266 hz of the ~ 1.5 khz "peak rate" recorded [84]) is dedicated to single-lepton triggers, due to their broad utility across a diverse set of analyses. Both electron and muon triggers rely on ID tracks, which are obtained in a two-step approach where fast-track finding is followed by a more precise algorithm using the previously-found space-points as seeds.

Electron triggers reconstruction operates in two stages to quickly reject poor candidates and avoid unnecessary processing. In the first, clusters are built from rectangular arrays of calorimeter cells within the L1 Trigger ROI and required to satisfy loose shower-shape criteria designed to reject candidates from hadronic showers. A 1 GeV matching track obtained from the fast-track finding algorithm is also required. In the second stage, an offline-like selection is used (see Section 4.4.2) with re-calibrated clusters and precision track inputs as well as a likelihood-based identification criterion. In 2016 data-taking, an isolation requirement $\sum p_{\mathrm{T}}/E_{\mathrm{T}} < 0.1$ using tracks in a cone of $\Delta R < 0.2$ is also enforced for the lowest un-prescaled trigger. This item is denoted `e24_lhtight_nod0_ivarloose`, where the E_{T} cut (24 GeV) and tight likelihood working point are labeled, as well as the p_{T}-dependent, loose isolation and the fact that the d_0 impact parameter is not included in the likelihood.

The muon trigger adds MDT measurements to the trigger chambers used in the L1 Trigger decision. The MS p_{T} is obtained from a look-up table after which the MS-only track is combined with a corresponding ID track to produce a combined measurement. The efficiency is improved by matching MS and ID tracks with both outside-in and inside-out strategies when necessary. Isolation requirements are also imposed in a manner similar to the electron case, with `mu26_ivarmedium` being the lowest-p_{T}threshold un-prescaled muon trigger in 2016.

Jet triggers

In the HLT, reconstruction of jets and $E_{\mathrm{T}}^{\mathrm{miss}}$ proceeds after reading out the entire calorimeter at full granularity and running the offline topo-clustering algorithm (see Section 4.4.4) to obtain inputs to each algorithm [85]. This allows jet reconstruction and calibration to proceed nearly identically to the manner in which it is carried out offline. The lowest un-prescaled jet trigger in 2016 required a 380 GeV jet, reconstructed from LC-scale clusters with the anti-$k_{\perp}$ algorithm with $R = 0.4$. As quarks and gluons are produced copiously at the LHC, jet trigger rates are large and so larger E_{T} must be required than is necessary for other reconstructed objects (e.g. a 26 GeV isolated electron) to record a manageable data-set. The primary users of the single-jet trigger are searches high-mass di-jet pairs (e.g. for a TeV-scale Z') and dark matter, via the “mono-jet” $pp \to \chi\bar{\chi} + j$ process. Requiring multiple jets allows lower thresholds, with items such as `4j100` and `6j60` used for measurements of hadronic $t\bar{t}$ decays. Similar triggers are critical for the HL-LHC, specifically to target the rare SM $hh \to b\bar{b}b\bar{b}$ process.

The most significant difference between online and offline jets is the level of possible energy calibration. In the HLT, limited track reconstruction prevents three offline corrections based on reconstructed vertices and the individual tracks associated to jets. The first corrects the origin of the jet four-vector based upon the location of the primary vertex (in z). The second applies a correction due to in-time PU based on the number of total reconstructed vertices in the event. The most important of the three is the Global Sequential Correction (GSC) [86], which primarily calibrates for non-uniformity in detector response to quark- and gluon-initiated jets. The energy calibration includes corrections based on the longitudinal structure of the jet shower and associated tracks as well as a muon segment-based "punch-through" correction irrelevant for trigger jet energies. The track inputs are the multiplicity associated to each jet as well as the angular moment

$$\text{track width} = \frac{\sum_{\text{tks}} p_{\text{T}}^{\text{tk}} \cdot \Delta R(\text{jet}, \text{tk})}{\sum_{\text{tks}} p_{\text{T}}^{\text{tk}}}. \tag{4.1}$$

As tracking is computationally expensive and is not otherwise required for jet triggers, none of these corrections were not applied prior to 2016 data-taking.

A crucial observation was made that the same L1 Trigger seed trigger used for single-jet events also seeds b jet items in the HLT, and that one might re-use these tracks for further jet energy corrections. After requiring a jet of moderate energy ($E_{\text{T}} \sim 200\,\text{GeV}$), b jet triggers further reduce the QCD rate by requiring a tight b-tag score, as computed from tracks associated to the jet. These tracks are obtained in a two-stage procedure, illustrated in Figure 4.9. First a fast tracking algorithm processes hits in a narrow ϕ window, but significant coverage in z. This allows the jet vertex to be identified so that a second, more precise algorithm can be run to identify all tracks in the jet ROIin a region narrow in z. Using these tracks, the HLT jet energy calibration can be improved through the application of the GSC. For jet energies near the single-jet threshold ($\approx 400\,\text{GeV}$), the correction from calorimeter-only corrections is significant, as shown in Figure 4.10, while for those near the multi-jet ($\approx 100\,\text{GeV}$) the track-based correction is much more significant.

$E_{\text{T}}^{\text{miss}}$**triggers**

$E_{\text{T}}^{\text{miss}}$ reconstruction is particularly challenging in the HLT, as true offline-like reconstruction would require complete reconstruction, calibration, and ambiguity resolution of many species of reconstructed objects. Calorimeter-based quantities are used in the trigger to approximate the offline calculation with a variety of different strategies:

- *Cell* $E_{\text{T}}^{\text{miss}}$ (`xe`) is constructed directly from the vector sum of all calorimeter cells with 2σ noise cuts applied, and treated as massless.
- *Topo-cluster* $E_{\text{T}}^{\text{miss}}$ (`xe_tc_lcw`) is built using a similar method, directly from topo-clusters after the local hadronic calibration scheme is applied (see Section 4.4.5).

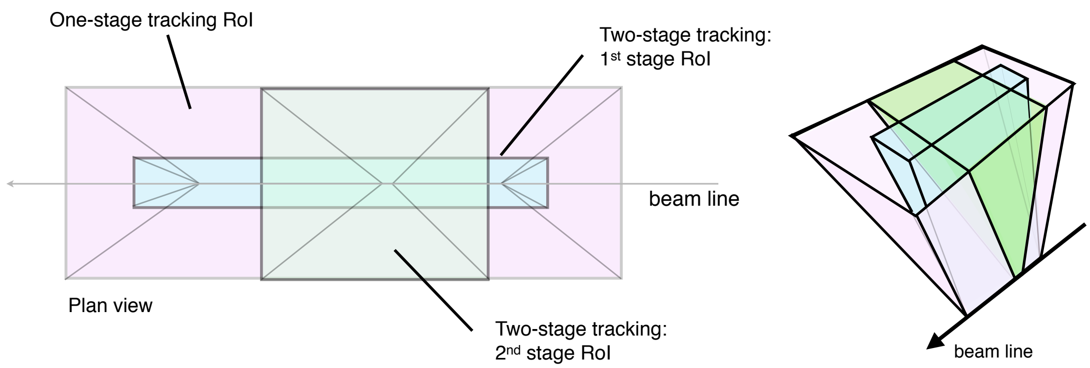

Figure 4.9: Regions considered in the two-step tracking procedure used for jet triggers is shown. First, a fast algorithm finds tracks in a region long in z and narrow in ϕ (pictured in blue) with the sole purpose of reconstructing the primary vertex associated to the jet. Next a more precise tracking algorithm is run over hits in a window narrow in z about the selected vertex, but comparable to the jet ROI in $\eta \times \phi$ (pictured in green).

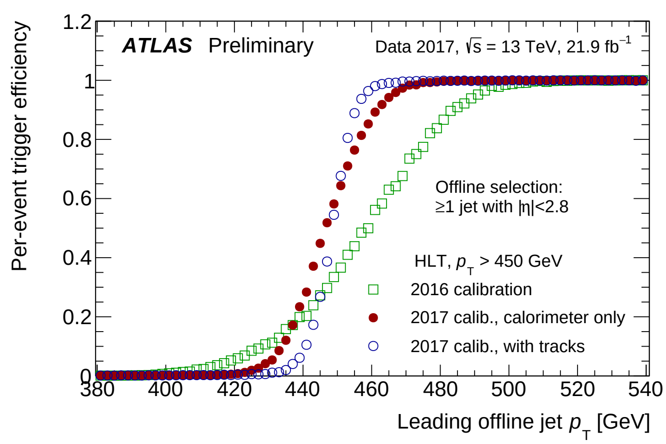

Figure 4.10: Efficiencies are compared for three configurations of single-jet HLT trigger accepting 400 GeV jets. In the green squares no GSC is applied, while in the red closed circles only the calorimeter-based corrections are applied and in blue open circles the ID track corrections are also applied. A more complete correction leads to tighter correspondence between the online and offline jet energies and thus a lower rate of events collected with offline jet p_T below the trigger threshold. Figure reproduced from Ref. [87].

- *Topo-cluster $E_{\mathrm{T}}^{\mathrm{miss}}$ with η-dependent PU correction* (`xe_tc_pueta`) is constructed as above, but with average pileup densities computed from $< 2\sigma$ topo-clusters in ten regions of η, which are subsequently subtracted from the topo-clusters used to build the $E_{\mathrm{T}}^{\mathrm{miss}}$.

- *Pile-up fit $E_{\mathrm{T}}^{\mathrm{miss}}$* (`xe_tc_pufit`) extends the η-dependent correction scheme by tiling the calorimeter into 0.8×0.8 regions which are divided in hard-scatter and PU dominated regions according to a total energy threshold criterion. The pileup densities in each hard-scatter region are obtained in a fit (assuming no $E_{\mathrm{T}}^{\mathrm{miss}}$ from PU) with the remaining energy used to compute the $E_{\mathrm{T}}^{\mathrm{miss}}$.

- *Jet-based $E_{\mathrm{T}}^{\mathrm{miss}}$* (`xe_tc_mht`) is computed using all $R = 0.4$ anti-$k_{\perp}$ jets reconstructed as described above with $p_{\mathrm{T}} > 7\,\mathrm{GeV}$. Retaining low-$p_{\mathrm{T}}$ jets gives an estimate of the soft-term.

The proliferation of methods is due to the significant dependence of $E_{\mathrm{T}}^{\mathrm{miss}}$ resolution on PU, when information from the ID is not used in the computation. Alternate methods have differing sensitivities to the level of PU, and also make requirements on energies calibrated at different scales (EM scale for cell $E_{\mathrm{T}}^{\mathrm{miss}}$, Local Hadronic Calibration (LC) scale for topoclusters, and particle-scale for fully calibrated jets). Figure 4.11 shows the efficiency for triggers of all types as well as the dependence of trigger rates on the average number of collisions per event. The increase in luminosity from 2015 to 2016 ($\langle\mu\rangle = 13$ to 25) required a more complicated trigger strategy, where combined requirements on different HLT $E_{\mathrm{T}}^{\mathrm{miss}}$ quantities were necessary.

4.4 Particle reconstruction

4.4.1 Charged particle tracks

The ID sub-detectors are used to reconstruct trajectories of charged particles from measurements of ionization in the active material ('hits'). The general track-finding procedure is as follows [88, 89]. Hits in the pixel and micro-strip silicon trackers are first converted into three-dimensional "space-points". For pixel sensors, this is trivially done by combining the two-dimensional measurement with the sensor position in a local-to-global lookup. For strip hits, measurements from opposite sides of each SCT layer (at a slight, stereo angle) are combined with a loose vertex constraint to produce a three dimensional measurement. Hits are reconstructed as track candidates in a series of finding and fitting algorithms. Track seeds are formed combinatorially by considering sequences of three hits in adjacent detector layers (pixel, strip, or a combination of both) and histogramming

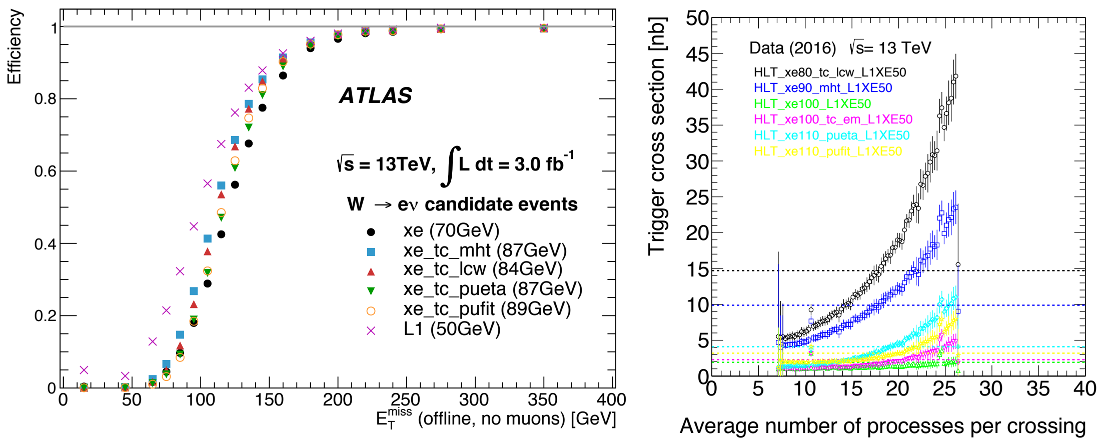

(a) (b)

Figure 4.11: At left, the efficiency is shown for several $E_{\mathrm{T}}^{\mathrm{miss}}$ triggers in 2015 data. The test efficiencies are computed by running $E_{\mathrm{T}}^{\mathrm{miss}}$ trigger algorithms on $W \to e\bar{\nu}$ candidate events, collected with lepton triggers, and shown as a function of the $E_{\mathrm{T}}^{\mathrm{miss}}$ as computed by the offline algorithm. Purple crosses show the efficiency for the L1 Trigger trigger requiring 50 GeV, while the remaining points compare different HLT algorithms. The efficiency for HLT items is computed as the fraction of events that path both the HLT item and its L1 Trigger seed (`L1_XE50`, also shown). The precise value of the $E_{\mathrm{T}}^{\mathrm{miss}}$ requirements are different for each HLT item, as different algorithms use energies calibrated to different scales, and are selected so that each item records events at the same rate. At right, the dependence of each HLT algorithm is shown on the average number of proton-proton interactions per bunch crossing ($\langle\mu\rangle$) for data collected in 2016. The rates are quantified by the corresponding trigger cross section: the number of events collected per unit luminosity. There is a large variation visible in the dependence of each algorithm on $\langle\mu\rangle$. The trend is less noticeable in the left plot, as the efficiencies are integrated over the full 2015 data set ($\langle\mu\rangle = 13$).

their extrapolated intersections with the beamline. This is the basis for a fast vertexing step, allowing additional constraints to narrow the range of acceptable seeds. Seeds are extrapolated into neighboring layers to search for additional consistent hits. For candidates of sufficient quality a Kalman filter-based 'track following' algorithm is employed, producing weighted assessments of the comparability of hits in additional layers with the existing track parameters. Track candidates produced in this process may share common hits, which are prioritized by a scoring metric based on measured of track quality. Tracks are extrapolated into the TRT to find extensions, associating straw hits to the existing track, after which a combined fit is performed. TRT extensions not associated to found tracks seed a second step of "outside-in" tracking, whereby TRT drift circles are associated with unassigned silicon space-points. This process is especially important to recover efficiency for tracks produced by converted photons, many of which do not leave hits in the inner silicon layers.

Tracks are used for the reconstruction of numerous higher-level objects, often in combination with measurements made in other sub-detectors. Track quality criteria are enforced, making minimum requirements on the number of silicon layers hit and maximum requirements on the number of 'holes' in layers where hits are anticipated. Generally only tracks with $p_{\mathrm{T}} > 400$ MeV and $|\eta| < 2.5$ are considered. Track characteristics and resolutions of the helix parameters $(p_{\mathrm{T}}, \eta, \phi, d_0, z_0)$ are measured in data and compared to simulation using 13 TeV data in Ref. [90]. Effects of material in the ID on track propagation and reconstruction are studied in Ref. [67].

Primary vertices corresponding to proton-proton interaction points are reconstructed using 500 MeV tracks in an iterative procedure beginning with all reconstructed tracks of sufficient quality [91]. The most probable location of a vertex in z is determined by histogramming the position of closest approach for all tracks, calculated with the Half-Sample Mode algorithm [92]. Tracks consistent with this position are locally linearized and the vertex position is determined by an adaptive fit with tracks weighted according to their consistency with the vertex hypothesis. Successfully reconstructed vertices are recorded and tracks removed from subsequent iterations of the algorithm. The reconstructed primary vertex with largest $\sum_{i \in \mathrm{tracks}} p_{\mathrm{T},i}$ is usually identified with the hard process of interest for general physics analyses. Both the vertex reconstruction efficiency and the resolution of reconstructed vertex parameters are measured in data, and compared to predictions from MC simulation [93]

4.4.2 Electrons and photons

Electrons are reconstructed in a three-step procedure of cluster-finding, track-finding, and track-to-cluster association [94]. Seed clusters are identified using a sliding-window algorithm that selects 3×5 towers of $\Delta\eta \times \Delta\phi = 0.025 \times 0.025$ longitudinally-summed EM calorimeter cells with transverse energy $E_{\mathrm{T}} > 2.5$ GeV. Track candidates with $p_{\mathrm{T}} > 400$ MeV are reconstructed from space-points constructed from hits in the silicon layers of the inner tracker, with a specialized pattern-recognition step allowing for bremsstrahlung energy loss at each material interface. Ambiguities due to shared hits are resolved and tracks are extended into the TRT [95, 96]. Subsequently tracks which loosely match clusters are fit using a specialized Gaussian sum filter (GSF) algorithm [97, 98] allowing for nonlinear effects from bremsstrahlung energy loss. Fit tracks are associated to clusters with tighter matching criteria, with the closes match deemed as the primary track in the case of multiple matches. Tracks without pixel hits and consistent with a secondary vertex are considered likely photon conversion candidates. Reconstructed clusters not matched to tracks are photon candidates.

Electrons are identified using a likelihood classifier based on observables relating to the calorime-

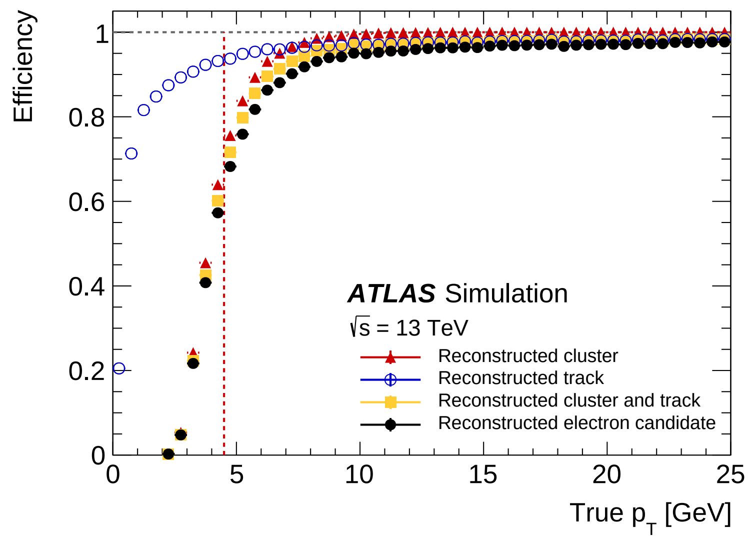

Figure 4.12: Efficiencies are separately shown as a function of truth p_{T} for the electron reconstruction steps. Red triangles show the efficiency to find a cluster corresponding to a 2.5 GeV EM-scale deposit in the electromagnetic calorimeter. Track reconstruction using standard methods is shown in open blue circles, while the combination of a cluster with GSF tracking is shown with yellow squares. Black closed circles represent the total efficiency also including the track-to-cluster matching criterion. Figure is reproduced from Ref. [94].

ter shower-shape, track parameters, and track-to-cluster matching. Photon identification is based on 'rectangular' requirements on shower-shape variables along. Calorimeter- and track-based isolation criteria are defined based on the additional activity in a ΔR cone about the reconstructed object. For both identification and isolation multiple working points are supported, allowing for variable signal efficiency and background rejection as a function of electron/photon E_{T}. Scale factors correcting the efficiencies predicted in MC simulation to those observed in data are obtained using tag-and-probe methods in $Z \to e^+e^-$ and $J/\Psi \to e^+e^-$ events. Such events are also used to measure electron and photon energy scale and resolution. The efficiency for reconstructing low-energy electrons is shown in Figure 4.12, separated into sub-components corresponding to track-finding, cluster-finding, and matching.

4.4.3 Muons

Muons are reconstructed from combined measurements with the inner detector, calorimeters, and muon spectrometer subsystems [99]. Reconstruction in the MS is seeded by segments obtained by a Hough transform-based pattern matching algorithm [100] in the MDT chambers combined with adjacent trigger chambers. A combinatorial algorithm seeded by segments in the intermediate layers combines measurements in each chamber to form track candidates. An overlap removal procedure is applied, and a χ^2 fit determined the final suite of candidates. "Recovery fits" are performed which allowing hits to be dropped in case the χ^2 is significantly improved.

MS segments are combined with information from other detector systems for combined reconstruction. Combined muons are reconstructed by performing a global re-fit to ID and MS tracks, using an 'outside-in' approach and allowing MS hits to be dropped to improve the fit. Segment-tagged muons are reconstructed when ID tracks are matched to a single MS segment and a full re-fit is not possible. Calorimeter-tagged muons are reconstructed by associating calorimeter energy deposits consistent with minimum-ionizing particles with ID tracks, and are used to recover efficiency in regions of low MS acceptance. Extrapolated muons are reconstructed in the MS only and require loose compatibility with the primary vertex, which if of primary utility beyond the range of the ID. Overlap removal is performed, preferring combined muons over segment-tagged and calo-tagged (in order of precedence) in the case of a shared ID track. MS segment overlap removal is also performed, preferring high-quality muons according to the number of hits and fit quality.

Identification requirements on muons are imposed by selecting which of the above-described populations should be accepted and what additional quality cuts should be imposed. Calorimeter- and track-based isolation requirements are considered and calibrated in an analogous manner to the electron case, with efficiency scale factors derived using $Z \to \mu^+\mu^-$ and $J/\psi \to \mu^+\mu^-$ events.

4.4.4 Jets

Hadronic showers are produced from decays of particles that are charged under QCD, which are reconstructed from calorimeter deposits as calorimeter 'jets'. Energy deposits measured by individual cells of the electromagnetic and hadronic calorimeters are combined by a local clustering algorithm to form composite topo-cluster objects [101] roughly corresponding to individually reconstructed particles. The algorithm relies on the 'significance' of the measured energy $E/\sigma(E)$, where $\sigma(E)$ corresponds to the root mean square (RMS) of the cell energy and is dominated in the Run 2 data set by fluctuating incidental contributions from soft particles produced in other proton-proton collisions. Cells with $E > 4\sigma(E)$ seed the clustering algorithm, accumulating all neighboring cells (in all 3 spatial dimensions) with 2σ energies. Finally, all cells neighboring the 2σ cells which have positive energies are added to the topocluster [3]. Topoclusters may be split according to local maxima crite-

[3] Cells may have negative energies due to noise suppression corrections

ria. The topocluster four-vector is taken as the sum of the raw, energy-weighted components of the constituent calorimeter cells, and is set to have zero mass. The resulting topoclusters are defined at the *EM scale*, so that the energy of electromagnetic showers should be faithfully measured.

Topoclusters are combined using the anti-$k_\perp$ algorithm [102] with radius parameter $R = 0.4$ to form jets. The procedure iteratively combines topoclusters with the nearest anti-$k_\perp$ distance

$$d_{ij} = \min(k_{t,i}^{-2}, k_{t,j}^{-2}) \frac{\Delta R_{ij}}{R} \tag{4.2}$$

until no candidates for combination are within $\Delta R_{ij} < R$. The procedure is efficiently implemented in the `FastJet` package [103, 104].

Reconstructed jets are calibrated to ensure a jet energy scale (JES) that is in agreement with the particle-level prediction from MC simulation, and is independent of: the jet energy and position in the detector; the species of parton initiating the jet; the level of additional hadronic activity in the detector due to PU. A multi-step calibration procedure corrects for each effect [105]. Jet energies are corrected from the initially clustered values based on their supposed origin from the primary vertex found in the event. The large catchment area of jets[4] leads their measured energies to be susceptible to contributions from both particles produced in simultaneous collisions in the same proton-proton bunch crossing ("in-time PU") and in previous bunch crossing ("out-of-time PU"). Corrections are made by energy subtraction terms constructed from the global PU density ρ multiplied the jet area (accounting for in- and out-of-time effects) as well as a dedicated correction for in-time PU based on the number of reconstructed track vertices in the event. The response of jets of various momenta following the origin- and PU-corrected steps is shown in Figure 4.13. Corrections derived from MC simulation are then applied to these PU-corrected jets to calibrate them to the energy of the underlying truth particles. Residual variations in the jet response with the species of showering parton and the longitudinal structure of the jet's shower are calibrated in a subsequent step (the global sequential correction, GSC). Finally, dependence on the simulation is removed in data-based *in-situ* corrections, where jets energies are corrected to balance well-measured reference objects (i.e. photons, leptonic Z boson decays, and systems of other jets).

To distinguish PU jets from proton-proton collisions other than the one of interest as well as jets due to calorimeter deposits from multiple collisions ("stochastic jets"), charged particle tracks are used to assess the hypothesis that a jet is due to the primary hard-scatter event. To find the correspondence between jets and tracks the *ghost-association* procedure is used, whereby tracks are included in the jet clustering procedure with infinitesimal momenta. Any constituent ghost

[4] An $R = 0.4$ jet corresponds to 3.2% of the central detector volume $|\eta| < 2.5$.

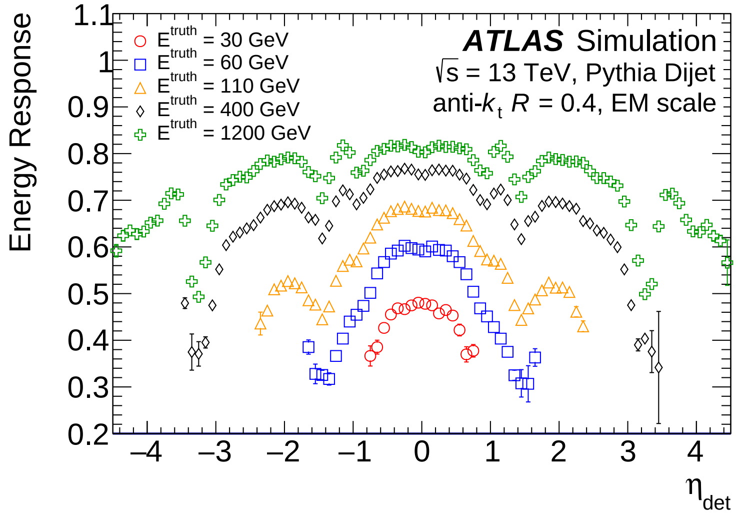

Figure 4.13: The jet response –the ratio of reconstructed to truth jet p_T– is shown as a function of pseudorapidity for a range of jet momenta. The only corrections to the jet energy already applied are the origin and PU corrections. Figure is reproduced from Ref. [105].

tracks are then associated to the corresponding calorimeter jet. The jet vertex fraction (JVF) is the p_T-weighted fraction of tracks associated to a jet that are matched to the primary vertex. The variable is subsequently corrected for dependence on the number of primary vertices. The ratio of the summed p_T of all such PV-associated tracks within a jet to the energy of the jet itself (R_{pT}) provides further information. These discriminants are combined using a likelihood-based approach to produce the jet vertex tagger (JVT) discriminant [106].

Flavor-tagging

Jets are identified as containing b hadrons using a boosted decision tree (BDT) multivariate algorithm to combine several lower-level algorithms targeting specific features of b hadron decays [107]. The IP2D/IP3D algorithm exploits the long lifetime of b hadrons through the track impact parameters d_0 and z_0 and their significances. A likelihood ratio technique incorporating track quality parameters is used to combine information from multiple tracks per jet. The secondary vertex (SV) algorithm considers two-track secondary vertex candidates, iteratively incorporating additional tracks and removing reconstructed any SVs due to long-lived particles and material interactions. The JetFitter algorithm [108] seeks to reconstruct the chain of b- and c-hadron decays inside jets by determining the flight path of the initial b hadron. This allows decays where only a single track is reconstructed to contribute information to the b jet hypothesis. These inputs are combined in the MV2c10 tagger, which uses a charm-enriched training sample (where the background jets are 7% charm and 93% light jets) to enhance the corresponding rejection power, as charms constitute the dominant background for many analyses. Multiple working points (WPs) are supported corresponding to b jet efficiency and light/charm-jet rejection factors. Scale factors are applied to MC simulation so that the efficiency is consistent with that measured in data.

4.4.5 Hadronic tau decays

Tau decays are split among the fully leptonic mode ($\mathcal{BR}(\tau^- \to \ell^- \bar{\nu}_\ell \nu_\tau) \approx 35\%$, $\ell = e, \mu$), other "one-prong" decays usually with a charged pion ($BR \approx 50\%$), and "three-prong" decays most often with three charged pions ($BR \approx 15\%$). Fully leptonic decays are inferred through reconstructed electrons and muons with accompanying $E_{\mathrm{T}}^{\mathrm{miss}}$, while hadronic tau decays are reconstructed using calorimeter jets, with the techniques detailed in Ref. [109]. Tau reconstruction is performed using $R = 0.4$ anti-$k_\perp$ calorimeter jets built from topo-clusters at the LC scale [110, 111]. The energies of these input clusters (different from the EM-scale inputs used in the jet reconstruction described in Section 4.4.4) are adjusted according to the cluster shape to account for different detector responses to electromagnetic and hadronic particle showers. The visible energy of the tau decay $\tau_{\text{had-vis}}$ p_{T} is set to the sum of cluster energies within $\Delta R < 0.2$ at the LC scale. One- and three-prong taus are reconstructed by determining the origin vertex of tracks associated with the $\Delta R < 0.2$ region (which may be different than the primary vertex (PV)) and requiring that either one or three tracks are matched to the vertex. Separate BDTs are trained for one- and three-prong tau candidates, based on inputs from the structure of the calorimeter shower and associated tracks. Selections targeting various signal efficiencies are defined, with efficiencies, scales, and resolutions calibrated using $Z \to \tau^+\tau^-$ events.

4.4.6 Missing transverse energy

Missing transverse energy ($E_{\mathrm{T}}^{\mathrm{miss}}$) is computed by summing visible object momenta in the plane transverse to the beamline (so that $p_{\mathrm{T}}^{\text{parton 1}} + p_{\mathrm{T}}^{\text{parton 1}} = 0$). The 2-dimensional vector $\vec{p}_{\mathrm{T}}^{\mathrm{miss}}$ denotes the quantity equal and opposite to this sum, while $E_{\mathrm{T}}^{\mathrm{miss}}$ is its magnitude. The visible objects included in the sum can be decomposed into those associated with the underlying hard-process, measured as electrons, photons, hadronic tau decays, muons, and jets, as well as those associated with the soft, unclustered energy deposits which may be accessed through charged particle tracks. Hard objects are selected which pass standard identification criteria and are accepted in the order listed above to avoid double-counting of energy deposits. For example, calorimeter deposits associated with an electron cannot be counted a second time for an identified tau lepton. Jets partially overlapping with other objects may fractionally contribute their energies. Particular care is taken in muon-jet overlap removal to remove jets due to catastrophic energy loss of muons in the calorimeter while retaining those due to muon final-state radiation (FSR). The soft term is built from quality tracks[5] associated to the PV and not with any other object, and as such is highly robust against variation in the number of simultaneous collisions. Complete details may be found in Ref. [112].

[5] No attempt is made to correct for soft neutral particles.

Chapter 5

Hardware Tracking for the Trigger

5.1 Trigger Upgrades for High Luminosity

The scope of the HL-LHC project [113] is to build on the physics capabilities of earlier LHC runs by collecting data from an unprecedented number of proton-proton collisions. The $3\,\mathrm{ab}^{-1}$ target data set size will be accomplished through a broad program of upgrades. These include upgrades to the LHC machine to enable the collision of proton-proton bunches at higher instantaneous luminosities as well as to the ATLAS detector so that these events may be effectively recorded and analyzed. A schedule of the coming LHC data-taking runs and upgrades is presented in Figure 5.1. The HL-LHC project will commence after the Phase-II upgrade to the ATLAS detector and is estimated to run from 2026 to 2038. The planned upgrades to the ATLAS detector to cope with the high-luminosity environment are described in a Letter of Intent [114], a Scoping Document [5], and Technical Design Reports for various detector sub-systems[6].

5.1.1 Physics Benchmarks

The requirements on the Phase-II upgrades to the ATLAS trigger system are driven by the physics goals of the HL-LHC. These include measurements of the new scalar particle observed in 2012 to assess its compatibility with the SM Higgs boson. In addition to precisely measuring its properties and couplings to the other SM particles, the HL-LHC presents the first opportunity to access the Higgs self-interaction through di-Higgs production. The large data set will also allow for improved measurements of the top-quark mass, scattering of vector bosons produced in association with high-mass jet pairs ($VVjj$), and electroweak precision observables in single W and Z events. The

[6] References to individual Technical Design Reports (TDRs) are provided in the relevant sections below.

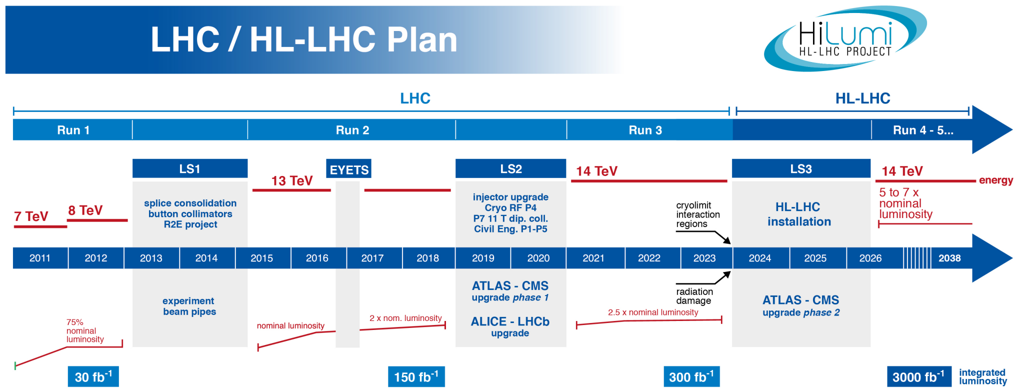

Figure 5.1: An overview of the LHC schedule, from the initial 7 TeV run to the ultimately-planned 14 TeV runs for the HL-LHC. At the time of writing, Run 2 has concluded, entering the period of Phase-I upgrades to the ATLAS detector. Run 3 will recommence at a planned energy of 14 TeV in 2021, after which data-taking will stop once more to allow for major Phase-II upgrades in 2024. This marks the beginning of the HL-LHC project, aiming to collect $3\,\text{ab}^{-1}$ of collision data over 10-12 years. Figure is reproduced from Ref. [10].

discovery potential for signatures of New Physics will also be significantly extended, particularly for scenarios with electroweak production cross-sections, compressed mass spectra, and unconventional signatures. For many of these targeted examples, the quality of future searches measurements relies on maximizing the trigger acceptance to each signature. As representative examples, we consider the case of SM (non-resonant) di-Higgs production and compressed SUSYin further detail.

The SM predicts a value of the Higgs boson self-coupling

$$\lambda_{hhh} = \frac{1}{2}\left(\frac{m_h}{v}\right)^2 \approx 0.13, \tag{5.1}$$

where m_h is the observed value of the Higgs mass and v the Higgs VEV (for a more detailed discussion see Section 2.2). The parameter can be extracted by measuring the production of pairs of Higgs bosons, which dominantly occurs through two diagrams and destructively interfere. These are shown in Figure 5.2. The first involves an s-channel h^* decaying to two (dominantly on-shell) Higgs bosons and the second a box loop of top quarks. Only the first is proportional to λ_{hhh}. The most promising channels to measure the rate of such events are in decays $hh \to b\bar{b}b\bar{b}$, $b\bar{b}\tau^+\tau^-$, and $b\bar{b}\gamma\gamma$. The sensitivity of the $b\bar{b}b\bar{b}$ and $b\bar{b}\tau^+\tau^-$ channels will completely rely on the ability to efficiently trigger on relatively low-energy b jets and hadronic tau candidates. Figure 5.3 shows the sensitivity of the $hh \to b\bar{b}b\bar{b}$ and $b\bar{b}\tau^+\tau^-$ analyses to the p_{T} requirement on the least-energetic jet or hadronic tau object. This dependence is used to set the requirements on the multi-jet and hadronic tau triggers to be used to collect HL-LHC data.

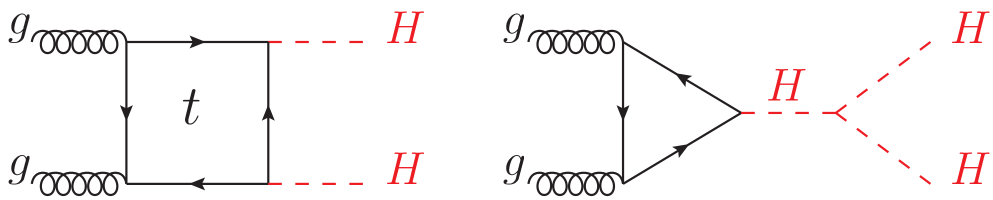

Figure 5.2: Feynman diagrams are shown depicting the dominant contributions to the $gg \to hh$ process. The box diagram with intermediate top quarks is shown at left, while the diagram with s-channel Higgs is shown at right. Only the second depends on the Higgs self-coupling. Figure reproduced from Ref. [1].

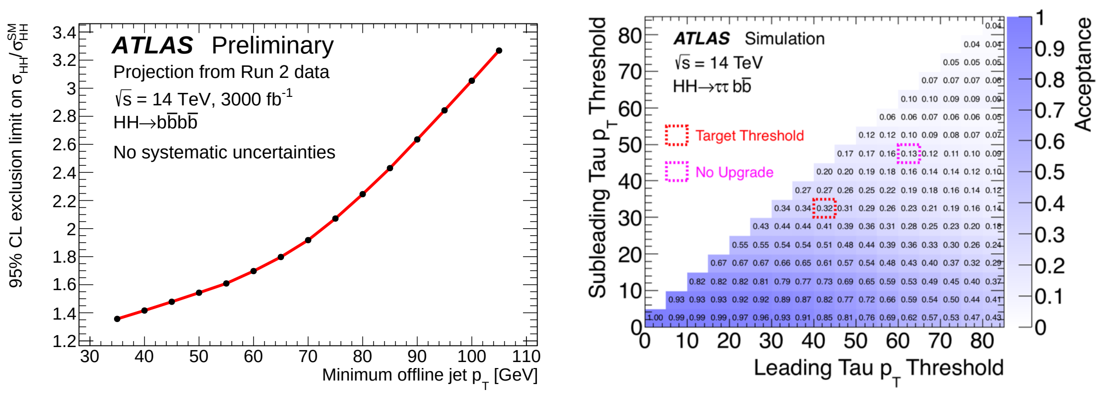

Figure 5.3: At left, the sensitivity of the $hh \to b\bar{b}b\bar{b}$ analysis to the p_{T} requirement on the fourth most energetic jet is shown. This is quantified by the corresponding excluded value of the di-Higgs production cross section with respect to the SM prediction $\sigma_{hh}/\sigma_{hh}^{\mathrm{SM}}$ as determined by a projected analysis of the full HL-LHC data set [115]. No systematic uncertainties are included and no combination is made with other decay channels. At right, the relative acceptance of the $hh \to b\bar{b}\tau^+\tau^-$ process as a function of the leading and sub-leading hadronic tau p_{T} thresholds is shown. Acceptances are highlighted which correspond to the capabilities of the current trigger system and proposed upgrades [10].

So-called "natural" scenarios of SUSY predict relatively light supersymmetric partners of the gluon, top quark, and electroweak bosons [116]. In general, the limits on gluino and stop sparticle masses will not significantly improve with additional data. This is because they may be pair-produced via the strong interaction and thus have large enough cross sections that large numbers of events should have already been seen, even for TeV-scale sparticle masses. However, limits on the allowed masses of the super-partners of the electroweak bosons are much weaker in scenarios where they are the only light sparticles, as they must be produced from s-channel W and Z bosons. In the naturalness-motivated scenario with a Higgsino LSP, a triplet of states is predicted with $\mathcal{O}(\mathrm{GeV})$ mass splittings. Cascade decays of these states to stable, undetectable LSPs via emission

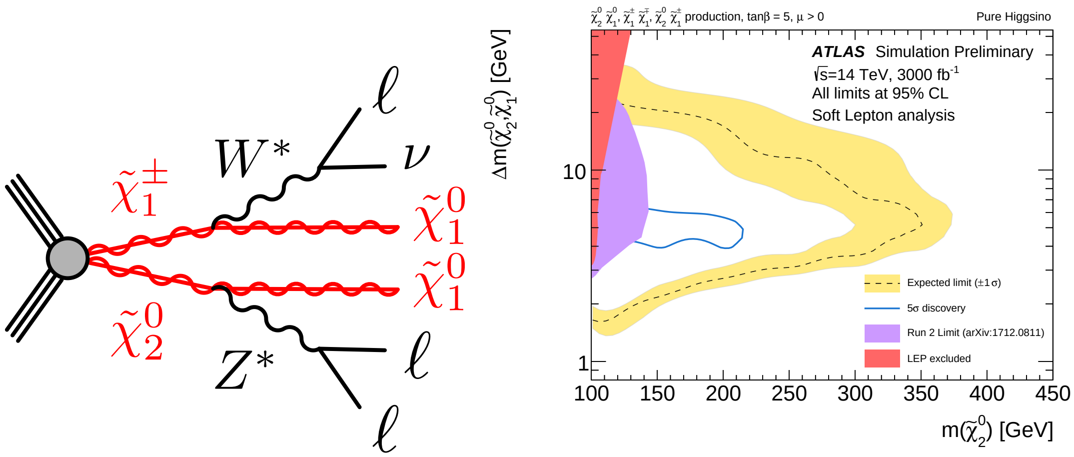

(a) (b)

Figure 5.4: At left, an illustration is shown of the $\tilde{\chi}_2^0\tilde{\chi}_1^{\pm}$ production process that leads to signatures with three leptons and missing transverse momentum. At right, the projected sensitivity of analyses of the full HL-LHC data set are shown as a function of the mass splitting of the electroweak super-partners [117].

of electroweak bosons, picture in Figure 5.4a, leads to a challenging signature with moderate $E_{\mathrm{T}}^{\mathrm{miss}}$ and multiple low-p_{T} leptons. The projected sensitivity to such scenarios was studied in Ref. [117] and is summarized in Figure 5.4b. Depending on the details of the model, triggers requiring $E_{\mathrm{T}}^{\mathrm{miss}}$, leptons, or a combination of both can provide the best signal acceptance. These are shown for benchmark SUSY model with $m_{\tilde{\chi}_2^0} - m_{\tilde{\chi}_1^0} = 20$ and 40 GeV in Figure 5.5.

5.1.2 Improvements from Hardware Tracking

The baseline Phase-II TDAQ upgrade is an extension of the two-level concept used in Run 2. The first level is the hardware-based Level-0 Trigger (L0 Trigger), which targets an output rate of 1 MHz (increased from 100 kHz in Run 2) and the second is the software-based Event Filter (EF), which shall ultimately select events at a 10 kHz rate (increased from the 1 kHz output rate of the HLT in Run 2). A second, evolved option is also being maintained that adds an intermediate hardware-based selection level. In the evolved scenario the L0 Trigger output is increased up to 4 MHz with a L1 Trigger output rate of 600 kHz (a variant with 2 MHz and 800 kHz rates, respectively, is also possible). A schematic overview of the evolved system design is shown in Figure 5.6.

In the baseline system, no tracking information is incorporated at the hardware level, with L0 Trigger rates controlled solely by upgrades to the readout and trigger electronics for the calorimeter

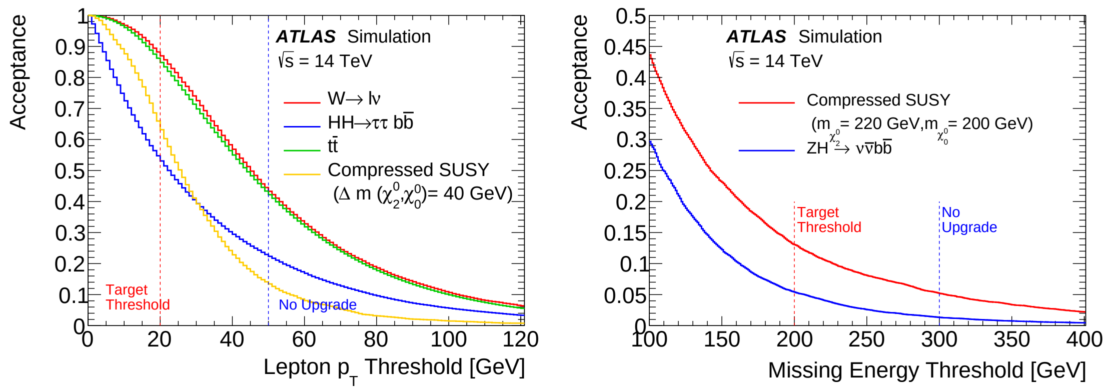

Figure 5.5: At left, the change in acceptance is shown as a function of the leading lepton p_{T} requirement for a variety of signal models. The SUSY scenario corresponds to the $\tilde{\chi}_2^0\tilde{\chi}_1^{\pm} \rightarrow W^{\pm *}\tilde{\chi}_1^0 Z^* \tilde{\chi}_1^0$ process with a mixture of Bino- and Higgsino-like light sparticle states, with $m_{\tilde{\chi}_2^0} - m_{\tilde{\chi}_1^0} = 40\,\mathrm{GeV}$. Leptonic decays of the W and Z bosons are assumed. Lowering the trigger lepton p_{T} threshold from 50 to 20 GeV improved the acceptance by more than a factor of four. (A factor of two improvement is also seen for the $hh \rightarrow b\bar{b}\tau^+\tau^-$ signature where one tau decays fully leptonically). At right, a similar comparison is shown as a function of the requirement on $E_{\mathrm{T}}^{\mathrm{miss}}$, now for a model with $m_{\tilde{\chi}_2^0} - m_{\tilde{\chi}_1^0} = 20\,\mathrm{GeV}$, essentially inaccessible with lepton triggers. Both sub-figures are reproduced from Ref. [10].

and muon systems. This information can also be further combined in the Global Trigger, a new sub-system considering full event data in an array of multiplexed field programmable gate arrays (FPGAs). The Hardware Tracking for the Trigger (HTT) system would act as a co-processor to the EF, providing tracks for a wide range of algorithms, such as object-to-vertex association, tau identification, b tagging, and building a $E_{\mathrm{T}}^{\mathrm{miss}}$ soft term. It's design and implementation build on the work of previous track triggers at the ATLAS (FTK [118]) and Collider Detector at Fermilab (CDF) (Silicon Vertex Tracker (SVT) [119]) experiments. In the evolved system tracks may also be used by the Global Trigger in the intermediate L1 Trigger, mainly to improve the reconstruction of hadronic and multi-object signatures.

Multi-jet Triggers

Focusing on the evolved scenario, the HTT system would significantly improve the trigger thresholds for the multi-jet and di-tau triggers necessary for the $hh \rightarrow b\bar{b}b\bar{b}$ and $hh \rightarrow b\bar{b}\tau^+\tau^-$ analyses. A large fraction of the four-jet trigger rate after an L0 Trigger accept is due to multiple high-p_{T} di-jet systems originating from the different proton-proton collisions. Because the luminous region is significantly extended in z (with a 3σ region of $|z| < 15\,\mathrm{cm}$), information from tracks associated to jets can be

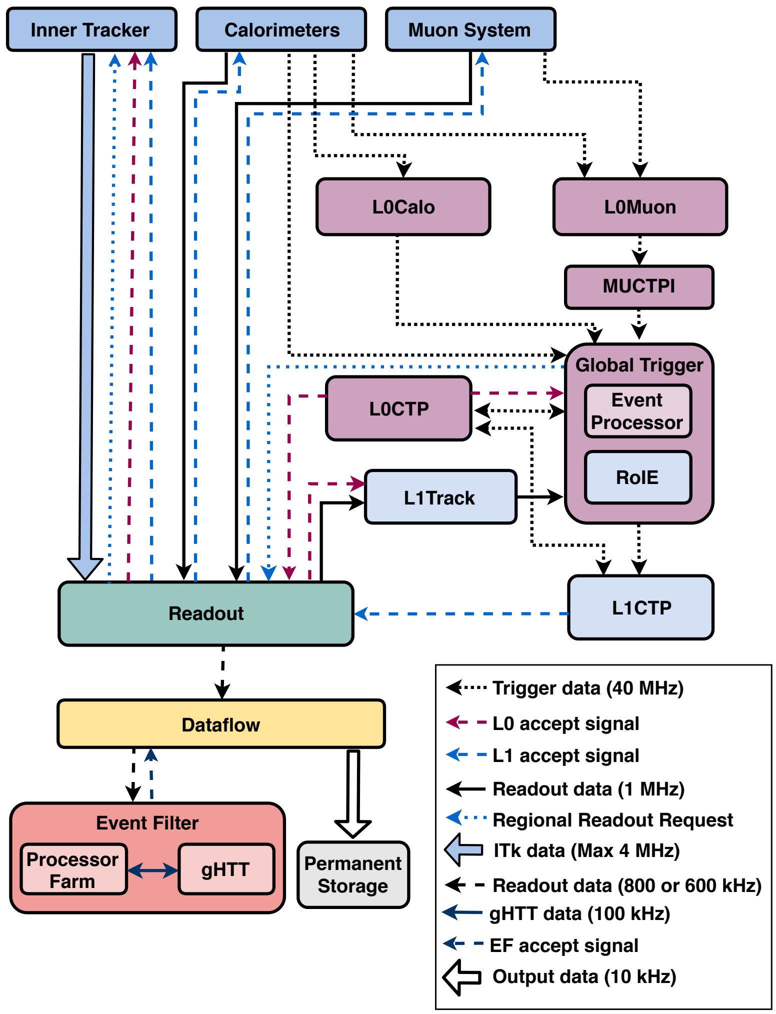

Figure 5.6: A schematic outline of the evolved Phase-II TDAQ system is shown [10]. Components of each of the three logical levels of the system are indicated, as well as the connecting trigger and readout paths. Compare to the layout of the Run 2 TDAQ system shown in Figure 4.8.

used to test the hypothesis that all jets have originated from a common vertex. In practice this can be accomplished with algorithms of varying complexity, two of which are illustrated in Figure 5.7. The figure shows a study using offline objects to set requirements on the track parameter resolutions needed in the case of each algorithm.

In both cases, tracking is run in ROIs with size 0.8×0.8 about the center of the jet, with tracks within $\Delta R < 0.4$ associated to the corresponding jet. An overlap removal procedure is enforced so that tracks matching to multiple jets are associated to the higher-energy jet. In the 'window' algorithm, a variant of the vertex-finding algorithm described in Section 4.4.1 is performed, with a z-binned histogram filled with each track of each jet. If any bin (corresponding to a particular 'window' in z) contains contributions from tracks belonging to at least N of the jets, the algorithm is passed. The track p_{T}, z histogram window size, and number N of jets contributing to the vertex are configurable parameters. Figure 5.7 shows the efficiency of $hh \to b\bar{b}b\bar{b}$ signal and minimum-bias background events passing a L0 Trigger `4j40` requirement to also pass the vertexing algorithm for a range of parameter requirements and 3-of-4 jet logic. A more complex JVF-based algorithm is also considered, where a JVF score (see Section 4.4.4) is calculated for each jet with respect to the maximum $\sum p_{\mathrm{T}}^2$ vertex and a minimum requirement is made on all or most of the jet scores.

$E_{\mathrm{T}}^{\mathrm{miss}}$ Triggers

The HTT system can be used in a similar way to improve the L0 Trigger $E_{\mathrm{T}}^{\mathrm{miss}}$ trigger decision. Due to the high-PU environment of the HL-LHC, the cell- and cluster-based $E_{\mathrm{T}}^{\mathrm{miss}}$ constructions are not projected to be feasible. Instead, the $\vec{H}_{\mathrm{T}}^{\mathrm{miss}}$ approach will be used, where the magnitude of the vector sum over L0 Trigger jets is taken as an estimate of the $E_{\mathrm{T}}^{\mathrm{miss}}$. HTT tracks would improve the performance by enabling $\vec{H}_{\mathrm{T}}^{\mathrm{miss}}$ to be built only from jets consistent with the primary vertex. The gain in performance is shown in Figure 5.8a as a function of the track p_{T} threshold available. This reduces the number of jets used in the sum and thus the susceptibility of the calculation to random energy measurement fluctuations due to the significant jet energy resolution (JER) of trigger-level jets. Further possible improvements to the $E_{\mathrm{T}}^{\mathrm{miss}}$ estimation with HTT include track-based energy corrections similar to those described in Section 4.3.2. Global tracking (not only confined to jet ROIs) also provides the possibility to estimate the soft-term in an offline-like manner.

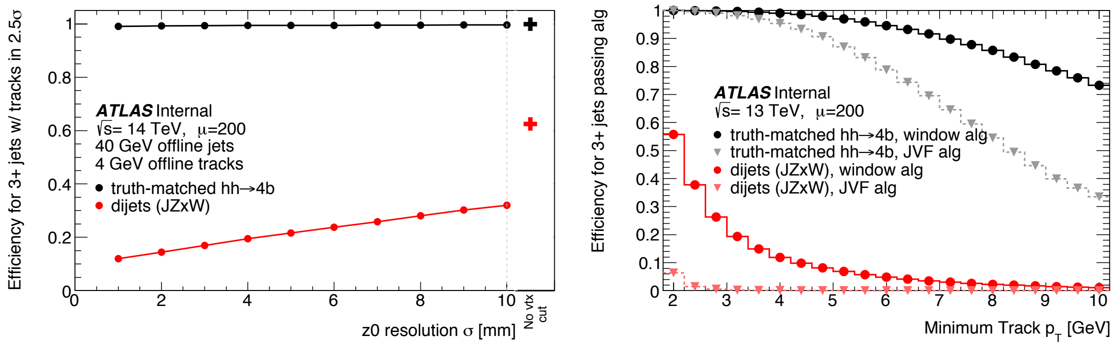

Figure 5.7: The efficiency is shown for events with four 40 GeV jets to satisfy a common vertex requirement is shown for a $hh \to b\bar{b}b\bar{b}$ signal process and for minimum bias events with $\langle\mu\rangle = 200$. Results are shown for the 'window' and JVF algorithms described in the text, where three of the four jets are required to satisfy the vertex criteria. Each plot shows the dependence of the algorithm performance on a fundamental parameter of the Level-1 Track Trigger (L1 Track) system: at left the resolution of the impact parameter along z, and at right the minimum p_{T} of the tracks provided. Tracks are associated to vertices with a characteristic size of $2.5\sigma(z_0)$, which is allowed to float with the track resolution considered. At left, efficiencies are shown for the window algorithm when 4 GeV tracks are considered, demonstrating a background rejection factor of 5x in the case where $\sigma(z_0) < 4$ mm. The rightmost point corresponds to no vertex cut, where only a requirement that one or more track be matched to the jets is enforced. The algorithm is over 99% efficient for the signal process for all working points. At right, the minimum track p_{T} is scanned, while the resolution is fixed at 2 mm. Results are shown for both the window (circle markers) and JVF algorithms (triangles). The more sophisticated JVF algorithm allows for significantly improved background rejection but provides lower signal efficiency, particularly for a minimum track p_{T} greater than 3 GeV.

Lepton Triggers

Finally, the HTT system would yield improved lepton triggers by requiring that an HTT track be found in an ROI near the reconstructed EM cluster or MS track. This allows a requirement to be placed on the more precise, track-based momentum measurement to further reduce the rate of backgrounds. For a working point 95-97% efficient for signal electrons, a rejection factor of 5x (3x) is estimated for the one- (two-)electron rate for a 20 GeV (10 GeV) threshold. A factor of 4x rejection is anticipated for the di-muon rate [10]. Efficiencies for single-particle triggers at the 10 GeV threshold are shown in Figure 5.8b. Further, isolation requirements could also be enforced using nearby tracks found in a cone about the lepton candidate. Tau identification is also possible through a consistency check of the one- or three-prong decay hypothesis.

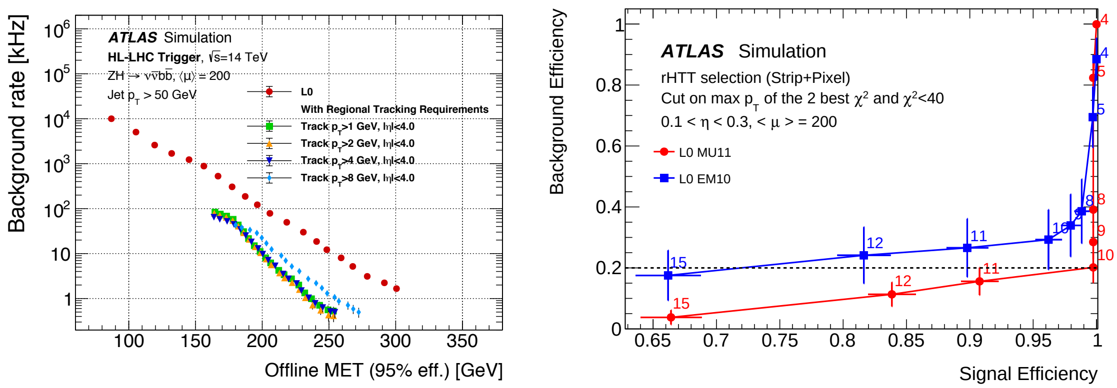

(a) (b)

Figure 5.8: At left, $E_{\mathrm{T}}^{\mathrm{miss}}$ trigger rates are shown as a function of the value of offline $E_{\mathrm{T}}^{\mathrm{miss}}$ for which the triggers become 95% efficient in $Zh \to \nu\bar{\nu}b\bar{b}$ events. In red circles, the trigger met is constructed as $\vec{H}_{\mathrm{T}}^{\mathrm{miss}}$ from all 50 GeV trigger jets, while for the remaining points HTT tracks are used to enforce vertex-matching criteria. Scenarios using tracks with minimum p_{T} ranging from 1 GeV to 8 GeV are shown. At right, minimum-bias background and real-lepton signal efficiencies are compared for events passing L0 Trigger electron (blue square) and muon (red circle) items. Requirements on the reconstructed HTT track $p_{\mathrm{T}}$are scanned, with specific requirements labeled on the Figure in GeV.

5.2 System concept

As discussed in the previous section, information from charged particle tracks is broadly useful in the trigger for identifying interesting signatures. The necessary track quality also significantly depends on the specifics of each algorithm, with fast estimates appropriate for requirements such as vertex association while greater precision is needed for b tagging and similar. The HTT system is designed to provide widespread tracking at the hardware and EF levels, with significant flexibility afforded by a two-stage design. The first stage of the system solves the problem that the number of track fits diverges combinatorially with large hit densities, though a pattern-based hit filter. Multi-layer sets of hits are retained only if they are consistent with a bank of patterns pre-stored in associative memory (AM) application-specific integrated circuits (ASICs). Patterns use a subset of the detector layers: typically eight of the nine outermost strip and pixel layers. Only hit sets associated to a matched pattern are passed to an FPGA which performs track fits, based on a local, linear approximation. These eight-layer tracks can be either directly passed to the component of the TDAQ system requesting a first-stage track (i.e. EFor L1 Track) or a second-stage fit can be performed. The second stage extrapolates the first-stage track into the remaining detector layers (in the barrel region this leads to a 13-layer track candidate) and performs another linear fit.

5.2.1 Impact of Baseline and Evolved Scenarios

In the baseline scenario, the HTT system functions purely as a co-processor to the EF, providing tracks on-request depending on the L0 Trigger that fires. The system is divided into two logical components, Regional Hardware Tracking for the Trigger (rHTT) and Global Hardware Tracking for the Trigger (gHTT). The rHTT system would provide tracks within ROIs associated with L0 Trigger trigger objects for use in EF decisions. This tracking would only be run on a subset of L0 Trigger items, processing an average of 10% of Inner Tracker (ITk) data at the 1 MHz rate. Such tracks are to be reconstructed in a single stage using the outermost detector layers targeting fast, efficient reconstruction with acceptable track parameter resolutions. Only tracks with p_{T} greater than 2 GeV will be reconstructed. The gHTT system is design to provide full-event track reconstruction at a rate of 100 kHz, including two reconstruction stages that make use of all layers of the detector. These near-offline-quality tracks would be reconstructed with a threshold of $p_{\mathrm{T}} > 1$ GeV and used for b tagging, $E_{\mathrm{T}}^{\mathrm{miss}}$ reconstruction, and lepton isolation.

In the evolved scenario the single-stage regional tracking system becomes a part of the L1 Trigger, providing inputs to the Global Trigger. These would include either tracks with $p_{\mathrm{T}} > 4$ GeV at a 4 MHz input rate or 2 GeV at 2 MHz. Instead of receiving ITk data over a network, the HTT receives it from the Front-End Link Exchange (FELIX) interface to the ITk front-end. This imposes a latency requirement of 30 μs on the entire L1 Trigger system, with the L1 Track component allowed a budget of 6 μs. The gHTT system would function similarly to the baseline scenario in this case. A smaller EF input rate in this scenario (600-800 kHz instead of 1 MHz) lowers the required readout rate of the ITk pixel system. It also allows for lower hadronic trigger thresholds at L0 Trigger, with L1 Track information used in Global Trigger algorithms chiefly to reduce rates of $E_{\mathrm{T}}^{\mathrm{miss}}$, multi-jet, and di-tau triggers.

5.2.2 Pattern Recognition

The goal of the pattern recognition step of the first stage is to reduce the number of tracks to be fit without compromising the track-finding efficiency. This is done by only fitting sets of hits consistent with a realistic track, i.e. those corresponding to a 'pattern'. Patterns are composed of groups of individual silicon sensors across multiple layers of the ID. In each layer of the detector, individual strips and pixels are grouped into one- or two-dimensional arrays denoted super-strips (SSs). A pattern is a set of SSs across multiple layers of the detector. Typically eight-layer patterns are considered in the central barrel region of the detector.

For a typical bank of patterns in the HTT system, SS sizes of 40 silicon strips and 33×403 pixels in $\eta \times \phi$ are used. Each of the possible SSs are denoted by a unique super-strip identifier (SSID) indicating the set of strips and pixels which must contain a hit for a pattern to fire, so that patterns are defined by a set of SSIDs for each detector layer. In strip layers, for example, an SSID of 00001_2 may correspond to hit clusters on strips 40 through 79.

As hit clusters from real tracks are usually less than a few strips or pixels in each dimension, the patterns are very 'wide' – patterns occupy a much larger larger volume in coordinate space than a track. For real HL-LHC conditions, the majority of matched patterns ('roads') will be due to random coincidences of hits across multiple layers, so that the rate of matched patterns depends on the product of SS sizes (and occupancies) across all layers. The don't care (DC) bit (also *ternary* bit) mechanism allows this volume to be tuned on a per-pattern basis.

Setting a DC bit in a single layer allows patterns with two different SSIDs to be combined. For example, setting the ternary bit (denoted 'X') to produce an SSID 0000X will match all hits with either SSID 00000 or 00001, i.e. strips with index 0 to 79 in the example above. Multiple DC bits may be set per layer, with N_{DC} increasing the effective SS size by a factor of $2^{N_{\mathrm{DC}}}$. DC bits may be set in multiple layers for a given pattern. Controlling the number of total DC bits to be set and the maximum number allowed in each layer gives precise control over the pattern bank performance. There is a distinction made between patterns and SSIDs with and without DC bits set, which is especially important for simulation in particular as the latter can always be re-derived from the former with re-configured DC bit settings. Patterns formed from binary SSIDs are denoted as thin-strip patterns (TSPs), with the binary SSIDs also denoted TSP SSIDs at times. Ternary bits are added to form the final patterns loaded into the AM chips, which are denoted as AM patterns, built from the ternary AM SSIDs with DC bits optionally set.

While DC bits allow pattern volumes to be reduced and thus reduce the fake rate of matched patterns due to random hit combinations for a given true track-finding efficiency, majority logic and wildcards (WCs) are required to maximize the efficiency of finding true tracks. True tracks may not leave hits in all layers used in the pattern-matching stage due to detector geometry, inactive material, non-functional modules, and sensor inefficiency, for example. One solution is to consider all patterns matched which have hits corresponding to $N-1$ or $N-2$ of the N layers (often denoted at 6/8 or 7/8 logic in the $N = 8$ layer case). However, a more nuanced strategy is possible if the location of the missing hits can be anticipated, as in the case of geometric inefficiency or known dead modules. In this case, a WC may be set on a per-pattern basis, essentially replacing the dead module (or similar) with a hit for every event. This way, patterns with $N-1$ hits are not fired if

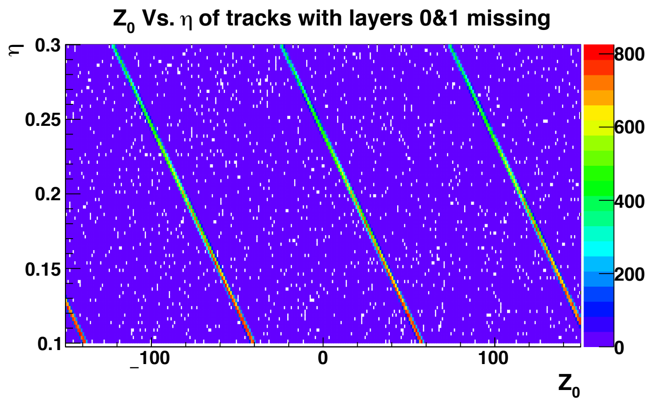

Figure 5.9: The η and z coordinates are shown for simulated muon tracks with misses in the first two ITk strip layers, corresponding to both components of the first double-sided layer. Due to correlated positions of the inactive material (sensor gaps) in each layer, a miss in one layer may accurately a missing hit in the second. This information can be used to set two WCs only for the patterns which correspond to tracks likely to fall outside the active area of the sensors in each layer. Figure is reproduced from Ref. [10].

the miss is in the wrong layer. Figure 5.9 shows the impact of correlated misses among double-sided strip layers, which can be mitigated by setting appropriate wildcards.

A bank of TSP patterns may be built from a set of muon tracks whose trajectories through the ITk have been simulated. For a given set of SS sizes, these tracks may be converted into SSIDs in the selected layers and banks of N-layer patterns (and potentially $N-1, N-2, \ldots$ if using wildcards) may be constructed. In a post-processing stage, this bank may be converted into the final AM pattern bank by setting WCs and DC bits. If a pattern is matched, a pattern identifier is passed to the track fitting machinery, in addition to the hits in each of the layers with SSIDs that match that of the AM pattern.

5.2.3 Track Fitting

The problem of track fitting is to determine the helix parameters corresponding to a charged particle track that has left hits in the detector. The central concept of the HTT fast track fitting procedure is that this relationship is approximately linear over a sufficiently small region in the space of helix parameters. In practice this is done by defining regions where each of the particular linear maps are valid (*sectors*) and by obtaining the linear coefficients (*constants*) for each map to be used in the fitting procedure. The constant banks can then be loaded into the local memory on HTT track-fitting boards to perform fits in real time.

Let x_i denote the vector of hit coordinates associated with a given track, where $i \in \{1, \ldots, N\}$ with N the total number of coordinates. The individual elements of the vector may correspond to local hit measurements in unique layers of the tracking detectors or to measurements in different dimensions by the same detector layer (i.e. for the silicon pixel detector). Let q_i denote the five true helix parameters of the track, taken here as $(p_T, \eta, \phi, d_0, z_0)$. The goal is to express the helix parameters as a linear function of the hits

$$q_i \approx \hat{q}_i \equiv c_{ij} x_j + k_i \tag{5.2}$$

so that the helix parameters q'_i of a similar track with hit parameters x'_i can be well-approximated by applying the same fit constants c_{ij} and k_i as for the original track. In the HTT system, the same constants are used for all sets of hits which are recorded in the same set of unique silicon sensors, usually distributed across multiple physical detector layers.

For each sector, fit constants can be obtained from a large sample of simulated muons, where both the hit information and truth track parameters are known. Henceforth consider a single sector, and let c_{ij} and k_i denote the constants to be determined. The constants can be found by minimizing the square difference between the true q_i and approximated $\hat{q}_i$ track parameters

$$\langle (q_i - \hat{q}_i)^2 \rangle = \langle (q_i - (c_{ij} x_j + k_i))^2 \rangle \tag{5.3}$$

over all tracks. Differentiating this expression with respect to k_l gives

$$\begin{aligned} 0 &= \frac{\partial}{\partial k_l} \langle (q_i - \hat{q}_i)^2 \rangle && (5.4) \\ &= \frac{\partial}{\partial k_l} \left[k^2 - 2 c_{ij} \langle x_i \rangle k_j - 2 k_i \langle q_i \rangle \right] && (5.5) \\ &= 2(k_l - c_{li} \langle x_i \rangle - \langle q_l \rangle) && (5.6) \\ & && (5.7) \end{aligned}$$

yielding the relation that

$$k_i = c_{ij} \langle x_j \rangle + \langle q_i \rangle \tag{5.8}$$

Now, differentiating with respect to c_{lm} gives

$$\begin{aligned} 0 &= \frac{\partial}{\partial c_{lm}} \langle (q_i - \hat{q}_i)^2 \rangle && (5.9) \\ &= \frac{\partial}{\partial c_{lm}} \left[c_{ij} c_{kj} \langle x_i x_k \rangle - 2 k_i c_{ij} \langle x_j \rangle - 2 c_{ij} \langle x_i q_j \rangle \right] && (5.10) \\ &= 2(c_{li} \langle x_i x_m \rangle - k_l \langle x_m \rangle - \langle x_l q_m \rangle) && (5.11) \\ & && (5.12) \end{aligned}$$

Combining this with Equation 5.8 and defining $V_{ij} = \langle x_i x_j \rangle - \langle x_i \rangle \langle x_j \rangle$ this gives

$$
\begin{aligned}
0 &= c_{li}\langle x_i x_m \rangle - (c_{li}\langle x_i \rangle + \langle q_l \rangle)\langle x_m \rangle - \langle x_l q_m \rangle && (5.13)\\
&= c_{li} V_{im} - \langle q_l \rangle \langle x_m \rangle - \langle x_l q_m \rangle && (5.14)\\
&= c_{li} V_{im} V^{-1}_{mj} - (\langle q_l \rangle \langle x_m \rangle + \langle x_l q_m \rangle) V^{-1}_{mj} && (5.15)\\
& && (5.16)
\end{aligned}
$$

and thus

$$c_{ij} = (\langle q_i \rangle \langle x_k \rangle + \langle x_i q_k \rangle) V^{-1}_{kj}. \tag{5.17}$$

The quality of a fit is excellent while x_i is near the average value $\langle x_i \rangle$, with the error being proportional to their square difference due to the limitation of the linear approximation. A useful quality metric is the χ^2, which further accounts for correlations among the coordinates and is computed as

$$\chi^2 = (x_i - \langle x_i \rangle) V^{-1}_{ij} (x_j - \langle x_j \rangle) \tag{5.18}$$

In order to fit tracks and compute a χ^2 value for each one, one must store the constants c_{ij} ($5N$ numbers), k_i (5 numbers), and V^{-1}_{ij} ($N(N+1)/2$ numbers, as V is symmetric). The number of parameters stored for V may be reduced by accounting for correlations among hits due to the constraint that they originate from a physical track. Thus, the eigenvalue decomposition of the (symmetric) matrix $V^{-1} = U^T \Lambda U$ is useful, with U a matrix of unit-normalized eigenvectors (let the components u_{ij} of U be the i component of vector j) and Λ a diagonal matrix of eigenvalues. Five eigenvalues will be nearly zero due to the track constraint, which can be dropped from the χ^2 computation. Thus, defining $A_{ij} = u_{ij}$ and $B_i = u_{ij}\langle x_j \rangle$, with $i = 1, \ldots, N-5$ indexing only the eigenvector components associated with the non-singular eigenvalues, the χ^2 can be approximated as

$$\chi^2 \approx (A_{ij} x_j - B_i)^2 \tag{5.19}$$

This requires storing $N(N-5)+(N-5) = (N+1)(N-5)$ numbers. However, this is only fewer than the $N(N+1)/2$ numbers before eigen-decomposition for $N < 10$. The real benefit of this approach is in reducing the number of sums and multiplications the FPGA must compute. Multiplying an $m \times n$-dimensional matrix $n \times p$-dimensional matrix requires mnp multiplications and $m(n-1)p$ sums. Thus the original χ^2 requires $N^2 + N$ multiplications and $N^2 + N - 1$ adds ($N \times N$ by $N \times 1$ then $1 \times N$ by $N \times 1$) while the approximate calculation requires $(N-5)N + (N-5) = (N+1)(N-5)$ multiplies and $(N-5)N + (N-5) + (N-6) = (N+2)(N-5) - 1$ adds, both improvements for all

N. In the case of tracks contained entirely in the barrel region of the ITk detectors ($|\eta| \lesssim 1$), hits in five pixel and four double-sided strip layers may be used, so that the hit vector is 18-dimensional. This requires $5 \cdot 18 + 5 = 95$ constants to be stored for track fitting (using $5N = 90$ multiplies and $5(N-1) + 5 = 5N = 90$ adds per fit). In addition, 247 constants are needed for the χ^2 calculation, each of which uses 247 multiplies and 259 adds (versus 152 constants, 380 multiplies, and 379 adds without eigen-decomposition).

In the first stage, the hits to be fit are determined by the matched patterns. If hits are present in all N layers, the corresponding constant set is retrieved based on the pattern identifier so that the fit proceeds with the full coordinate set. The track χ^2 is also computed, with tracks only retained if a loose requirement is satisfied.

Fits with $< N$ layers must be conducted when either hits are not present in each of the N layers (missing coordinates) or if the χ^2 for the N-layer track is poor (a *recovery fit*). This requires a modification to the N-layer fit procedure either by: using a separate, lower-dimensional constant set, or; substituting *dummy* hit coordinates into the fully-dimensional constant set. Both strategies have been investigated in the context of the HTT system, with each incurring costs in different parts of the system (memory versus fit resources). In the latter configuration, hit coordinates are guessed which minimize the χ^2 of the corresponding track fit. At this point, the resulting first-state fit tracks may be passed back to the EF or extrapolated into the remaining layers of the detector for an expanded second-stage fit, making use of the additional coordinates.

An overlap removal (historically denoted as the 'Ghostbuster' or hit warrior (HW) algorithm) may also be applied (at several possible stages) to reduce the number of tracks which share common coordinates. The algorithms removes tracks which share hits in common, deciding which to retain based on the χ^2 of each fit and the number of hits associated to each track. Often first-stage tracks are required to have at least three unique hits.

5.2.4 Extrapolation and Second-Stage Fit

First-stage tracks are associated to the additional detector layers used in the second-stage fit with a two-step extrapolation procedure. Recall that a fit sector (the region over which a particular set of fit constants is valid) is defined to be a union of single modules in each layer of the detector. A single first-stage sector, built from modules in each of the first-stage layers, may correspond to a subset of second-stage sectors. This is to say that multiple 13-layer sectors (in the ITk barrel, for example) may share the same 8-layer subset in the first-stage layers. A *connection* denoted the association of a first-state sector to a second-stage sector, so that many potential connections are possible per first-stage sector. For each connection, the corresponding all-layer fit constants may be used to extrapolate the first-stage track into the remaining modules using the same hit-guessing machinery described in the previous section. The extrapolation window may be set on a per-layer basis to optimize the extrapolation efficiency for true tracks, with all hits falling within the window considered in the all-layer fit. Thus for each connection and for each all-layer hit combination a full fit is executed.

A similar set of configurable parameters is available to the second stage as is used in the first-stage. In addition to the number of connections considered per first-stage track and the range ('window') of hit coordinates considered about the extrapolated ('guessed') coordinate, hits may be required in only a subset of the new layers. In the barrel, typically only three or four hits are required in the five additional layers, with wildcards also considered, with dedicated $N - 1$ hit constant sets used to anticipate missing hits. Variable requirements on the track χ^2 can also be used to run recovery fits and control the rate of fake tracks. Overlap removal criteria may also be set in a manner similar to that described for first-stage tracks, with at least six of thirteen hits often required to be unique.

5.3 Simulated Performance

The performance of the HTT system design has been simulated using the `FTKSim` package originally developed for the FTK [118] and the online SVT [119] for the CDF experiment. Each conceptual step of the track finding and fitting processes is implemented in the simulation, though not in a manner designed to perfectly match the hardware implementation of each process. For example, constants are stored with floating-point precision instead of fixed-point, and data organization and pathways are simplified. This allows for increased simulation speed, simplified design, and quick configurability. Separate bit-level simulations of low-level processes exist elsewhere and are planned to be integrated into the developing `HTTSim` software framework.

The HTT system must achieve high efficiency for real tracks while achieving a low rate of fake tracks. The real track efficiency can be studied in detail by considering single muon events. Performance is also checked in single pions and electrons, for which efficiencies can be lower due to bremsstrahlung and multiple scattering. Fake track rates are studied using minimum-bias events, where true tracks with p_{T} above several GeV from PU collisions are generally rare, compared to matches from random coincidences of hits from various low-p_{T} tracks. For ROI-seeded tracking, the rate of tracks within jets is also relevant, producing a larger track rate.

As the HTT system is not yet fully defined, a number of configurations were compared to optimize the system design parameters. A region in the central barrel was selected to measure the performance using the latest available ITk geometry[7] The region with $0.1 < \eta < 0.3$ and $0.3 < \phi < 0.5$ is studied (roughly corresponding to the single hardware processor unit described below), which is covered by the five concentric pixel layers and four double-sided strip layer of the ITk. Based on earlier optimizations prior to the release of the Phase-II TDAQ TDR [10], seven strip and one pixel layers were selected to be used in the first stage: the outermost pixel layer, the innermost strip layer, and the six outermost strip layers. The second-innermost strip layer and four innermost pixel layers are considered in the second stage. The SS sizes indicated above were also found to perform well in pattern-matching studies in this early round of optimization.

5.3.1 First Stage Simulation and Performance

The pattern-matching performance is studied for the configuration with one pixel and seven strip layers. For strip layers, a TSP SS size of 40 strips is chosen. Pixels are also ganged together into SSs that are long in the z coordinate (403 pixels, corresponding to half of the sensor), so that not so many patterns are spent finding tracks that are very similar in z. To maintain a relatively small SS area in the pixel layer, the SS is selected to be 33 pixels wide in the bending coordinate.

TSP pattern banks are produced with this configuration from a large set of single muons (up to a few billion). In the gHTT scenario, a final AM bank of 3.75 million patterns per 0.2×0.2 region in $\eta \times \phi$ is foreseen to reconstruct tracks with $p_{\mathrm{T}} > 1\,\mathrm{GeV}$. To ensure high efficiency in this region, patterns are generated from muons in a slightly larger region of phase space, corresponding to 0.24×0.24 in $\eta \times \phi$ and $p_{\mathrm{T}} > 800\,\mathrm{MeV}$. The RMS of the beamspot in z is foreseen to be 5 cm, so the target fiducial region is selected to be $|z| < 3\sigma = 15\,\mathrm{cm}$. Tracks are considered with $d_0 < 2\,\mathrm{mm}$. The training sample of single muons is drawn with flat priors on the particle z_0, d_0, η, ϕ, and $1/p_{\mathrm{T}}$ in the ranges specified. For each muon with hits in all $8 - N_{\mathrm{WC}}$ layers, the SSID of each hit is stored as a pattern in the bank. The number of independent muons producing the same pattern is also recorded, so that only the most ‘popular’ patterns can be used for the final bank if desired.

A second strategy for pattern bank generation is also possible, instead of the one using fully-simulated single muons described above. The ‘fast inversion’ strategy uses the constants from the linear track fit (mapping 9-dimensional track coordinate space to 5-dimensional helix parameter

[7] In the results presented below, this is the “Step 2.2” geometry used in the pixel detector TDR [120], in which the description of the silicon strip detector is largely unchanged from the corresponding TDR [121].

space) to generate hit coordinates from random track parameters. In this method, five helix parameters are randomly chosen in the specified range and the sector corresponding to these parameters is selected (with the most popular sector selected in the case of multiple matches). The corresponding fit constants are used along with $9 - 5 = 4$ random Gaussian constraints to produce pseudo-track coordinates which are converted to SSIDs and then a pattern. Both strategies are compared, with the latter having the advantage of being significantly less computationally intensive, as muons are only needed to generate fit constants and not each pattern.

To produce the final AM bank these ($\mathcal{O}(100\,\mathrm{M})$) TSP patterns are combined by setting DC bits to produce a bank of 3.75 million patterns. Up to two SSs may be combined for the pixel layer with DC bits in each dimension, while three are allowed in the strip layers. The maximum number of DC bits set per pattern allowed is scanned, with the optimal number found to be small enough so that the per-layer maximum number of DC bits has little impact. AM patterns are produced with an iterative procedure considering TSP patterns ranked by the number of (pseudo-)tracks that have produced each pattern. The most popular TSP pattern is added to the AM bank. Subsequent TSP patterns are combined with existing patterns in the bank by setting DC bits in existing AM patterns if possible, else new patterns are added to the bank. Once the AM bank contains the full 3.75 million patterns, still-to-be-considered TSP patterns can no longer be added to the bank, but may still be used to set further DC bits in the existing AM patterns, so long as the per-pattern limits on the total and per-layer number of DC bits is respected.

Figure 5.10 shows the single muon efficiency versus the average number of matched patterns (roads) per event in a minimum-bias sample for a variety of configurations. Banks are compared which have been produced using the fast inversion technique as well as the fully-simulated single muon patterns. The fast inversion generally does not perform as well, but the procedure should continue to be studied and tuned in order to perform its performance relative to the fully-simulated bank. The performance is also compared for banks produced with either one or two WCs, and for matching criteria that requires only six or seven out of eight matching hits. A requirement that hits are present in all eight layers was found not to give acceptable efficiency for all configurations. For all configurations, the relative volume of patterns in the bank is varied by scanning the maximum number of DC bits allowed per pattern. A high efficiency ($> 98\%$) is obtained for a number of configurations, with the full-simulation muon bank with two WCs, seven-of-eight logic, and a maximum of five DC bits per pattern yielding the lowest number of roads per event (220 roads, 98.6% efficient).

Each combination of hits corresponding to matched patterns are fit, with the number of fits

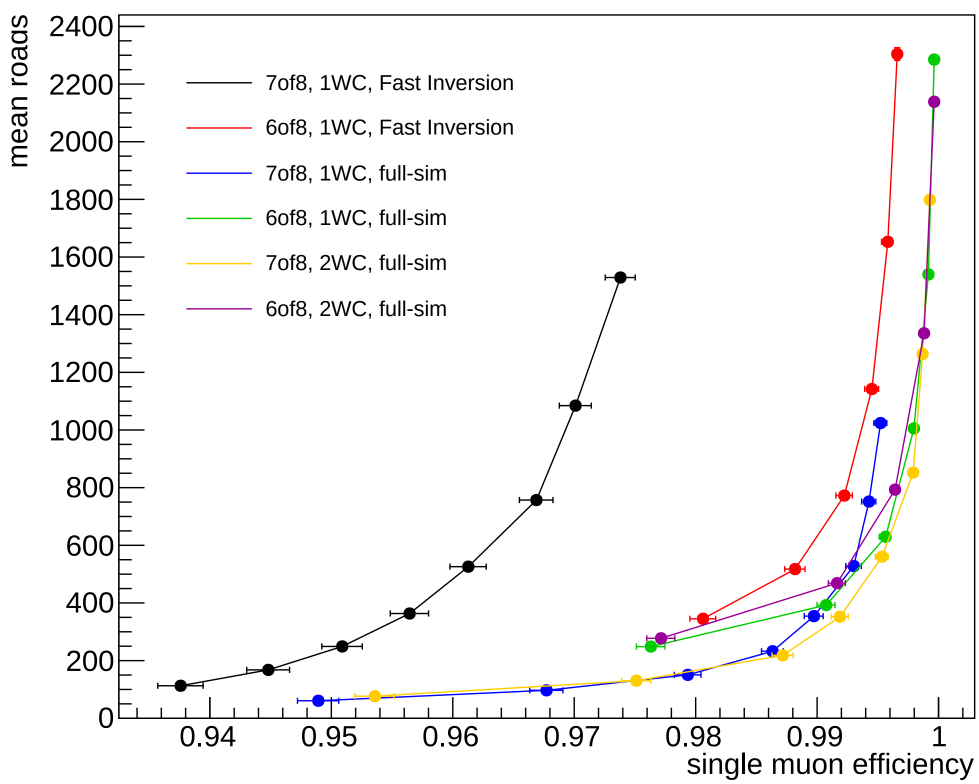

Figure 5.10: The efficiency to find muon tracks is compared to the number of matched patterns (roads) as a function of the pattern bank and matching logic. Banks are compared where the TSP bank has been produced using fully simulated single muon events as well as 'fast inversion' pseudo-tracks produced from the eight-layer fit constants. Banks with one and two WCs are compared, as well as matching logic requiring six- or seven-of-eight hits. For each of these configurations (denoted by distinct colors) the number of maximum DC bits per pattern is scanned, with more DC bits giving both higher efficiency as well as a larger number of matched patterns.

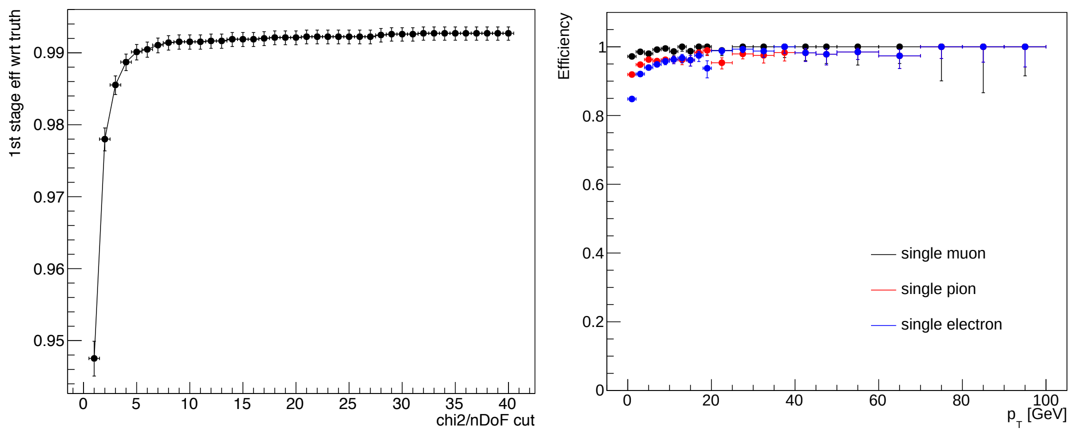

(a) (b)

Figure 5.11: At left, the efficiency is shown for single muon events as a function of the χ^2/nDOF requirement. The default requirement of 40 is very loose, nominally to ensure a high signal efficiency for tracks extrapolated into the second stage, and could be tightened upon further optimization. At right, efficiencies are compared for single muon, pion, and electron samples. Efficiencies are poorest for electrons due to bremsstrahlung energy losses leading to 'kinked' tracks, but could be mitigated by incorporating additional particle species into the sample of training events.

given by the product of hit multiplicities over each layer of the road. A loose requirement on the fit quality (χ^2 divided by the number of degrees of freedom (nDOF) less than 40) is made and HW logic is set to retain tracks which have at least three unique hits. Overlaps are resolved by selecting tracks with more hit coordinates and a lower χ^2/nDOF. Figure 5.11a shows the change in efficiency as a function of the χ^2/nDOF cut for single muon events. The relative efficiency of single muons, pions, and electrons is shown in Figure 5.11b for a benchmark configuration requiring seven-of-eight matches, one WC at most four DC bits per pattern, and a full-simulation TSP bank.

The dependence of the number of first-stage tracks on the number of matched patterns is shown for a number of configurations in Figure 5.12a. The rate of fake tracks is further quantified in Figure 5.12b using truth information associated to each track. Each hit is assigned the an identifying 'barcode' denoting which truth particle in the event record deposited a plurality of the hit's charge. The 'barcode fraction' of a reconstructed track gives the fraction of hits originating from the same truth particle, maximized over all truth particles. For example, an eight-layer track with barcode 0.25 would have only two hits originating from the same truth particle, with the other four coming from random hits from other tracks. A requirement on the barcode fraction (often above 70% or 80%) may be used as a sensible definition of fake tracks.

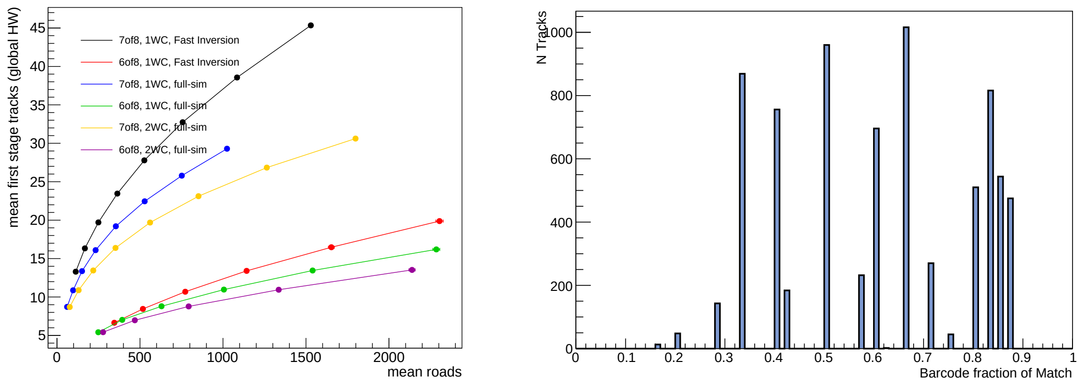

(a) (b)

Figure 5.12: At left, the relation between the number of matched patterns (roads) and first-stage tracks is shown for the same variety of configurations considered in Figure 5.10. At right, the barcode fraction for the set of accepted first-stage tracks is shown for the optimal previously selected in Figure 5.10 (using the full-simulation muon bank with two WCs, seven-of-eight logic, and a maximum of five DC bits per pattern yielding 220 roads and 13 tracks). The entry corresponding to tracks with 100% barcode fraction is suppressed, with 36% of first-stage tracks found to have a barcode fraction of less than 70%.

5.3.2 Second Stage Simulation and Performance

Each first-stage track is extrapolated into the second-stage layers, with multiple connections per event studied. Optimization studies showed little benefit to considering more than eight connections per first-stage track. A best-fit coordinate is obtained for each layer of the extrapolation, with hits falling within a range of that coordinate considered for further fits. A two-sigma window (with errors propagated from the covariance matrix of the first-stage fit) was found to be sufficient to retain excellent signal efficiency while combinatorially reducing the number of track fits to consider. An extrapolation is considered successful when at least one hit is within the extrapolation window in three or four of the five additional layers. In the other layers, either hits may be guessed or additional dedicated $(N-1)$-layer constant sets may be used with WCs. As incorporating WCs would reduce the number of hit guesses, the performance is compared in Table 5.1. With the current implementation, WCs are only set when simulated muons fail to impinge on all thirteen layers of the detector. While the performance improvement is not significant when adding wildcards, and the four-of-five configuration with one wildcard does not match the performance of three-of-five logic even when allowing up to 20 connections per first-stage track, it is possible that a more aggressive strategy would offer further improvements.

The resolutions of the first- and second-stage track parameters are presented in Table 5.2 and are compared to the values obtained using offline algorithms. Second stage tracks are found to have near-offline quality, with all resolutions within a factor of two.

5.3.3 Simulation and Performance in the Forward Region

In addition to the central barrel region described above, further forward regions were studied in which the choice of layers to use in each fit stage can be more complex. The region with $1.2 < \eta < 1.4$ includes the transition between the ITk strip barrel and endcap. Simulation shows results comparable to that of the central barrel region and will not be described in further detail here. However, the far forward region $3.0 < \eta < 3.2$ poses significant new challenges, as tracks enter only the innermost layers of the ITk Pixel Detector. In this region all tracks leave at least nine hits in the detector, with an average of 13 hits on track. The ITk geometry as described in the Pixel TDR [120] and considered in the studies documented herein is shown in Figure 5.13, alongside a more recently update design [122].

AM Chip Inputs and Logical Layer Assignment

The AM pattern recognition chip input bus takes eight channels of ITk data, which were assigned to independent layers of the strip and pixel detectors (seven strip and one pixel) for the barrel region discussed above. In the forward region, the detector layers must be assigned to the AM bus differently, as muons impinge may only on the three innermost pixel layers. Instead of using layers of

Table 5.1: A comparison of the single-muon efficiencies and data-flow metrics for five separate configurations of the second stage. The number of hits required in the addition five detector layers is varied between three and four, while one WC is also optionally allowed. For the configuration requiring hits in four layers and one WC, a configuration allowing up to 20 connections per first-stage track is also considered instead of eight.

Configuration	Required hits	3	3	4	4	4
	Wildcards	0	1	0	1	1
	Max connections per 1st-stage track	8	8	8	8	20
Single-muon efficiency	vs. Offline	0.964	0.964	0.941	0.943	0.952
	vs. 1st stage	0.976	0.977	0.952	0.954	0.964
Data flow in minimum-bias	Extrapolations	3.6	3.7	3.0	3.0	3.0
	Combinations	41	42	29	30	34
	Tracks	2.8	2.8	2.7	2.7	2.7

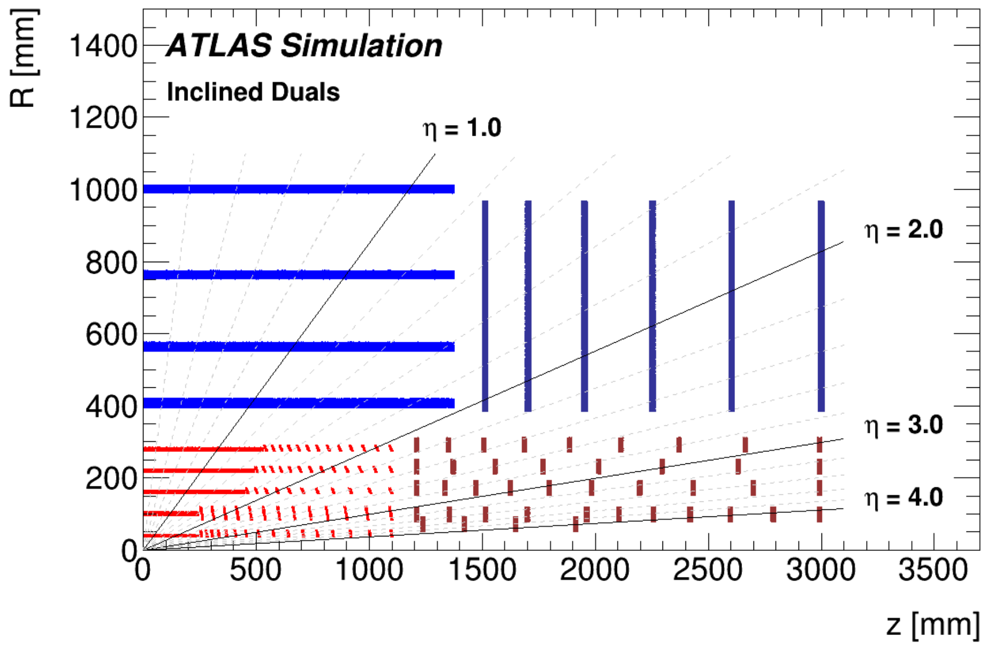

(a) The ITk design presented in the Pixel TDR [120]

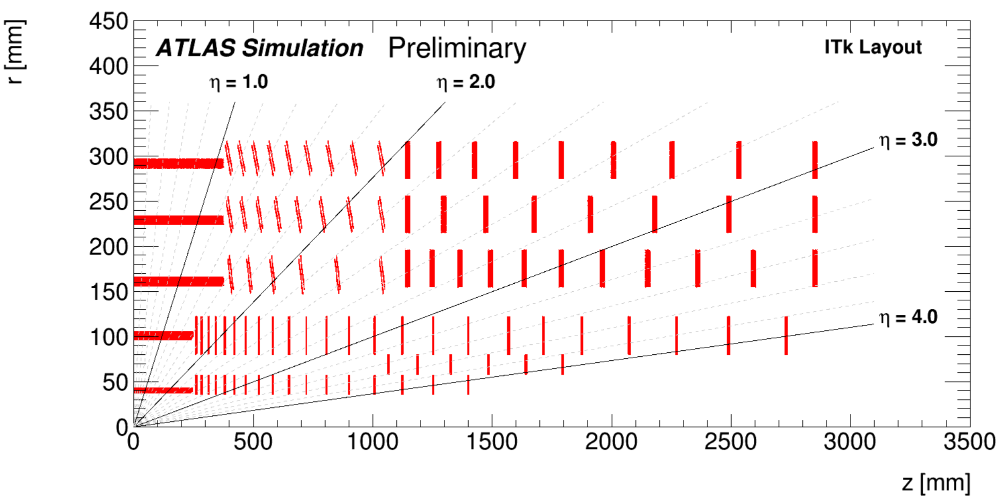

(b) The updated ITk Pixel Detector layout [122]

Figure 5.13: The geometry is shown as presented in the ITk Pixel Detector TDR [120] (top) alongside the recently updated layout of the Pixel detector [122] (bottom).

sensors in r, eight 'logical layers' may be defined by combining detector modules that should contain hits from all muons in the η range targeted. Because all patterns in the region would be loaded onto a single pattern recognition hardware unit, there is strong motivation to utilize the same set of logical layers for all muons in the region.

Defining logical layers in this manner involves partitioning the set of modules[8] hit by all tracks into disjoint subsets. Several algorithms were studied to develop these partitions, using the guiding principle that modules should be combined which are not tightly overlapping and which contribute orthogonal hit information. This information is captured in a module correlation matrix

$$M(\text{module } i, \text{ module } j) = \frac{\text{sum of muons with hits in modules } i \text{ and } j}{\text{sum of muons with hits in module } i} \tag{5.20}$$

shown in Figure 5.14, where off-diagonal entries represent the relative fraction of shared hits between two modules. A coverage map is also displays the fraction of muons leaving hits each module, which shows that only about 25 modules have an appreciable number of hits from muons in this η region.

Three algorithms were investigated to partition these roughly 25 modules into eight-layer sets providing maximal coverage for all simulated muons. The 'greedy' algorithm forms the first logical layer using the highest-coverage module and then adds modules to this layer that provide coverage for the largest number of additional muons. Layers are deemed complete when a set of configurable criteria are met: either a maximum coverage met by the layer (e.g. 95%, 98%) or with a maximum number of modules included in the layer (2 or 3). The 'democratic' algorithm first distributes the eight highest-coverage modules to each of the eight logical layers, then adds modules to the lowest-coverage layer first, continuing until all modules have been utilized. The 'pair/triplet' algorithm

Table 5.2: Helix parameter resolutions are compared for 1 GeV tracks matching truth muons, reconstructed with the first- and second-stage gHTT configurations as well as the offline reconstruction in the region $0.1 < \eta < 0.3$ and $0.3 < \phi < 0.5$. Additional pixel layers considered in the second stage dramatically improve the impact parameter resolutions with respect to the first stage, leading to resolutions within a factor of two of the offline-reconstructed performance.

Resolutions for 1 GeV tracks with $0.1 < \eta < 0.3$			
Helix parameter	First stage	Second Stage	Offline
q/p_{T} [GeV^{-1}]	0.01	0.01	0.01
η	0.003	0.002	0.002
ϕ	0.002	0.002	0.002
d_0 [mm]	0.42	0.10	0.07
z_0 [mm]	0.9	0.14	0.07

[8]Modules with identical ϕ coordinates are always assigned to the same layer, so that the individual models considered are those shown in the $r - z$ view of the detector in Figure 5.13, near $\eta \sim 3$.

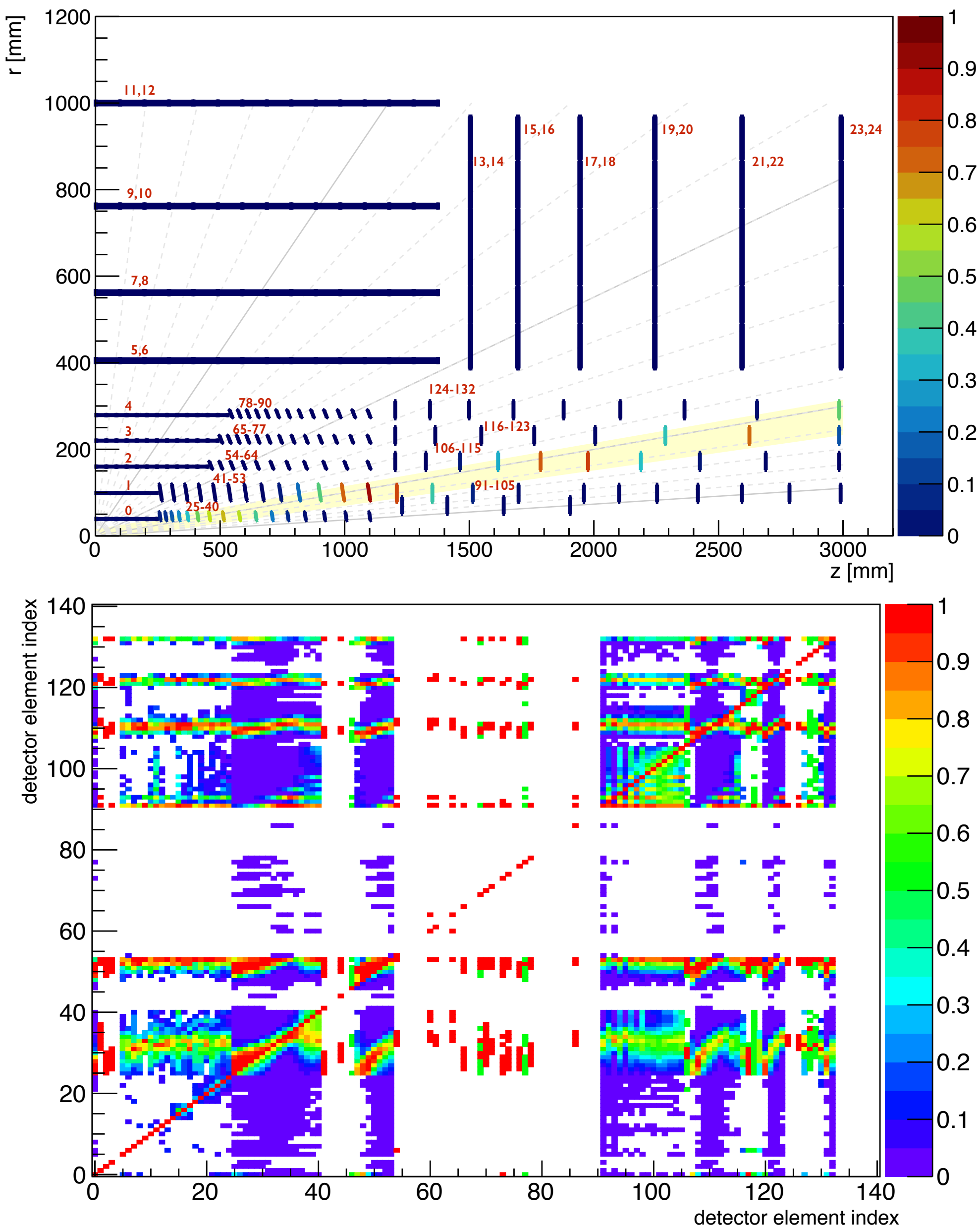

Figure 5.14: An analysis is shown of the per-module coverage and correlation for muons in the region $3.0 < \eta < 3.2$. Top: an $r - z$ display of the ID is shown with each module colored according to the fraction of simulated muons penetrating the respective sensor. The shaded light yellow region illustrates the fiducial region of all tracks, accounting for the full ranges of simulated η and z_0. Bottom: the module-to-module hit correlations are shown, with a per-module index (indicated on the Figure at left) shown on the horizontal and vertical axes. Each entry $M(i, j)$ represents is the fraction of muons leaving hits in module i which also leave hits in module j.

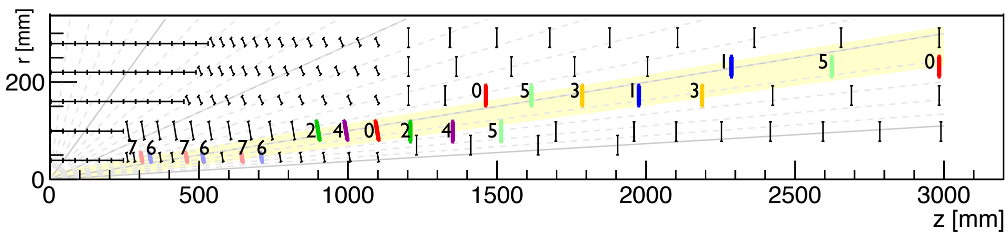

Figure 5.15: The optimal assignment of detector modules to logical layers obtained using the doublet/triplet algorithm described in the text is shown. Modules are labeled by color for each layer and numbered from zero through seven. Six logical layers are constructed using the outermost pixel layers, with the final two using the innermost layer, whose readout may present challenges in some HTT scenarios.

computes the coverage of all pairs of modules and selects the partition (built from non-overlapping pairs) where the coverage of the lowest-coverage layer is maximized. Naively, a large set of partitions must be checked in the last algorithm, with 25 modules giving $\binom{25}{2} = 25!/(23!\,2!)$ possible pairs so that the number of partitions is $\binom{25}{2} \cdot \binom{23}{2} \cdots \binom{17}{2} = 25!/(15!\,2^8) \approx 46\,\text{billion}$. This computational challenge can be solved by using the output of one of the previous algorithms as a seed – though these solutions may not provide the absolute best solution, they should provide a close approximation. With this strategy, many pairs and partitions can be efficiently discarded so that a much smaller set can be explicitly tested to find the optimal partition. While is it not computationally feasible to repeat the algorithm with module triplets instead of doublets, the doublet solution produced by this algorithm may be augmented by adding the $\approx 25 - 2 \cdot 8 = 9$ unused modules to existing logical layers to improve coverage. The optimal solution found by this algorithm for the $3.0 < \eta < 3.2$ region is shown in Figure 5.15.

Studies with Limited Layer Availability

The pair/triplet algorithm was also used to study the ability to reconstruct tracks at large η in scenarios where the full ID is not available for readout. This is relevant in the L1 Track scenario, where the large data rate of the innermost pixel regions may prevent their use in a high-rate track trigger. While the impact on pattern recognition for central regions would be minimal, the lack of an inner layer would inhibit forward tracking, where multiple logical layers are built from the same detector layer. To study this dependence, the total number of modules hits per muon and the performance of logical layer assignment was studied for a range of eta regions, as shown in Figure 5.16.

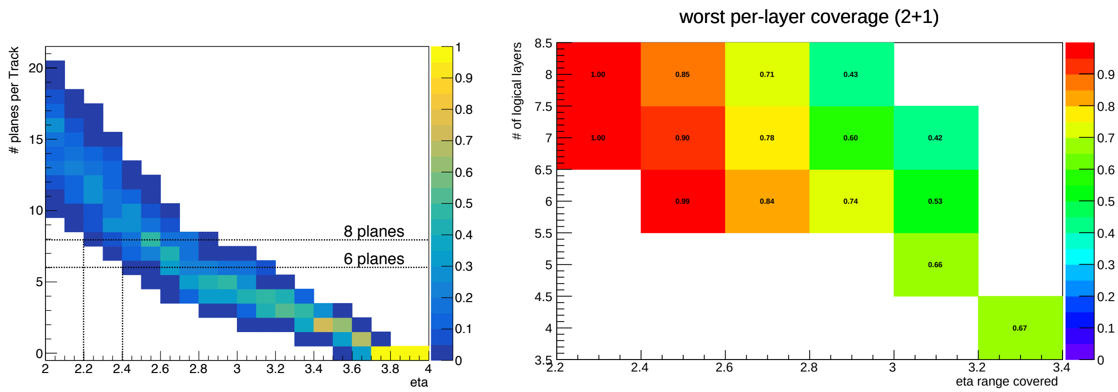

Figure 5.16: At left, the number of modules (modulo phi) hit per muon track is shown for muons in the range $2 < \eta < 4$, where only the three outermost pixel layers are considered. The normalization is arbitrary, with zero entries suppressed. Beyond $\eta = 2.2$ (2.4), tracks are found which leave hits in fewer than 8 (6) modules. In each region of $\Delta\eta = 0.2$, the triplet logical layer assignment algorithm is run for a range of target logical layers. At right, the fraction of muons leaving hits in the layer of poorest coverage is shown for each configuration. For $2.2 < \eta < 2.4$, eight logical layers may be assigned that give 100% coverage, while for the adjacent region $2.4 < \eta < 2.6$ only six logical layers may be constructed that are hit by 99% of all muons. In the farther forward region the coverage is significantly lower, even for configurations with a reduced number of logical layers.

Simulated gHTT Performance

Using the layer mappings described above, tracking performance is tested in the forward region $3.0 < \eta < 3.2$. The logical layers defined in Figure 5.15 were used, nominally with only the outermost six layers (numbered 0-5) used in the first stage and the remaining two layers in the second stage. The SS sizes are set to be constant functions of the physical detector layers, and were optimized in a two-step procedure. In the first step, SSs are fixed to have the same number of pixels in η and ϕ and the relative sizes in each layer are scanned, while in the second step the optimal per-layer aspect ratios are determined. The resulting sizes from inner layer to outer are 18×32 in $\eta \times \phi$, followed by 22×22, 36×25, and 58×40. With five-of-six-layer pattern matching, a maximum of five set DC bits was found to be optimal with up to two bits allowed per layer, leading to an efficiency of 98.8% for single muons with an average of 60 matched patterns in $\langle\mu\rangle = 200$ minimum bias events.

Extrapolating into the final two logical layers leads to eight-layer tracks with 16 measured coordinates, comparable to the 18 (5×2 pixel + 8 strip) measured in the inner barrel region. The track parameter resolutions for six-layer and eight-layer tracks are presented in Table 5.3 and compared to the offline quantities.

5.4 Hardware Implementation and System Design

The hardware implementation of the HTT system is comprised of 96 independent "HTT units" functioning as independent tracking engines that together provide full detector coverage. Each unit receives a fraction of the raw ITk data and processes it as a part of the first- or second-stage HTT subsystems. The main component of the system is the Track Processor (TP), an Advanced Telecommunications Computing Architecture (ATCA) board that can be configured to host two species of mezzanine card: either a Pattern Recognition Mezzanine (PRM) or a Track-Fitting Mezzanine (TFM). The HTT unit is comprised of seven interconnected TP boards, six of which are configured with PRMs and denoted Associative Memory Track Processors (AMTPs) while the remaining one is configured with TFMs and denoted an Second-Stage Track Processor (SSTP).

The TP is responsible for unpacking, clustering, and synchronizing ITk data, which it receives either over a commercial network via the HTT Interface (HTTIF) to the EF in the baseline scenario or directly from the front-end via FELIX cards. Data is transmitted to the board through optical multi-gigabit transceivers through the Rear Transition Module (RTM) and routed to the main FPGA for further processing. Clustering for a single event may be split across multiple TPs with the outputs shared across the backplane and sent to the appropriate board for further processing, so that the pixels in particular need not be clustered multiple times per unit.

For first-stage processing, clustered data for a single region of a single event are collected on a common AMTP, where they are transmitted to a PRM. The PRM is composed of a series of AM chips [123], each loaded with a set of eight-layer patterns, in addition to an FPGA and potentially an external memory source. In the FPGA firmware, SSIDs are associated to each cluster and

Table 5.3: Helix parameter resolutions are compared for 1 GeV tracks matching truth muons, reconstructed with the six- and eight-layer gHTT configurations as well as the offline reconstruction in the region $3.0 < \eta < 3.2$ and $0.3 < \phi < 0.5$. Considering additional pixel hits in the second stage may significantly improve resolutions that do not currently reproduce projected offline-reconstruction performance.

Resolutions for 1 GeV tracks with $3.0 < \eta < 3.2$			
Helix parameter	Six-layer HTT	Eight-layer HTT	Offline
q/p_{T} [GeV^{-1}]	0.09	0.07	0.01
θ	0.005	0.004	0.0006
ϕ	0.008	0.004	0.004
d_0 [mm]	0.42	0.17	0.16
z_0 [mm]	4.2	2.2	2

recorded in a Data Organizer (DO) unit before being sent to the AM ASICs which returns a list of matched patterns. The DO retrieves the hits corresponding to SSIDs of the matched patterns as well as the fit constants (based on the sector associated to the road identifier), and passes this information to the track fitting engines. Successful fit results are relayed to the AMTP, including helix parameters, the fit χ^2, and road and sector identifiers. Overlap removal may be performed in the AMTP before transmitting first-stage tracks to either the Global Trigger / EF systems or the second-stage processing unit.

When second-stage processing is requested, first-stage track information is propagated from one of the six AMTPs to the single SSTP associated to the HTT unit. Due to the large volume of pixel data needed for the additional detector layers used in the second-stage fits, the pixel clustering burden must also be shared among the AMTPs and transmitted to the SSTP for the final fits. The SSTP organizes these inputs and transmits them to the TFM, which is essentially composed of a single FPGA with large internal memory for fast access to the large fit constant matrices needed in the second-stage fits. The firmware is divided into extrapolator, track-fitting, and DO units that associate first-stage tracks to clusters, perform the fits, and facilitate cluster, track, and constant assignments, respectively. Overlap removal may also be performed at this stage after the fit tracks are transmitted to the SSTP. The final tracks are sent to the EF via the HTTIF.

Physics Impact on Hardware Organization

The HTT system is designed to enable a trigger menu more aggressive and ambitious that would be possible without an upgrade to the present TDAQ system. The targeted physics signatures, menu design, and detector geometry all place inter-related constraints on the design and organization of the HTT system.

In the L1 Track and rHTT scenarios the entire detector need not be read out, but only the region about the physics object of interest. The trigger menu thus dictates what fraction of the detector must be processed by the HTT for each event. Consider the illustrative case of a regional tracking request following a L1 Trigger muon accept. The item will produce tracking requests in ROIs with η values distributed across the region $|\eta| < 2.5$ and all of phi. Assuming the requests are uniform in η and ϕ, one can assess the fraction of such events for which each module in the detector need be read out. This is done using simulated single muons across the region and asking in which detector modules each has left a hit. Figure 5.17 shows this fraction for each module, averaged over the ϕ coordinate. Note that due to the spread of the beam-spot in z it can be necessary to process

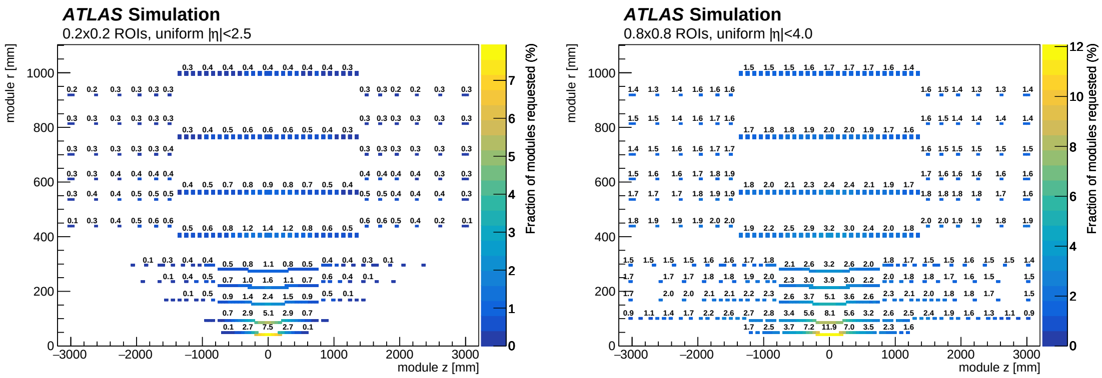

Figure 5.17: The relative fraction of events for which each detector module must be read out is shown for two sets of L1 Trigger ROIs, as a function of $r - z$. At left (right) the usage fractions are shown for muon (jet) ROIs that are uniformly distributed in the region $|\eta| < 2.5$ (4.0).

detector modules with $|\eta_{\text{det}}| > 2.5$. The central pixel modules must be read out for a large fraction of events due to their large areas in projective $\eta - \phi$ space. The corresponding information for jet ROIs (0.8×0.8) over the full detector η range is also shown. The $E_{\text{T}}^{\text{miss}}$ ($\vec{H}_{\text{T}}^{\text{miss}}$) trigger requires tracking in an average of five such jet ROIs per event.

Similar information for all trigger menu items can be combined according to their rates to produce a projected average request fraction across all events. This is shown in Figure 5.18 in addition to a contingency factor. For all but the innermost pixel layers, the average readout fraction is below 10%, with the pixel and central-most modules required much more frequently than those at large η. The asymmetry places limits on the HTT hardware, determining the data-throughput to be supported, as well as suggesting load-balancing strategies to share the computational burden across large regions of η.

Duplication of data among the 96 HTT units and various hardware sub-units motivates strategic division of the detector. The large size of the beam-spot in z leads to the innermost pixel modules being necessary to reconstruct tracks with vastly different polar angles. Similarly, the large bending angles of low-p_{T} tracks means that the outer strip layers must be duplicated among adjacent units in ϕ. Because of the sheer volume of pixel data, the HTT unit configuration found to minimize the total duplication is to have three units in η and 32 in ϕ. A more detailed account of the data rates and processing division among processing units may be found in Ref [10].

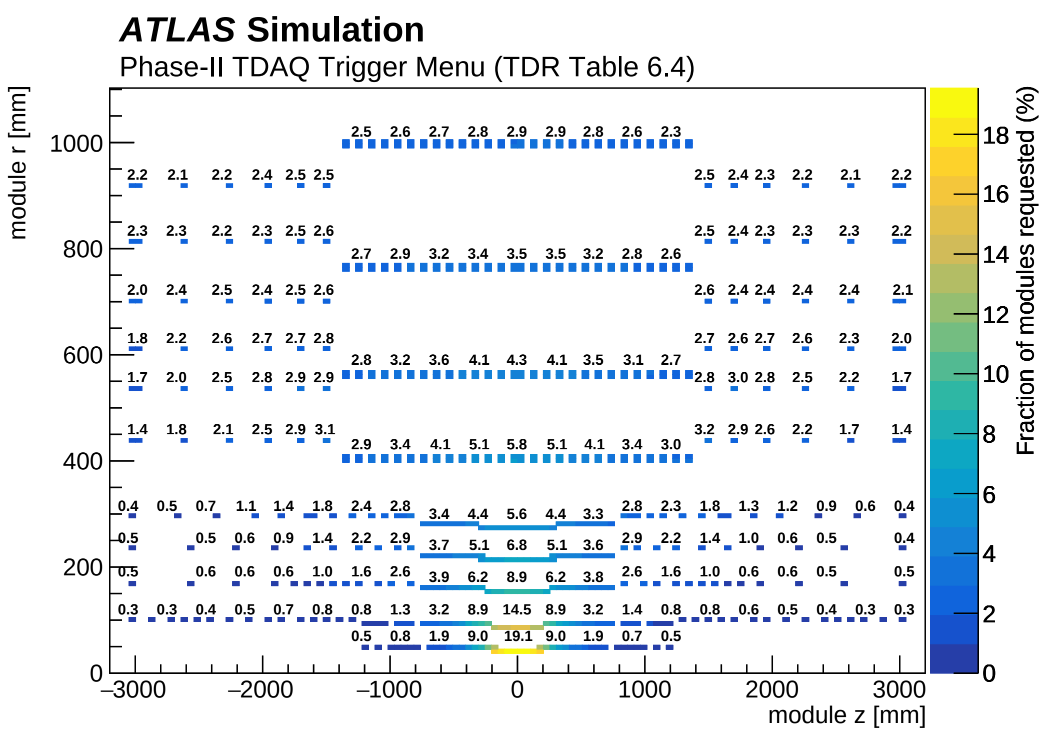

Figure 5.18: The relative fraction of events for which each detector module must be read out is shown assuming the trigger menu stated in the Phase-II TDAQ TDR [10].

Chapter 6

A Search for Top Squarks

6.1 Collider Phenomenology

In Chapter 3, we introduced the framework of SUSY and the MSSM Lagrangian, which is the minimal extension of the SM Lagrangian that respects SUSY. Further, the soft SUSY breaking terms were discussed, which generate larger masses for the superpartners than those that are realized for the SM particles. The masses of the scalar partner of the top quarks $\tilde{t}_1$ and $\tilde{t}_2$ are controlled by the m_{q3L} and m_{TR} soft masses, in addition to the trilinear coupling A_t and the ratio of up- and down-type Higgs VEVs $\tan\beta$. The m_{q3L} parameter is associated with the superpartner of the left-handed top quark and thus also gives mass to the left-handed bottom quark residing in the same SU(2) doublet. The m_{TR} parameter is associated with the right-handed, SU(2) singlet top quark, with a separate parameter setting the mass of the right-handed sbottom. In general, the stop mass eigenstates are mixtures of the left- and right-handed components. Thus, if the lighter of the two physical top squarks ($\tilde{t}_1$) is primarily left-handed, a sbottom should generically also have similar mass. In the following discussion, the "stop" $\tilde{t}$ will refer to the lighter of the two top squarks $\tilde{t}_1$, with the heavier $\tilde{t}_2$ assumed to be inaccessible at the LHC.

The natural target for $\tilde{t}$ searches at the LHC is to consider top squark-anti-squark ($\tilde{t}\tilde{t}^*$) pair production. Because the $\tilde{t}$ is charged under SU(3), this process can proceed via s-channel gluon diagrams and does not depend on the spectra of any remaining SUSY particles. The cross section for this process is large at the LHC, as shown in Figure 6.1. For a stop mass of 500 GeV, the production cross section is 610 fb, yielding 22 000 events in the recorded 2015+2016 data sample of 36 fb^{-1}. The $\tilde{t}\tilde{t}^*$ cross section is lower than for gluino pair production for common sparticle masses, as the gluinos enjoy a larger color multiplicity factor that enhances their relative cross section.

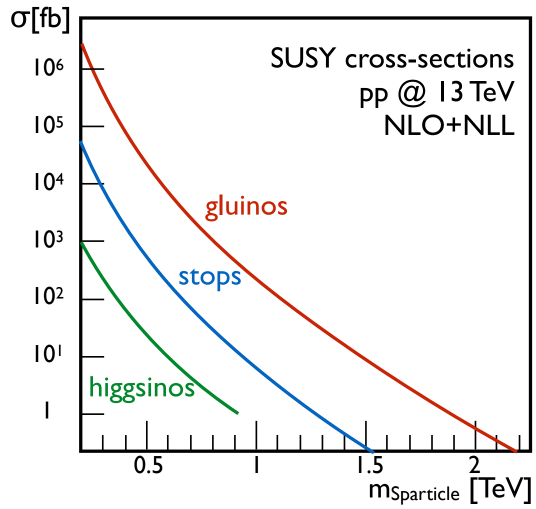

Figure 6.1: Cross sections (in femtobarns) for sparticle-anti-sparticle pair production in proton-proton collisions at a center of mass energy of $\sqrt{s} = 13\,\text{TeV}$. Rates are shown as a function of sparticle mass for three species. The top squark cross section is for only the lightest of the two mass eigenstates, $\tilde{t}_1$. The Higgsino cross section shown is the sum of $\tilde{\chi}_1^0\tilde{\chi}_2^0/\tilde{\chi}_2^0\tilde{\chi}_1^{\pm}/\tilde{\chi}_1^{\pm}\tilde{\chi}_1^{\mp}$. In all cases, production cross sections are presented assuming that all other SUSY particles are decoupled. These data are taken from calculations presented in Refs. [124, 125].

However, it is much larger than for the direct production of light electroweakinos, which must be produced via the weak interaction.

When considering the production of $\tilde{t}\tilde{t}^*$ pairs, generally the contributions of other sparticles to the cross section is not considered. Light gluinos, for example, could significantly enhance the rate at which stop pairs are produced, but are not considered to reduce the model-dependence of the stop search. This is a reasonable choice because gluinos light enough to enhance the $\tilde{t}\tilde{t}^*$ cross section for stop masses considered in this search have already been excluded by analyses of Run 1 LHC data.

However, model-dependence must be introduced when considering how the stop can decay. The first logical possibility is that the stop is the LSP. In this case, its decay is forbidden by R-parity conservation, and the stop must form a color-neutral R-hadron in association with SM quarks and gluons. Dedicated searches for R-hadrons have been conducted by ATLAS and CMS, using techniques particular to slow-moving, massive particles: measurements of ionization energy losses in the silicon tracker and time of flight (ToF) obtained from the tile calorimeter and muon system [126, 127].

An electromagnetically neutral, stable sparticle could serve as an excellent dark matter candidate, motivating the consideration of such particles as the LSP. Charged, stable LSPs would generally lead to anomalously heavy nuclei, and are constrained by heavy hydrogen searches (see, for example Ref. [128]). A neutrino superpartner is one LSP candidate, though in general the annihilation rate is too large to produce the observed relic abundance [129–131]. This possibility is also severely constrained by direct detection experiments (find latest Refs. in Sect. 2.4) and measurements of the invisible width of the Z boson [132].

The remaining LSP candidates are the neutralinos, partner to the B, W^0, and Higgs (h_u^0, and h_d^0) bosons. Each of these LSP candidates, denoted $\tilde{\chi}_B^0$, $\tilde{\chi}_W^0$, and $\tilde{\chi}_h^0$, is controlled by an independent parameter (the soft masses M_1 and M_2, and the SUSY Higgs mass parameter μ, respectively). Thus the lightest neutralino $\tilde{\chi}_1^0$, a mass eigenstate, may be dominantly composed of any of these three species. We consider each case separately.

- *Bino-like LSP*: When the Bino mass parameter M_1 is much less than M_2 and μ, the $\tilde{\chi}_B^0$ is the only light electroweakino. The state may be arbitrarily light and cannot be produced directly at collider experiments due to SM symmetries. Thus a Bino LSP can only be identified as the decay product of other sparticles.

- *Wino-like LSP*: The Wino mass parameter M_2 controls the mass of the SU(2) doublet containing $\tilde{\chi}_1^0$ and $\tilde{\chi}_1^\pm$. The latter has a mass which is 150-165 MeV larger than the neutral component, a splitting dominated by one-loop electroweak corrections [133]. The $\tilde{\chi}_1^\pm$ must be heavier than roughly 100 GeV to evade constraints from LEP experiments [62, 134–139].

- *Higgsino-like LSP*: The four physical states $\tilde{\chi}_1^0$,$\tilde{\chi}_1^\pm$,$\tilde{\chi}_2^0$ of the Higgsino SU(2) triplet have masses set by the parameter μ. A splitting of 355 MeV between the charged and lighter neutral states is expected in the decoupling limit [140]. The accompanying chargino thus also constrains the Higgsino LSP to have a mass above 100 GeV.

In all cases, the top squark may decay to a top quark and neutralino $\tilde{t} \to t\tilde{\chi}_1^0$ if the channel is kinematically allowed. This process is shown schematically in Figure 6.3(a). If not, various many-body decays can become important, among them $\tilde{t} \to bW^\pm\tilde{\chi}_1^0$, $\tilde{t} \to bf\bar{f}'\tilde{\chi}_1^0$, where f and $\bar{f}'$ are fermions from an off-shell W boson decay, and even $\tilde{t} \to c\tilde{\chi}_1^0$. The regions where each decay channel is important is shown in Figure 6.2. In the wino and Higgsino cases, the $\tilde{t} \to b\tilde{\chi}_1^\pm$ decay channel may also be open, as shown in Figure 6.3(b). In such cases, the $\tilde{\chi}_1^\pm$ is unstable and thus decays to the LSP via emission of a virtual W boson. The decay fraction for each sub-process depends on details of the sparticle mass spectra as well as other parameters of the full theory (electroweakino mixing, $\tan\beta$, signs of mass terms, and so on).

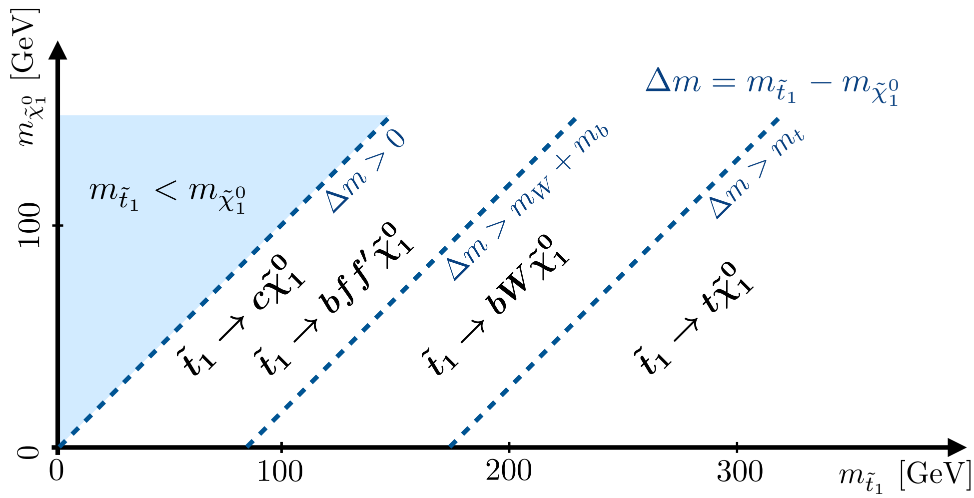

Figure 6.2: A map in the space of sparticle masses where various decays of the top squark are allowed to proceed. The stop mass is scanned on the x-axis, while the neutralino LSP mass is scanned on the y-axis. The blue region where the LSP mass is greater than the stop is not physically meaningful and thus not considered. When the stop mass is greater than the sum of the LSP and top-quark masses the tN decay dominated. While the other decays pictures for smaller mass splittings are also possible, they are strongly suppressed by the top-quark line-shape.

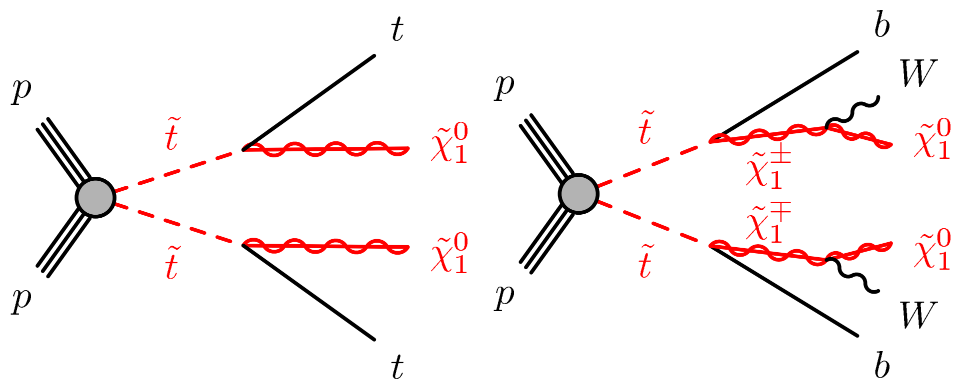

(a) top-neutralino decay mode

(b) bottom-chargino decay mode

Figure 6.3: Schematic diagrams of $\tilde{t}\tilde{t}^*$ pair production with subsequent decays to (a) top quarks and neutralino LSPs, (b) bottom quarks and chargino next-to-lightest supersymmetric particles (NLSPs).

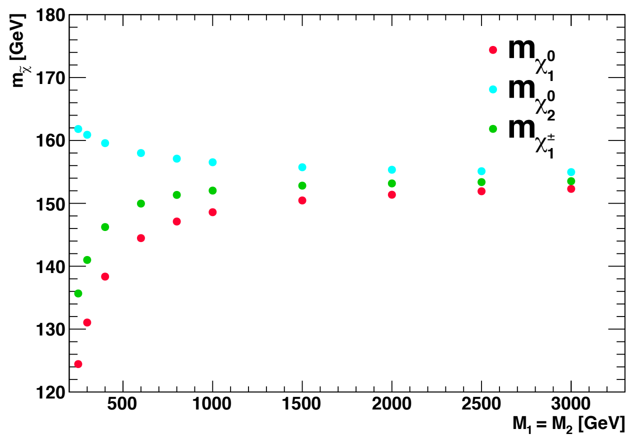

Figure 6.4: The masses of the dominantly-Higgsino physical eigenstates $\tilde{\chi}_1^0$,$\tilde{\chi}_1^{\pm}$, and $\tilde{\chi}_2^0$ are shown as a function of a scanned common gaugino mass parameter ($M_1 = M_2$). Here the Higgsino mass parameter μ is fixed to 150 GeV. At large values of the common gaugino mass parameter the splitting $dM(\tilde{\chi}_1^0, \tilde{\chi}_1^{\pm})$ approaches 355 MeV, though splittings as large as 4 GeV are found when the gaugino mass is set to 1 TeV. Conversely, mixing effects are very significant when the mass parameter is set to 250 GeV, with $dM(\tilde{\chi}_1^0, \tilde{\chi}_1^{\pm}) = 10$ GeV and $dM(\tilde{\chi}_1^0, \tilde{\chi}_2^0) \approx 40$ GeV.

In the following discussion of the search for $\tilde{t}\tilde{t}^*$ production, only the cases where the LSP is dominantly bino and Higgsino will be considered. The experimental signature in the case of a bino LSP (with all other sparticles decoupled) is generally the same as SM production of top-quark pairs, plus a significant momentum imbalance among the reconstructed objects, due to the presence of additional undetected LSPs in the event. Top quarks may not be reconstructed if the LSP-stop mass splitting is small, as discussed above. In the case of a Higgsino LSP, the additional decays $\tilde{t} \to b\tilde{\chi}_1^+$ and $\tilde{t} \to t\tilde{\chi}_2^0$ to the other members of the Higgsino multiplet are possible, with subsequent decays $\tilde{\chi}_1^+ \to W^*\tilde{\chi}_1^0$ and $\tilde{\chi}_2^0 \to Z^*\tilde{\chi}_1^0$. While the decay products of these virtual bosons are not detectable when the $\tilde{\chi}_1^0$ is pure Higgsino ($dM(\tilde{\chi}_1^0, \tilde{\chi}_1^{\pm}) = 355$ MeV), the mass splitting increases significantly when mixing with the other neutralinos is considered. As shown in Figure 6.4, splittings of $\mathcal{O}(10\,\text{GeV})$ are predicted from the mass matrix diagonalization, even when the gaugino mass terms are as large as 1 TeV. Such a scenario presents the opportunity to directly reconstruct low-momentum ("soft") leptons stemming from the decays of the far off-shell electroweak bosons.

The scenario for a Wino LSP allows for a fundamentally different search strategy. Because of the very small mass splitting between the neutral and charges states, the decay of the charged component is highly suppressed, leading to a lifetime of about 0.2 ns. This enables dedicated searches for "disappearing tracks", where the charged wino leaves hits only in the innermost layers of the

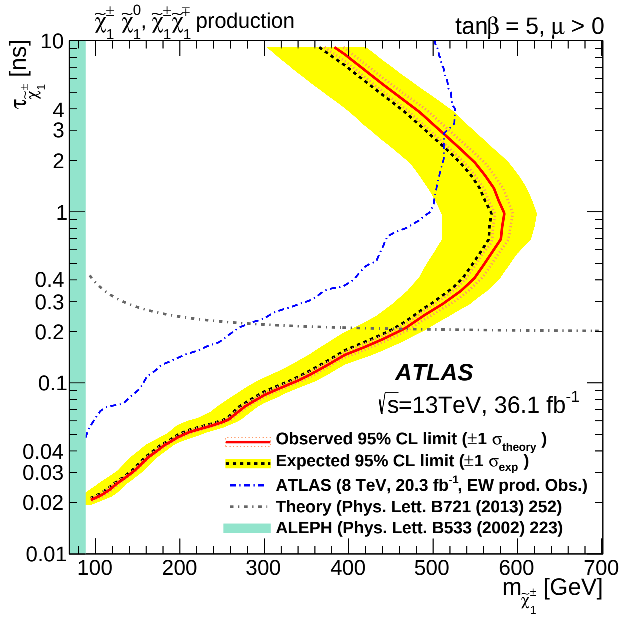

Figure 6.5: Limits on direct production of charged winos obtained by ATLAS, based on a search for disappearing tracks in the inner detector [141]. Limits are set as a function of the wino lifetime and mass, with the upper left section of the plot inside the red band being excluded. The theoretical prediction of the charged wino lifetime as a function of its mass is shown as a black dot-dashed line. Assuming this relation, chargino masses of up to 460 GeV are excluded at the 95% confidence level.

tracker, before decaying to a neutralino and very low-momentum (undetected) charged pion. ATLAS sets limits on this scenario up to masses of 460 GeV, as shown in Figure 6.5, considering direct electroweak production of $\tilde{\chi}_1^{\pm}\tilde{\chi}_1^0$and $\tilde{\chi}_1^{\pm}\tilde{\chi}_1^{\mp}$pairs [141].

Previous searches have been conducted for top squarks using Run 1 ATLAS and CMS data [142–148] as well as a small data set of early Run 2 data taken in 2015 [149–152]. Prior to this, similar searches were conducted at the Tevatron by the CDF and D0 Collaborations [153, 154].

6.2 Search strategy

The following Sections will describe a search for pair production of top squarks [7]. The aim of this section is to describe the search strategy in general terms, in accordance with the expected experimental signature described in Section 6.1.

The search described in this document is conducted in final states with one charged lepton. Each of the top quarks produced in the $\tilde{t}\tilde{t}^* \to t\bar{t}\tilde{\chi}_1^0\tilde{\chi}_1^0$ process decays to a b quark and W boson, the latter of which decays to electrons and muons about 25% of the time[9], so that the large majority of events are produced with zero (56%) or one (38%) lepton. Focusing on one-lepton events allows for large acceptance to the $\tilde{t}\tilde{t}^*$ signal while allowing for excellent control over difficult background processes, as will be discussed in the following chapters.

The dominant backgrounds to the $\tilde{t}\tilde{t}^*$ signal are SM processes with prompt leptons, large $E_{\mathrm{T}}^{\mathrm{miss}}$, b-tagged jets, and additional hadronic activity. The two largest contributions come from SM $t\bar{t}$ production as well as W bosons produced in association with jets. The rarer process $t\bar{t}Z$ can be challenging when the Z boson decays invisibly, as well as $t\bar{t}W$ to a lesser extent. Despite the low cross section, single top (tW) backgrounds are also important because of difficulties in distinguishing these process from the stop signal in certain SUSY scenarios.

The analysis strategy is to identify observables which can be used to disentangle a SUSY signal from the SM backgrounds. For stop masses significantly heavier than the weak scale, one can exploit the presence of high-energy objects in the event, large $E_{\mathrm{T}}^{\mathrm{miss}}$, and related quantities. Top reconstruction techniques are also useful, to remove backgrounds such as W+jets, where no real top quark was produced. One may then define a "signal region" (signal region (SR)) as the class of data events which satisfy requirements on a number of such observables. The region should have relatively acceptance to the $\tilde{t}\tilde{t}^*$ signal, and the number of SM events entering this region should be small and accurately predicted.

MC simulation (see Section 2.3) can be used to estimate the expected backgrounds in the SR due to SM processes. However, MCs have limitations due to many factors (missing phase space, absent higher-order corrections, reliance on 'tuned' parameters, etc), which can lead to large theoretical uncertainties on the pure MC-based predictions. In the searches to be described, all major backgrounds are estimated in a data-driven manner, where the benefits of MC-based predictions are combined with in-situ, data-based corrections. This strategy is based on the use of control regions (CRs), each of which is chosen to be very purely populated by events from a specific background process, and allow the use of observed data to correct MC predictions. Instead of relying on an MC estimate of the number of events entering the SR, the MC is only relied on to extrapolate from one region of phase-space to another. Specifically, the number of measured data events in the CR is multiplied by an MC-derived *transfer factor* that gives the predicted ratio of events in the CR to the SR. With this strategy, deficiencies in the MC modeling which are correlated between regions cancel each other, allowing a more robust prediction. However, the strategy is most successful when the

[9] The W decays 11% of the time to each generation of $\ell^{\pm}\nu_{\ell}$ pairs. In decays to third-generation leptons, 35% of tau particles decay in the fully leptonic channel to the lighter generations $\tau^{\pm} \to \ell^{\pm}\bar{\nu}_{\ell}\nu_{\tau}$.

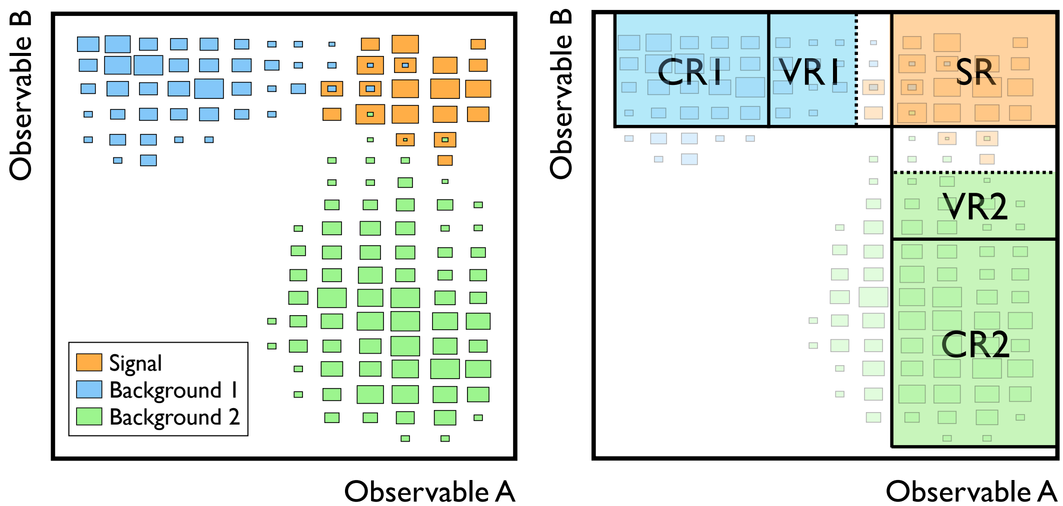

(a) Predicted signal and background event yields

(b) Resulting CR/VR/SR definitions

Figure 6.6: An illustrative example of the background estimation strategy used in the $\tilde{t}\tilde{t}^*$ search. At left, three populations of events are shown, due to two separate background processes (blue and green) as well as signal (orange). The distribution of events is shown differentially in two variables ("Observable A" and "Observable B"), with the number of events each process contributes to a given bin of 2D phase space represented by the size of the box of corresponding color. The signal process is dominant at extreme values of each observable. At right, the control, validation, and signal regions (CR, VR, and SR, respectively), selected based on the yields reported in (a) are shown. `CR1` is selected as a region rich in Background 1, with `VR1` validating the extrapolation of this estimate to large values of Observable A. The validation region is selected to minimize potential contamination from signal events. Corresponding regions (`CR2`, `VR2`) are defined to estimate Background 2 and validate the extrapolation in Observable B. The number of events entering the SR due to Background 1 and 2 is estimated as described in the text.

extrapolation from CR to SR is simple and well-modeled by the MC. This premise is usually checked in an intermediate validation region (validation region (VR)), where the data-driven prediction of VR events can be compared explicitly against the number of observed VR events to check that the method closes. VRs must have minimal contamination from a potential signal process in order to allow an unambiguous cross-check of the estimation. The method is further illustrated with an example in Figure 6.6.

The background estimation process results in an SR definition with an expected number of events to be observed from SM processes alone. A significant excess above this estimate would constitute potential evidence for a BSM signal. To quantify the agreement of the observed number of events in the SR with the SM expectation, a statistical test is performed. This involves the construction of a likelihood function $\mathcal{L}(s)$ as a product of Poisson (statistical) and Gaussian (systematic "nuisance parameter") terms, which the quantifies the agreement of the data with the predicted number of events $b + s$. Here b is the number of predicted SM background events and s is the number of additional events that may enter due to some BSM process. Values of s are excluded which lead to large values of $-2 \log \mathcal{L}$, with processes "excluded" which contribute more than s_{95} events to the SR. If one were to repeat the experiment many times under the SM-only hypothesis, one expects to observe $b + s_{95}$ or more events in less than 5% of trials. A similar procedure is used to set even more restrictive limits on specific models by combining observations across multiple signal regions.

In the following Sections, the details of this strategy will be described as they pertain to several searches conducted as a part of Ref. [7]. In addition to the analyses described below, complementary searches for other signatures of $\tilde{t}\tilde{t}^*$ production were carried out using data collected over the same period by ATLAS [155–160] as well as CMS [161–170].

6.3 Simulation Tools

6.3.1 Standard Model Processes

Samples of events simulated using MC techniques are generated to predict differential distributions for a variety of SM processes. For an less technical review of the elements of such calculations the reader is referred to Section 2.3.

The $t\bar{t}$ process is simulated with the `hvq` process implemented in `POWHEG-BOX v2` [171]. The ME is calculated at NLO in the strong coupling constant α_S, with top-quarks treated in the narrow width approximation (NWA). Events are weighted to approximate the effects of off-shell tops. The renormalization scale μ_R and factorization scales μ_F are both set to the geometric mean of the top mass and $p_T$for the underlying Born configuration. The `hdamp` parameter, which controls the level of high-$p_T$radiation off of the top-quark system, is set to be equal to the top mass. The NLO `CT10` PDF set is employed. This calculation is matched to a parton shower, implemented in Pythia 6 [29], using the `Powheg` method. The Perugia 2012 (P2012) set of configurable parameters ("tune") is used to enhance the agreement of the shower model with measurements, accounting for high-multiplicity perturbative effects, non-perturbative physics, and multi-parton interactions. `EVTGEN` is used, replacing the decay of heavy-flavor hadrons from `PYTHIA`, to produce an accurate and consistent description of b quark fragmentation and hadronization across generators [172]. All $t\bar{t}$ samples are normalized to the theoretical cross section of 830 pb, calculated at NNLO with next-to-next-to-leading logarithm soft gluon resummation [33].

Alternative $t\bar{t}$ simulations are used to assess the dependence of the results on modeling choices and assumptions. To assess the impact of variations in μ_R and μ_F, accounting to missing higher-order corrections, two alternative samples are produced with both scales coherently varied up and down by a factor of two. These are referred to as "low radiation" and "high radiation" variations, the latter of which also modifies the `hdamp` parameter to twice the top mass. At the same time in each sample, the value of α_S is modified in the shower (in addition to several other technical parameters) to reflect the alternative scale choice, using the corresponding low/high radiation P2012 tunes. To compare the parton shower model, an alternative sample is generated using `HERWIG++` [30] in place of `PYTHIA`. The shower is tunes with the `UE-EE-5` set of configurable parameters [173] as well as the `CTEQ6L1` PDF set [174]. To compare choices of the NLO matching scheme an alternative sample is generated with `Madgraph5_aMC@NLO` 2.2.1 (`MG5_aMC@NLO`) [27]. The renormalization and factorization scales are set to $\mu = \sqrt{m_t^2 + 0.5(p_{T,t} + p_{T,\bar{t}})}$. This sample uses the same `HERWIG++` shower configuration as described in the previous sample.

More detailed information about the top-quark generator setups described above may be found in Refs. [175, 176].

The tW single top process is simulated with a nominal setup and systematic variations nearly identical to those for the $t\bar{t}$ process described above. Five-flavor scheme PDFs are used, as the tW final state demands a b from the proton at LO. At NLO, the process received large corrections, as the final state becomes identical to that of $t\bar{t}$ if the additional QCD emission in the final state is a b quark (tWb). This effect demands a careful treatment to avoid double-counting when combining with predictions obtained using the $t\bar{t}$ calculations described above. Two sample variants are simulated to compare the sensitivity of the measurement to different models of the overlap and interference among these two processes: diagram removal (DR) and diagram subtraction (DS). Finally, a LO `MG5_aMC@NLO` sample of $W^{\pm}W^{\mp}b\bar{b}$ events is generated (using the four-flavor scheme), with and without interference between $t\bar{t}$ and single top diagrams, to provide further information regarding overlap and interference effects. A detailed description of the $t\bar{t} - tWb$ interference issue and a comparison of calculations to best describe the process is provided in Section 7.1.

To reduce the statistical uncertainty on the predicted number of events with kinematics which produce a large transverse momentum imbalance, a filtering strategy is used to over-sample this region which contributes only a small fraction to the overall cross section. This strategy is applied to both $t\bar{t}$ and tW single top events. In addition to samples which are inclusive in $E_{\mathrm{T}}^{\mathrm{miss}}$, dedicated samples are produced to populate regions with $E_{\mathrm{T}}^{\mathrm{miss}} > 200$, as well as further selections of 300, and 400 GeV for $t\bar{t}$ only. In the $E_{\mathrm{T}}^{\mathrm{miss}} > 200$ GeV sample, only events with $E_{\mathrm{T}}^{\mathrm{miss}}$ calculated from the particle-level (fully showered) event are reconstructed, allowing the sample to be combined with the inclusive one with a corresponding veto imposed. The samples with $E_{\mathrm{T}}^{\mathrm{miss}} > 300$ and 400 GeV are obtained by making requirements on the parton-level configurations and showering only a subset of events to further reduce the computational cost of the production. The filtering procedures are verified to be fully efficient in the phase space of the analyses described below.

Production of single W and Z bosons as well as dibosons $VV = WW/WZ/WW$ in association with jets is modeled with SHERPA [40], using matrix elements from Comix [177] and OpenLoops [178]. Events with up to extra QCD two emissions are modeled at NLO while LO accuracy in the ME is retained for three and four emissions. The SHERPA parton shower model is employed and the merging of the hard process calculations is done with the ME+PS@NLO method [179]. The CKKW-L scheme [38] is used to match and merge in a manner that avoids double counting among calculations corresponding to various jet multiplicities, with the merging scale set to 20 GeV. For diboson processes (SHERPA 2.1), the NLO CT10 PDF set is used with $\alpha_{\mathrm{S}} = 0.118$ and the values of μ_R and μ_f are set according to a clustering of multi-parton emissions for the underlying n-leg hard process. For V+jets processes (SHERPA 2.2), the NNPDF3.0 PDF set is employed, along with various other technical improvements. Alternative samples are produced using modified matching scales (15 GeV and 30 GeV), μ_R (factor of two up and down), μ_f (factor of two up and down), and resummation scales (factor of two up and down) to assess theory modeling uncertainties. Dedicated samples are produced in regions of varying boson p_{T} and jet activity (via filtering on dijet-mass or the sum of jet momenta) to reduce the MC statistical uncertainty on predictions in extreme regions of phase space probed by searches. Further information regarding the technical setup for these processes may be found in Ref. [180].

MG5_aMC@NLO interfaced with PYTHIA 8 [29] is used to simulate the production of $t\bar{t}$ pairs in association with vector bosons $V = Z, W$ at NLO in α_{S}. The NNPDF3.0 PDF set is used in the ME, with μ_R and μ_f set to $H_T/2$, one half of the sum of top-quark, vector boson, and jet transverse momenta for the hard process configuration. The Madspin program [181] is used to decay the top quarks and vector bosons, preserving the correlation of spins among each of the states. The A14 tune is used for the PYTHIA configuration, with the NNPDF2.3 PDF set. Events are weighted to enable systematic variations of the factorization and renormalization scales as well as various PDF eigenvectors. An additional LO multi-leg sample generated with SHERPA 2.2 is used to assess further uncertainties in the modeling of additional QCD emissions. Details of this setup are similar to those described above for the V+jets and multi-boson processes.

6.3.2 SUSY signals

SUSY signals processes are simulated using MG5_aMC@NLO interfaced to PYTHIA 8 with "multi-leg" hard processes calculated at LO with up to two extra partons and merged using the CKKW-L scheme. The production cross section for top-squark pairs is computed at NLO+next-to-leading logarithm (NLL) [182–184] with a variety of choices of PDF sets and μ_R and μ_f scales to establish the central value and uncertainty [124]. Cross sections are computed assuming pure strong production, which is to say that contributions from any additional light SUSY particles (e.g. other squarks or gluinos) is neglected. Thus the cross section depends only on the mass of the $\tilde{t}$and not on the lighter spectrum of (weakly interacting) sparticles.

Details of the signal model generation depends on the SUSY scenario considered. Three are considered in this document:

- *Bino LSP*: The only light sparticles considered are the stop and the singlet Bino LSP. The signal model is fully specified by the $\tilde{t}$ and $\tilde{\chi}_1^0$ masses.
- *Higgsino LSP*: The stop is assumed to decay to the Higgsino LSP and multiplet partners with all other SUSY particles assumed to be sufficiently heavy to decouple. The mass splitting among the Higgsino states and their intermediate decays depend on the particular model assumptions adopted. A variety of these are considered, with the parameters scanned discussed in the text below.
- *Bino LSP with light Higgsino*: Both the Bino and Higgsino are assumed to be light, motivated by naturalness considerations and the dark matter relic density. The scenario is treated similarly to the Higgsino LSP scenario, with all other sparticles decoupled.
- *Bino LSP with light Wino*: The Wino doublet is assumed to have a mass between the Bino and top squarks, so that the top squark decays dominantly to the Wino NLSP (due to the chiral structure of the weak interaction). This scenario is considered due to its different signature of high-p_{T} b jets, not from top decays.

The particular settings and configuration of the simulation configurations are described in the following for each of these scenarios.

Bino LSP

The hard process simulated using MG5_aMC@NLO is $\tilde{t}\tilde{t}^*$ pairs, with decays of the top squarks handled by PYTHIA. Stop decays use only phase-space considerations and not the full ME. These decays of unpolarized stops are re-weighted to consider the case where the $\tilde{t}_1$ is dominantly left- and right-handed, which affects the polarization of the tops produced in their decays [185, 186]. The top polarization affects the resulting lepton kinematics and therefore the signal acceptance, so that various assumptions must be considered. Madspin is used to reproduce the proper decay product kinematics for signals where the top quark is forced to be off-shell.

Higgsino LSP

The Higgsino LSP scenario is studied in the framework of the pMSSM (for further details see Section 3.3.1). The choice of pMSSM parameter values is used to calculate physical observables using HDecay 3.4 [187], SDecay 1.5(a) [188], and SoftSusy 3.7.3 [189, 190], including sparticle mass spectra and decay rates. These physical observables are then used to develop a set of simplified models, inspired by studies of the pMSSM, with particular particle masses and branching fractions considered for each of the model points specified by hand. All decays are assumed to proceed promptly. This strategy minimizes unnecessary variation within the space of models considered, while being informed by the representative behavior obtained from pMSSM scans. The free parameters among the model points (often "grid points") considered are the stop mass, the LSP Higgsino mass, and the mass splitting among the Higgsino triplet of states which is constrained to be from 2 to 30 GeV. Scenarios with left- and right-handed stops are considered for an intermediate value of $\tan\beta = 20$, in addition to a large-$\tan\beta$ scenario ($\tan\beta = 60$) where polarization effects are found to be negligible. The results of scanned pMSSM parameters motivating these choices are shown in Figure 6.7. In the $\tilde{t}_1 \sim \tilde{t}_L$ scenario, the $\tilde{t}$ is found to decay via $\tilde{t} \to t\tilde{\chi}_1^0$ and $\tilde{t} \to t\tilde{\chi}_2^0$ modes 45% of the time each, with the $\tilde{t} \to b\tilde{\chi}_1^\pm$ decay occurring 10% of the time. In the $\tilde{t}_1 \sim \tilde{t}_R$ scenario, the $\tilde{t}$ is found to decay via $\tilde{t} \to t\tilde{\chi}_1^0$ and $\tilde{t} \to t\tilde{\chi}_2^0$ modes 25% of the time each, with the $\tilde{t} \to b\tilde{\chi}_1^\pm$ decay occurring 50% of the time. Finally, in the large-$\tan\beta$ scenario, each decay mode of the stop is found to be equally likely.

Due to the small mass splittings between the Higgsino states, the decays of the $\tilde{\chi}_2^0$ and $\tilde{\chi}_1^\pm$ occur via off-shell Z/γ^* and W bosons, respectively. The stops are thus decayed by Madspin in this scenario to properly reproduce the low-p_{T} lepton kinematics, which are critical to correctly modeling their reconstruction efficiency. In all models, the mass difference $\Delta M(\tilde{\chi}_1^0, \tilde{\chi}_2^0)$ is set to twice the difference $\Delta M(\tilde{\chi}_1^0, \tilde{\chi}_1^\pm)$, as was found to be a good approximation when $\mu < M_1, M_2$ in

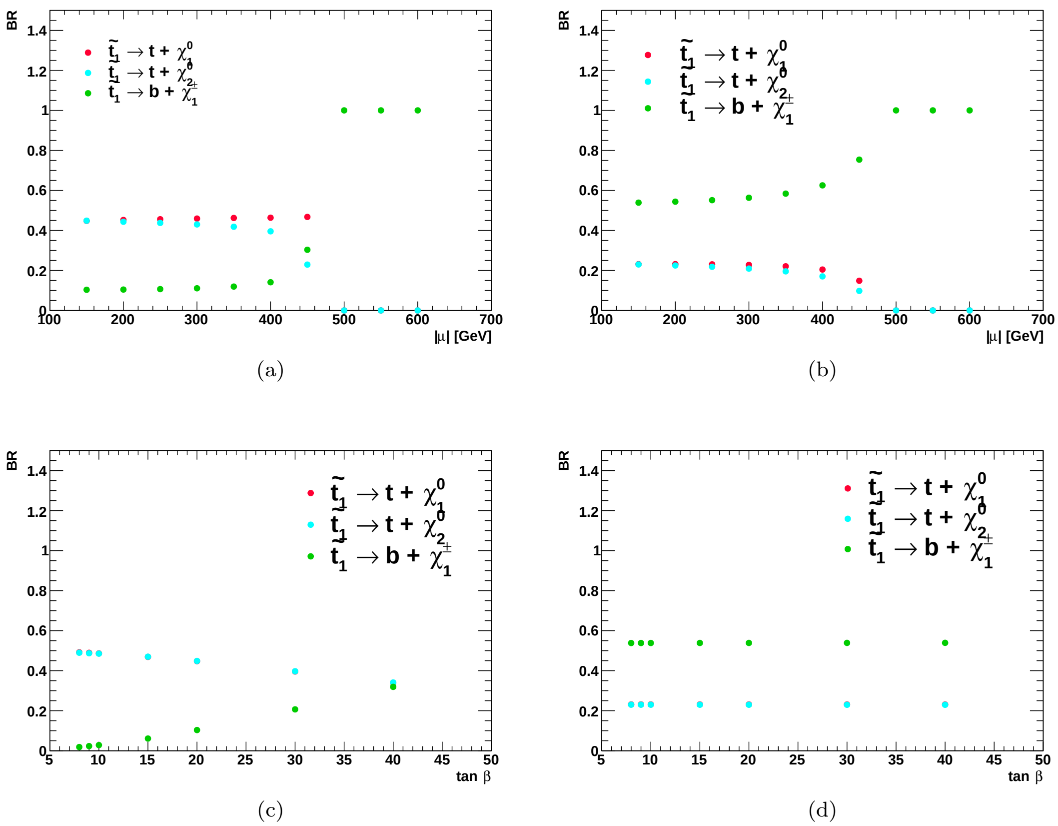

Figure 6.7: At top left, a scan of the $\tilde{t}_1$ branching fraction as a function of the Higgsino mass parameter μ in a scenario with the mass m_{q3L} of the $\tilde{t}_1 \sim \tilde{t}_L$ set to 600 GeV. Decays mediated by top quarks are in general favored, but become unimportant as the $\tilde{t}$–$\tilde{\chi}_1^0$ mass splitting becomes small. At top right, a analogous scan for the case $\tilde{t}_1 \sim \tilde{t}_R$, where the $\tilde{t} \rightarrow b\tilde{\chi}_1^\pm$decay is found to dominate. At lower left, the effect of varying $\tan\beta$ is shown for the case $\tilde{t}_1 \sim \tilde{t}_L$, where $m_{q3L} = 600$ GeV and $\mu = 150$ GeV. In this scenario, all decays of the $\tilde{t}_1$ become equally likely as $\tan\beta$ becomes large. Ar lower right, the analogous plot for the right-handed $\tilde{t}_1$ is shown (with $m_{TR} = 600$ GeV), where changes to $\tan\beta$ are found to have no effect on the stop decay widths.

the study pictured in Figure 6.4.

Bino LSP with light Higgsino

The models considered within the context of scenarios with light Bino and Higgsino states are obtained by a scan of pMSSM parameters. Here $\tan\beta$ is taken to be 20, the breaking scale is set to $m_S = 0.7 - 1.3\,\text{TeV}$ (to reproduce the observed Higgs mass), the gluino mass parameter is set to $1.8\,\text{TeV}$ to evade experimental constraints. The Wino mass parameter is set to $2\,\text{TeV}$. Two independent parameters are varied, corresponding to the $\tilde{t}$ mass and scale of the light Bino and Higgsino states. The m_{q3L} (m_{TR}) and M_1 parameters are varied in the scenario with left- (right-)handed $\tilde{t}_1$. The precise masses and mixing of the electroweak sector are calculated to reproduce the correct relic density $0.10 < \Omega h^2 < 0.12$. (This is commonly referred to as the "well-tempered neutralino" scenario [191].) The relic density is calculate using the MicrOMEGAs 4.3.1f program [192,193], with the μ parameter varied to achieve the proper value. This generally leads to $\Delta(\mu, M_1) \approx 20 - 50\,\text{GeV}$. In cases where $\tilde{t}_1 \sim \tilde{t}_L$, a light bottom squark is also expected and the pair production of sbottoms is also simulated, as $\tilde{b} \to t\tilde{\chi}_1^{\pm}$ decays produce a similar experimental signature to $\tilde{t} \to t\tilde{\chi}_1^0$. All other pMSSM parameters are set to large masses ($> 3\,\text{TeV}$) and thus decouple from the low-energy phenomena relevant to LHC searches.

Bino LSP with light Wino

A similar approach is taken to the previous scenario, now with the Higgsino mass parameter set to a large value ($\mu = \pm 3\,\text{TeV}$) and the Wino mass parameter M_2 scanned. Differences with respect to the previous scenario are as follows. The gluino mass parameter M_3 is set to $2.2\,\text{TeV}$, the breaking scale is varied within to $m_S = 0.9 - 1.2\,\text{TeV}$, and the Bino mass parameter is set to $M_1 = 2M_2$. The $\tilde{t}_1$ is assumed to be left-handed and thus sbottom pair production is also considered. In this scenario the stop decays dominants to the Wino states (with $\mathcal{BR}(\tilde{t} \to b\tilde{\chi}_1^{\pm}) \sim 2 \cdot \mathcal{BR}(\tilde{t} \to t\tilde{\chi}_2^0)$), as decays to the Bino are chirality-suppressed. Both signs of the μ parameter are considered, as this controls the relative importance of $\tilde{\chi}_2^0 \to h\tilde{\chi}_1^0$ ($\mathcal{BR} \sim 95\%$ when $\mu > 0$) and $\tilde{\chi}_2^0 \to Z\tilde{\chi}_1^0$ ($\mathcal{BR} \sim 75\%$ when $\mu < 0$) decays.

An overview of the parameter setting used in the generation of the pMSSM(-inspired) models is given in Table 6.1.

Table 6.1: An overview of the parameter settings used in the pMSSM(-inspired) models defined in the text. All parameters which are not specified are set to values above 3 TeV and do not impact the details of the low-energy phenomena that is simulated. In addition, an estimate of the decay branching fractions for stops (and sbottoms, where relevant) is shown. In the Higgsino LSP scenario, the three sets of branching fractions correspond to $\tilde{t}_1 \sim \tilde{t}_R$, $\tilde{t}_1 \sim \tilde{t}_L$, and the large $\tan\beta$ scenario, respectively. In the Bino LSP scenario with light Higgsinos, the two columns represent $\tilde{t}_1 \sim \tilde{t}_L$ (left) and $\tilde{t}_R$ (right) cases.

Scenario	Wino NLSP	Higgsino LSP	Bino/Higgsino mix
Models	pMSSM	simplified	pMSSM
Mixing parameters		$X_t/M_S \sim \sqrt{6}$	
$\tan\beta$	20	20 or 60	20
M_S [TeV]	0.9–1.2	1.2	0.7–1.3
M_3 [TeV]	2.2	2.2	1.8
Scanned mass parameters	$(M_1,\, m_{q3L})$	$(\mu,\, m_{q3L}/m_{tR})$	$(M_1,\, m_{q3L}/m_{tR})$
Electroweakino masses [TeV]	$\mu = \pm 3.0$	$M_2 = M_1 = 1.5$	$M_2 = 2.0$
	$M_2 = 2M_1 \ll \lvert\mu\rvert$	$\mu \ll M_1 = M_2$	$M_1 \sim -\mu,\, M_1 < M_2$
Additional requirements	–	–	$0.10 < \Omega h^2 < 0.12$
Sbottom pair production	considered	–	considered
$\tilde{t}_1$ decay modes and their BR [%]	$\tilde{t}_1 \sim \tilde{t}_L$	$\tilde{t}_L$ / $\tilde{t}_R$ / $\tan\beta$=60	$\tilde{t}_L$ / $\tilde{t}_R$
$\tilde{t} \to t\tilde{\chi}_1^0$	< 5	$\sim 25/\sim 45/\sim 33$	$< 10/< 10$
$\tilde{t} \to b\tilde{\chi}_1^\pm$	~ 65	$\sim 50/\sim 10/\sim 33$	$\sim 50/\sim 10$
$\tilde{t} \to t\tilde{\chi}_2^0$	~ 30	$\sim 25/\sim 45/\sim 33$	$\sim 20/\sim 40$
$\tilde{t} \to t\tilde{\chi}_3^0$	–	–	$\sim 20/\sim 40$
$\tilde{b}_1$ decay modes and their BR [%]	$\tilde{b}_1 \sim \tilde{t}_L$	–	$\tilde{b}_1 \sim \tilde{b}_L$
$\tilde{b} \to b\tilde{\chi}_1^0$	< 5	–	< 5
$\tilde{b} \to t\tilde{\chi}_1^\pm$	~ 65	–	~ 85
$\tilde{b} \to b\tilde{\chi}_2^0$	~ 30	–	< 5
$\tilde{b} \to b\tilde{\chi}_3^0$	–	–	< 5

6.4 Data set

The data-set of proton-proton collisions at $\sqrt{s} = 13$ TeV that was collected over LHC physics runs in 2015 and 2016 are included in the analysis. The recorded data corresponds to $36.1\,\text{fb}^{-1}$, as determined using the methods described in Ref. [194]. Only data is included which passes a Good Runs List (GRL), recording which runs and luminosity blocks contain events suitable for analysis. All events were recorded with un-prescaled $E_{\text{T}}^{\text{miss}}$ triggers, the details of which were described in Section 4.3. For the 2015 period, the cell-based `HLT_xe70_L1XE50` trigger was used, while the jet-based `HLT_xe110_mht_L1XE50` trigger[10] was used to record events in 2016. Figure 6.8 shows the

[10] For runs early in the year recorded at lower instantaneous luminosity, lower threshold triggers were un-prescaled and are thus also used in the analysis.

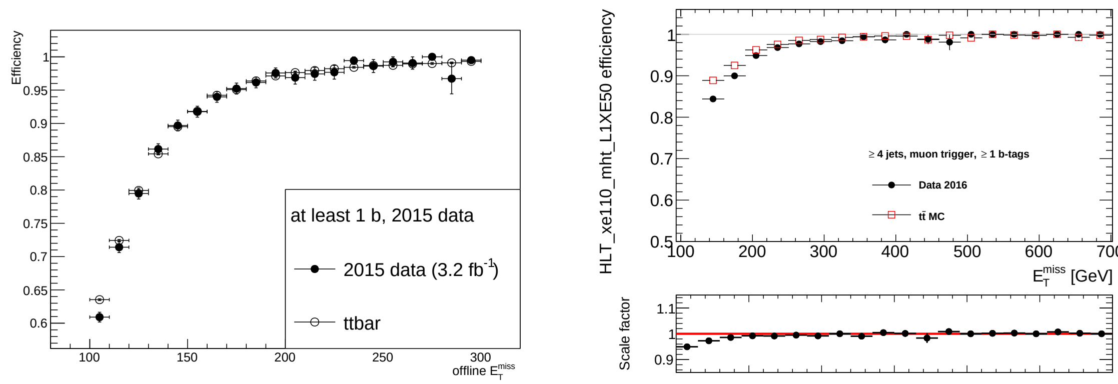

Figure 6.8: The efficiency of the $E_{\mathrm{T}}^{\mathrm{miss}}$ trigger is shown separately for 2015 (left) and 2016 (right). In 2015 a cell-based HLT $E_{\mathrm{T}}^{\mathrm{miss}}$ algorithm was used, while a jet-based calculation was used for the data-taking periods in 2016. The efficiency is measured using data collected with a single-lepton trigger and requiring four jets, at least one of which must be b-tagged. Good agreement is seen between simulated $t\bar{t}$ events and data, with a plateau in efficiency reached for events with offline $E_{\mathrm{T}}^{\mathrm{miss}} > 250\,\mathrm{GeV}$.

efficiency for triggers in each year for a signal-like selection as a function of the calculated offline $E_{\mathrm{T}}^{\mathrm{miss}}$. Events are selected for further analysis which have offline $E_{\mathrm{T}}^{\mathrm{miss}} > 250\,\mathrm{GeV}$, beyond which there is no significant change in the trigger efficiency. Studies showed that also including lepton triggers would improve the acceptance to $t\bar{t}$ events by only 1.2% for events with $E_{\mathrm{T}}^{\mathrm{miss}} > 250\,\mathrm{GeV}$, so this was not pursued.

Additional data-quality requirements are imposed on reconstructed jets to ensure that events are well-reconstructed. All signal jets are required to pass "cleaning" requirements [195] to reduce spurious jets caused by beam-induced backgrounds, cosmic-ray showers, and calorimeter noise spikes [196]. These are based on quality measures of the calorimeter pulse shapes as well as consistency checks on the relative fraction of energy deposited in each layer of the calorimeter and between the jet and constituent track p_{T} measurements. The efficiency of a combined selection on these quantities is found to be greater than 99.5% in an inclusive sample of di-jet events.

6.5 Object identification

High-granularity measurements of the detector are combined to form reconstructed particle candidates. This analysis requires the reconstruction of electrons, muons, jets, photons, and hadronic tau decays to characterize each of the recorded events and test the SM and BSM hypotheses. The algorithms used to reconstruct individual objects were presented in Section 4.4. Here we discuss analysis-specific choices, balancing the efficiency of reconstructing the targeted objects with the purity of the sample obtained. These reconstructed objects are used to build more complicated full-event observables.

Generally two sets of objects are defined. Baseline objects make loose requirements on identification criteria and kinematics and are used for the purposes of overlap removal. This procedure ensures that detector signatures are not reconstructed as multiple objects and energies double-counted. A tighter 'signal' selection is applied to baseline quantities which satisfy the overlap removal criteria, providing the ultimate objects used for the final analysis selections.

6.5.1 Electrons

Electron candidates are selected which satisfy selections on the identification and isolation parameters described in Section 4.4.2. Two classes of signal electrons are defined to be used in separate analyses. Loose leptons are used by default and use relaxed identification and isolation criteria to maximize acceptance to high-p_{T} signals where other selections efficiently reduce backgrounds from non-prompt and mis-identified leptons. Tight leptons are used in specialized search regions targeting signatures with low-p_{T} leptons where tighter identification is useful. Due to the lower requirement on p_{T}, tight signal leptons are not a subset of loose leptons. The selection criteria for baseline and signal leptons is summarized in Table 6.2.

The likelihood operating points used are denoted 'VeryLooseLH', 'LooseAndBLayerLH', and 'TightLLH'. The VeryLooseLH and LooseAndBLayerLH requirements are variations of the Loose working point which is found to be 93% efficient for prompt electrons with $E_{\mathrm{T}} = 40$ GeV. The former requires only a single hit in the pixel detector, while the latter requires two, one of which must be in the innermost pixel layer. The tight operating point is determined to be 80% efficient for 40 GeV electrons.

Isolation variables are defined requiring that tracks (calorimeter deposits) that are not associated to the reconstructed electron but are within $\Delta R = 0.2$ have $E_{\mathrm{T,cone}}^{\mathrm{iso}}$ ($p_{\mathrm{T,cone}}^{\mathrm{iso}}$) less than a particular value. The 'LooseTrackOnly' isolation criterion does not enforce the calorimeter requirement and achieves an efficiency of 99% independent of electron E_{T} and η. The 'FixedCutTight' criterion requires that both $E_{\mathrm{T,cone}}^{\mathrm{iso}}$ and $p_{\mathrm{T,cone}}^{\mathrm{iso}}$ be less than 6% of the electron p_{T}.

6.5.2 Muons

Baseline muons are identified using the Loose working point, which accepts all four varieties of muon described in Section 4.4.3. The majority of reconstructed muons are combined muons (approximately 97.5% of muons satisfying $|\eta| < 2.5$), with extrapolated muons are allowed only in the region beyond the ID coverage $2.5 < |\eta| < 2.7$, and calo-tagged (1.5%) and segment-tagged (1.0%) muons accepted only in the region $|\eta| < 0.1$. Additional requirements on the number of MS segments and the significance of the muon p_{T} are enforced. Signal muons are required to additionally pass the Medium identification criteria, which rejects calo-tagged and segment-tagged muon candidates. A comparison of the efficiency to reconstruct muons with the Loose and Medium working points, as measured in $Z \to \mu^+\mu^-$ events is shown in Figure 6.9.

Signal muons are further required to the pass the 'FixedCutTightTrackOnly' isolation requirement which requires that $p_{\mathrm{T,cone}}^{\mathrm{iso}}$ be less than 6% of the muon p_{T}, where the isolation variable in this case is computed from tracks within a cone of $\Delta R = 0.3$. The selection criteria for baseline and signal muons is summarized in Table 6.3.

In the following description of the stop analysis, leptons are collectively referred to as passing the 'loose' or 'tight' identification criteria; while variable criteria are used for electrons, no change is made for muons. The only distinctions is that lower p_{T} muons (to 4 GeV) are included in analyses using tight leptons.

6.5.3 Hadronic tau decays

ttbar decays with hadronic taus comprise a significant source of background for some signal selections, motivating the use of loose tau identification criterion. Only a single category of tau (reconstructed as described in Section 4.4.5) is used in the analysis, with those selected satisfying

Table 6.2: Selection criteria for electrons is summarized. In addition to baseline objects defined for overlap removal, 'loose' and 'tight' categories of signal leptons are defined. Tight electrons are defined at lower E_{T} and use tighter identification and isolation criteria.

Selection criteria	Baseline	Loose signal	Tight signal
E_{T}	> 5 GeV	> 25 GeV	> 5 GeV
$\|\eta\|$		< 2.47	
Identification	VeryLooseLH	LooseAndBLayerLH	TightLLH
Isolation	–	LooseTrackOnly	FixedCutTight
d_0 significance	–	< 5	
$z_0 \sin\theta$	–	< 0.5 mm	

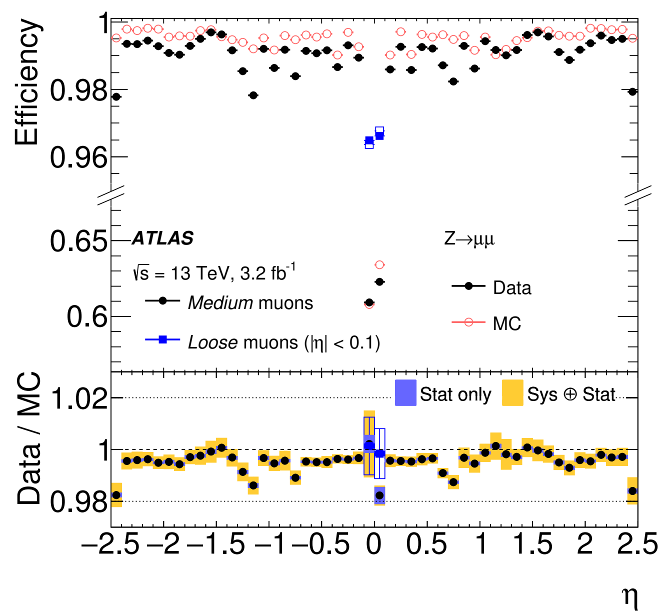

Figure 6.9: The reconstruction efficiencies for muons identified with the Loose and Medium working points are compared as a function of pseudorapidity. In the top panel, efficiencies for data and MC are shown with the corresponding ratio ("scale factors") shown in the lower panel. Loose muons include calo-tagged and segment-tagged muons in the region $|\eta| < 0.1$, allowing for significantly enhanced efficiency in this region. Figure is reproduced from Ref. [99].

Table 6.3: Selection criteria is summarized for muons, with identification and isolation working points are defined in the text. Muons as low in p_T as 4 GeV are utilized only for the soft lepton analysis targeting the Higgsino LSP signatures.

Selection criteria	Baseline	Signal
E_T	> 5 GeV	> 4 or 25 GeV
$\lvert\eta\rvert$	< 2.7	
Identification	Loose	Medium
Isolation	–	FixedCutTightTrackOnly
d_0 significance	–	< 3
$z_0 \sin\theta$	–	< 0.5 mm

$p_{\mathrm{T}} > 20$ GeV and $|\eta| < 2.5$. Candidates are identified using the looses working point, found to be 60% (50%) efficient for one-prong (three-prong) decays. The total charge of the tracks associated with the tau is required to be opposite to that of the identified lepton.

6.5.4 Jets

Jets are clustered using the anti-$k_{\perp}$ algorithm with radius parameter $R = 0.4$ as described in Section 4.4.4. Jets from SM backgrounds and SUSY signals are generally expected to be central, so jets are only considered in the region $|\eta| < 2.5$ which is also well-covered by the inner tracker. For low-p_{T} jets in the tracker acceptance, jets from pile-up can be efficiently rejected by requiring that the charged particle tracks within the jet cone originate from the primary vertex. This is accomplished with a requirement on the JVT discriminant that is found to be 92% efficient in signal jets from the hard-scatter.

Jets are considered b-tagged which pass a MV2c10 tagging requirement that was found to be 77.0% efficient for b jets in $t\bar{t}$ events. The corresponding rejection rates (inverse of efficiency) are 134 for light jets, 6.21 for charm and 22.0 for taus.

6.5.5 $E_{\mathrm{T}}^{\mathrm{miss}}$

$E_{\mathrm{T}}^{\mathrm{miss}}$ is defined as described in Section 4.4.6, using baseline objects described above as inputs. Photons and hadronic taus are not included, but may enter as electrons, jets, or via the soft term.

6.5.6 Overlap removal

To avoid double-counting of momenta from physics objects reconstructed from the same detector outputs an overlap removal (OR) procedure is enforced. Categories of baseline objects are com-

Table 6.4: A summary of selection criteria for calorimeter jets used in the analysis. JVT is a requirement on the 'jet vertex tagger' which removed pileup jets at low-p_{T}.

Selection criteria	Baseline jets	Signal jets
E_{T}	> 20 GeV	> 25 GeV
$\|\eta\|$	< 2.5	< 2.5
JVT	–	for $p_{\mathrm{T}} < 60$ GeV and $\|\eta\| < 2.4$

pared to check for overlaps in an ordered procedure so that removed objects are not considered in subsequent steps. The comparisons considered are, in order of precedence:

1. **Muon & electron**. If $\Delta R < 0.01$: the muon is removed only if it is calo-tagged, else the electron is removed.

2. **Electron & non-b-tagged jet**. If $\Delta R < 0.2$: the jet is removed.

3. **Muon & non-b-tagged jet**. If $\Delta R < 0.2$ and $\frac{p_{\mathrm{T}}(\mathrm{muon})}{p_{\mathrm{T}}(\mathrm{jet})} > 0.7$: the jet is removed.

4. **Non-b-tagged jet & lepton**. If $\Delta R < \min(0.4, 0.04 + \frac{10\ \mathrm{GeV}}{p_{\mathrm{T}}(\ell)})$: the lepton is removed.

5. **Electron & tau**. If $\Delta R < 0.1$: the tau is removed.

Surviving objects that also pass the signal selection criteria in each category are considered well-measured signal objects used to define the remainder of the analysis selection.

6.6 Event reconstruction

As was shown in Section 6.1, the existence of stops within the reach of the LHC could provide a diverse range of experimental signatures. The simplest scenario may be that of a high-mass stop (compared with the electroweak-scale SM particles) with a sizable production cross section. In this case, the signature is sufficiently different from any SM process that a simple selection (e.g. requiring many high-energy jets) could be enough to isolate a large set of BSM events. However, if nature is not so kind, prospects may be more difficult. For a intermediate-mass stop with a complicated spectrum of electroweakinos at lower masses, these BSM events with many soft objects may be very difficult to disentangle from the copious SM background processes. In the following, we will briefly describe the sophisticated set of tools used to (hopefully!) isolate signatures of BSM physics from SM impostors.

$E_{\mathrm{T}}^{\mathrm{miss}}$ significance

A generic signature of $\tilde{t}\tilde{t}^{*}$ production is the presence of many energetic objects and large $E_{\mathrm{T}}^{\mathrm{miss}}$. As such, each of the signal selections used in this analysis makes requirements on energetic jets. In the Bino LSP scenario, four energetic jets are expected, with three generally resulting from the fully hadronic decay of one (anti-)top quark and a b jet from the decay of the other. SM backgrounds with a significant amount of hadronic activity can be reconstructed as having larger $E_{\mathrm{T}}^{\mathrm{miss}}$ than expected from the invisible particles produced in the process due to mis-measurement of jet energies. To determine whether the reconstructed $E_{\mathrm{T}}^{\mathrm{miss}}$ in an event is consistent with mis-measured jets, the $\vec{H}_{\mathrm{T,sig}}^{\mathrm{miss}}$ observable is defined as

$$\vec{H}_{\mathrm{T,sig}}^{\mathrm{miss}} = \frac{|\vec{H}_{\mathrm{T}}^{\mathrm{miss}}| - M}{\sigma_{\vec{H}_{\mathrm{T}}^{\mathrm{miss}}}}. \tag{6.1}$$

Here $\vec{H}_{\mathrm{T}}^{\mathrm{miss}}$ is the vector sum of the p_{T} for all jets in the event as well as the signal lepton, i.e. an object-level proxy for the $E_{\mathrm{T}}^{\mathrm{miss}}$. The numerator is constructed from its magnitude, less an overall scale $M = 100$ GeV corresponding to the average activity in a typical event. The denominator is computed as the spread in $\vec{H}_{\mathrm{T}}^{\mathrm{miss}}$ values based on the energy resolution for each jet in the event. This quantity is calculated using toy data sets where $\vec{H}_{\mathrm{T}}^{\mathrm{miss}}$ is computed from jets whose "toy momenta" are randomly drawn according to their per-object uncertainties, which vary according to the p_{T} and η of the jet. The quantity $\sigma_{\vec{H}_{\mathrm{T}}^{\mathrm{miss}}}$ is calculated as the 1σ variation over all toy data sets, so that $\vec{H}_{\mathrm{T,sig}}^{\mathrm{miss}}$ may naturally be interpreted as the "significance" of the measured object-based $E_{\mathrm{T}}^{\mathrm{miss}}$.

Hadronic top and W reconstruction

In the benchmark $t\bar{t} + E_{\mathrm{T}}^{\mathrm{miss}}$ signature of $\tilde{t}\tilde{t}^*$production, reconstructing the constituent jets of the hadronically-decaying top quark allows an additional handle to isolate the signal from backgrounds without real hadronic top decays (chiefly di-leptonic $t\bar{t}$ and W+jets). Previous analyses have excluded stop masses below 600 GeV in the Bino LSP scenarios for a range of LSP masses, allowing the use of dedicated reconstruction techniques that rely on high-p_{T} tops. The opening angle between two objects from a decaying resonance of mass M and momentum $\vec{p}$ is given by

$$\theta = \frac{2M}{|\vec{p}|} \tag{6.2}$$

assuming that the decay plane is perpendicular to $\vec{p}$. For a stop produced at rest, the $\vec{p}$ of its top quark daughter is $m_{\tilde{t}}/2$, so that the top decay products will, on average, be found within an $\eta - \phi$ cone of size $\Delta R \sim 2m_t/p_{\mathrm{T}} \sim 4m_t/m_{\tilde{t}}$. As an example, the typical angular separation is 1.0 for a 700 GeV stop.

This motivated the *recursive reclustering* algorithm used to identify top-quark candidates, which is conducted in steps:

1. All jets are reclustered using the anti-$k_{\perp}$algorithm with radius parameter $R = R_0$.

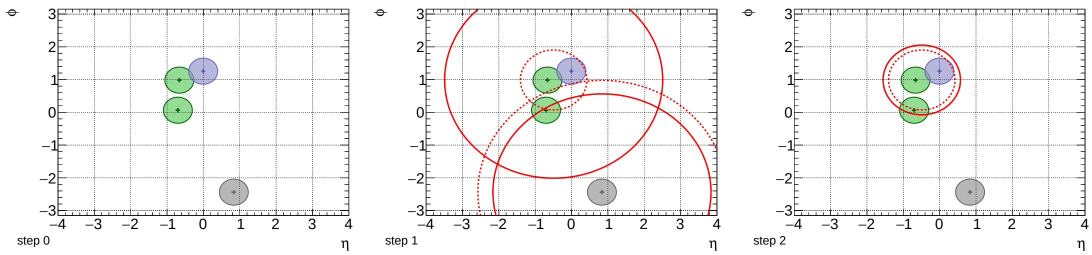

(a) All jets (b) Initial clustering (c) Final candidates

Figure 6.10: An illustration of the recursive reclustering algorithm for a single semi-leptonic $t\bar{t}$ decay event. All signal jets are shown in 6.10a, colored green (W decay), blue (b jetfrom top-quark), or gray (other), to indicate their origin. 6.10b shows the candidates clustered with radius R_0 (solid red circles), as well as the optimal radius $R(p_{\mathrm{T}})$ (dashed red circles). The result of the iterative procedure is shown in 6.10c, where only one candidate has been retained and the final radii are shown.

2. For each reclustered jet, the "optimal radius" is computed according to the constituent jet momenta from the heuristic $R(p_{\mathrm{T}}) = 2m_t/p_{\mathrm{T}}$. The radius of the reclustered jet R_{reclus} is now compared to its optimal radius $R(p_{\mathrm{T}})$:

   a) If $R(p_{\mathrm{T}}) < R_{\mathrm{reclus}} - R_{\mathrm{down}}$: then the constituents are reclustered with radius $R = \max\{R(p_{\mathrm{T}}) + \frac{1}{2}R_{\mathrm{down}}, \frac{1}{2}R_{\mathrm{reclus}}\}$ and Step 2 is repeated for each new reclustered jet.

   b) If $R(p_{\mathrm{T}}) > R_{\mathrm{reclus}} + R_{\mathrm{up}}$: the jet is rejected.

   c) Else: the jet is accepted as a hadronic top candidate.

The parameters R_0, R_{down}, and R_{up} are configurable. R_0 is taken to be 300 GeV: the top decay products for nearly all models considered should have momenta above this scale. R_{down} and R_{up} parameters control the tolerance of the approximate angular separation formula and are set to 0.5 and 0.3, respectively. The maximum taken in Step 2(a) controls the rate which the jet radii are allowed to shrink to prevent discarding genuine high-p_{T} top-quark decays. The reclustered jets which are retained in Step 2(c) comprise the reconstructed top-quark candidates. An analogous procedure is used to reconstruct hadronic decays of W bosons, where b jetsare not included as inputs.

An example event display for this procedure is shown in Figure 6.10. Figure 6.11 shows the efficiency to reconstruct hadronic tops and resulting reconstructed mass distributions for $t\bar{t}$ events. In particular, the recursive reclustering algorithm is found to outperform a naive strategy using anti-$k_\perp$ jets with $R = 1.0$ even for top quarks with $p_{\mathrm{T}} > 2m_{\mathrm{top}}$, illustrating the power of the adaptively-selected radius strategy.

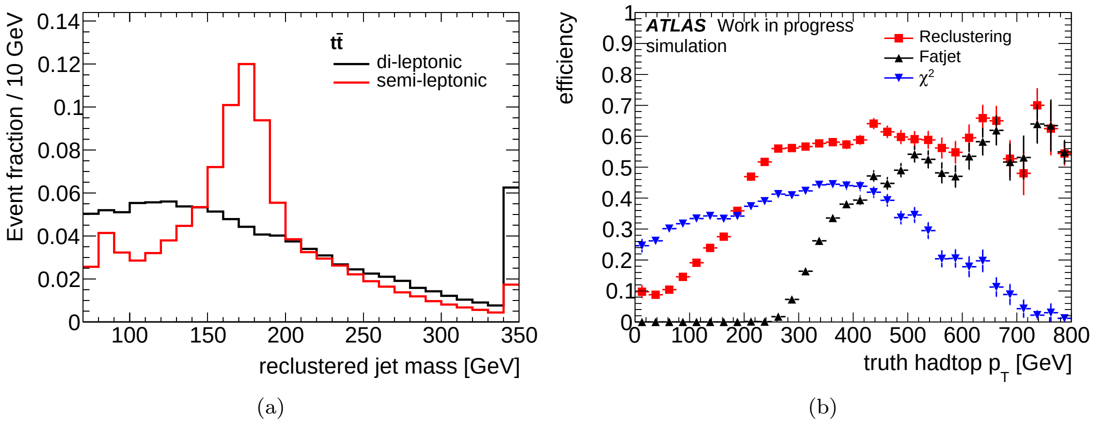

Figure 6.11: At left, the mass of reconstructed top-quark candidates is shown for semi- and di-leptonic $t\bar{t}$events. The reconstructed mass peaks at m_{top} for events with a true hadronically-decaying top quark, while it is smooth and unshaped for those without. At right, the reconstruction efficiency of the recursive reclustering algorithm is compared to several other in semi-leptonic $t\bar{t}$ events. The blue curve corresponds to a χ^2-minimization technique used in analyses targeting low-momentum top quarks which are not described further here. The method performs best only at low p_{T}, and produces mass distributions which peak at the top mass even for events where no hadronically decaying top is present, in contrast to 6.11a. The black curve shows a reconstruction algorithm where the anti-$k_{\perp}$ algorithm with $R = 1.0$ is run directly on the signal jet constituents. This method is efficient for high-p_{T} top quarks only due to the fixed radius size.

Transverse mass

Transverse masses are estimators of the mass of parent particles that decay semi-invisibly, as in the case of the W boson decay to an electron and neutrino $W \to e\bar{\nu}_e$. Because the momenta of invisible daughter particles may only be inferred in the plane perpendicular to the beam-line at a proton-proton collider the complete parent mass cannot be reconstructed. The transverse mass m_{T} is constructed assuming massless decay products, written here as a visible charged lepton ℓ and an invisible neutrino ν as

$$m_{\mathrm{T}} = \sqrt{(E_T^{\ell} + E_T^{\nu})^2 - (p_T^{\ell} + p_T^{\nu})^2} \quad (6.3)$$

$$= \sqrt{2 \cdot p_{\mathrm{T}}^{\ell} \cdot p_{\mathrm{T}}^{\nu}(1 - \cos \Delta\theta(\ell, \nu)}. \quad (6.4)$$

Requiring that events have $m_{\mathrm{T}} > m_W$ is very effective in removing SM backgrounds where the $E_{\mathrm{T}}^{\mathrm{miss}}$ and identified lepton are from a W decay. The m_{T} distribution for events with a well-identified lepton and $E_{\mathrm{T}}^{\mathrm{miss}} > 200$ GeV is shown in Figure 6.12a.

After selecting events with large m_{T} the dominant background to the $t\bar{t}$+$E_{\mathrm{T}}^{\mathrm{miss}}$ signature of

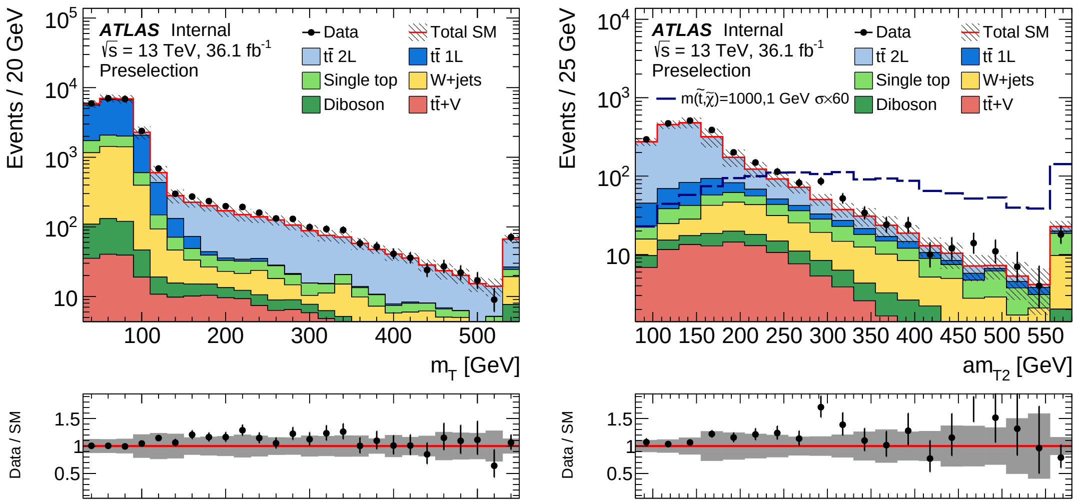

(a) (b)

Figure 6.12: The transverse mass variables m_{T} and am_{T2} shown for events with a well-identified lepton and $E_{\mathrm{T}}^{\mathrm{miss}} > 200$ GeV. Note the logarithmic scales. In (a), an endpoint near the W mass is clearly observed, below which the vast majority of semi-leptonic $t\bar{t}$ and $W+$jets events are found. In (b), a requirement that $m_{\mathrm{T}} > 120$ GeV is additionally enforced to reduce contamination from events with a single leptonically decaying W boson. The contribution from di-leptonic $t\bar{t}$ decays is significantly reduced when $am_{T2} > m_{\mathrm{top}}$. In contrast, the majority of the am_{T2} spectrum from a 1 TeV stop falls beyond the kinematic endpoint.

$\tilde{t}\tilde{t}^*$ production is di-leptonic $t\bar{t}$ events where one of the leptons is not identified. Such events may pass the m_{T} endpoint because momentum is carried by two invisible particles. This can be due to acceptance or failure to identify the lepton, the latter of which is particularly problematic for top quark decays involving tau leptons. To distinguish such events from the $\tilde{t}\tilde{t}^*$ signal, the m_{T} variable is generalized to the m_{T2} class of observables, targeting decay structures with two invisible particles [197, 198].

In the case of pair-produced particles X each decaying semi-invisibly (say to visible particle V and invisible particle I), the event can be split into two "legs", each of which correspond to one of the X particles. The one may compute m_{T} for each leg of the decay in the same manner as Eqn. 6.3:

$$(m_{T,i})^2 = (E_{T,i}^V + E_{T,i}^I)^2 - (p_{T,i}^V + p_{T,i}^I)^2 \tag{6.5}$$

, where $i = 1, 2$ indexes the decay products of the pair-produced particles X_i. The fact that there are multiple legs with invisible particles presents the problem that ATLAS only measured $E_{\mathrm{T}}^{\mathrm{miss}}$

and not individual invisible particle momenta. Thus one cannot distinguish between the various configurations which give $|p^I_{T,1} + p^I_{T,2}| = E_{\mathrm{T}}^{\mathrm{miss}}$. However, for the correct assignment of invisible particles $\max\{m_{T,1}, m_{T,2}\}$ must be less than the mass of particle X. It follows that

$$m_{T2} = \min_{|p^I_{T,1}+p^I_{T,2}|=E_{\mathrm{T}}^{\mathrm{miss}}} \{\max(m_{T,1}, m_{T,2})\}, \tag{6.6}$$

with $m_{T,i}$ defined as in Eqn. 6.3, must also take a value below the mass of X.

The most useful definition of m_{T2} is specific to the analysis goal, with several variants are used in the $\tilde{t}\tilde{t}^*$ search. Di-leptonic $t\bar{t}$ events are targeted with the asymmetric m_{T2} ("am_{T2}") variable. In this construction, each leg corresponds to the decay of a (anti-)top quark. In one leg, the visible particles are a b jet and a lepton and the invisible particle is the neutrino. In the other leg, the lepton is also undetected, so the invisible particle is a W boson, while the visible particle is second b jet[11]. This assignment is shown in Figure 6.13a. The invisible masses in the m_{T2}calculation are accordingly set to $m_\nu \approx 0$ and m_W in the calculation ("hence the asymmetric"). Further, both pairings of the b jet and the lepton are considered, with a minimum taken over the two possible combinations, so that we define

$$am_{T2} = \min_{|p^I_{T,\nu}+p^I_{T,W}|=E_{\mathrm{T}}^{\mathrm{miss}}} \{\min_{b-\ell \text{ pairs}} [\max(m_T(\ell, b, \nu), m_T(b', W))]\}. \tag{6.7}$$

The second m_{T2} variable constructed is m^τ_{T2}, which targets decays where the one of the top quarks decays with a hadronic tau. The topology and assignment of masses is shown in Figure 6.13b, with m^τ_{T2} defined analogously to Eqn. 6.7, except that b jetsare not included in the calculation and the invisible mass is set to zero for both legs. This reproduces an endpoint at the W boson mass in the limit of colinear neutrinos. A veto is constructed based on this variable for events with a reconstructed tau candidate (defined in Sect. 6.5), which rejects events when $m^\tau_{T2} < 100$ GeV[12]. This veto is found to be 99% percent efficient for a signal model with 800 GeV stops, each decaying to a massless LSP and a top quark, for the `tN_med` signal region, to be defined in the following Section. Conversely, about 40% of $t\bar{t}$ events with a hadronic tau are rejected. The variable is shown for events with a preselection of $m_{\mathrm{T}} > 150$ GeV and $E_{\mathrm{T}}^{\mathrm{miss}} > 200$ GeV in Figure 6.14.

[11]The W boson is only truly invisible if the lepton is outside of the detector acceptance. If it is an electron that is reconstructed as a jet, for example, the mass of the invisible system will be overestimated, broadening the resolution of this observable.

[12]Upon further optimization, it was decided to loosen this requirement to 80 GeV.

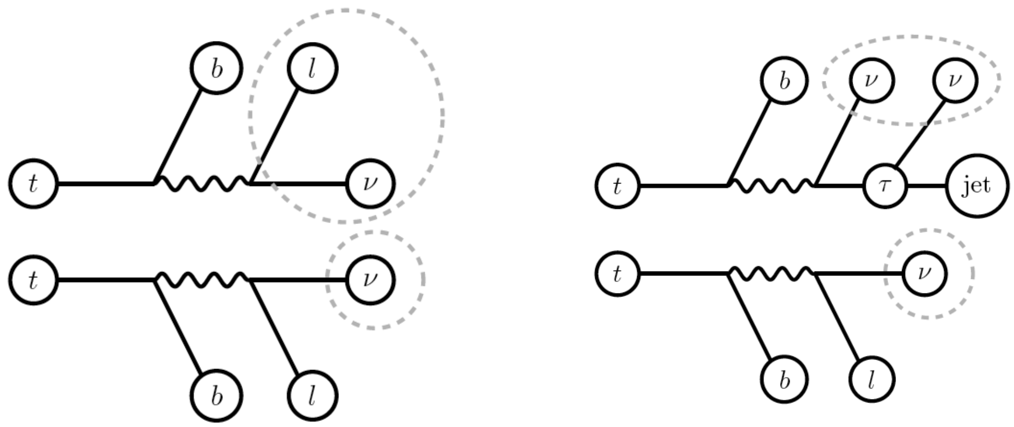

(a) am_{T2} (b) m_{T2}^{τ}

Figure 6.13: The assignment of visible and invisible objects when constructing the am_{T2} (left) and m_{T2}^{τ} (right) observables. A transverse mass is computed for each (anti-)top quark leg shown, with the invisible system circles with dashed lines. For m_{T2}^{τ}, the b jets are not included in the calculation, so that the endpoint occurs at m_W and not m_{top}.

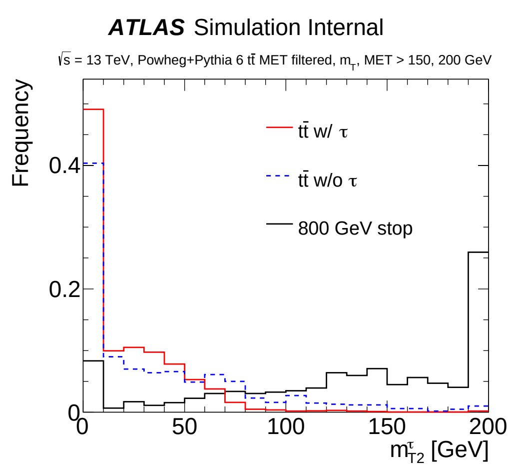

Figure 6.14: The m_{T2}^{τ} distribution is shown for $t\bar{t}$ events with and without a hadronically decaying tau lepton as well as for $\tilde{t}\tilde{t}^*$ events. All displayed events have a reconstructed tau candidate and have $m_{\text{T}} > 150$ GeV and $E_{\text{T}}^{\text{miss}} > 200$ GeV. The endpoint at the W mass is clear for $t\bar{t}$ with tau decays, while the other events may pass this value. After the selection shown, the majority of the signal distribution has large reconstructed m_{T2}^{τ} due to the large $E_{\text{T}}^{\text{miss}}$ in the event. Events due to $t\bar{t}$ without a real hadronic tau decay are still reconstructed as having low values of m_{T2}^{τ} here as the majority of fake tau candidates are due to low-energy jets near the threshold of 20 GeV.

6.7 Search Regions and Background Estimation

In Section 6.1, we discussed the phenomenology of $\tilde{t}\tilde{t}^*$ pair production accessible at the LHC. Here we will further discuss the searches tailored for each of the signatures described. In particular, dedicated selections are developed for the case of the Bino LSP, the Bino LSP with light Wino, and the Higgsino LSP. Though a dedicated search region is not designed for the well-tempered neutralino scenario (Bino LSP with light Higgsino) other regions are sensitive to this signature.

The space of possible $\tilde{t}\tilde{t}^*$ decay signatures is vast so, while it is not possible to describe in this document all of the search selections targeted in the one-lepton channel, we will take care to discuss a broad and representative set. The selections described will focus on $\tilde{t} \to t\tilde{\chi}_1^0$ decays for high-mass stops (relevant to all scenarios), $\tilde{t} \to b\tilde{\chi}_1^\pm$ decays of high-mass stops (relevant for the Wino NLSP scenario), and soft-lepton regions (targeting Higgsino LSPs).

6.7.1 High-mass stop decays to $t\tilde{\chi}_1^0$

Two SRs are defined to target high-mass stops with large mass splittings between the $\tilde{t}$ and LSP. The previous, Run 1 ATLAS analysis in this channel excluded top squarks up to nearly 700 GeV in the case where the LSP is massless and $\mathcal{BR}(\tilde{t} \to t\tilde{\chi}_1^0) = 100\%$ [3]. The models excluded in this scenario by the 8 TeV analysis are shown in Figure 6.15. The first signal region `tN_high` targets the case of the massless Bino, where the most energetic top quarks are emitted from the $\tilde{t}$ decay. The second signal region `tN_med` targets the intermediate phase space, optimized based on the point $(m_{\tilde{t}}, m_{\tilde{\chi}_1^0}) = (600\ \text{GeV}, 300\ \text{GeV})$. Each of these regions is named `tN` in reference to the top quark t plus neutralino $\tilde{\chi}_1^0$ final state, in addition to the mass range of the stop which is targeted. Specialized SRs for lower stop masses in the "corridor" regions where $\Delta(m_{\tilde{t}}, m_{\tilde{\chi}_1^0}) \sim m_{\text{top}}$ or $\Delta(m_{\tilde{t}}, m_{\tilde{\chi}_1^0}) \sim m_W$ (see Figure 6.15) are also defined but require dedicated analysis techniques and will not be further discussed in this document.

Event preselection

The $E_{\text{T}}^{\text{miss}}$ trigger is used to collect events for each of these signal regions, with the precise menu items described in Section 6.4. The trigger is found to be fully efficient for values of "offline" $E_{\text{T}}^{\text{miss}}$ above 230 GeV. In addition to passing the trigger, events are required to contain exactly one 'loose' lepton with $p_{\text{T}} > 25$ GeV, and no additional baseline leptons. In addition two jets with p_{T} of at least 25 GeV are required as well as $m_{\text{T}} > 30$ GeV to suppress fake lepton backgrounds. Further, events must pass data-quality checks: all jets must pass "cleaning" requirements (defined in Sect. 6.5) as

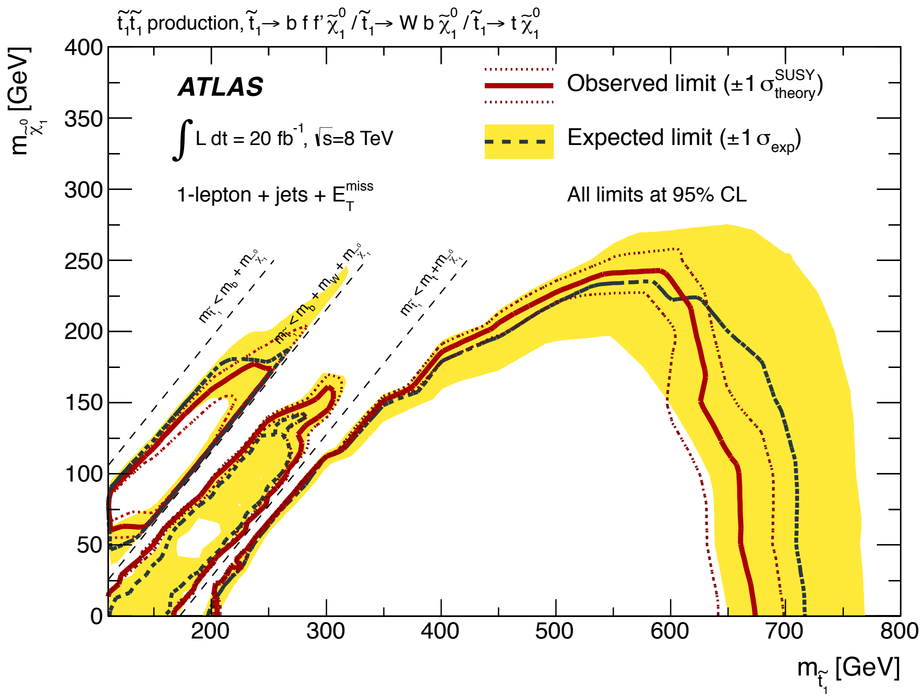

Figure 6.15: Exclusion contours established after the 8 TeV analysis in the one-lepton channel. Figure reproduced from Ref. [3].

well as having at least two 400 MeV tracks associated with the primary vertex. These requirements are summarized in Table 6.5 and define the common tN preselection.

Optimization procedure

The tN signal regions are optimized using the discriminating variables described in Section 6.6, as well as other basic event kinematics. The precise signal selection is determined by an optimization algorithm, which maximizes the expected significance of a signal. This is done sequentially by considering the improvement in significance that could be achieved by cutting on each of the observables to consider. A selection is made on the variable which produces the best significance, but at a looser value than that which would maximize the significance. The procedure is then repeated until no additional requirements would substantially change the significance. There are free parameters in the algorithm corresponding to: the "annealing factor" of how aggressively to cut on the best-significance variable, at risk of being too aggressive at the expense of placing powerful cuts on other variables; what level of additional significance is required to place an additional cut instead of terminating the algorithm; and what model should be used to assess the signal significance. Re-

Table 6.5: Preselection requirements for signal regions targeting Bino and Higgsino LSPs. The main difference between selections is the lepton p_T range targeted, which results in a difference choice of lepton identification and isolation working point.

Selection	**hard-lepton**	**soft-lepton**
Trigger	E_T^{miss} triggers only	
Data quality	jet cleaning, primary vertex	
Second-lepton veto	no additional baseline leptons	
Number of leptons, tightness	= 1 'loose' lepton	= 1 'tight' lepton
Lepton p_T [GeV]	> 25	> 4 for μ
		> 5 for e
Number of (jets, b-tags)	$(\geq 2, \geq 0)$	$(\geq 2, \geq 1)$
Jet p_T [GeV]	$> (25,\ 25)$	
E_T^{miss} [GeV]	> 230	
m_T [GeV]	> 30	–

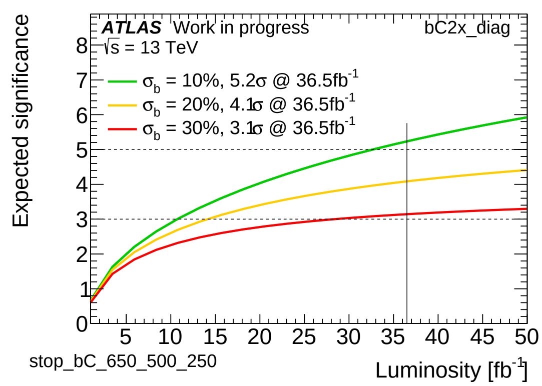

Figure 6.16: An example diagnostic plot from the optimization procedure. The expected significance of a particular selection is shown as a function of the recorded luminosity. Here, a SR targeting $\tilde{t} \to b\tilde{\chi}_1^{\pm}$ decays described in Sect. 6.7.2 is shown, though the procedure is the same as was used for all SRs. The expected sensitivity is shown for assumed systematic uncertainties of 10, 20, and 30% of the total estimated SM background.

quirements may also be placed on the maximum MC statistical uncertainty, leading to looser SR definitions. Each of these parameters was scanned in the optimization process to attain the final selections. Figure 6.16 demonstrates the expected sensitivity of a test selection to the BSM signal as a function of data luminosity, where various levels of systematic uncertainties are compared. Distributions of several important observables used to select events in each SR are shown after the hard-lepton preselection in Figures 6.17 and 6.18.

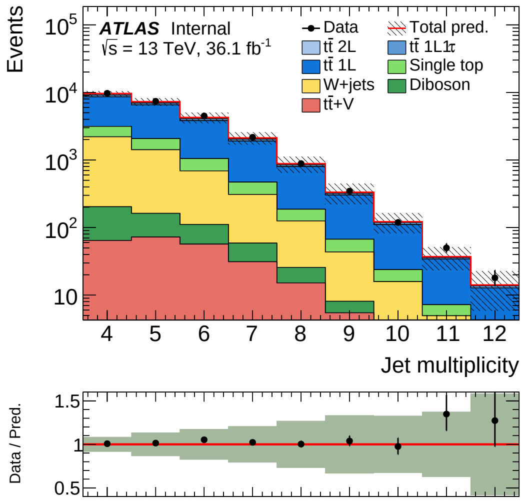

(a) Number of jets

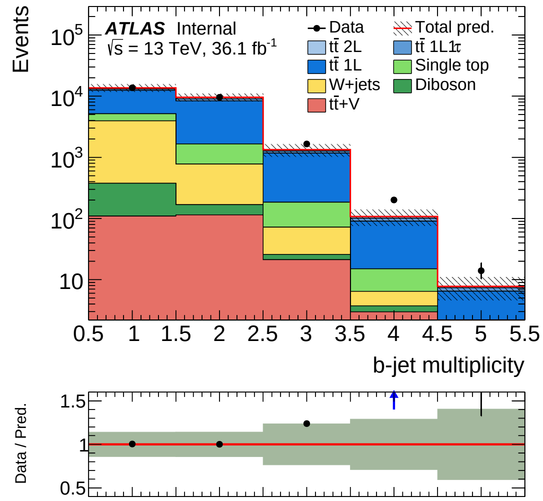

(b) Number of b jets

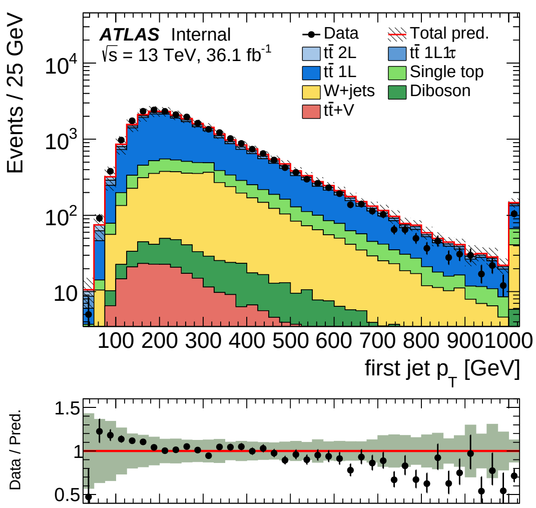

(c) Leading jet p_{T}

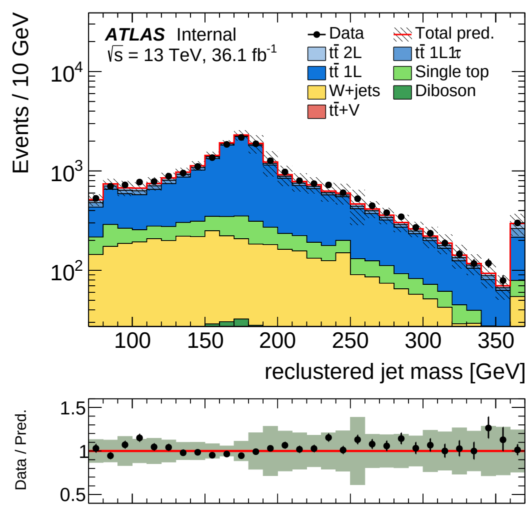

(d) Hadronic top candidate mass

Figure 6.17: Comparisons of data with predicted yields based on MC simulation, with differential distributions shown for a variety of observables. Prediction histograms are stacked, corresponding to contribution from different SM processes, indicated in the legend. Only statistical uncertainties are displayed. Clockwise from top-left, distributions are shown for the number of jets, b-tagged jets, hadronic top candidate mass, and leading jet p_{T}. In general the data and MC agree well, with two notable exceptions. The leading jet p_{T}, most often from initial-state radiation off of the $t\bar{t}$system, is over-estimated in simulation. Second, the number of b jets is under-predicted at high-multiplicity, corresponding to additional gluon radiation off of the top quarks, which subsequently split to b quark pairs. The background estimation strategy is designed to be robust against each mis-modeling.

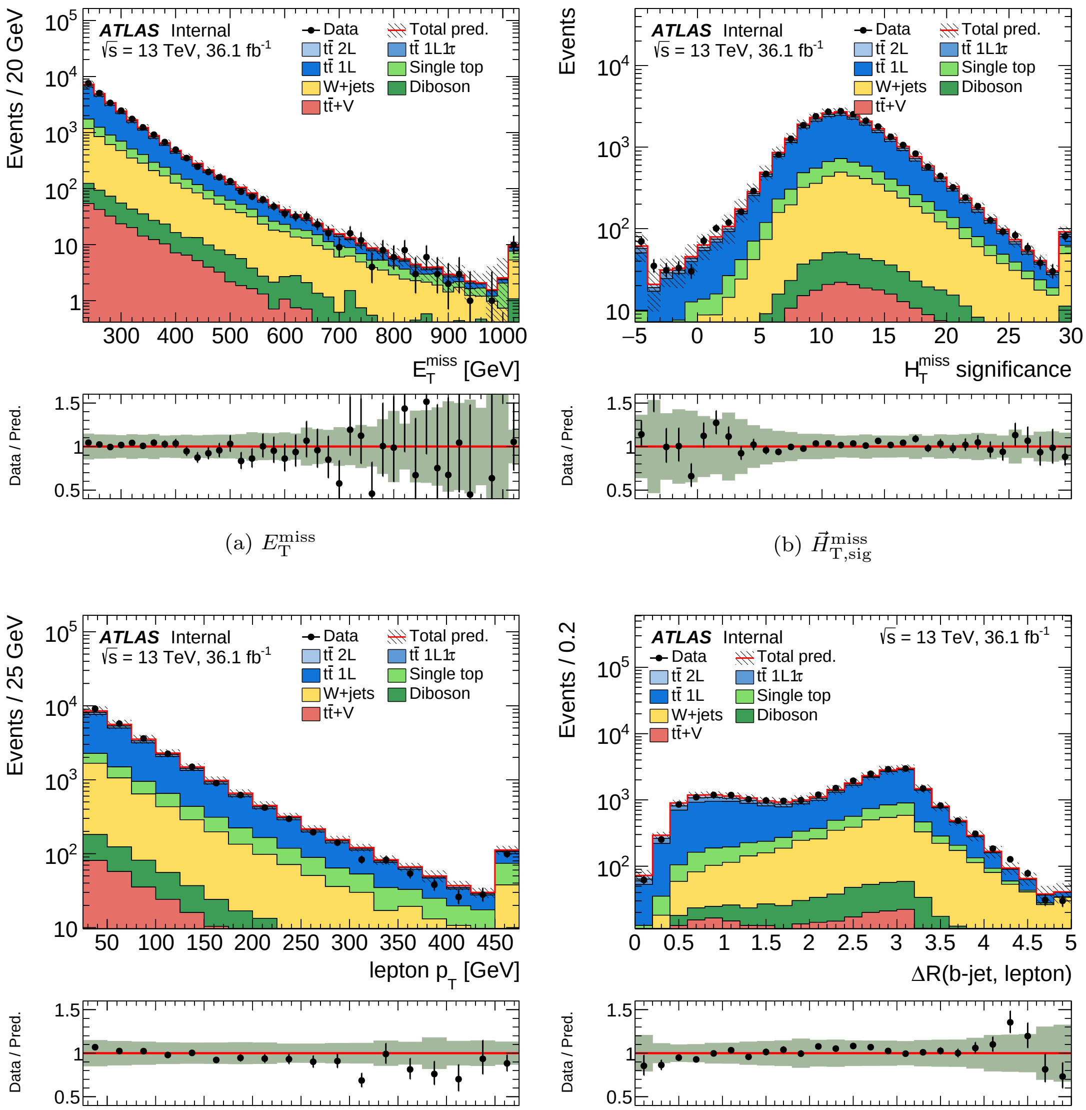

(a) $E_{\mathrm{T}}^{\mathrm{miss}}$

(b) $\vec{H}_{\mathrm{T,sig}}^{\mathrm{miss}}$

(c) Lepton p_{T}

(d) $\Delta R(b, \ell)$

Figure 6.18: Comparisons of data with predicted yields based on MC simulation, with differential distributions shown for a variety of observables. Prediction histograms are stacked, corresponding to contribution from different SM processes, indicated in the legend. Only statistical uncertainties are displayed. Clockwise from top-left, distributions are shown for the missing energy, $\vec{H}_{\mathrm{T,sig}}^{\mathrm{miss}}$, lepton p_{T}, and the angular distance between the lepton and the closest b jet. The data and MC generally agree well.

Signal region definitions

The `tN_high` SR is defined to be the set of events passing several selections on top of those described in the preselection above. It is optimized to discover the decays of a TeV stop to a massless LSP and top quark. Four jets are required: one must have p_{T} greater than 100 GeV, another 80 GeV, another 50 GeV, and a fourth with p_{T} at least 30 GeV. At least one signal jet must be b-tagged. The reconstructed $E_{\mathrm{T}}^{\mathrm{miss}}$ should be at least 550 GeV. The $E_{\mathrm{T}}^{\mathrm{miss}}$ is required to be well-measured and originating from true invisible particles by requiring $\vec{H}_{\mathrm{T,sig}}^{\mathrm{miss}} > 27$ and $\Delta\phi(\mathrm{jet}, \vec{p}_{\mathrm{T}}^{\mathrm{miss}}) > 0.4$ for each of the two leading jets. A hadronic top candidate is required with $m_{\mathrm{top}}^{\mathrm{reclustered}} > 130$ GeV. No upper requirement is enforced to maximize the signal acceptance. Requirements are made on the transverse mass variables $m_{\mathrm{T}} > 160$ GeV and $am_{T2} > 175$ GeV. The b jetclosest to the lepton must satisfy $\Delta R(b, \ell) < 2.0$. Finally, the m_{T2}-based tau veto is enforced.

The selection for the `tN_med` SR is similar, with looser requirements on the four jets of 60, 50, 40, and 40 GeV. A modest cut of $E_{T,\perp}^{\mathrm{miss}} > 230\ GeV$ is enforced. This quantity is the $E_{\mathrm{T}}^{\mathrm{miss}}$ projected onto the leptonic top system (b jet, neutrino, and lepton) where the ambiguity in choice of b jet[13] is solved by minimizing a χ^2 which assigns the four leading jets to W boson and top quark parents. The mass of the hadronic top candidate is tightened to $m_{\mathrm{top}}^{\mathrm{reclustered}} > 150$ GeV, while the $\vec{H}_{\mathrm{T,sig}}^{\mathrm{miss}}$ significance requirement is loosened to 14. This region is subdivided into several “bins” based on $E_{\mathrm{T}}^{\mathrm{miss}}$, with boundaries defined by $[250, 350, 450, 600, \mathrm{inf})$ GeV. If an excess of events is observed, the significance of single bins may be quoted. Otherwise, bins may be combined to set more powerful limits on $\tilde{t}\tilde{t}^*$ signals with a broad $E_{\mathrm{T}}^{\mathrm{miss}}$ distribution by combining regions with various ratios of signal-to-background. The selection for each `tN` region is summarized in Table 6.6.

Background Estimation

The composition of the expected SM backgrounds is shown for each SR in Table 6.7. In `tN_med` the largest contributions come from $t\bar{t}$ and $t\bar{t}Z$ processes. In `tN_high` the expected background is very small (4 events), with $t\bar{t}Z$ and $W+$jets processes being the most important.

Following the strategy outlined in Section 6.2, CRs and VRs are defined to estimate the SM backgrounds which are anticipated to be dominant based on MC studies and to assess the quality of this estimation. Separate CRs are defined for semi-leptonic $t\bar{t}$, di-leptonic $t\bar{t}$ (including hadronic taus), $W+$jets and tW single top processes. Precise definitions of each region are presented in

[13] Because only one b jet is required in this SR, the second candidate for the purposes of this algorithm is taken as the jet with the next largest probability to be a b jet, as determined by the nominal b tagging algorithm

Table 6.6: Event selection criteria for the `tN_med` and `tN_high` SRs. The top panel shows the definition of the SRs used for the model-independent results. To enhance exclusion capabilities for stop models, multi-bin regions are also defined for `tN_med`.

Signal region	`tN_med`	`tN_high`
Preselection	high-$E_{\mathrm{T}}^{\mathrm{miss}}$ preselection	
Number of (jets, b-tags)	$(\geq 4, \geq 1)$	$(\geq 4, \geq 1)$
Jet p_{T} [GeV]	$>(60,\ 50,\ 40,\ 40)$	$>(100,\ 80,\ 50,\ 30)$
$E_{\mathrm{T}}^{\mathrm{miss}}$ [GeV]	>250	>550
$E_{T,\perp}^{\mathrm{miss}}$ [GeV]	>230	–
$\vec{H}_{\mathrm{T,sig}}^{\mathrm{miss}}$	>14	>27
$m_{\mathrm{top}}^{\mathrm{reclustered}}$ [GeV]	>150	>130
m_{T} [GeV]	>160	
am_{T2} [GeV]	>175	
$\Delta R(b,\ell)$	<2.0	
$\lvert\Delta\phi(j_{1,2},\vec{p}_{\mathrm{T}}^{\mathrm{miss}})\rvert$	>0.4	
m_{T2}^{τ} based τ-veto [GeV]	>80	
Exclusion technique	shape-fit in $E_{\mathrm{T}}^{\mathrm{miss}}$	cut-and-count
Bin boundaries in $E_{\mathrm{T}}^{\mathrm{miss}}$ [GeV]	$[250, 350, 450, 600, \inf)$	

Table 6.8, with the same preselection enforced as was described for the SRs above. The background from semi-leptonic $t\bar{t}$ events is estimated by inverting the transverse mass selection. The corresponding CR is defined in the background rich region $m_{\mathrm{T}} < 90$ GeV, while the extrapolation past the kinematic endpoint at the W boson mass is checked in the VR ($90 < m_{\mathrm{T}}/\mathrm{GeV} < 120$). Di-leptonic $t\bar{t}$ is estimated by inverting the hadronic top tag requirement. The am_{T2} selection is also reversed for both sets of $t\bar{t}$ regions. Backgrounds due to $W+$jets are also estimated from

Table 6.7: Predicted composition of the SM backgrounds to the `tN` signal regions. Yields here are normalized to the SM cross sections, before any data-driven corrections are applied. All sub-regions of `tN_med` are combined, inclusive in $E_{\mathrm{T}}^{\mathrm{miss}}$.

Signal region	`tN_med`	`tN_high`
$t\bar{t}$ 2L	7.15 ± 0.94	0.34 ± 0.18
$t\bar{t}$ 1L1τ	7.11 ± 0.83	0.28 ± 0.18
$t\bar{t}$ 1L	0.35 ± 0.14	0.00 ± 0.00
Single top	3.66 ± 0.41	0.31 ± 0.09
W+jets	5.16 ± 0.82	1.30 ± 0.53
Diboson	1.78 ± 0.40	0.32 ± 0.12
$t\bar{t}$+V	12.39 ± 0.39	1.50 ± 0.12
Total SM	37.60 ± 1.66	4.04 ± 0.62

events which tail the top-tag requirement at large values of am_{T2} (as $W+$jets need not respect the top mass endpoint). The CR and VR are defined in regions of low and intermediate m_{T} in the same manner used for semi-leptonic $t\bar{t}$ decays. A small angle between the two jets deemed most likely to contain B-hadrons is required, exploiting their probable origin from gluon splitting in $W+$jets events. The single top CR is defined with an analogous selection with an inverted angular requirement on the b jets. No validation region is defined for the background as the small number of predicted tW events for these SRs make it difficult and unnecessary. (Contributions from $t\bar{t}Z$ are estimated using a different strategy, which is common to all SRs and is based on 3-lepton events from $t\bar{t}(Z\to\ell^+\ell^-)$. A dedicated treatment is provided in the following Section.) In each of these regions some SR requirements are relaxed to obtain a larger sample of events where normalization factors can be derived. In particular, the requirement on $\vec{H}_{\mathrm{T,sig}}^{\mathrm{miss}}$ is loosened for all CRs and VRs after verifying that this observable is well-modeled. Figure 6.19 shows several distributions for the CRs and VRs associated with the `tN_med` and `tN_high` SRs. The full statistical machinery used to obtain precise predictions and uncertainties on the expected SM contributions to the SRs will be described in Section 6.9.

ttZ Estimation

The $t\bar{t}(Z\to\nu\bar{\nu})$ process is an irreducible background to the $t\bar{t}$+$E_{\mathrm{T}}^{\mathrm{miss}}$ signal and must be estimated using a different strategy than for the other processes. In previous analyses (e.g. the final Run 1 result [3] as well as early results with the Run 2 data [149]) this background was estimated by exploiting similarities between the $t\bar{t}+\gamma$ and $t\bar{t}+Z$ processes. Each involved the production of an electroweak boson in association with top quark pairs, and as such should be similarly affected by theoretical uncertainties associated to the modeling of each process. Differences arise from the finite mass of the Z boson[14], but become less important at high boson p_{T}. Enhanced bremsstrahlung of photons off of top quarks is also reduced at large energies, and is further suppressed by angular requirements between the boson and reconstructed top decay products. Such $t\bar{t}+\gamma$ events can serve as a proxy for the $t\bar{t}(Z\to\nu\bar{\nu})$ process if $E_{\mathrm{T}}^{\mathrm{miss}}$-based observables are rebuilt for photon events, with the photon treated as invisible. Distributions of $E_{\mathrm{T}}^{\mathrm{miss}}$ and m_{T} defined in this way, selecting a $t\bar{t}+\gamma$-enriched region by Ref. [149] are shown in Figure 6.20a.

It is also possible to estimate the $t\bar{t}(Z\to\nu\bar{\nu})$ background using $t\bar{t}(Z\to\ell^+\ell^-)$ events. The primary disadvantage of this strategy is that the Z boson branching fraction to electrons and muons

[14] The contributing Feynman diagrams are identical up to the radiation of Z bosons off of neutrinos from top-quark decays.

Table 6.8: The definition of CRs and VRs used to estimate and validate the level of SM backgrounds expected in the tN_med and tN_high signal regions is shown. Each of the defined regions is orthogonal, with CRs designed to be enriched in the specified background. T1LCR/VR (T2LCR/VR) refers to the semi-leptonic (di-leptonic) $t\bar{t}$ process control and validation regions while WCR/VR targets the $W+$jets process and STCR targets single top. A validation region is not defined for the single top estimates derived for these SRs.

	tN_med	T1LCR/VR	T2LCR/VR	WCR/VR	STCR
Preselection	high-$E_{\mathrm{T}}^{\mathrm{miss}}$ preselection				
Number of (jets, b-tags)	$(\geq 4, \geq 1)$	$(\geq 4, \geq 1)$	$(\geq 4, \geq 1)$	$(\geq 4, \geq 1)$	$(\geq 4, \geq 2)$
Jet p_{T} [GeV]	$>(60,\ 50,\ 40,\ 40)$				
b-tagged jet p_{T} [GeV]	>25				$>(25,\ 25)$
$E_{\mathrm{T}}^{\mathrm{miss}}$ [GeV]	>250				
$E_{T,\perp}^{\mathrm{miss}}$ [GeV]	>230				
m_{T} [GeV]	>160	$[30,90]$ / $[90,120]$	>120	$[30,90]$ / $[90,120]$	$[30,120]$
$\vec{H}_{\mathrm{T,sig}}^{\mathrm{miss}}$	>14	>10	>10	>10	>10
$m_{\mathrm{top}}^{\mathrm{reclustered}}$ [GeV]	>150	>150	top veto / >150	top veto	top veto
am_{T2} [GeV]	>175	<200	<200 / <130	>200	>200
$\Delta R(b,\ell)$	<2.0	–	–	–	–
$\Delta R(b_1,b_2)$	–	–	–	<1.2	>1.2
Lepton charge	–	–	–	$+1$	–
$\lvert\Delta\phi(j_{1,2},\vec{p}_{\mathrm{T}}^{\mathrm{miss}})\rvert$	>0.4				
m_{T2}^{τ} based τ-veto [GeV]	>80				

	tN_high	T1LCR/VR	T2LCR/VR	WCR/VR	STCR
Preselection	high-$E_{\mathrm{T}}^{\mathrm{miss}}$ preselection				
Number of (jets, b-tags)	$(\geq 4, \geq 1)$	$(\geq 4, \geq 1)$	$(\geq 4, \geq 1)$	$(\geq 4, \geq 1)$	$(\geq 4, \geq 2)$
Jet p_{T} [GeV]	$>(100,\ 80,\ 50,\ 30)$				
b-tagged jet p_{T} [GeV]	>25				$>(25,\ 25)$
$E_{\mathrm{T}}^{\mathrm{miss}}$ [GeV]	>550	>350	>350	>350	>350
m_{T} [GeV]	>160	$[30,90]$ / $[90,120]$	>120	$[30,90]$ / $[90,120]$	$[30,120]$
$\vec{H}_{\mathrm{T,sig}}^{\mathrm{miss}}$	>27	>10	>10	>10	>10
$m_{\mathrm{top}}^{\mathrm{reclustered}}$ [GeV]	>130	>130	top veto / >130	top veto	top veto
am_{T2} [GeV]	>175	<200	<200 / <130	>200	>200
$\Delta R(b,\ell)$	<2.0	–	–	–	–
$\Delta R(b_1,b_2)$	–	–	–	<1.2	>1.2
Lepton charge	–	–	–	$+1$	–
$\lvert\Delta\phi(j_{1,2},\vec{p}_{\mathrm{T}}^{\mathrm{miss}})\rvert$	>0.4				
m_{T2}^{τ} based τ-veto [GeV]	>80				

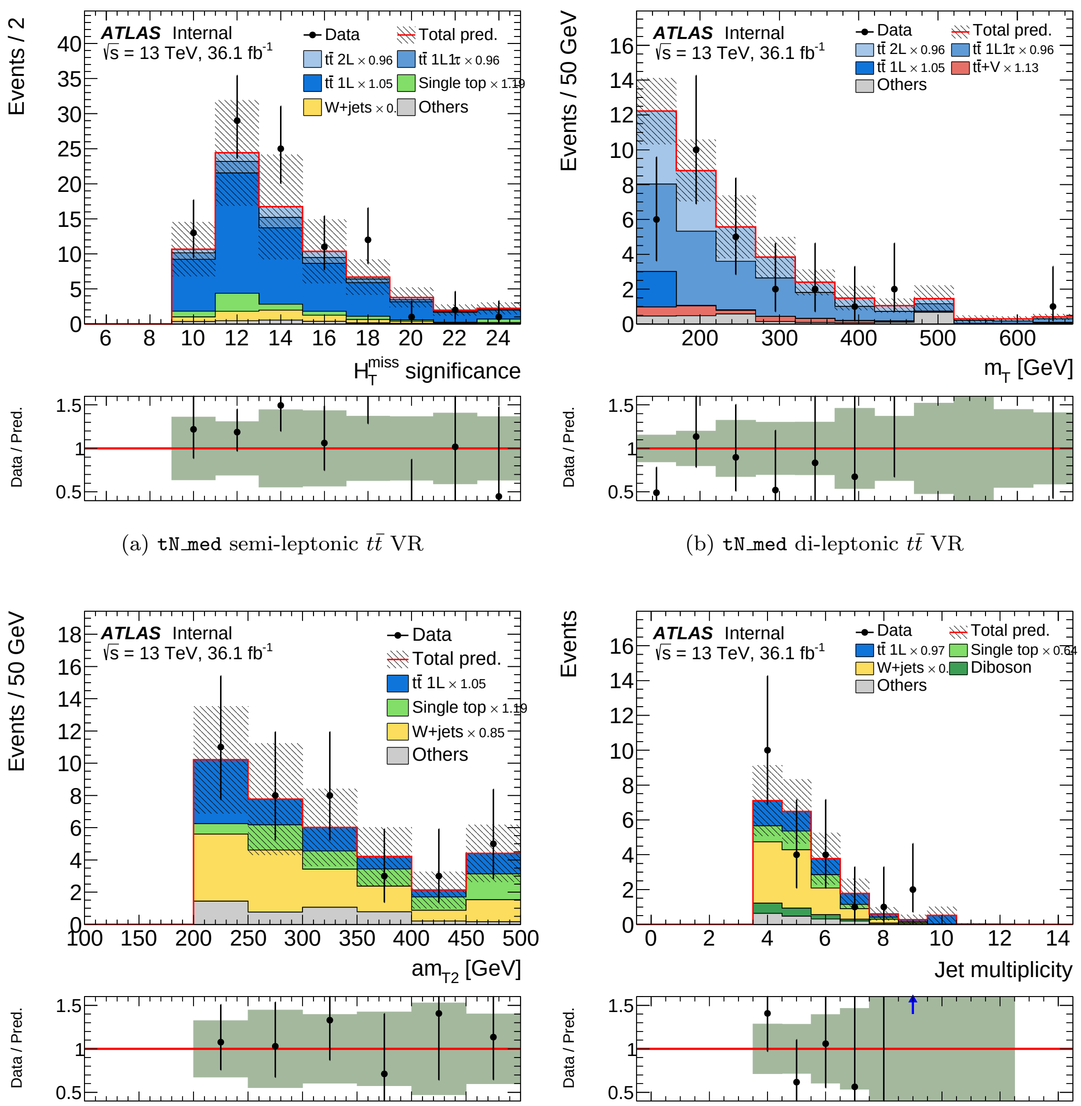

(a) `tN_med` semi-leptonic $t\bar{t}$ VR

(b) `tN_med` di-leptonic $t\bar{t}$ VR

(c) `tN_med` $W+$jets VR

(d) `tN_high` $W+$jets VR

Figure 6.19: Data to MC comparisons of the predicted distributions for key observables in each of the major background control and validation regions corresponding to the `tN_med` and `tN_high` SRs. The normalization of $t\bar{t}$, $W+$jets, and single top predictions is fixed in a fit to the CR yields, so that inclusive agreement is good in the CRs by construction. The resulting normalizations are used to predict the events in VRs, which quantify the performance of the fit.

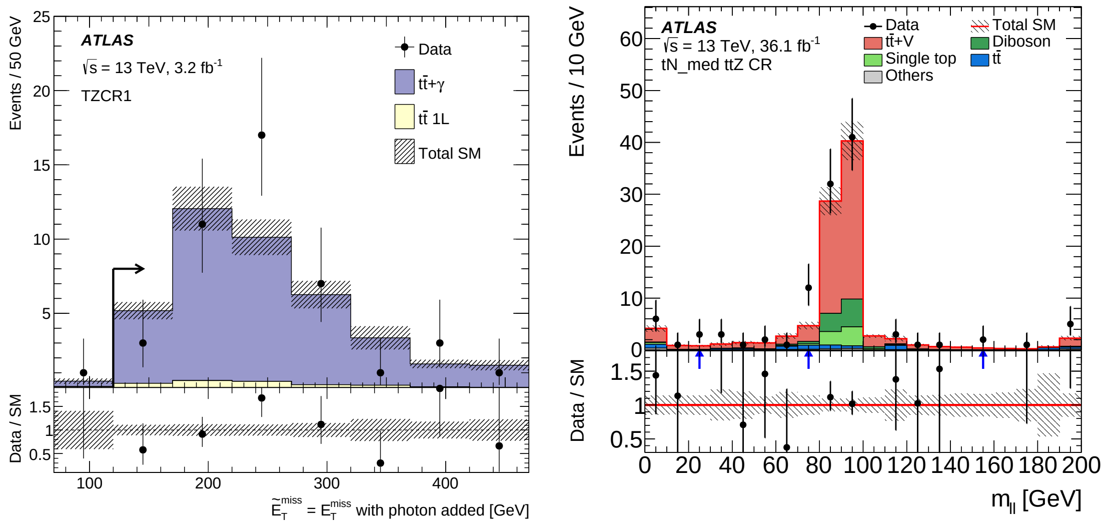

(a) $t\bar{t}+\gamma$, 3.2/fb analysis (b) $t\bar{t}(Z\to\ell^+\ell^-)$, 36.1/fb analysis

Figure 6.20: At left, the corrected $E_{\mathrm{T}}^{\mathrm{miss}}$ distribution with photon treated as invisible, shown in a sample of events with one lepton, real $E_{\mathrm{T}}^{\mathrm{miss}}$, and a photon. This region was used as a $t\bar{t}Z$ CR in a previous analysis [149]. At right, the di-lepton mass distribution used to select three-lepton events for the $t\bar{t}(Z\to\ell^+\ell^-)$ control region used in the analysis of the 2015+16 data set.

is three times smaller than that to neutrinos. Further, acceptance effects further reduce the number of $Z\to\ell^+\ell^-$ events available to estimate the background. However, this strategy was used to define a $t\bar{t}Z$ CR for the 36.1fb^{-1} analysis described within this chapter. A $t\bar{t}Z$ CR preselection is defined as events having: four signal jets, one of which is b-tagged, three leptons, two of which are consistent with the decay of a Z boson, and satisfying the hard-lepton preselection, where the reconstructed Z treated as invisible. Lepton triggers are used to collect these events, so that one of the three leptons is required to pass the 'tight' identification criteria. The Z-consistency requirement is that the event contain an e^+e^- or $\mu^+\mu^-$ pair which has $|m_{\ell^+\ell^-} - m_Z| < 10$ GeV. Events passing this selection except for the final $m_{\ell^+\ell^-}$ requirement are shown in Figure 6.20b. The region is relatively pure in the $t\bar{t}(Z\to\ell^+\ell^-)$ process, with remaining contributions from diboson and tZ single top. The diboson modeling is assessed by considering events where the b-tag has been inverted; a normalization factor of 0.8 is found in this region and applied to diboson contributions in the $t\bar{t}Z$ CRs. Dedicated $t\bar{t}Z$ CRs are defined for each of the SRs described in this and the following Section, namely including `tN_med` and`tN_high`. These CRs are the subset of events passing the $t\bar{t}(Z\to\ell^+\ell^-)$ preselection as well as the jet p_{T} requirements additionally demanded in each SR. Other requirements, such as those on m_{T}, am_{T2}, and such are not enforced. This allows an estimation which is robust against systematic uncertainties affecting jet modeling, top-quark and boson p_{T}, and angular distributions, while retaining a sufficient population of events to extract the overall normalization by allowing the MC to model the extrapolation in other variables.

The two strategies of using $t\bar{t}+\gamma$ and $t\bar{t}(Z \to \ell^+\ell^-)$ events to estimate $t\bar{t}(Z \to \nu\bar{\nu})$ contributions to the SRs were checked in parallel through the course of the analysis. The advantage of the $t\bar{t}+\gamma$ method is the process's relatively large cross section, which allows a $t\bar{t}+\gamma$ CR definition which is more closely related to the SR. The $t\bar{t}(Z \to \ell^+\ell^-)$ method was chosen, however, due to the inadequacy of the $p_{T,Z}, m_Z \ll 1$ assumption, particularly in the low-$E_{\mathrm{T}}^{\mathrm{miss}}$ regions of the `tN_med` SR. However, both methods were pursued and found to give similar estimates of the size of the $t\bar{t}(Z \to \nu\bar{\nu})$ contribution in each of the SRs considered.

6.7.2 High-mass stop decays to $b\tilde{\chi}_1^{\pm}$

Two additional SRs are defined to target high-mass stops that decay to a much lighter chargino, which subsequently decays to a low-mass LSP. These regions are motivated by scenarios with a Wino NLSP that has twice the mass of the Bino LSP, which occurs when the SUSY breaking parameters satisfy $M_2 = 2M_1$ a relation predicted by gauge unification arguments (see Sec. 6.1). Relevant results from the Run 1 analysis [3] in this channel are shown in Figure 6.21. Instead of conducting a pMSSM scan (as is done for the Run 2 result detailed in this document and introduced in Sect. 6.1), simplified models were considered where the stop always decays via the $\tilde{t} \to b\tilde{\chi}_1^{\pm}$ channel, as in Fig.6.21a. To demonstrate the change in sensitivity to scenarios with more "realistic" branching fractions to several final states, a scan in the relative decay rate of $\tilde{t} \to t\tilde{\chi}_1^0$ and $\tilde{t} \to b\tilde{\chi}_1^{\pm}$ was conducted, shown in Fig. 6.21b. For models with significant $\tilde{t} \to b\tilde{\chi}_1^{\pm}$ branching fractions, stop masses up to about 500 GeV are excluded for LSPs in the range from 50 to 200 GeV. Lighter LSPs are not considered, as in this model a 50 GeV LSP corresponds to a 100 GeV chargino, which is on the boundary of states excluded at the LEP experiments (see Sect. 6.1).

Two signal regions, denoted `bC2x_med` and `bC2x_diag`, are optimized to be sensitive to models where stops decay without top quarks in the decay chain. The strategy is similar to that described in Section 6.7.1, with the main difference being that hadronic top-tagging is not possible. Instead, a similar strategy is followed, using W-tagging to target the hadronic leg of the $\tilde{\chi}_1^{\pm} \to W^{\pm}\tilde{\chi}_1^0$. The preselection is identical to that described in Section 6.7.1 and detailed in Table 6.5 (denoted "hard lepton") and the same optimization technique is used.

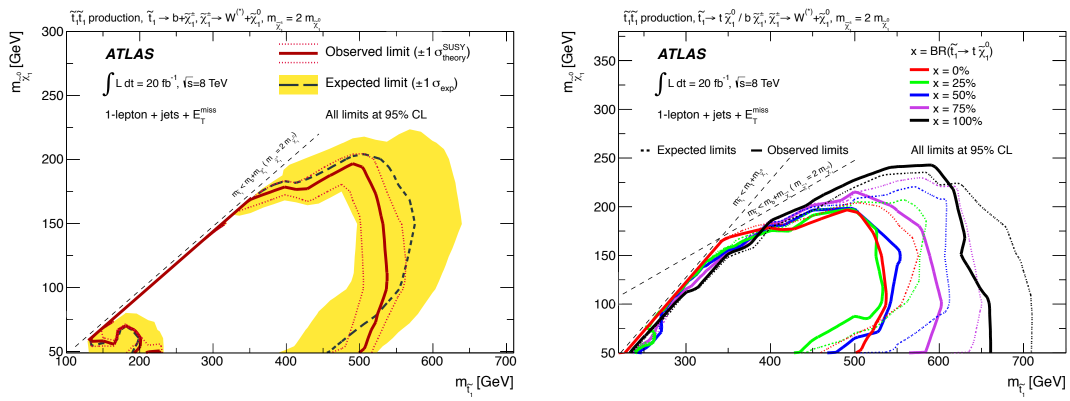

(a) Pure $\tilde{t} \to b\tilde{\chi}_1^{\pm}$ decays (b) Mixed $\tilde{t} \to t\tilde{\chi}_1^0$ and $\tilde{t} \to b\tilde{\chi}_1^{\pm}$

Figure 6.21: At left, contours are shown corresponding to the space of excluded sparticle masses when $m_{\tilde{\chi}_1^{\pm}} = 2m_{\tilde{\chi}_1^0}$ and the stop decays via $\tilde{t} \to b\tilde{\chi}_1^{\pm}$ 100% of the time. At right, the change in exclusions are shown as a function of the top squark branching ratios to $\tilde{t} \to t\tilde{\chi}_1^0$ versus $\tilde{t} \to b\tilde{\chi}_1^{\pm}$. Figures are reproduced from Ref. [3].

Signal region definitions

The characteristics of the `bC2x` signals depend on the mass splitting $\Delta M(\tilde{t}, \tilde{\chi}_1^{\pm})$, which leads to energetic b jets from the $\tilde{t} \to b\tilde{\chi}_1^{\pm}$ decay, and on the splitting $\Delta M(\tilde{\chi}_1^{\pm}, \tilde{\chi}_1^0)$, which leads to an energetic W boson from the $\tilde{\chi}_1^{\pm} \to W^{\pm}\tilde{\chi}_1^0$ decay. The `bC2x_med` region is optimized for the model with $(m_{\tilde{t}}, m_{\tilde{\chi}_1^{\pm}}, m_{\tilde{\chi}_1^0}) = (750\ \text{GeV}, 300\,\text{GeV}, 150\,\text{GeV})$ so that two highly-energetic b jetsare expected. In addition to strict requirements on these energetic jets, this allows an aggressive requirement on am_{T2} ($>$ 300 GeV), as the invariant mass also includes these jets. These requirements efficiently reduce $t\bar{t}$ backgrounds to a negligible level, with tW single top remaining as the dominant background. Because a second, real b jet in this process (i.e., tWb) does not originate from a top resonance, it cannot be removed by the am_{T2} transverse mass variable. In fact, a large theoretical uncertainty on this background prevents the establishment of another SR –the would-be `bC2x_high`– targeting even lighter LSPs. The difficulties surrounding this process are discussed in great detail in Chapter 7.

The `bC2x_diag` region focuses on the phase space where the mass splitting between the $\tilde{t}$ and the $\tilde{\chi}_1^{\pm}$ becomes small, and is optimized for the model with $(m_{\tilde{t}}, m_{\tilde{\chi}_1^{\pm}}, m_{\tilde{\chi}_1^0}) = (650\,\text{GeV}, 500\,\text{GeV}, 250\,\text{GeV})$. Thus, the two required b jets are allowed to be as soft as 30 GeV, though at least three of the four selected jets must have $p_{\text{T}} > 75$ GeV, exploiting the frequency of initial-state radiation (ISR) off of the $\tilde{t}\tilde{t}^*$ system. Lower-momentum b jets skew the signal am_{T2} shape to smaller values, so the corresponding requirement is reduced with respect to the `bC2x_med` case, to 175 GeV. The full selection

Table 6.9: Event selection criteria for the `bC2x_diag` and `bC2x_med` SRs.

Signal region	`bC2x_diag`	`bC2x_med`
Preselection	high-$E_{\mathrm{T}}^{\mathrm{miss}}$ preselection	
Number of (jets, b-tags)	$(\geq 4, \geq 2)$	
Jet p_{T} [GeV]	$> (75,\ 75,\ 75,\ 30)$	$> (200,\ 140,\ 25,\ 25)$
b-tagged jet p_{T} [GeV]	$> (30,\ 30)$	$> (140,\ 140)$
$E_{\mathrm{T}}^{\mathrm{miss}}$ [GeV]	> 230	
$\vec{H}_{\mathrm{T,sig}}^{\mathrm{miss}}$	> 13	> 10
m_{T} [GeV]	> 180	> 120
am_{T2} [GeV]	> 175	> 300
$\lvert\Delta\phi(j_1, \vec{p}_{\mathrm{T}}^{\mathrm{miss}})\rvert$	> 0.7	> 0.9
$\lvert\Delta\phi(j_2, \vec{p}_{\mathrm{T}}^{\mathrm{miss}})\rvert$	> 0.7	> 0.9
$m_{\mathrm{W}}^{\mathrm{reclustered}}$ [GeV]	> 50	
$\lvert\Delta\phi(j_{1,2}, \vec{p}_{\mathrm{T}}^{\mathrm{miss}})\rvert$	> 0.4	
m_{T2}^{τ} based τ-veto [GeV]	> 80	
Exclusion technique	cut-and-count	cut-and-count

for both regions is shown in Table 6.9.

Background Estimation

With the selection as described above, the main backgrounds remain the $t\bar{t}$, single top, $W+$jets, and $t\bar{t}Z$ processes. Exact yields for each process, based on pure, uncorrected simulation estimates, are shown in Table 6.10. Diboson processes are negligible in these regions due to the requirement of a second b jet.

A similar CR strategy is employed for the `bC2x` regions as was used for the `tN` regions described

Table 6.10: Predicted composition of the SM backgrounds to the `bC2x` signal regions. Yields here are normalized to the SM cross sections, before any data-driven corrections are applied.

Signal region	`bC2x_diag`	`bC2x_med`
$t\bar{t}$ 2L	2.50 ± 0.61	0.64 ± 0.25
$t\bar{t}$ 1L1τ	3.23 ± 0.56	1.35 ± 0.47
$t\bar{t}$ 1L	0.36 ± 0.15	0.18 ± 0.15
Single top	3.02 ± 0.45	2.85 ± 0.41
W+jets	1.76 ± 0.33	0.45 ± 0.11
$t\bar{t}$+V	7.12 ± 0.31	0.66 ± 0.07
Total SM	17.99 ± 1.05	6.13 ± 0.70

in the previous section. The main difference is that the hadronic top tag requirement ($m_{\text{top}}^{\text{reclustered}} \gtrsim 150\,\text{GeV}$) is replaced with a hadronic W boson requirement ($m_{\text{W}}^{\text{reclustered}} > 50\,\text{GeV}$) instead. With this substitution, the same strategy is used to define semi-leptonic $t\bar{t}$ control regions at low m_{T} and di-leptonic control regions with a W veto. The W + jets and single top control regions are both defined with the W veto as well as low m_{T}requirement. As previously, angular requirement on the opening angle between the b jets differentiates the two. In some cases, the requirement on the number of b jets is loosened in the CR/VR definition to increase the corresponding samples of events. The precise definitions of each of the CRs and VRs for each background source and each SR are shown in Table 6.11. Comparisons of the MC modeling of critical variables with the observed data distributions are shown in Figure 6.22 for `bC2x_med` and `bC2x_diag`. The $t\bar{t}Z$ background is estimated using the same strategy as was described in Section 6.7.1.

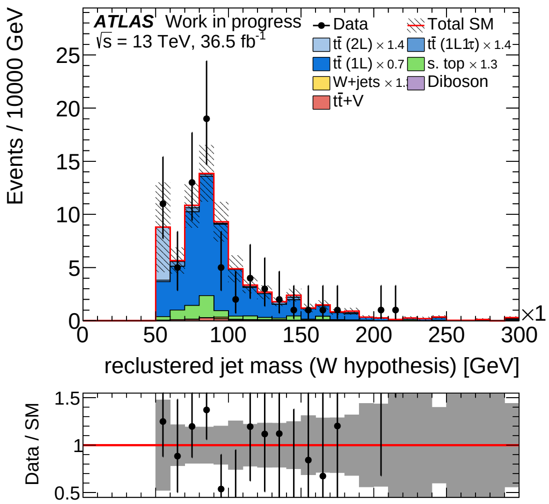

(a) bC2x_med semi-leptonic $t\bar{t}$ CR

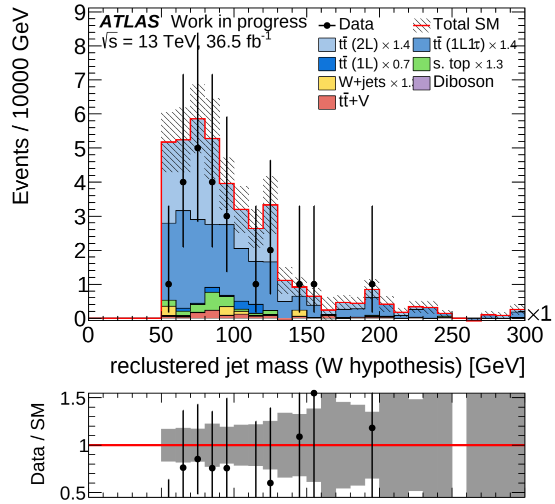

(b) bC2x_med di-leptonic $t\bar{t}$ VR

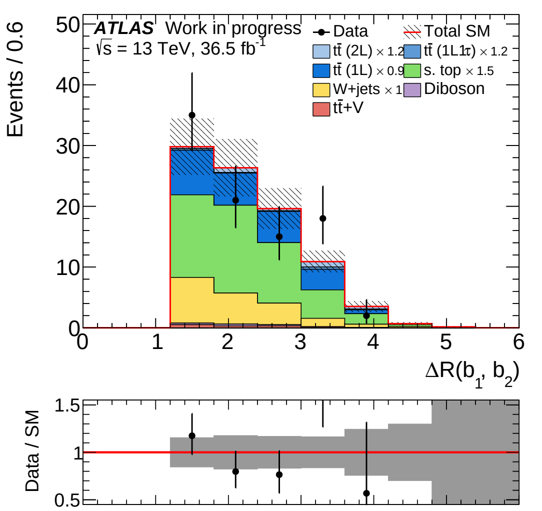

(c) bC2x_diag single top CR

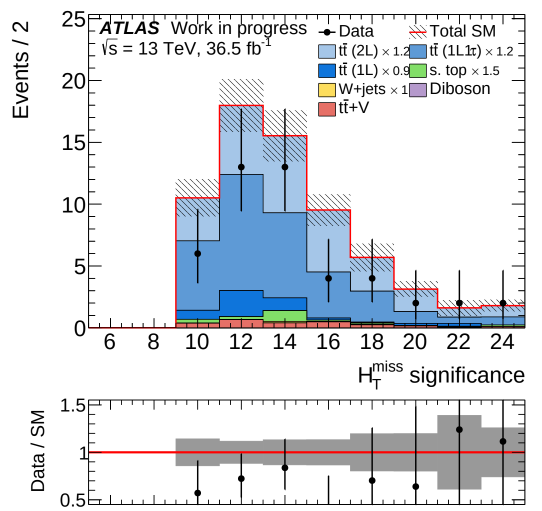

(d) bC2x_diag di-leptonic $t\bar{t}$ VR

Figure 6.22: Data to MC comparisons of the predicted distributions for key observables in each of the major background control and validation regions corresponding to the bC2x_med and bC2x_diag SRs. The normalization of $t\bar{t}$, $W+$jets, and single top predictions is fixed in a fit to the CR yields, so that inclusive agreement is good in the CRs by construction. The resulting normalizations are used to predict the events in VRs, which quantify the performance of the fit.

Table 6.11: The definition of CRs and VRs used to estimate and validate the level of SM backgrounds expected in the `bC2x_diag` and `bC2x_med` signal regions is shown. Each of the defined regions is orthogonal, with CRs designed to be enriched in the specified background. T1LCR/VR (T2LCR/VR) refers to the semi-leptonic (di-leptonic) $t\bar{t}$ process control and validation regions while WCR/VR targets the $W+$jets process and STCR targets single top. A validation region is not defined for the single top estimates derived for these SRs.

	`bC2x_diag`	T1LCR/VR	T2LCR/VR	WCR/VR	STCR
Preselection			high-$E_{\mathrm{T}}^{\mathrm{miss}}$ preselection		
Number of (jets, b-tags)	$(\geq 4, \geq 2)$	$(\geq 4, \geq 2)$	$(\geq 4, \geq 2)$	$(\geq 4, \geq 1)$	$(\geq 4, \geq 2)$
Jet p_{T} [GeV]			$>(75,\ 75,\ 75,\ 30)$		
b-tagged jet p_{T} [GeV]	$>(30,\ 30)$	$>(30,\ 30)$	$>(30,\ 30)$	$>(30,\ -)$	$>(30,\ 30)$
$E_{\mathrm{T}}^{\mathrm{miss}}$ [GeV]			>230		
$\vec{H}_{\mathrm{T,sig}}^{\mathrm{miss}}$	>13	>13	>10	>13	>10
m_{T} [GeV]	>180	$[30,90]$ / $[90,120]$	>120	$[30,90]$ / $[90,120]$	$[30,120]$
am_{T2} [GeV]	>175	<200	<200 / <130	>200	>200
$\lvert\Delta\phi(\mathrm{jet}_i,\vec{p}_{\mathrm{T}}^{\mathrm{miss}})\rvert(i=1,2)$			>0.7		
$m_{\mathrm{W}}^{\mathrm{reclustered}}$ [GeV]	>50	>50	W veto / >50	W veto	W veto
$\Delta R(b_1,b_2)$	–	–	–	<1.2	>1.2
Lepton charge	–	–	–	$=+1$	–
$\lvert\Delta\phi(j_{1,2},\vec{p}_{\mathrm{T}}^{\mathrm{miss}})\rvert$			>0.4		
m_{T2}^{τ} based τ-veto [GeV]			>80		
	`bC2x_med`	T1LCR/VR	T2LCR/VR	WCR/VR	STCR
Preselection			high-$E_{\mathrm{T}}^{\mathrm{miss}}$ preselection		
Number of (jets, b-tags)	$(\geq 4, \geq 2)$	$(\geq 4, \geq 2)$	$(\geq 4, \geq 1)$	$(\geq 4, \geq 1)$	$(\geq 4, \geq 2)$
Jet p_{T} [GeV]			$>(200,\ 140,\ 25,\ 25)$		
b-tagged jet p_{T} [GeV]	$>(140,\ 140)$	$>(140,\ 140)$	$>(140,\ -)$	$>(140,\ -)$	$>(140,\ 140)$
$E_{\mathrm{T}}^{\mathrm{miss}}$ [GeV]			>230		
$\vec{H}_{\mathrm{T,sig}}^{\mathrm{miss}}$	>10	>10	>10	>10	>6
m_{T} [GeV]	>120	$[30,90]$ / $[90,120]$	>120	$[30,90]$ / $[90,120]$	$[30,120]$
am_{T2} [GeV]	>300	<200	<200 / <130	>200	>200
$\lvert\Delta\phi(\mathrm{jet}_i,\vec{p}_{\mathrm{T}}^{\mathrm{miss}})\rvert(i=1,2)$			>0.9		
$m_{\mathrm{W}}^{\mathrm{reclustered}}$ [GeV]	>50	>50	W veto / >50	W veto	W veto
$\Delta R(b_1,b_2)$	–	–	–	<1.2	>1.2
Lepton charge	–	–	–	$=+1$	–
$\lvert\Delta\phi(j_{1,2},\vec{p}_{\mathrm{T}}^{\mathrm{miss}})\rvert$			>0.4		
m_{T2}^{τ} based τ-veto [GeV]			>80		

6.7.3 Stop decays to Higgsino LSP

The case of a Higgsino LSP can produce new signatures, which are not probed by the search regions defined in previous sections. In particular, if the charged lepton is not produced directly from the top-quark decay products, but in the secondary decay of the chargino $\tilde{\chi}_1^{\pm}$ via a highly off-shell W boson, then the leptons will have too low momenta to be selected according to the methods described in Section 6.7.2. Similar models were considered in Run 1 searches, with selected results shown in Figure 6.23 for models parameterized by the physical sparticle masses (simplified models, Fig. 6.23a) and by the pMSSM mass parameters (pMSSM scan, Fig. 6.23b). In this work, signal models are considered for a range of stop masses (> 350 GeV) and Higgsino LSP masses (> 100 GeV), as well as a range of values for the $\tilde{\chi}_1^{\pm}$-$\tilde{\chi}_1^0$mass splitting (0 GeV $< \Delta M <$ 30 GeV). Details of the dedicated search regions exploiting the soft-lepton signature associated with Higgsino LSPs is described below.

Signal region definitions

In the $\tilde{t}\tilde{t}^*$ cascade decay, one or both stops may decay via the $\tilde{t} \to b\tilde{\chi}_1^{\pm}$ process which leads to soft leptons in the Higgsino LSP scenario. Dedicated signal regions are developed targeting each scenario. The `bCsoft_med` SR targets the mixed scenario $\tilde{t}\tilde{t}^* \to tb\tilde{\chi}_1^{\pm}\tilde{\chi}_1^0$ for a broad range of stop masses, while the `bCsoft_high` SR is optimized for very high-mass stop pairs decaying $\tilde{t}\tilde{t}^* \to b\bar{b}\tilde{\chi}_1^{+}\tilde{\chi}_1^{-}$. Both of these regions are defined to be orthogonal to the `tN_med` SR so that they can be statistically combined to give maximum coverage of all $\tilde{t}\tilde{t}^*$ decay chains. Finally, a specialized SR `bCsoft_diag` is defined to target scenarios where $\Delta M(\tilde{t}, \tilde{\chi}_1^0) < m_{\text{top}}$ and the stop decays exclusively via $\tilde{t} \to b\tilde{\chi}_1^{\pm}$. This SR is not statistically combined with other signal regions.

The preselection demanded for the `bCsoft` regions has been introduced in Table 6.5. Major differences include: a reduced p_{T} threshold for signal leptons (5 GeV electrons and 4 GeV muons); tighter lepton identification requirements to allow for the estimation of fake and non-prompt backgrounds; the absence of any requirement on m_{T}; the requirement that one of the two required 25 GeV signal jets satisfies the b tagging requirement. Because the lepton p_{T} is very low for the targeted signal processes, the m_{T} (proportional to the geometric mean of the lepton p_{T} and the $E_{\text{T}}^{\text{miss}}$) is as well. For this reason, an upper cut on m_{T} is used to enforce orthogonality of the `bCsoft` SRs with `tN_med`, which requires $m_{\text{T}} >$ 160 GeV. The low signal m_{T} also leads to processes with one real lepton comprising the dominant background, as opposed to the `tN` regions. The full description of the `bCsoft` SRs is given in Table 6.12.

The `bCsoft_diag` SR is designed to capture stop signals when an energetic jet recoils off of the

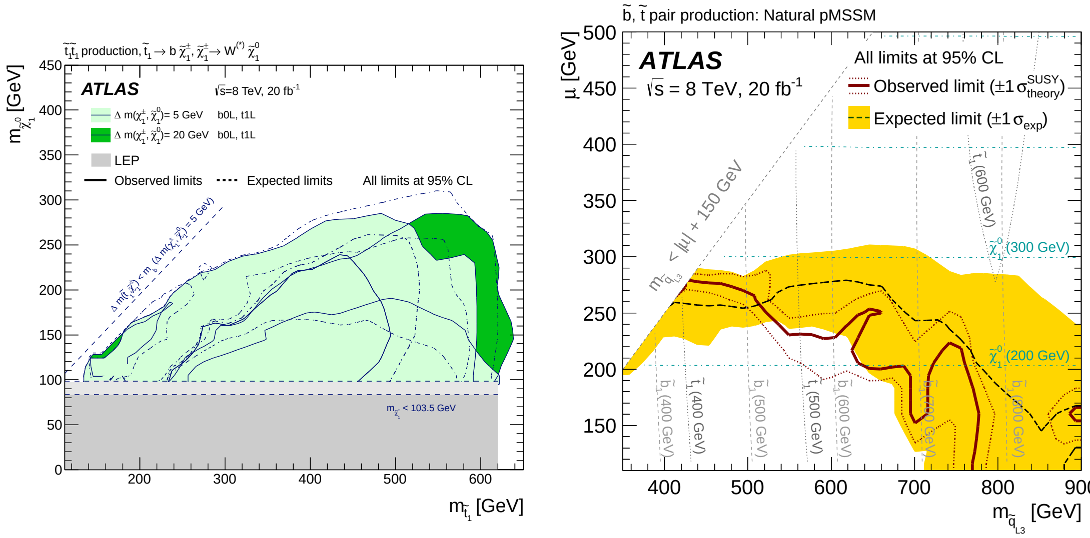

(a) Higgsino simplified model

(b) pMSSM parameter scan

Figure 6.23: At left, search results are presented as exclusions on a space of models with $\Delta M(\tilde{\chi}_1^0, \tilde{\chi}_1^\pm) = 5$ (light green shaded region) and 20 GeV (dark green), as a function of the stop and LSP mass. Limits on direct chargino production are also shown for each $\Delta M(\tilde{\chi}_1^0, \tilde{\chi}_1^\pm)$ assumption based on LEP searches. Results are combinations of analyses considering final states with one soft lepton [3] and zero leptons, with 2 high-p_{T} b jets [199]. At right, related results are presented as a function of the SUSY mass parameters m_{q3L} (the third generation left-handed squark mass) and μ (the Higgsino mass parameter). Dotted and dashed lines are overlaid denoting the physical sparticle masses. Both figures are reproduced from Ref. [142].

$\tilde{t}\tilde{t}^*$ pair. The large ISR boosts the $\tilde{t}\tilde{t}^*$ pairs, leading to larger momenta of their decay products in the rest frame of the detector. Thus, `bCsoft_diag` requires a leading jet of at least 400 GeV, in addition to a second signal jet, which must be b-tagged. A hadronic top veto reduces the (largest) background from semi-leptonic top decays.

The `bCsoft_high` SR requires two high-p_{T} jets, both of which must be b-tagged, in accordance with the anticipated signature of the $\tilde{t}\tilde{t}^* \to b\bar{b}\tilde{\chi}_1^\pm\tilde{\chi}_1^\mp$ signal for large stop masses. While the $E_{\mathrm{T}}^{\mathrm{miss}}$ cut is low for this region (only large enough so that the trigger efficiency has reach a plateau) a strict requirement is instead made on p_{T}^W. The reconstructed W boson transverse momentum p_{T}^W is the combined p_{T} of the combined lepton-$E_{\mathrm{T}}^{\mathrm{miss}}$ system, which is a proxy for the W p_{T} in SM events such as semi-leptonic $t\bar{t}$ and tW single top. Because the lepton p_{T} is much smaller than the $E_{\mathrm{T}}^{\mathrm{miss}}$ for signal events, this requirement is effectively a $E_{\mathrm{T}}^{\mathrm{miss}}$ cut. The benefit of this choice is related to the estimation of backgrounds and is given in the following section. An aggressive requirement on am_{T2} is also made to reduce the $t\bar{t}$ and single top backgrounds. The `bCsoft_med` signal region is a

Table 6.12: Event selection criteria for the bCsoft_diag, bCsoft_med, and bCsoft_high SRs. The top panel shows the definition of the SRs used for the model-independent results. To enhance exclusion capabilities for stop models, multi-bin regions are also defined.

Signal region	bCsoft_diag	bCsoft_med	bCsoft_high
Preselection	soft-lepton preselection		
Number of (jets, b-tags)	$(\geq 2, \geq 1)$	$(\geq 3, \geq 2)$	$(\geq 2, \geq 2)$
Jet p_{T} [GeV]	$> (400,\ 25)$	$> (120,\ 60,\ 40)$	$> (100,\ 100)$
b-tagged jet p_{T} [GeV]	> 25	$> (120,\ 60)$	$> (100,\ 100)$
$E_{\mathrm{T}}^{\mathrm{miss}}$ [GeV]	> 300	> 230	> 230
m_{T} [GeV]	< 50	< 160	< 160
p_{T}^{W} [GeV]	–	> 400	> 500
$p_{\mathrm{T}}^{\ell}/E_{\mathrm{T}}^{\mathrm{miss}}$	< 0.02	< 0.03	< 0.03
am_{T2} [GeV]	–	> 200	> 300
$m_{\mathrm{top}}^{\mathrm{reclustered}}$ [GeV]	top veto	–	–
$\min(\Delta\phi(b\text{-jet}_i, \vec{p}_{\mathrm{T}}^{\mathrm{miss}}))$	< 1.5	> 0.8	> 0.4
$\Delta R(b_1, b_2)$	–	–	> 0.8
$\lvert\Delta\phi(j_{1,2}, \vec{p}_{\mathrm{T}}^{\mathrm{miss}})\rvert$		> 0.4	
Exclusion technique	shape-fit in $p_{\mathrm{T}}^{\ell}/E_{\mathrm{T}}^{\mathrm{miss}}$		
Bin boundaries in $p_{\mathrm{T}}^{\ell}/E_{\mathrm{T}}^{\mathrm{miss}}$	$[0, 0.01, 0.015, 0.02]$	$[0, 0.015, 0.03, 0.1]$	$[0, 0.015, 0.03, 0.1]$

effectively a looser version of bCsoft_high, which targets mixed decays $\tilde{t}\tilde{t}^* \to tb\tilde{\chi}_1^{\pm}\tilde{\chi}_1^0$.

For all regions, the key discriminant is $p_{\mathrm{T}}^{\ell}/E_{\mathrm{T}}^{\mathrm{miss}}$, which is required to be small. The fit exploits multiple bins of $p_{\mathrm{T}}^{\ell}/E_{\mathrm{T}}^{\mathrm{miss}}$ to retain sensitivity to a large range of lepton momenta stemming from various Higgsino mass splittings.

Background Estimation

The background procedure for the bCsoft_med and bCsoft_high regions relies on extrapolations on $p_{\mathrm{T}}^{\ell}/E_{\mathrm{T}}^{\mathrm{miss}}$ instead of hadronic top and W boson taggers as were used for the previous regions. The critical observation for this strategy is that the SM backgrounds relevant for the SRs defined above feature $E_{\mathrm{T}}^{\mathrm{miss}}$ and a lepton that originate from the same decay of a W boson. This can be seen from the predicted SR yields shown in Table 6.13. For backgrounds, this the lepton p_{T} and $E_{\mathrm{T}}^{\mathrm{miss}}$ should generally be of a similar size, though this is sculpted at preselection by the $E_{\mathrm{T}}^{\mathrm{miss}}$ trigger requirement. For signal, the lepton p_{T} is proportional to the mass splitting of the Higgsino states (typically $\mathcal{O}(\mathrm{GeV})$), while the $E_{\mathrm{T}}^{\mathrm{miss}}$ is proportional to $\Delta M(\tilde{t}, \tilde{\chi}_1^{\pm}) \sim m_{\tilde{t}}$ so that $p_{\mathrm{T}}^{\ell}/E_{\mathrm{T}}^{\mathrm{miss}}$ should in general be quite small. SM backgrounds may also attain small values of this ratio if the angle of the lepton from the W boson decay is small, with respect to the W boson momentum in the lab frame.

This difference is illustrated in Figure 6.24. However, the difference between SM backgrounds that pass and fail the SR selection is only due to this decay angle, which is precisely predicted in the SM and thus should be well-modeled in the SM simulation. Thus, the strategy for background estimation in the `bCsoft` regions is to normalize backgrounds in regions with W-neutrino decay angles producing high-p_{T} leptons, while controlling for the p_{T} of the W boson itself. Thus, any systematic uncertainties that affect the W boson p_{T} modeling (whether in $W+$jets, $t\bar{t}$, or single top processes) should cancel in the extrapolation.

tW single top and $W+$jets are the dominant backgrounds for the `bCsoft_high` and `bCsoft_med` SRs and are estimated from events with large $p_{\mathrm{T}}^{\ell}/E_{\mathrm{T}}^{\mathrm{miss}}$. The precise definition of each CR and VR is presented in Table 6.14. The `bCsoft_high` SR requires $p_{\mathrm{T}}^{\ell}/E_{\mathrm{T}}^{\mathrm{miss}} < 0.03$, with the tW and $W+$jets CRs defined with $p_{\mathrm{T}}^{\ell}/E_{\mathrm{T}}^{\mathrm{miss}} > 0.2$ and the VRs in the intermediate region. For the tW CR and VR all other selection criteria are identical to the SR. For the $W+$jets CR and VR events are required to have exactly one b jet. The distribution of $p_{\mathrm{T}}^{\ell}/E_{\mathrm{T}}^{\mathrm{miss}}$ for events entering these regions is displayed in Figure 6.25. A $t\bar{t}$ CR and VR are also defined by inverting the selection on am_{T2}. The strategy used for the `bCsoft_med` regions is similar, with some regions of intermediate $p_{\mathrm{T}}^{\ell}/E_{\mathrm{T}}^{\mathrm{miss}}$ unusable as VR due to potential signal contamination.

For the `bCsoft_diag` region, a similar strategy is used to the hard-lepton regions. CRs and VRs are defined for $t\bar{t}$ and $W+$jets backgrounds, while single top is taken from simulation as it is less important in this region. The $t\bar{t}$ regions are defined by inverting the hadronic top veto. The $W+$jets regions are defined by inverting the angular requirement on the $E_{\mathrm{T}}^{\mathrm{miss}}$ and nearest b jet. For $W+$jets, these are expected to be back-to-back while for signal (and $t\bar{t}$) they stem from a top or stop decay and thus are boosted in a common direction. For both backgrounds, the CR is defined

Table 6.13: Predicted composition of the SM backgrounds to the `bCsoft` signal regions. Yields here are normalized to the SM cross sections, before any data-driven corrections are applied. Entries corresponding to less than 0.01 events are marked as "–".

Signal region	`bCsoft_diag`	`bCsoft_med`	`bCsoft_high`
$t\bar{t}$ 1L	8.92 ± 0.83	3.55 ± 0.56	1.67 ± 0.36
$t\bar{t}$ 1L1τ	2.57 ± 0.50	–	–
$t\bar{t}$ 2L	1.04 ± 0.29	0.07 ± 0.07	–
Single top	3.60 ± 0.82	3.27 ± 0.32	5.91 ± 0.47
V+jets	6.93 ± 0.66	4.31 ± 0.39	3.55 ± 0.22
$t\bar{t}$+V	0.14 ± 0.06	0.47 ± 0.10	0.42 ± 0.06
Diboson	2.14 ± 1.01	0.50 ± 0.26	–
Total SM	25.34 ± 1.78	12.17 ± 0.81	11.55 ± 0.63

Table 6.14: The definition of CRs and VRs used to estimate and validate the level of SMs backgrounds expected in the `bCsoft_diag` and `bCsoft_med` signal regions is shown. Each of the defined regions is orthogonal, with CRs designed to be enriched in the specified background. T1LCR/VR (T2LCR/VR) refers to the semi-leptonic (di-leptonic) $t\bar{t}$ process control and validation regions while WCR/VR targets the $W+$jets process and STCR targets single top. A validation region is not defined for the single top estimates derived for these SRs.

	`bCsoft_diag`	TCR/VR	WCR/VR
Preselection	soft-lepton preselection		
Number of (jets, b-tags)	$(\geq 2, \geq 1)$	$(\geq 2, \geq 1)$	$(\geq 2, = 1)$
Jet p_{T} [GeV]	$> (120,\ 25)$		
b-tagged jet p_{T} [GeV]	> 25		
$E_{\mathrm{T}}^{\mathrm{miss}}$ [GeV]	> 300		
m_{T} [GeV]	< 50	< 160	< 160
$p_{\mathrm{T}}^{\ell}/E_{\mathrm{T}}^{\mathrm{miss}}$	< 0.02	$[0.03, 0.10]$ / < 0.03	$[0.03, 0.10]$ / < 0.03
$m_{\mathrm{top}}^{\mathrm{reclustered}}$ [GeV]	top veto	> 150	top veto
$\min(\Delta\phi(b\text{-jet}_i, \vec{p}_{\mathrm{T}}^{\mathrm{miss}}))$	< 1.5	< 1.5	> 1.5
$\lvert\Delta\phi(j_{1,2}, \vec{p}_{\mathrm{T}}^{\mathrm{miss}})\rvert$	> 0.4		

	`bCsoft_med`	TCR/VR	WCR/VR	STCR/VR
Preselection	soft-lepton preselection			
Number of (jets, b-tags)	$(\geq 3, \geq 2)$	$(\geq 3, \geq 2)$	$(\geq 3, = 1)$	$(\geq 3, \geq 2)$
Jet p_{T} [GeV]	$> (120,\ 60,\ 40,\ 25)$			
b-tagged jet p_{T} [GeV]	$> (120,\ 60)$	$> (120,\ 60)$	> 120	$> (120,\ 60)$
$E_{\mathrm{T}}^{\mathrm{miss}}$ [GeV]	> 230			
m_{T} [GeV]	< 160			
p_{T}^{W} [GeV]	> 400			
$p_{\mathrm{T}}^{\ell}/E_{\mathrm{T}}^{\mathrm{miss}}$	< 0.03	> 0.03 / < 0.03	> 0.20 / $[0.1, 0.2]$	> 0.20 / $[0.1, 0.2]$
am_{T2} [GeV]	> 200	< 200	> 200	> 200
$\min(\Delta\phi(b\text{-jet}_i, \vec{p}_{\mathrm{T}}^{\mathrm{miss}}))$	> 0.8	–	$[0.8, 2.5]$	> 0.8
$\Delta R(b_1, b_2)$	–	–	–	> 1.2
$\lvert\Delta\phi(j_{1,2}, \vec{p}_{\mathrm{T}}^{\mathrm{miss}})\rvert$	> 0.4			

	`bCsoft_high`	TCR/VR	WCR/VR	STCR/VR
Preselection	soft-lepton preselection			
Number of (jets, b-tags)	$(\geq 2, \geq 2)$	$(\geq 2, \geq 2)$	$(\geq 2, = 1)$	$(\geq 2, \geq 2)$
Jet p_{T} [GeV]	$> (100,\ 100)$			
b-tagged jet p_{T} [GeV]	$> (100,\ 100)$			
$E_{\mathrm{T}}^{\mathrm{miss}}$ [GeV]	> 230			
m_{T} [GeV]	< 160			
p_{T}^{W} [GeV]	> 500			
$p_{\mathrm{T}}^{\ell}/E_{\mathrm{T}}^{\mathrm{miss}}$	< 0.03	> 0.10 / < 0.10	$[0.1, 0.4]$ / < 0.10	> 0.30 / $[0.1, 0.3]$
am_{T2} [GeV]	> 300	< 300	> 300	> 300
$\min(\Delta\phi(b\text{-jet}_i, \vec{p}_{\mathrm{T}}^{\mathrm{miss}}))$	> 0.4			
$\Delta R(b_1, b_2)$	> 0.8	> 0.8	–	> 0.8
$\Delta R(b, \ell)$	–	–	> 0.8	–
$\lvert\Delta\phi(j_{1,2}, \vec{p}_{\mathrm{T}}^{\mathrm{miss}})\rvert$	> 0.4			

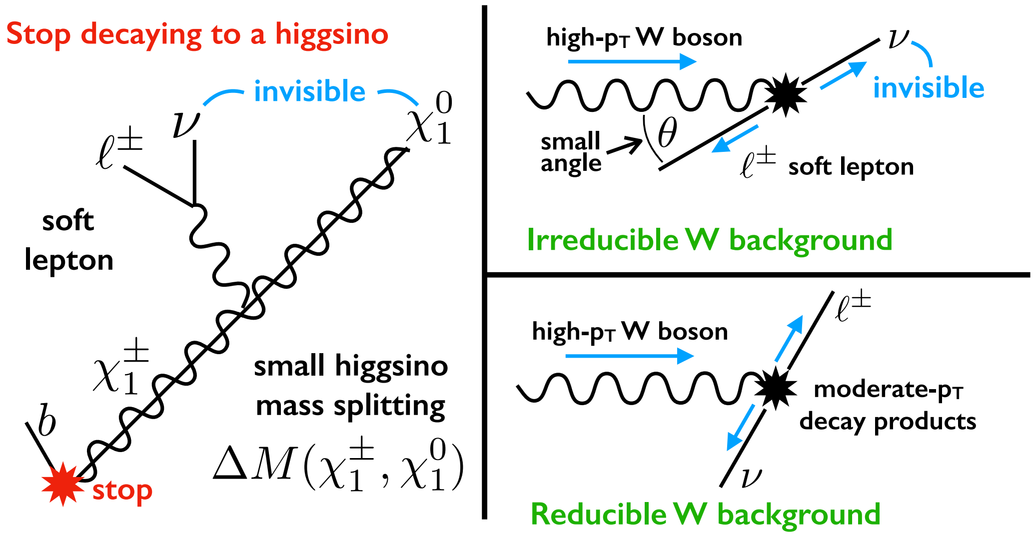

Figure 6.24: An illustration of the behavior of the $p_{\mathrm{T}}^{\ell}/E_{\mathrm{T}}^{\mathrm{miss}}$ observable for signal (left) and SM background events with a single leptonically decaying W boson (right). For the signal process, the low lepton p_{T} is related to the Higgsino mass splitting and is essentially uncorrelated with the large $E_{\mathrm{T}}^{\mathrm{miss}}$ due to the large stop mass. For backgrounds, the low lepton p_{T} for events entering the SRs is specifically due to the small decay angle between the W boson and its daughter neutrino (upper left), the magnitude of which can be estimated using large-angle decays (bottom left).

at large $p_{\mathrm{T}}^{\ell}/E_{\mathrm{T}}^{\mathrm{miss}}$ and the VR assesses the extrapolation to low values of $p_{\mathrm{T}}^{\ell}/E_{\mathrm{T}}^{\mathrm{miss}}$.

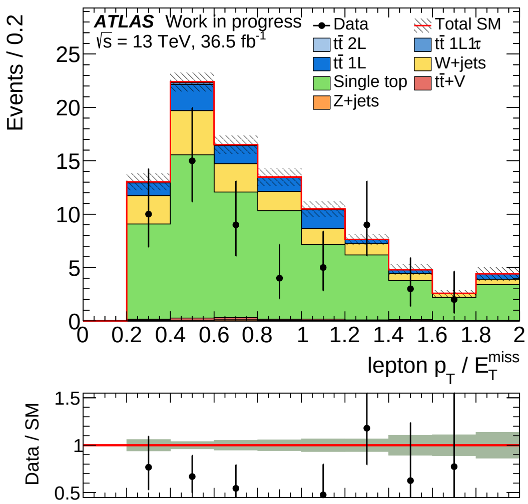

(a) tW CR, before normalization

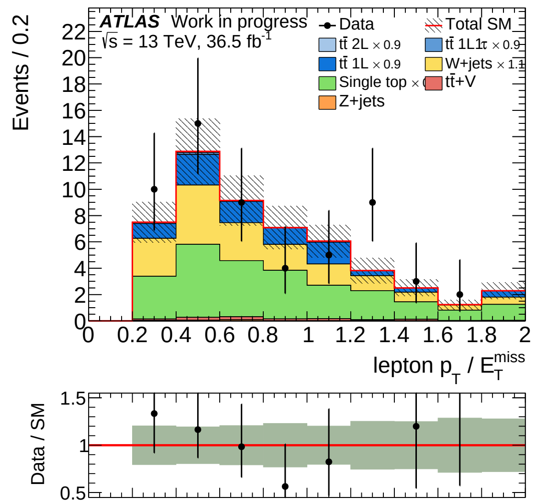

(b) tW CR, after normalization

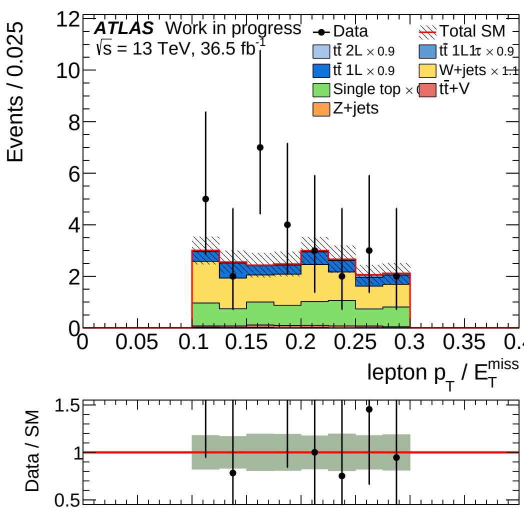

(c) tW VR

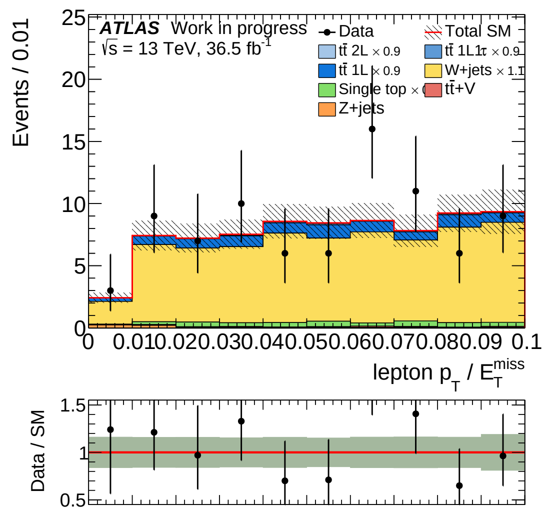

(d) $W+$jets VR

Figure 6.25: The observed distribution of $p_{\mathrm{T}}^{\ell}/E_{\mathrm{T}}^{\mathrm{miss}}$ in data is compared to MC prediction for a variety of regions and configurations. At top left, the data are shown in the tW control region alongside MC prediction where each process is normalized to the theoretical cross-section. At top right, the same data are shown with MC whose normalization has been corrected in the fitting procedure. The fit assigns the tW process a significantly smaller normalization than the calculated cross section. At bottom left, the fit results are validated in a tW-rich region defined at lower values of $p_{\mathrm{T}}^{\ell}/E_{\mathrm{T}}^{\mathrm{miss}}$, where generally good agreement is observed. At bottom right, the same distribution is shown in the region validating the modeling of the $W+$jets process.

6.8 Uncertainties

6.8.1 Experimental Sources

The effects imperfect object reconstruction on the measurement are considered by assigning nuisance parameter (NP) to individual sources which can affect the calibration of individual objects. Each nuisance parameter usually corresponds to $\pm 1\sigma$ variations (i.e. for scale and efficiency uncertainties) for individual sources, while for others a one-sided $+1\sigma$ uncertainty is assessed (i.e. for resolutions). Uncertainties are only considered in the full statistical procedure which give a significant impact on the final results. Those related to jets, $E_{\mathrm{T}}^{\mathrm{miss}}$, and flavor tagging are most critical for the stop analysis.

Jet energy scale A set of 88 uncertainties are considered from the JES calibration Ref. [105]. Of those, 75 are due to various assumptions made in the in-situ calibrations regarding the event topology, MC simulation, event statistics, and uncertainties on other reference objects used in the calibration. An eigenvector decomposition is used to reduce these to 6 NPs, retaining the vast majority of the correlation uncertainties to produce 19 in total. The remaining NPs stem from uncertainty in the modeling of pile-up in simulation, the flavor composition of jets entering event samples and their distinct responses, high-p_{T} corrections for jets not full contained within the calorimeter and calibrated with single-particle measurements, and non-closure in the calibration methods as a function of η_{det}. A final NP as assigned to backgrounds estimated using fast detector simulation. In the present analysis, the impact of preserving all correlations is found to be negligible, so a further set of strongly reduced NPs is used so that a four-NP scheme is used.

Jet energy resolution The jet energy resolution is measured through *in-situ* comparisons of the relative momenta in di-jet events, based on the techniques described in Ref. [200]. The uncertainties relating to the extrapolation of Run 1 measurements to Run 2 conditions are dominant and have similar shapes, so are combined in a correlated manner into a single NP. Jet energies are smeared according to the resolution to estimate the impact of this variation.

$E_{\mathrm{T}}^{\mathrm{miss}}$ **soft term** Uncertainties are assessed on the determination of the scale and resolution of the soft term, as described in Ref. [112]. Scale uncertainties are obtained by comparisons of the $E_{\mathrm{T}}^{\mathrm{miss}}$ component along the p_{T} of the hard process (in $Z \to \mu^+\mu^-$ events) in simulation and data. The distribution of variances of the $E_{\mathrm{T}}^{\mathrm{miss}}$ components parallel and perpendicular to the hard process are used to extract corresponding resolution terms.

Flavor tagging Variations in efficiency scale factors are provided by comparing data and simulation in regions enhanced in jets of specific flavors. Dedicated NPs are assigned for each flavor in addition to NPs associated to extrapolation from the measured region to high-p_{T} jets. The latter is based on variations of parameters affecting the tagging efficiency such as track resolution, multiplicity, and material effects.

Electron efficiency Separate NPs are considered to account for changes in the efficiency scale factors due to the reconstruction, identification, and isolation. Scale and resolution uncertainties on electrons are found to be negligible and thus are not considered.

Muon efficiency Scale factor variations impacting the measured reconstruction and isolation efficiency for muons are considered with separate NPs for statistical and systematic sources. Additional NPs are considered for low-p_{T} muons.

Pileup re-weighting The sensitivity of the results to the PU profile simulated in MC is assessed by re-weighting events. The average pileup can be measured in terms of the average number of collisions $\langle\mu\rangle$ per bunch crossing as well as by the number of reconstructed vertices per event N_{PV}. The correspondence between each parameter reflects the relative fraction of high-p_{T} interactions (leading to reconstructed vertices), which is configurable in MC simulation. A correction is necessary such that events simulated with a value of $\langle\mu\rangle$ fixed to data are re-scaled to have 9% fewer reconstructed vertices. The uncertainty on PU re-weighting is obtained by varying the underlying pileup profile of simulated event samples by the full size of this correction in each direction.

6.8.2 Theoretical Sources

Uncertainties stemming from the finite calculational accuracy of simulations of physical processes are considered. Predictions are separately obtained for each SM background and a set of parameter variations corresponding to modeling choices are assigned to each, assumed to be uncorrelated among processes. The sources considered are described separately below for each SM background. Technical details of the various samples of simulated events were introduced in Section 6.3.1.

$t\bar{t}$ and tW single top Uncertainties are considered corresponding to variations in scale choices, parton shower modeling, and the NLO matching scheme. Scale uncertainties are assessed by comparisons of the low- and high-radiation samples with altered values of the μ_R, μ_f, and `hdamp` parameters. Uncertainties due to modeling of the parton shower, including fragmentation and hadronization effects is obtained by comparing the nominal powheg+PYTHIA sample to an alternate one where the HERWIG++ shower program is utilized. The difference between MC@NLO and POWHEG calculations with fixed parton shower determined the uncertainties due to choices in the various matching parameters. Uncertainties due to PDFs are found to be negligible compared to the remaining effects and are not explicitly considered. The uncertainty related to overlapping contributions from diagrams with one and two resonant top quarks and their interference is assessed by comparing predictions using the DR and DS schemes. A cross section uncertainty is assessed on the tW single top process in regions where its normalization is not derived from a dedicated control region.

$W+$jets and $Z+$jets The effect of separate variations in the renormalization, factorization, and resummation scales are considered by a factor of two in each direction. The CKKW-L merging scale defined the phase space to be included in the NLO- versus LO-accurate ME calculation. Nominally it is set to 20 GeV, and is variations of 15 GeV and 30 GeV are considered. A further uncertainty is assessed comparing the nominal SHERPA prediction to a multi-leg LO MG5_aMC@NLO+PYTHIA 8 calculation. Cross section uncertainties are not needed for $W+$jets, which is normalized in all regions. The contribution of $Z+$jets to all SRs is so small that the cross section uncertainty is irrelevant.

Diboson Variations of the renormalization, factorization, and resummation are considered. Cross section uncertainties are also considered for each VV sub-process.

$t\bar{t}V$ The renormalization and factorization scales are independently varied by factors of two in each direction, with the envelope giving the uncertainty on the predicted transfer factor. 100 NNPDF eigenvector variations are also considered, with the associated uncertainty calculated as the RMS across variations.

Signal Uncertainty in the signal production cross sections are evaluated. Further uncertainties on the signal shape due to PDF and scale variations are assessed for several benchmark points and found to be everywhere negligible in comparison to the experimental uncertainties.

6.8.3 Summary

The relative impact of each of the sources of systematic uncertainty is summarized in Table 6.15 and compared to the (statistical) uncertainty on the normalization factor for each fitted background.

6.9 Statistical Procedure

The control regions defined in Section 6.7 are used to predict the number of SM background events entering the corresponding signal regions. In some cases, multiple signal regions (and their corresponding CRs) are combined in a fit to obtain tighter constraints on BSM models. In the stop analysis, the statistical framework is implemented in the HistFitter package [201]. Before discussing specifics of the statistical interpretation of the results of the stop search, we briefly review the profile likelihood ratio framework used to quantify agreement of the observed data with the predicted SM background and the CL_S prescription [202] used to set limits on BSM signal models.

Table 6.15: The contribution to the total uncertainty on the SM background enter each SR due to the data-driven normalization factors and systematic uncertainties. The uncertainty on the SR yields is shown as a percentage of the total SM prediction for three selected SRs. Normalization uncertainties are dominated by the sample size of the corresponding CR(s), while systematic uncertainties reflect residual effects not canceled in the transfer factor construction. Individual contributions may not sum to the total uncertainty shown due to their correlations.

Signal Region Uncertainty (%)	`tN_med`	`bC2x_med`	`bCsoft_med`
$t\bar{t}+Z$ normalization	11	6.8	–
$t\bar{t}$ (2L) normalization	4.7	3.3	2.6
Wt normalization	3.0	17	3.4
W+jets normalization	2.5	2.1	8.1
$t\bar{t}+Z$ modeling	11	1.2	< 1.0
$t\bar{t}$ radiation	4.3	1.9	4.6
$t\bar{t}$ generator	3.6	1.7	4.6
$t\bar{t}$ hadronization	2.5	5.8	3.9
Wt–$t\bar{t}$ interference	< 1.0	13	< 1.0
Single-top generator	< 1.0	4.9	< 1.0
Single-top hadronization	< 1.0	11	< 1.0
JER	2.8	6.8	2.4
JES	2.8	1.4	2.1
Mis-b-tag (c-quark)	2.3	4.9	13
Mis-b-tag (light quark)	2.0	2.0	4.6
Pile-up	2.5	3.8	2.0
Total systematic uncertainty	18	22	15

The Profile Likelihood Ratio

The fit model is described by a likelihood function which is a product of probabilities involving observed yields $\mathbf{d}$, predicted yields due to some arbitrary sources $\mathbf{m}^i$, and parameters controlling the effects of systematic uncertainties $\boldsymbol{\theta}$:

$$L(\mathbf{d}, \mathbf{m}^i, \boldsymbol{\theta}) = P(\mathbf{d}, \mathbf{m}^i, \boldsymbol{\theta}) \times C(\boldsymbol{\theta}). \tag{6.8}$$

For concreteness, here $\mathbf{d} = (d_{\mathrm{SR}}, d_{t\bar{t}\ \mathrm{CR}}, d_{W+\mathrm{jets\ CR}}, \ldots)$ and a similar vector exists for each process $\mathbf{m}^{t\bar{t}}, \mathbf{m}^{tW}, \ldots$, which each also contribute to all regions. The term $P(\mathbf{d}, \mathbf{m}_i, \boldsymbol{\theta})$ is a product of Poisson constraints for each signal and control region

$$P(\mathbf{d}, \mathbf{m}^i, \boldsymbol{\theta}) = \prod_{r \in \mathrm{Regions}} \frac{(\sum_i m_r^i(\boldsymbol{\theta}))^{d_r} e^{-\sum_i m_r^i(\boldsymbol{\theta})}}{d_r!} \tag{6.9}$$

with $\boldsymbol{\theta}$ parameterizing the effect of each systematic uncertainty on the yield for each process in each region. Each of the NPs θ is modeled as a random variable with unit Gaussian probability density function (pdf)[15]) that simultaneously controls the variation in the yields for all bins and processes $\mathbf{m}_i = \mathbf{m}_i(\boldsymbol{\theta})$. The constraint term $C(\boldsymbol{\theta})$ is the product of Gaussian constraints for all NPs. In this formulation the dependence of the yields predicted in a specific region for a specific process due to NP θ may be parameterized as $m_r^i(\boldsymbol{\theta}) = m_r^i|_{\mathrm{no\ syst}} + \theta \cdot \Delta_r^i$, where the Δ_r^i are precisely the variations in predicted yields which were obtained in Section 6.8. A single source of uncertainty may be "decorrelated" among bins by representing its effects on various regions and processes through many NPs, each of which may vary independently. In the case of jet energy scale uncertainties, for example, effects are taken to be correlated across all processes and regions. On the other hand, while modeling uncertainties due to μ_R/μ_f variations are decorrelated among processes they must be correlated among regions. This is critical to obtain the cancellation of effects in the "transfer factor" construction. In Eqn. 6.9, each m_r^i is required to be non-negative.

Among the $\mathbf{m}_i$, the contribution of the signal process is unique in that its normalization is unknown, so that conventionally its contribution is written as $\mu_{\mathrm{sig}}\mathbf{m}_i$, with the signal strength parameter μ_{sig} controlling the normalization of the contribution. The "shape" of the signal (relative contribution to each region) is encoded in the $\mathbf{m}_i$, as with all other processes, and may be nonzero in regions other than the SR.

[15] Here we do not capitalize the abbreviation to distinguish from the parton distribution function (PDF) described above.

It is useful to take advantage of convenient properties of the likelihood function to derive a further test statistic, the profile likelihood ratio $\lambda(\mu)$ and its normalized transform q_μ, defined

$$\lambda(\mu) = \frac{L(\mu, \hat{\hat{\boldsymbol{\theta}}})}{L(\hat{\mu}, \hat{\boldsymbol{\theta}})} \tag{6.10}$$

$$q_\mu = -2 \log \lambda(\mu). \tag{6.11}$$

In the first line $\hat{\mu}$ and $\hat{\boldsymbol{\theta}}$ refer to the parameters which minimize L and $\hat{\hat{\boldsymbol{\theta}}}$ refers to the $\boldsymbol{\theta}$ that minimizes L given μ. We assume that μ and $\hat{\mu}$ are non-negative. Wilks' theorem states that q_μ follows a χ^2 distribution with one degree of freedom in the limit of large event samples [203].

The Background-only fit

A "background-only" fit is first conducted to determine the data-driven corrections to the background processes and check the fit behavior before considering SR data. This is done by removing SRs, VRs, and any signal processes from the $\mathbf{m}_i$ contributing to the likelihood defined in Equation 6.8. In this setup the NPs included in $\boldsymbol{\theta}$ include all of the background systematic uncertainties described in Section 6.8 as well as normalization factors (NFs) μ_i for each of the background processes for which a CR has been defined. For backgrounds with floating normalization, only the shape (the relative contribution of the process to all regions) is taken from simulation so that $\mathbf{m} \to \mu_i \mathbf{m}$ for these processes. The values for each normalization factor give useful information regarding the quality of the MC simulation's description of the data, with NFs far from unity indicating potential systematic biases. The covariance matrix for $\boldsymbol{\theta}$ can be obtained from the likelihood function as

$$V_{ij}^{-1} = \frac{\partial^2 L}{\partial \theta_i \partial \theta_j} \tag{6.12}$$

assuming large event samples[16]. The values of $\hat{\hat{\boldsymbol{\theta}}}$ and their associated 1σ values indicate whether the fit has constrained any systematic uncertainties. This "profiling" is usually undesirable, exposes an inconsistency between the method used to obtain uncertainties and the setup of the fit model itself. Inspecting the correlation matrix for $\boldsymbol{\theta}$ is also necessary to ensure that, for example, extracted normalizations are not strongly correlated with theoretical uncertainties, confounding the two effects.

The background-only fit may be extrapolated to provide an estimate of the SM yield in the SR. This estimate may be written in terms of the NFs as

$$m_{\mathrm{SR}}^{i,(\text{data-driven})} = m_{\mathrm{SR}}^{i,(\text{Pure MC})} \cdot \mu_i \approx m_{\mathrm{SR}}^{i,(\text{Pure MC})} \left[\frac{d_{\mathrm{CR}_i}}{m_{\mathrm{CR}_i}^{i,(\text{Pure MC})}} \right] \tag{6.13}$$

[16] When this approximation breaks down ($\mathcal{O}(10)$ expected events), toy data sets with varied $\boldsymbol{\theta}$ vectors may be used to recover the full covariance matrix.

where the last relation is an equality if no other processes contribute to CR_i and no other regions constrain the process. It can also be useful to write the estimate of $m_{\mathrm{SR}}^{i,(\text{data-driven})}$ as a MC-based transfer factor $t_i^{\mathrm{CR}_i \to \mathrm{SR}}$ which extrapolates observed yields in a CR to an SR prediction:

$$m_{\mathrm{SR}}^{i,(\text{data-driven})} \approx d_{\mathrm{CR}_i} \cdot t_i^{\mathrm{CR}_i \to \mathrm{SR}} = d_{\mathrm{CR}_i} \left[\frac{m_{\mathrm{SR}}^{i,(\text{Pure MC})}}{m_{\mathrm{CR}_i}^{i,(\text{Pure MC})}} \right]. \tag{6.14}$$

This extrapolation provides a full description of the predicted SR yields and uncertainties, except for any of the $\boldsymbol{\theta}$ whose effects cannot be extrapolated from the other regions (e.g. limited MC stats in the SR).

Testing the SM hypothesis

For each SR, the agreement of the observed data with the SM prediction is quantified by quoting a p-value corresponding to the SM-only hypothesis. If this p-value corresponds to more than a few σ, either our model of the SM prediction is inadequate or it constitutes evidence for BSM physics. In this case, the signal prediction is set to zero in all regions except the SR, where μ_{sig} then parameterizes the number of BSM events entering the region. To test this hypothesis, all observed data and SM estimates in the CRs and the SR are included in likelihood function, as well as the BSM signal. If the best-fit $\hat{\mu}_{\mathrm{sig}}$ is negative a p-value of 0.5 is quoted, as the choice is made to consider only signals leaving positive contributions to the SR. Otherwise, the test statistic q_0 gives the desired likelihood ratio and the pdf of the test statistic can be integrated up to calculate a p-value

$$p_0 = \int_{q_{0,\ \mathrm{obs}}}^{\infty} \mathrm{pdf}(q_0 \mid \mu_{\mathrm{sig}} = 0)\, \mathrm{d}q_0. \tag{6.15}$$

In the asymptotic case, the pdf is approximates a χ^2 distribution, with $p_0 \approx \sqrt{q_0}$ [204].

Model-independent exclusions

For each SR, a model-independent limit may be placed on the number of non-SM events entering the region, provided that the SM provides a good description of the data. The setup is similar to that of the previous section where the BSM process is assumed to contribute only to the SR. However, the test statistic q_μ is now calculated for a range of signal strengths $\mu \geq \hat{\mu}$ to assess the compatibility of the observed data with a particular signal strength μ_{sig}. These p-values are capped at 0.5, with $q_\mu \equiv 0$ for $\mu < \hat{\mu}$ in this scenario.

The $\mathrm{CL_S}$ prescription [202] is used to obtain the excluded signal strength instead of the p-value defined in Eqn. 6.15 to avoid setting extreme limits in the case where a deficit of data, below the SM prediction, is observed. Thus, for each signal strength μ_{sig} the corresponding CL_S value is computed as

$$\text{CL}_\text{S}(\mu_{\text{sig}}) = p_{\mu_{\text{sig}}}/p_0, \tag{6.16}$$

the ratio of the compatibility of the signal + background versus the that of the background-only hypotheses. When the observation perfect matches the SM prediction, the penalty factor p_0 is 0.5, so that limits are more conservative than those obtained from the signal p-value alone (i.e. $p_\mu = 0.05 \mapsto \text{CL}_\text{S} = 0.10$).

Thus, for a scanned range of μ values, the corresponding CL_S is computed, using toys if necessary. The number of BSM events corresponding to the μ_{sig} for which $\text{CL}_\text{S}(\mu_{\text{sig}}) = 0.05$ is defined as $S^{\text{obs}}_{\text{excl},95\%}$. An expected value $S^{\text{exp}}_{\text{excl},95\%}$ is similarly obtained by replacing $L(\hat{\mu}, \hat{\boldsymbol{\theta}})$ in the denominator of the likelihood ratio with $L(0, \hat{\boldsymbol{\theta}})$, where the value for the NPs obtained from the full fit including observed data are still included[17].

Model-dependent exclusions

In the context of this statistical framework, each specific BSM model predicts the relative number of extra events expected in each region entering the fit (ideally, many events in the SR(s) and few in the CR(s)) as well as a potential overall normalization (signal cross section). A similar procedure to the model-independent case may then be followed. The value of μ_{sig} corresponding to $\text{CL}_\text{S}(\mu_{\text{sig}}) = 0.05$ is obtained as above, with the model excluded if $\mu^{\text{obs}}_{\text{excl},95\%} < 1$. The limit may also be translated into a limit on the cross section times branching ratio $\sigma \times \mathcal{BR}$ to the targeted final state, using the acceptance and efficiency predicted for the signal model

$$(\sigma \times \mathcal{BR}_{\text{model}})^{\text{obs}}_{\text{excl},95\%} = \mu^{\text{obs}}_{\text{excl},95\%} \cdot (\sigma \times \mathcal{BR}_{\text{model}}). \tag{6.17}$$

The latter is particularly useful in the case of new BSM particles that may decay via a number of channels. For example, assuming the strong $\tilde{t}\tilde{t}^*$ production cross sections, limits may be set on the individual $\tilde{t} \to t\tilde{\chi}^0_1$ and $\tilde{t} \to b\tilde{\chi}^\pm_1$ branching fractions.

While each of the `bCsoft` regions are not orthogonal to each other (i.e. some events may enter both `bCsoft_med` and `bCsoft_high`), they are designed to be orthogonal to the `tN` regions so that they may be combined. In this manner, a combined likelihood function can be built from the `tN_med` regions (five CRs and four SRs) and one of the `bCsoft` regions (e.g. three CRs and three SRs for `bCsoft_high`). The signal sensitivity is increased by considering its contribution to all seven SRs at

[17] The choice to retain the values of the NPs derived from data is made to facilitate more direct comparisons between the expected and observed limits

once. The background treatment becomes more complicated, with two sets of processes receiving separate normalizations for the hard- and soft-lepton CRs and SRs. The optimal choice of how to correlate systematics among regions in this approach is not obvious, but in practice they are generally taken to be uncorrelated among the two sets of fit regions.

6.10 Results

6.10.1 Model-independent results

Background-only fits are conducted for the each of the SRs. The predicted SR yields and uncertainties are compared to the observed data in each VR and SR in Figures 6.26 and 6.27. The full comparison of predicted and observed events is presented in Table 6.16, in addition to the observed significance and model-independent exclusions for each signal region. In each of these results, the "discovery regions" are used when considering SRs in which multiple sub-regions for model-dependent fits are also defined. No significant excesses are observed, the largest being 1.6σ in `tN_high`.

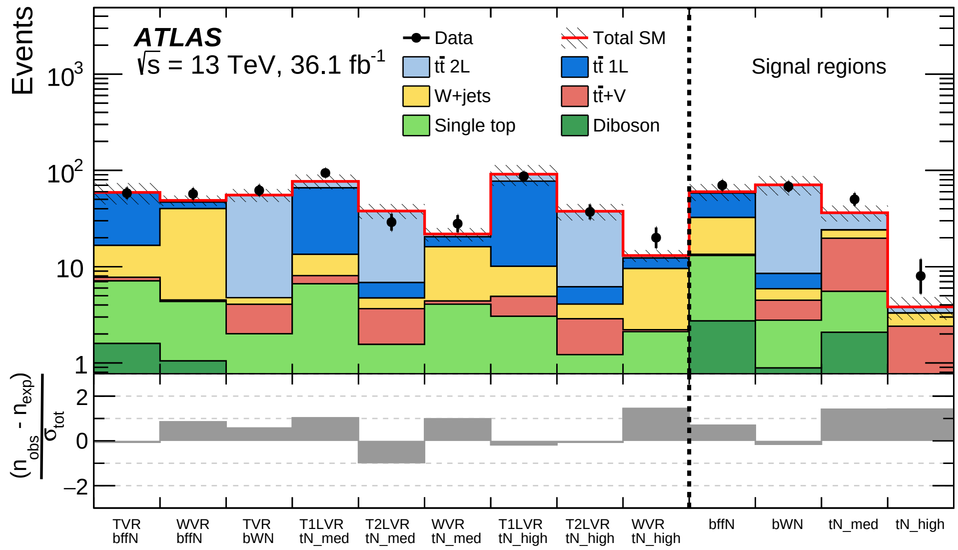

(a) tN regions

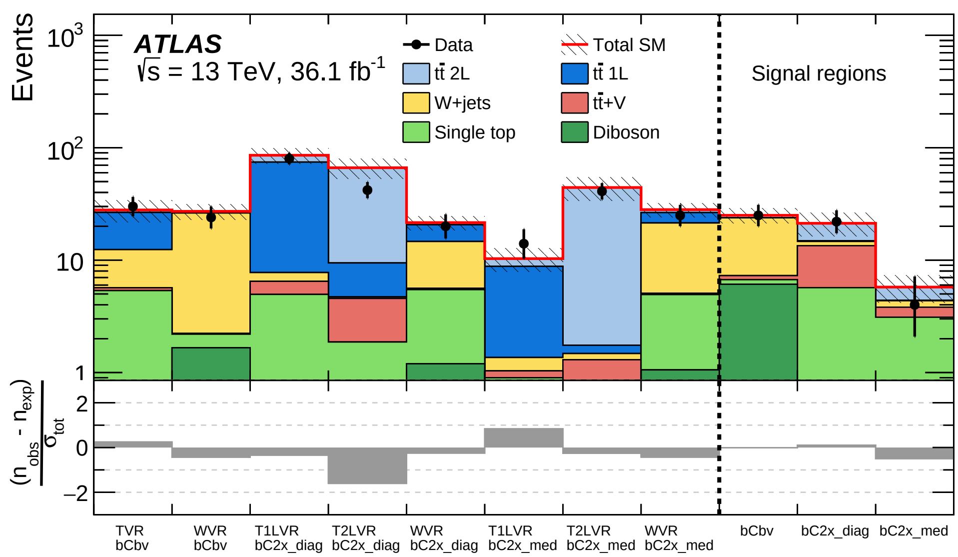

(b) bC2x regions

Figure 6.26: The observed data in the (a) tN_med and tN_high and (b) bC2x_med and bC2x_diag SRs and VRs are compared with the SM yields predicted by the background-only fit. Contributions from each process are shown in colored, stacked histograms indicated in the legends. The "pull" distributions are given in the corresponding lower panels, showing the difference between observed and predicted yields in units of the expected total uncertainty. The bWN, bffN, and bCbv regions pictured target scenarios where $\Delta M(\tilde{t}, \tilde{\chi}_1^0) < m_{\text{top}}$. A detailed description of these regions has been omitted from the text for brevity.

Table 6.16: The observed number of events in all SRs is compared with the corresponding SM prediction, broken into individual components according to the SM process. The SM predictions are the result of the background-only fit where the normalization of each process are allowed to float. The normalizations for each process obtained from the fit to CR data is also shown in the table. Finally, the comparability of the observed number of events in each region with the SM prediction is quantified with a p-value (capped at 0.5) corresponding to the background-only hypothesis and the significance σ, quoted as the equivalent for a Gaussian-distributed random variable. Model-independent limits on the number of non-SM events entering each region are also quoted ($N^{\text{limit}}_{\text{non-SM}}$ obs.) in addition to the expected value $N^{\text{limit}}_{\text{non-SM}}$ exp. Each Background whose contribution does not float in the fit is normalized to its theoretical cross section. For the `bCsoft` regions the $t\bar{t}$ estimate is not divided into explicit sub-components, so that a single SR prediction and associated NF are obtained.

Signal region	`tN_high`	`tN_med`	`bC2x_diag`	`bC2x_med`	`bCsoft_diag`	`bCsoft_med`	`bCsoft_high`
Observed	8	50	22	4	33	19	2
Total SM	3.8 ± 1.0	36.3 ± 6.6	21.3 ± 5.0	5.8 ± 1.6	24.7 ± 3.1	13.7 ± 2.1	1.8 ± 0.3
$t\bar{t}$ 2ℓ	0.51 ± 0.18	12.1 ± 2.9	6.4 ± 2.4	1.36 ± 0.49	-	-	-
$t\bar{t}$ 1ℓ	0.020 ± 0.001	0.19 ± 0.05	0.28 ± 0.18	$0.04^{+0.13}_{-0.04}$	10.3 ± 2.4	4.9 ± 1.5	0.36 ± 0.15
$t\bar{t} + V$	1.86 ± 0.90	14.2 ± 5.5	7.8 ± 3.3	0.71 ± 0.38	0.14 ± 0.06	0.44 ± 0.10	0.05 ± 0.02
Single top	0.13 ± 0.10	3.5 ± 1.2	5.5 ± 2.4	3.0 ± 1.5	3.5 ± 1.5	1.6 ± 0.5	0.23 ± 0.11
W+jets	0.88 ± 0.24	4.3 ± 1.1	1.22 ± 0.35	0.54 ± 0.14	8.0 ± 2.0	6.4 ± 2.0	1.06 ± 0.24
Diboson	0.42 ± 0.16	2.08 ± 0.70	0.23 ± 0.08	0.07 ± 0.04	2.21 ± 0.93	0.31 ± 0.16	0.04 ± 0.01
Z+jets	-	-	-	-	0.60 ± 0.55	0.17 ± 0.16	0.04 ± 0.04
$t\bar{t}$ 2ℓ NF	1.01 ± 0.15	0.96 ± 0.13	1.28 ± 0.17	1.58 ± 0.22	-	-	-
$t\bar{t}$ 1ℓ NF	0.97 ± 0.08	1.05 ± 0.09	0.96 ± 0.08	0.75 ± 0.15	0.73 ± 0.11	0.92 ± 0.07	0.93 ± 0.16
$t\bar{t} + V$ NF	1.11 ± 0.35	1.13 ± 0.32	1.18 ± 0.39	0.95 ± 0.52	-	-	-
Single top NF	0.64 ± 0.37	1.19 ± 0.37	1.59 ± 0.45	1.17 ± 0.37	-	0.47 ± 0.14	0.37 ± 0.15
W+jets NF	0.82 ± 0.17	0.85 ± 0.18	0.80 ± 0.24	1.11 ± 0.25	1.19 ± 0.26	1.35 ± 0.24	1.11 ± 0.19
p_0 (σ)	0.05 (1.6)	0.07 (1.4)	0.45 (0.11)	0.5 (-)	0.09 (1.34)	0.12 (1.17)	0.44 (0.16)
$N^{\text{limit}}_{\text{non-SM}}$ exp.	5.8	19	14	6.4	13	9.6	4.1
$N^{\text{limit}}_{\text{non-SM}}$ obs.	10	31	14	5.2	20	14	4.3

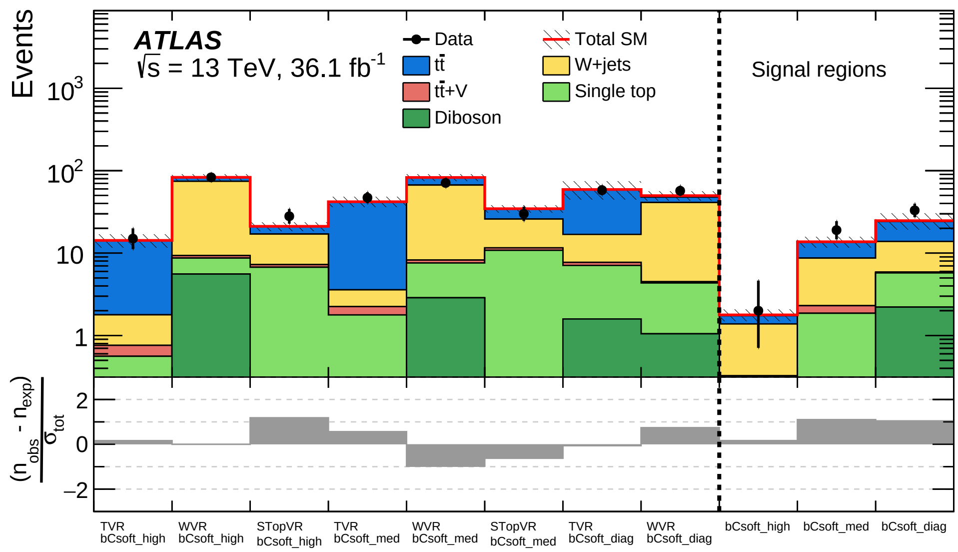

Figure 6.27: The observed data in the `bCsoft_high`, `bCsoft_med`, and `bCsoft_diag` SRs and VRs are compared with the SM yields predicted by the background-only fit. Contributions from each process are shown in colored, stacked histograms indicated in the legend. The "pull" distribution is shown in the lower panel, showing the difference between observed and predicted yields in units of the expected total uncertainty.

6.10.2 Limits on SUSY Scenarios

As no significant excesses are observed, limits are set on the allowed space of SUSY models which may still be consistent with the data. For each of the models considered, the SR which achieves the best expected exclusion is selected; if the model is not allowed by that region it is considered to be excluded. The SRs considered in this process are the single-bin `tN_high`, `bC2x_med`, and `bC2x_diag` regions, as well as the multi-bin regions `tN_med`, `bCsoft_diag`, `bCsoft_med`, and `bCsoft_high`. The bin-by-bin breakdown for the shape fit regions is shown separately in Table 6.17 and displayed in Figure 6.28.

Figure 6.29 shows the space of excluded models in the Bino LSP scenario, where no other light sparticles are assumed so that the stop may only decay via $\tilde{t} \to t\tilde{\chi}_1^0$. Modest excesses of data in the `tN_high` and `tN_med` regions limit the exclusion to stop masses of about 900 GeV for LSP masses up to about 350 GeV. Exclusions based on the results of other SRs defined in Ref. [7] are also shown.

Limits on the Bino LSP model with Wino LSP are presented in Figure 6.30. Signal models are generated for a scan of pMSSM mass parameters corresponding to the left-handed stop (m_{q3L}) as well as the Bino mass M_1, with $M_2 = 2M_1$. As the left-handed stop is part of an SU(2) doublet,

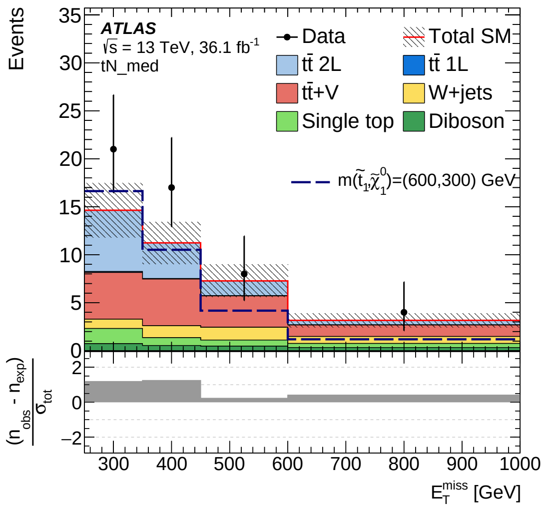

(a) `tN_med` SR

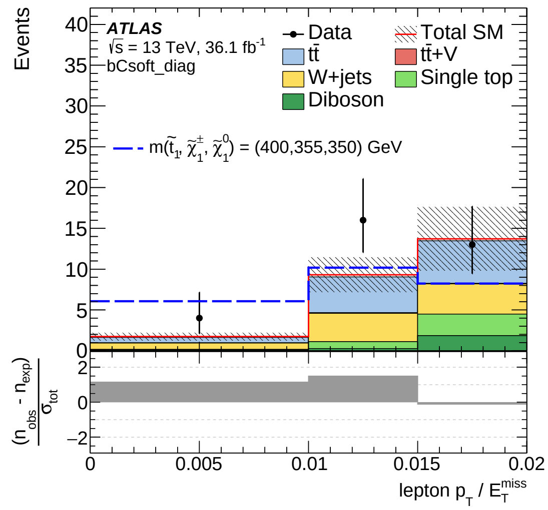

(b) `bCsoft_diag` SR

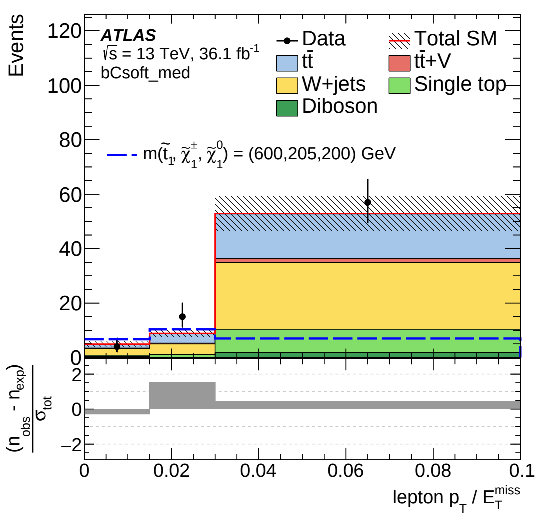

(c) `bCsoft_med` SR

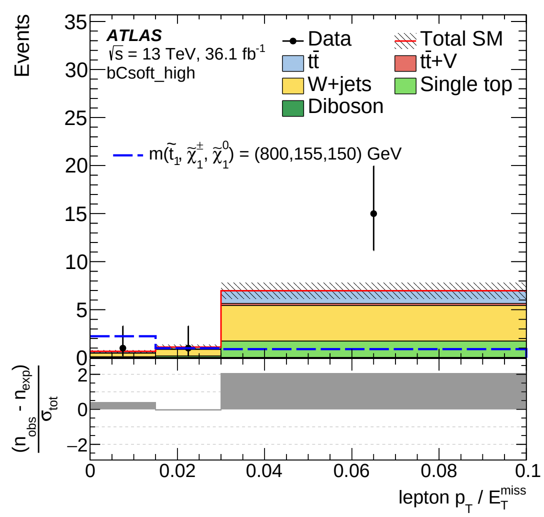

(d) `bCsoft_high` SR

Figure 6.28: Comparisons are shown between the predicted SM yields and observed data for SRs where a multiple sub-regions are used in the exclusion fit.

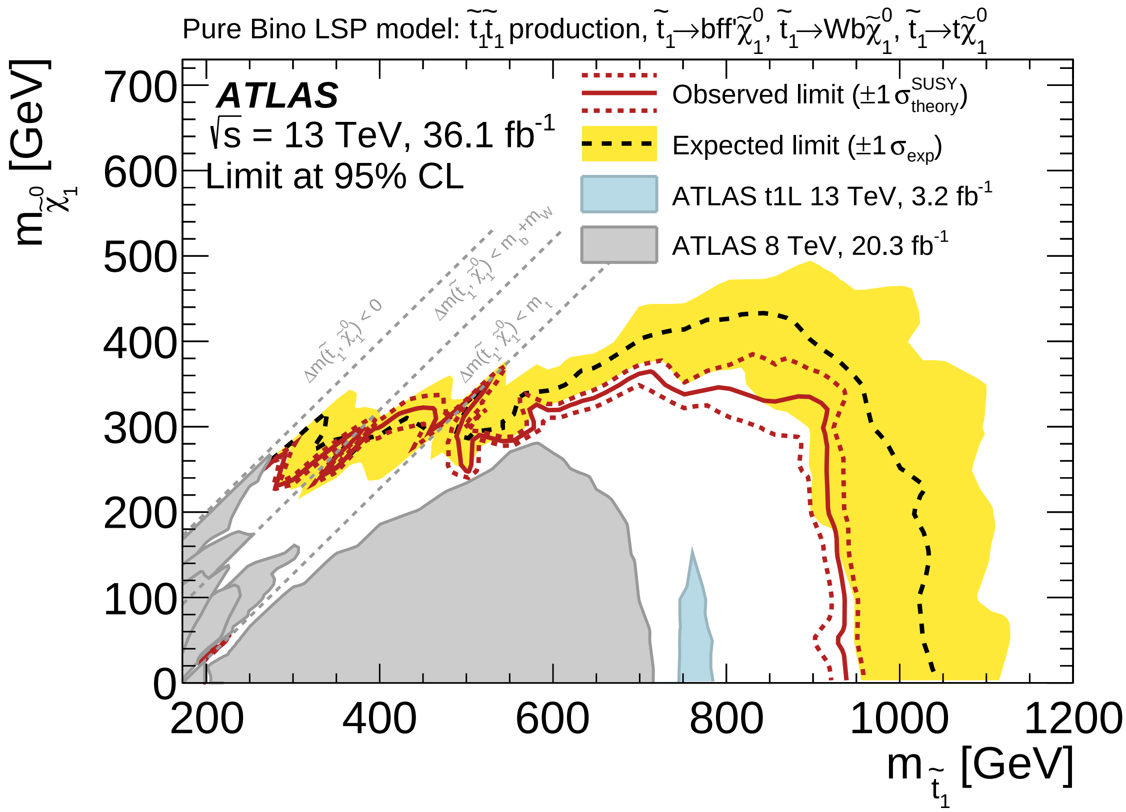

Figure 6.29: The expected and observed exclusion contours are shown for the simplified model where $\mathcal{BR}(\tilde{t} \to t\tilde{\chi}_1^0) = 100\%$, inspired by scenarios with a Bino LSP. The region inside the red solid line is excluded at the 95% confidence level, with dotted red lines indicating the exclusion for variation of the $\tilde{t}\tilde{t}^*$ production cross section within its theory uncertainty. The expected limit based on the prediction of SM yields is shown a a black dashed line, with the yellow band indicating the corresponding experimental uncertainty. Exclusions for models with $\Delta M(\tilde{t}, \tilde{\chi}_1^0) > 250$ GeV are obtained with the `tN_med` and `tN_high`regions. Generally `tN_high` is the most sensitive region for stop masses above 900 GeV. Exclusions for lower values of $\Delta M(\tilde{t}, \tilde{\chi}_1^0)$ are shown for completeness, but are obtained from other search regions defined in Ref. [7]. Results from previous analyses of 8 TeV [3] and 13 TeV [149] data are also included.

production of sbottom pairs at similar mass scales is also considered. Stop masses up to 900 GeV are excluded for LSPs between 100 GeV and 300 GeV, with limits roughly independent of the sign of μ. Models cannot be excluded which have $50 < m_{\tilde{\chi}_1^0}/\text{GeV} < 100$ for the full range of stop masses considered. In this corridor, $\Delta M(\tilde{\chi}_1^0, \tilde{\chi}_1^{\pm}) \sim 50 - 100$ GeV so that the acceptance is low for both hadronic W-tagging regions (where the W boson is less boosted) and for the soft-lepton regions (which targets lower lepton p_{T}).

Results based on the combination of soft-lepton `bCsoft` signal regions and hard-lepton `tN_med` regions are shown in Figure 6.31. Models are considered with a fixed Higgsino mass splittings $\Delta M(\tilde{\chi}_1^0, \tilde{\chi}_1^{\pm}) = 5$ GeV and $\Delta M(\tilde{\chi}_1^0, \tilde{\chi}_2^0) = 10$ GeV, where stops are excluded up to 800 to 900 GeV in the case of a 100 GeV chargino. Variations in the observed exclusions are observed depending on the choice of pMSSM parameters controlling the stop handedness ($\tilde{t}_1 \sim \tilde{t}_L$ versus $\tilde{t}_R$) and $\tan\beta$. Stronger limits are set in the case $\tilde{t}_1 \sim \tilde{t}_L$, as the stop decays more frequently via $\tilde{t} \to t\tilde{\chi}_1^0$, where looser selections can be made on the lepton, which has higher-momentum that that emitted in the $\tilde{t} \to b\tilde{\chi}_1^{\pm}$ decay. Limits up to 400 GeV are also observed for the case when $\Delta M(\tilde{t}, \tilde{\chi}_1^0) < m_{\text{top}}$ and the $\tilde{t}$ must always decay via $\tilde{t} \to b\tilde{\chi}_1^{\pm}$.

Higgsino LSP models are also considered with mass splittings $\Delta M(\tilde{\chi}_1^0, \tilde{\chi}_1^{\pm})$ varied from 0 to 30 GeV, with exclusions shown in Figure 6.32. The $\tilde{\chi}_1^{\pm}$ mass is assumed to be 150 GeV. The shape fit in $p_{\text{T}}^{\ell}/E_{\text{T}}^{\text{miss}}$ provides a broad expected sensitivity across Higgsino mass splittings, with exclusions independent of $\Delta M(\tilde{\chi}_1^0, \tilde{\chi}_1^{\pm})$ down to approximately 4 GeV. At even lower mass splittings,

Table 6.17: The number of events observed in each bin of the SRs where shape fits are used to improve sensitivity to difficult models of $\tilde{t}\tilde{t}^*$ pair production. Observed data is compared to the SM prediction in each bin, which are labeled according to increasing values of the binning variable ($E_{\text{T}}^{\text{miss}}$ or $p_{\text{T}}^{\ell}/E_{\text{T}}^{\text{miss}}$).

Signal region	Fitted variable		bin 1	bin 2	bin 3	bin 4
`tN_med`	$E_{\text{T}}^{\text{miss}}$	Observed	21	17	8	4
		Total background	14.6 ± 2.8	11.2 ± 2.2	7.3 ± 1.7	3.16 ± 0.74
`bCsoft_diag`	$p_{\text{T}}^{\ell}/E_{\text{T}}^{\text{miss}}$	Observed	4	16	13	–
		Total background	1.69 ± 0.47	9.3 ± 2.1	13.6 ± 2.8	–
`bCsoft_med`	$p_{\text{T}}^{\ell}/E_{\text{T}}^{\text{miss}}$	Observed	4	15	57	–
		Total background	4.92 ± 0.90	8.9 ± 1.3	52.9 ± 6.2	–
`bCsoft_high`	$p_{\text{T}}^{\ell}/E_{\text{T}}^{\text{miss}}$	Observed	1	1	15	–
		Total background	0.67 ± 0.13	1.11 ± 0.22	6.98 ± 0.81	–

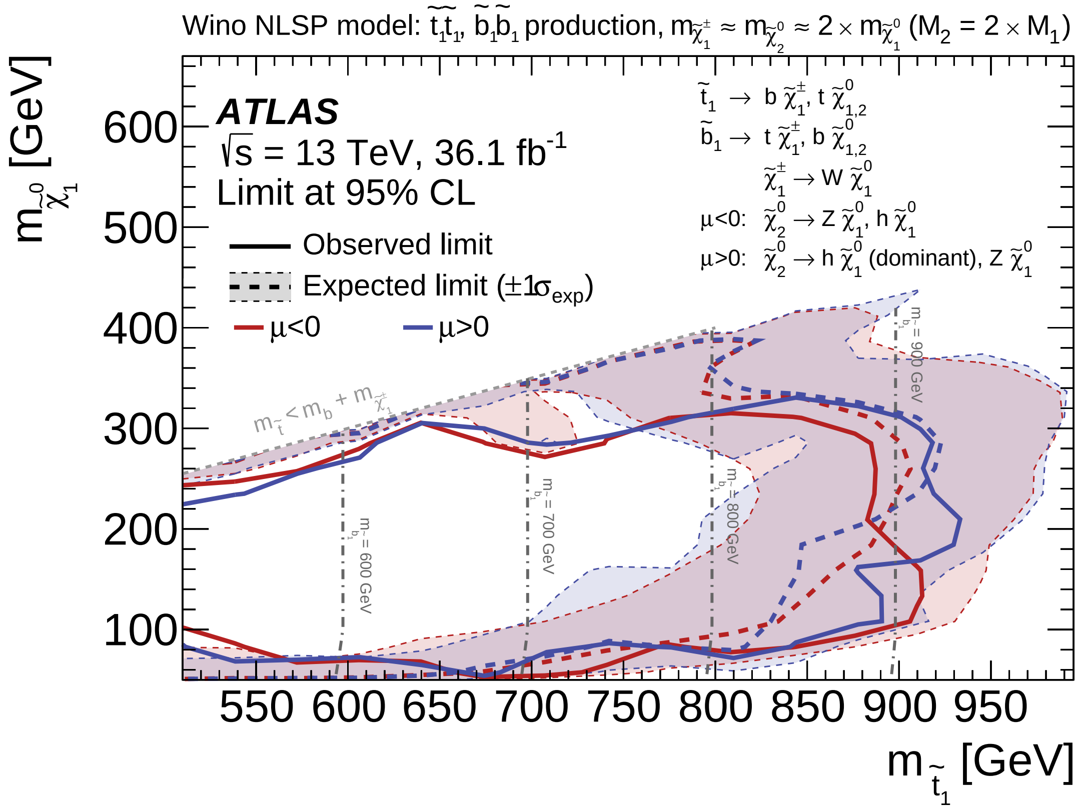

Figure 6.30: Expected and observed exclusion contours are shown for the Bino LSP / Wino NLSP pMSSM model. The pMSSM mass parameters are scanned to evenly populate the grid of physical stop and LSP masses shown here, with separate grids for the $\mu > 0$ and $\mu < 0$ cases. The main effect of the sign of μ is to alter the fraction of $\tilde{\chi}_2^0$ decays to $\tilde{\chi}_1^0$ via emission of a Z of Higgs boson. As these decay products are not reconstructed, the exclusions in each scenario are similar. Stop masses up to 900 GeV are excluded for LSPs between 100 GeV and 300 GeV. Models with light LSPs and charginos near the LEP limit are allowed, independent of stop mass. For the majority of phase space the strongest constraints from the the `bC2x` signal regions. Near the diagonal region $m_{\tilde{t}} \sim m_b + m_{\tilde{\chi}_1^\pm}$ the combination of `bCsoft` and `tN_med` regions are most sensitive, but only exclude stop masses below 700 GeV. $\tilde{b}\tilde{b}^*$ production is also included, as $\tilde{t}_1 \approx \tilde{t}_L$ in this model, with the $\tilde{b}$ mass indicated by the vertical gray dashed lines. Sbottom decays via $\tilde{b} \rightarrow b\tilde{\chi}_2^0$ and $\tilde{b} \rightarrow t\tilde{\chi}_1^\pm$ can produce signatures to which the stop search signal regions have good sensitivity.

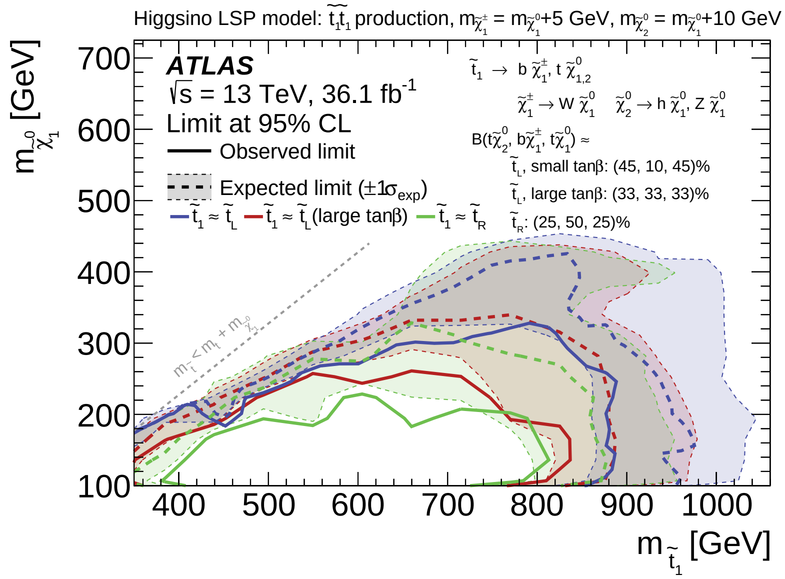

(a) Exclusions for the region $\Delta M(\tilde{t}, \tilde{\chi}_1^0) > m_{\text{top}}$

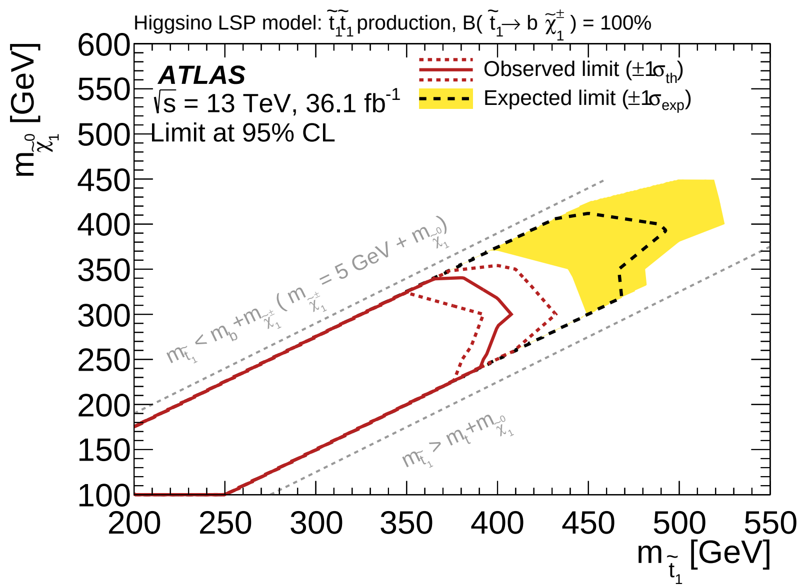

(b) Exclusions for the region $\Delta M(\tilde{t}, \tilde{\chi}_1^0) < m_{\text{top}}$

Figure 6.31: Expected (dashed) and observed (solid) exclusion contours are presented for several variants of the Higgsino LSP simplified model. In (a), models are shown in which $\Delta M(\tilde{t}, \tilde{\chi}_1^0) > m_{\text{top}}$. Colors indicate different assumed pMSSM parameters: $\tilde{t}_1 \sim \tilde{t}_L$ (blue), $\tilde{t}_1 \sim \tilde{t}_R$ (green), and $\tilde{t}_1 \sim \tilde{t}_L$ with large $\tan\beta$ (red). These assumptions alter the relative fraction of stop decays via $\tilde{t} \rightarrow t\tilde{\chi}_1^0$, $\tilde{t} \rightarrow b\tilde{\chi}_1^\pm$, and $\tilde{t} \rightarrow t\tilde{\chi}_2^0$. In (b), models are shown with $\Delta M(\tilde{t}, \tilde{\chi}_1^0) < m_{\text{top}}$, having $\mathcal{BR}(\tilde{t} \rightarrow b\tilde{\chi}_1^\pm) = 1$. In all models $\Delta M(\tilde{\chi}_1^0, \tilde{\chi}_1^\pm)$ is fixed to 5 GeV.

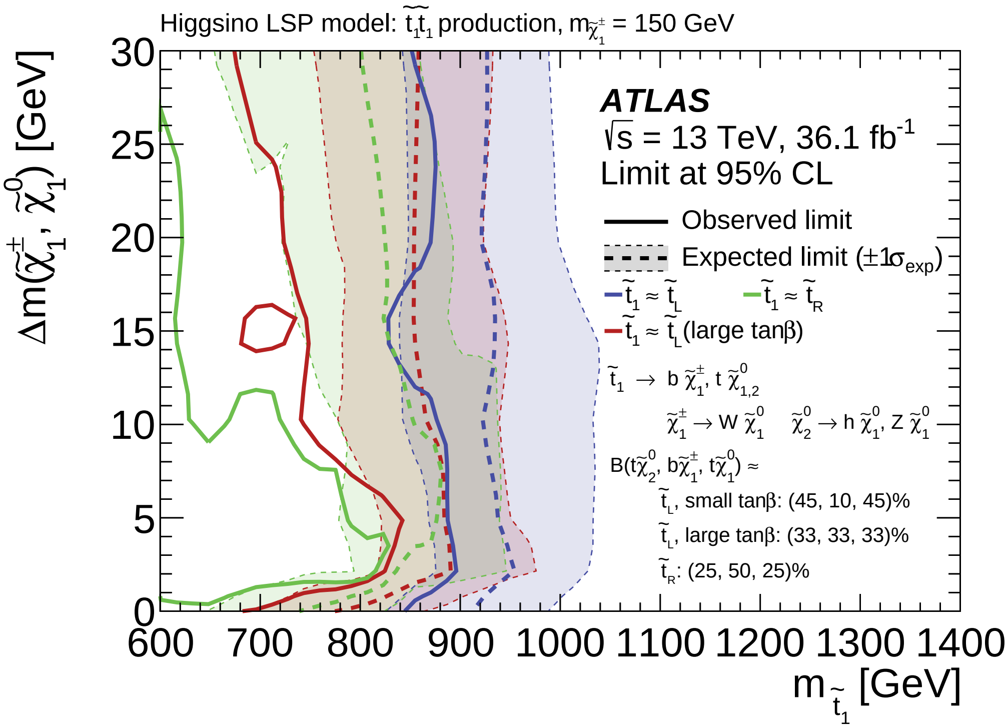

Figure 6.32: Higgsino LSP models are shown where $m_{\tilde{\chi}_1^\pm} = 150$ GeV and the stop mass and $\Delta M(\tilde{\chi}_1^0, \tilde{\chi}_1^\pm)$ are varied. Colors indicate different assumptions of pMSSM parameter values: $\tilde{t}_1 \sim \tilde{t}_L$ (blue), $\tilde{t}_1 \sim \tilde{t}_R$ (green), and $\tilde{t}_1 \sim \tilde{t}_L$ with large $\tan\beta$ (red). These assumptions alter the relative fraction of stop decays via $\tilde{t} \to t\tilde{\chi}_1^0$, $\tilde{t} \to b\tilde{\chi}_1^\pm$, and $\tilde{t} \to t\tilde{\chi}_2^0$, which are specified in the Figure legend. The red "island" contour near $(m_{\tilde{t}}, \Delta M) = (700\text{ GeV}, 15\text{ GeV})$ is an artifact of an insufficient number of simulated events and may be ignored.

models are still excluded due to the $\tilde{t} \to t\tilde{\chi}_1^0$ and $\tilde{t} \to t\tilde{\chi}_2^0$ decay channels. A small excess of events in `bCsoft_high` produces weaker-than-expected limits in the large mass-splitting scenario $\Delta M(\tilde{\chi}_1^0, \tilde{\chi}_1^\pm) > 10$ GeV.

Finally, limits are set on models in the "well-tempered neutralino" model with a Bino LSP and Higgsino NLSP, as shown in Figure 6.33. Given the value of M_1, The Higgsino mass parameter μ is set to reproduce the DM relic density, leading to mass splittings of $\Delta M(\tilde{\chi}_1^0, \tilde{\chi}_2^0) \sim 20-50$ GeV. Scenarios are considered both where the light stop is left-handed (with a corresponding light sbottom) and right-handed. No dedicated SR was optimized for this model, with the best sensitivity coming from the `bCsoft_med` and `bCsoft_high` regions, combined with `tN_med`. However, this scenario is not well-covered by the existing SRs. The acceptance is low for `tN_med` because the 'secondary' leptons (not from a top decay) produced in the cascade decays of the $\tilde{\chi}_2^0$,$\tilde{\chi}_1^\pm$, and $\tilde{\chi}_3^0$ lead these events to

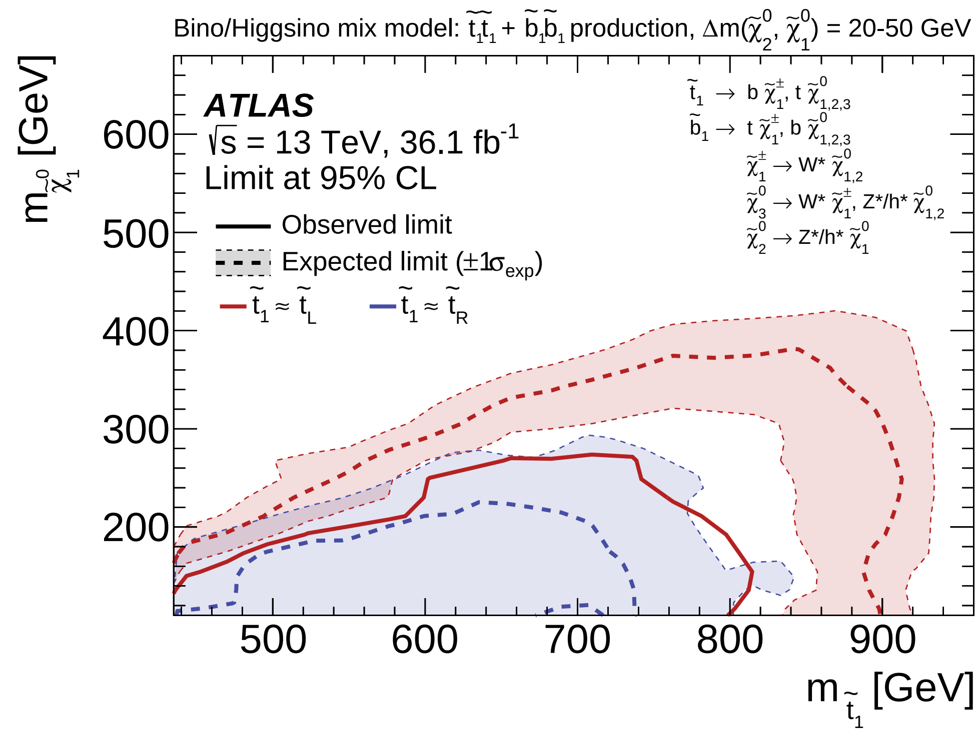

Figure 6.33: Expected (dashed) and observed (solid) exclusion contours are presented for the "well-tempered neutralino" scenario with a Bino LSP and Higgsino LSP with mass parameters set to reproduce the observed dark matter relic density. Scenarios where the lightest stop is left- and right-handed are considered, where a light bino is also assumed in the left-handed scenario. Stops and sbottoms decay to all of the $\tilde{\chi}^0_1$, $\tilde{\chi}^\pm_1$, $\tilde{\chi}^0_2$, and $\tilde{\chi}^0_3$ states with branching fractions set by the pMSSM parameters. In the case of a left-handed stop, exclusions reach up to 800 GeV in stop mass but are limited to $\Delta M(\tilde{t}, \tilde{\chi}^0_1) > 300 - 350$ GeV. In the right-handed case, somewhat weaker exclusions are expected due to the lack of an accompanying sbottom state, but no observed limits can be set due to small excesses of events observed in several SRs.

fail the one-lepton selection. For events where one lepton is produced in these cascade decays, its p_{T} spectrum is harder than the low-energy signal used to optimize the `bCsoft` Higgsino regions. In the left-handed scenario (assuming also a low-mass sbottom), limits are set for stop masses up to 800 GeV and LSP masses up to 275 GeV, while no models were excluded in the right-handed case (no light sbottom). A complementary search in zero-lepton events sets limits of to 600 GeV on right-handed stop production in this scenario [158].

Chapter 7

Quantum Interference in Top-Quark Production

7.1 Theory Introduction

The LHC creates a large number of top quarks, most often through the process of $t\bar{t}$ pair production. At LO in the strong coupling constant, this process can occur through parton-anti-parton annihilation via an s-channel gluon, or via t-channel top-quark exchange from initial-state gluons, as shown in Figure 7.1a. The cross section for top-quark pair production at 13 TeV, calculated at NNLO+next-to-next-to-leading logarithm (NNLL) and assuming $m_{\text{top}} = 172.5$ GeV, is[18] [33, 208–211]

$$\sigma_{t\bar{t}} = 831.76^{+19.77}_{-29.20}\ (\text{scale}) \pm 35.06\ (\text{PDF}+\alpha_{\text{S}})^{+23.18}_{-22.45}\ (m_{\text{top}})\,\text{pb}. \tag{7.1}$$

However, top quarks may also be singly-produced via electroweak processes, leading to the three distinct final states shown in Figures 7.1b-7.1d. Production of a single top-(anti)quark via the t-channel exchange of a W boson ("t-channel single top") has the largest predicted (NLO) cross section of 217^{+7}_{-6} pb [212, 213]. The tW-channel process has the next-largest cross section of 72 ± 4 pb [214], while that for a single top quark produced via the decay of an s-channel W boson ("s-channel single top") is only 10.3 ± 0.4 pb [215, 216].

The ATLAS and CMS Collaborations have measured the production of $t\bar{t}$ pairs most recently at 13 TeV [217–221], and have measured single top in the t-channel at 13 TeV [222, 223] as well

[18] The quoted cross section is calculated using the Top++ program, with an uncertainty prescription using a set of input parameters agreed upon by the ATLAS and CMS Collaborations [205]. The uncertainty due to imperfect knowledge of the pdf is computed using the `PDF4LHC` prescription, described in more detail in Section 7.5.4. The top mass is varied up and down by 1.0 GeV, about the size of uncertainties reported by recent measurements of the top-quark mass [206, 207].

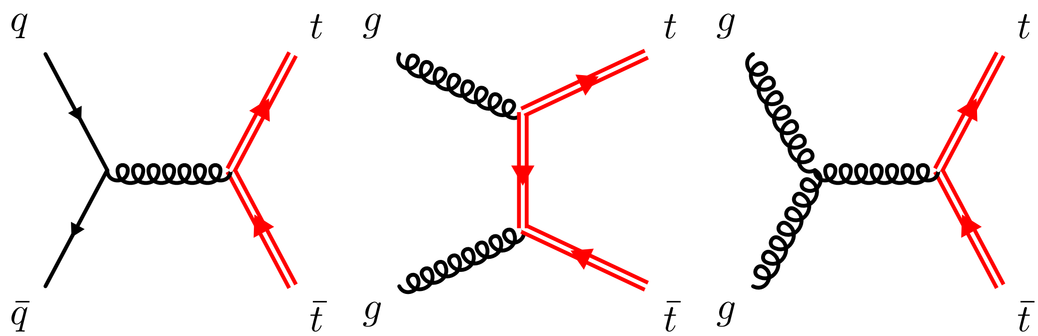

(a) Top-quark pair production diagrams

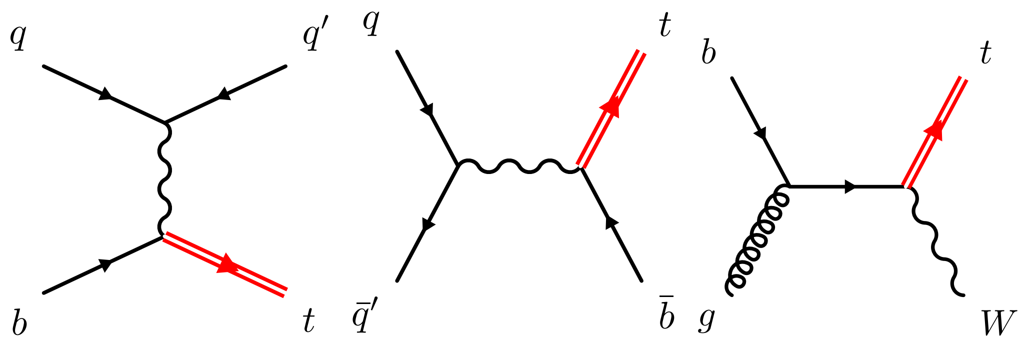

(b) t-channel single top (c) s-channel single top (d) tW-channel single top

Figure 7.1: Representative Feynman diagrams are shown for production of top-quark pairs (a) and single top quarks (b,c,d) at leading order. t- and s-channel single top processes refer to the intermediate W boson propagator, while tW refers to the final state particles.

as in the tW-channel at 13 TeV [224, 225]. At 8 TeV, ATLAS established evidence for s-channel production [226].

At LO, the only diagram contributing to the tW single top process is that shown in Figure 7.1c. This assumes five active flavors of quark in the proton PDF; i.e. that the incomping b quark may be obtained from the proton. The NLO correction to this process thus includes all emissions of extra partons, including processes where a second b-quark appears in the final state, sometimes written explicitly as "tWb". In the four-flavor scheme, the initial state b quark in Figure 7.1c must come from a split gluon, so that the LO contribution is already that of the tWb process. A difficulty emerges from this observation: because the tWb single-top process shares the same final state as $t\bar{t}$ pair-production the two must be considered together and their interference considered. The ME for the full $W^+W^-b\bar{b}$ final state has contributions from each of the diagrams of Figure 7.2 and can be

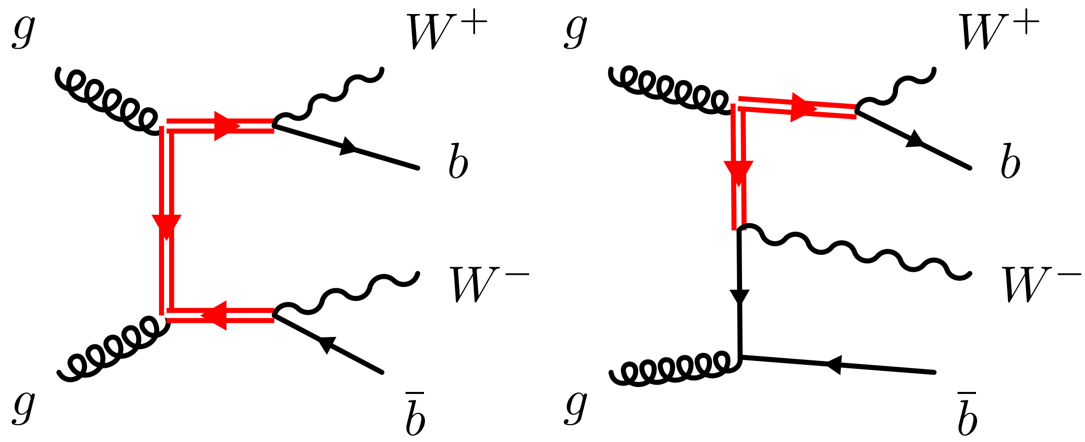

(a) $gg \to t\bar{t}$ (b) $gg \to tWb$

Figure 7.2: Leading contributions to $W^+W^-b\bar{b}$ production from gluons are shown, due to diagrams with two (a) or one (b) time-like top-quark propagators. Internal top-quark lines are shown doubled and in red.

written schematically as

$$|\mathcal{M}_{WWbb}|^2 = |\mathcal{M}_{t\bar{t}}|^2 + 2\mathcal{R}(\mathcal{M}_{t\bar{t}}\mathcal{M}_{tWb}) + |\mathcal{M}_{tWb}|^2, \tag{7.2}$$

where we have neglected the contribution from diagrams without top quarks. The critical issue is how to obtain accurate calculations for colliders of the inclusive $W^+W^-b\bar{b}$ process, particularly in regions without two on-shell top quarks. The following sections review current state-of-the-art calculations, motivating the need for new measurements in the non-resonant regime.

Calculations of the $t\bar{t}$ and tW single top processes

The comparison of SM predictions with ATLAS data requires precise predictions of collider observables. As discussed in Section 2.3 this requires an MC parton shower, which describes the evolution of high-energy interactions to Λ_{QCD}. While leading order calculations of the $t\bar{t}$ process matched to a PS have been available for some time, the NLO corrections are known to be significant and are required for precision study of the top quark at the LHC.Calculations involving the production of top-quark pairs with NLO ME calculations matched to a PS are possible using the `MC@NLO` [39] and `Powheg` [41] approaches (the latter as the "`hvq`" process [227]). In these calculations only production is calculated at NLO, where top quarks are treated as stable particles so that spin correlations of their decay products are not automatically preserved. In the `hvq` implementation, these "on-shell" events are subsequently "deformed" into events with top-quark decays, with off-shell effects that are correct to LO. The ME calculation is performed using the four-flavor scheme (4FS).

NLO calculations of tW are performed in the five-flavor scheme (5FS), with LO diagrams requiring an initial-state b-quark, so that tWb diagrams are encountered at NLO. This causes the NLO correction to the tW process to be much larger than the LO cross section, due to the resonant enhancement from configurations where the mass of the second Wb pair is near m_{top}. To combine an NLO tW prediction obtained in this way with the $t\bar{t}$ process described above, the overlapping $t\bar{t}$-like phase space must not be double-counted. Two schemes were initially proposed to produce a well-defined tW prediction at NLO in Ref. [228]. The diagram removal (DR) definition of tW omits all contributions from amplitudes $\mathcal{M}_{t\bar{t}}$ so that the single top process includes only the third term of Eqn. 7.2. The diagram subtraction (DS) definition includes all MEs of Eqn. 7.2, cancelling the overlapping contribution from $t\bar{t}$ with a gauge-invariant subtraction term Φ. The subtraction term is constructed from the $t\bar{t}$ amplitude squared, calculated from the Wb decay products that have been reshuffled to reproduce the top mass. After a final re-scaling by Breit-Wigner distributions (BWs) to recover the original Wb line-shape, this produces

$$\Phi = \frac{\text{BW}(m_{Wb})}{\text{BW}(m_t)} |\mathcal{M}_{t\bar{t}}(Wb)|^2_{\text{reshuffled}}. \tag{7.3}$$

The standard practice among LHC experiments is to use the DR definition of the process and assess the full DR/DS difference as a systematic uncertainty. Since the proposals of DR and DS, further ones have been suggested [176, 229, 230]. In particular, a second diagram removal scheme (DR2) was proposed that neglects only the squared $t\bar{t}$ amplitudes from the single top calculation, so that the tW prediction is given by the second and third term of Eqn. 7.2.

Both treatments of the tW process are approximate and it is unclear *a priori* whether one should provide a better description of the real data when combined with corresponding $t\bar{t}$ simulation. Comparisons shown in Figure 7.3 indicate the large difference in predictions between the two schemes at kinematic extremes. Fig. 7.3b shows that the difference is negligible when tW and $t\bar{t}$ are combined and an inclusive phase-space is considered. However, in a region where the $t\bar{t}$ contribution can be effectively vetoed, the difference between the two treatments may be tested. This is the goal of the measurement described herein.

More recently, the complete NLO calculation of the $pp \to \ell^+\nu_\ell\, l^-\bar{\nu}_l\, b\,\bar{b}$ process has become available [231–235]. These ME calculations from OpenLoops have been PS-matched in the `b_bbar_4l` process recently implemented in `POWHEG BOX RES` [42, 236]. This calculation includes full off-shell effects, with top quarks produced at NLO and decayed at NLO. It also includes contributions from

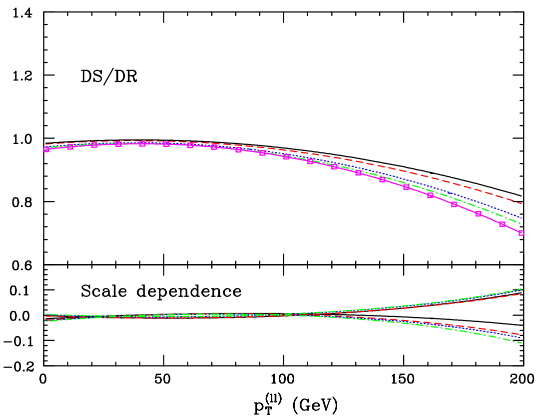

(a) $gg \to t\bar{t}$

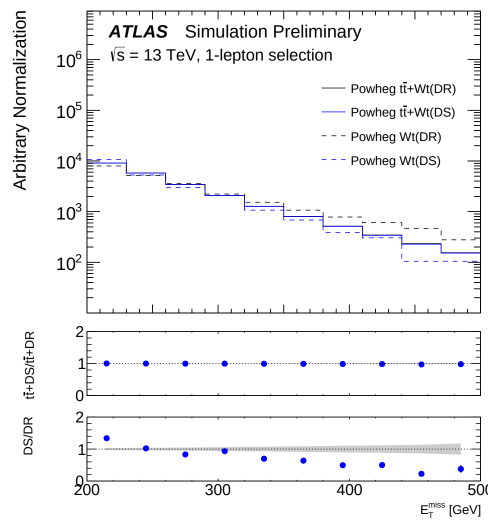

(b) $gg \to tWb$

Figure 7.3: Comparisons of the agreement of the DR and DS scheme as a function of kinematic variables. At left, the ratio of predictions is shown as a function of the di-lepton mass for tW events. Various curves are shown for different choices of scale, with their relative difference shown in the lower panel. The figure is reproduced from Ref. [228]. At right, the ATLAS implementation of the two processes are shown separately (dashed lines) and together with the Powheg $t\bar{t}$ prediction (solid lines). Relative differences between the DR and DS setups are shown, with and without $t\bar{t}$ included, in the lower panels.

"cross-talk" diagrams, where gluons connect initial and final states. Exact spin correlations are included as well as interference. The major technical accomplishment of the `POWHEG BOX RES` framework is proper maintenance of resonance histories in the parton shower so that an NLO+PS accurate calculation is achieved while simultaneously preserving the masses of top-quark decay products.

7.2 Measurement Strategy

As seen in the previous section, theoretical choices in the modeling of the tW process can lead to large differences in predictions for LHC experiments. Previous measurements of the tW cross section have been designed to minimize sensitivity to this effect [224,225,237–241]. However, the uncertainty surrounding this effect can become large in the phase space important for BSM searches [142, 149, 156,158,242,243], as was shown in Chapter 6 in the context of a search for SUSY top-quark partners. This motivates a new measurement of non-resonant top-quark production that could provide the first constraints on interference models from LHC data.

The strategy is to measure the $t\bar{t} + tWb$ process in a region that gives maximal sensitivity to the interference effect. Instead of targeting tW in the inclusive phase-space where previous measurements have been made, the analysis will employ the sophisticated tools developed by BSM searches to effectively eliminate on-shell $t\bar{t}$ events. The analysis is conducted in the di-lepton channel (targeting $\ell^+\ell^-\nu\bar{\nu}b\bar{b}$ events), and measures a version of the m_{T2} variable described in Chapter 6 in the context of stop searches. However, as this analysis does not search for new BSM physics leading to invisible particles, $E_{\mathrm{T}}^{\mathrm{miss}}$ is not necessary to include. We define

$$m_{b\ell}^{\mathrm{minimax}} = \min\{\max(m_{b\ell}, m_{b'\ell'}), \max(m_{b\ell'}, m_{b'\ell})\} \tag{7.4}$$

as the interference-sensitive variable to be measured. Without using $E_{\mathrm{T}}^{\mathrm{miss}}$, no neutrino momenta need be minimized over, and it is no longer necessary to restrict to *transverse* masses. For $t\bar{t}$ events with two on-shell tops, at LO the b quark-lepton invariant mass $m_{b\ell}$ is bounded above by $\sqrt{m_t^2 - m_w^2}$. Beyond this value, the relative contribution is much higher from tWb events where the second bW pair is non-resonant. A differential measurement of this variable is shown to be sensitive to the interference effect. The measurement will be unfolded to particle-level to better enable comparisons to new theoretical models of the interference effect.

7.3 Analysis of Reconstructed Events

7.3.1 Objects

The selection of reconstructed objects is identical to that described in Chapter 6, with only minor exception. First, the use of lepton triggers requires that the "tight" lepton requirement (introduced in Section 6.5) be applied. Second, the use of b tagging criteria is slightly more nuanced, with "tight" and "loose" categories of b jets both defined. Jets are classified as originating from a hadronizing b quark through the use of a multivariate classifier, which exploits the relatively long b hadron lifetime. Figure 7.4a displays the output of the classifier for jets originating from b quarks, c quarks, and the remaining "light-flavor" quarks plus gluons. Figure 7.4b shows the corresponding rejection factors (inverse of tag efficiency) for charm and light-flavor jets as a function of the b jet efficiency.

A requirement on the classifier corresponding to "loose" b jets is 85% efficient for real b jets produced in top-quark decays. This gives a corresponding rejection rate of 27.3 for light-flavor jets, 3.25 for charm-initiated jets, and 7.97 for hadronic tau leptons. A subset of these jets also pass the "tight" requirement, which is 60% efficient for b jets. The corresponding rejection rate is 1160 for light-flavor, 36.8 for charm, and 171 for tau jets.

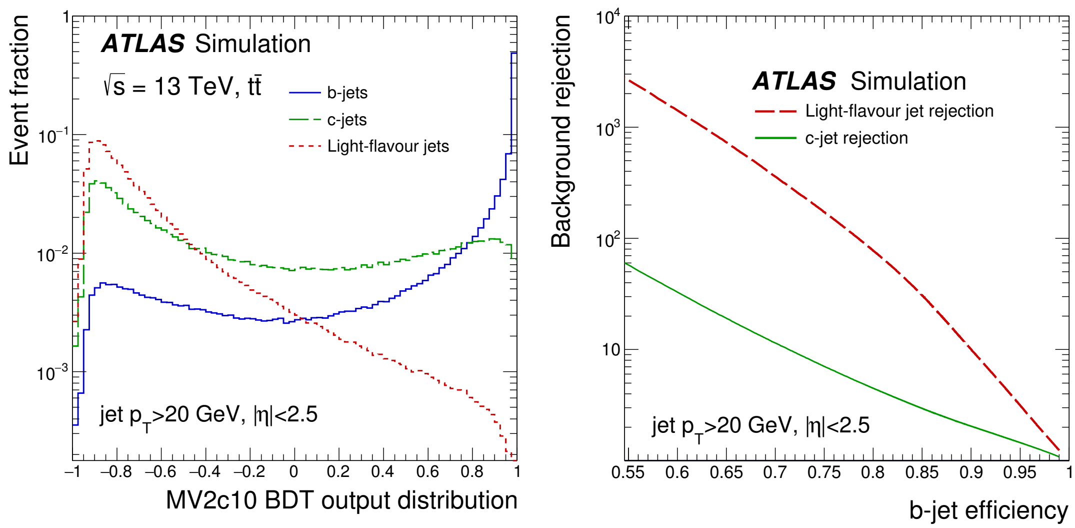

(a) (b)

Figure 7.4: At left, the output of the MV2c10 b tagging discriminant is shown for simulated $t\bar{t}$ events, separately for jets that contain b hadrons, c hadrons, or neither. At right, the charm and light jet rejection factors are shown as a function of the tagging efficiency for real b jets. As c-jets are more difficult to distinguish from b jets than are light jets, the charm content of the event sample used to train the algorithm is enhanced, leading to improved rejection rates. In the interference analysis, two working points are employed corresponding to 85% and 60% b jet efficiency. Figures are reproduced from Ref. [107].

As lepton triggers are used to collect data, the corresponding p_{T} requirements on selected leptons are slightly more restrictive than in the analysis described in Chapter 6. The requirements on signal objects are summarized in Table 7.1.

Table 7.1: The selection criteria for reconstructed objects are briefly summarized. Explicit definitions of all working points are given in Section 6.5 of the text.

Object	p_{T} requirement	$\lvert\eta\rvert$ requirement	Additional comments
Electron	> 28 GeV	< 2.47	TightLLH ID, FixedCutTight isolation
Muon	> 28 GeV	< 2.5	Medium ID, FixedCutTightTrackOnly isolation
Jet	> 25 GeV	< 2.5	JVT for $p_{\mathrm{T}} < 60$ GeV and $\lvert\eta\rvert < 2.4$ 85% (loose) and 60% (tight) b-tag WPs

7.3.2 Event Selection

This analysis targets the $\ell^- \nu \ell^+ \bar{\nu} b\bar{b}$ final state produced by di-leptonic top decays, using a simple selection. The only objects used in the analysis are leptons and b jets. Selections on $E_{\mathrm{T}}^{\mathrm{miss}}$ were investigated to exploit the undetected neutrino signature, but was ultimately not included in the analysis. Requirements on events which pass the signal selection (or enter the signal region (SR)) are detailed in the following.

Events are only considered which pass a suite of single lepton triggers which, combined, ran without prescale over the 2015 and 2016 data-taking periods. These items are summarized in Table 7.2 (see Section 4.3 for a review of the trigger algorithms and naming conventions). Scale factors are assigned to all simulated events according to the trigger lepton kinematics to correct the MC efficiency to match that measured in data. Requirements on signal lepton p_{T} are chosen so that the trigger is fully efficient with respect to the offline identification criteria.

Events are required to contain exactly two leptons of opposite charge. All $e^+e^-, \mu^+\mu^-, e^\pm\mu^\mp$ pairs are considered, with addition requirements made on on those with same-flavor, opposite-sign (SFOS) lepton pairs. In these events the di-lepton invariant mass $m_{\ell^+\ell^-}$ must be greater than 10 GeV to avoid contributions from light resonances. Events with $|m_{\ell^+\ell^-} - m_Z| < 15$ GeV are also rejected to reduce the contamination from Z boson decays.

To reduce backgrounds from non-top quark processes, two tight b jets are required. This requirement leads to the single largest decrease in efficiency, but it critical to the removal of background

Table 7.2: The selection of trigger items, at least one of which is required to pass in order for an event to be accepted. The most selective single electron items require calorimeter isolation criteria at L1 Trigger ('L1EM20VH') as well as tight identification ('lhtight') and isolation ('ivarloose') criteria in the HLT. The most selective muon trigger enforces isolation ('ivarmedium') in the HLT. In 2016 these un-prescaled triggers required leptons with $p_{\mathrm{T}} > 26$ GeV. Triggers with looser identification and isolation requirements and higher p_{T} cuts are also considered in the analysis.

Single-Electron	Single-Muon
2015 Triggers	
e24_lhmedium_L1EM20VH e60_lhmedium e120_lhloose	HLT_mu20_iloose_L1MU15 HLT_mu40
2016 Triggers	
e26_lhtight_nod0_ivarloose e60_lhmedium_nod0 e140_lhloose_nod0	HLT_mu26_ivarmedium HLT_mu50

contributions in phase space that is otherwise highly enriched in tWb events. With this tight selection, the $t\bar{t}+b\bar{b}$ process contribution also becomes important, as it can fake the tWb signal if only two b jets pass the tight b tagging requirement. To reduce this background, selected events are required to have no more than two loose b jets. Thus, even though tight b jets tagged at the 60% efficiency working point are required for the analysis, any event which also has a third jet passing the loose, 85% efficient b-tag is rejected. The full event selection is summarized in Table 7.3.

While the $m_{b\ell}^{\text{minimax}}$ distribution is the main interference-sensitive variable targeted in the analysis, others are also investigated. For example, the di-lepton p_{T} and $E_{\text{T}}^{\text{miss}}$ were seen to produce large discrepancies in the DR and DS schemes in Figure 7.3. Thus a tighter version of the signal selection, the "interference SR", is defined as events passing $m_{b\ell}^{\text{minimax}} > 200$ GeV. This selection dramatically reduces the population of $t\bar{t}$ events so that other observables may be investigated. The next most sensitive distribution to the interference effect was found to be the leading lepton p_{T}.

7.3.3 Signal Extraction

Selecting events with two high-p_{T} leptons and b jets selects a sample of events that is overwhelmingly dominated by the $t\bar{t}$ process. However, in regions of large $m_{b\ell}^{\text{minimax}}$ this is no longer true, and a careful estimate must be made of the non-top-quark contributions. The largest absolute background is $Z+$jets, where a gluon splits to a pair of b quarks. This is efficiently reduced by selecting on the invariant mass of the lepton pair ($|m_{\ell^+\ell^-} - m_Z| > 15$ GeV), though the off-shell contribution is still significant enough that it must be estimated from data. This is done through the use of events with an inverted $m_{\ell^+\ell^-}$ selection. The contribution from misidentified and non-prompt leptons ("fake leptons") is much smaller, but more difficult to model in simulation and so is also obtained in a

Table 7.3: The full signal selection criteria. The subset of selected events with $m_{b\ell}^{\text{minimax}} > 200$ GeV also pass the interference SR selection.

Selection	Comments
Single lepton trigger	Individual items defined in Table 7.2
jet cleaning	veto events containing a jet failing the loose jet cleaning criteria
exactly two signal leptons	opposite-sign, and no additional baseline (4 (μ), 5 (el) GeV) leptons
exactly 2 signal b-jets	b-taggedat 60% working point
veto third loose-ID b-jet	b-taggedat 85% working point
$m_{\ell^+\ell^-} > 10$ GeV	for same-flavor lepton pairs only
$\lvert m_{\ell^+\ell^-} - m_Z\rvert > 15$ GeV	for same-flavor lepton pairs only
$m_{b\ell}^{\text{minimax}} > 200$ GeV	interference SR only

data-driven manner from events with like-charge leptons. $t\bar{t}+b\bar{b}$ events are considered a background in this analysis and are also subtracted from the signal process. When only two of the b jets are identified, this background can have $m_{b\ell}^{\mathrm{minimax}}$ above the kinematic endpoint, faking the interference signal. An event sample where three jets are b-tagged is enriched in this process and so is used to estimate the size of the $t\bar{t}+b\bar{b}$ background in the signal region. Backgrounds from diboson (VV) production and $t\bar{t}V$ ($V = W, Z$) are found to be small and so are estimated from MC alone. This technically includes fully non-resonant $WW + b\bar{b}$ events which also interfere with the $t\bar{t}+tWb$ signal process, though the cross section is so small that the effect is not considered. The background estimation strategy is summarized in Table 7.4. Separate estimates are obtained for the inclusive SR, in bins of $m_{b\ell}^{\mathrm{minimax}}$, as well as for the subset with $m_{b\ell}^{\mathrm{minimax}} > 200$ GeV, in bins of leading lepton p_{T}.

Estimation of $Z+$jets backgrounds

As the signal selection uses all $e^+e^-, \mu^+\mu^-, e^\pm\mu^\mp$ pairs, $Z+$jets backgrounds are important to consider. While these are generally only important for same-flavor leptons, a very small contribution is also expected to different-flavor events from Z decays to taus[19]. The quality of the MC description of the process is assessed in a $Z+$jets CR, defined in the same manner as the SR, but selecting only e^+e^- and $\mu^+\mu^-$ events with $|m_{\ell^+\ell^-} - m_Z| < 15$ GeV. The $Z+$jets MC sample may be divided into $Z+b$, $Z+c$, and Z+light components by checking the truth record for heavy-flavor partons. The overwhelming majority of Z+jets events entering both the $Z+$jets CR and SR contain real

Selection	Signal	$Z+$jets CR	Fake lepton CR	$t\bar{t}+b\bar{b}$ CR
Signal leptons	$=2$	$=2$	$=2$	$=2$
Lepton charges	opposite	opposite	same	opposite
Lepton flavor	–	$ee/\mu\mu$	–	–
$\lvert m_{\ell^+\ell^-} - m_Z\rvert < 15$ GeV	veto	require	veto	veto
b-tagged jets 85% eff. WP	$=2$	$=2$	$=2$	≥ 3
b-tagged jets 60% eff. WP	$=2$	$=2$	$=2$	≥ 3

Table 7.4: Overview of the control regions defined to estimate the backgrounds due to $Z+$jets, events with fake leptons, and $t\bar{t}$produced in association with extra b quarks. "Z veto" denotes that events are rejected which have a pair of opposite-sign, same-flavor leptons with reconstructed mass within 15 GeV of the Z boson. Table entries denoted "–" imply that no selection is made for this region.

[19] The predicted Z yield in the region of $m_{b\ell}^{\mathrm{minimax}} > 200$ GeV comes nearly entirely from the same-flavor channel (and *not* from $Z \to \tau\tau \to e\mu + E_{\mathrm{T}}^{\mathrm{miss}}$); the nominal **SHERPA** $Z+$jets MC predicts less than one $e\mu$ event per bin in this region.

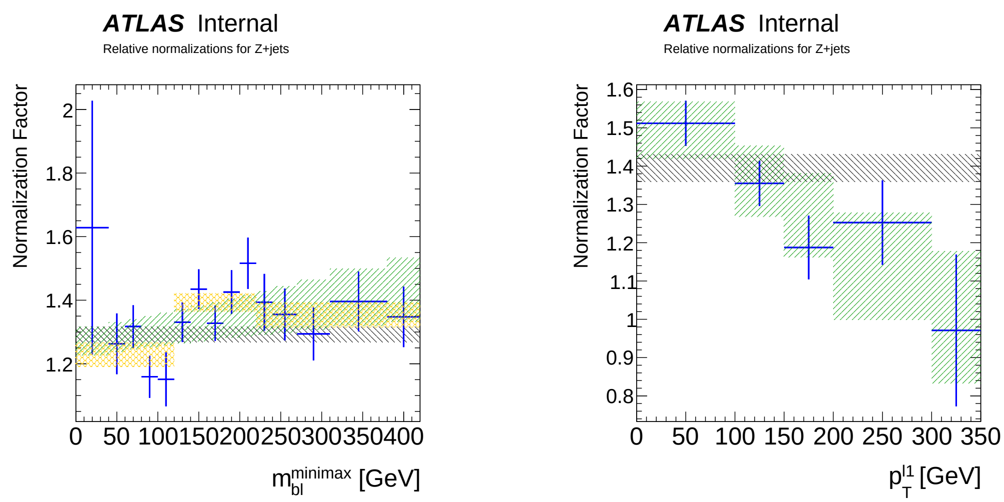

Figure 7.5: At left the individual normalization factors (blue crosses), derived per bin of $m_{b\ell}^{\text{minimax}}$, are compared to several methods of combining the factors to decrease the per-bin statistical uncertainty on the $Z+$jets estimate. The green bin shows a linear fit to the binned NFs, while the results of a coarser binning of the events used to derive the NFs into a single bin (black hashed band) and 3 bins (orange band) are shown. The 3-bin coarsification strategy (yellow band) is chosen for the final $Z+$jets estimate. At right the same information is shown for the lepton p_{T} distribution in the high-$m_{b\ell}^{\text{minimax}}$ $Z+$jets CR, where the linear scheme is employed.

b-hadrons, with the Sherpa MC predicting 1.2±0.6% (1.6±0.7%) of events with $Z+c$ and 1.0±1.0% (2.2±1.2%) of events from Z+light in the inclusive signal region (the $Z+$jets CR).

The general approach used to estimate this background is to compare the predicted Z+jets contribution to the $Z+$jets CR in MC to the observed data in the region. From this, a normalization factor (NF) for the process is derived such that the MC yield multiplied by the NF matches the observed data. With this approach, the estimate of Z+jets in the i-th bin of a distribution in the SR is given generically by

$$N^{\text{SR}}_{i,\ Z+\text{jets prediction}} = \mu_i \cdot N^{\text{SR}}_{i,\ Z+\text{jets MC}}$$

where μ_i is the NF applied in the i-th bin. Note that NFs may be allowed to vary from bin-to-bin to improve shape agreement or a single, global NF may be used when appropriate. Several possible strategies used to estimate the contribution of Z+jets to the signal selection are compared in Figure 7.5, including a coarser binning of the NFs in $m_{b\ell}^{\text{minimax}}$, a linear fit to the binned NFs, and a global NF used across all bins.

Ultimately, the approach of using three distinct NFs for different ranges of $m_{b\ell}^{\text{minimax}}$ was settled on, as it is found to balance good data MC agreement in the $Z+$jets CR with the corresponding statistical uncertainty on the background estimate. To estimate the Z+jets background as a function of lepton p_{T} in the interference SR, a linear NF is employed. The values of each of the NFs used are provided in Table 7.5. Monte Carlo studies indicate that all contributions to the Z+jets control regions from mis-identified leptons are negligible.

Estimation of fake lepton backgrounds

The background of processes entering the signal region due to the mis-identification of jets and photons as leptons ("fake leptons" or "fakes") is estimated by considering events with two same-sign leptons, using the same strategy as Ref. [244].

The fake lepton CRs are defined with a selection identical to the inclusive and interference SRs, except that the opposite-sign (OS) charge requirement on the leptons is inverted, requiring instead a same-sign (SS) pair. The contribution of fakes is estimated by subtracting the prediction of prompt SM backgrounds $N_{\mathrm{SS}}^{\text{scaled MC, } i}$ from the observed data in this SS region $N_{\mathrm{SS}}^{\text{data, } i}$, both in the i-th bin, where the MC prediction of fakes is vetoed by requiring all reco-level objects to match to a prompt lepton at truth-level. The ratio of the number of SS and OS events with fake leptons $f_{\mathrm{OS/SS}}^{\mathrm{MC}}$ is taken from MC and can be applied to the observed data in the fake-lepton CR to give a prediction in the SRs. This gives an estimate of the fake contribution to the ith bin

$$\begin{aligned} N_{\mathrm{OS}}^{\text{Fakes, } i} &= f_{\mathrm{OS/SS}}^{\mathrm{MC}} \times N_{\mathrm{SS}}^{\text{Fakes, } i} \\ &= \frac{N_{\mathrm{OS}}^{\text{MC Fakes}}}{N_{\mathrm{SS}}^{\text{MC Fakes}}} \times (N_{\mathrm{SS}}^{\text{data, } i} - N_{\mathrm{SS}}^{\text{prompt MC, } i}). \end{aligned} \tag{7.5}$$

Table 7.5: Summary of the normalization factors extracted from the $Z+$jets control region. Estimates are separately obtained in the e^+e^- and $\mu^+\mu^-$ channels, with the inclusive NF shown only for illustrative purposes. The first three columns show the NFs used to estimate the Z+jets background in the inclusive SR, broken into sub-regions of $m_{b\ell}^{\text{minimax}}$. The fourth column shows the NF applied to $Z+$jets in the interference SR, which requires $m_{b\ell}^{\text{minimax}} > 200$ GeV. Here the NF is presented as a linear function of the leading lepton p_{T}.

$m_{b\ell}^{\text{minimax}}$ Selection	All flavors	ee channel	$\mu\mu$ channel
$\in [0, 120)$ GeV	1.23 ± 0.04	1.22 ± 0.05	1.23 ± 0.05
$\in [120, 220)$ GeV	1.39 ± 0.03	1.35 ± 0.04	1.42 ± 0.04
$\in [220, \infty)$ GeV	1.35 ± 0.04	1.36 ± 0.06	1.34 ± 0.05
> 200 GeV	$(-0.18 \pm 0.05) \cdot \frac{p_{\mathrm{T}}^{\ell}}{100\ \mathrm{GeV}} + (1.58 \pm 0.07)$	$(-0.23 \pm 0.07) \cdot \frac{p_{\mathrm{T}}^{\ell}}{100\ \mathrm{GeV}} + (1.64 \pm 0.11)$	$(-0.15 \pm 0.07) \cdot \frac{p_{\mathrm{T}}^{\ell}}{100\ \mathrm{GeV}} + (1.55 \pm 0.09)$

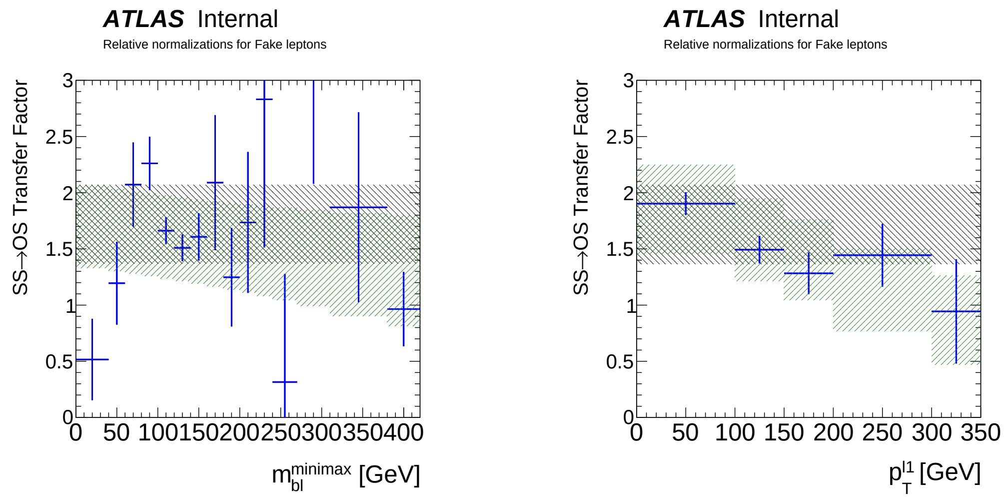

Figure 7.6: The ratios of the OS-to-SS transfer factors derived for fake lepton process when using the binned and global approaches. Transfer factors (TFs) are derived by comparing the non-prompt MC prediction in the SR with opposite-sign leptons to the fake CR with same-sign leptons. The global approach derives a single TF using all non-prompt MC events entering the SR and fake CR. The binned approach derives a separate transfer factor in each bin of $m_{b\ell}^{\text{minimax}}$. The uncertainties on the binned TFs (shown with blue error bars) are due only to limited MC statistics. The uncertainty on the global TF (shown as a hashed band about unity) is due to MC statistics, plus a 20% fake composition uncertainty. The green hashed band shows a linear fit to the binned NFs. At left the normalization factors are shown in bins of $m_{b\ell}^{\text{minimax}}$ in the inclusive region, while at left they are shown for events passing the interference criterion ($m_{b\ell}^{\text{minimax}} > 200$ GeV) and binned in leading lepton p_{T}.

This transfer factor from SS to OS events is computed independently of $m_{b\ell}^{\text{minimax}}$, with the same factor $f_{\text{OS/SS}}^{\text{MC}}$ being applied to each bin of the unfolded distribution. Figure 7.6 shows that there is no significant trend in $m_{b\ell}^{\text{minimax}}$; however as some dependence is seen with respect to the leading lepton p_{T}, a linear fit is performed to the p_{T}-binned transfer factors to extract the final predicted fake yields in the interference SR.

MC studies show that the fakes in both regions are dominated by electron conversions, with smaller contributions from other sources. Fakes from simulation are categorized according to the flavor of the fake lepton, in addition to its origin process, determined using the MC truth particle record. Fake electrons are classified as coming from heavy flavor decays, photon conversions, or other non-prompt sources. Fake muons are classified as coming from heavy flavor decays or other sources. The "other" categories in each case are populated by various hadronic decays. A 20% uncertainty is applied to $f_{\text{OS/SS}}^{\text{MC}}$ to account for the differences in fake composition between the two regions. Table 7.6 provides a breakdown of the SS and OS yields by fake-lepton type, as well as a comparison of the total fake MC yield to that derived from the data-driven procedure. Figure 7.7 compares the shapes of the fake estimates from data and simulation. They are found to be in close agreement in nearly all bins, with the largest difference coming in the bulk of the $t\bar{t}$ core distribution where the fakes contribute at the sub-percent level. The two estimates are found to agree well on the leading lepton p_{T} spectrum as well.

Estimation of $t\bar{t} + b\bar{b}$ backgrounds

By construction of the $m_{b\ell}^{\mathrm{minimax}}$ variable, $t\bar{t}$ events can have $m_{b\ell}^{\mathrm{minimax}}$ above the top mass bound only due to energy resolution and off-shell top effects, both of which fall off rapidly with increasing $m_{b\ell}$. This supposes that the two reconstructed leptons and b-jets are indeed those from the $t\bar{t}$ decay.

The remaining $t\bar{t}$ events which enter the region of large $m_{b\ell}^{\mathrm{minimax}}$ do so because we fail to reconstruct the correct b jets from the top-quark decay; these events fall into two further categories. First, "mis-tagged" $t\bar{t}$ events can enter when one of the two identified b jets is actually a light jet – in this case we *both* fail to reconstruct a real b jet due to efficiency or acceptance effects *and* additionally mis-tag a light flavor jet as a b jet. Such contributions are heavily suppressed by the requirement that both b jets be tagged with the tight WP. Second, $t\bar{t}$ events can be produced in association with additional, real heavy-flavor jets (i.e. from an ISR gluon splitting to $b\bar{b}$). This population of $t\bar{t} + b\bar{b}$ events enters the signal region with large $m_{b\ell}^{\mathrm{minimax}}$ when a b jet from a top-quark decay fails to be b-tagged (due to the inefficiency of the tagger), while an additional real b jet, usually from gluon

Table 7.6: Number of events in opposite- and same-sign regions used to determine the OS-to-SS transfer factor. Yields are broken into categories based on the origin of the faking lepton. Additionally, the fake MC prediction in the same-sign fake CR and opposite-sign inclusive SR is compared with the observed data in the region, used for the nominal (data-driven) fake estimate.

Component	OS	SS	(OS/SS)
Heavy flavor e	5.2 ± 1.4	1.6 ± 0.7	3.2 ± 1.7
Conversion e	524.6 ± 14.1	340.4 ± 11.4	1.5 ± 0.1
Other e	18.9 ± 2.1	2.0 ± 0.6	9.2 ± 3.1
Heavy flavor μ	40.3 ± 4.0	3.8 ± 1.2	10.6 ± 3.4
Other μ	9.9 ± 1.4	0.5 ± 0.3	21.2 ± 16.0
Total Fake MC	598.9 ± 15.0	348.3 ± 11.5	1.7 ± 0.1
Data-Driven	624.2 ± 149.1	363.1 ± 25.0	–

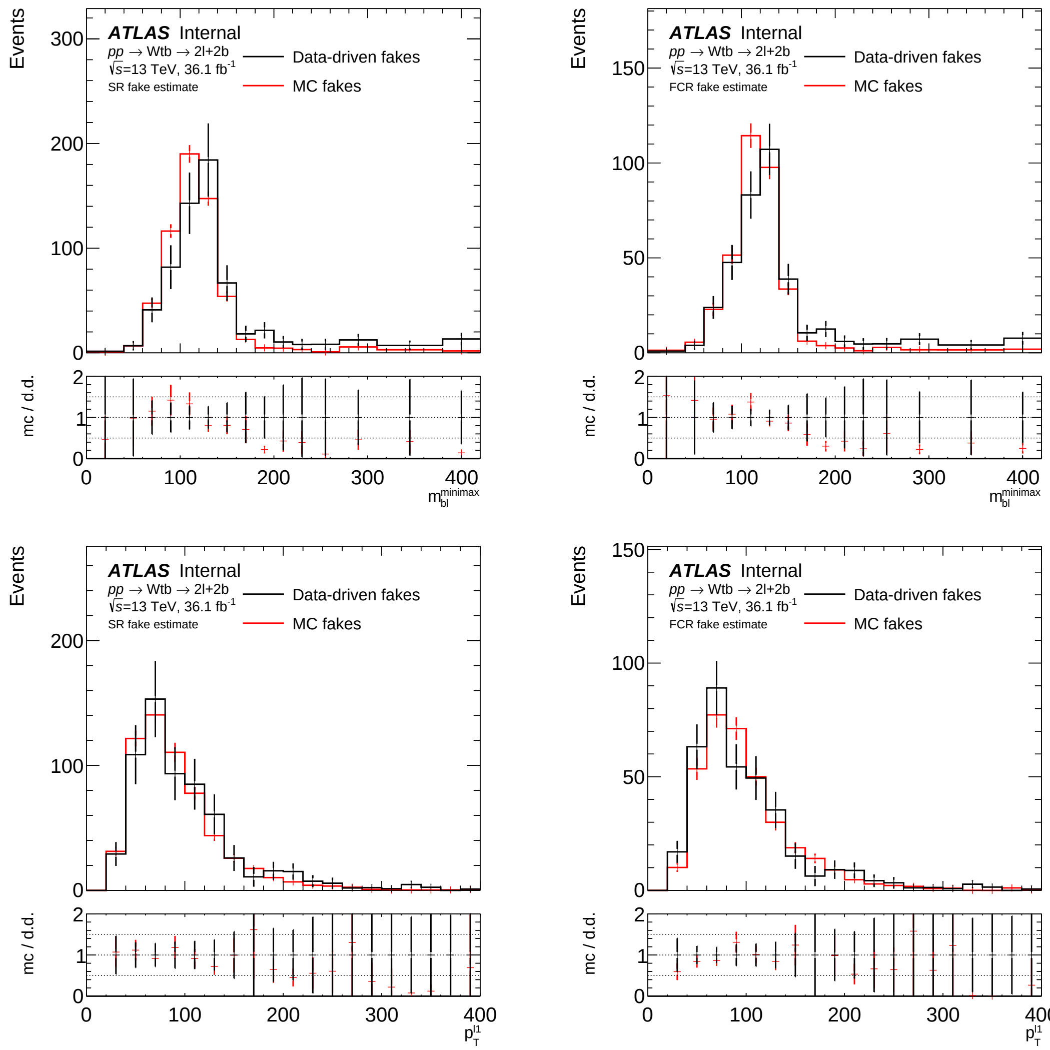

Figure 7.7: The data-driven fake estimates are compared to those predicted from the simulated samples in bins of $m_{b\ell}^{\mathrm{minimax}}$ in the opposite-sign inclusive SR (top left) and same-sign fake-lepton CR (top right). The comparison is also shown for the leading lepton p_{T} distributions for the inclusive SR (bottom left) and same-sign fake-lepton CR (bottom right).

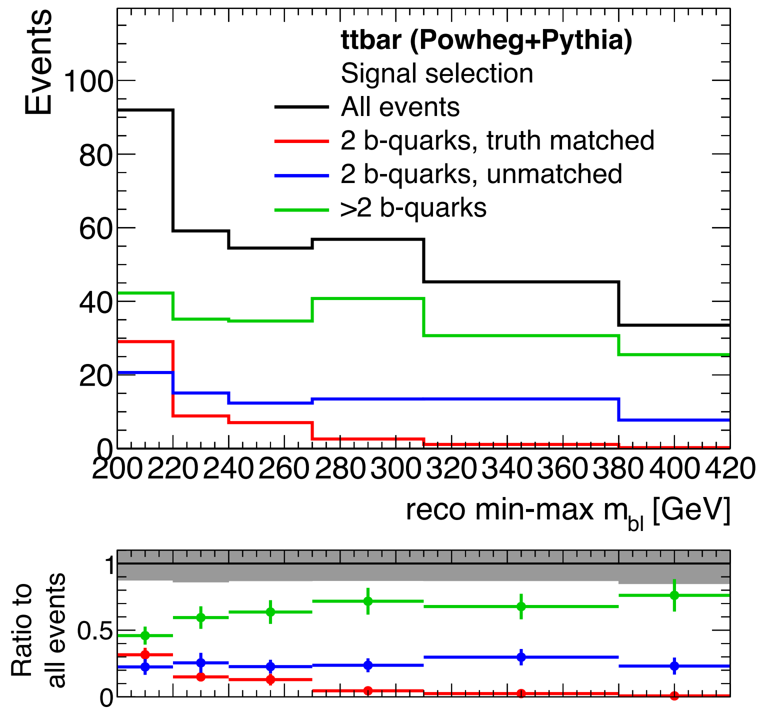

Figure 7.8: The spectrum of all high-$m_{b\ell}^{\mathrm{minimax}}$ $t\bar{t}$ events passing the signal selection is shown in black, as obtained from Powheg+Pythia MC simulation. The total is broken into three components, with individual predictions overlaid in the top panel and fractional composition given in the lower panel as a function of $m_{b\ell}^{\mathrm{minimax}}$. $t\bar{t}$ entering due to resolution effects is shown in red and it only important in the lowest bins of the observable. It is identified by selecting events with exactly two final-state b-quarks in the truth record, each of which are truth-matched to the reconstructed b jets. Events entering due to mis-tags are shown in blue, selecting events where two final-state b-quarks are found in the truth record, at least one of which is not matched to the reconstructed b jets. Finally events entering the region due to additional gluon splittings to $b\bar{b}$ pairs are identified as having > 2 truth b quarks in the event, and are displayed in green. Gluon splitting and, to a lesser extent, mis-tags dominate $t\bar{t}$ events at large values of the interference variable.

splitting, is tagged. The precise composition of the $t\bar{t}$ events entering the signal region is shown in Figure 7.8.

Top-quark pair production in association with additional heavy-flavor jets has been found to be poorly modeled in previous measurements [245], making it crucial to derive our $t\bar{t} + b\bar{b}$ estimation from data. Any mis-modeling of $t\bar{t} + b\bar{b}$ in the region of large $m_{b\ell}^{\mathrm{minimax}}$ could be conflated with the interference effect, so it is crucial to derive a reliable estimation. Because the $t\bar{t} + b\bar{b}$ process has a distinct final state from the $W^+W^-b\bar{b}$ state that this analysis seeks to measure, the $t\bar{t} + b\bar{b}$ process is treated as a *background* (separate from the remainder of $t\bar{t}$ events) and is subtracted before the

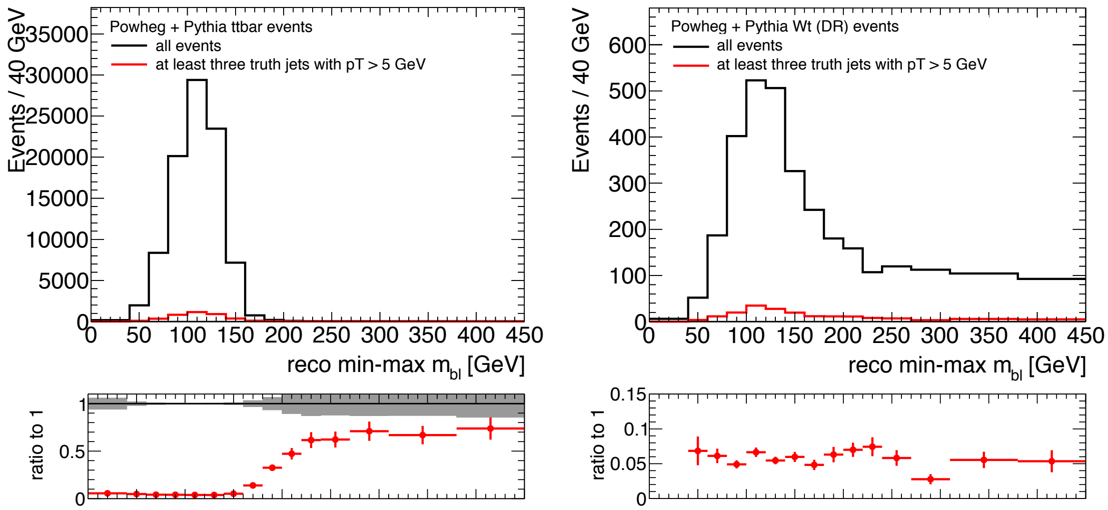

Figure 7.9: The reconstructed $m_{b\ell}^{\text{minimax}}$ spectrum obtained from simulation is shown for $t\bar{t}$ (left) and tW (right) events. The total contribution is shown in black, while the subset of events with three truth b jets is shown in red. The fraction of such events (which are treated as backgrounds due to the additional heavy flavor jets) is shown in the lower panels. For $t\bar{t}$ events at large $m_{b\ell}^{\text{minimax}}$ the relative fraction of events with extra b jets is large, while it is only at the 5% level for the $tW(b)$ process. Also, notably the $m_{b\ell}^{\text{minimax}}$ spectrum is much flatter in $m_{b\ell}^{\text{minimax}}$ for tW than for $t\bar{t}$ events.

$t\bar{t}$+tWb process is unfolded.

For the purpose of this analysis, $t\bar{t} + b\bar{b}$ is defined as the subset of simulated $t\bar{t}$ events which contain at least 3 $R = 0.4$ anti-$k_{\perp}$ particle-level jets with $p_{\text{T}} > 5$ GeVand which have a b-hadron ghost-associated to them. Only $|\eta| < 5$ is required of these jets. The complement of these events are referred to as "$t\bar{t}$ plus light flavor" or often simply $t\bar{t}$ when the distinction is clear, as it is this subset of $t\bar{t}$ events alone which enter the particle-level fiducial region. The fraction of simulated $t\bar{t}$ and tW events classified as having extra b jets is shown as a function of $m_{b\ell}^{\text{minimax}}$ in Figure 7.9.

The $t\bar{t} + b\bar{b}$ background passing the signal selection is estimated from the MC prediction, which is scaled by a global normalization factor to match the observed data in a dedicated $t\bar{t} + b\bar{b}$ control region. The $t\bar{t} + b\bar{b}$ CR is defined to be identical to the inclusive SR (no cut on $m_{b\ell}^{\text{minimax}}$), except to require at least three b jets that are tagged at the tight WP (recall that exactly two are required in the signal region). This is a natural definition, as it captures the $t\bar{t} + b\bar{b}$ process when both of the b quarks from the top decay are reconstructed as b-tagged jets in addition to the third real b. It is highly pure in real $t\bar{t}$ + heavy flavor events. We find that in subset of the SR with $m_{b\ell}^{\text{minimax}}$>200 GeV, roughly equal fractions of $t\bar{t} + b\bar{b}$ events are reconstructed as having either exactly two or greater than two b jets.

A single normalization factor is derived in the $t\bar{t}+b\bar{b}$ CR and is applied to the MC $t\bar{t}+b\bar{b}$ prediction in both the inclusive and interference SRs. The derived NF and its variation by lepton flavor channel is provided in Table 7.7.

Background subtraction

Schematically, the NF μ^{MC} is defined for a given process so that the relation

$$N^{\mathrm{CR}}_{\mathrm{data}} = \mu^{\mathrm{MC}} \times N^{\mathrm{CR}}_{\mathrm{target\ MC}} + N^{\mathrm{CR}}_{\mathrm{other}}$$

is satisfied, where $N^{\mathrm{CR}}_{\mathrm{data}}$ is the observed data in the SR, $N^{\mathrm{CR}}_{\mathrm{target\ data}}$ is the MC prediction for the background to be adjusted, and $N^{\mathrm{CR}}_{\mathrm{other}}$ is the predicted contribution of all other processes to the CR.

Because NFs are derived for multiple backgrounds, some ambiguity is introduced in the treatment of the $N^{\mathrm{CR}}_{\mathrm{other}}$ term, specifically whether NFs for other processes estimated from data should be also be included[20]. This is resolved by applying NFs to the background iteratively, calculated in order for $t\bar{t}+b\bar{b}$, $Z+$jets, and then fake leptons. With this method, no backgrounds entering the $N^{\mathrm{CR}}_{\mathrm{other}}$ term used in the determination of the $t\bar{t}+b\bar{b}$ NF are scaled by their respective NFs. In the determination of the $Z+$jets NF, the corresponding $N^{\mathrm{CR}}_{\mathrm{other}}$ term includes only the NF already derived for the $t\bar{t}+b\bar{b}$ process. Similarly, the $Z+$jets and $t\bar{t}+b\bar{b}$ backgrounds are both scaled by their respective NFs before being subtracted from the fake CR. The impact of the choice to use such a strategy instead of a simultaneous fit is small, due to the purity of the control regions. For example, the $Z+$jets process' contribution to the $t\bar{t}+b\bar{b}$ CR is at the % level, and thus an order unity NF does not impact the extracted $t\bar{t}+b\bar{b}$ NF.

The yields in the signal region are shown in Table 7.8 in bins of $m^{\mathrm{minimax}}_{b\ell}$. Table 7.9 shown yields in bins of leading lepton p_{T}, after a requirement is made that $m^{\mathrm{minimax}}_{b\ell} > 200$ GeV. The

3 b-tag region	All flavors	ee channel	$e\mu$ channel	$\mu\mu$ channel
$m^{\mathrm{minimax}}_{b\ell}$-inclusive	1.49 ± 0.05	1.61 ± 0.13	1.51 ± 0.07	1.38 ± 0.10
$m^{\mathrm{minimax}}_{b\ell} > 200$ GeV	1.40 ± 0.04	1.41 ± 0.06	1.39 ± 0.05	1.39 ± 0.05

Table 7.7: Summary of the normalization factors extracted from the $t\bar{t}+b\bar{b}$ control regions. The lepton flavor-channel breakdown is shown only for illustration, with the inclusive NF applied to all events.

[20] In the case of the stop one-lepton analysis described in Chapter 6, the NFs for each process are applied to all regions in a simultaneous fit. More pure CRs allow a simpler strategy to be adopted here.

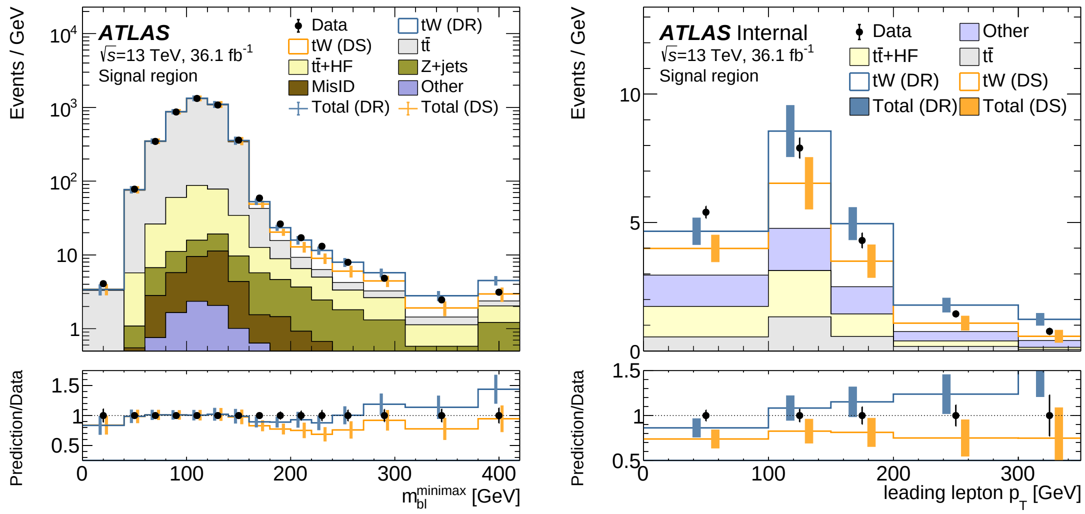

Figure 7.10: Data is compared to the predicted event yields for SM processes passing the signal selection, shown in stacked histograms. The tW single top contribution is included as an unfilled histogram, stacked above each of the other contributions. Totals obtained using both DR and DS schemes are shown, in blue and orange respectively, with corresponding errors included on the total prediction. At left, yields are shown in bins of $m_{b\ell}^{\mathrm{minimax}}$, while at right the leading lepton p_{T} is shown for events satisfying $m_{b\ell}^{\mathrm{minimax}} > 200$ GeV.

corresponding information is shown visually in Figures 7.10, with estimates from both DR and DS models of the interference shown for comparison.

Table 7.8: The observed number of events passing the signal selection is shown, compared to the predicted background from all SM processes. Yields are presented in bins of $m_{b\ell}^{\text{minimax}}$. Predicted backgrounds estimates are after all normalization.

SR yields for $m_{b\ell}^{\text{minimax}}$ [GeV]	0-40	40-60	60-80	80-100	100-120	120-140	140-160	160-180
Observed data	163	1557	6916	17336	26452	21587	7200	1180
$t\bar{t}$	116.8 ± 6.2	1388.3 ± 23.7	6338.6 ± 50.3	16016.8 ± 79.4	24452.4 ± 99.2	20065.8 ± 90.0	6146.3 ± 50.0	602.1 ± 15.6
tW (DR)	3.8 ± 0.7	34.2 ± 2.1	130.6 ± 3.8	299.4 ± 5.5	427.0 ± 6.8	422.6 ± 6.8	284.4 ± 5.5	200.6 ± 4.7
$t\bar{t}+b\bar{b}$	10.1 ± 2.3	92.6 ± 7.4	390.5 ± 16.6	979.9 ± 32.7	1434.1 ± 42.1	1175.0 ± 36.6	494.3 ± 22.4	138.5 ± 10.2
$t\bar{t}V$	0.4 ± 0.1	3.5 ± 0.2	13.2 ± 0.4	31.1 ± 0.7	44.7 ± 0.9	39.1 ± 0.8	18.2 ± 0.5	8.2 ± 0.3
VV	0.2 ± 0.1	0.7 ± 0.1	1.8 ± 0.3	1.9 ± 0.3	2.3 ± 0.3	2.2 ± 0.2	1.9 ± 0.2	4.5 ± 2.8
$Z+$jets	3.4 ± 2.6	10.7 ± 9.3	77.9 ± 10.6	108.4 ± 11.8	126.4 ± 10.6	158.1 ± 10.7	106.4 ± 9.1	83.5 ± 7.6
Fake leptons	1.5 ± 1.8	6.8 ± 4.5	41.1 ± 11.9	81.8 ± 20.9	142.9 ± 29.4	184.2 ± 35.0	66.8 ± 16.9	18.1 ± 7.8
Total SM estimation	136.2 ± 7.3	1536.8 ± 27.0	6993.8 ± 55.4	17519.3 ± 89.4	26629.8 ± 112.5	22047.1 ± 104.0	7118.2 ± 58.3	1055.5 ± 22.3

SR yields for $m_{b\ell}^{\text{minimax}}$ [GeV]	180-200	200-220	220-240	240-270	270-310	310-380	>380
Observed data	526	342	262	238	193	172	125
$t\bar{t}$	136.0 ± 8.4	55.5 ± 7.0	26.7 ± 5.0	26.9 ± 4.1	24.9 ± 4.0	21.8 ± 3.3	13.7 ± 3.0
tW (DR)	155.0 ± 4.0	132.2 ± 3.8	103.5 ± 3.4	112.2 ± 3.4	99.4 ± 3.3	95.0 ± 3.3	84.8 ± 2.9
$t\bar{t}+b\bar{b}$	84.9 ± 7.0	56.9 ± 6.5	50.9 ± 5.6	45.9 ± 5.4	52.5 ± 6.1	38.6 ± 4.6	32.8 ± 4.2
$t\bar{t}V$	6.5 ± 0.3	5.4 ± 0.2	4.0 ± 0.2	4.2 ± 0.2	3.8 ± 0.2	3.2 ± 0.2	3.1 ± 0.2
VV	1.1 ± 0.2	2.7 ± 1.2	1.5 ± 0.9	2.3 ± 0.9	1.0 ± 0.1	1.1 ± 0.2	1.0 ± 0.1
$Z+$jets	63.4 ± 4.8	54.8 ± 6.0	35.5 ± 2.6	39.4 ± 2.7	35.5 ± 2.3	28.9 ± 2.1	31.2 ± 3.5
Fake leptons	21.5 ± 7.8	10.4 ± 5.8	8.0 ± 5.4	8.2 ± 5.4	12.4 ± 5.8	7.1 ± 4.7	13.3 ± 6.0
Total SM estimation	468.4 ± 14.8	317.9 ± 13.3	230.0 ± 10.2	239.0 ± 9.7	229.5 ± 10.1	195.7 ± 8.3	179.9 ± 9.1

Table 7.9: The observed number of events passing the signal selection and with $m_{b\ell}^{\text{minimax}} > 200$ GeV is shown, compared to the predicted background from all SM processes. Yields are presented in bins of leading lepton p_{T}. Predicted backgrounds estimates are after all normalization.

SR yields for $m_{b\ell}^{\text{minimax}}$ [GeV]	0-100	100-150	150-200	200-300	>300
Observed data	540	395	215	144	38
$t\bar{t}$	54.4 ± 5.3	66.3 ± 8.3	28.2 ± 4.0	17.6 ± 3.5	3.0 ± 1.1
tW (DR)	170.8 ± 4.2	189.3 ± 4.6	122.8 ± 3.7	103.1 ± 3.2	41.2 ± 2.1
$t\bar{t}+b\bar{b}$	118.7 ± 8.8	90.1 ± 7.5	43.8 ± 5.0	21.2 ± 4.8	4.0 ± 1.4
$t\bar{t}V$	6.3 ± 0.2	6.7 ± 0.3	4.5 ± 0.2	4.0 ± 0.2	2.0 ± 0.1
VV	1.7 ± 0.2	2.4 ± 0.7	3.4 ± 1.5	1.6 ± 0.6	0.5 ± 0.1
$Z+$jets	98.1 ± 7.9	58.9 ± 5.1	36.4 ± 2.8	22.4 ± 2.3	8.0 ± 1.4
Fake leptons	15.9 ± 7.8	14.3 ± 6.5	8.7 ± 4.7	8.4 ± 4.2	2.8 ± 2.1
Total SM estimation	465.9 ± 15.7	428.0 ± 14.6	247.8 ± 9.3	178.4 ± 8.3	61.4 ± 3.7

7.4 Unfolding

The procedure of unfolding seeks to remove the dependence of observed cross-sections on the details of the particular detector used to measure them. Experiments aim to measure the particles from a high-energy reactions to investigate the the underlying physical processes which lead to their production. A perfect detector would be able to exactly measure and identify all particles produced in a proton-proton collision. However, realistic measurements of these processes are "folded" with effects specific to the detector used to measure them. This section describes methods of removing these effects, through the use of simulations of the underlying physical processes and of the detector's response to particle signals, to "unfold" measurements of reconstructed objects to particle-level[21].

7.4.1 Background information

To discuss unfolding, we first consider the measured and simulated inputs to the process. Let t_i denote a differential cross-section defined in terms of truth-level observables, which is also represented in bins of some such observable. A measurement d_i of this quantity may be attempted using a particle detector, where experimental outputs are used to reconstruct proxies for the underlying particle-level objects. In general, the reconstructed and idealized distributions will differ due to acceptance, efficiency, and resolution effects. *Acceptance* denotes phase space that is inaccessible to the detector, such as events with low-p_{T} leptons that cannot be triggered. The impact of this on the unfolded result should be minimal, so long as the particle-level selection is chosen to closely correspond to the measurement region. *Efficiency* denotes the imperfect ability to reconstruct and identify the event; b tagging and lepton identification are common sources of inefficiency. Mis-identification can also lead to extra events entering the reconstruction-level distribution (i.e. tagging a charm jet as a b), necessitating a *fake factor* correction. *Resolution* is the difference between the true and measured quantities in fully reconstructed events, for example imperfect jet energy measurements from a sampling calorimeter. The response matrix R_{ij} encodes the relation between particle-level and detector-level quantities:

$$d_i = \sum_j R_{ij} t_j. \tag{7.6}$$

Though the reconstructed distribution d_i is what an experiment measures, the unfolded distribution t_i is more useful for comparisons with theoretical models and measurements conducted with different experimental apparatuses. Naively, it is not difficult to relate the two – multiplying the

[21] In this section, truth- or particle-level will be used to refer to the particles produced in proton-proton collisions, while reconstruction- or detector-level will refer to observables calculated from the measured detector outputs.

measured distribution d_i by R^{-1} should recover the unfolded distribution t_i. Unfortunately it does not work well in practice to use R^{-1} as the unfolding matrix. Measurements are an intrinsically probabilistic statements and small fluctuations in d_i can lead to large, non-physical instabilities in the unfolded yields when the inverse matrix is used. Instead, a regularization scheme must be adopted.

The most basic approach is “bin-by-bin” unfolding, where all off-diagonal terms of $\mathbf{R}$ are ignored. While this can be appropriate (it is the scheme used by Higgs differential cross-section measurements [246, 247]), it is not suitable when migration effects are important to consider. Two further schemes are commonly used to regularize the process: the Bayesian iterative and singular value decomposition (SVD) approaches.

Bayesian iterative unfolding

In the Bayesian approach [248], the unfolding matrix is written

$$t_i = \sum_j \mathrm{P}(T_i \mid M_j) d_j, \tag{7.7}$$

where $\mathrm{P}(T_i \mid M_j)$ is the probability for a measured value in bin j to correspond to a true value in bin i. This may be rewritten by using Bayes' theorem

$$\mathrm{P}(T \mid M) = \frac{\mathrm{P}(M \mid T)\mathrm{P}(T)}{\mathrm{P}(M)} \tag{7.8}$$

and by using conservation of probability to rewrite $\mathrm{P}(M)$ as a sum over true states to obtain

$$\mathrm{P}(T_i \mid M_j) = \frac{\mathrm{P}(M_j \mid T_i)\mathrm{P}(T_i)}{\sum_k \mathrm{P}(M_j \mid T_k)\mathrm{P}(T_k)}. \tag{7.9}$$

This gives the unfolding matrix as a pure function of the response matrix $\mathrm{P}(M \mid T)$ and some particle-level prior $\mathrm{P}(T)$. The approach is made iterative by updating this prior so that the unfolded result after n iterations is

$$t_i^{(n)} = \sum_j \mathrm{P}(T_i \mid M_j) d_j = \sum_j \left\{ \frac{\mathrm{P}(M_j \mid T_i)\mathrm{P}(t_i^{(n-1)})}{\sum_k \mathrm{P}(M_j \mid T_k)\mathrm{P}(t_k^{(n-1)})} \right\} d_j, \tag{7.10}$$

where $t^{(0)}$ is usually taken as the prior from pure MC prediction. A small number of iterations increase reliance on the simulated model, which may lead to large theoretical systematic uncertainties. With a large number of iterations, the initial model becomes less important, but the statistical uncertainty on the unfolded distribution may become large, due to increased reliance on the measured distribution. The number of iterations is chosen to balance these effects.

Singular Value Decomposition unfolding

While the Bayesian iterative technique described above is the nominal one used in the analysis, the singular value decomposition (SVD) method [249] is also investigated as an alternate. This method applies singular value decomposition to the response matrix and regularizes the inversion of the matrix by neglecting the smallest singular values, which can amplify statistical fluctuations in the measured distribution. The number of singular values retained may be tuned to control the degree of regularization introduced in the unfolding matrix, in principle running from 1 to all n bins of the unfolded distribution. The authors of Ref. [249] propose some criteria to select this parameter, though in practice we test the effect of scanning all possible choices of the number of singular values to be retained.

Efficiency and mis-identification effects

While the response matrix formalism can absorb all effects stemming from detector acceptance, mis-identification, and resolution, it is convenient to treat them separately. Define the *fake factor* f_i to be the fraction of reconstructed events which are due to the targeted truth-level process. Define the *inefficiency factor* c_i as the fraction of truth-level events which hare reconstructed by the detector. Acceptance effects should be small due to the choice of particle-level fiducial region. Then we may define an unfolding matrix U where the particle- and detector-level inputs have already been corrected for these quantities which satisfy

$$\hat{d}_i = d_i \cdot f_i \tag{7.11}$$

$$\hat{t}_i = t_i \cdot c_i \tag{7.12}$$

$$\hat{t}_i = \sum_j U_{ij} \hat{d}_i. \tag{7.13}$$

The full machinery of the Bayesian iterative and SVD processes can thus be applied to the corrected variables $\hat{d}_i$ and $\hat{t}_i$, so that resolution effects are separately considered. The `RooUnfold` framework [250] is used as the technical implementation of the various unfolding prescriptions considered.

7.4.2 Particle-level physics objects

Particle-level objects are built from the collection of stable truth particles, defined to have $c\tau >$ 10 mm. Leptons (electrons and muons) are selected which are not produced from the decays of hadrons. All photons satisfying $\Delta R(\ell, \gamma) < 0.1$ are deemed to be final-state radiation and their four-vectors are combined with the "bare" lepton to form a "dressed" lepton. Jets are clustered from particles using the anti-$k_\perp$ algorithm with radius parameter $R = 0.4$. b hadrons are not included in the collection of stable particles, but are used to identify a subset of b jets that contain a b hadron with $p_\mathrm{T} > 5$ GeV. This is done via the ghost-association procedure, in which b hadrons four-vectors are re-scaled to have infinitesimal momenta and are included in the jet clustering procedure. A b hadron is associated to a jet if it belongs to its collection of constituent particles. The full object selection criteria, including kinematic acceptance, is given in Table 7.10. An overlap removal (OR) procedure is applied to the b-tagged and non-b-tagged jets and the dressed leptons, to avoid double-counting of particles among multiple objects. Baseline objects are used, with looser kinematic requirements than those for the signal objects. The same procedure is followed for particle-level and detector-level objects. Briefly, overlapping objects are eliminated in a multi-step procedure as follows:

1. Non-b-tagged jets are removed which are within $\Delta R < 0.2$ of a baseline electron.
2. Non-b-tagged jets are removed which are within $\Delta R < 0.2$ of a baseline muon and have $p_\mathrm{T}(\ell)/p_\mathrm{T}(\text{jet}) > 0.7$.
3. Leptons are removed which are within $\Delta R < \min(0.4, 0.04 + \frac{10\text{ GeV}}{p_\mathrm{T}(\ell)})$ of a jet.

The choice of OR is inspired by Ref. [7] and is motivated in greater detail in Chapter 6.

Table 7.10: A summary of the definitions of particle-level objects used in the analysis. Requirements are generally selected to mirror those made on detector-reconstructed objects. Lepton momenta are dressed with nearby photons and b hadrons are ghost-associated to jets. Baseline and signal objects are defined with the former used in the overlap removal procedure. Signal requirements are enforced on top of those already specified for the baseline objects.

Object	Requirements	Comments
Electrons	Baseline : $p_\mathrm{T} > 7$ GeV and $\lvert\eta\rvert < 2.47$ Signal : $p_\mathrm{T} > 28$ GeV	Dressed
Muons	Baseline : $p_\mathrm{T} > 6$ GeV and $\lvert\eta\rvert < 2.5$ Signal : $p_\mathrm{T} > 28$ GeV	Dressed
Jets	Baseline : $p_\mathrm{T} > 20$ GeV and $\lvert\eta\rvert < 2.5$ Signal : $p_\mathrm{T} > 25$ GeV	anti-$k_\perp$, $R = 0.4$
b jet	b hadron with $p_\mathrm{T} > 5$ GeV	ghost-associated

7.4.3 Optimization of the unfolding parameters

A selection of possible binnings of the distributions to be unfolded were considered, where a candidate was chosen which minimized the average per-bin uncertainty while retaining maximal shape information. A simplified setup was used where only the statistical and interference uncertainties (the bias from unfolding DS tW with the DR tW response matrix, expected to be the dominant theoretical uncertainty) were considered. Configurations with 4-12 bins of $m_{b\ell}^{\text{minimax}}$ in the interference region ($m_{b\ell}^{\text{minimax}} > 200$ GeV) were investigated, with the bin limits chosen to yield a fixed number of reco-level events in each bin. For each binning, the uncertainties were scanned for 1-15 iterations of Bayesian unfolding.

Below $m_{b\ell}^{\text{minimax}} < 200$ GeV, the signal is dominated by $t\bar{t}$ events and the interference effect becomes small. In this region a simple strategy is adopted taking fixed width bins of 20 GeV, except for the [0 GeV, 20 GeV] and [20 GeV, 40 GeV] bins, which are merged because of the low number of expected events. This choice is fixed during in the optimization of the high-$m_{b\ell}^{\text{minimax}}$ binning.

The results of the optimization are shown in Figure 7.11 for the $m_{b\ell}^{\text{minimax}}$distribution, where the two scan dimensions (bin multiplicity and unfolding iterations) have been linearized for readability. The 4-, 5-, and 6-bin setups are all found to produce minimal average uncertainties for some choice of iterations and thus the 6-bin setup is selected to preserve maximal shape information from the unfolded distribution. The precise bin limits are shown in Table 7.11.

The strategy for binning the leading-lepton p_{T} distribution is adjusted slightly for the interference SR. A 3-bin scheme with boundaries at 100 and 150 GeV is considered, having a similar number of events in each bin. Additional bins are added by splitting the most sensitive bin (characterized by the 'significance' (DR-DS)/σ_{tot}), up to 7 bins when the statistical uncertainties become very large. The number of bins is selected to maximize the per-bin average of (DR-DS)/σ_{tot}. Figure 7.12 shows the average value of this 'significance' as a function of the number of bins and iterations considered. The 5-bin scheme is selected, as adding additional bins is found not to be helpful. The conclusion is checked using toy pseudodata generated with both the DR and DS assumptions.

The final number of iterations is selected via the same procedure used to choose the binning, though now with all uncertainties described in Section 7.5 included. Figure 7.13 shows the evolution of the per-bin uncertainty as a function of the number of iterations used for both DR and DS pseudodata. The per-bin uncertainty is generally minimized using a single iteration of the procedure, so this value is chosen. The resulting uncertainties are also cross-checked with the alternate SVD unfolding method, which is found to obtain similar results. Figure 7.14 shows the analogous study

Table 7.11: Bin limits used to unfold the $m_{b\ell}^{\text{minimax}}$ observable in the inclusive SR and leading lepton p_{T} in the interference SR, defined from the optimization procedure described in the text.

Signal Region	Number of bins	Bin limits
Inclusive	15 bins in $m_{b\ell}^{\text{minimax}}$	[0 GeV, 40 GeV], then 20 GeV bins up to 200 GeV [200 GeV, 220 GeV], [220 GeV, 240 GeV], [240 GeV, 270 GeV], [270 GeV, 310 GeV], [310 GeV, 380 GeV], and ¿380 GeV
Interference	5 bins in p_{T}^{ℓ}	[0 GeV, 100 GeV], [100 GeV, 150 GeV], [150 GeV, 200 GeV], [200 GeV, 300 GeV], and ¿300 GeV

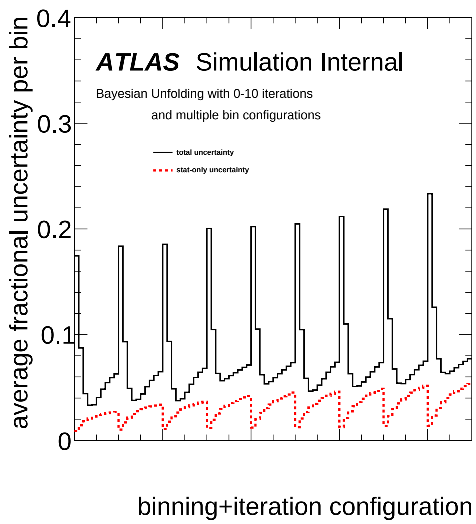

Figure 7.11: The $m_{b\ell}^{\text{minimax}}$ distribution is unfolded for $t\bar{t}$+tW (DR) events with a number of unfolding configurations considered. The average fractional uncertainty per bin of the unfolded distribution is shown for each configuration, calculated as the sum in quadrature of the components from limited data statistics in the detector-level region and the non-closure $t\bar{t}$+tW (DS) when unfolded with response matrices and correction factors from $t\bar{t}$+tW (DR). Both total (solid black) and stat-only uncertainties (dotted red) are shown . Each unfolding configuration consists of the number of bins considered and the number of iteration performed. The binnings are defined to select a constant number of events per bin in the signal region for $m_{b\ell}^{\text{minimax}}$>200 GeV. The 2-dimensional scan over number of bins and iterations is linearized, with each set of 10 contiguous bins corresponding to scanning over the number of iterations performed for a fixed binning. Four iterations are generically seen to minimize the uncertainty for all binnings. The best performance is found with the 4-, 5-, and 6-bin configurations, with an average fractional uncertainty of 4% per bin with 4 iterations. The 6-bin configuration is selected to preserve maximal shape information.

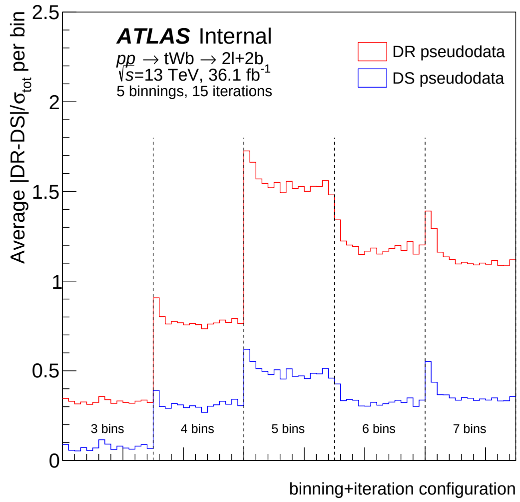

Figure 7.12: The leading lepton p_{T} distribution in the interference signal region is unfolded for toy $t\bar{t}$+tW events with various unfolding configurations considered. For a given unfolding setup, displayed is the average 'significance' per-bin: the average difference in particle-level DR and DS predictions divided by the per-bin uncertainty. Five possible binnings of the lepton p_{T} distribution are considered (from 3-7 bins), with the same distribution unfolded with 1 to 15 iterations, so that the result for unfolding $3+n$ bins with m iterations is found in the $(15n+m)$-th bin of the histogram. The red (blue) line displays results where the pseudodata is generated using the DR (DS) prediction. Because the DS sample predicts fewer events in the SR the corresponding statistical uncertainties are larger, resulting in lower significances. The 5-bin configuration is found to be optimal in cases of both DR- and DS-like observed data yields.

for the unfolded lepton p_{T} spectrum in the interference region, where 3 iterations are selected.

The evolution of the central values of the unfolded $m_{b\ell}^{\mathrm{minimax}}$ distribution is shown in Figure 7.15 for 1 to 15 iterations with statistical uncertainties determined from an ensemble of toys. Also illustrated separately is the $t\bar{t}$ + DS single top signal unfolded with the nominal (DR) response matrix, demonstrating the that theoretical unfolding bias from the interference effect is much smaller than the raw DR/DS difference. This is also seen in Figure 7.16, which shows the (quick) convergence of the unfolded values over many iterations and the fact that the interference uncertainty is small compared to the statistical contribution to the final measurement.

7.4.4 Response matrices, efficiency and acceptance factors

The nominal inputs to the unfolding procedure which were obtained after the optimization described in Section 7.4.3. The response matrix, fake, and inefficiency factors for the nominal unfolding setup using $t\bar{t}$and DR single top events MC is presented in Figure 7.17 (top). The corresponding

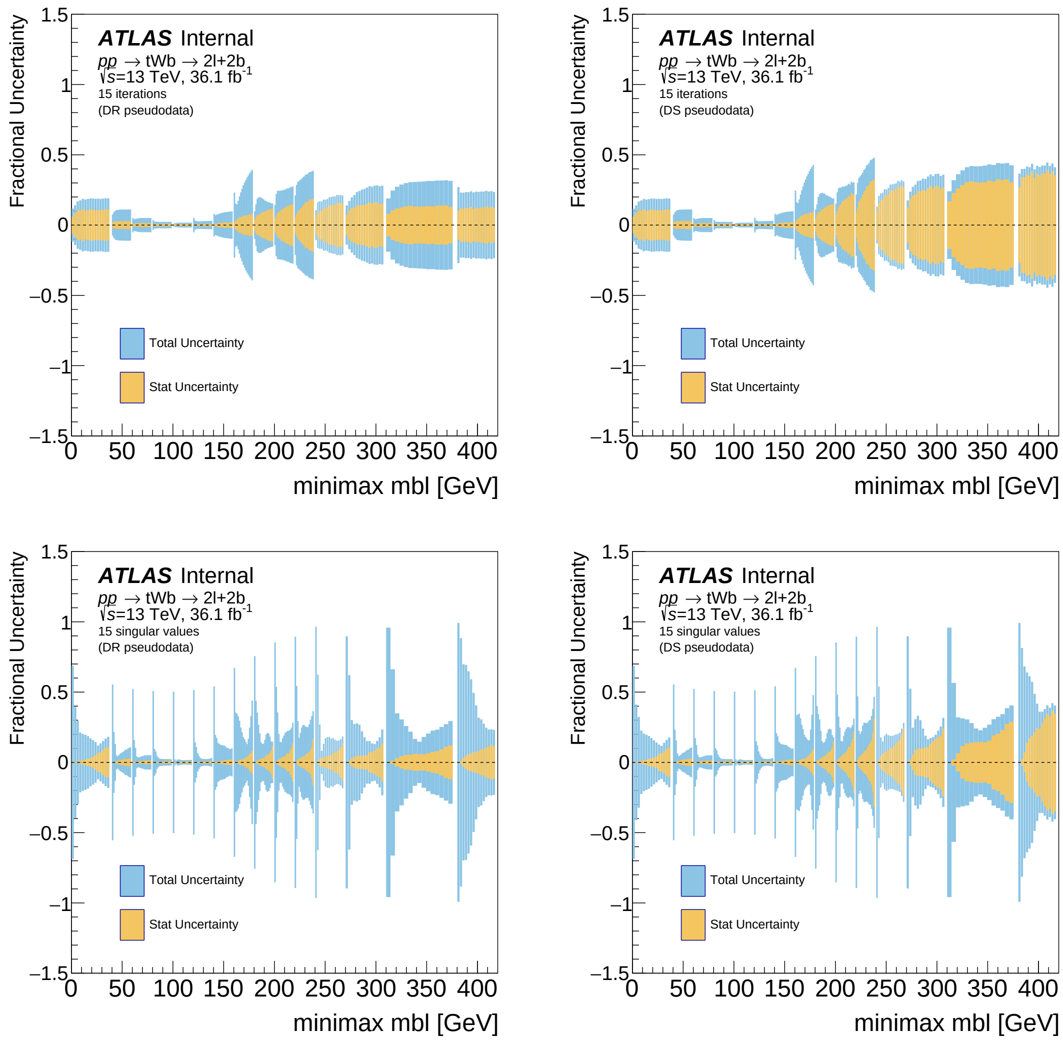

Figure 7.13: The per-bin $m_{b\ell}^{\text{minimax}}$ uncertainties are shown using both the Bayesian iterative (top) and SVD (bottom) methods, where the relevant regularization parameter is scanned (the number of iterations or the number of singular values retained). Pseudodata in the signal region is considered, generated from either $t\bar{t}$ and DR (left) or DS (right) single top MC. Uncertainties are broken into statistical and systematic components, with all major uncertainties included. The statistical uncertainty is larger for DS pseudodata as it predicts that fewer events enter the SR. Total uncertainties in the interference-sensitive region are generally minimized after a single iteration, motivating the choice to use one iteration when unfolding the data. The SVD method leads to similar results for the proper choice of the regularization hyper-parameter.

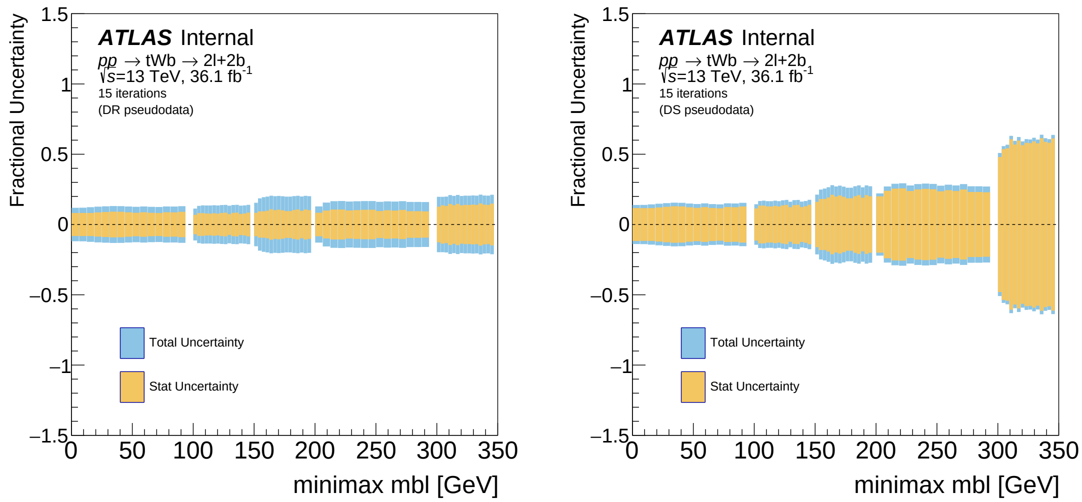

Figure 7.14: The uncertainties are shown in bins of leading-lepton p_{T}, scanning over the number of iterations employed. Pseudodata is generated in the signal region, generated from $t\bar{t}$ and DR (left) or DS (right) single top MC. Uncertainties are broken into statistical and systematic components, with all major uncertainties included. The statistical uncertainty is larger for DS pseudodata as it predicts that fewer events enter the SR. The total uncertainties do not depend strongly on the number of iterations employed, with 3 iterations chosen to avoid unnecessarily inflating the statistical component.

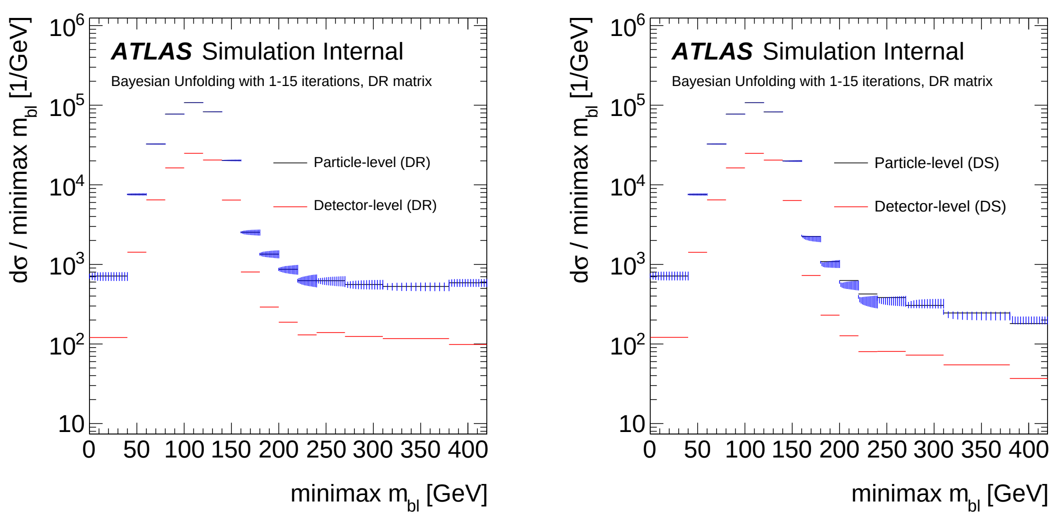

Figure 7.15: At left, the reco- and truth-level DR distributions are shown as well as the unfolded central values and their uncertainties after 1 to 15 iterations. The central unfolded values precisely match the truth, indicating no technical bias in the unfolding machinery. At right, the reco- and truth-level DS distributions are shown as well as the reco-level DS distribution unfolded with the DR response matrix. Vertical bars indicate the statistical uncertainty associated with each iteration of the unfolding.

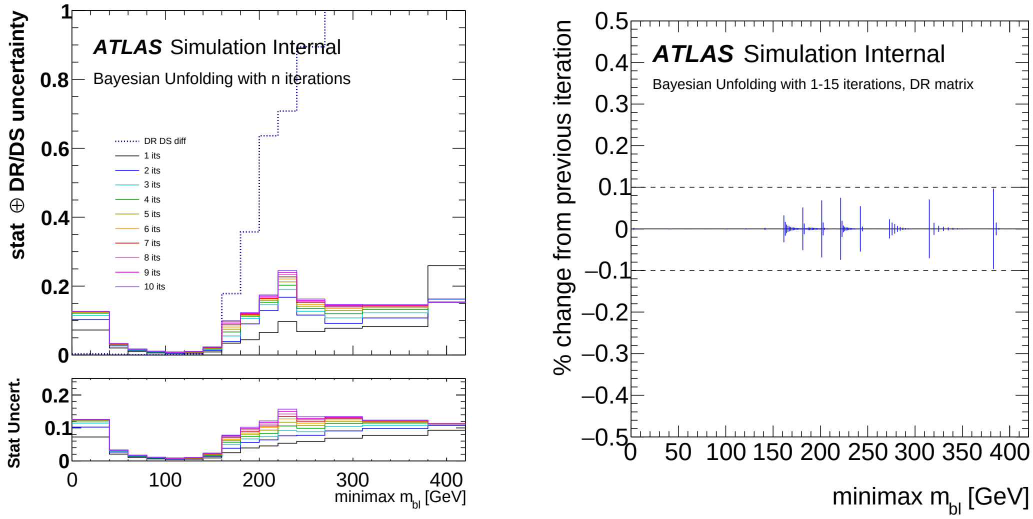

Figure 7.16: At left, the top panel shows the sum in quadrature of the statistical uncertainty and the non-closure the $t\bar{t}$+tW(DS) when unfolded with response matrices and correction factors from $t\bar{t}$+tW(DR). Different colors indicate different numbers of iterations in the iterative Bayesian unfolding. For comparison, the difference between the particle level predictions for the $t\bar{t}$+tW(DR) and $t\bar{t}$+tW(DS) models is also shown in the black dotted line. The contribution from the statistical uncertainty alone is plotted in the bottom sub-figure. At right, the relative change per bin is shown as a function of the number of iterations when unfolding the DS distribution with the DR response matrix.

information for the unfolding setup using DS single top events is shown in the bottom row. The off-diagonal elements for both response matrices are generally small and in good agreement with each other. There is a slightly larger fake factor for the DS sample at high $m_{b\ell}^{\text{minimax}}$, inflated by the softer population of b jets that may more easily fluctuate out of acceptance. Figure 7.18 presents the analogous information for leading lepton p_{T} in the interference region. Here resolution effects are negligible, due to the cleaner observable.

7.4.5 Stress tests

$t\bar{t}$ shape injections

In order to check that the unfolding procedure is robust against Monte Carlo mis-modeling of the tWb shape, stress tests are performed. The inclusive tWb process may be broken into $t\bar{t}$ and single top constituents. The single top component is stressed by comparing the DR and DS schemes of modeling the interference, which can disagree by factors of 2-3 in the interference region. The robustness of the unfolding to DR/DS differences is further studied in Section 7.5. This section will

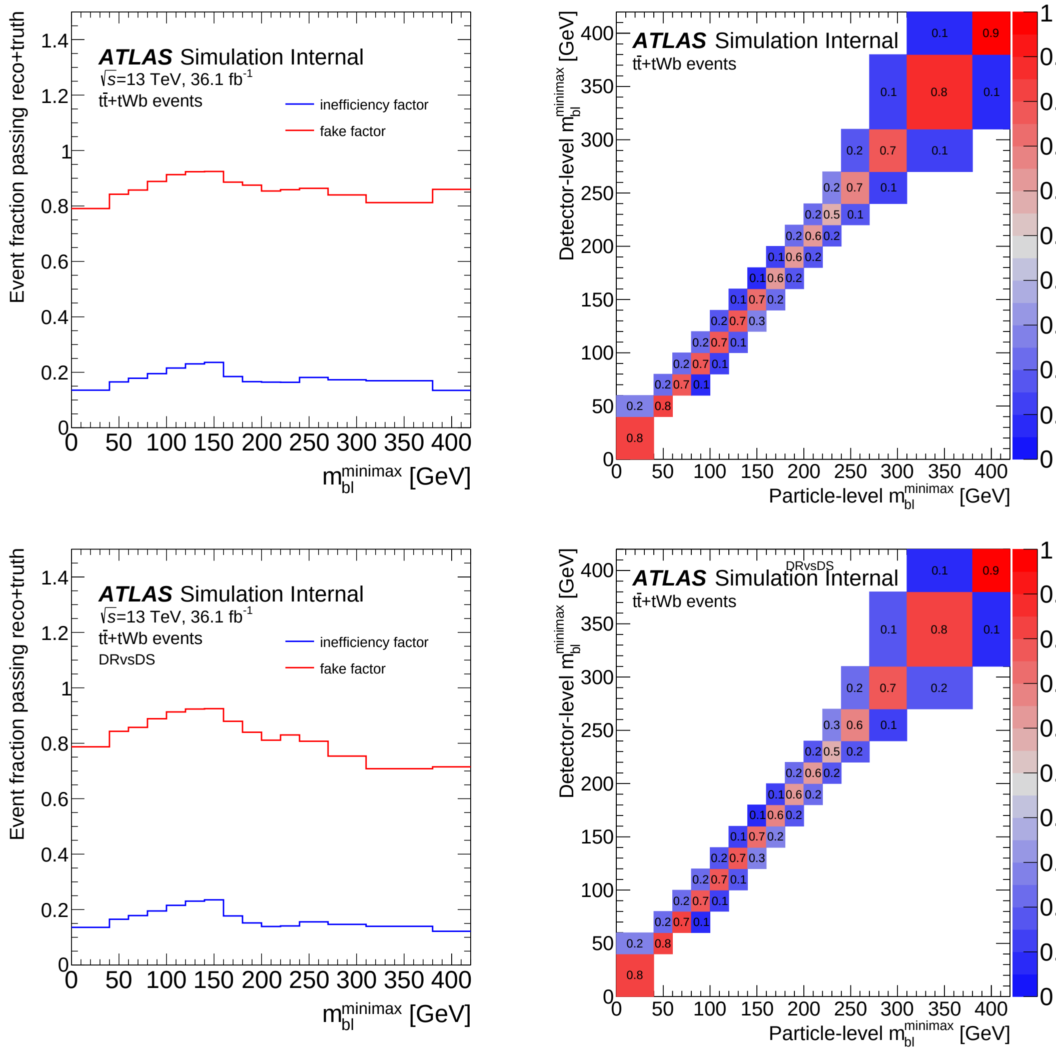

Figure 7.17: The acceptance and efficiency factors are shown at left in bins of $m_{b\ell}^{\text{minimax}}$ for events passing the signal selection, which are derived from the nominal $t\bar{t}$+tWb simulation. The response matrices are presented at right. Off-diagonal terms in the response matrices are found to be generally small, with bin-to-bin migration dominated by the jet energy resolution. The top row shows quantities derived using the DR interference scheme, while the bottom row is calculated using the DS scheme. The difference in the unfolding inputs pictured here for the two schemes is relatively small demonstrating that, while DR and DS give dramatically different predicted $m_{b\ell}^{\text{minimax}}$ spectra, these differences do not lead to a bias in the unfolding model.

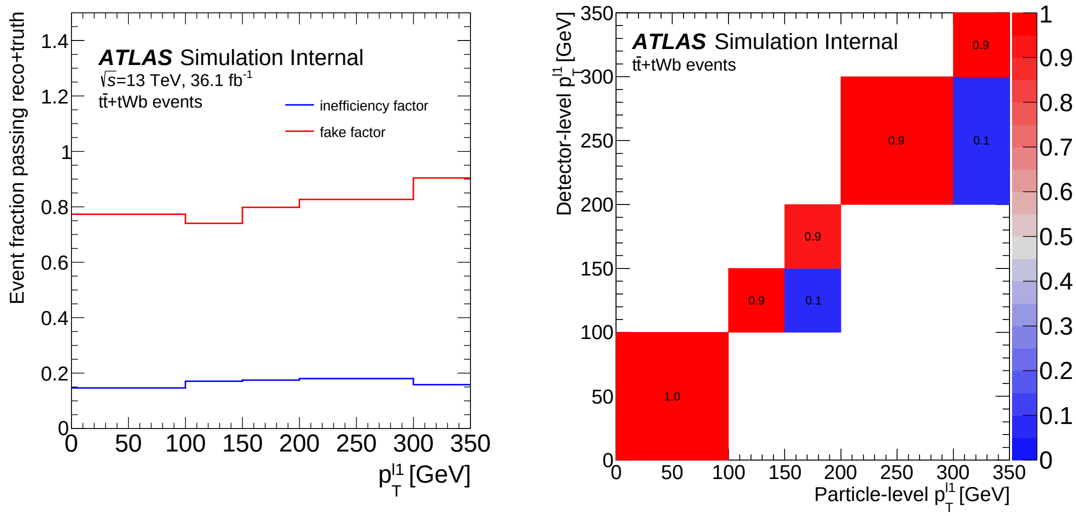

Figure 7.18: The acceptance and efficiency factors are shown at left in bins of leading-lepton p_{T} for events entering the interference selection ($m_{b\ell}^{\mathrm{minimax}} > 200$ GeV). The response matrices are presented at right and the nominal $t\bar{t}$+tWb simulation is use. Only results using the DR scheme are shown, as the difference with respect to DS is found to be minimal.

focus on additional stresses to the $t\bar{t}$ component, which dominates the region of $m_{b\ell}^{\mathrm{minimax}} \lesssim m_{\mathrm{top}}$.

Stress tests are performed to check whether a shift in the $t\bar{t}$ contribution can be properly unfolded, by multiplying the MC predictions by Gaussian and sinusoidal shifts. The shifts are applied to the bins dominated by $t\bar{t}$ (chosen here as those with $0 < m_{b\ell}^{\mathrm{minimax}} < 180$ GeV) with the size of the variation governed by the largest fractional uncertainty of all bins within that range $\sigma_t\bar{t}^{\max}$ (this is roughly 25%). For the Gaussian shift, the height is taken to be $\sigma_t\bar{t}^{\max}$, with the mean set to the midpoint of the range considered (90 GeV) and width set to 45 GeV so that a "2σ" range is used. For the sinusoidal modification, the weights are set to deviate from unity with a period of 180 GeVand amplitude such that the peak-to-peak difference is $\sigma_t\bar{t}^{\max}$.

For each variation, the resulting linear weights w_i are multiplied by the original truth-level $t\bar{t}$ distributions t_i to obtain a weighted test distributions $\tilde{t}_i = w_i t_i$. A test detector-level distribution $\tilde{r}$ is then produced by applying the response matrix to $\tilde{t}$. Figure 7.19 shows the differences in the unfolded $\tilde{r}_i$ distribution and the weighted truth $\tilde{t}_i$ for the Gaussian and sinusoidal perturbations, which provide some estimate of the robustness of the procedure against differences in the $t\bar{t}$ shape. The differences are found to be small in magnitude, everywhere covered by the data-driven non-closure uncertainty (see Section 7.5), and everywhere insignificant compared to the total uncertainty.

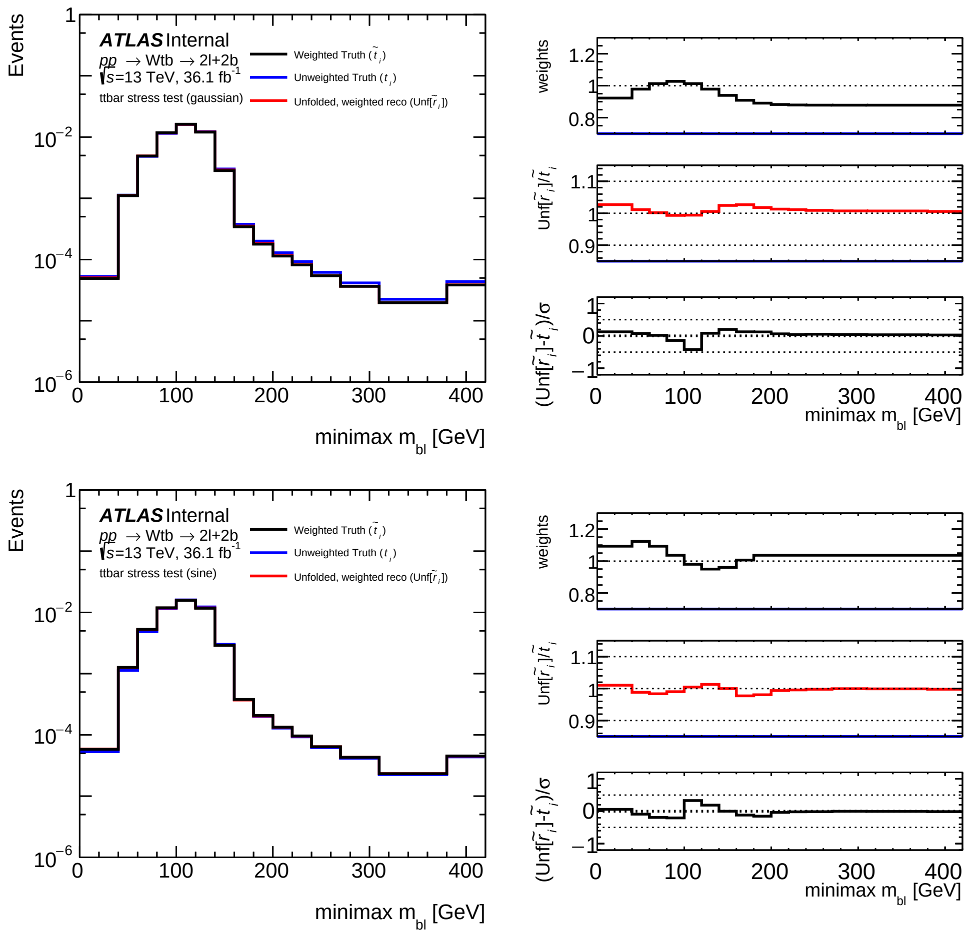

Figure 7.19: The top panel reviews the $t\bar{t}$ unfolding stress tests with Gaussian shape injection. At left, the $m_{b\ell}^{\text{minimax}}$ distribution for truth $W^+W^-b\bar{b}$ events with nominal MC (black), weighted $W^+W^-b\bar{b}$ MC (blue), and the unfolded, weighted reco-level distribution (red). At upper right, the Gaussian weights are shown which are applied to derive both the weighted truth- and reco-level distributions for testing. At middle right, the difference between the unfolded, weighted reco-level distribution and the weighted truth distribution are shown. At lower right a "pull" plot compares this difference to the uncertainty in the unfolding due to data statistics. The lower panel displays the corresponding plots for the sinusoidal shape injection. The differences are found to be small in magnitude, everywhere covered by the data-driven non-closure uncertainty (see Section 7.5), and everywhere insignificant compared to the total uncertainty.

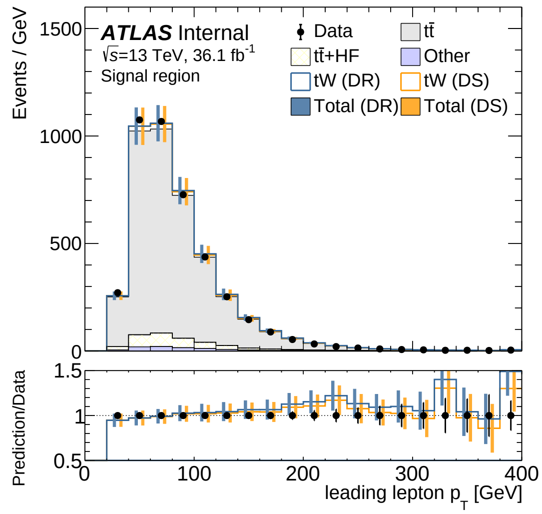

Figure 7.20: The leading lepton p_{T} distribution is shown for events entering the signal region (NFs are applied). A slight trend of harder leptons in simulation than data is observed, motivating a check of the impact with a dedicated unfolding stress test.

Lepton p_{T} re-weighting

In the inclusive SR, a minor trend is seen in the leading lepton p_{T} where the data spectrum is softer than that predicted by the MC simulation. This can be observed in Figure 7.20. While the deviation is not significant compared to the uncertainty on the MC estimate, the impact on the unfolding procedure was checked by re-weighting the predicted $WWbb$ distribution to match the observed data. The re-weighting test is summarized in Figure 7.21.

Re-weighting factors are computed in bins of lepton p_{T} of 20 GeV width, ranging from 20 to 300 GeV, where the last bin includes overflow events. These weights are derived from the data and MC distributions shown in Figure 7.20 and the correlation between lepton p_{T} and $m_{b\ell}^{\mathrm{minimax}}$ leads to the weights in bins of $m_{b\ell}^{\mathrm{minimax}}$observed in the top-right panel of Figure 7.21. These weights are used to perform a stress test using a similar procedure to the $t\bar{t}$ shape injection tests discussed above. Weights are applied directly to the truth-level distribution, denoted $\tilde{t}_i$. This distribution is folded, using the response matrix, to produce a weighted reco-level distribution, $\tilde{r}_i$. The bias due to the re-weighting is then computed as the difference between the weighted truth distribution and the unfolded, weighted reco-level distribution, shown in the right-center panel of Figure 7.21, in percent. The right-lower panel of Figure 7.21 compares the size of the effect to the data-driven non-closure uncertainty in each bin.

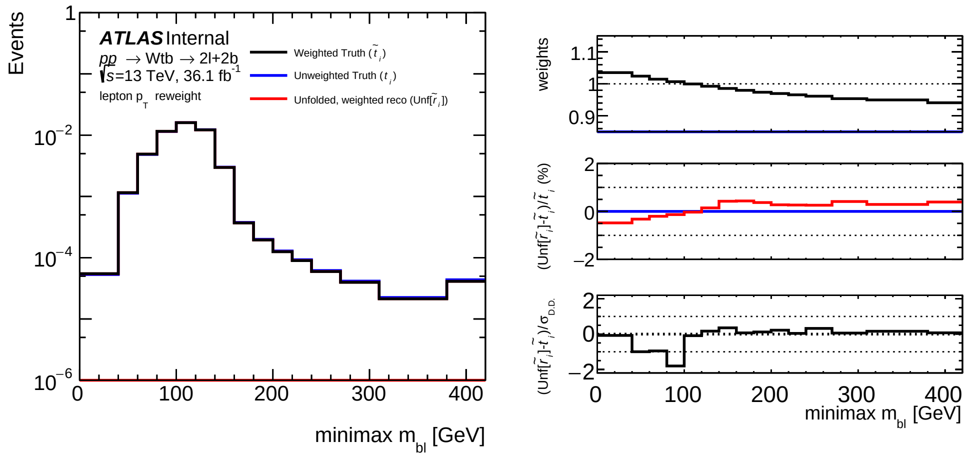

Figure 7.21: At left, the $m_{b\ell}^{\mathrm{minimax}}$ distribution for truth $W^+W^-b\bar{b}$ events with nominal MC (black), weighted WWbb MC (blue), and the unfolded, weighted reco-level distribution (red). At upper right, weights are shown which re-weight the nominal WWbb MC so that the leading lepton p_{T} distribution matches the observed data. The weights are used to derive both the weighted truth- and reco-level distributions for testing. At middle right, the difference between the unfolded, weighted reco-level distribution and the weighted truth distribution are shown. At lower right a "pull" plot compares this difference to the data-driven non-closure uncertainty.

The size of the re-weighting effect is found to be everywhere less than 0.5% and is less than the quoted data-driven non-closure uncertainty in all but one bin. In this bin ($80 < m_{b\ell}^{\mathrm{minimax}} < 100$ GeV) the non-closure uncertainty is 0.07% and the re-weighting effect is 0.14%, while the total (stat-only) uncertainty is 4.9% (0.5%) in that bin. We conclude that no additional uncertainty need be considered to account for this small effect.

7.5 Uncertainties

Systematic uncertainties from a variety of sources are considered which affect the final unfolded distributions. Uncertainties may affect the reconstruction-level signal extracted from the data, the MC-based unfolding procedure, or both simultaneously. Uncertainties stem from the limited number of simulated MC events, the calibration of reconstructed objects, accuracy of theoretical models, and choices in the unfolding procedure.

7.5.1 Monte Carlo Statistical Uncertainties

Figure 7.5.1 illustrates the size of the MC statistical uncertainty. The MC statistical uncertainty is calculated by generating an ensemble of pseudo-experiments where each bin of the response matrix

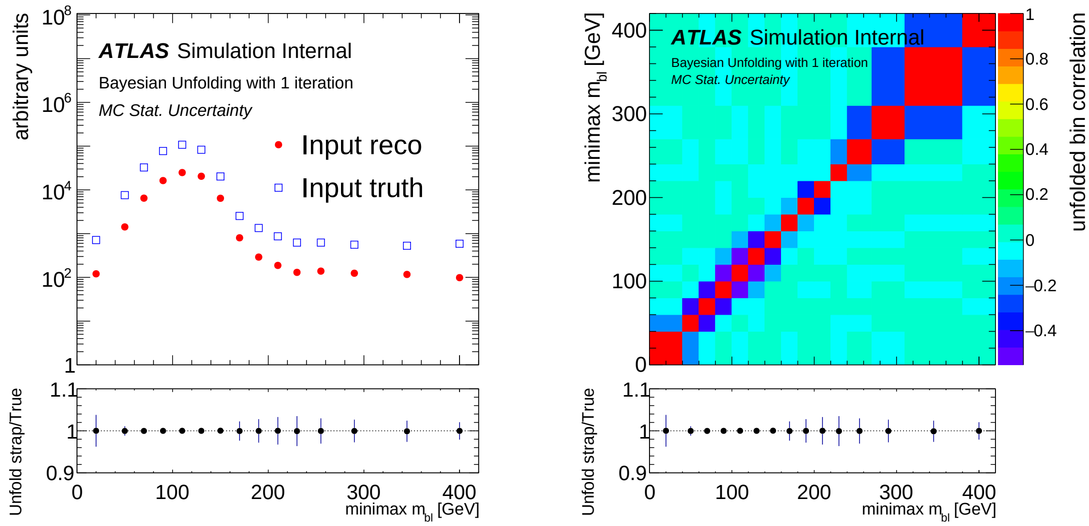

Figure 7.22: At left, the top panel shows the input reco and truth-level distributions. The bottom panel shows the the median over the pseudo-experiments per bin and the error bar is one-half the inter-quartile range (IQR) over pseudo-experiments. For each pseudo-experiment, the entries in the response matrix are fluctuated according to the MC statistical uncertainty. At right, the upper panel shows the statistical correlations between bins induced from the unfolding.

is fluctuated within its uncertainty. Pseudo-reco and truth distributions are generated from this response matrix by projections, to take into account correlations between the fluctuations. This removes the need for fake and inefficiency corrections factors. The nominal response matrix is used to generate nominal projected reco and projected truth distributions. The bottom plot of the left figure in Fig. 7.22 show the median over the pseudo-experiments per bin and the error bar is one-half the IQR over pseudo-experiments. The right plot further shows the statistical correlations between bins induced from the unfolding.

7.5.2 Experimental Systematic Uncertainties

The following uncertainties correspond to variations in the reconstruction of experimental objects. For each uncertainty, the complete analysis is repeated with the varied setup to produce new unfolded distributions. These uncertainties can affect the reconstruction-level differential cross-sections (in the “usual way” of modifying transfer factors and causing migration among bins of $m_{b\ell}^{\mathrm{minimax}}$ and leading-lepton p_{T}) as well as the fake factors and response matrix inputs to the unfolding process. The majority of uncertainties considered correspond to the same sources described for the SUSY search in Section 6.8.1 with the exception of the $E_{\mathrm{T}}^{\mathrm{miss}}$ soft term, which is not relevant for the present analysis. Here we highlight additional experimental uncertainties considered in the measurement as well as relevant modifications to those previously described.

Jet energy scale The same sources of uncertainties are considered as in Section 6.8.1. Additional correlation information is retained, with a total of 19 parameterized variations considered.

Jet energy resolution Treatment is identical to that described in Section 6.8.1.

Electron efficiency The treatment of efficiency scale factors is identical to that described in Section 6.8.1, with variations considered from reconstruction, identification, and isolation effects.

Electron scale and resolution Uncertainties on the scale and resolution are considered using a simplified scheme, where all contributing sources are assumed to be fully correlated in η_{det} and are summed in quadrature.

Muon efficiency The treatment of efficiency scale factors is identical to that described in Section 6.8.1, with variations considered from reconstruction and isolation.

Muon scale and resolution Uncertainties are considered to account for mis-alignments in the ID and MS as well as for uncertainty on the momentum scale.

Flavor tagging Uncertainties impacting the efficiency scale factors for light flavor, charm, and b jets are considered where extended correlations are retained with respect to the scheme described in Section 6.8.1. Sixteen independent variations are considered that impact light-flavor jets, in addition to three for c-jets and six for b jets. A proper treatment of correlations among tight-tagged, loose-not-tight-tagged, and un-tagged jets is provided in the context of the "pseudo-continuous" calibration. For c jets with $p_{\text{T}} > 140$ GeV and b jets with $p_{\text{T}} > 300$ GeV, an insufficient sample of calibration events prevents the use of pseudo-continuous uncertainties. For these jets (found in only a small fraction of the total population of selected events) a simplified scheme is used where uncertainties are calculated under assumptions where the uncertainties on tight and loose tagged jets are fully-correlated and fully-uncorrelated. For each measurement the most pessimistic of the two approaches is adopted.

Pile-up re-weighting The same sources of uncertainties are considered as in Section 6.8.1.

7.5.3 Background Subtraction Uncertainty

Events enter the signal regions which stem from physical processes other than the $W^+W^-b\bar{b}$ target. They must be subtracted from the SR distributions before unfolding the data.

$Z+$jets and $t\bar{t}+b\bar{b}$ backgrounds are estimated from data with dedicated control regions and are described in Section 7.3.3. Uncertainties enter on these estimates due to the limited data statistics used to derive the corresponding normalization factor. Experimental and theoretical systematic uncertainties also affect the estimated SR yields for these processes, though only though variations in transfer factors.

The estimation of backgrounds from mis-identified and non-prompt leptons is also estimated from data in control regions, as described in Section 7.3.3. Uncertainty on this background enters from the limited data statistics in each bin of the same-sign analogues of the SR distributions. An uncertainty is also propagated to the background estimate via the flavor composition uncertainty assessed on the transfer factor used to extrapolate from the same-sign to opposite-sign regions.

Scale variation uncertainties on Z+jets events are applied, yielding a small change to the predicted shape and thus the extracted binned normalization factors. These are computed by taking the full envelope of the 7-point variations of the factorization and renormalization scales . The maximum variation is chosen separately for every unique bin of the unfolded distribution, and no correlation among bins is assumed.

Figure 7.23 shows the ratio of predicted $Z+$jets yields in the inclusive signal region using the approach of individual $m_{b\ell}^{\text{minimax}}$ bins versus the nominal approach of deriving combined normalization factors across multiple bins of $m_{b\ell}^{\text{minimax}}$. The difference is compared to the size of the uncertainty on the nominal estimate due to (a) data statistics only in the yellow band, and (b) data statistics and scale variations in the black band. Additional details on the methods can be found in Section 7.3.3.

Other backgrounds are minor and are taken entirely from MC. They are varied by the 3.2% luminosity uncertainty as well as within their theoretical uncertainties.

7.5.4 Theoretical systematic uncertainties

Systematic uncertainties on the $t\bar{t}$+tWb signal impact the magnitude and shape of the extracted signal as well as the unfolded yields obtained from it. Uncertainties are assessed using the same set of samples and general techniques described in Section 6.8.2, so that here we describe only the choices particular the the present analysis.

In general, the distinction between $t\bar{t}$ and tWb processes in the region of large interference is artificial, so often uncertainties are treated as correlated between the two. The $t\bar{t}+b\bar{b}$ process is treated separately, so that theoretical uncertainties on this component (defined in Section 7.3.3) are considered to be uncorrelated with those on other signal processes. The sources of theoretical

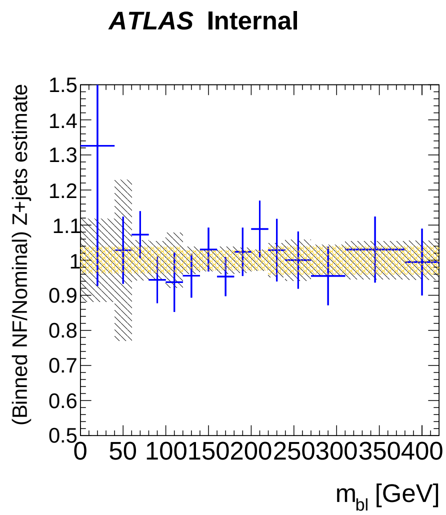

Figure 7.23: The ratio of the predicted Z + jets yields in the inclusive signal region is shown in blue crosses, using two methods of estimation. The numerator of the ratio is given by the prediction using an estimation strategy with a unique normalization factor employed for each bin of $m_{b\ell}^{\text{minimax}}$. The denominator estimate uses the nominal procedure of combining several adjacent bins to determine average normalization factors across a broader region. (The bins are $m_{b\ell}^{\text{minimax}} \leq 120$, $120 < m_{b\ell}^{\text{minimax}} \leq 220$, and $m_{b\ell}^{\text{minimax}} > 220$ GeV). The yellow hashed band represents the fractional uncertainty on the nominal estimate due to limited data statistics in the Z+jets control region, while the black band also includes uncertainty due to scale variations. The specific procedures are described in Section 7.3.3. (The scale uncertainty is derived from an envelope of 7-point variations to μ_R/μ_f. The large uncertainty in the second bin is due to a large weight (statistical fluctuation) in one of the samples used to compute the envelope.)

uncertainty on the signal process are summarized as follows:

MC generator / NLO matching. Predictions from `POWHEG` and `MG5_aMC@NLO` are compared, with the uncertainty given as the symmetrized, full difference between samples. The contributions to $t\bar{t}$ and tW are decorrelated, as the tWb process is calculated to a different accuracy in the two sets of ME calculations.

Fragmentation / hadronization. Predictions from `PYTHIA` and `HERWIG++` are compared, with the uncertainty taken as the full difference between samples, symmetrized. The models are fully correlated between $t\bar{t}$ and tW samples.

Scale variations. Low and high radiation samples obtained from scale variations (defined explicitly in Section 6.3.1) are compared, with the uncertainty calculated as one half of the difference, symmetrized. As variations account for missing higher-order diagrams and the tWb MEs are calculated at different orders for the $t\bar{t}$ and tW processes, the variations are taken to be uncorrelated.

Interference. The DR and DS prescriptions are compared, with the full difference between predictions taken as an uncertainty.

PDF. The `PDF4LHC` prescription is followed, using the internal eigenvectors obtained in the combination of the `CT14`, `MMHT14`, and `NNPDF3.0` sets [251]. However, because the nominal $t\bar{t}$ and tW samples use the `CT10` PDF, which is *n*ot used in the `PDF4LHC` combination, the difference between the `CT10` and `PDF4LHC` nominal sets is also be checked. The total uncertainty is then taken as sum in quadrature of the full difference of the `CT10` to `PDF4LHC` sets with the internal uncertainty taken from the `PDF4LHC` combination and is generally dominated by the latter.

Top + additional heavy flavor. The fragmentation / hadronization and radiation uncertainties are applied to $t\bar{t}$+$b\bar{b}$ predictions using the same methods described for the orthogonal $t\bar{t}$sample. Due to insufficient MC statistics, the `MG5_aMC@NLO`comparison is replaced by one with a 4FS `SHERPA`$t\bar{t} + b\bar{b}$ calculation.

The individual components of the top theory uncertainties are displayed in Figure 7.24 separately for the $t\bar{t}$+light, $t\bar{t} + b\bar{b}$ and tWb components.

Uncertainties on the theoretical cross sections calculated for each process are also considered and are summarized in Table 7.12. Cross section uncertainties on $t\bar{t}$ and single top are included as they lead to (small) changes in the composition of the inclusive $W^+W^-b\bar{b}$ sample.

7.5.5 Unfolding Non-closure

The same method introduced in Section 7.4.5 to test the robustness of the unfolding machinery to signal injections is used to check the closure of the procedure in data. The unfolding procedure

Table 7.12: Summary of the theoretical cross section uncertainties considered.

Process	Relative Uncertainty	Reference
V+jets	5%	[252]
VV	6%	[252]
ttV	13%	[2]
$t\bar{t}$	5%	[33, 205]
tW	5%	[253]

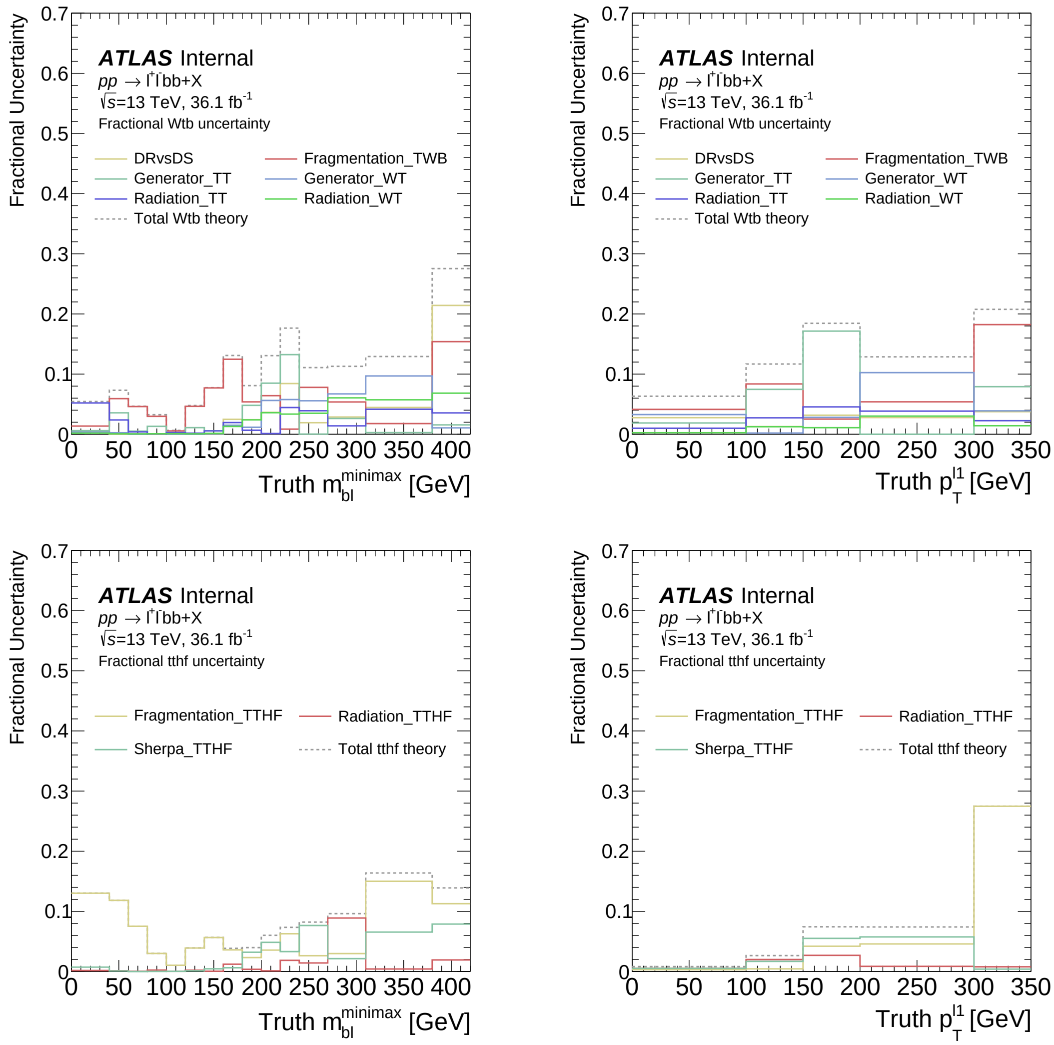

Figure 7.24: The fractional uncertainty due to each $t\bar{t}$+light, tWb single top (both top tow), and $t\bar{t}+b\bar{b}$ (bottom row) theory source is shown in bins of the unfolded variables $m_{b\ell}^{\text{minimax}}$ (left column) and leading lepton p_{T} (right column). The uncertainties are computed directly on the data by varying the response matrix used in the unfolding.

inherently assumes that the data is similar to the reconstruction-level distribution, using this as the basis of the procedure to correct the distribution for detector effects. The reliance on this model is reduced by the iterative Bayesian procedure, whereby the observed data is used to adjust the prior and improve the procedure's estimate.

To assess the non-closure of the procedure due to differences between the extracted signal shape and that of the MC distribution, the ratio of the two is used to a set of weights. These weights are then applied to the truth-level distribution t_i (this is assumed to produce a *reasonable prior* for the purposes of this test, as the response matrix is not far from diagonal) to produce a test distribution $\tilde{t}_i$. The response matrix can then be used to fold $\tilde{t}_i$ into a test reco-level distribution $\tilde{d}_i$. While unfolding procedure precisely recovers t_i from d_i by construction, the difference between $\tilde{t}_i$ and the truth distribution recovered from unfolding $\tilde{d}_i$ is used to estimate the bias in the procedure. This assessment provides a data-driven non-closure uncertainty.

The method is illustrated in Figure 7.25 for the unfolded $m_{b\ell}^{\text{minimax}}$ and leading-lepton p_{T} distributions. A comparison of reco-level and truth-level distributions are shown. The folded, re-weighted MC prediction is shown to give a better description of the data than that from pure MC alone. The bias of the method for the test data set is found to be less than an 8% (5%) effect in all bins of $m_{b\ell}^{\text{minimax}}$ (leading-lepton p_{T}).

7.5.6 Summary of all uncertainties

The composition of the uncertainty in each bin of the unfolded distributions is shown graphically in Figure 7.26, with individual components grouped according to the definitions in Table 7.13.

Table 7.13: Uncertainty categories used in the display of systematic uncertainties for covariance and correlation matrices.

Systematic group name	List of uncertainty components included
Lepton	electron/muon efficiency, resolution, scale
Jet	JES, JER, η-intercalibration
b-tag	b, c, light, and high-p_{T}extrapolation
Theory	top generator, fragmentation, radiation
DR/DS	interference uncertainty
Background subtraction	NFs/TFs from ZCR, 3bCR, and FCRs
XS/lumi	Cross-section uncertainties for all backgrounds, luminosity
MC stat.	limited MC stats for all samples
Non-closure	data-driven non-closure
PDF	`PDF4LHC` eigenvectors, `CT10` to `PDF4LHC`

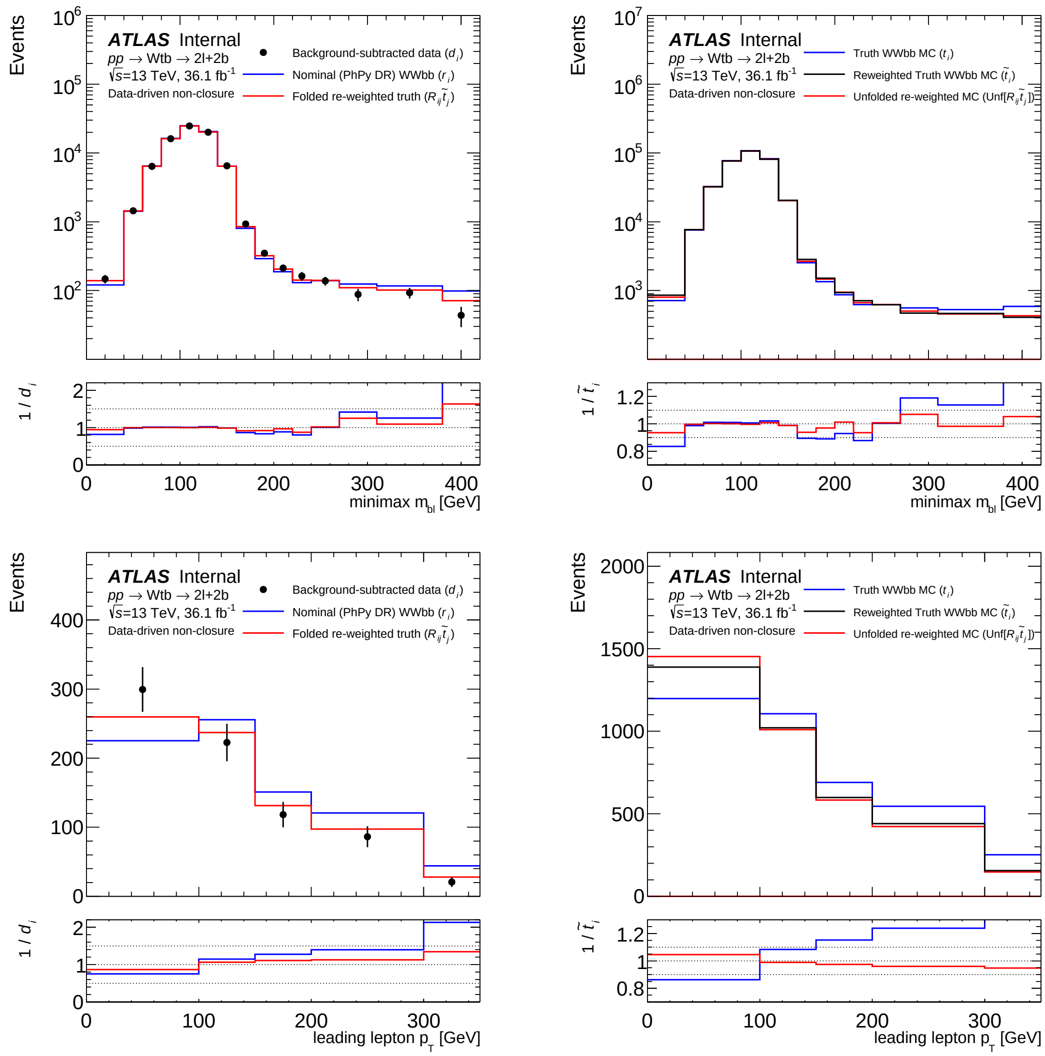

Figure 7.25: At left, the reco-level distributions for background-subtracted data d_i (black points) and the nominal MC prediction r_i (blue). At right, the particle-level truth MC prediction t_i (blue) and the test distribution $\tilde{t}_i$ (black) re-weighted according to the relative difference in reco-level MC prediction and data. The test distribution, folded with the response matrix ($R_{ij}\tilde{t}_j$, red) is also shown at left, displaying better data agreement with respect to the pure simulation estimate. The unfolded, folded test distribution (Unf$[R_{ij}\tilde{t}_j]$, red) is also shown at right for comparison with the initial test distribution, with their relative difference used to assess a non-closure systematic uncertainty. The top row shows the procedure applied to bins of $m_{b\ell}^{\text{minimax}}$, while the bottom row corresponds to the unfolded leading-lepton p_{T} distribution.

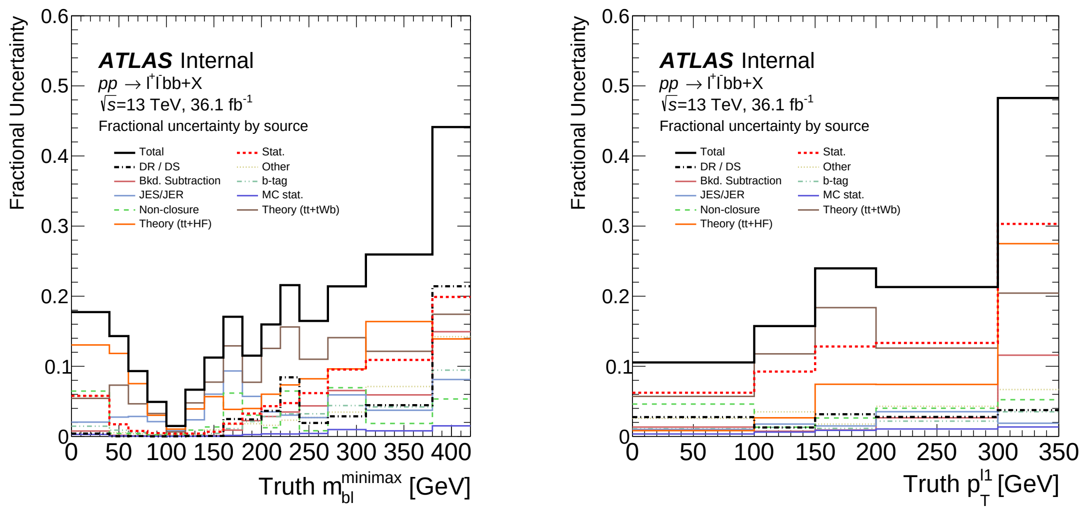

Figure 7.26: The fractional uncertainty due to each source is shown in bins of the unfolded variables $m_{b\ell}^{\text{minimax}}$ (left) and leading lepton p_{T} (right). The uncertainties are computed directly on the data by varying the response matrix used in the unfolding.

7.6 Results

The unfolded $m_{b\ell}^{\text{minimax}}$ spectrum is presented in Figure 7.27 alongside `POWHEG` predictions using three approaches of interference modeling. The unfolded leading-lepton p_{T} distribution in the region with $m_{b\ell}^{\text{minimax}} > 200$ GeV is shown in Figure 7.28. Figure 7.29 shows a further suite of comparisons to alternative $t\bar{t}$+tWb signal models in the $m_{b\ell}^{\text{minimax}}$ observable.

χ^2 tests

To quantitatively compare the unfolded data with various models of the interference a χ^2 test statistic is defined to be

$$\chi^2 = \sum_{i,j}(d_i^{(1)} - m_i^{(1)})^T \cdot (\Sigma^{(1)})_{ij}^{-1} \cdot (d_i^{(1)} - m_i^{(1)}), \tag{7.14}$$

where d_i is the observed data, m_i is the model prediction, and Σ is the full covariance matrix. The superscripts indicate that a single entry has been removed from each distribution for the purpose of the χ^2 calculation to account for the fact that the distributions are normalized. Entries corresponding to the first bin are removed for each distribution, though the choice is irrelevant as the information contained in the removed bin is fully redundant due to the normalization condition.

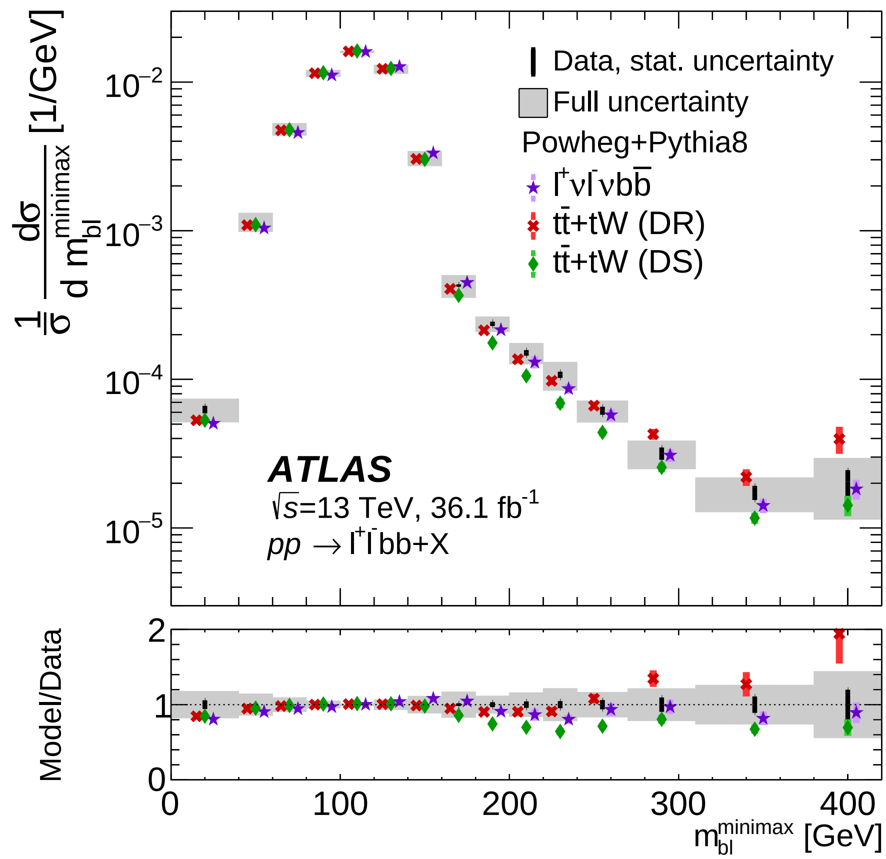

Figure 7.27: The unfolded, normalized differential fiducial cross section in bins of $m_{b\ell}^{\text{minimax}}$ is presented in the upper panel. Data points are indicated by points with black error bars representing the statistical component of the uncertainty on the data. The gray band includes all sources of uncertainty including systematics. Colored markers show predictions for three samples of events generated with POWHEG+PYTHIA 8, with corresponding bands representing uncertainties from PDF and scale variations. Red crosses (green diamonds) indicate the process generated with the Diagram Removal (Diagram Subtraction) interference scheme for combining separate NLO calculations of the $t\bar{t}$ and tW processes. Purple stars represent the NLO+PS calculation of inclusive $pp \to \ell^+\nu_\ell\, l^-\bar{\nu}_l\, b\,\bar{b}$ using the b_bbar_4l process implemented in the POWHEG BOX RES framework. The lower panel shows the ratio of predictions to data.

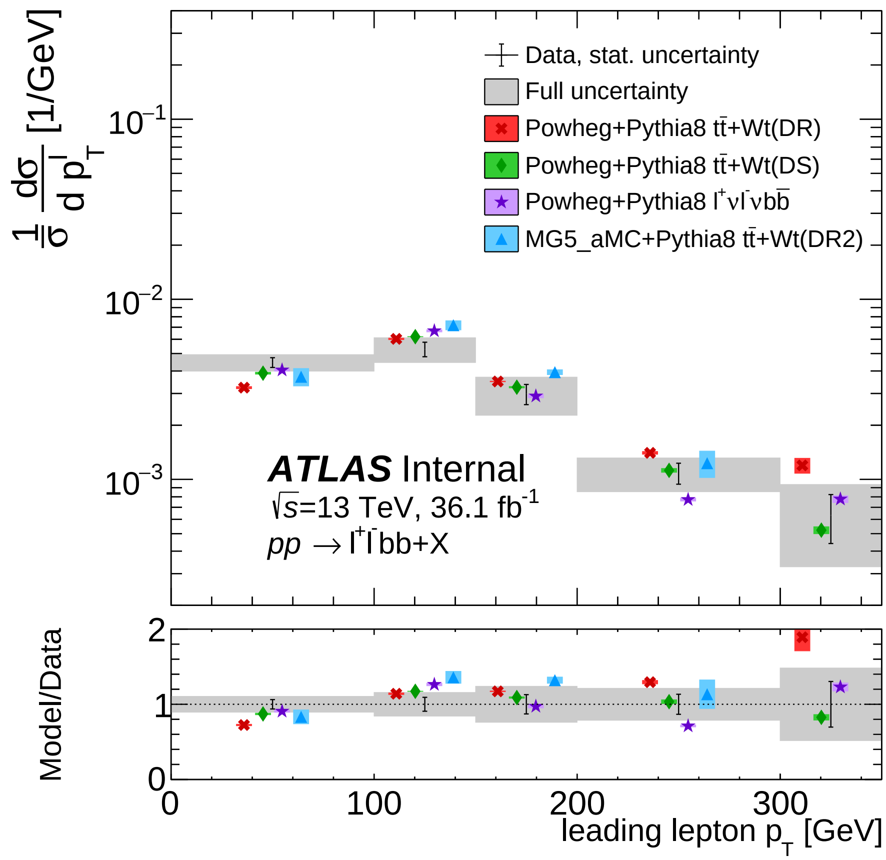

Figure 7.28: The unfolded, normalized differential fiducial cross section in bins of leading-lepton p_{T} is presented in the upper panel. Data points are indicated by points with black error bars representing the statistical component of the uncertainty on the data. The gray band includes all sources of uncertainty including systematics. Colored markers show predictions for four samples of events generated, with corresponding bands representing uncertainties from PDF and scale variations. Red crosses (green diamonds) indicate the process generated POWHEG+PYTHIA 8 using the Diagram Removal (Diagram Subtraction) interference scheme for combining separate NLO calculations of the $t\bar{t}$ and tW processes. Purple stars represent the NLO+PS calculation of inclusive $pp \to \ell^+ \nu_\ell \, l^- \bar{\nu}_l \, b \, \bar{b}$ using the b_bbar_4l process implemented in the POWHEG BOX RES framework. Blue triangles represent the NLO calculations of the $t\bar{t}$ and tW processes using MG5_aMC@NLO with the DR2 diagram removal scheme. This calculation predicts zero events in the bin of largest lepton p_{T}. The lower panel shows the ratio of predictions to data.

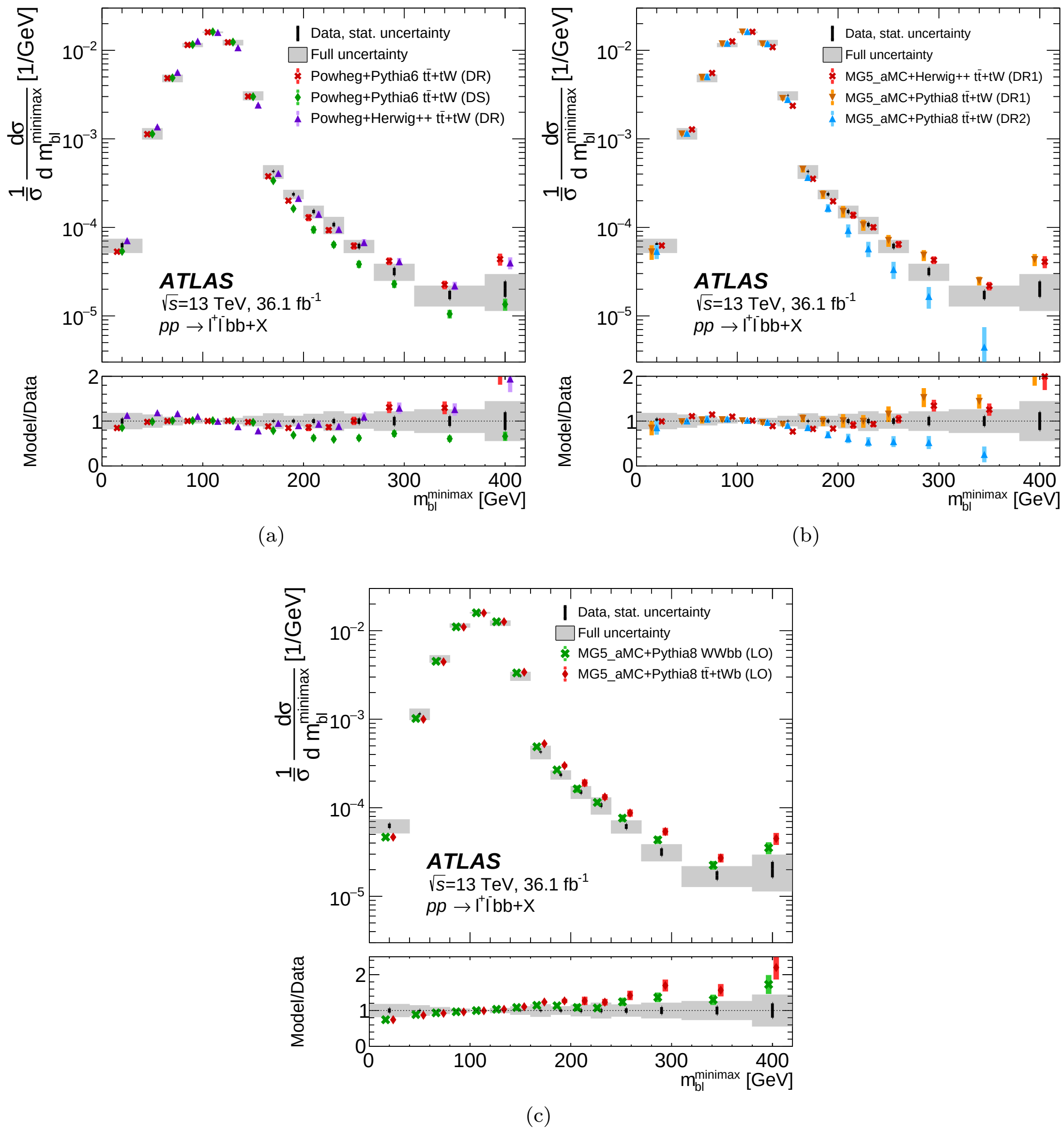

Figure 7.29: The unfolded, normalized differential fiducial cross section in bins of $m_{b\ell}^{\mathrm{minimax}}$ is presented, compared to a suite of predictions from various MC generator setups. In (a), the nominal POWHEG+PYTHIA 6 prediction used to model reconstruction-level objects and extract the $t\bar{t}$+tWb signal is shown for both the DR and DS schemes. An alternative sample using the HERWIG++ parton shower model is also displayed. In (b) samples produced with the MG5_aMC@NLO generator are displayed with the HERWIG++ and PYTHIA 8 shower models. Two variants of the PYTHIA sample are shown using the diagram removal scheme with (DR1) and without (DR2) the interference amplitudes removed from the calculation. The DR2 sample predicts no events in the bin with largest $m_{b\ell}^{\mathrm{minimax}}$. Figure (c) shows the comparisons to a LO calculation using MG5_aMC@NLO. Variants are shown where the interference is included (denoted $W^+W^-b\bar{b}$) and neglected ($t\bar{t}$+tWb).

Pseudo-experiments are performed by generating sets of pseudo-data obtained by throwing a random variable $X(\mu, \Sigma)$ from a multivariate Gaussian distribution with mean μ and covariance Σ set by the observed data yields and covariance matrix. For each pseudo-experiment, the χ^2 statistic is computed for the pseudo-data as in Equation 7.14, producing an expected distribution, given the measured data and its uncertainty.

A set of χ^2 values are also computed for each theoretical model considered, taking into account PDF and scale variations. For each model, the prediction is varied according to its per-bin uncertainties, generating a distribution of χ^2 values. A p-value is then computed for each prediction, using both the data and corresponding model χ^2 distributions. Table 7.14 presents the χ^2 and p-values obtained for each distribution.

Comparing the various interference schemes considered (DR(1),DR2,DS, plus `b_bbar_4l`) several trends emerge. The DR1 scheme that is used by ATLAS and CMS for the standard tW simulation appears to significantly differ from the data in the region of maximal interference. When $m_{b\ell}^{\text{minimax}} >$ 200 GeV, this scheme over-predicts the number of events in the bins of highest $m_{b\ell}^{\text{minimax}}$and leading lepton p_{T}. The DS scheme does not display a significant trend different than data in this region in either observable considered, but does appear to underestimate the relative contribution of the tWb process as a whole to the region beyond the $t\bar{t}$ kinematic endpoint. Altogether, the two

Table 7.14: Results are shown for χ^2 tests assessing the compatibility of the data with various MC predictions. Three sets of values are displayed: one using data from all bins of $m_{b\ell}^{\text{minimax}}$, a second only using the bins $m_{b\ell}^{\text{minimax}} > 160$ GeV most sensitive to the interference modeling, and a third using the leading-lepton p_{T} spectrum in the region $m_{b\ell}^{\text{minimax}} > 200$ GeV. Columns labeled χ^2/n denote the median value of the χ^2 test statistic for each sample over the number of degrees of freedom. The data and MC distributions for the statistic is used to calculate a p-value from toys, denoted p_0. PDF and scale uncertainties are considered for all simulated samples.

Model	All $m_{b\ell}^{\text{minimax}}$		High $m_{b\ell}^{\text{minimax}}$		$p_{\text{T}}(\ell_1)$	
	χ^2/n	p_0	χ^2/n	p_0	χ^2/n	p_0
Powheg+Pythia8 $t\bar{t}+tW$ (DR)	10/14	0.71	8.5/8	0.40	9.6/4	0.04
Powheg+Pythia8 $t\bar{t}+tW$ (DS)	10/14	0.77	6.6/8	0.56	2.3/4	0.64
Powheg+Pythia8 $\ell^+\nu\ell^-\nu bb$	5.9/14	0.92	2.0/8	0.95	7.3/4	0.10
MG5_aMC+Pythia8 $t\bar{t}+tW$ (DR1)	26/14	0.14	13/8	0.17	–	
MG5_aMC+Pythia8 $t\bar{t}+tW$ (DR2)	36/14	0.02	20/8	0.08	11/4	0.02
Powheg+Herwig++ $t\bar{t}+tW$ (DR)	26/14	0.07	7.3/8	0.48	11/4	0.02
MG5_aMC+Herwig++ $t\bar{t}+tW$ (DR)	30/14	0.04	11/8	0.23	10/4	0.03
Powheg+Pythia6 $t\bar{t}+tW$ (DR)	14/14	0.49	11/8	0.23	12/4	0.01
Powheg+Pythia6 $t\bar{t}+tW$ (DS)	14/14	0.49	10/8	0.32	2.2/4	0.66
MG5_aMC+Pythia8 (LO) $WWbb$	12/14	0.68	8.2/8	0.42	–	
MG5_aMC+Pythia8 (LO) $WWbb$, no int.	28/14	0.05	22/8	0.005	–	

predictions generally bracket the data, justifying the DR/DS comparison used to assess systematic uncertainties by LHC experiments. The diagram removal variant where interfering amplitudes are retained (DR2) predicts large destructive interference that does not agree well with data for values of $m_{b\ell}^{\text{minimax}} > 160$ GeV. Comparatively, the `b_bbar_4l` calculation provides a better description of the inclusive $m_{b\ell}^{\text{minimax}}$ spectrum, and agreed particularly with the data for large values of $m_{b\ell}^{\text{minimax}}$. In the region of the distribution dominated by on-shell $t\bar{t}$ events the simulation predicts a slightly harder spectrum than seen in data, though the size of the effect is covered by the data uncertainty. The DR description of the leading-lepton p_{T} spectrum is not as good as that given by the DS scheme.

Alternative samples used to estimated systematic uncertainties are found not to significantly improve the predictions for the standard DR scheme. The `HERWIG++` parton shower sample has little impact in the $m_{b\ell}^{\text{minimax}}$ tail and appears to worsen agreement in the $t\bar{t}$ bulk region. The NLO `MG5_aMC@NLO` prediction may give a slight improvement with respect to `POWHEG` in the description of $t\bar{t}$ events which migrate past the endpoint in the region from 180 GeV $< m_{b\ell}^{\text{minimax}} <$ 240 GeV. Significant differences across the $m_{b\ell}^{\text{minimax}}$ spectrum are observed comparing the LO `MG5_aMC@NLO` prediction with data. The destructive interference for $m_{b\ell}^{\text{minimax}}$ values beyond the $t\bar{t}$ kinematic endpoint improves this agreement.

Chapter 8

A New Measurement of the Top-Quark Width

The first measurement of top quarks in the pure off-shell and singly-resonant regime [8], described in Chapter 7, poses the question of whether any further properties of top quarks may be learned from this new data set. It is possible that the measured distribution could be sensitive to properties of SM top quarks and also potential signatures of BSM physics. Both possibilities are explored in the following chapter, which describes an extraction of the top quark width from the data obtained in Ref. [8], as well as a limit on top decays to non-SM particles ($\mathcal{BR}(t \to \text{BSM})$) and potential constraints on BSM charged currents.

8.1 Top-quark width in the SM (and beyond)

The top quark was discovered nearly 25 years ago [254,255] and a broad program has been established to measure its mass using a wide variety of methods [256–274]. Individual analysis channels as well as combined measurements have reached sub-percent precision. Theoretical uncertainties of these measurements are now comparable to Λ_{QCD}, raising questions of how the extracted mass parameter of the color-charged particle should be interpreted[22]. In contrast, direct measurements of the top quark width have uncertainties of 50% or worse [259, 276, 277]! Other measurements have been recast as indirect measurements of the top-quark width [278, 279], but their utility is limited by the restrictive assumptions required to do so.

[22]For an excellent discussion of interpretations of the top quark mass extracted from measurements using MCs, see Ref. [275]

The top-quark width at NLO is given [1] by:

$$\Gamma_t^{\mathrm{NLO}} = \frac{G_F m_t^3}{8\sqrt{2}\pi}\left(1-\frac{m_W^2}{m_t^2}\right)^2\left(1+2\frac{m_W^2}{m_t^2}\right)\left[1-\frac{2\alpha_{\mathrm{S}}}{3\pi}\left(\frac{2\pi^2}{3}-\frac{5}{2}\right)\right], \tag{8.1}$$

where the b-quark mass is neglected and terms of $\mathcal{O}(\alpha_{\mathrm{S}}\frac{m_W^2}{m_t^2})$ are omitted to significantly simplify the expression. This was first computed in Refs. [280–282], where finite b-quark mass, W width, and full NLO corrections may be found. Since then, the NNLO computation of the inclusive width has been completed [283–285], as well as the fully differential decay rate [286, 287]. The most recent calculation [286] also includes finite W boson and b quark mass effects and NLO electroweak correction and, assuming $m_{\mathrm{top}} = 172.5$ GeV and $\alpha_{\mathrm{S}} = 0.1181$, gives a predicted width equal to 1.322 GeV. Associated scale uncertainties are estimated to be less than one percent. Thus an improved measurement of the top-quark width could provide a stringent test of the SM top sector.

The top-quark width may be modified in extensions of the SM where additional interaction of the top quark are present. This can include the opening of additional decay channels of the top quark, as well as modifications to the tWb coupling, and the presence of new radiative corrections. These can occur in two-Higgs doublet models (2HDMs), SUSY models, as well as top-color technicolor. In top color models, this may be induced either by mixing between the SM W boson and a new heavier W' state or by tree-level contributions from vector-like quarks (VLQs) [288]. Similar ideas have been considered in top flavor models, where a new SU(2) symmetry is introduced for the existing third-generation particles of the SM [289–291]. These models can be combined with scenarios involving SUSY and additional Higgs doublets to be more readily consistent with the observation of a 125 GeV Higgs [292].

8.2 Previous measurements

Since its discovery at the Tevatron, the top quark's width has been measured with two different methods. The first "direct" category of measurements, made by the CDF [276], ATLAS [259], and CMS [277] Collaborations, relies on kinematic reconstruction of a b jet and charged lepton from the decay of one (anti-)top quark in $t\bar{t}$ events. These measurements have been conducted in both "leptons+jets" and di-leptonic $t\bar{t}$ decays. Mass templates are produced for various values of the top-quark width and the best-fit value is extracted from the measured distribution. However, a major shortcoming of this method is the weak dependence of the observable on the top-quark width parameter. The width of the measured distribution (shown in Fig. 8.1 for the most-sensitive measurement [259]) is the convolution of the BW width with the kinematic widening of the distribution

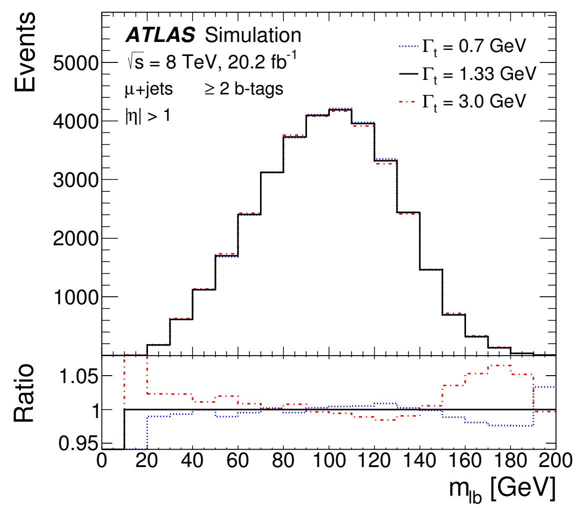

Figure 8.1: The reconstructed lepton and b jet invariant mass for several values of the top-quark width. This figure is reproduced from Ref. [259].

due to the unmeasured neutrino momentum in addition to fragmentation effects from the b quark. As can be seen, the width of the measured distribution is ≈ 35 GeV, and high-precision measurements are required to constrain widths on the order of 1 GeV. This measurement has obtained a value

$$\Gamma_t^{(\text{Direct})} = 1.76 \pm 0.33(\text{stat.})^{+0.79}_{-0.68}(\text{syst.})\ \text{GeV}. \tag{8.2}$$

A second "indirect" method of extracting the top-quark width has been performed by the D0 [278] and CMS [279] Collaborations, by combining measurements of the t-channel single top cross section with the relative branching fraction $\mathcal{BR}(t \to Wb)/\mathcal{BR}(t \to Wq)$. In the t-channel process,the NWA may be applied to the final-state top quark so that the production cross section is proportional to its width. Writing the cross section schematically as

$$\sigma_{t\text{-channel}} = \Gamma_t \mathcal{BR}_{\text{in}} \mathcal{BR}_{\text{out}} = \Gamma_t \left(\frac{\Gamma_{\text{in}}}{\Gamma_t}\right)\left(\frac{\Gamma_{\text{out}}}{\Gamma_t}\right) \tag{8.3}$$

allows one to compare theoretical calculations with experimental limits to obtain the width. Taking Γ_{in} to be the rate of proton-proton to single top quarks and $\mathcal{BR}_{\text{out}}$ to be the fraction of events where the top decays to Wb one can write

$$\sigma_{t\text{-channel}}^{\text{measured}} = \Gamma_{\text{in}} \mathcal{BR}_{\text{out}} = \Gamma_{\text{in}} \frac{\mathcal{BR}(t \to Wb)}{\mathcal{BR}(t \to Wq)}, \tag{8.4}$$

where in the last line it is assumed that the top quark must always decay to Wq. Then one can substitute Γ_{in} for the theoretical expression to find

$$\Gamma_t = \frac{\sigma^{\text{measured}}_{t\text{-channel}} \cdot \Gamma(t \to Wb)}{\sigma^{\text{theory}}_{t\text{-channel}} \cdot \frac{\mathcal{BR}(t\to Wb)}{\mathcal{BR}(t\to Wq)}}. \tag{8.5}$$

Using this method, Ref. [279] finds the most precise estimate of $\Gamma_t = 1.36 \pm 0.02$ (stat.) $^{+0.14}_{-0.11}$ (syst.).

8.3 Inspiration from measurements of the Higgs width

A third method to measure the top-quark width is possible, which is inspired by methods currently used to access the Higgs width. It is linearly dependent on Γ_t, unlike the direct method described above, and does not require the restrictive assumptions needed for the indirect method. The SM predicts $\Gamma_h \approx 4$ MeV, which is below the experimental resolution one could ever hope to achieve at the LHC or any futuristic e^+e^- machine.

It was suggested to study the Higgs boson width through the comparison of on- and off-shell cross section [293–296]. The motivation is plainly seen from the BW expression for a resonance[23]

$$\sigma(s) \sim \frac{\Gamma^2 M^2}{(s - M^2)^2 + M^2\Gamma^2}, \tag{8.6}$$

which (for narrow resonance $\Gamma/M \ll 1$) implies that the on-shell cross section is independent of the width, while the off-shell cross section is not. In the Higgs case, this is best illustrated in the $h \to 4\ell$ decay channel, where there are large enhancements in the off-shell cross section at both $2m_Z$ and $2m_t$ due to threshold effects in the decay and production, respectively. The differential cross section in four-lepton invariant mass is shown in Figure 8.2. Here, after integrating the Higgs line-shape, the cross section ratio depends linearly on Γ_h

$$\sigma^{\text{off-shell}}_{gg\to h\to ZZ} / \sigma^{\text{on-shell}}_{gg\to h\to ZZ} \sim \frac{m_h \Gamma_h}{(2m_Z)^2}, \tag{8.7}$$

where we have written the off-shell cross section as being dominated at the on-shell ZZ threshold.

This measurement technique has interesting sensitivity to BSM contributions to the Higgs width, and has been discussed extensively since being proposed [297–304]. In the originally proposed context of four-lepton mass scans it has been pointed out that the procedure does not establish a fully model-independent limit on Γ_h. Counter-example models of BSM physics exist which might modify the gluon-gluon fusion Higgs production loop, affecting the cross sections in a devious way that

[23] See the *Resonances* review and related chapters of Ref. [1] for an excellent discussion of the derivation and applicability of this expression.

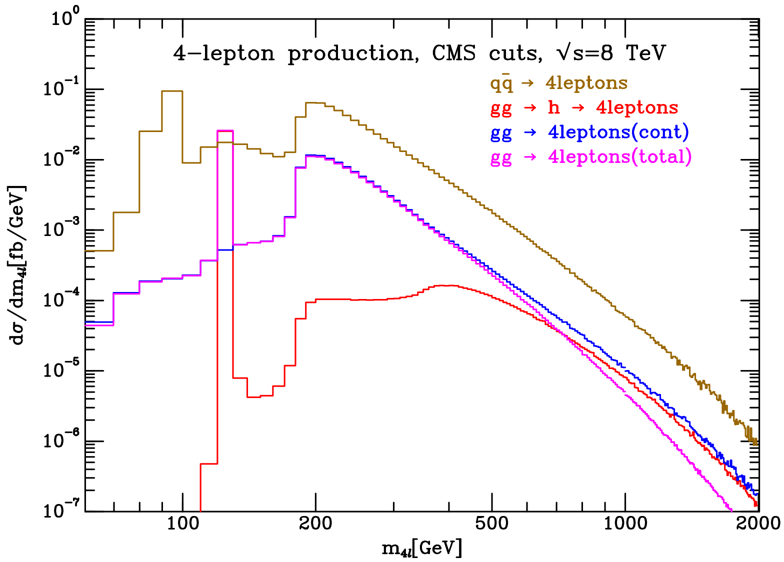

Figure 8.2: Several cross sections are shown, differentially in the four-lepton invariant mass. The rate of $gg \to h \to 4\ell$ is shown in red, with the other lines corresponding to background $pp \to 4\ell$ processes. The purple line shows the large destructive interference between Higgs and non-Higgs contributions for large masses. Beyond the maximum cross section at the Higgs mass, enhancements at $2m_Z$ (due to a threshold effect in the $\Gamma(h \to ZZ)$ partial width) and $2m_t$ (due to top-quark thresholds in the gluon-gluon fusion triangle loop) are observed. This figure is reproduced from Ref. [295].

invalidates the constraint on Γ_h. However, this can be avoided by conducting a similar analysis in a different channel (vector boson fusion (VBF) $h \to W^+W^-$, where the Higgs boson production and decay are mediated by the same hWW coupling) to establish more robust limits [297]. The method has been used (in the four-lepton final state) by the CMS [305–308] and ATLAS [309] Collaborations to obtain limits on the width.

The idea to utilize the same method to measure the top-quark width has been considered in the past in the context of e^+e^- [310] and proton-proton [311,312] collider measurements. However these studies were only completed at parton-level and did not propose a physical observable that could be used to perform such a study. A different idea has also recently been proposed to extract the width in proton-proton collisions using b jet charge asymmetries in t-channel production, though reconstruction effects were not considered [313].

8.4 Samples of simulated events

The primary calculation used to model the $W^+W^-b\bar{b}$ signal is the `b_bbar_4l` [236] generator implemented in `POWHEG BOX RES` [42]. It includes NLO QCD corrections and matching with the parton shower (PS) based on the Powheg method [41,314]. The process is described in terms of exact matrix elements for $pp \to \ell^+\nu_\ell\, l^-\bar{\nu}_l\, b\,\bar{b}$, dominated by top-pair topologies with leptonic W-boson decays, with massive b quarks provided by the OpenLoops program [178]. The `b_bbar_4l` generator combines for the first time: consistent NLO+PS treatment of top-quark resonances, including quantum corrections to top-quark propagators and off-shell top-quark decay chains; exact spin correlations at NLO, interference between NLO radiation from top-quark production and decays, full NLO accuracy in $t\bar{t}$ production and decays; NLO accuracy in b-quark kinematics; access to phase-space regions with unresolved b quarks and/or jet vetoes.

The nominal event sample was obtained using the `NNPDF30_nlo_as_0118` PDF set and the input top-quark mass value $m_t = 172.5$ GeV. Additional samples were generated with a range of top-quark widths $\Gamma_t \in \{0.66, 1, \Gamma_t^{\mathrm{SM}}, 1.66, 2\}$ GeV (with $m_t = 172.5$ GeV and[24] $\Gamma_t^{\mathrm{SM}} = 1.3328$ GeV) to enable the extraction of the best-fit value from data, with a range of top-quark mass values $m_t \in \{171.5, 172.5, 173.5\}$ GeV (with $\Gamma_t = \Gamma_t^{\mathrm{SM}}$) in order to estimate the uncertainty due to the top-quark mass, and a range of α_S values in the PDF $\alpha_S \in \{0.115, 0.118, 0.121\}$ (with $m_t = 172.5$ GeV and $\Gamma_t = \Gamma_t^{\mathrm{SM}}$) to explore the uncertainty due to variation of scale of the shower evolution. The central renormalization and factorization scales are set to the geometric average of transverse masses of the top quark and anti-top quark, and the value of `hdamp` is always set equal to the input value of the top-quark mass. The samples include all possible combinations of different family final state leptons (corresponding to the `channel 7` setting). Events also feature additional weights due to standard 7-point scale variation and due to PDF variation. Up to three hardest emissions are kept with the `allrad 1` setting, one from the production process and one from each of the top-quark resonances, and matching to Pythia 8.2 [29] makes use of both the PowhegHooks and PowhegHooksBB4L [315] vetoes, and A14 set of tuned parameters [173]. In the samples with $\alpha_S \in \{0.115, 0.121\}$ the `SpaceShower:alphaSValue` parameter of shower evolution in Pythia 8.2 is set correspondingly.

In addition, a LO calculation of the $W^+W^-b\bar{b}$ process is used from `Madgraph5_aMC@NLO` 2.6.4 with up to 2 extra jets, matched to a parton shower implemented in Pythia 8.240. This sample of events was simulated using the `NNPDF23_nlo_as_0118` PDF set, the A14 set of tuned parameters, $m_t =$

[24]The value of Γ_t^{SM} is the NLO top-quark width calculated by `b_bbar_4l` from all the other input values.

172.5 GeV, and $\Gamma_t \in \{0.66, 1, 1.33, 1.66, 2\}$ GeV. Alternative samples were produced with α_S varied as described above, as well as with alternative top-quark mass hypotheses $m_t \in \{170, 175\}$ GeV.

Event samples are analyzed and compared to data using the selection criteria of Ref. [8] as implemented in the `Rivet` toolkit [316]. Briefly, leptons and jets are reconstructed at particle-level with selections based upon the acceptance of the ATLAS detector. Leptons are dressed with nearby photons and are required to have transverse momentum $p_T > 28$ GeV and pseudorapidity $|\eta| < 2.47$ (2.5) for electrons (muons). Jets are reconstructed with the anti-k_T algorithm using a radius parameter of $R = 0.4$ [102–104] and considered in the analysis only if $p_T > 25$ GeV and $|\eta| < 2.5$. They are b-tagged if a B-hadron with $p_T > 5$ GeV is found within the jet cone. Events are selected which have two leptons, two b-tagged jets, with same-flavor lepton events vetoed if the di-lepton mass $m_{\ell\ell} < 10$ GeV or satisfies $|m_{\ell\ell} - m_Z| < 15$ GeV.

The `b_bbar_4l` simulation produces events with different-flavor leptons and must be corrected to account for same-flavor contributions. The ee and $\mu\mu$ contribution is obtained by re-weighting the generated $e\mu$ events which satisfy same-flavor $m_{\ell\ell}$ requirements. Good closure of this technique is found using the LO `Madgraph5_aMC@NLO` simulation, which includes all leptonic decays of the W boson. Further, the contribution of di-τ events (with fully leptonic τ decays) is found to be negligible and is not considered.

8.5 Recasting the interference measurement

A technique similar to that used by the Higgs width measurements can be used to reinterpret the analysis described in Chapter 7 as a limit on Γ_t. To very briefly summarize the key aspects of the analysis, a differential measurement of $m_{b\ell}^{\text{minimax}}$ was done in events with two charged leptons and b jets. The final state is inclusively sensitive to contributions from $t\bar{t}$ and tWb diagrams, with events with two on-shell tops obeying $m_{b\ell}^{\text{minimax}} < \sqrt{m_t^2 - m_W^2}$ at LO. Larger values of $m_{b\ell}^{\text{minimax}}$ are sensitive to off-shell and non-resonant events. The measurement was designed to assess the validity of different schemes to model interference effects in this region. The `b_bbar_4l` simulation includes exact interference effects at NLO and describes the data well. This allows the possibility of using this MC to extract a value of the top-quark width.

There are two manners in which changes to Γ_t can impact the $m_{b\ell}^{\text{minimax}}$ spectrum. First, a large population of events beyond the $\sqrt{m_t^2 - m_W^2}$ endpoint in $m_{b\ell}^{\text{minimax}}$ are due to $t\bar{t}$ pair production where one of the top quarks is off-shell. The cross section due to this contribution scales as

$$\frac{d\sigma}{dm_{Wb}^2} \sim \frac{1}{(m_{Wb}^2 - m_t^2)^2 + m_t^2\Gamma_t^2}. \tag{8.8}$$

and thus is enhanced by a larger top-quark width. Sufficiently beyond the top quark mass endpoint, this produces an overall linear scale factor to the signal cross section [317], in analogy to the situation described in Section 8.3.

Second, the relative fraction of events with $m_{b\ell}^{\text{minimax}}$ above $\sqrt{m_t^2 - m_W^2}$ has contributions from two classes of Feynman diagrams, with one and two time-like top quark propagators. The effect of scaling Γ_t on the number of events predicted from each class of amplitudes will not be the same. Thus, changes to Γ_t will scale each of the contributions (plus a third contribution from their interference) by a different factor, producing an overall change to the shape of the distribution.

Extraction

As the interference measurement [8] makes many measurement of $m_{b\ell}^{\text{minimax}}$ beyond the $\sqrt{m_t^2 - m_W^2}$ endpoint, the unfolded data in these bins may be compared to `b_bbar_4l` predictions for various values of Γ_t to extract a range of allowed values to this SM parameter. This extraction is done through the construction of a χ^2 test statistic, which quantifies the measured data values d_i in bins of $m_{b\ell}^{\text{minimax}}$ with the corresponding predictions m_i for some specific model. The statistic is defined as

$$\chi^2 = \sum_{i,j}(d_i - m_i) \cdot V_{ij}^{-1} \cdot (d_j - m_j), \tag{8.9}$$

using the same method described in Chapter 7. Here V_{ij} is the covariance matrix of uncertainties which allows information from multiple bins of $m_{b\ell}^{\text{minimax}}$ to be combined. Here both d_i and m_i correspond to normalized cross sections and the bin index runs only over the region where $m_{b\ell}^{\text{minimax}} >$ 160 GeV (past the kinematic endpoint $\sqrt{m_t^2 - m_W^2}$), as the bins with lower values are not sensitive to variations in the width.

To evaluate the effect of variations in the width, `b_bbar_4l` simulation is used, with settings identical to those used in the analysis described within Chapter 7, with the exception that each of the lepton family combinations $e^{\pm}\mu^{\mp}$,$e^{\pm}\tau^{\mp}$,and $\tau^{\pm}\mu^{\mp}$. Independent samples are generated with various values of Γ_t: 1.33, 0.66 GeV, 1.0 GeV, 1.66 GeV, and 2.0 GeV as described in Section 8.4. Using the event selection and procedure described in Chapter 7, the predicted $m_{b\ell}^{\text{minimax}}$ spectrum for each value of top-quark width is obtained. To smoothly interpolate predictions as a function of Γ_t, yields in each bin of $m_{b\ell}^{\text{minimax}}$ are fit to obtain a parameterized prediction $m_i = F_i(\Gamma_t)$. Quadratic functions are found to be a sufficient choice for the F_i, which can in principle be non-linear due to the changes in the shape of the distribution with varying Γ_t. After these fits, we obtain a prediction $m_i(\Gamma_t)$ and thus, given the nominal model and observed data, can write the χ^2 purely as a function of the top-quark width: $\chi^2 = \chi^2(\Gamma_t \mid d, m)$. Since this is a polynomial[25] in the width parameter, it is trivial to minimize the χ^2 and extract the corresponding best-fit width $\hat{\Gamma}_t$.

8.6 Uncertainties

The unfolded data and covariance matrix from Ref. [8] includes statistical and systematic uncertainties necessary to unfold the data (including experimental systematics as well as theory uncertainties on the unfolding model). To obtain an uncertainty on the width that is extracted using the procedure above, an additional set of uncertainties must be considered on the ($W^+W^-b\bar{b}$) signal model: namely, due to the PDF and corresponding value of α_S, the factorization and renormalization scales, and the value of the top quark mass. For each systematic m_i^{var}, the difference is computed with respect to the nominal prediction m_i^{nom} in each bin of $m_{b\ell}^{\mathrm{minimax}}$, assuming the SM value of Γ_t. This relative difference is then applied to the nominal predictions for all values of Γ_t to obtain

$$m_i^{\mathrm{var}}(\Gamma_t) = m_i^{\mathrm{nom}}(\Gamma_t) \cdot \frac{m_i^{\mathrm{var}}(\Gamma_t = \Gamma_t^{\mathrm{SM}})}{m_i^{\mathrm{nom}}(\Gamma_t = \Gamma_t^{\mathrm{SM}})}, \tag{8.10}$$

assuming that the two effects are uncorrelated. A width can then be extracted for each of the varied signal models $m_i^{\mathrm{var}}(\Gamma_t)$ using the same prescription as described in Section 8.5.

To calculate the PDF uncertainty, the matrix element calculation is repeated for each of the 100 eigenvector components of the `NNPDF` PDF set to obtain weights for each simulated event. Each of these 100 eigenvectors is used to re-weight the $m_{b\ell}^{\mathrm{minimax}}$ distribution and to extract a corresponding width. The uncertainty on Γ_t is then computed as standard deviation of the set of values obtained for each variation [318]. The affect of altering the value of α_S in the PDF is also considered, in addition to a coherent variation in the parton shower for initial-state radiation (`Var3c`) [173]. Independent events are generated with $\alpha_\mathrm{S} = 0.115$ (0.121) in the PDF and corresponding values of 0.115 (0.140) in the shower for the up (down) variations. This uncertainty is computed as one-half of the difference between the results obtained with the two variations. The effects of scale variations are considered by calculating event weights corresponding to varied μ_R and μ_f scales, up and down by a factor of two (not considering un-physical variations where the scales are altered in different directions) The uncertainty is computed as the envelope which covers the difference between each of

[25] Because nonlinear effects are small, it is practically a parabola.

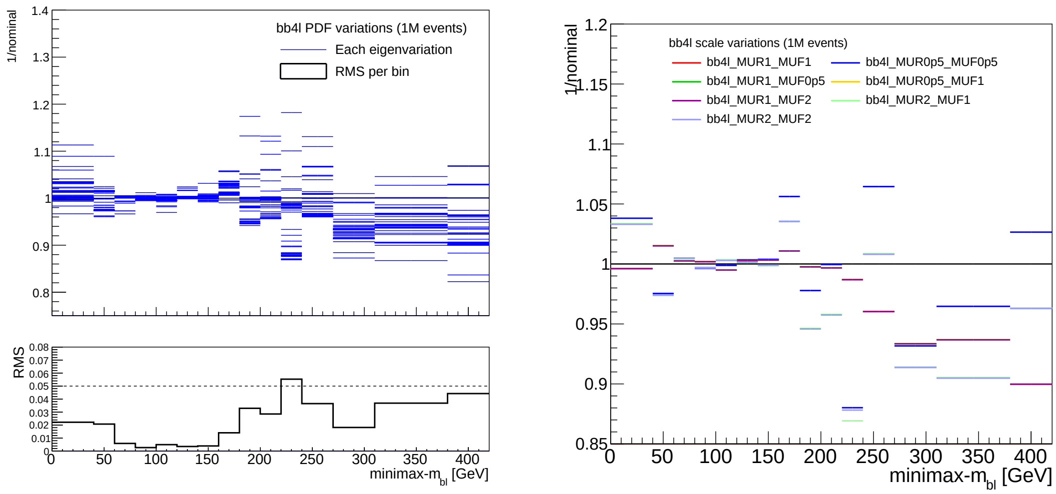

Figure 8.3: The full $m_{b\ell}^{\text{minimax}}$ distribution recalculated for systematic variations of the PDF set (left) and renormalization and factorization scales (right). The displayed values are the ratio of the varied yields to those of the nominal sample. For PDF uncertainties, the uncertainty is computed as the RMS of predictions, while the envelope is used for the scale variations.

the "seven-point" variations and the nominal prediction. Finally, alternate samples are generated with the top quark mass set to 171.5 and 173.5 GeV , with the corresponding uncertainty set to one-half the difference. Figure 8.3 displays the relative size of the PDF and scale uncertainties.

Uncertainties due to variations of α_S and m_{top} are assessed by generating independent sets of events. Because `b_bbar_4l` events are not perfectly unweighted even very large samples of events suffer from a relatively poor effective number of events beyond $\sqrt{m_t^2 - m_W^2}$ in the $m_{b\ell}^{\text{minimax}}$ distribution. To maximize the statistical power of the full set of simulated events and to ameliorate the impact of statistical fluctuations on the uncertainties which are not estimated with event weights, a fit is performed to the yields, parameterized in α_S, m_{top}, and $m_{b\ell}^{\text{minimax}}$. The fit model assumes a linear dependence on the α_S and m_{top} parameters, which is derived separately in each bin of $m_{b\ell}^{\text{minimax}}$ so that

$$m_i(\alpha_s, m_t) = \bar{m}_i(\alpha_s^{\text{SM}}, m_t^{\text{SM}}) + \bar{a}_i(\alpha_s - \alpha_s^{\text{SM}}) + \bar{b}_i(m_t - m_t^{\text{SM}}) \tag{8.11}$$

with the nominal value also allowed to float in the fit, so that the three parameters $\bar{m}$, $\bar{a}$, and $\bar{b}$ are obtained from the five variations (nominal, plus up and down variations for α_S and m_{top}), separately in each bin of $m_{b\ell}^{\text{minimax}}$. After this procedure a second step is performed that allows bin-to-bin cross-talk for the systematic variations to further reduce the un-physical statistical variation. This step requires that the variations across all eight bins of $m_{b\ell}^{\text{minimax}}$ vary quadratically in the observable[26]. The original distributions for all `b_bbar_4l` samples in addition to the parameterized predictions after the first and second fits are shown in Figure 8.4.

The calculation of the effect of uncertainty on the data itself is computed from the full covariance matrix though the use of "toys" (also "pseudo-data"). The unfolded results of Ref. [8] specify a probability density function corresponding to a vector in the measurement space of bins of $m_{b\ell}^{\text{minimax}}$. Uncertainties on the yields are generically correlated. For example, though statistical uncertainties due to the limited number of events observed in bins of the reconstructed $m_{b\ell}^{\text{minimax}}$ distribution are uncorrelated among bins, a non-diagonal response matrix implies that this is no longer true for the particle-level, unfolded distribution. Thus using the most probable values extracted from the data (d_i) as well as their covariance matrix V_{ij}, we can generate a large data set of toy data samples that encodes these relative probabilities. This is simply a multivariate Gaussian with mean $\mathbf{d}$ and covariance $\mathbf{V}$. To reflect the uncertainty in the data, the width is extracted for each toy data set, the distribution of which is shown in Figure 8.5. The median Γ_t is the nominal extracted value, with the (potentially asymmetric) 68% and 95% confidence intervals also obtained from this distribution.

Finally, the uncertainty due to the limited number of generated MC events is assessed by similar means, independently varying the original predictions m_i each simulated sample, and performing new interpolations to extract a new value of $\hat{\Gamma}_t$ from the resulting χ^2 distribution. The ensemble of extracted values of Γ_t is also shown in Figure 8.5. A summary of the uncertainties on the width extracted using both signal models is presented in Table 8.1.

For the `MG5_aMC@NLO` signal model, an identical set of uncertainties are assessed, employing the

Table 8.1: Uncertainty on the top-quark width extracted for data, with individual contributions shown from experimental, theoretical, and statistical sources.

Uncertainty [GeV]		`b_bbar_4l`	`MG5_aMC@NLO`
Experimental		+0.27/-0.26	±0.20
Theory	PDF	±0.06	±0.04
	Scale	±0.10	±0.06
	m_t	±0.03	±0.03
	α_s	±0.06	±0.04
	Combined	±0.14	±0.10
Simulation Stats.		±0.04	±0.04
Total		±0.30	±0.22

[26] In the case of the `MG5_aMC@NLO` prediction, samples are generated with 170 GeV and 175 GeV top-quark masses, instead of the 1 GeV up/down variations taken as the nominal uncertainty. As a result, the fitted variations are re-scaled by a factor of 2.5 GeV/1 GeV.

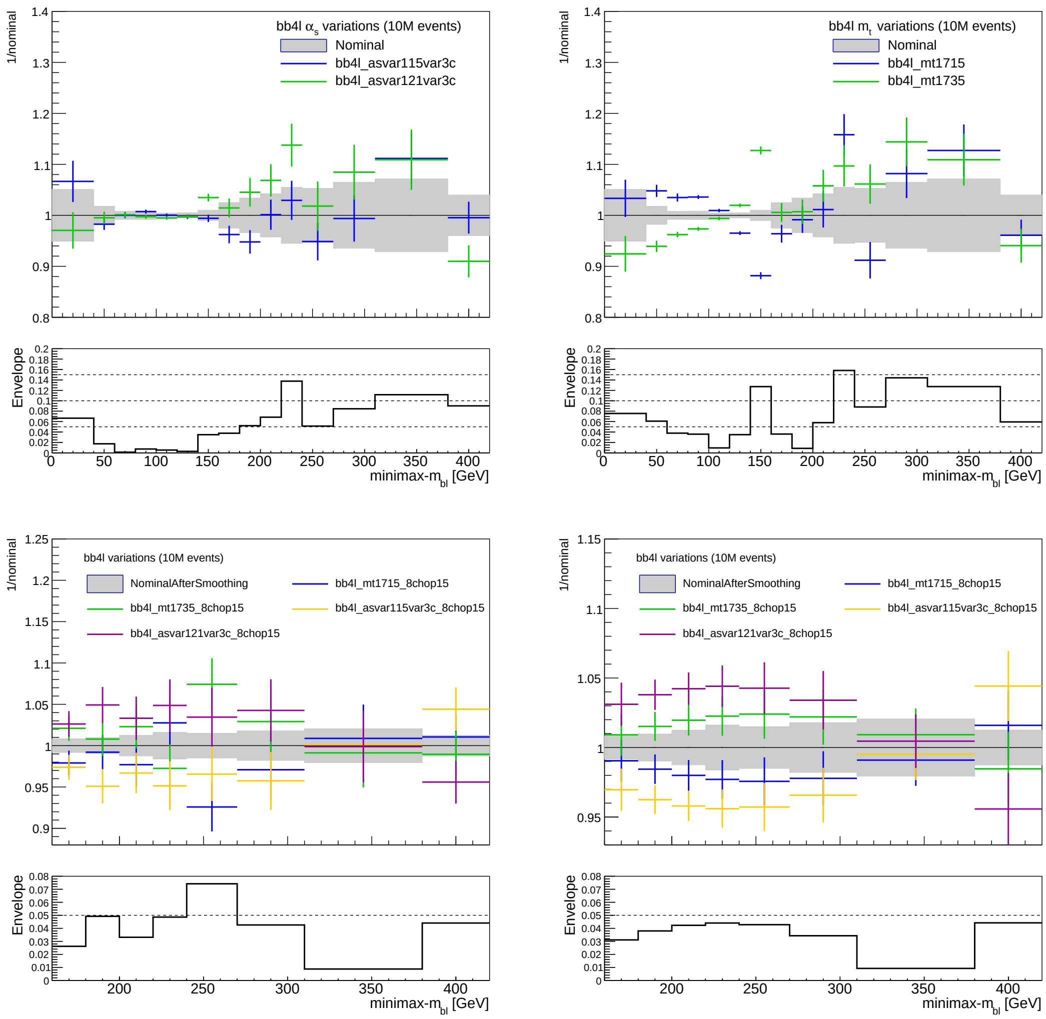

Figure 8.4: The full $m_{b\ell}^{\mathrm{minimax}}$ distribution is shown for variations of α_{S} in the PDF and parton shower (top left) as well as the top-quark mass (top right). These predictions are obtained with independently-generated sets of events and are simultaneously fit (see the text for details) to obtain a parameterized prediction of the effects of m_{top} and α_{S}, shown in stages in the lower two plots, for the range of $m_{b\ell}^{\mathrm{minimax}}$ values considered in the width extraction. The yields before (after) allowing bin-to-bin correlation for systematic variations is shown at bottom left (right).

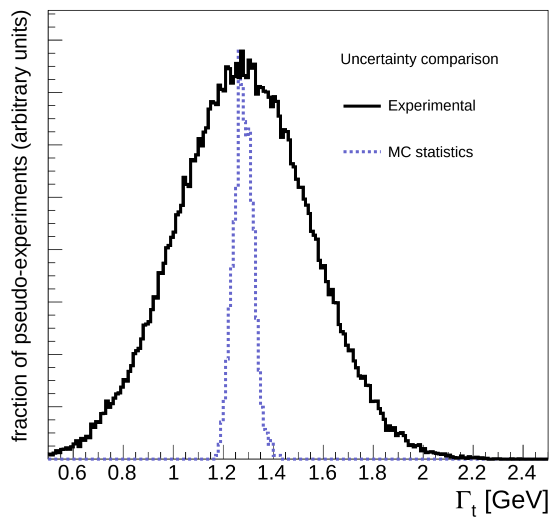

Figure 8.5: In black, the extracted Γ_t values are shown for an ensemble to 100 million toy data sets. The median is the nominal extracted value of $\Gamma_t = 1.28$ GeV, with 1σ uncertainties of 0.27 GeV up and 0.26 GeV down. Also pictured in blue is the uncertainty due to the limited number of generated MC events in the nominal samples generated for all considered values of Γ_t, leading to an uncertainty of 0.04 GeV. Values are shown for the `b_bbar_4l` signal model.

same estimation methods, with the following modification: the `NNPDF23_nlo_as_0119` PDF set is used as the nominal value for this sample. The top-quark mass uncertainty is assessed using samples with $m_t = 170, 175$ GeV, interpolating to obtain the same 1 GeV variations as used above.

8.7 Results

Comparisons of the `b_bbar_4l` and `MG5_aMC@NLO` models to the data are shown in Figures 8.6 and 8.7, respectively. As in Ref. [8], the `b_bbar_4l` model is found to model the data well, while some slope is seen in the `MG5_aMC@NLO` prediction. A width of 1.28 ± 0.30 GeV (1.33 ± 0.29 GeV expected) is extracted, from the data, as is shown in Figure 8.8. This result is more precise than the previous best direct measurement of ($1.76^{+0.86}_{-0.76}$ GeV) [259].

The value extracted using `MG5_aMC@NLO` is 1.18 ± 0.22 GeV (1.33 ± 0.23 GeV expected). The dependence of the fractional yields in this region are found to depend more strongly on the width for the `MG5_aMC@NLO` model than for `b_bbar_4l`. As a result, the uncertainty on the extracted width is found to be narrower for the `MG5_aMC@NLO` sample.

The extracted width can be compared to SM prediction in order to obtain a bound on the branching fraction of the top quark to new physics channels $\Gamma_h(t \to \text{BSM})$. Using the `b_bbar_4l`

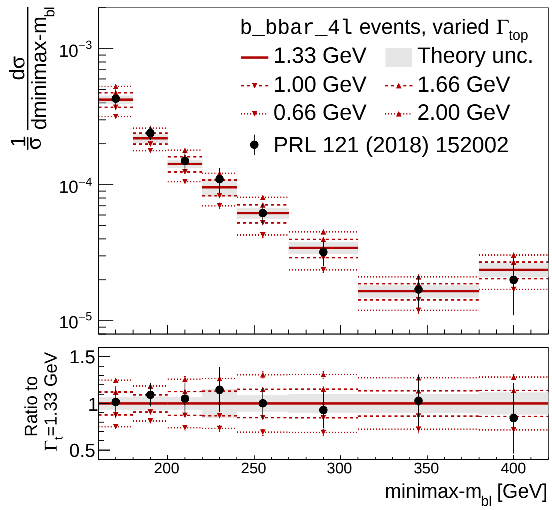

Figure 8.6: The $m_{b\ell}^{\mathrm{minimax}}$ spectrum predicted using `b_bbar_4l` is shown for various values of the top-quark width. Data from the unfolded ATLAS measurement are included for comparison. The gray band shows the theoretical uncertainty for the simulated sample corresponding to the predicted SM value of the width.

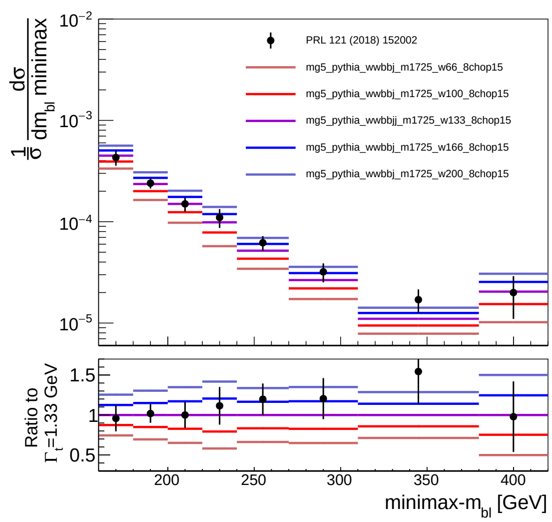

Figure 8.7: The $m_{b\ell}^{\mathrm{minimax}}$ spectrum predicted using `MG5_aMC@NLO` is shown for various values of the top-quark width. Data from the unfolded ATLAS measurement are included for comparison.

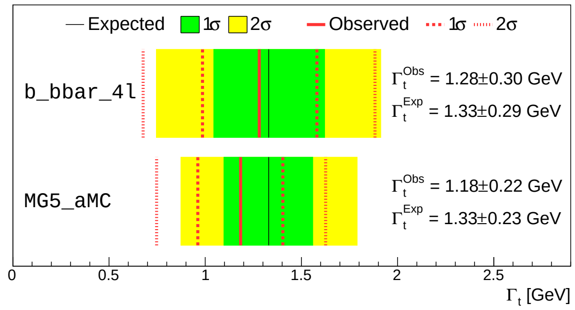

Figure 8.8: Observed and expected top-quark widths for the `b_bbar_4l` and `MG5_aMC@NLO` signal models.

signal mode, we constrain the width to be less than $\Gamma^{+95\%} = 1.88$ at the 95% confidence level. Thus we find a corresponding limit

$$\mathcal{BR}(t \to \text{BSM}) < \frac{\Gamma^{+95\%} - \Gamma^{\text{SM}}}{\Gamma^{+95\%}} = 29\%. \tag{8.12}$$

The expected value is $\mathcal{BR}(t \to \text{BSM}) < 25\%$.

8.8 Further constraints on BSM physics

Model-specific BSM constraints are also possible for processes which have a significant effect in the off-shell region defined by high $m_{b\ell}^{\text{minimax}}$. For example, a charged Higgs H^+ produced via its btH^+ coupling and then decaying via $\tau\nu$ would preferentially enhance this region. However, limits from this measurement are not as strong as direct searches [319–321] because of the rate penalty from requiring the τ decay to e or μ with sufficient transverse momentum to pass selection.

From the direct width extraction procedure presented above, constraints may be placed on BSM theories which allow yet-undetected top-quark decays. However, if a new particle coupling to the top quark is sufficiently heavy, it may have little or not contribution to the width. This is accomplished in models including additional charged Higgs particles $H^\pm$ or a $W'^\pm$ that couples preferentially to third-generation fermions. Such processes may still modify the $m_{b\ell}^{\text{minimax}}$ spectrum when produced in association with a single top quark and thus can be constrained from data using a similar approach as was taken to measure the top-quark width.

Signal models are studied using the `MG5_aMC@NLO` Monte Carlo generator interfaced to `Pythia` using the same settings described above. Events from the $bbH^\pm W^\mp$ process are simulated, where the $H^\pm$ is produced via a coupling to top and bottom quarks g_{Htb} and decays via $H^+ \to \tau^+\nu_\tau$ with coupling strength $g_{H\tau\nu}$. We assume that the new particle is narrow, so that interference effects with

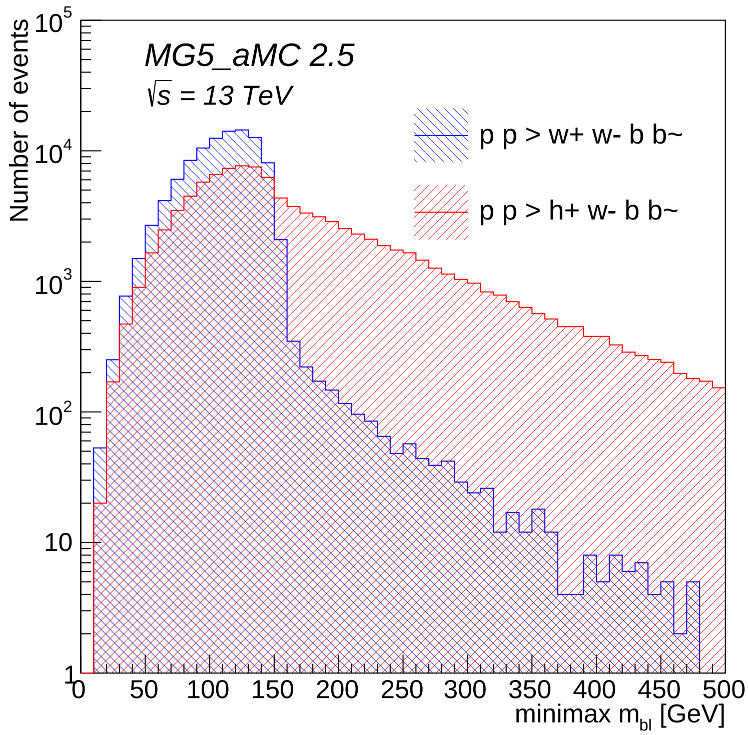

Figure 8.9: The parton-level $m_{b\ell}^{\mathrm{minimax}}$ distribution for $W^+W^-b\bar{b}$ and $H^+W^-b\bar{b}$ events is compared. Events are shown which pass the two charged lepton and two b quark selection for the width extraction analysis. The charged Higgs is assumed to only couple to third generation particles and is forced here to decay $H^+ \to \tau^+\nu_\tau$ with the τ^+ subsequently yielding a e^+ or μ^+. A charged Higgs contribution would significantly increase the number of observed events in the region $m_{b\ell}^{\mathrm{minimax}} > m_{\mathrm{top}}$.

the top quark may be neglected. For charged Higgs masses $m_{H^\pm} > m_t$, only single-top production modes are relevant and both the signal acceptance and shape in $m_{b\ell}^{\mathrm{minimax}}$ are found to be largely insensitive to $m_{H^\pm}$ over the studied range.The shape comparison is shown in Figure 8.9, where the $m_{b\ell}^{\mathrm{minimax}}$ observable is plotted for $W^+W^-b\bar{b}$ events as well as $H^+W^-b\bar{b}$. Here the charged Higgs mass is set to 250 GeV. As the charged Higgs events have a much longer tail for $m_{b\ell}^{\mathrm{minimax}} > m_{\mathrm{top}}$, which should cause an observable difference in the measured $m_{b\ell}^{\mathrm{minimax}}$ tail probed in Ref. [8].

`MG5_aMC@NLO` is used to calculate the cross section for the $H^+W^-b\bar{b}$ process as a function of the charges Higgs mass. In addition to the mass dependence, this requires an assumption on the value of g_{Htb}. Figure 8.10 shows the mass dependence where this coupling has been set equal to the SU(2) coupling so that $\sigma(H^+W^-b\bar{b}) = \sigma(W^+W^-b\bar{b})$ when $m_{H^+} = m_{W^+}$. The cross section falls rapidly as m_{H^+} approaches m_{top}, after which the top decay closes and only the single-Higgs production

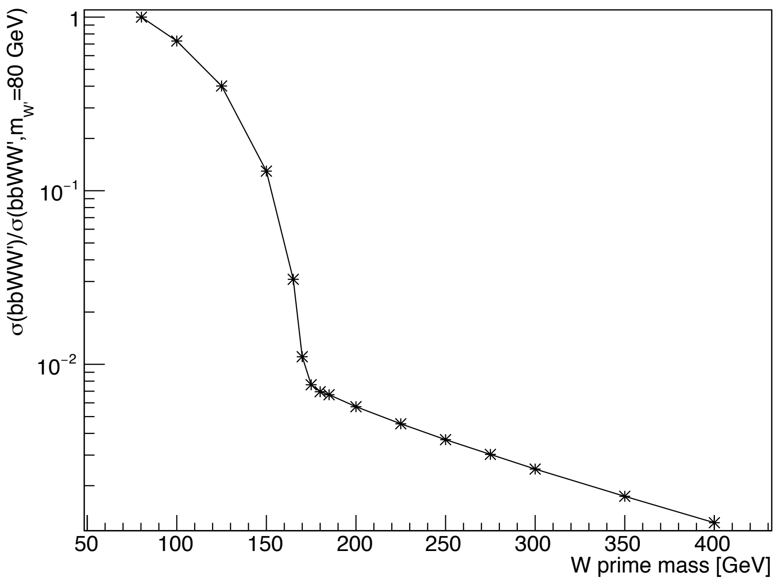

Figure 8.10: The cross section to produce $H^+W^-b\bar{b}$ events is presented as a function of the charged Higgs mass. The g_{Htb} coupling leading to Higgs production is taken to be identical to the SU(2) weak coupling g_{Wtb} so that $\sigma(H^+W^-b\bar{b}) = \sigma(W^+W^-b\bar{b})$ when $m_{H^+} = m_{W^+}$. The cross section can be obtained for other coupling values by rescaling ($\sigma(H^+W^-b\bar{b}) \propto g^2_{Htb}$). For charged Higgs masses below the top-quark mass, the dominant production process is through $t\bar{t}$ diagrams, while single-top diagrams dominate for larger Higgs masses.

channel remains open.

A constraint can be placed on $H^{\pm}/W'$ production taking `b_bbar_4l` simulation as the SM background prediction, where nominal values are set for each of the configurable parameters. A similar $\chi^2(d_i, m_i)$ construction is used as above, with the model m_i to test consisting of contributions from the `b_bbar_4l` background prediction b_i and the $bbH^{\pm}W^{\mp}$ signal, with a contribution controlled by signal strength parameter μ:

$$m_i(\mu) = b_i + \mu \cdot s_i \tag{8.13}$$

The distribution of the test statistic under the background-only hypothesis $\mu = 0$ is determined from an ensemble of pseudo-experiments where the data is varied within uncertainties. The excluded signal strength μ^{excl} is the value such that $\chi^2(d_i, m_i(\mu = \mu^{\text{excl}}))$ is larger than $\chi^2(d_i, m_i(\mu = 0))$ for 95% of the toy experiments described above.

Using this method we set limits on the g_{Htb} coupling as a function of the charged Higgs mass, shown in Figure 8.11. For a mass of 250 GeV, the coupling is constrained to be less than unity, while the coupling is ust be less than the weak coupling $g_2/\sqrt{2}$ if $m_{H^+} = m_{\text{top}}$. For large values of

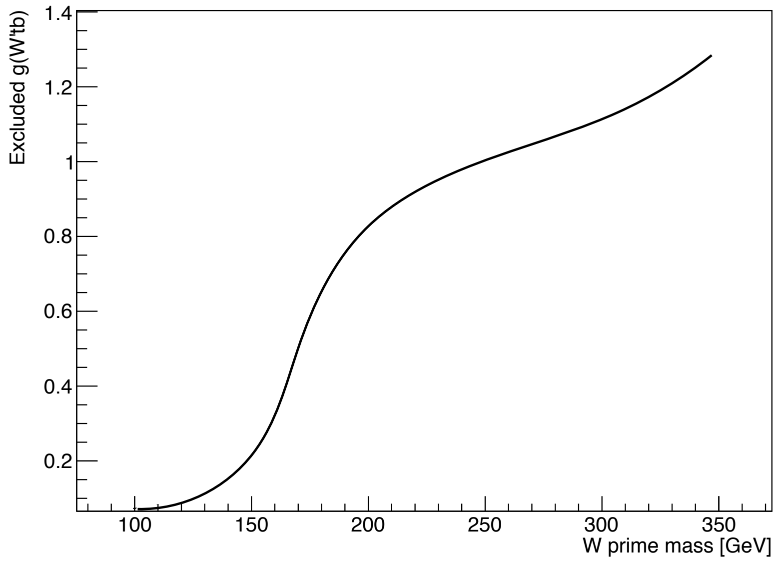

Figure 8.11: The value of the coupling between a $W'^{\pm}$ (or $H^{\pm}$), top, and bottom quark $g_{W'tb}$ that is excluded at the 95% confidence level, as a function of the W' mass. Limits are obtained from the data presented in Ref. [8] treating the W' in the NWA and assume that $\mathcal{BR}(W' \to \tau\nu) = 100\%$. See the text for a discussion of these assumptions for large W' masses.

g_{Htb} a more careful treatment is required, as the decay width $\Gamma_{H^+ \to t\bar{b}}$ becomes significant enough that (a) this second decay channel should be considered, and (b) the NWA may no longer be a good approximation. As an example, for the excluded value[27] of $g = 0.8$ for $m_{H^+} = 200\,\text{GeV}$ we find $\Gamma_{H^+}/m_{H^+} \approx 10\%$ and $\mathcal{BR}(H^+ \to \tau^+\nu_\tau) \approx 90\%$. This largely justifies the assumptions, while for $m_{H^+} = 250\,\text{GeV}$ the width is 20% the mass and $\mathcal{BR}(H^+ \to \tau^+\nu_\tau) \approx 50\%$ so that a more nuanced analysis should be adopted.

These results present a complimentary strategy to charged Higgs searches by the ATLAS and CMS Collaborations [319–321]. The current most stringent limit of $\sigma(bbH^+W^-) \times \mathcal{BR}(H^+ \to \tau^+\nu_\tau) < 0.2$ pb for $m_{H^\pm} = 200$ GeV comes from an ATLAS analysis of 13 TeV data [319]. The recast limit is weaker than dedicated analyses, as it relies on fully leptonic tau decays significantly decreasing the signal acceptance. However, the technique could be easily extended to hadronic tau decays, presenting a simple and powerful alternative to conventional search strategies.

[27] This corresponds to an excluded $H^+W^-b\bar{b}$ cross section of about 5.0 pb.

Chapter 9

Conclusions and Outlook

The paradigm of naturalness suggests that the top quark will play a central role in explaining the light mass of the recently-observed Higgs boson. Thus, the main work described in this dissertation has explored how the top quark may be used to shed light on the nature of this new physics. This has been completed in the form of a direct search for new particles associated with SUSY, as well as with a measurement of top-quark properties, sensitive to new physics effects.

A search for pair-production of supersymmetric partners of the top quark using events with one isolated lepton dramatically increased the experiment's sensitivity to stops, with respect to previous searches. In the minimal simplified model interpretation where only a stop and stable LSP are introduced (with the $\tilde{t}\tilde{t}^* \rightarrow t\bar{t}\tilde{\chi}_1^0\tilde{\chi}_1^0$ decay considered) stops are excluded up to masses of about 1 TeV. This represents a significant improvement with respect to the previous best limits, obtained with the 8 TeV Run 1 LHC data, which excluded stops up to a mass of about 650 GeV. This scenario has also been tightly constrained in the experimentally challenging regime where the mass difference $\Delta(m_{\tilde{t}}, m_{\text{LSP}})$ is small and the associated decay products have low transverse momenta.

Strong constraints were also set on models motivated more directly by naturalness, where the LSP is part of a Higgsino multiplet. A broad analysis was designed to maximize sensitivity to all possible decay modes of the stop in this scenario, with particular effort towards the identification of soft leptons from Higgsino cascade decays. Following improvements over the 8 TeV analysis, limits in the Higgsino scenario are significantly more robust. These limits on the allowed stop mass values are now largely independent of SUSY model parameters that may, for example, reduce the relative fraction of decays in the most-extensively-studied $\tilde{t} \rightarrow t\tilde{\chi}_1^0$ mode. Further, the sensitivity is largely independent of the Higgsino mass splitting $\Delta(m_{\tilde{\chi}_1^\pm}, m_{\tilde{\chi}_1^0})$ down to values as small as 2 GeV.

In the course of the stop analysis, the theoretical uncertainty associated with the modeling of interference between $t\bar{t}$ pair production and tWb single top production was found to be large. A two-prong approach was taken in response to these studies. First, the search regions most sensitive to this effect were redesigned to use a data-driven background estimation technique that reduced the size of the effect. Second, a new measurement (Ref. [8]) was designed to push forward progress in understanding the theoretical origins of the effect. The resulting differential measurement of the $m_{b\ell}^{\text{minimax}}$ spectrum in events with two leptons and b jets provided a first direct test of the two standard theoretical schemes used to approximate the effect. Neither of these standard schemes described the data well, though the conventional practice of assigning their difference as an uncertainty appears justified. However, a recent state-of-the-art NLO+PS calculation of the $\ell^+ l^- \nu\bar{\nu}b\bar{b}$ process was also directly compared to data for the first time, with excellent agreement observed. The success of this next-generation MC tool will pave the way for its expanded use in future top-quark measurements and searches where precise modeling is critical.

9.1 Perspectives on Measurements of Top-Quark Production

Having completed a period of intense analysis of top-quark processes, it is a natural opportunity to reflect on this work and to consider the future of such measurements and what exciting prospects may lie ahead. As both analyses of the $m_{b\ell}^{\text{minimax}}$ differential distribution, as a constraint on $t\bar{t}-tWb$ interference and on the top-quark width, were performed for the first time there are likely many related directions that one could explore.

First, the width extraction in Ref. [9] was a re-interpretation of the existing ATLAS measurement so that the analysis itself was not optimized for sensitivity to this parameter. Despite this, a world's-best direct constraint was obtained and the top-quark branching fraction to new physics channels was limited to be less than 29%. While an interesting first result, the BSM models discussed in Chapter 8 typically lead to effects on the order of five percent. Thus, it will be critical for LHC experiments to conduct a fully optimized analysis in the future.

One important lesson from this work was that the constraining power on Γ_{top} came dominantly from measurements of $m_{b\ell}^{\text{minimax}}$ in the region just beyond the on-shell $t\bar{t}$ kinematic endpoint: roughly 160-220 GeV. In contrast, sensitivity to the interference term is maximized at the largest measured values of the $m_{b\ell}^{\text{minimax}}$ spectrum, where the analysis is dominated by a different set of uncertainties. Improving the precision on the extracted width will depend on the reliability of models of b-quark hadronization and fragmentation, as these effects allow on-shell $t\bar{t}$ to fluctuate above the $m_{b\ell}^{\text{minimax}}$ kinematic endpoint. Fortunately, MC shower programs continue to provide improved descriptions of data, driven by theoretical advances as well as an ever-increasing set of LHC measurements for comparison. In tandem, important experimental uncertainties related to the determination of the jet energy scale and resolution should improve as the full Run 2 data-set allows for enhanced determinations. Thus, there is reason to believe that an improved understanding of experimental and theoretical factors would bring increased precision to a dedicated width measurement. A sub-10% measurement would serve as an interesting theoretical target.

At the same time, the full Run 2 data-set presents an interesting opportunity to better understand the interference effect, and to provide more useful comparisons for new MC programs. While neither of the traditional DR nor DS schemes for modeling the interference agreed well with the data, the difference between the two predictions in the interference-sensitive region was typically at the 2σ level. While already useful for relative comparisons of these two schemes with the NLO+PS $\ell^+ l^- \nu\bar{\nu} b\bar{b}$ prediction, a more precise measurement might provide further evidence towards the use of one scheme over the other.[28] For the largest values of $m_{b\ell}^{\text{minimax}}$ that drive the sensitivity of this measurement to the interference effect, the largest uncertainties come from data statistics, $t\bar{t} + b\bar{b}$ modeling, and the impact of interference on the unfolding procedure. Each of these uncertainties should be reduced in a future analysis: data statistics will see a $\sqrt{N}$ improvement with a 13 TeV data-set now collected that is ≈ 4 times larger than that analyzed in Ref. [8]; $t\bar{t} + b\bar{b}$ modeling has improved significantly following intense interest from the experimental [322–327] and theoretical [328–332] communities (driven by its importance as a background for $t\bar{t}(H \to b\bar{b})$ measurements); a dedicated DR-versus-DS uncertainty is no longer necessary with an NLO+PS calculation of the interference effect available. Understanding top-quark processes with high precision relies on a diverse program of top-quark measurements, and will aid in the continued quest to identify subtle BSM phenomena.

9.2 Perspectives on Searches for Natural Supersymmetry

Following the impressive suite of analyses of LHC data to date, there has been no clear experimental indication for the presence of SUSY. A large variety of searches have been conducted, severely constraining the space of SUSY models that are consistent with present experimental results. However, for the reasons described in Chapter 3, SUSY remains an attractive property of BSM theories, and in particular the argument for TeV-scale SUSY remains compelling. If TeV-scale SUSY has indeed been realized in nature, current null results may be explained either by sparticle masses that are

[28] Even given the superior description of `b_bbar_4l`, the relative agreement of DR and DS schemes remains interesting as they can be combined with separate, widely-studied calculations of the $t\bar{t}$ process in the on-shell regime.

beyond the reach of present collider searches or a SUSY mass spectra that yields experimentally difficult signatures.

If SUSY is simply beyond the reach of present analyses, it is useful to investigate the improvements anticipated for future LHC searches. This has been explored in detail in a number of studies motivating upgrades to the ATLAS detector in addition to other future collider scenarios. Ref. [333] studied the gluino pair-production process, comparing results obtained at the end of Run 3 ($300\,\text{fb}^{-1}$) with those of the full HL-LHC program ($3\,\text{ab}^{-1}$). For the case of a massless LSP, the 10x larger data-set improves the excluded gluino mass from 2.4 TeV to 2.9 TeV. The corresponding limit with $36\,\text{fb}^{-1}$ of 13 TeV data is 2.1 TeV [334]. Ref. [335] projects an increase in the mass reach for top squarks in the massless LSP scenario of $m_{\tilde{t}} < 1.6$ TeV with $3\,\text{ab}^{-1}$, focusing on the zero-lepton final state. This is a 600 GeV increase with respect to the Run 2 analysis [336], which was conducted with a factor of 100x less data. For direct Higgsino production, limits have been set as a function of the Higgsino mass splitting $\Delta(m_{\tilde{\chi}_1^0}, m_{\tilde{\chi}_1^\pm})$, with chargino masses up to 150 GeV excluded (for $\Delta m \sim 4$ to 5 GeV) with the $36\,\text{fb}^{-1}$ data-set [337]. With $3\,\text{ab}^{-1}$ the reach is projected to extend as far as 350 GeV (for $\Delta m \sim 2$ to 3 GeV[29]) [117]. The excluded sparticle masses are compared for each data-set in Table 9.1.

The message of these projections is that the upgrade to a *pp* collision center-of-mass energy of $\sqrt{s} = 14$ TeV and HL-LHC integrated luminosity of $3\,\text{ab}^{-1}$ (or more) will promise to open up new

Table 9.1: Actual and projected excluded sparticle masses are shown as a function of the collected data-set for benchmark SUSY signatures. In all scenarios the LSP is assumed to be massless. See the text for a description of the description of the experimental signatures considered as well as references to each analysis. Analyses for which no projections are available are marked as '–'.

	Period	2015+16	Run 3	HL-LHC
Data-set	$\int \mathcal{L}$	$36\,\text{fb}^{-1}$	$300\,\text{fb}^{-1}$	$3\,\text{ab}^{-1}$
	$\sqrt{s}$	13 TeV	14 TeV	14 TeV
(Projected) masses exclusion limit	Gluino $\tilde{g} \to q\bar{q}\tilde{\chi}_1^0$	2.1 TeV	2.4 TeV	2.9 TeV
	Stop $\tilde{t} \to t\tilde{\chi}_1^0(0\ell)$	1.0 TeV	–	1.6 TeV
	Higgsino $(2\ell + E_{\text{T}}^{\text{miss}})$	150 GeV	–	350 GeV

[29] While technically the quoted mass reach is highly dependent on the mass splitting and thus the quoted Higgsino mass exclusions are not directly comparable, it is reasonable to assume that with a further optimized analysis the HL-LHC sensitivity will extend to larger mass splittings.

parameter space for a range of interesting sparticle masses. However, the message is also that each subsequent improvements to the analyses, measured in hundreds of GeV of sparticle mass probed, comes at progressively longer intervals of time. The 13 TeV data-set increased by a factor of ten from 2015 to 2016. The next factor of ten will not likely come before the end of Run 3 in 2023. The final factor of ten is projected as the ultimate HL-LHC goal to be attained perhaps near 2038, requiring fifteen further years of operations.

It is critical that the large program of SUSY searches in place continue as the integrated luminosity accumulates over the operational lifetime of the LHC to make maximal progress towards a discovery of SUSY. However, the long time-scale associated with these searches highlights the importan of the second possibility to consider – what if the production cross section for TeV-scale SUSY particles is significant, but the specific signature has not yet been accessed by current searches? This may be because most such events are difficult to reconstruct, identify, or trigger on, as is the case with small-mass-splitting Higgsinos. Or it may that the analysis would be perfectly tractable except that no one has conducted it yet, either due to technical difficulty or lack of imagination. Various models of R-parity violating SUSY may enter the latter category.

A compelling scenario in the context of stop searches is the well-tempered neutralino (Bino LSP with light Higgsino) scenario introduced in Section 6.3.2. This model provides a DM candidate satisfying the relic density constraint, as well as including a light Higgsino and a light stop, thus fulfilling all three of SUSY's most idealistic promises: to unify the gauge couplings, to provide a DM candidate, and to solve the hierarchy problem. The combined exclusions in this scenario are shown in Figure 9.1, based on the zero- and one-lepton stop analyses (Refs. [336] and [7]). It is observed that viable models remain where the Higgsinos are as light as 250 GeV and the stop as light as 500 GeV.[30] The future direction of stop searches must include renewed efforts to access this and similar phase-space to ensure that such attractive models are covered where possible.

Finally, supersymmetric theories should continue to be considered regardless of whether they provide a DM candidate, which may only be suggested (but not required!) to be a weak-scale particle. In fact, supersymmetric theories with axion DM provide a novel target for future LHC searches (see Ref. [338] for example). Decoupling this requirement opens a larger range of interesting models into consideration, including the R-parity violating $B - L$ MSSM models discussed in Section 3.4 and investigated further in Appendices A and B. These theories predict a range of long-lived BSM particles that may be targeted with specialized analysis techniques and often require non-standard trigger strategies. Further, effective lepton-number violating operators in $B - L$ MSSM theories lead

[30] Perhaps even lighter stops remain feasible, as 500 GeV is the lightest mass considered in this exercise.

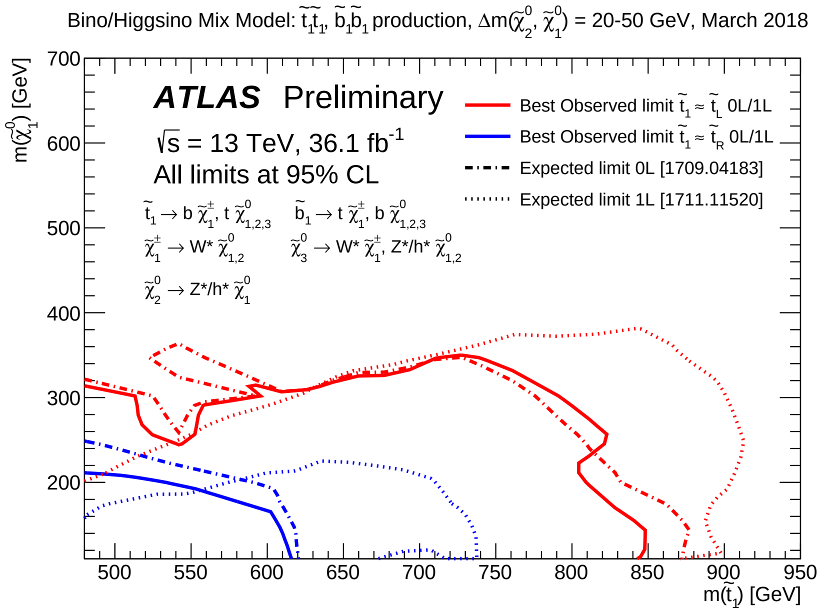

Figure 9.1: Combined exclusions in the well-tempered neutralino scenario from the zero- and one-lepton stop searches [7, 336].

the LSPs (inferred in R-parity conserving (RPC) SUSY searches as $E_{\mathrm{T}}^{\mathrm{miss}}$) to decay in combinations of charged and neutral leptons. This could suggest a broad program of converting existing RPC searches into RPV-targeted ones by looking in "four-lepton plus X" events with moderate $E_{\mathrm{T}}^{\mathrm{miss}}$. Related strategies have been considered in the past by ATLAS [339], targeting electroweakino and gluino production. Other interesting signatures to pursue in the future may include stop production and exotic decays of the Higgs boson.

Appendix A

A Bino LSP in the $B - L$ MSSM

In Section 3.4.1 the $B - L$ MSSM was introduced, which extends the MSSM with three right-handed neutrinos, one of which has a sneutrino partner that develops a VEV and breaks SUSY. This also leads to VEVs for the left-handed sneutrinos, which directly lead to RPV (lepton-number violating) terms.

A.1 Random Parameter Scan

In a series of results, the possible LHC-energy phenomena predicted by this model have been studied by Ovrut and collaborators [11,58,61,340–343]. In the absence of a complete description of the SUSY-breaking mechanism that would dictate the soft SUSY-breaking mass terms, the phenomenology of the model is tested with a random scan and statistical evaluation of these parameters. The soft masses are scanned at the SUSY-breaking scale (typically taken to be several TeV to avoid the development of a new hierarchy) and the one-loop RG equations are used to run the parameters to the electroweak scale. With this technique, the physical masses are not distributed with complete randomness, but rather encode the physical information of the RG equations. The most striking effect is that this causes the Bino to be the LSP more than any other sparticle, despite its respective SUSY-breaking scale mass parameter being randomly thrown in the same manner as each of the others. The full distribution of LSPs obtained in the scan conducted in Ref. [11] was shown in Figure 3.2 in Chapter 3. All points in the random scan are required to break electroweak symmetry, satisfy all experimental lower bounds on sparticle masses, and to reproduce the observed Higgs boson mass. The population of points satisfying each of these criteria is shown in Figure A.1. The distribution of LSPs found in the scan was shown in Figure 3.2 of Chapter 3 and the masses of the

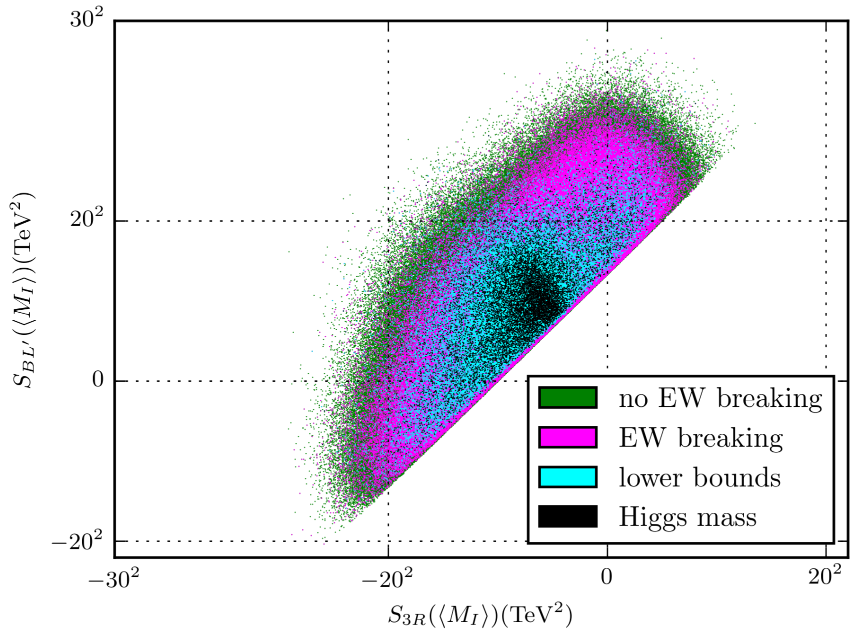

Figure A.1: The population of all studied model points obtained in the random parameter scan, colored according to whether they pass each of the electroweak symmetry-breaking, sparticle bounds, and Higgs mass criteria. Points are plotted versus two S-terms corresponding to different sets of squared soft mass terms and are defined in Ref. [343].

LSPs that are majority-Bino are shown in Figure A.2.

A.2 Decays of the Bino LSP

Due to the presence of RPV terms, the Bino LSP may decay. These decays proceed via the emission of electroweak gauge bosons as illustrated in the vertices shown in Figure A.3. The lepton number violating terms are generated by the development of a VEV by one of the sneutrinos and are thus do not generally maintain the principle of lepton flavor universality apparently respected by the SM. Thus, the RPV couplings associated to each of the vertices in Fig. A.3 may attain a different value for each lepton generation.

From this information the partial widths may be separately calculated for each of the $3 \times 3 = 9$ decay channels via each lepton flavor and electroweak boson. These widths are shown for the case $m_{\tilde{\chi}^0_B} > 100\,\text{GeV}$ in Figure A.4. If all amplitudes for RPV processes are small, and since no other decay modes for the Bino are possible, the Bino could live for a significant time before decaying. Thus the partial widths for each decay channel are shown in units of millimeters in

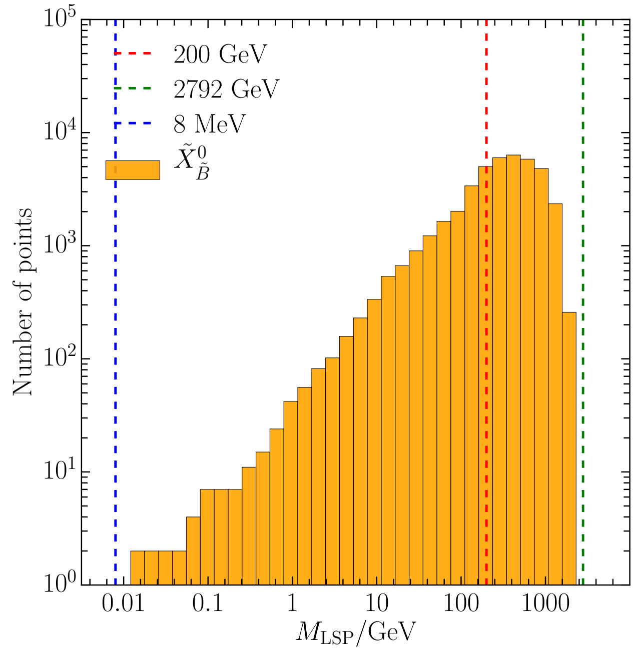

Figure A.2: The mass of the LSP for points in the random scan where the particle is a neutralino with majority Bino component. All soft masses are scanned in a range from 200 GeV to 10 TeV, resulting in a lightest (heaviest) Bino LSP of 8 MeV (2792 GeV). Note that a significant number of Bino masses are smaller than the M_1 lower bound of 200 GeV due to RG running and cancellations among contributing terms.

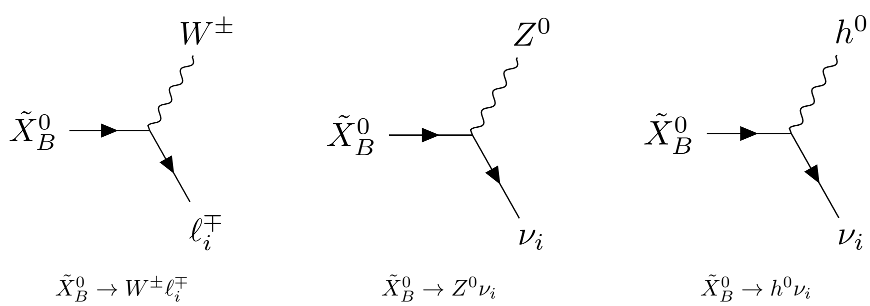

Figure A.3: Lepton number violating vertices present in the $B - L$ MSSM allowing the decay of the Bino LSP.

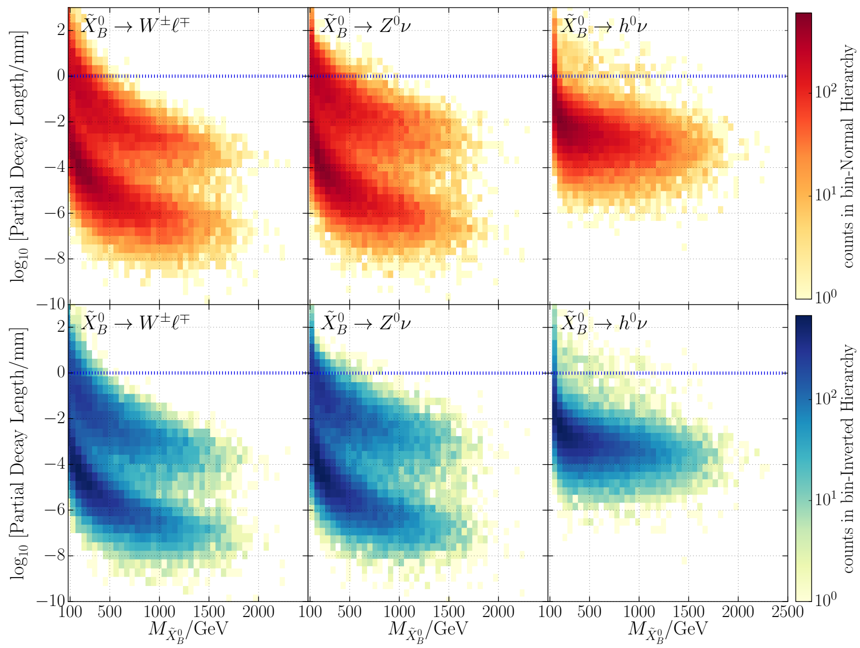

Figure A.4: The partial decay widths are shown as a function of the Bino mass seperately for the decay modes corresponding to each of the three electroweak boson decay channels, in the case that the $\tilde{\chi}^0_B$ is greater than 100 GeV. The reciprocal of the widths are expressed to give "partial decay lengths", comparing the size of the contribution relative to that needed to produce promptly reconstructable objects in the detector (roughly 1 mm). Note that the lengths add as $1/l_{\text{tot}} = \sum_i 1/l_i$ to produce shorter overall lifetimes. Values of the lifetime are shown separately for each assumption on the neutrino mass hierarchy.

Fig. A.4, roughly corresponding to the scale at which prompt object reconstruction is relevant for collider experiments[31].

A.3 Low Mass Bino LSPs

In the case of $m_{\tilde{\chi}^0_B}$ greater than the mass of the electroweak bosons, the calculation is straightforward, with analytic expressions for the decays given in Ref. [58]. For Bino LSP's lighter than the Higgs boson mass, the widths may be calculated in a similar manner, simply by ignoring the Higgs channel, whose off-shell contribution is negligible due to its very small width. For practical purposes, this is also true for Bino particles in the range $m_W < m_{\tilde{\chi}^0_B} < m_Z$, with the width dominated by the on-shell W channel. In the case of an even lighter Bino, a numerical calculation is used to evaluate

[31] Note however that the total decay length is not computed additively from the partial decay lengths $l_{\text{partial}} = c\tau_{\text{partial}} \sim 1/\Gamma_{\text{partial}}$, but rather as $1/l_{tot} = \sum_i 1/l_i$, since it the reciprocal of the total width.

the amplitudes. This is necessary because the on-shell approximation is no longer valid and instead the full electroweak bosons' line-shapes must be taken into account. This calculation is done using `MG5_aMC@NLO` 2.6.4 [27] with a trick used to avoid having to implement the specific details of each $B-L$ MSSM point in model space.

Consider the RPV decay $\tilde{\chi}_B^0 \to \tau^+(W^{-(*)} \to e^-\bar{\nu}_e)$ proceeding via the emission of a virtual W boson. This is similar to the structure of the SM process $\mu^- \to \nu_\mu(W^{-(*)} \to e^-\bar{\nu}_e)$ with the following important differences: the muon mass is fixed while the Bino mass is a free parameter to be scanned; the coupling structure associated with the W emission is the weak coupling instead of an RPV one, and; a massless neutrino is emitted instead of a τ^+. Thus the second (SM) process may be used to obtain results for the first process, making the appropriate substitutions. Namely, for this process the muon and muon neutrino masses must be reset in the program to the desired Bino mass and the tau mass, respectively. Further, the weak coupling in the SM process must be replaced by an effective RPV coupling, using the scaling relation $\Gamma \propto g^2$ between the width Γ and Bino decay coupling g.

The extension to all possible W decay channels is straightforward, while the generalization to Z- and h-mediated decays is more subtle. In the latter cases both couplings in the $\mu^- \to \nu_\mu(W^{-(*)} \to e^-\bar{\nu}_e)$ process must be replaced either by the Z boson's coupling to the various fermion-anti-fermion pairs and the relevant Higgs Yukawa and gauge couplings. In addition to coupling effects, the mass and width of the intermediate boson lead to differences in the relative rates of the off-shell decays. These can be accounted for by directly altering the value of the W mass and width in the `MG5_aMC@NLO` configuration. For the case of the intermediate Z boson the masses of the subsequent decay products can become relevant (most notably the $Z \to b\bar{b}$ decay) at low Bino mass, so the individual partial widths are calculated separately and combined. The case of Higgs decays is complicated by the fact that the Higgs decay products may also be off-shell, as in the $h \to W^+W^-$ and $h \to ZZ$ decays, so the relative rates as a function of the Higgs virtuality is taken from Ref. [2].

Figure A.5 shows the dependence of the partial width for decays corresponding to each electroweak boson on the Bino mass. Here the partial width corresponding to all W boson-mediated decays (for example) is written as

$$\Gamma_{\tilde{\chi}_B^0 \to We} = g^2_{\tilde{\chi}_B^0 \to We} \mathcal{F}(m_{\tilde{\chi}_B^0}, m_W, \Gamma_W, m_e) \sum_{f,f'} g^2_{W \to ff'} \tag{A.1}$$

where the coupling dependence and kinematic dependence have been factorized. Note that if the massless approximation for the boson decay products is poor then the kinematic function $\mathcal{F}$ must be separately computed for each decay mode yielding a more complicated equation than the one given

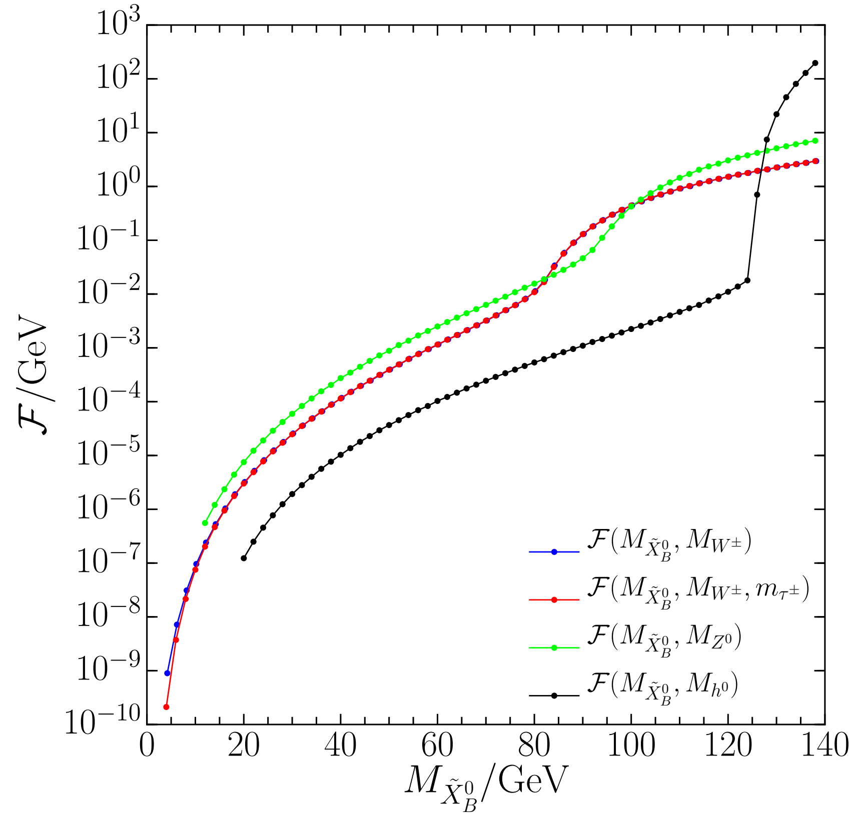

Figure A.5: The dependence of each Bino partial width on the Bino mass, with coupling contributions factorized out. See the text for detailed definitions and explanation.

above. In such cases in Fig. A.5, we have combined the separate functions into a single effective function by means of a coupling-weighted average. Separate functions are provided for each of the decays via $W/Z/h$. Because the neutrinos are mass degenerate, the only differences amongst the three sets of $\tilde{\chi}^0_B \to Z\nu_i$ and $\tilde{\chi}^0_B \to h\nu_i$ decays are due to the values of the RPV coupling which may vary for each point in model space considered. In the case of $\tilde{\chi}^0_B \to W^\pm \ell^\mp_i$ there is also a weak dependence on generation that enters via the charged lepton mass. The small size of the effect is shown by presenting the kinematic function for a massless lepton as well as for a massive tau. Tables A.1 and A.2 show the relative branching fraction of the electroweak bosons to each fermion pair for the case of an intermediate Z and h particle as a function of the Bino mass (an effective proxy for the off-shell boson mass). As the W boson decay products are all essentially massless the on-shell SM values remain valid. The partial widths for the case where no on-shell decays are allowed are shown in Figure A.6.

Table A.1: Branching fractions for decays of the virtual Z boson for the $Z \to \overline{f}f$ process for several values of the $\tilde{\chi}^0_B$ mass. The reference values for on-shell Z decays ($m_{\tilde{\chi}^0_B} > m_Z$) are taken from Ref. [1].

Process	Z^0 branching fractions for $Z^0 \to \overline{f}f$ decays (in %)		
	$M_{\tilde{\chi}^0_B} > M_{Z^0}$	$M_{\tilde{\chi}^0_B} = 60$ GeV	$M_{\tilde{\chi}^0_B} = 30$ GeV
$Z^0 \to e^{\pm}e^{\mp}$	3.4	3.4	3.6
$Z^0 \to \mu^{\pm}\mu^{\mp}$	3.4	3.4	3.6
$Z^0 \to \tau^{\pm}\tau^{\mp}$	3.4	3.4	3.4
$Z^0 \to \nu\overline{\nu}$	20.0	20.3	21.3
$Z^0 \to u\overline{u}$	11.6	11.7	12.4
$Z^0 \to c\overline{c}$	12.0	12.0	12.2
$Z^0 \to d\overline{d}$	15.6	15.8	16.6
$Z^0 \to s\overline{s}$	15.6	15.8	16.6
$Z^0 \to b\overline{b}$	15.1	14.3	10.3

Table A.2: Branching fractions for decays of the virtual Higgs boson for the $h \to \overline{f}f$ process for several values of the $\tilde{\chi}^0_B$ mass. These values are adapted from the Higgs branching fractions presented as a function of mass, published in Ref. [2]. Decay modes which contribute $< 0.01\%$ for all values of the Bino LSP mass are suppressed.

Process	h^0 branching fractions for $h^0 \to \overline{f}f$ decays (in %)		
	$M_{\tilde{\chi}^0_B} > M_{h^0}$	$M_{\tilde{\chi}^0_B} = 60$ GeV	$M_{\tilde{\chi}^0_B} = 30$ GeV
$h^0 \to b\overline{b}$	58.9	84.2	87.0
$h^0 \to c\overline{c}$	2.9	4.1	4.4
$h^0 \to \tau^{\pm}\tau^{\mp}$	6.3	8.0	6.9
$h^0 \to \mu^{\pm}\mu^{\mp}$	0.02	0.03	0.02
$h^0 \to gg$	7.8	3.5	1.7
$h^0 \to W^{\pm}W^{\mp}$	21.0	0.02	< 0.01
$h^0 \to Z^0Z^0$	2.6	0.01	< 0.01
$h^0 \to \gamma\gamma$	0.23	0.07	0.01
$h^0 \to Z^0\gamma$	0.15	< 0.01	< 0.01

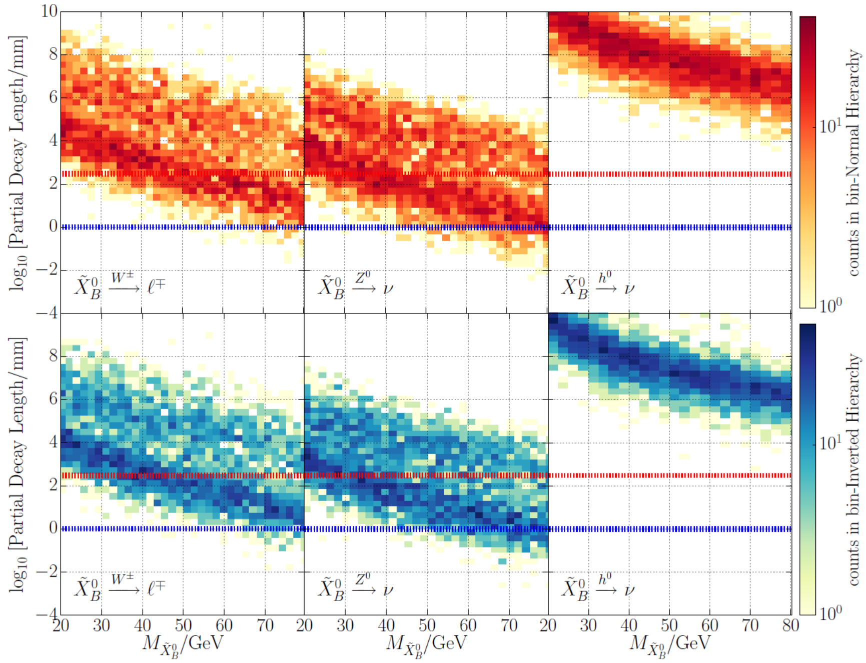

Figure A.6: The partial decay widths are shown as a function of the Bino mass seperately for the decay modes corresponding to each of the three electroweak boson decay channels, in the case that the $\tilde{\chi}_B^0$ is greater less than 80 GeV. The reciprocal of the widths are expressed to give "partial decay lengths", comparing the size of the contribution relative to that needed to produce promptly reconstructable objects in the detector (roughly 1 mm). Note that the lengths add as $1/l_{\rm tot} = \sum_i 1/l_i$ to produce shorter overall lifetimes. Values of the lifetime are shown separately for each assumption on the neutrino mass hierarchy.

A.4 Lifetimes and Branching Fractions of the Bino LSP

Combining the information computed above for each range in Bino mass, we obtain the statistical spread in Bino lifetime as a function of the Bino mass in Figure A.7. The relative decay rates to each of the channels is given in Figure A.8 for the high-mass Bino and in Figure A.9 for the low-mass Bino. If the Bino is heavier than the W boson it will decay promptly in the vast majority of simulated points in $B-L$ MSSM parameter space. For small values of $\tan\beta$ in this scenario it decays mostly via W and Z bosons, while for large $\tan\beta$ the Higgs mode can also become large. For a Bino mass below the W boson, there is a large spread in decay lengths, reaching as large as tens of kilometers when $m_{\tilde{\chi}_B^0}$ approaches 20 GeV. However, for a large number of points with $m_{\tilde{\chi}_B^0} \gtrsim 40$ GeV the lifetime falls in a range from 1 mm to 0.3 m that corresponds to the region in which displaced vertex searches are most powerful. Here displaced lepton and jet signatures have

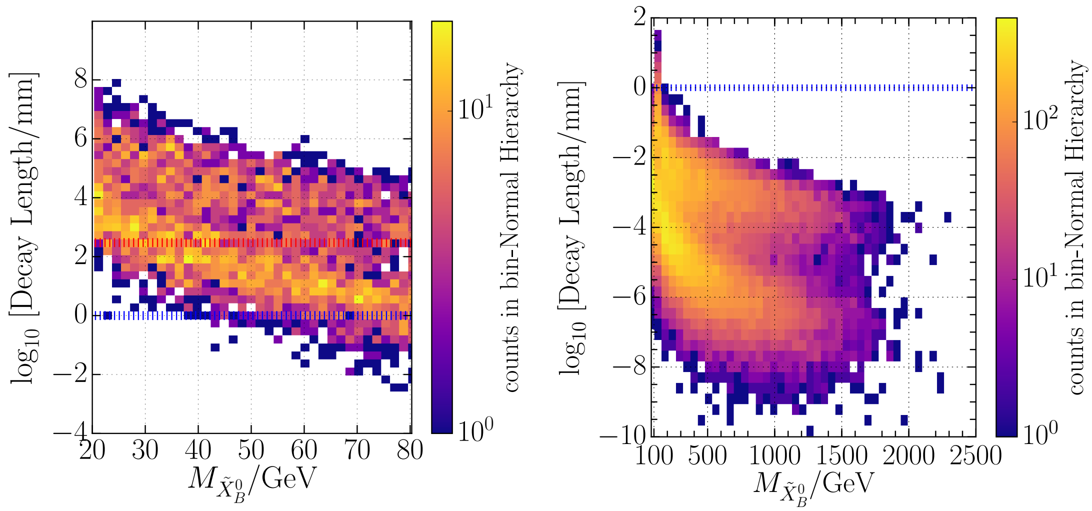

Figure A.7: The lifetime of the Bino LSP in each of the points in $B-L$ MSSM model space considered is shown as a function of the Bino mass. Results are presented separately for masses below (left) and above (right) the electroweak scale. Here the normal neutrino mass hierarchy is assumed. For high-mass Binos the vast majority of decays are found to be prompt, while for the low-mass case there a large spread in values. For a wide range of Bino masses, a large fraction of models considered produce decays between 1 mm and 0.3 m that provide an interesting target for displaced-decay collider searches.

the potential to be identified with large acceptance and to lead to searches that are essentially free of background. For these low-mass Bino LSPs the Higgs channel is completely suppressed due to its narrow width, with decays occurring dominantly in the Zv channel. Finally, the branching fraction as a function of lepton generation is shown in Figure A.10, separately for each electroweak boson decay channel. The relative fraction of each leptonic decay mode is given once per point under two sets of assumptions on the value of $\sin^2\theta_{23}$ as well as for both the normal and inverted hierarchies.

A.5 Experimental Outlook

These studies demonstrate that the Bino LSP is a viable candidate for direct detection at the LHCacross a wide range of masses. For very low masses of the Bino LSP, the existing search program for R-parity conserving SUSYscenarios should be sensitive to final states with this new "detector-stable" particle. Such searches may also be sensitive in the case of prompt Bino LSP decays to neutrinos (that is, $\tilde{\chi}^0_B \to Z^0\nu$ and $\tilde{\chi}^0_B \to h^0\nu$). A similar idea to this is discussed for the case of a Wino LSP in Appendix B. Generally, a diverse set of searches for RPV decays using prompt objects should also be pursued. In particular, maximal sensitivity could be obtained by

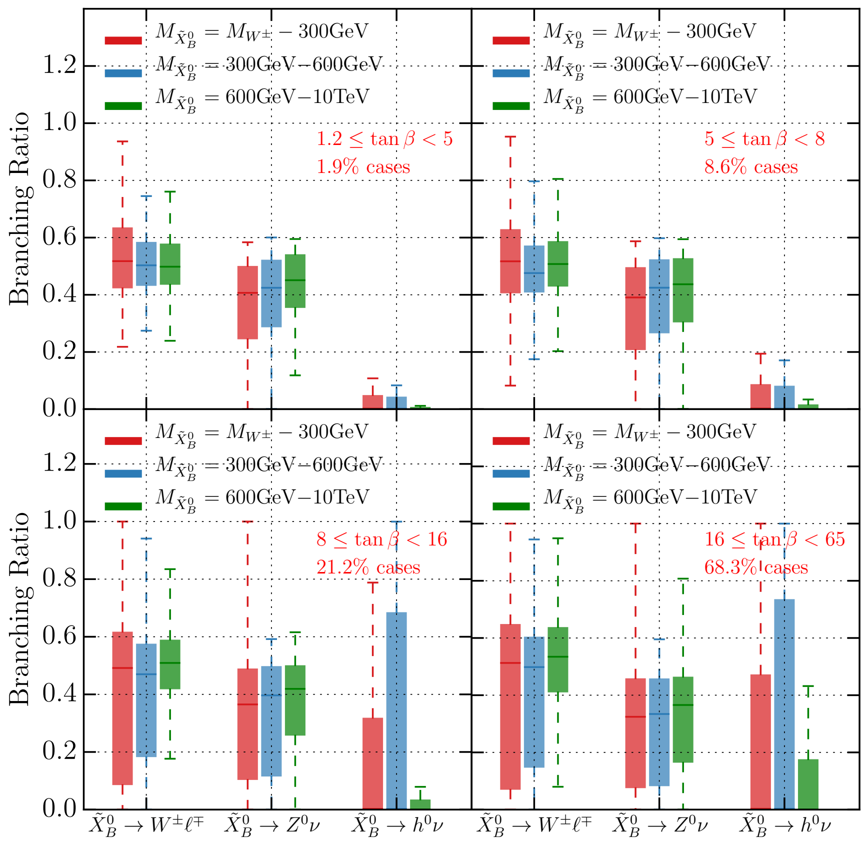

Figure A.8: The branching fraction of the Bino LSP is shown for three ranges of masses greater than the W boson mass. Branching fractions are shown for four categories of $\tan\beta$. The median (solid, darkened horizontal line), inter-quartile range (shaded box), and maximum and minimum values obtained (extended dashed lines) are shown for each population of events. Depending on the phase space each of the three decay modes may contribute substantially.

taking advantage of the unconventional signatures produced in Bino LSP decays, such as W-lepton resonances. Finally, the calculated distribution of possible lifetimes makes it abundantly clear that searches for displaced leptons and jets are an invaluable tool, particularly when the Bino LSP is lighter than the W boson.

The Bino presents an attractive candidate to the experimentalist, as it is by far the most prevalent LSP in the space of models considered in the present analysis. As has been shown, it may also be arbitrarily lighter than the soft SUSY breaking scale, due to canceling contributions from unrelated soft mass terms. On the other hand, pure Bino pairs cannot be produced directly from SM particle decays, so that experimental prospects will in general depend on the detailed spectrum of heavier

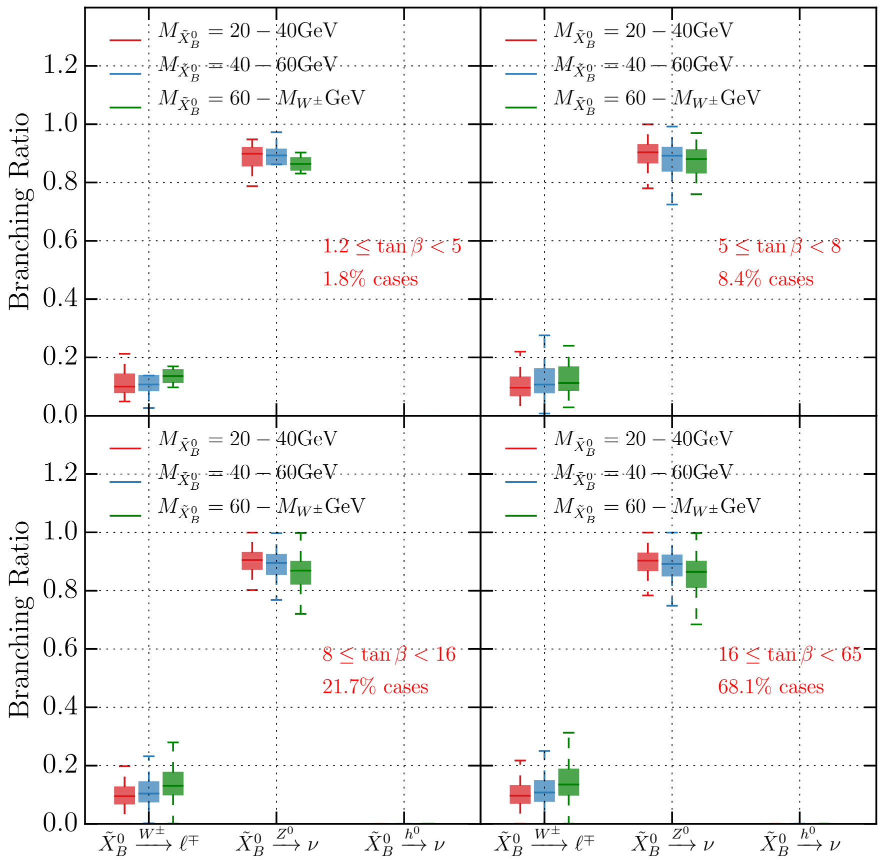

Figure A.9: The branching fraction of the Bino LSP is shown for three ranges of masses less than the W boson mass. Branching fractions are shown for four categories of $\tan\beta$. The median (solid, darkened horizontal line), inter-quartile range (shaded box), and maximum and minimum values obtained (extended dashed lines) are shown for each population of events. Generally the Z boson-mediated decay is most significant (typically near the 90% level) and in all cases the Higgs decay mode is suppressed to an extent so as not to appear.

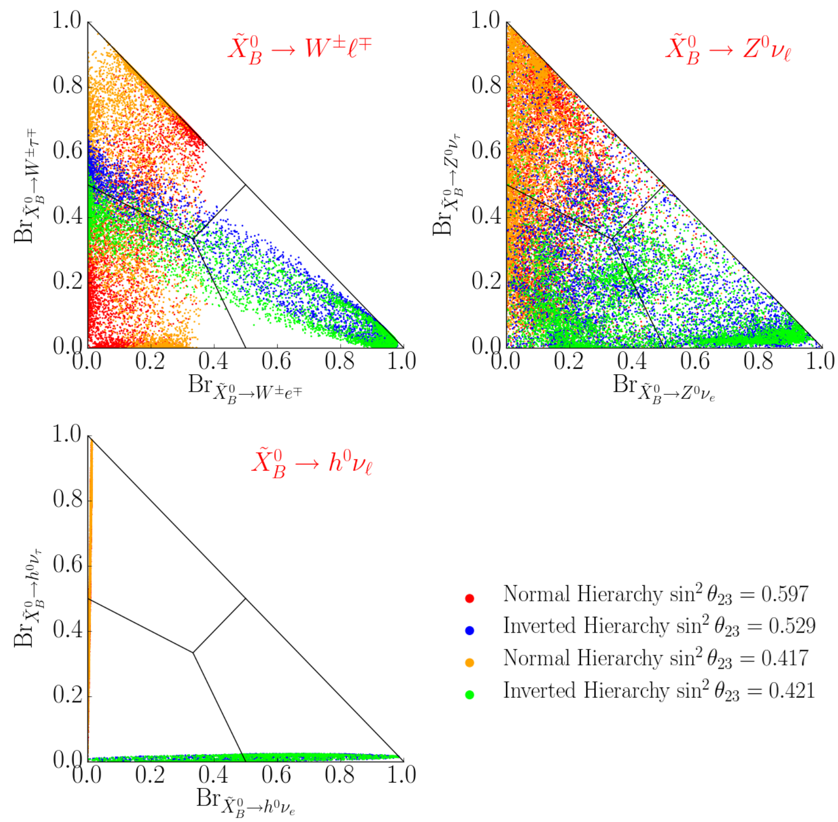

Figure A.10: The relative branching fraction of the Bino to each generation of charged and neutral lepton is shown separately for each electroweak boson decay channel. First and third generation fractions are plotted on the x- and y-axis, respectively, with the second generation fraction given as the complement. Model points are displayed under various assumptions on the neutrino mass hierarchy as well as $\sin^2\theta_{23}$. There is a strong correlation between the mass hierarchy and the relative branching fractions in the case of W and h-mediated decays, while the correlation is much weaker in the case of the Z. In particular, electron-flavor decays are essentially absent in the Higgs channel for the normal hierarchy, while the tau channel is absent in the inverted case. While notable, this difference has little experimental consequence at a collider where neutrino flavor cannot be measured. The correlation is potentially helpful in the W boson decay channel, though the lepton-universality preserving scenario remains a possibility in this channel under all assumptions considered.

SUSY particles. However, this makes the prediction of a long-lived Bino LSP intriguing, as it is a process with no SM background. This enables Bino LSP searches to be conducted without regard to the potentially complicated mechanism responsible for their production. Hence, searches for displaced leptons and jets (independent of other activity in the detector) present a completely orthogonal method of probing otherwise challenging spectra of sparticle masses.

Appendix B

Limits on RPV Scenarios from RPC Searches

The $B-L$ MSSM was introduced in Chapter 3 and studied in further in Appendix A in the case of the Bino LSP. This Appendix is devoted to exploring the effectiveness of using traditional searches for (R-parity conserving) SUSY to constrain the allowed space of $B-L$ MSSM models. The idea is that the R-parity violating operators allowing the LSP to decay in the $B-L$ MSSM can often lead to an abundance of final-state neutrinos, producing relatively large-$E_{\mathrm{T}}^{\mathrm{miss}}$ final states that may contribute to invisible-LSP signal regions.

As an example we consider the case of charged Wino pair production. The phenomenology of this scenario was detailed in Refs. [58] and [61]. Briefly, the Wino neutralino and chargino are government by a common mass parameter M_2 and do not mix significantly with the other charged and neutral states. This leads to two nearly-degenerate charged and neutral states with a mass splitting of $\approx 160\,\mathrm{MeV}$ [133] producing a lifetime of about 200 ps ($c\tau \approx 6\,\mathrm{cm}$). In the MSSM the neutral state is assumed to be lightest, with chargino searches (Ref. [141], for example) based on the "disappearing track" signature of the charged particle passing through several layers of the inner tracker before decaying before any hits are left in the outermost layers. In the $B-L$ MSSM the chargino may decay via four lepton number violating operators shown as vertices in Figure B.1, via emission of a vector or Higgs boson in addition to a lepton. Similar decays of the neutralino are possible, without a corresponding photon channel. These decays were found in Ref. [61] to occur promptly enough that the chargino would decay via this RPV coupling even if it were the NLSP with a LSP Wino neutralino.

We investigate the production of one neutralino and chargino. The cross section of this process has been calculated at NLO plus NLL precision in the limit that all other sparticles are decoupled

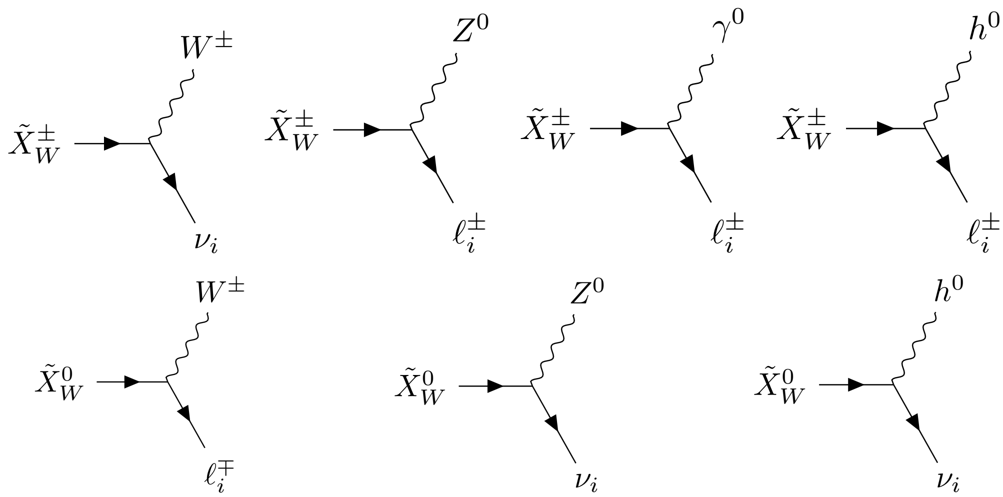

Figure B.1: Lepton number violating vertices present in the $B-L$ MSSM allowing Wino decays. Top row: decays of the chargino. Bottom row: decays of the neutralino.

with the `Resummino` program [344, 345], and varies from 5.2 pb at $m_{\chi_W} = 150\,\text{GeV}$ to 1.3 fb at $m_{\chi_W} = 1\,\text{TeV}$. The branching fraction of charginos and neutralinos are shown in Figures B.2 and B.3, respectively. To minimize the number of free parameters we assume that $\mathcal{BR}(\tilde{\chi}_W^0 \to W^{\pm}\ell^{\mp}) = 1$ for the remainder of the analysis but allow the chargino decay to vary.[32] If the chargino decay proceeds as $\tilde{\chi}_1^{\pm} \to W^{\pm}\nu$ and the W boson decays leptonically the resulting process is

$$pp \to (\tilde{\chi}_1^{\pm} \to W^{\pm}\nu \to \ell^{\pm}\nu\nu)(\tilde{\chi}_1^0 \to W^{\pm}\ell^{\mp} \to \ell^{\pm}\nu\ell^{\mp}) \sim \ell^{\pm}\ell^{\pm}\ell^{\mp}\nu\nu\nu, \tag{B.1}$$

yielding three leptons (none of which form a Z boson) and missing energy. In fact, this is a fairly generic signature of the Wino LSP scenario. If the chargino instead decays to a Z boson, a similar signature to that of the $\tilde{\chi}_1^{\pm} \to W^{\pm}\nu \to \ell^{\pm}\nu\nu$ process is produced instead by $\tilde{\chi}_1^{\pm} \to Z\ell^{\pm} \to \ell^{\pm}\nu\nu$ with the invisible Z decay providing the missing energy.

A similar signature was studied by the ATLAS Experiment [4] in the context of electroweakino production with slepton-mediated decays. The relevant diagram for the R-parity conserving SUSY search is shown in Figure B.4, alongside a mapping onto the RPV signature. Due to the similarity of the signatures the ATLAS result may be recast as a limit on the $B-L$ MSSM scenario.

[32]The branching fraction to the $\ell^+\ell^-\nu$ final state via the decay $\tilde{\chi}_W^0 \to W^{\pm}\ell^{\mp})$ was found to be dominant in preliminary studies related to the work presented in Ref. [61]. Though no longer fully realistic, the scenario continues to present an interesting case study and the results are anticipated to largely translate to the closely-related $(Z \to \ell^+\ell^-)\nu$ final state.

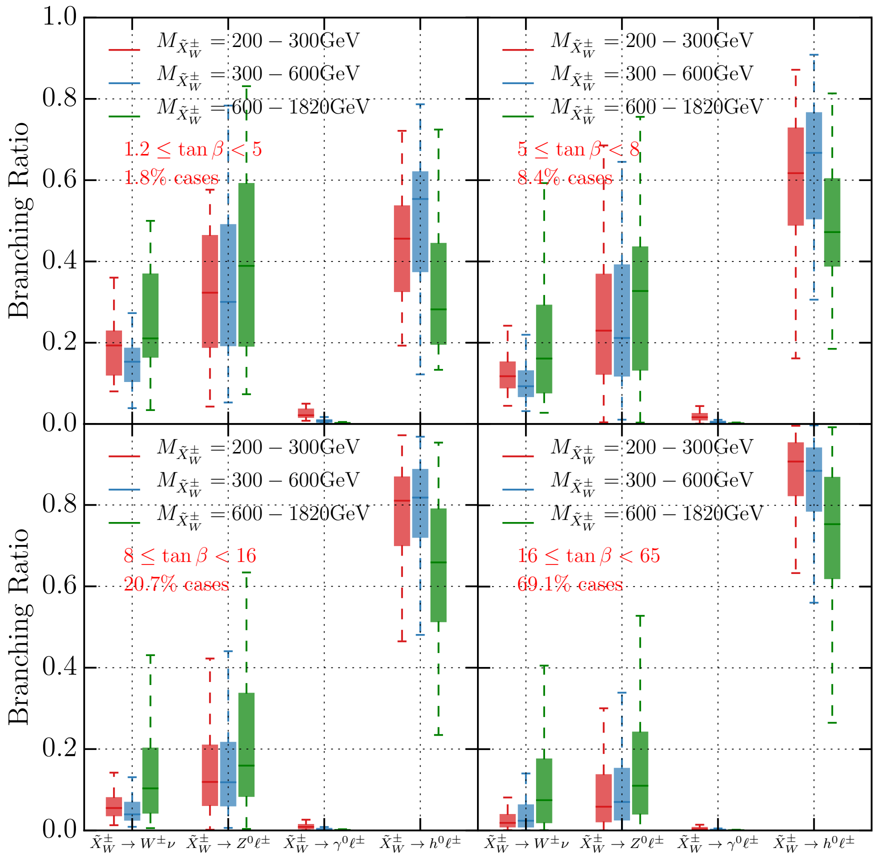

Figure B.2: The branching fraction of the Wino chargino is shown for a range of masses. Branching fractions are shown for four categories of $\tan\beta$. The median (solid, darkened horizontal line), inter-quartile range (shaded box), and maximum and minimum values obtained (extended dashed lines) are shown for each population of events. Depending on the phase space each of the four decay modes may contribute substantially.

B.1 The ATLAS analysis

The search described in Ref. [4] targets a variety of signatures, though here we focus only on the three-lepton signal region targeting SUSY scenarios where no SFOS lepton pair is consistent with the Z mass. The selection for the slepton-mediated regions (labeled as `SR3-slep-a` through `SR3-slep-e` in the ATLAS paper) is briefly summarized here. Three leptons are required, two of which must have p_{T} larger than 25 GeV, while the third may have p_{T}¿20 GeV. These thresholds are selected so that lepton triggers may be used to collect events. No selection is made on the number of b-tagged jets. Events are required to have missing transverse energy $E_{\mathrm{T}}^{\mathrm{miss}} > 130$ GeV and transverse mass $m_{\mathrm{T}} > 110$,GeV (significantly above the W boson mass), and to have a SFOS lepton pair with

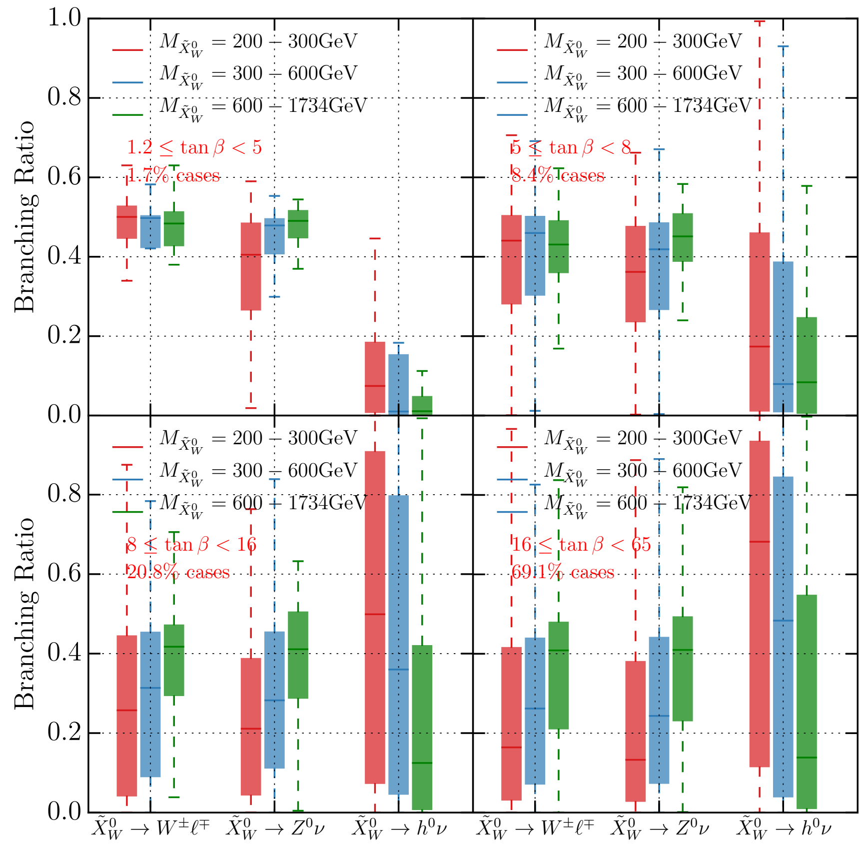

Figure B.3: The branching fraction of the Wino neutralino is shown for a range of masses. Branching fractions are shown for four categories of $\tan\beta$. The median (solid, darkened horizontal line), interquartile range (shaded box), and maximum and minimum values obtained (extended dashed lines) are shown for each population of events. Depending on the phase space each of the three decay modes may contribute substantially.

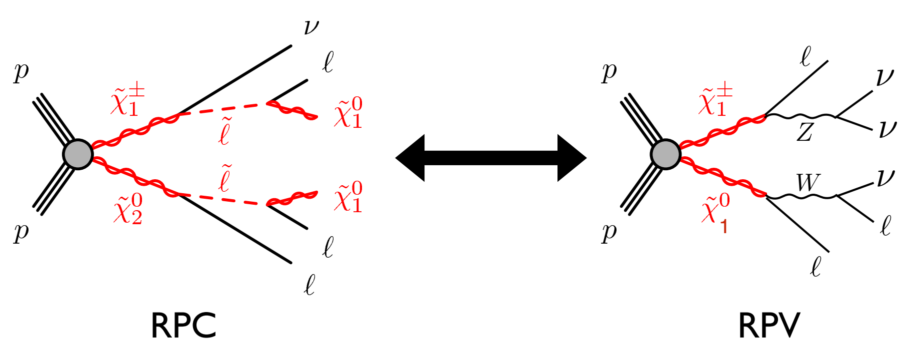

Figure B.4: The electroweakino production process and slepton-mediated decay in the RPC SUSY scenario is compared to an $B - L$ MSSM-inspired process violating R-parity.

3ℓ exclusive signal region definitions							
m_{SFOS} [GeV]	$E_{\mathrm{T}}^{\mathrm{miss}}$ [GeV]	$p_{\mathrm{T}}^{\ell_3}$ [GeV]	$n_{\text{non-}b\text{-tagged jets}}$	$m_{\mathrm{T}}^{\mathrm{min}}$ [GeV]	$p_{\mathrm{T}}^{\ell\ell\ell}$ [GeV]	$p_{\mathrm{T}}^{\mathrm{jet1}}$ [GeV]	Bins
<81.2	> 130	20–30 > 30		> 110			SR3-slep-a SR3-slep-b
>101.2	> 130	20–50 50–80 > 80		> 110			SR3-slep-c SR3-slep-d SR3-slep-e

Figure B.5: The signal selection criteria for slepton-mediated electroweakino decays are presented for the ATLAS three-lepton analysis [4].

Signal channel	Region	N_{obs}	N_{exp}	$\langle\epsilon\sigma\rangle_{\mathrm{obs}}^{95}$[fb]	S_{obs}^{95}	S_{exp}^{95}	$p(s{=}0)$	Z
	slep-a	4	2.2 ± 0.8	0.19	6.8	$4.7^{+2.3}_{-0.5}$	0.23	0.72
	slep-b	3	2.8 ± 0.4	0.14	5.2	$5.1^{+1.9}_{-1.2}$	0.47	0.08
	slep-c	9	5.4 ± 0.9	0.29	10.5	$6.8^{+2.9}_{-1.3}$	0.09	1.4
	slep-d	0	1.4 ± 0.4	0.08	3.0	$3.6^{+1.2}_{-0.6}$	0.5	0
	slep-e	0	1.1 ± 0.2	0.09	3.3	$3.6^{+1.3}_{-0.5}$	0.5	0

Figure B.6: The electroweakino production process and slepton-mediated decay in the RPC SUSY scenario is compared to an $B-L$ MSSM-inspired process violating R-parity.

$|m_{\ell^+\ell^-} - m_Z| > 10\,\mathrm{GeV}$. All events passing this selection are categorized into five regions according to whether $m_{\ell^+\ell^-}$ is above or below the Z boson mass, and depending on the third lepton p_{T}. No requirements are made on any hadronic activity in the event. The signal selection are summarized in Figure B.5.

Figure B.6 presents the number of observed and expected events for each of the five signal regions. As no significant excess was found, the analyzers proceeded to set model-independent limits for each region, given in the column denoted S_{obs}^{95}. Any signal model that predicts more than S_{obs}^{95} enter any of the five signal regions defined in the analysis can be excluded at the 95% confidence level.

B.2 Estimation of the RPV Signal

The chargino-neutralino signal process is simulated with `MG5_aMC@NLO` 2.6.2 [27] with up to two additional jets, interfaced to the Pythia 8.240 parton shower [29]. In the generated sample, the neutralino is forced to always decay through the $\tilde{\chi}_1^0 \to W^\pm \ell^\mp$ channel, while equal parts are generated of the $\tilde{\chi}^\pm \to Z\ell^\pm/h\ell^\pm/W^\pm\nu$ processes. Events are also generated assuming lepton universality in the RPV coupling structure, with results re-weighted to vary this assumption. All electroweak bosons are decayed with Pythia and all decay channels are considered when computing acceptance (i.e. not only $W \to \ell\nu$ and so forth). Notably, all Higgs decay channels are included. The common Wino mass is scanned from 150 GeV to 1 TeV in steps of 50 GeV, and each sample is normalized to the NLO+NLL cross sections computed with `Resummino` [344, 345].

Particle-level are passed to a fast simulation of the ATLAS detector using the `DELPHES` package [346]. A custom configuration of the simulation is used, based on the standard one, updating important parameters to reflect the analysis criteria as well as updated efficiencies and resolutions for the physics objects of interest. This setup is validated by comparing against the public results of Ref. [4]. To do so, a grid of signal samples is produced identical to the slepton model investigated in the paper (using an identical setup to the software used to generate the RPV model) and signal yields compared. Figure B.7 shows excellent agreement between the exclusion reported by Ref. [4] and that derived using the fast detector simulation. At high Wino masses, the full analysis excludes models corresponding to a cross section roughly 20% larger than that of the emulated one. The source of this discrepancy was investigated and several theories were not borne out, including: lepton selection and efficiency, with the discrepancy persisting even with super-optimistic lepton acceptance; $E_{\mathrm{T}}^{\mathrm{miss}}$ resolution was tested by varying the selection and noise of the $E_{\mathrm{T}}^{\mathrm{miss}}$ constituent objects to little effect; multi-region combination effects were ruled out, as the sensitivity was driven by one signal region at high-mass. The results were also verified by comparing the number of events remaining after a series of nested signal selection criteria. This comparison was available for only a single signal model point reported by Ref. [4] and is shown in Table B.1. In any case, the emulated results herein were found to be generally conservative and agreement was found within 10% or so for a range of validation methods.

Figure B.8 shows the number of baseline (20 GeV) leptons for all generated signal events, for a range of Wino masses. After all signal region selections are enforced, the missing transverse momentum, dilepton mass, transverse mass, and third lepton p_{T} were plotted in Figure B.9. The signal regions populated by each of the models specified by the various Wino mass parameters are determined by the third lepton p_{T} and $m_{\ell^+\ell^-}$ distributions.

B.3 Results

Following the validation of the signal generation and detector simulation, we present results for the $B-L$ MSSM models considered. For the lighted Wino mass considered in the analysis, 150 GeV, we check the number of expected events in each signal region against the number of BSM events excluded by the ATLAS analysis. Based on the truth information in the chargino decay, the signal

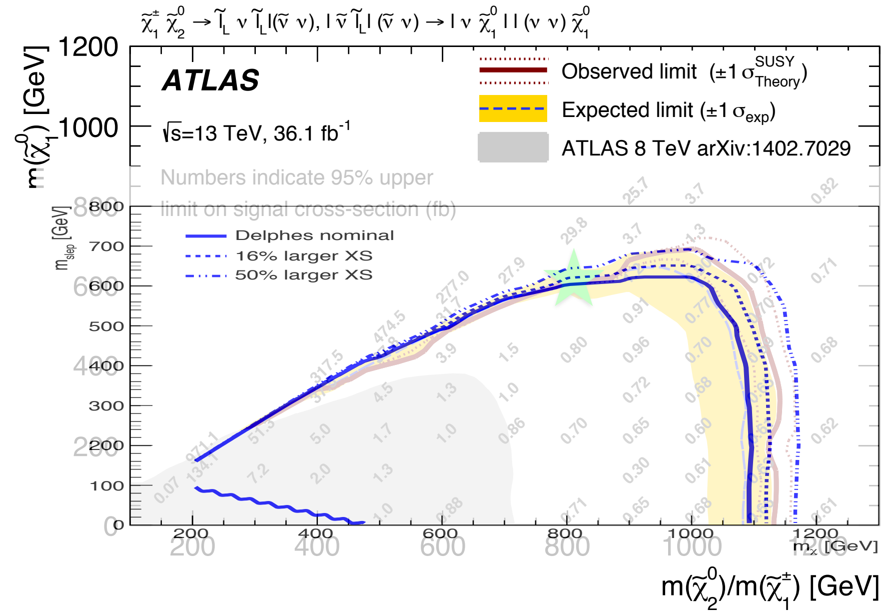

Figure B.7: A comparison is shown between the grid of signal models excluded by the ATLAS [4] and emulated analyses. The ATLAS observed exclusion is shown in solid red, while the emulated analysis result is shown in blue. The dotted and dash-dot lines show the emulated exclusions obtained by re-scaling the signal cross sections by factor of 1.16 and 1.5, respectively.

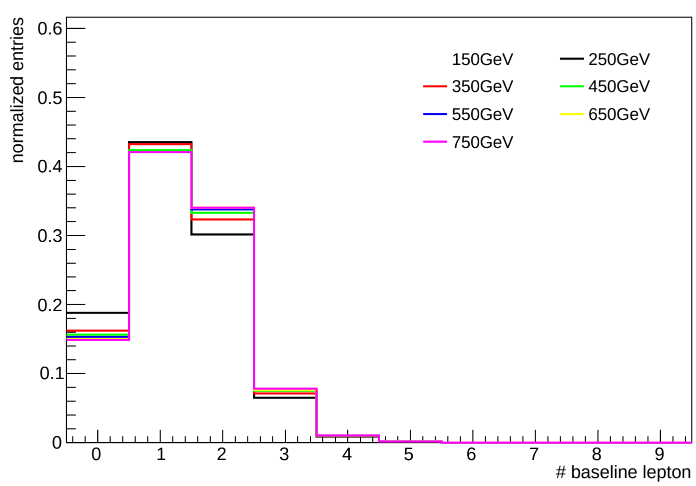

Figure B.8: The number of baseline leptons as defined in the ATLAS analysis [4] is shown before any further selection for a variety of signal models. Distributions are shown as normalized histograms for a range of Wino masses considered.

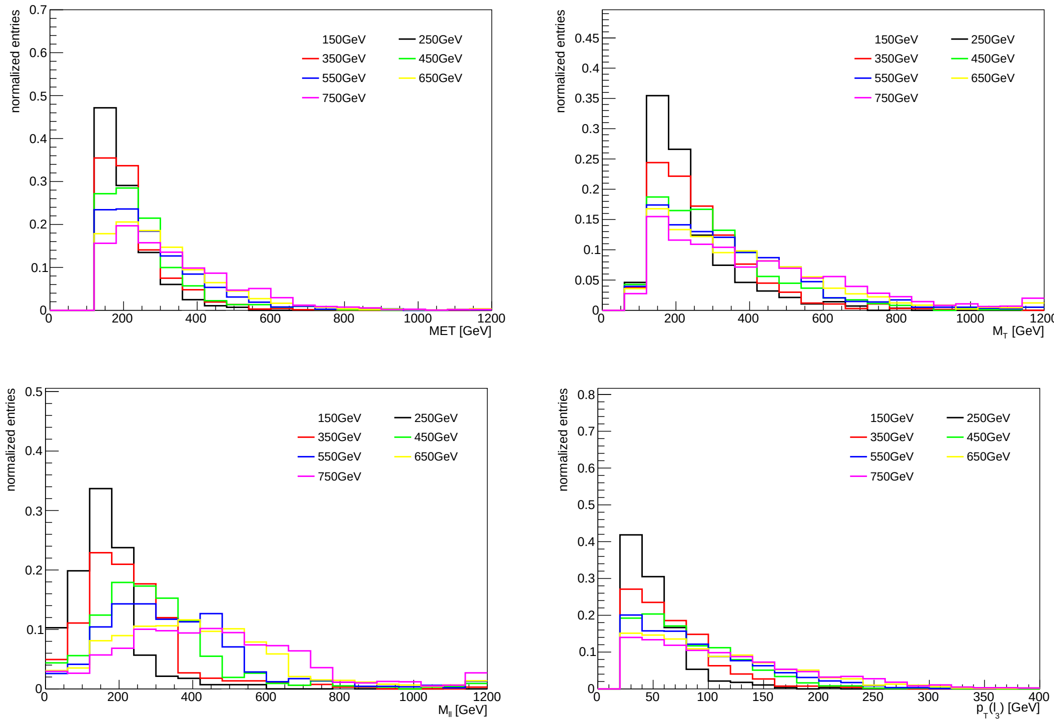

Figure B.9: The number of baseline leptons as defined in the ATLAS analysis [4] is shown before any further selection for a variety of signal models. Distributions are shown as normalized histograms for a range of Wino masses considered.

is re-weighted to the emulate the yields of points with non-universal decays to leptons and the three massive bosons.[33] This leaves $\mathcal{BR}(\tilde{\chi}_1^{\pm} \to W^{p}m + X)$, $\mathcal{BR}(\tilde{\chi}_1^{\pm} \to Z^0 + X)$, $\mathcal{BR}(\tilde{\chi}_1^{\pm} \to e/\nu_e + X)$, and $\mathcal{BR}(\tilde{\chi}_1^{\pm} \to \tau/\nu_\tau + X)$ as free parameters, with the branching fractions to H and μ set by conservation of probability. To avoid scanning all four parameters simultaneously, two are fixed while the other two are scanned. Figure B.10 shows the case where lepton universality is assumed and decay rates to the electroweak bosons are varied. Figure B.11 shows the case where decay rates to the different lepton flavors are scanned while charginos are assumed equally likely to decay to all bosons. For each branching ratio configuration shown in the figures, the ratio of events predicted to events excluded by ATLAS is shown, using the most sensitive signal region for each model point. As all ratios are greater than unity, a Wino mass of 150 GeV is excluded by the ATLAS analysis for all of the branching ratio configurations studied.

Following this, higher-mass Wino particles are considered so that, for each set of branching ratios,

[33] Photon decays are ignored as they were found to be negligible in Figure B.2.

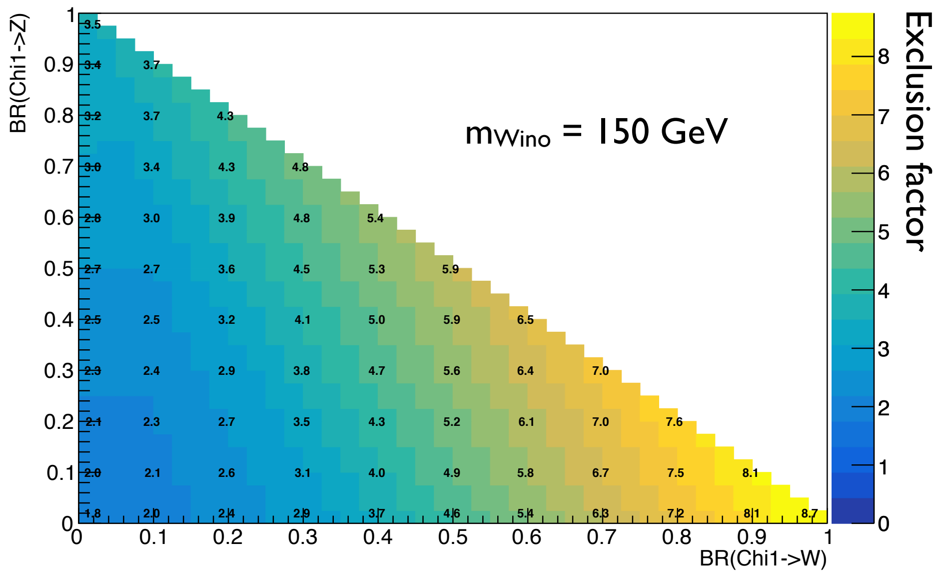

Figure B.10: The ratio of predicted events in the $B - L$ MSSM model to number of events excluded by the ATLAS analysis [4] is shown as a function of the chargino branching fraction to the various electroweak bosons, for a Wino mass of 150 GeV. Decays to leptons are assumed to occur at equal rates, and the maximum value is taken over all signal regions, separately for each combination of branching ratios. All models considered predict more events than the exclusion limit and thus the Wino LSP is completely excluded in this scenario for a mass of 150 GeV.

the Wino mass is obtained for which the model can no longer be excluded. These are presented in Figures B.12 and B.13 for the cases of universal lepton and boson decays, respectively, as considered for the 150 GeV Wino masses.

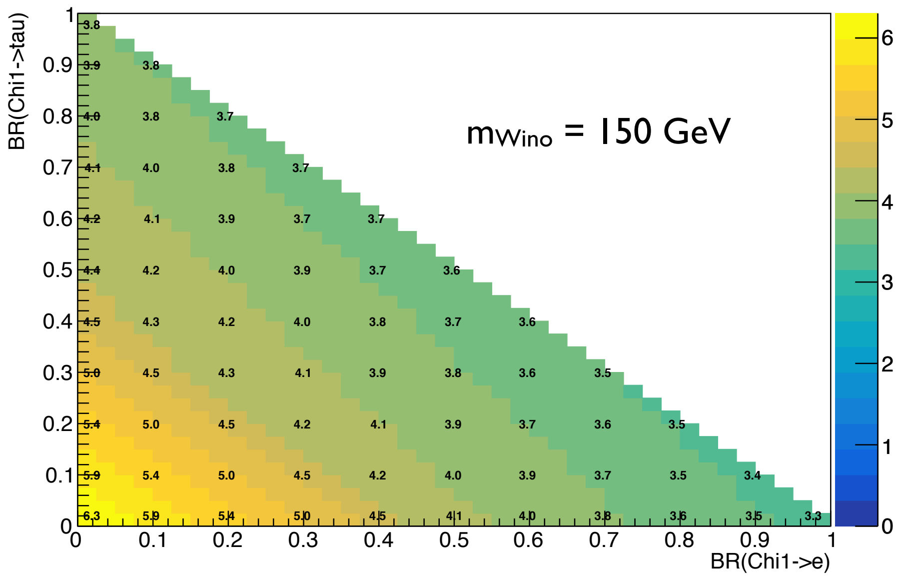

Figure B.11: The ratio of predicted events in the $B - L$ MSSM model to number of events excluded by the ATLAS analysis [4] is shown as a function of the chargino branching fraction to the various flavor of leptons, for a Wino mass of 150 GeV. Decays to electroweak bosons are assumed to occur at equal rates, and the maximum value is taken over all signal regions, separately for each combination of branching ratios. All models considered predict more events than the exclusion limit and thus the Wino LSP is completely excluded in this scenario for a mass of 150 GeV.

Table B.1: The number of events passing the signal selection after a sequence of iterative requirements is presented for the ATLAS analysis and the emulated one, for a SUSY signal with 800 GeV Wino and 600 GeV Bino decaying via sleptons. Categories not included in the ATLAS cut-flow and those not emulated in the fast analysis are denoted at '–'. All requirements are enforced sequentially up to the $m_{\ell^+\ell^-}$ requirement, after which all selections are exclusive. Agreement within 10% is found for all regions except for `SR2-slep-a` which is not relevant for the Wino masses considered in this analysis.

Selection	Full Analysis	Emulation
All events	172	172
Trigger	25.4	–
Three leptons	25.1	25.2
Event cleaning	23.5	–
b jet veto	–	24.8
SFOS pair	–	24.7
$m_{\mathrm{T}} > 101\,\mathrm{GeV}$	14.4	15.3
$E_{\mathrm{T}}^{\mathrm{miss}} > 130\,\mathrm{GeV}$	10.2	10.7
$m_{\ell^+\ell^-} < 81.2\,\mathrm{GeV}$	2.10	–
$m_{\ell^+\ell^-} > 101.2\,\mathrm{GeV}$	6.80	–
pass $m_{\ell^+\ell^-}$	–	9.4
`SR2-slep-a`	0.11	0.15
`SR2-slep-b`	1.99	2.18
`SR2-slep-c`	2.53	2.79
`SR2-slep-d`	3.01	3.08
`SR2-slep-e`	1.25	1.20

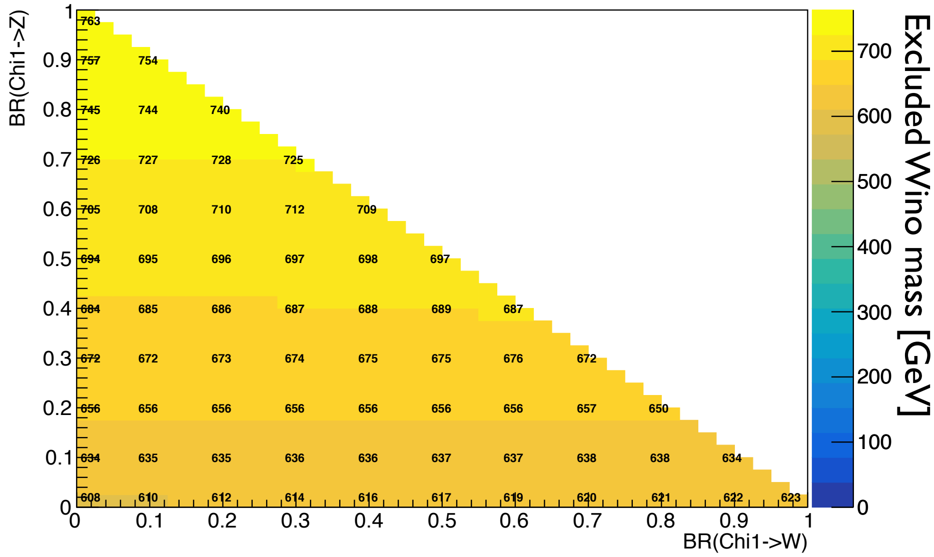

Figure B.12: The largest excluded Wino mass in the $B-L$ MSSM model considered is shown as a function of the chargino branching fraction to the various electroweak bosons, assuming decays to leptons at equal rates. The maximum value is taken over all signal regions, separately for each combination of branching ratios. Masses up to 610 GeV (100% Higgs branching fraction) to 760 GeV (100% Z boson branching fraction) are excluded.

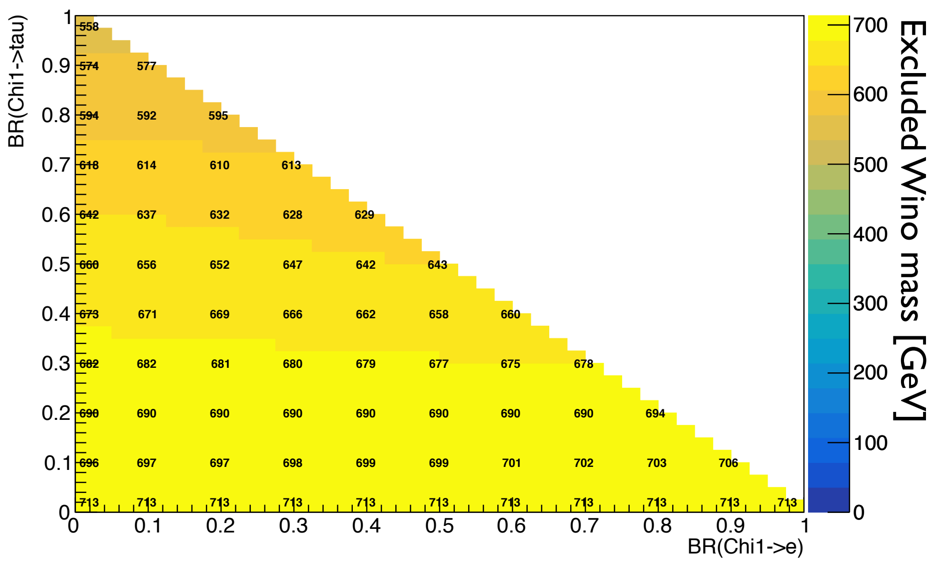

Figure B.13: The largest excluded Wino mass in the $B-L$ MSSM model considered is shown as a function of the chargino branching fraction to the various electroweak bosons, assuming decays to leptons at equal rates. The maximum value is taken over all signal regions, separately for each combination of branching ratios. Masses up to 560 GeV (100% tau branching fraction) to 710 GeV (0% tau branching fraction) are excluded.

B.4 Conclusions

For the $B-L$ MSSM model considered, we find that the ATLAS analysis [4] excludes Wino masses from 150 GeV up to 560 GeV to 760 GeV depending on the model assumptions. Constraints are weakened in the case where the chargino decays predominantly to τ leptons, due to the fact that hadronic tau decays are not directly reconstructed, and to Higgs bosons, which do not produce invisible momentum as is the case with Z and W boson decays. The strongest exclusions are found when the branching fraction to τ leptons is zero and the branching fraction to Z bosons is large, driven by the invisible Z decay. Only a single type of analysis was considered in this study, with potential increases in sensitivity coming from additional channel. In particular, two-lepton and four-lepton analyses show promise for enhanced exclusion. Ref. [339] specifically targets lepton-violating SUSY in the four-lepton signature. For high-mass Wino LSPs, additional analysis efforts may further improve constraints by directly reconstructing visible Wino decays.

Bibliography

[1] Particle Data Group, *Review of Particle Physics*, Phys. Rev. D **9**8 (Aug, 2018) 030001. Cited on pages xiii, 6, 55, 205, 207, and 234.

[2] LHC Higgs Cross Section Working Group Collaboration, *Handbook of LHC Higgs Cross Sections: 4. Deciphering the Nature of the Higgs Sector*, arXiv:1610.07922 [hep-ph]. Cited on pages xiii, 194, 232, and 234.

[3] ATLAS Collaboration, *Search for top squark pair production in final states with one isolated lepton, jets, and missing transverse momentum in $\sqrt{s} = 8$ TeV pp collisions with the ATLAS detector*, JHEP **1**1 (2014) 118, arXiv:1407.0583 [hep-ex]. Cited on pages xvi, 112, 113, 119, 123, 124, 130, and 149.

[4] ATLAS Collaboration, *Search for electroweak production of supersymmetric particles in final states with two or three leptons at $\sqrt{s} = 13$ TeV with the ATLAS detector*, Eur. Phys. J. C **7**8 (2018) 995, arXiv:1803.02762 [hep-ex]. Cited on pages xviii, 242, 243, 245, 246, 247, 248, 249, 250, and 253.

[5] ATLAS Collaboration, *ATLAS Phase-II Upgrade Scoping Document*, Tech. Rep. CERN-LHCC-2015-020. LHCC-G-166, CERN, Geneva, Sep, 2015. `http://cds.cern.ch/record/2055248`. Cited on pages xxvi and 53.

[6] T. Herwig and Atlas Collaboration, *ATLAS jet trigger performance in 2015 data*, in *Proceedings of the 38th International Conference on High Energy Physics (ICHEP2016). 3-10 August 2016. Chicago*, p. 854. Jan, 2016. Cited on page xxvi.

[7] ATLAS Collaboration, *Search for top-squark pair production in final states with one lepton, jets, and missing transverse momentum using 36 fb^1 of $\sqrt{s} = 13$ TeV pp collision data with the ATLAS detector*, JHEP **0**6 (2018) 108, arXiv:1711.11520 [hep-ex]. Cited on pages xxvii, 89, 92, 147, 149, 178, 226, and 227.

[8] ATLAS Collaboration, *Probing the quantum interference between singly and doubly resonant top-quark production in pp collisions at $\sqrt{s} = 13$ TeV with the ATLAS detector*, Phys. Rev. Lett. **1**21 (2018) no. 15, 152002, arXiv:1806.04667 [hep-ex]. Cited on pages xxvii, 204, 210, 211, 212, 214, 216, 219, 221, 223, and 224.

[9] C. Herwig, T. Ježo, and B. Nachman, *Extracting the Top-Quark Width from Non-Resonant Production*, Phys. Rev. Lett. **122** (2019) no. 23, 231803, arXiv:1903.10519 [hep-ex]. Cited on pages xxvii and 223.

[10] ATLAS Collaboration, *Technical Design Report for the Phase-II Upgrade of the ATLAS TDAQ System*, Tech. Rep. CERN-LHCC-2017-020. ATLAS-TDR-029, CERN, Geneva, Sep, 2017. http://cds.cern.ch/record/2285584. Cited on pages xxvii, 54, 55, 57, 58, 60, 64, 69, 82, and 83.

[11] S. Dumitru, C. Herwig, and B. A. Ovrut, *R-parity Violating Decays of Bino Neutralino LSPs at the LHC*, arXiv:1906.03174 [hep-ph]. Cited on pages xxvii, 26, and 228.

[12] E. Wigner, *On unitary representations of the inhomogeneous Lorentz group*, Annals of Mathematics **40** (1939) pp. 149–204. Cited on page 4.

[13] C. N. Yang and R. L. Mills, *Conservation of isotopic spin and isotopic gauge invariance*, Phys. Rev. **96** (1954) 191–195. Cited on page 5.

[14] K. G. Wilson and J. Kogut, *The renormalization group and the ϵ expansion*, Physics Reports **12** (1974) no. 2, 75 – 199. Cited on page 5.

[15] C. G. Callan, *Broken Scale Invariance in Scalar Field Theory*, Phys. Rev. D **2** (Oct, 1970) 1541–1547. Cited on page 5.

[16] K. Symanzik, *Small distance behaviour in field theory and power counting*, Communications in Mathematical Physics **18** (Sep, 1970) 227–246. Cited on page 5.

[17] F. Englert and R. Brout, *Broken symmetry and the mass of gauge vector mesons*, Phys. Rev. Lett. **13** (1964) 321–323. Cited on page 7.

[18] P. W. Higgs, *Broken symmetries, massless particles and gauge fields*, Physics Letters **12** (1964) 132–133. Cited on page 7.

[19] P. W. Higgs, *Broken symmetries and the masses of gauge bosons*, Phys. Rev. Lett. **13** (1964) 508–509. Cited on page 7.

[20] G. S. Guralnik, C. R. Hagen, and T. W. B. Kibble, *Global conservation laws and massless particles*, Phys. Rev. Lett. **13** (1964) 585–587. Cited on page 7.

[21] V. Gribov and L. Lipatov, *Deep inelastic e-p scattering in perturbation theory*, Sov.J.Nucl.Phys. **15** (1972) 438–450. Cited on page 9.

[22] G. Altarelli and G. Parisi, *Asymptotic freedom in parton language*, Nucl.Phys.B **126** (1977) 298. Cited on page 9.

[23] Y. L. Dokshitzer, *Calculation of the structure functions for deep inelastic scattering and e^+e^- annihilation by perturbation theory in quantum chromodynamics.*, Sov.Phys.JETP **46** (1977) 641–653. Cited on page 9.

[24] NNPDF Collaboration, R. D. Ball et al., *Parton distributions from high-precision collider data*, Eur. Phys. J. **C77** (2017) no. 10, 663, arXiv:1706.00428 [hep-ph]. Cited on pages 9 and 10.

[25] S. Dulat, T.-J. Hou, J. Gao, M. Guzzi, J. Huston, P. Nadolsky, J. Pumplin, C. Schmidt, D. Stump, and C. P. Yuan, *New parton distribution functions from a global analysis of quantum chromodynamics*, Phys. Rev. **D93** (2016) no. 3, 033006, arXiv:1506.07443 [hep-ph]. Cited on page 9.

[26] A. D. Martin, W. J. Stirling, R. S. Thorne, and G. Watt, *Parton distributions for the LHC*, Eur. Phys. J. **C63** (2009) 189–285, arXiv:0901.0002 [hep-ph]. Cited on page 9.

[27] J. Alwall, R. Frederix, S. Frixione, V. Hirschi, F. Maltoni, O. Mattelaer, H. S. Shao, T. Stelzer, P. Torrielli, and M. Zaro, *The automated computation of tree-level and next-to-leading order differential cross sections, and their matching to parton shower simulations*, JHEP **07** (2014) 079, arXiv:1405.0301 [hep-ph]. Cited on pages 12, 93, 232, and 245.

[28] T. Sjostrand, S. Mrenna, and P. Z. Skands, *PYTHIA 6.4 physics and manual*, JHEP **05** (2006) 026, arXiv:hep-ph/0603175 [hep-ph]. Cited on page 12.

[29] T. Sjostrand, S. Mrenna, and P. Z. Skands, *A brief introduction to PYTHIA 8.1*, Comput. Phys. Commun. **178** (2008) 852–867, arXiv:0710.3820 [hep-ph]. Cited on pages 12, 92, 94, 209, and 245.

[30] M. Bahr et al., *Herwig++ physics and manual*, Eur. Phys. J. C **58** (2008) 639–707, arXiv:0803.0883 [hep-ph]. Cited on pages 12 and 93.

[31] S. Catani, L. Cieri, G. Ferrera, D. de Florian, and M. Grazzini, *Vector Boson Production at Hadron Colliders: A Fully Exclusive QCD Calculation at Next-to-Next-to-Leading Order*, Phys. Rev. Lett. **103** (2009) 082001, arXiv:0903.2120 [hep-ph]. Cited on page 13.

[32] S. Catani and M. Grazzini, *An NNLO subtraction formalism in hadron collisions and its application to Higgs boson production at the LHC*, Phys. Rev. Lett. **98** (2007) 222002, arXiv:hep-ph/0703012 [hep-ph]. Cited on page 13.

[33] M. Czakon and A. Mitov, *Top++: A program for the calculation of the top-pair cross-section at hadron colliders*, Comput. Phys. Commun. **185** (2014) 2930, arXiv:1112.5675 [hep-ph]. Cited on pages 13, 92, 155, and 194.

[34] K. Hamilton, P. Nason, E. Re, and G. Zanderighi, *NNLOPS simulation of Higgs boson production*, JHEP **10** (2013) 222, arXiv:1309.0017 [hep-ph]. Cited on page 13.

[35] M. Grazzini, *NNLO predictions for the Higgs boson signal in the H —¿ WW —¿ lnu lnu and H —¿ ZZ —¿ 4l decay channels*, JHEP **02** (2008) 043, arXiv:0801.3232 [hep-ph]. Cited on page 13.

[36] M. L. Mangano, M. Moretti, F. Piccinini, and M. Treccani, *Matching matrix elements and shower evolution for top-quark production in hadronic collisions*, JHEP **01** (2007) 013, arXiv:hep-ph/0611129 [hep-ph]. Cited on page 13.

[37] S. Catani, F. Krauss, R. Kuhn, and B. R. Webber, *QCD matrix elements + parton showers*, JHEP **11** (2001) 063, arXiv:hep-ph/0109231 [hep-ph]. Cited on page 13.

[38] L. Lonnblad, *Correcting the color dipole cascade model with fixed order matrix elements*, JHEP **05** (2002) 046, arXiv:hep-ph/0112284 [hep-ph]. Cited on pages 13 and 94.

[39] S. Frixione and B. R. Webber, *Matching NLO QCD computations and parton shower simulations*, JHEP **0206** (2002) 029. Cited on pages 14 and 157.

[40] T. Gleisberg, S. Hoeche, F. Krauss, M. Schonherr, S. Schumann, F. Siegert, and J. Winter, *Event generation with SHERPA 1.1*, JHEP **02** (2009) 007, arXiv:0811.4622 [hep-ph]. Cited on pages 14 and 94.

[41] P. Nason, *A New method for combining NLO QCD with shower Monte Carlo algorithms*, JHEP **11** (2004) 040, arXiv:hep-ph/0409146 [hep-ph]. Cited on pages 14, 157, and 209.

[42] T. Ježo and P. Nason, *On the Treatment of Resonances in Next-to-Leading Order Calculations Matched to a Parton Shower*, JHEP **12** (2015) 065, arXiv:1509.09071 [hep-ph]. Cited on pages 14, 158, and 209.

[43] G. Chapline, *Cosmological effects of primordial black holes*, Nature (London), v. 253, no. 5489, pp. 251-252 . Cited on page 15.

[44] G. Chapline and P. H. Frampton, *A new direction for dark matter research: intermediate mass compact halo objects*, JCAP **1611** (2016) no. 11, 042, arXiv:1608.04297 [gr-qc]. Cited on page 15.

[45] P. H. Frampton, *Searching for dark matter constituents with many solar masses*, Modern Physics Letters A **31** (2016) no. 16, 1650093. Cited on page 15.

[46] B. Carr, M. Raidal, T. Tenkanen, V. Vaskonen, and H. Veermäe, *Primordial black hole constraints for extended mass functions*, Phys. Rev. **D96** (2017) no. 2, 023514, arXiv:1705.05567 [astro-ph.CO]. Cited on page 15.

[47] R. Peccei and H. R. Quinn, *CP Conservation in the Presence of Pseudoparticles*, Phys. Rev. Lett. **38** (1977) 1440–1443. Cited on page 15.

[48] R. Peccei and H. R. Quinn, *Constraints imposed by CP conservation in the presence of pseudoparticles*, Phys. Rev. D **16** (1977) 1791–1797. Cited on page 15.

[49] S. P. Martin, *A Supersymmetry primer*, arXiv:hep-ph/9709356 [hep-ph]. [Adv. Ser. Direct. High Energy Phys.18,1(1998)]. Cited on pages 20 and 21.

[50] R. Dermisek and I. Low, *Probing the Stop Sector and the Sanity of the MSSM with the Higgs Boson at the LHC*, Phys. Rev. **D77** (2008) 035012, arXiv:hep-ph/0701235 [HEP-PH]. Cited on page 21.

[51] Z. Han, G. D. Kribs, A. Martin, and A. Menon, *Hunting quasidegenerate Higgsinos*, Phys. Rev. **D89** (2014) no. 7, 075007, arXiv:1401.1235 [hep-ph]. Cited on page 22.

[52] B. Altunkaynak, M. Holmes, P. Nath, B. D. Nelson, and G. Peim, *SUSY Discovery Potential and Benchmarks for Early Runs at $\sqrt{s} = 7$ TeV at the LHC*, Phys. Rev. **D82** (2010) 115001, arXiv:1008.3423 [hep-ph]. Cited on page 23.

[53] MSSM Working Group, *The Minimal supersymmetric standard model: Group summary report*, in *GDR (Groupement De Recherche) - Supersymetrie Montpellier, France, April 15-17, 1998*. 1998. arXiv:hep-ph/9901246 [hep-ph]. Cited on page 23.

[54] C. F. Berger, J. S. Gainer, J. L. Hewett, and T. G. Rizzo, *Supersymmetry Without Prejudice*, JHEP **0902** (2009) 023, arXiv:0812.0980 [hep-ph]. Cited on page 23.

[55] V. Braun, Y.-H. He, B. A. Ovrut, and T. Pantev, *A Heterotic standard model*, Phys. Lett. **B**618 (2005) 252–258, arXiv:hep-th/0501070 [hep-th]. Cited on page 25.

[56] V. Braun, Y.-H. He, B. A. Ovrut, and T. Pantev, *The Exact MSSM spectrum from string theory*, JHEP **05** (2006) 043, arXiv:hep-th/0512177 [hep-th]. Cited on page 25.

[57] V. Braun, Y.-H. He, and B. A. Ovrut, *Supersymmetric Hidden Sectors for Heterotic Standard Models*, JHEP **09** (2013) 008, arXiv:1301.6767 [hep-th]. Cited on page 25.

[58] S. Dumitru, B. A. Ovrut, and A. Purves, *The R-parity Violating Decays of Charginos and Neutralinos in the B-L MSSM*, JHEP **02** (2019) 124, arXiv:1810.11035 [hep-ph]. Cited on pages 26, 228, 231, and 241.

[59] ATLAS Collaboration, *A search for $B-L$ R-parity-violating scalar top decays in $\sqrt{s}=8$ TeV pp collisions with the ATLAS experiment*, ATLAS-CONF-2015-015, 2015. https://cds.cern.ch/record/2002885. Cited on page 26.

[60] ATLAS Collaboration, *Search for $B-L$ R-parity-violating top squarks in $\sqrt{s}=13$ TeV pp collisions with the ATLAS experiment*, Phys. Rev. D **97** (2018) 032003, arXiv:1710.05544 [hep-ex]. Cited on page 26.

[61] S. Dumitru, B. A. Ovrut, and A. Purves, *R-parity Violating Decays of Wino Chargino and Wino Neutralino LSPs and NLSPs at the LHC*, arXiv:1811.05581 [hep-ph]. Cited on pages 26, 228, 241, and 242.

[62] ALEPH, DELPHI, L3, OPAL Collaborations, *Combined LEP Chargino Results, up to 208 GeV for low DM*, LEPSUSYWG/02-04.1, 2002. http://lepsusy.web.cern.ch/lepsusy/www/inoslowdmsummer02/charginolowdm_pub.html. Cited on pages 26 and 86.

[63] L. Evans and P. Bryant, *LHC Machine*, JINST **3** (2008) S08001. Cited on pages 28 and 29.

[64] ATLAS Collaboration, *The ATLAS Experiment at the CERN Large Hadron Collider*, JINST **3** (2008) S08003. Cited on pages 30 and 35.

[65] ATLAS Collaboration, *ATLAS pixel detector electronics and sensors*, JINST **3** (2008) P07007. Cited on page 32.

[66] A. Collaboration, *ATLAS Insertable B-Layer Technical Design Report*, Tech. Rep. CERN-LHCC-2010-013. ATLAS-TDR-19, Sep, 2010. https://cds.cern.ch/record/1291633. Cited on page 32.

[67] ATLAS Collaboration, *Study of the material of the ATLAS inner detector for Run 2 of the LHC*, JINST **12** (2017) P12009, arXiv:1707.02826 [hep-ex]. Cited on pages 32 and 46.

[68] A. Yamamoto et al., *Progress in ATLAS central solenoid magnet*, IEEE Transactions on Applied Superconductivity **10** (March, 2000) 353–356. Cited on page 33.

[69] ATLAS Collaboration, *Readiness of the ATLAS Tile Calorimeter for LHC collisions*, Eur. Phys. J. C **70** (2010) 1193, arXiv:1007.5423 [hep-ex]. Cited on page 34.

[70] ATLAS Collaboration, *ATLAS liquid-argon calorimeter: Technical Design Report*. Technical Design Report ATLAS. CERN, Geneva, 1996. https://cds.cern.ch/record/331061. Cited on pages 33 and 36.

[71] B. Aubert et al., *Development and Construction of Large Size Signal Electrodes for the ATLAS Electromagnetic Calorimeter*, Nucl. Instrum. Methods Phys. Res., A **5**39 (May, 2004) 558–594. 43 p. https://cds.cern.ch/record/737956. Cited on page 34.

[72] M. Andrieux et al., *Construction and test of the first two sectors of the ATLAS barrel liquid argon presampler*, Nuclear Instruments and Methods in Physics Research Section A: Accelerators, Spectrometers, Detectors and Associated Equipment **479** (2002) no. 2, 316 – 333. Cited on page 35.

[73] ATLAS Collaboration, *Drift Time Measurement in the ATLAS Liquid Argon Electromagnetic Calorimeter using Cosmic Muons*, Eur. Phys. J. **C**70 (2010) 755–785, arXiv:1002.4189 [physics.ins-det]. Cited on page 35.

[74] ATLAS Collaboration, *ATLAS tile calorimeter: Technical Design Report*. Technical Design Report ATLAS. CERN, Geneva, 1996. http://cds.cern.ch/record/331062. Cited on page 35.

[75] ATLAS Collaboration, M. Aleksa et al., *Construction, assembly and tests of the ATLAS electromagnetic end-cap calorimeters*, JINST **3** (2008) P06002. Cited on page 36.

[76] A. Artamonov et al., *The ATLAS forward calorimeters*, JINST **3** (2008) P02010. Cited on page 36.

[77] ATLAS Collaboration, *ATLAS muon spectrometer: Technical design report*, Tech. Rep. CERN-LHCC-97-22, ATLAS-TDR-10, CERN, Geneva, 1997. https://cds.cern.ch/record/331068. Cited on page 36.

[78] P. Vedrine et al., *Manufacturing and integration progress of the ATLAS barrel toroid magnet at CERN*, IEEE Transactions on Applied Superconductivity **14** (June, 2004) 491–494. Cited on page 36.

[79] J. Rey et al., *Cold Mass Integration of the ATLAS Barrel Toroid Magnets at CERN*, IEEE Transactions on Applied Superconductivity **16** (June, 2006) 553–556. Cited on page 36.

[80] D. E. Baynham et al., *Engineering status of the superconducting end cap toroid magnets for the ATLAS experiment at LHC*, IEEE Transactions on Applied Superconductivity **10** (March, 2000) 357–360. Cited on page 36.

[81] ATLAS Collaboration, *Performance of the ATLAS trigger system in 2015*, Eur. Phys. J. C **77** (2017) 317, arXiv:1611.09661 [hep-ex]. Cited on pages 37 and 38.

[82] ATLAS Collaboration, *Performance of the ATLAS Trigger System in 2010*, Eur. Phys. J. C **72** (2012) 1849, arXiv:1110.1530 [hep-ex]. Cited on page 37.

[83] R. Achenbach et al., *The ATLAS level-1 calorimeter trigger*, JINST **3** (2008) P03001. Cited on page 39.

[84] ATLAS Collaboration, *Trigger Menu in 2016*, ATL-DAQ-PUB-2017-001, 2017. https://cds.cern.ch/record/2242069. Cited on page 40.

[85] ATLAS Collaboration, *The performance of the jet trigger for the ATLAS detector during 2011 data taking*, Eur. Phys. J. C **76** (2016) 526, arXiv:1606.07759 [hep-ex]. Cited on page 41.

[86] ATLAS Collaboration, *Jet global sequential corrections with the ATLAS detector in proton–proton collisions at* $\sqrt{s} = 8$ *TeV*, ATLAS-CONF-2015-002, 2015. https://cds.cern.ch/record/2001682. Cited on page 42.

[87] ATLAS Collaboration, *Trigger Menu in 2017*, ATL-DAQ-PUB-2018-002, 2018. https://cds.cern.ch/record/2625986. Cited on page 43.

[88] ATLAS Collaboration, *Expected performance of the ATLAS experiment: detector, trigger and physics*. CERN, Geneva, 2008. arXiv:0901.0512. Cited on page 44.

[89] T. Cornelissen, M. Elsing, S. Fleischmann, W. Liebig, E. Moyse, and A. Salzburger, *Concepts, Design and Implementation of the ATLAS New Tracking (NEWT)*, Tech. Rep. ATL-SOFT-PUB-2007-007. ATL-COM-SOFT-2007-002, CERN, Geneva, Mar, 2007. https://cds.cern.ch/record/1020106. Cited on page 44.

[90] ATLAS Collaboration, *Track Reconstruction Performance of the ATLAS Inner Detector at* $\sqrt{s} = 13$ *TeV*, ATL-PHYS-PUB-2015-018, 2015. https://cds.cern.ch/record/2037683. Cited on page 46.

[91] ATLAS Collaboration, *Reconstruction of primary vertices at the ATLAS experiment in Run 1 proton–proton collisions at the LHC*, Eur. Phys. J. C **77** (2017) 332, arXiv:1611.10235 [hep-ex]. Cited on page 46.

[92] T. Robertson and J. D. Cryer, *An Iterative Procedure for Estimating the Mode*, Journal of the American Statistical Association **69** (1974) no. 348, 1012–1016. Cited on page 46.

[93] ATLAS Collaboration, *Vertex Reconstruction Performance of the ATLAS Detector at*$\sqrt{s} = 13$ *TeV*, ATL-PHYS-PUB-2015-026, 2015. https://cds.cern.ch/record/2037717. Cited on page 46.

[94] ATLAS Collaboration, *Electron reconstruction and identification in the ATLAS experiment using the 2015 and 2016 LHC proton-proton collision data at* $\sqrt{s}$ *= 13 TeV*, Submitted to: Eur. Phys. J. (2019) , arXiv:1902.04655 [physics.ins-det]. Cited on pages 46 and 47.

[95] T. Cornelissen, M. Elsing, I. Gavrilenko, W. Liebig, E. Moyse, and A. Salzburger, *The new ATLAS track reconstruction (NEWT)*, Journal of Physics: Conference Series **119** (July, 2008) 032014. Cited on page 46.

[96] T. G. Cornelissen, M. Elsing, I. Gavrilenko, J.-F. Laporte, W. Liebig, M. Limper, K. Nikolopoulos, A. Poppleton, and A. Salzburger, *The global* $\chi 2$ *track fitter in ATLAS*, Journal of Physics: Conference Series **119** (July, 2008) 032013. Cited on page 46.

[97] ATLAS Collaboration, *Improved electron reconstruction in ATLAS using the Gaussian Sum Filter-based model for bremsstrahlung*, ATLAS-CONF-2012-047, 2012. https://cds.cern.ch/record/1449796. Cited on page 46.

[98] R. Frühwirth, *A Gaussian-mixture approximation of the Bethe-Heitler model of electron energy loss by bremsstrahlung*, Computer Physics Communications **154** (2003) no. 2, 131 – 142. Cited on page 46.

[99] ATLAS Collaboration, *Muon reconstruction performance of the ATLAS detector in proton–proton collision data at* $\sqrt{s} = 13$ *TeV*, Eur. Phys. J. C **76** (2016) 292, arXiv:1603.05598 [hep-ex]. Cited on pages 47 and 103.

[100] J. Illingworth and J. Kittler, *A survey of the hough transform*, Computer Vision, Graphics, and Image Processing **44** (1988) no. 1, 87 – 116. Cited on page 47.

[101] ATLAS Collaboration, *Topological cell clustering in the ATLAS calorimeters and its performance in LHC Run 1*, Eur. Phys. J. C **77** (2017) 490, arXiv:1603.02934 [hep-ex]. Cited on page 48.

[102] M. Cacciari, G. P. Salam, and G. Soyez, *The anti-k_t jet clustering algorithm*, JHEP **04** (2008) 063, arXiv:0802.1189 [hep-ph]. Cited on pages 49 and 210.

[103] M. Cacciari and G. P. Salam, *Dispelling the N^3 myth for the k_t jet-finder*, Phys. Lett. **B**641 (2006) 57–61, arXiv:hep-ph/0512210 [hep-ph]. Cited on pages 49 and 210.

[104] M. Cacciari, G. P. Salam, and G. Soyez, *FastJet User Manual*, Eur. Phys. J. **C**72 (2012) 1896, arXiv:1111.6097 [hep-ph]. Cited on pages 49 and 210.

[105] ATLAS Collaboration, *Jet energy scale measurements and their systematic uncertainties in proton–proton collisions at $\sqrt{s} = 13$ TeV with the ATLAS detector*, Phys. Rev. D **96** (2017) 072002, arXiv:1703.09665 [hep-ex]. Cited on pages 49, 50, and 136.

[106] ATLAS Collaboration, *Performance of pile-up mitigation techniques for jets in pp collisions at $\sqrt{s} = 8$ TeV using the ATLAS detector*, Eur. Phys. J. C **76** (2016) 581, arXiv:1510.03823 [hep-ex]. Cited on page 50.

[107] ATLAS Collaboration, *Measurements of b-jet tagging efficiency with the ATLAS detector using $t\bar{t}$ events at $\sqrt{s} = 13$ TeV*, JHEP **08** (2018) 089, arXiv:1805.01845 [hep-ex]. Cited on pages 50 and 161.

[108] G. Piacquadio and C. Weiser, *A new inclusive secondary vertex algorithm for b-jet tagging in ATLAS*, Journal of Physics: Conference Series **119** (July, 2008) 032032. Cited on page 50.

[109] ATLAS Collaboration, *Identification and energy calibration of hadronically decaying tau leptons with the ATLAS experiment in pp collisions at $\sqrt{s} = 8$ TeV*, Eur. Phys. J. C **75** (2015) 303, arXiv:1412.7086 [hep-ex]. Cited on page 51.

[110] ATLAS Liquid Argon HEC Collaboration, B. Dowler et al., *Performance of the ATLAS hadronic end-cap calorimeter in beam tests*, Nucl. Instrum. Meth. **A**482 (2002) 94–124. Cited on page 51.

[111] T. Barillari et al., *Local Hadronic Calibration*, ATL-LARG-PUB-2009-001, 2008. `https://cds.cern.ch/record/1112035`. Cited on page 51.

[112] ATLAS Collaboration, *Performance of missing transverse momentum reconstruction with the ATLAS detector using proton–proton collisions at $\sqrt{s} = 13$ TeV*, Eur. Phys. J. C **78** (2018) 903, arXiv:1802.08168 [hep-ex]. Cited on pages 52 and 136.

[113] G. Apollinari, O. Brüning, T. Nakamoto, and L. Rossi, *High Luminosity Large Hadron Collider HL-LHC*, CERN Yellow Rep. (2015) no. 5, 1–19, arXiv:1705.08830 [physics.acc-ph]. Cited on page 53.

[114] ATLAS Collaboration, *Letter of Intent for the Phase-II Upgrade of the ATLAS Experiment*, . `https://cds.cern.ch/record/1502664`. Cited on page 53.

[115] ATLAS Collaboration, *Measurement prospects of the pair production and self-coupling of the Higgs boson with the ATLAS experiment at the HL-LHC*, ATL-PHYS-PUB-2018-053, 2018. https://cds.cern.ch/record/2652727. Cited on page 55.

[116] Michele Papucci, Joshua T. Ruderman, Andreas Weiler, *Natural SUSY Endures* , JHEP **09** (2012) , arXiv:1110.6926 [hep-ex]. Cited on page 55.

[117] ATLAS Collaboration, *ATLAS sensitivity to winos and higgsinos with a highly compressed mass spectrum at the HL-LHC*, ATL-PHYS-PUB-2018-031, 2018. https://cds.cern.ch/record/2647294. Cited on pages 56 and 225.

[118] M. Shochet, L. Tompkins, V. Cavaliere, P. Giannetti, A. Annovi, and G. Volpi, *Fast TracKer (FTK) Technical Design Report*, Tech. Rep. CERN-LHCC-2013-007. ATLAS-TDR-021, Jun, 2013. https://cds.cern.ch/record/1552953. ATLAS Fast Tracker Technical Design Report. Cited on pages 57 and 68.

[119] CDF Collaboration, J. A. Adelman et al., *The Silicon Vertex Trigger upgrade at CDF*, Nucl. Instrum. Meth. **A**572 (2007) 361–364. Cited on pages 57 and 68.

[120] ATLAS Collaboration, *Technical Design Report for the ATLAS Inner Tracker Pixel Detector*, Tech. Rep. CERN-LHCC-2017-021. ATLAS-TDR-030, CERN, Geneva, Sep, 2017. https://cds.cern.ch/record/2285585. Cited on pages 69, 74, and 75.

[121] ATLAS Collaboration, *Technical Design Report for the ATLAS Inner Tracker Strip Detector*, Tech. Rep. CERN-LHCC-2017-005. ATLAS-TDR-025, CERN, Geneva, Apr, 2017. http://cds.cern.ch/record/2257755. Cited on page 69.

[122] ATLAS Collaboration, *Expected Tracking Performance of the ATLAS Inner Tracker at the HL-LHC*, ATL-PHYS-PUB-2019-014, 2019. https://cds.cern.ch/record/2669540. Cited on pages 74 and 75.

[123] A. Annovi, G. Calderini, F. Crescioli, F. De Canio, L. Frontini, T. Kubota, V. Liberali, P. Luciano, F. Palla, S. R. Shojaii, C. Sotiropoulou, A. Stabile, and G. Traversi, *A low-power and high-density Associative Memory in 28 nm CMOS technology*, in *2017 6th International Conference on Modern Circuits and Systems Technologies (MOCAST)*, pp. 1–4. May, 2017. Cited on page 80.

[124] C. Borschensky, M. Kramer, A. Kulesza, M. Mangano, S. Padhi, T. Plehn, and X. Portell, *Squark and gluino production cross sections in pp collisions at $\sqrt{s}$ = 13, 14, 33 and 100 TeV*, Eur. Phys. J. C **7**4 (2014) no. 12, 3174, arXiv:1407.5066 [hep-ph]. Cited on pages 85 and 95.

[125] J. Fiaschi and M. Klasen, *Neutralino-chargino pair production at* NLO + NLL *with resummation-improved parton density functions for LHC Run II*, Phys. Rev. D **9**8 (Sep, 2018) 055014. Cited on page 85.

[126] ATLAS Collaboration, *Search for heavy charged long-lived particles in the ATLAS detector in 31.6 fb^{-1} of proton-proton collision data at $\sqrt{s} = 13$ TeV*, arXiv:1902.01636 [hep-ex]. Cited on page 85.

[127] CMS Collaboration, *Search for long-lived charged particles in proton-proton collisions at $\sqrt{s}$ = 13 TeV*, Phys. Rev. **D**94 (2016) no. 11, 112004, arXiv:1609.08382 [hep-ex]. Cited on page 85.

[128] T. Yamagata, Y. Takamori, and H. Utsunomiya, *Search for anomalously heavy hydrogen in deep sea water at 4000-m*, Phys. Rev. **D**47 (1993) 1231–1234. Cited on page 86.

[129] T. Falk, K. A. Olive, and M. Srednicki, *Heavy sneutrinos as dark matter*, Phys. Lett. **B**339 (1994) 248–251, arXiv:hep-ph/9409270 [hep-ph]. Cited on page 86.

[130] L. J. Hall, T. Moroi, and H. Murayama, *Sneutrino cold dark matter with lepton number violation*, Phys. Lett. **B**424 (1998) 305–312, arXiv:hep-ph/9712515 [hep-ph]. Cited on page 86.

[131] N. Arkani-Hamed, L. J. Hall, H. Murayama, D. Tucker-Smith, and N. Weiner, *Small neutrino masses from supersymmetry breaking*, Phys. Rev. **D**64 (2001) 115011, arXiv:hep-ph/0006312 [hep-ph]. Cited on page 86.

[132] ALEPH, DELPHI, L3, OPAL, SLD, LEP Electroweak Working Group, SLD Electroweak Group, SLD Heavy Flavour Group, *Precision electroweak measurements on the Z resonance*, Phys. Rept. **427** (2006) 257–454, arXiv:hep-ex/0509008 [hep-ex]. Cited on page 86.

[133] M. Ibe, S. Matsumoto, and R. Sato, *Mass Splitting between Charged and Neutral Winos at Two-Loop Level*, Phys. Lett. **B**721 (2013) 252–260, arXiv:1212.5989 [hep-ph]. Cited on pages 86 and 241.

[134] ALEPH Collaboration, *Absolute mass lower limit for the lightest neutralino of the MSSM from e^+e^- data at $\sqrt{s}$ up to 209 GeV*, Phys. Lett. B **5**83 (2004) 247–263. Cited on page 86.

[135] DELPHI Collaboration, *Searches for supersymmetric particles in e^+e^- collisions up to 208 GeV and interpretation of the results within the MSSM*, Eur. Phys. J. C **31** (2003) 421–479, arXiv:hep-ex/0311019. Cited on page 86.

[136] OPAL Collaboration, *Search for anomalous production of dilepton events with missing transverse momentum in e^+e^- collisions at $\sqrt{s}$ = 183 GeV to 209 GeV*, Eur. Phys. J. C **32** (2004) 453–473, arXiv:hep-ex/0309014. Cited on page 86.

[137] ALEPH Collaboration, *Search for charginos nearly mass degenerate with the lightest neutralino in e^+e^- collisions at center-of-mass energies up to 209 GeV*, Phys. Lett. B **533** (2002) 223–236, arXiv:hep-ex/0203020. Cited on page 86.

[138] L3 Collaboration, *Search for charginos with a small mass difference with the lightest supersymmetric particle at $\sqrt{s}$ = 189 GeV*, Phys. Lett. B **4**82 (2000) 31–42, arXiv:hep-ex/0002043. Cited on page 86.

[139] OPAL Collaboration, *Search for nearly mass degenerate charginos and neutralinos at LEP*, Eur. Phys. J. C **2**9 (2003) 479–489, arXiv:hep-ex/0210043. Cited on page 86.

[140] S. D. Thomas and J. D. Wells, *Phenomenology of Massive Vectorlike Doublet Leptons*, Phys. Rev. Lett. **8**1 (1998) 34–37, arXiv:hep-ph/9804359 [hep-ph]. Cited on page 86.

[141] ATLAS Collaboration, *Search for long-lived charginos based on a disappearing-track signature in pp collisions at $\sqrt{s} = 13$ TeV with the ATLAS detector*, JHEP **06** (2018) 022, arXiv:1712.02118 [hep-ex]. Cited on pages 89 and 241.

[142] ATLAS Collaboration, *ATLAS Run 1 searches for direct pair production of third-generation squarks at the Large Hadron Collider*, Eur. Phys. J. C **7**5 (2015) 510, arXiv:1506.08616 [hep-ex]. Cited on pages 89, 130, and 159.

[143] CMS Collaboration, *Search for top squark pair production in compressed-mass-spectrum scenarios in proton-proton collisions at $\sqrt{s}$ = 8 TeV using the α_T variable*, Phys. Lett. **B**767 (2017) 403–430, arXiv:1605.08993 [hep-ex]. Cited on page 89.

[144] CMS Collaboration, *Search for top-squark pairs decaying into Higgs or Z bosons in pp collisions at $\sqrt{s}$=8 TeV*, Phys. Lett. **B**736 (2014) 371–397, arXiv:1405.3886 [hep-ex]. Cited on page 89.

[145] CMS Collaboration, *Search for top squark and higgsino production using diphoton Higgs boson decays*, Phys. Rev. Lett. **1**12 (2014) 161802, arXiv:1312.3310 [hep-ex]. Cited on page 89.

[146] CMS Collaboration, *Search for top-squark pair production in the single-lepton final state in pp collisions at $\sqrt{s}$ = 8 TeV*, Eur. Phys. J. **C**73 (2013) no. 12, 2677, arXiv:1308.1586 [hep-ex]. Cited on page 89.

[147] CMS Collaboration, *Search for Supersymmetry in Hadronic Final States with Missing Transverse Energy Using the Variables α_T and b-Quark Multiplicity in pp collisions at* $\sqrt{s} = 8$ *TeV*, Eur. Phys. J. **C**73 (2013) no. 9, 2568, arXiv:1303.2985 [hep-ex]. Cited on page 89.

[148] CMS Collaboration, *Search for supersymmetry with razor variables in pp collisions at $\sqrt{s}$=7 TeV*, Phys. Rev. **D**90 (2014) no. 11, 112001, arXiv:1405.3961 [hep-ex]. Cited on page 89.

[149] ATLAS Collaboration, *Search for top squarks in final states with one isolated lepton, jets, and missing transverse momentum in* $\sqrt{s} = 13$ *TeV pp collisions with the ATLAS detector*, Phys. Rev. D **9**4 (2016) no. 5, 052009, arXiv:1606.03903 [hep-ex]. Cited on pages 89, 119, 122, 149, and 159.

[150] CMS Collaboration, *Searches for pair production of third-generation squarks in* $\sqrt{s} = 13$ *TeV pp collisions*, Eur. Phys. J. **C**77 (2017) no. 5, 327, arXiv:1612.03877 [hep-ex]. Cited on page 89.

[151] CMS Collaboration, *A search for new phenomena in pp collisions at* $\sqrt{s} = 13$ *TeV in final states with missing transverse momentum and at least one jet using the* α_{T} *variable*, Eur. Phys. J. **C**77 (2017) no. 5, 294, arXiv:1611.00338 [hep-ex]. Cited on page 89.

[152] CMS Collaboration, *Inclusive search for supersymmetry using razor variables in pp collisions at $\sqrt{s}$ = 13 TeV*, Phys. Rev. **D**95 (2017) no. 1, 012003, arXiv:1609.07658 [hep-ex]. Cited on page 89.

[153] CDF Collaboration, *Search for Pair Production of Supersymmetric Top Quarks in Dilepton Events from p anti-p Collisions at S**(1/2) = 1.96 TeV*, Phys. Rev. Lett. **1**04 (2010) 251801, arXiv:0912.1308 [hep-ex]. Cited on page 89.

[154] D0 Collaboration, *Search for the lightest scalar top quark in events with two leptons in $p\bar{p}$ collisions at $\sqrt{s}$ = 1.96-TeV*, Phys. Lett. **B**675 (2009) 289–296, arXiv:0811.0459 [hep-ex]. Cited on page 89.

[155] ATLAS Collaboration, *Search for supersymmetry in events with b-tagged jets and missing transverse momentum in pp collisions at* $\sqrt{s} = 13$ *TeV with the ATLAS detector*, JHEP **1**1 (2017) 195, arXiv:1708.09266 [hep-ex]. Cited on page 92.

[156] ATLAS Collaboration, *Search for direct top squark pair production in final states with two leptons in $\sqrt{s} = 13$ TeV pp collisions with the ATLAS detector*, Eur. Phys. J. C **77** (2017) 898, arXiv:1708.03247 [hep-ex]. Cited on pages 92 and 159.

[157] ATLAS Collaboration, *Search for direct top squark pair production in events with a Higgs or Z boson, and missing transverse momentum in $\sqrt{s} = 13$ TeV pp collisions with the ATLAS detector*, JHEP **08** (2017) 006, arXiv:1706.03986 [hep-ex]. Cited on page 92.

[158] ATLAS Collaboration, *Search for a scalar partner of the top quark in the jets plus missing transverse momentum final state at $\sqrt{s}$=13 TeV with the ATLAS detector*, JHEP **12** (2017) 085, arXiv:1709.04183 [hep-ex]. Cited on pages 92, 154, and 159.

[159] ATLAS Collaboration, *Search for supersymmetry in final states with charm jets and missing transverse momentum in 13 TeV pp collisions with the ATLAS detector*, JHEP **09** (2018) 050, arXiv:1805.01649 [hep-ex]. Cited on page 92.

[160] ATLAS Collaboration, *Search for supersymmetry in final states with two same-sign or three leptons and jets using 36 fb^{-1} of $\sqrt{s} = 13$ TeV pp collision data with the ATLAS detector*, JHEP **09** (2017) 084, arXiv:1706.03731 [hep-ex]. Cited on page 92.

[161] CMS Collaboration, *Search for new phenomena with the M_{T2} variable in the all-hadronic final state produced in protonproton collisions at $\sqrt{s} = 13$ TeV*, Eur. Phys. J. **C**77 (2017) no. 10, 710, arXiv:1705.04650 [hep-ex]. Cited on page 92.

[162] CMS Collaboration, *Search for top squark pair production in pp collisions at $\sqrt{s} = 13$ TeV using single lepton events*, JHEP **10** (2017) 019, arXiv:1706.04402 [hep-ex]. Cited on page 92.

[163] CMS Collaboration, *Search for direct production of supersymmetric partners of the top quark in the all-jets final state in proton-proton collisions at $\sqrt{s} = 13$ TeV*, JHEP **10** (2017) 005, arXiv:1707.03316 [hep-ex]. Cited on page 92.

[164] CMS Collaboration, *Search for the pair production of third-generation squarks with two-body decays to a bottom or charm quark and a neutralino in protonproton collisions at $\sqrt{s} = 13$ TeV*, Phys. Lett. **B**778 (2018) 263–291, arXiv:1707.07274 [hep-ex]. Cited on page 92.

[165] CMS Collaboration, *Search for supersymmetry in proton-proton collisions at 13 TeV using identified top quarks*, Phys. Rev. **D**97 (2018) no. 1, 012007, arXiv:1710.11188 [hep-ex]. Cited on page 92.

[166] CMS Collaboration, *Search for top squarks and dark matter particles in opposite-charge dilepton final states at $\sqrt{s} = 13$ TeV*, Phys. Rev. **D**97 (2018) no. 3, 032009, arXiv:1711.00752 [hep-ex]. Cited on page 92.

[167] CMS Collaboration, *Search for new physics in events with two soft oppositely charged leptons and missing transverse momentum in proton-proton collisions at $\sqrt{s} = 13$ TeV*, Phys. Lett. **B**782 (2018) 440–467, arXiv:1801.01846 [hep-ex]. Cited on page 92.

[168] CMS Collaboration, *Search for top squarks decaying via four-body or chargino-mediated modes in single-lepton final states in proton-proton collisions at $\sqrt{s} = 13$ TeV*, JHEP **09** (2018) 065, arXiv:1805.05784 [hep-ex]. Cited on page 92.

[169] CMS Collaboration, *Inclusive search for supersymmetry in pp collisions at $\sqrt{s}$ = 13 TeV using razor variables and boosted object identification in zero and one lepton final states*, JHEP **03** (2019) 031, arXiv:1812.06302 [hep-ex]. Cited on page 92.

[170] CMS Collaboration, *Search for the pair production of light top squarks in the $e^{\pm}\mu^{\mp}$ final state in proton-proton collisions at $\sqrt{s}$ = 13 TeV*, arXiv:1901.01288 [hep-ex]. Cited on page 92.

[171] S. Alioli, P. Nason, C. Oleari, and E. Re, *A general framework for implementing NLO calculations in shower Monte Carlo programs: the POWHEG BOX*, JHEP **06** (2010) 043, arXiv:1002.2581 [hep-ph]. Cited on page 92.

[172] D. J. Lange, *The EvtGen particle decay simulation package*, Nuclear Instruments and Methods in Physics Research Section A: Accelerators, Spectrometers, Detectors and Associated Equipment **462** (2001) no. 1, 152 – 155. BEAUTY2000, Proceedings of the 7th Int. Conf. on B-Physics at Hadron Machines. Cited on page 92.

[173] ATLAS Collaboration, *ATLAS Pythia 8 tunes to* 7 *TeV data*, ATL-PHYS-PUB-2014-021, 2014. `https://cds.cern.ch/record/1966419`. Cited on pages 93, 209, and 212.

[174] J. Pumplin, D. R. Stump, J. Huston, H. L. Lai, P. M. Nadolsky, and W. K. Tung, *New generation of parton distributions with uncertainties from global QCD analysis*, JHEP **07** (2002) 012, arXiv:hep-ph/0201195 [hep-ph]. Cited on page 93.

[175] ATLAS Collaboration, *Simulation of top-quark production for the ATLAS experiment at* $\sqrt{s} = 13$ *TeV*, ATL-PHYS-PUB-2016-004, 2016. `https://cds.cern.ch/record/2120417`. Cited on page 93.

[176] ATLAS Collaboration, *Studies on top-quark Monte Carlo modelling for Top2016*, ATL-PHYS-PUB-2016-020, 2016. `https://cds.cern.ch/record/2216168`. Cited on pages 93 and 158.

[177] T. Gleisberg and S. Hoeche, *Comix, a new matrix element generator*, JHEP **12** (2008) 039, arXiv:0808.3674 [hep-ph]. Cited on page 94.

[178] F. Cascioli, P. Maierhofer, and S. Pozzorini, *Scattering Amplitudes with Open Loops*, Phys. Rev. Lett. **108** (2012) 111601, arXiv:1111.5206 [hep-ph]. Cited on pages 94 and 209.

[179] S. Hoeche, F. Krauss, M. Schonherr, and F. Siegert, *QCD matrix elements + parton showers: The NLO case*, JHEP **04** (2013) 027, arXiv:1207.5030 [hep-ph]. Cited on page 94.

[180] ATLAS Collaboration, *Monte Carlo Generators for the Production of a W or Z/γ^* Boson in Association with Jets at ATLAS in Run 2*, ATL-PHYS-PUB-2016-003, 2016. `https://cds.cern.ch/record/2120133`. Cited on page 94.

[181] P. Artoisenet, R. Frederix, O. Mattelaer, and R. Rietkerk, *Automatic spin-entangled decays of heavy resonances in Monte Carlo simulations*, JHEP **03** (2013) 015, arXiv:1212.3460 [hep-ph]. Cited on page 94.

[182] W. Beenakker, M. Kramer, T. Plehn, M. Spira, and P. M. Zerwas, *Stop production at hadron colliders*, Nucl. Phys. **B**515 (1998) 3–14, hep-ph/9710451. Cited on page 95.

[183] W. Beenakker, S. Brensing, M. Kramer, A. Kulesza, E. Laenen, et al., *Soft-gluon resummation for squark and gluino hadroproduction*, JHEP **0**912 (2009) 041, arXiv:0909.4418 [hep-ph]. Cited on page 95.

[184] W. Beenakker et al., *Squark and gluino hadroproduction*, Int.J.Mod.Phys. **A**26 (2011) 2637–2664, arXiv:1105.1110 [hep-ph]. Cited on page 95.

[185] I. Low, *Polarized charginos (and top quarks) in scalar top quark decays*, Phys. Rev. D **8**8 (2013) no. 9, 095018, arXiv:1304.0491 [hep-ph]. Cited on page 96.

[186] M. Perelstein and A. Weiler, *Polarized Tops from Stop Decays at the LHC*, JHEP **03** (2009) 141, arXiv:0811.1024 [hep-ph]. Cited on page 96.

[187] A. Djouadi, J. Kalinowski, and M. Spira, *HDECAY: A Program for Higgs boson decays in the standard model and its supersymmetric extension*, Comput. Phys. Commun. **1**08 (1998) 56–74, arXiv:hep-ph/9704448 [hep-ph]. Cited on page 96.

[188] A. Djouadi, M. M. Muhlleitner, and M. Spira, *Decays of supersymmetric particles: The Program SUSY-HIT (SUspect-SdecaY-Hdecay-InTerface)*, Acta Phys. Polon. **B**38 (2007) 635–644, arXiv:hep-ph/0609292 [hep-ph]. Cited on page 96.

[189] B. C. Allanach, *SOFTSUSY: a program for calculating supersymmetric spectra*, Comput. Phys. Commun. **1**43 (2002) 305–331, arXiv:hep-ph/0104145 [hep-ph]. Cited on page 96.

[190] B. C. Allanach, P. Athron, L. C. Tunstall, A. Voigt, and A. G. Williams, *Next-to-Minimal SOFTSUSY*, Comput. Phys. Commun. **1**85 (2014) 2322–2339, arXiv:1311.7659 [hep-ph]. Cited on page 96.

[191] N. Arkani-Hamed, A. Delgado, and G. F. Giudice, *The Well-tempered neutralino*, Nucl. Phys. **B**741 (2006) 108–130, arXiv:hep-ph/0601041 [hep-ph]. Cited on page 98.

[192] G. Belanger et al., *MicrOMEGAs 2.0: A Program to calculate the relic density of dark matter in a generic model*, Comput. Phys. Commun. **1**76 (2007) 367, arXiv:hep-ph/0607059 [hep-ph]. Cited on page 98.

[193] G. Belanger et al., *micrOMEGAs: A Tool for dark matter studies*, Nuovo Cim. C033N2 (2010) 111, arXiv:1005.4133 [hep-ph]. Cited on page 98.

[194] ATLAS Collaboration, *Luminosity determination in pp collisions at* $\sqrt{s} = 8$ *TeV using the ATLAS detector at the LHC*, Eur. Phys. J. C **7**6 (2016) 653, arXiv:1608.03953 [hep-ex]. Cited on page 99.

[195] ATLAS Collaboration, *Selection of jets produced in* 13 *TeV proton–proton collisions with the ATLAS detector*, ATLAS-CONF-2015-029, 2015. `https://cds.cern.ch/record/2037702`. Cited on page 100.

[196] ATLAS Collaboration, *Characterisation and mitigation of beam-induced backgrounds observed in the ATLAS detector during the 2011 proton–proton run*, JINST **8** (2013) P07004, arXiv:1303.0223 [hep-ex]. Cited on page 100.

[197] C. G. Lester and D. J. Summers, *Measuring masses of semiinvisibly decaying particles pair produced at hadron colliders*, Phys. Lett. **B**463 (1999) 99–103, arXiv:hep-ph/9906349 [hep-ph]. Cited on page 109.

[198] A. Barr, C. Lester, and P. Stephens, *m(T2): The Truth behind the glamour*, J. Phys. **G**29 (2003) 2343–2363, arXiv:hep-ph/0304226 [hep-ph]. Cited on page 109.

[199] ATLAS Collaboration, *Search for direct third-generation squark pair production in final states with missing transverse momentum and two b-jets in $\sqrt{s} = 8$ TeV pp collisions with the ATLAS detector*, JHEP **10** (2013) 189, arXiv:1308.2631 [hep-ex]. Cited on page 130.

[200] ATLAS Collaboration, *Jet energy resolution in proton–proton collisions at $\sqrt{s} = 7$ TeV recorded in 2010 with the ATLAS detector*, Eur. Phys. J. C **73** (2013) 2306, arXiv:1210.6210 [hep-ex]. Cited on page 136.

[201] M. Baak, G. J. Besjes, D. Côte, A. Koutsman, J. Lorenz, and D. Short, *HistFitter software framework for statistical data analysis*, Eur. Phys. J. **C**75 (2015) 153, arXiv:1410.1280 [hep-ex]. Cited on page 139.

[202] A. L. Read, *Presentation of search results: The CL_s technique*, J. Phys. G **2**8 (2002) 2693. Cited on pages 139 and 142.

[203] S. S. Wilks, *The Large-Sample Distribution of the Likelihood Ratio for Testing Composite Hypotheses*, Ann. Math. Statist. **9** (03, 1938) 60–62. Cited on page 141.

[204] G. Cowan, K. Cranmer, E. Gross, and O. Vitells, *Asymptotic formulae for likelihood-based tests of new physics*, Eur. Phys. J. **C**71 (2011) 1554, arXiv:1007.1727 [physics.data-an]. [Erratum: Eur. Phys. J.C73,2501(2013)]. Cited on page 142.

[205] ATLAS, CMS Collaborations, *Recommended predictions for top-quark-pair cross sections using the Top++v2.0 program*, 2014. `https://twiki.cern.ch/twiki/bin/view/LHCPhysics/TtbarNNLO`. Cited on pages 155 and 194.

[206] Tevatron Electroweak Working Group, *Combination of CDF and D0 Results on the Mass of the Top Quark using up to 9.7 fb^{-1} at the Tevatron*, arXiv:1407.2682 [hep-ex]. Cited on page 155.

[207] ATLAS and CMS Collaborations, *Combination of ATLAS and CMS results on the mass of the top-quark using up to* 4.9 *fb^{-1} of $\sqrt{s} = 7$ TeV LHC data*, ATLAS-CONF-2013-102, 2013. `https://cds.cern.ch/record/1601811`. Cited on page 155.

[208] M. Botje et al., *The PDF4LHC Working Group Interim Recommendations*, arXiv:1101.0538 [hep-ph]. Cited on page 155.

[209] A. D. Martin, W. J. Stirling, R. S. Thorne, and G. Watt, *Uncertainties on alpha(S) in global PDF analyses and implications for predicted hadronic cross sections*, Eur. Phys. J. **C**64 (2009) 653–680, arXiv:0905.3531 [hep-ph]. Cited on page 155.

[210] J. Gao, M. Guzzi, J. Huston, H.-L. Lai, Z. Li, P. Nadolsky, J. Pumplin, D. Stump, and C. P. Yuan, *CT10 next-to-next-to-leading order global analysis of QCD*, Phys. Rev. **D**89 (2014) no. 3, 033009, arXiv:1302.6246 [hep-ph]. Cited on page 155.

[211] R. D. Ball et al., *Parton distributions with LHC data*, Nucl. Phys. B **8**67 (2013) 244–289, arXiv:1207.1303 [hep-ph]. Cited on page 155.

[212] J. M. Campbell, R. Frederix, F. Maltoni, and F. Tramontano, *Next-to-Leading-Order Predictions for t-Channel Single-Top Production at Hadron Colliders*, Phys. Rev. Lett. **1**02 (2009) 182003, arXiv:0903.0005 [hep-ph]. Cited on page 155.

[213] P. Kant, O. M. Kind, T. Kintscher, T. Lohse, T. Martini, S. M olbitz, P. Rieck, and P. Uwer, *HatHor for single top-quark production: Updated predictions and uncertainty estimates for single top-quark production in hadronic collisions*, Comput. Phys. Commun. **191** (2015) 74–89, arXiv:1406.4403 [hep-ph]. Cited on page 155.

[214] N. Kidonakis, *Theoretical results for electroweak-boson and single-top production*, PoS **D**IS2015 (2015) 170, arXiv:1506.04072 [hep-ph]. Cited on page 155.

[215] N. Kidonakis, *Theoretical results for top-quark cross sections and distributions*, PoS **I**CHEP2016 (2016) 654, arXiv:1609.07404 [hep-ph]. Cited on page 155.

[216] N. Kidonakis, *NNLL resummation for s-channel single top quark production*, Phys. Rev. **D**81 (2010) 054028, arXiv:1001.5034 [hep-ph]. Cited on page 155.

[217] ATLAS Collaboration, *Measurements of top-quark pair differential cross-sections in the lepton+jets channel in pp collisions at $\sqrt{s} = 13$ TeV using the ATLAS detector*, JHEP **11** (2017) 191, arXiv:1708.00727 [hep-ex]. Cited on page 155.

[218] ATLAS Collaboration, *Measurements of top-quark pair differential cross-sections in the $e\mu$ channel in pp collisions at $\sqrt{s} = 13$ TeV using the ATLAS detector*, Eur. Phys. J. C **77** (2017) 292, arXiv:1612.05220 [hep-ex]. Cited on page 155.

[219] CMS Collaboration, *Measurement of normalized differential $t\bar{t}$ cross sections in the dilepton channel from pp collisions at $\sqrt{s} = 13$ TeV*, JHEP **04** (2018) 060, arXiv:1708.07638 [hep-ex]. Cited on page 155.

[220] CMS Collaboration, *Measurements of differential cross sections of top quark pair production as a function of kinematic event variables in proton–proton collisions at $\sqrt{s} = 13$ TeV*, JHEP **06** (2018) 002, arXiv:1803.03991 [hep-ex]. Cited on page 155.

[221] CMS Collaboration, *Measurement of differential cross sections for the production of top quark pairs and of additional jets in lepton+jets events from pp collisions at $\sqrt{s} = 13$ TeV*, Phys. Rev. D **97** (2018) 112003, arXiv:1803.08856 [hep-ex]. Cited on page 155.

[222] ATLAS Collaboration, *Measurement of the inclusive cross-sections of single top-quark and top-antiquark t-channel production in pp collisions at $\sqrt{s}$ = 13 TeV with the ATLAS detector*, JHEP **04** (2017) 086, arXiv:1609.03920 [hep-ex]. Cited on page 155.

[223] CMS Collaboration, *Measurement of the single top quark and antiquark production cross sections in the t channel and their ratio in proton-proton collisions at $\sqrt{s}$ = 13 TeV*, arXiv:1812.10514 [hep-ex]. Cited on page 155.

[224] ATLAS Collaboration, *Measurement of the cross-section for producing a W boson in association with a single top quark in pp collisions at $\sqrt{s} = 13$ TeV with ATLAS*, JHEP **01** (2018) 063, arXiv:1612.07231 [hep-ex]. Cited on pages 156 and 159.

[225] CMS Collaboration, *Measurement of the production cross section for single top quarks in association with W bosons in proton-proton collisions at $\sqrt{s} = 13$ TeV*, JHEP **10** (2018) 117, arXiv:1805.07399 [hep-ex]. Cited on pages 156 and 159.

[226] ATLAS Collaboration, *Evidence for single top-quark production in the s-channel in proton–proton collisions at $\sqrt{s} = 8$ TeV with the ATLAS detector using the Matrix Element Method*, Phys. Lett. B **756** (2016) 228, arXiv:1511.05980 [hep-ex]. Cited on page 156.

[227] S. Frixione, P. Nason, and G. Ridolfi, *A Positive-weight next-to-leading-order Monte Carlo for heavy flavour hadroproduction*, JHEP **09** (2007) 126, arXiv:0707.3088 [hep-ph]. Cited on page 157.

[228] S. Frixione, E. Laenen, P. Motylinski, C. D. White, and B. R. Webber, *Single-top hadroproduction in association with a W boson*, JHEP **07** (2008) 029, arXiv:0805.3067 [hep-ph]. Cited on pages 158 and 159.

[229] W. Hollik, J. M. Lindert, and D. Pagani, *NLO corrections to squark-squark production and decay at the LHC*, JHEP **03** (2013) 139, arXiv:1207.1071 [hep-ph]. Cited on page 158.

[230] F. Demartin, B. Maier, F. Maltoni, K. Mawatari, and M. Zaro, *tWH associated production at the LHC*, Eur. Phys. J. C **77** (2017) no. 1, 34, arXiv:1607.05862 [hep-ph]. Cited on page 158.

[231] A. Denner, S. Dittmaier, S. Kallweit, and S. Pozzorini, *NLO QCD corrections to WWbb production at hadron colliders*, Phys. Rev. Lett. **106** (2011) 052001, arXiv:1012.3975 [hep-ph]. Cited on page 158.

[232] A. Denner, S. Dittmaier, S. Kallweit, and S. Pozzorini, *NLO QCD corrections to off-shell top-antitop production with leptonic decays at hadron colliders*, JHEP **10** (2012) 110, arXiv:1207.5018 [hep-ph]. Cited on page 158.

[233] G. Bevilacqua, M. Czakon, A. van Hameren, C. Papadopoulos, and M. Worek, *Complete off-shell effects in top quark pair hadroproduction with leptonic decay at next-to-leading order*, JHEP **02** (2011) 083, arXiv:1012.4230 [hep-ph]. Cited on page 158.

[234] F. Cascioli, S. Kallweit, P. Maierhfer, and S. Pozzorini, *A unified NLO description of top-pair and associated Wt production*, Eur. Phys. J. **C**74 (2014) no. 3, 2783, arXiv:1312.0546 [hep-ph]. Cited on page 158.

[235] R. Frederix, *Top Quark Induced Backgrounds to Higgs Production in the $WW^{(*)} \rightarrow ll\nu\nu$ Decay Channel at Next-to-Leading-Order in QCD*, Phys. Rev. Lett. **112** (2014) no. 8, 082002, arXiv:1311.4893 [hep-ph]. Cited on page 158.

[236] T. Ježo, J. M. Lindert, P. Nason, C. Oleari, and S. Pozzorini, *An NLO+PS generator for $t\bar{t}$ and Wt production and decay including non-resonant and interference effects*, Eur. Phys. J. **C**76 (2016) no. 12, 691, arXiv:1607.04538 [hep-ph]. Cited on pages 158 and 209.

[237] ATLAS Collaboration, *Measurement of differential cross-sections of a single top quark produced in association with a W boson at $\sqrt{s} = 13$ TeV with ATLAS*, Eur. Phys. J. C **78** (2018) 186, arXiv:1712.01602 [hep-ex]. Cited on page 159.

[238] ATLAS Collaboration, *Measurement of the production cross-section of a single top quark in association with a W boson at 8 TeV with the ATLAS experiment*, JHEP **01** (2016) 064, arXiv:1510.03752 [hep-ex]. Cited on page 159.

[239] CMS Collaboration, *Observation of the associated production of a single top quark and a W boson in pp collisions at $\sqrt{s}$ =8 TeV*, Phys. Rev. Lett. **112** (2014) no. 23, 231802, arXiv:1401.2942 [hep-ex]. Cited on page 159.

[240] CMS Collaboration, *Evidence for associated production of a single top quark and W boson in pp collisions at $\sqrt{s}$ = 7 TeV*, Phys. Rev. Lett. **110** (2013) 022003, arXiv:1209.3489 [hep-ex]. Cited on page 159.

[241] ATLAS Collaboration, *Evidence for the associated production of a W boson and a top quark in ATLAS at* $\sqrt{s} = 7$ *TeV*, Phys. Lett. **B**716 (2012) 142–159, arXiv:1205.5764 [hep-ex]. Cited on page 159.

[242] ATLAS Collaboration, *Search for bottom squark pair production in proton-proton collisions at* $\sqrt{s} = 13$ *TeV with the ATLAS detector*, Eur. Phys. J. C **76** (2016) no. 10, 547, arXiv:1606.08772 [hep-ex]. Cited on page 159.

[243] ATLAS Collaboration, *Search for gluinos in events with an isolated lepton, jets and missing transverse momentum at* $\sqrt{s}$ *= 13 Te V with the ATLAS detector*, Eur. Phys. J. C **76** (2016) no. 10, 565, arXiv:1605.04285 [hep-ex]. Cited on page 159.

[244] ATLAS Collaboration, *Measurement of the* $t\bar{t}$ *production cross-section using* $e\mu$ *events with b-tagged jets in pp collisions at* $\sqrt{s}$*=13 TeV with the ATLAS detector*, Phys. Lett. **B**761 (2016) 136–157, arXiv:1606.02699 [hep-ex]. Cited on page 166.

[245] ATLAS Collaboration, *Measurements of fiducial cross-sections for* $t\bar{t}$ *production with one or two additional b-jets in pp collisions at* $\sqrt{s}$ *=8 TeV using the ATLAS detector*, Eur. Phys. J. **C**76 (2016) no. 1, 11, arXiv:1508.06868 [hep-ex]. Cited on page 170.

[246] ATLAS Collaboration, *Measurements of Higgs boson properties in the diphoton decay channel with* $36\,fb^{-1}$ *of pp collision data at* $\sqrt{s} = 13$ *TeV with the ATLAS detector*, Phys. Rev. D **98** (2018) 052005, arXiv:1802.04146 [hep-ex]. Cited on page 176.

[247] ATLAS Collaboration, *Measurement of inclusive and differential cross sections in the* $H \to ZZ^* \to 4\ell$ *decay channel in pp collisions at* $\sqrt{s} = 13$ *TeV with the ATLAS detector*, JHEP **10** (2017) 132, arXiv:1708.02810 [hep-ex]. Cited on page 176.

[248] G. D'Agostini, *A Multidimensional unfolding method based on Bayes' theorem*, Nucl. Instrum. Meth. A **362** (1995) 487–498. Cited on page 176.

[249] A. Hocker and V. Kartvelishvili, *SVD approach to data unfolding*, Nucl. Instrum. Meth. **A**372 (1996) 469–481, arXiv:hep-ph/9509307 [hep-ph]. Cited on page 177.

[250] T. Adye, *Unfolding algorithms and tests using RooUnfold*, arXiv:1105.1160 [physics.data-an]. Cited on page 177.

[251] J. Butterworth et al., *PDF4LHC recommendations for LHC Run II*, J. Phys. G **43** (2016) 023001, arXiv:1510.03865 [hep-ph]. Cited on page 194.

[252] ATLAS Collaboration, *Single Boson and Diboson Production Cross Sections in pp collisions at* $\sqrt{s} = 7$ *TeV*, ATL-COM-PHYS-2010-695, 2010. `https://cds.cern.ch/record/1287902`. Cited on page 194.

[253] N. Kidonakis, *Two-loop soft anomalous dimensions for single top quark associated production with a* W^- *or* H^-, Phys. Rev. D **82** (2010) 054018, arXiv:1005.4451 [hep-ph]. Cited on page 194.

[254] CDF Collaboration, *Observation of top quark production in* $\bar{p}p$ *collisions*, Phys. Rev. Lett. **74** (1995) 2626–2631, arXiv:hep-ex/9503002 [hep-ex]. Cited on page 204.

[255] D0 Collaboration, *Observation of the top quark*, Phys. Rev. Lett. **74** (1995) 2632–2637, arXiv:hep-ex/9503003 [hep-ex]. Cited on page 204.

[256] ATLAS, CDF, CMS, D0 Collaboration, *First combination of Tevatron and LHC measurements of the top-quark mass*, arXiv:1403.4427 [hep-ex]. Cited on page 204.

[257] ATLAS Collaboration, *Measurement of the top quark mass in the $t\bar{t} \rightarrow$ dilepton channel from $\sqrt{s} = 8$ TeV ATLAS data*, Phys. Lett. B **761** (2016) 350, arXiv:1606.02179 [hep-ex]. Cited on page 204.

[258] ATLAS Collaboration, *Top-quark mass measurement in the all-hadronic $t\bar{t}$ decay channel at $\sqrt{s} = 8$ TeV with the ATLAS detector*, JHEP **09** (2017) 118, arXiv:1702.07546 [hep-ex]. Cited on page 204.

[259] ATLAS Collaboration, *Direct top-quark decay width measurement in the $t\bar{t}$ lepton+jets channel at $\sqrt{s} = 8$ TeV with the ATLAS experiment*, Eur. Phys. J. C **78** (2018) 129, arXiv:1709.04207 [hep-ex]. Cited on pages 204, 205, 206, and 216.

[260] ATLAS Collaboration, *Measurement of lepton differential distributions and the top quark mass in $t\bar{t}$ production in pp collisions at $\sqrt{s} = 8$ TeV with the ATLAS detector*, Eur. Phys. J. C **77** (2017) 804, arXiv:1709.09407 [hep-ex]. Cited on page 204.

[261] ATLAS Collaboration, *Measurement of the top quark mass in the $t\bar{t} \rightarrow$ lepton+jets channel from $\sqrt{s} = 8$ TeV ATLAS data and combination with previous results*, Eur. Phys. J. (2018) , arXiv:1810.01772 [hep-ex]. Cited on page 204.

[262] ATLAS Collaboration, *Measurement of the top-quark mass in $t\bar{t} + 1$-jet events collected with the ATLAS detector in pp collisions at $\sqrt{s} = 8$ TeV*, arXiv:1905.02302 [hep-ex]. Cited on page 204.

[263] CMS Collaboration, *Measurement of the top quark mass using proton–proton data at $\sqrt{s} = 7$ and 8 TeV*, Phys. Rev. D **93** (2016) 072004, arXiv:1509.04044 [hep-ex]. Cited on page 204.

[264] CMS Collaboration, *Measurement of the $t\bar{t}$ production cross section in the $e\mu$ channel in proton–proton collisions at $\sqrt{s} = 7$ and 8 TeV*, JHEP **08** (2016) 029, arXiv:1603.02303 [hep-ex]. Cited on page 204.

[265] CMS Collaboration, *Measurement of the top quark mass using charged particles in pp collisions at $\sqrt{s} = 8$ TeV*, Phys. Rev. D **93** (2016) 092006, arXiv:1603.06536 [hep-ex]. Cited on page 204.

[266] CMS Collaboration, *Measurement of the mass of the top quark in decays with a J/ψ meson in pp collisions at 8 TeV*, JHEP **12** (2016) 123, arXiv:1608.03560 [hep-ex]. Cited on page 204.

[267] CMS Collaboration, *Measurement of the $t\bar{t}$ production cross section using events with one lepton and at least one jet in pp collisions at $\sqrt{s} = 13$ TeV*, JHEP **09** (2017) 051, arXiv:1701.06228 [hep-ex]. Cited on page 204.

[268] CMS Collaboration, *Measurement of the top quark mass using single top quark events in proton–proton collisions at $\sqrt{s} = 8$ TeV*, Eur. Phys. J. C **77** (2017) 354, arXiv:1703.02530 [hep-ex]. Cited on page 204.

[269] CMS Collaboration, *Measurement of the jet mass in highly boosted $t\bar{t}$ events from pp collisions at $\sqrt{s} = 8$ TeV*, Eur. Phys. J. C **77** (2017) 467, arXiv:1703.06330 [hep-ex]. Cited on page 204.

[270] CMS Collaboration, *Measurement of the top quark mass in the dileptonic $t\bar{t}$ decay channel using the mass observables $M_{b\ell}$, M_{T2}, and $M_{b\ell v}$ in pp collisions at $\sqrt{s} = 8$ TeV*, Phys. Rev. D **96** (2017) 032002, arXiv:1704.06142 [hep-ex]. Cited on page 204.

[271] CMS Collaboration, *Measurement of the top quark mass with lepton+jets final states using pp collisions at $\sqrt{s} = 13$ TeV*, Eur. Phys. J. C **78** (2018) 891, arXiv:1805.01428 [hep-ex]. Cited on page 204.

[272] CMS Collaboration, *Measurement of the $t\bar{t}$ production cross section, the top quark mass, and the strong coupling constant using dilepton events in pp collisions at $\sqrt{s} = 13$ TeV*, Eur. Phys. J. (2018) , arXiv:1812.10505 [hep-ex]. Cited on page 204.

[273] CMS Collaboration, *Measurement of the top quark mass in the all-jets final state at $\sqrt{s} = 13$ TeV and combination with the lepton+jets channel*, Eur. Phys. J. (2018) , arXiv:1812.10534 [hep-ex]. Cited on page 204.

[274] CMS Collaboration, *Measurement of $\mathrm{t\bar{t}}$ normalised multi-differential cross sections in pp collisions at $\sqrt{s} = 13$ TeV, and simultaneous determination of the strong coupling strength, top quark pole mass, and parton distribution functions*, Submitted to: Eur. Phys. J. (2019) , arXiv:1904.05237 [hep-ex]. Cited on page 204.

[275] P. Nason, *The Top Mass in Hadronic Collisions*, in *From My Vast Repertoire ...: Guido Altarelli's Legacy*, A. Levy, S. Forte, and G. Ridolfi, eds., pp. 123–151. 2019. arXiv:1712.02796 [hep-ph]. Cited on page 204.

[276] CDF Collaboration, *Direct Measurement of the Total Decay Width of the Top Quark*, Phys. Rev. Lett. **111** (2013) no. 20, 202001, arXiv:1308.4050 [hep-ex]. Cited on pages 204 and 205.

[277] CMS Collaboration, *Bounding the top quark width using final states with two charged leptons and two jets at* $\sqrt{s} = 13$ TeV, CMS-PAS-TOP-16-019 (2016) . `https://cds.cern.ch/record/2218019`. Cited on pages 204 and 205.

[278] D0 Collaboration, *An Improved determination of the width of the top quark*, Phys. Rev. **D**85 (2012) 091104, arXiv:1201.4156 [hep-ex]. Cited on pages 204 and 206.

[279] CMS Collaboration, *Measurement of the ratio $\mathcal{B}(t \to Wb)/\mathcal{B}(t \to Wq)$ in pp collisions at $\sqrt{s} = 8$ TeV*, Phys. Lett. **B**736 (2014) 33–57, arXiv:1404.2292 [hep-ex]. Cited on pages 204, 206, and 207.

[280] M. Ježabek and J. Kühn, *QCD corrections to semileptonic decays of heavy quarks*, Nuclear Physics B **3**14 (1989) no. 1, 1 – 6. Cited on page 205.

[281] A. Czarnecki, *QCD corrections to the decay $t \to Wb$ in dimensional regularization*, Phys. Lett. B **2**52 (1990) 467–470. Cited on page 205.

[282] C. Li, R. J. Oakes, and T. Yuan, *QCD corrections to $t \to W^+ + b$*, Phys. Rev. D **43** (Jun, 1991) 3759–3762. Cited on page 205.

[283] A. Czarnecki and K. Melnikov, *Two-loop QCD corrections to top quark width*, Nuclear Physics B **5**44 (1999) no. 3, 520 – 531. Cited on page 205.

[284] K. G. Chetyrkin, R. Harlander, T. Seidensticker, and M. Steinhauser, *Second order QCD corrections to $\Gamma(t \to Wb)$*, Phys. Rev. D **60** (Nov, 1999) 114015, arXiv:hep-ph/9906273 [hep-ph]. Cited on page 205.

[285] I. Blokland, A. Czarnecki, M. Ślusarczyk, and F. Tkachov, *Heavy-to-Light-Quark Decays with Two-Loop Accuracy*, Phys. Rev. Lett. **93** (Aug, 2004) 062001, arXiv:hep-ph/0403221 [hep-ph]. Cited on page 205.

[286] J. Gao, C. Li, and H. Zhu, *Top Quark Decay at Next-to-Next-to Leading Order in QCD*, Phys. Rev. Lett. **110** (2013) no. 4, 042001, arXiv:1210.2808 [hep-ph]. Cited on page 205.

[287] M. Brucherseifer, F. Caola, and K. Melnikov, $\mathcal{O}(\alpha_s^2)$ *corrections to fully-differential top quark decays*, JHEP **04** (2013) 059, arXiv:1301.7133 [hep-ph]. Cited on page 205.

[288] P. Batra and T. M. P. Tait, *Measuring the W-t-b Interaction at the ILC*, Phys. Rev. **D74** (2006) 054021, arXiv:hep-ph/0606068 [hep-ph]. Cited on page 205.

[289] R. S. Chivukula, E. H. Simmons, and J. Terning, *Limits on noncommuting extended technicolor*, Phys. Rev. **D53** (1996) 5258–5267, arXiv:hep-ph/9506427 [hep-ph]. Cited on page 205.

[290] E. Malkawi, T. M. P. Tait, and C. P. Yuan, *A Model of strong flavor dynamics for the top quark*, Phys. Lett. **B385** (1996) 304–310, arXiv:hep-ph/9603349 [hep-ph]. Cited on page 205.

[291] D. J. Muller and S. Nandi, *Top flavor: A Separate SU(2) for the third family*, Phys. Lett. **B383** (1996) 345–350, arXiv:hep-ph/9602390 [hep-ph]. Cited on page 205.

[292] P. Batra, A. Delgado, D. E. Kaplan, and T. M. P. Tait, *The Higgs mass bound in gauge extensions of the minimal supersymmetric standard model*, JHEP **02** (2004) 043, arXiv:hep-ph/0309149 [hep-ph]. Cited on page 205.

[293] N. Kauer and G. Passarino, *Inadequacy of zero-width approximation for a light Higgs boson signal*, JHEP **08** (2012) 116, arXiv:1206.4803 [hep-ph]. Cited on page 207.

[294] F. Caola and K. Melnikov, *Constraining the Higgs boson width with ZZ production at the LHC*, Phys. Rev. **D88** (2013) 054024, arXiv:1307.4935 [hep-ph]. Cited on page 207.

[295] J. M. Campbell, R. K. Ellis, and C. Williams, *Bounding the Higgs width at the LHC using full analytic results for* $gg- > e^-e^+\mu^-\mu^+$, JHEP **04** (2014) 060, arXiv:1311.3589 [hep-ph]. Cited on pages 207 and 208.

[296] J. M. Campbell, R. K. Ellis, and C. Williams, *Bounding the Higgs width at the LHC: Complementary results from* $H \to WW$, Phys. Rev. **D89** (2014) no. 5, 053011, arXiv:1312.1628 [hep-ph]. Cited on page 207.

[297] C. Englert and M. Spannowsky, *Limitations and Opportunities of Off-Shell Coupling Measurements*, Phys. Rev. **D90** (2014) 053003, arXiv:1405.0285 [hep-ph]. Cited on pages 207 and 208.

[298] G. Cacciapaglia, A. Deandrea, G. Rochelle, and J. Flament, *Higgs couplings: disentangling New Physics with off-shell measurements*, Phys. Rev. Lett. **113** (2014) no. 20, 201802, arXiv:1406.1757 [hep-ph]. Cited on page 207.

[299] A. Azatov, C. Grojean, A. Paul, and E. Salvioni, *Taming the off-shell Higgs boson*, Zh. Eksp. Teor. Fiz. **147** (2015) 410–425, arXiv:1406.6338 [hep-ph]. [J. Exp. Theor. Phys.120,354(2015)]. Cited on page 207.

[300] M. Ghezzi, G. Passarino, and S. Uccirati, *Bounding the Higgs Width Using Effective Field Theory*, PoS **LL**2014 (2014) 072, arXiv:1405.1925 [hep-ph]. Cited on page 207.

[301] M. Buschmann, D. Goncalves, S. Kuttimalai, M. Schonherr, F. Krauss, and T. Plehn, *Mass Effects in the Higgs-Gluon Coupling: Boosted vs Off-Shell Production*, JHEP **02** (2015) 038, arXiv:1410.5806 [hep-ph]. Cited on page 207.

[302] J. S. Gainer, J. Lykken, K. T. Matchev, S. Mrenna, and M. Park, *Beyond Geolocating: Constraining Higher Dimensional Operators in $H \to 4\ell$ with Off-Shell Production and More*, Phys. Rev. **D**91 (2015) no. 3, 035011, arXiv:1403.4951 [hep-ph]. Cited on page 207.

[303] C. Englert, Y. Soreq, and M. Spannowsky, *Off-Shell Higgs Coupling Measurements in BSM scenarios*, JHEP **05** (2015) 145, arXiv:1410.5440 [hep-ph]. Cited on page 207.

[304] D. Goncalves, T. Han, and S. Mukhopadhyay, *Off-Shell Higgs Probe of Naturalness*, Phys. Rev. Lett. **120** (2018) no. 11, 111801, arXiv:1710.02149 [hep-ph]. [Erratum: Phys. Rev. Lett.121,no.7,079902(2018)]. Cited on page 207.

[305] CMS Collaboration, *Constraints on the Higgs boson width from off-shell production and decay to Z-boson pairs*, Phys. Lett. **B**736 (2014) 64–85, arXiv:1405.3455 [hep-ex]. Cited on page 208.

[306] CMS Collaboration, *Search for Higgs boson off-shell production in proton-proton collisions at 7 and 8 TeV and derivation of constraints on its total decay width*, JHEP **09** (2016) 051, arXiv:1605.02329 [hep-ex]. Cited on page 208.

[307] CMS Collaboration, *Limits on the Higgs boson lifetime and width from its decay to four charged leptons*, Phys. Rev. **D**92 (2015) no. 7, 072010, arXiv:1507.06656 [hep-ex]. Cited on page 208.

[308] CMS Collaboration, *Measurements of properties of the Higgs boson decaying into the four-lepton final state in pp collisions at $\sqrt{s} = 13$ TeV*, JHEP **11** (2017) 047, arXiv:1706.09936 [hep-ex]. Cited on page 208.

[309] ATLAS Collaboration, *Constraints on off-shell Higgs boson production and the Higgs boson total width in $ZZ \to 4\ell$ and $ZZ \to 2\ell 2\nu$ final states with the ATLAS detector*, Phys. Lett. **B**786 (2018) 223–244, arXiv:1808.01191 [hep-ex]. Cited on page 208.

[310] S. Liebler, G. Moortgat-Pick, and A. S. Papanastasiou, *Probing the top-quark width through ratios of resonance contributions of $e^+e^- \to W^+W^-b\bar{b}$*, JHEP **03** (2016) 099, arXiv:1511.02350 [hep-ph]. Cited on page 208.

[311] A. Baskakov, E. Boos, and L. Dudko, *Model independent top quark width measurement using a combination of resonant and non resonant cross sections*, Phys. Rev. **D**98 (2018) no. 11, 116011, arXiv:1807.11193 [hep-ph]. Cited on page 208.

[312] A. Baskakov, E. Boos, and L. Dudko, *On the top-quark width measurement using a combination of resonant and non resonant cross sections.*, EPJ Web Conf. **158** (2017) 04007. Cited on page 208.

[313] P. Giardino and C. Zhang, *Probing the top-quark width using the charge identification of b jets*, Phys. Rev. **D**96 (2017) no. 1, 011901, arXiv:1702.06996 [hep-ph]. Cited on page 208.

[314] S. Frixione, P. Nason, and C. Oleari, *Matching NLO QCD computations with Parton Shower simulations: the POWHEG method*, JHEP **11** (2007) 070, arXiv:0709.2092 [hep-ph]. Cited on page 209.

[315] S. Ferrario Ravasio, T. Ježo, P. Nason, and C. Oleari, *A theoretical study of top-mass measurements at the LHC using NLO+PS generators of increasing accuracy*, Eur. Phys. J. **C**78 (2018) no. 6, 458, arXiv:1801.03944 [hep-ph]. Cited on page 209.

[316] A. Buckley, J. Butterworth, L. Lonnblad, D. Grellscheid, H. Hoeth, J. Monk, H. Schulz, and F. Siegert, *Rivet user manual*, Comput. Phys. Commun. **184** (2013) 2803–2819, arXiv:1003.0694 [hep-ph]. Cited on page 210.

[317] N. Kauer and D. Zeppenfeld, *Finite width effects in top quark production at hadron colliders*, Phys. Rev. **D**65 (2002) 014021, arXiv:hep-ph/0107181 [hep-ph]. Cited on page 211.

[318] R. D. Ball et al., *Parton distributions for the LHC Run II*, JHEP **04** (2015) 040, arXiv:1410.8849 [hep-ph]. Cited on page 212.

[319] ATLAS Collaboration, *Search for charged Higgs bosons decaying via $H^{\pm} \to \tau^{\pm}\nu_{\tau}$ in the τ+jets and τ+lepton final states with 36 fb^{-1} of pp collision data recorded at $\sqrt{s} = 13$ TeV with the ATLAS experiment*, JHEP **09** (2018) 139, arXiv:1807.07915 [hep-ex]. Cited on pages 218 and 221.

[320] ATLAS Collaboration, *Search for charged Higgs bosons decaying into top and bottom quarks at $\sqrt{s}$ = 13 TeV with the ATLAS detector*, JHEP **11** (2018) 085, arXiv:1808.03599 [hep-ex]. Cited on pages 218 and 221.

[321] CMS Collaboration, *Search for a charged Higgs boson in pp collisions at $\sqrt{s} = 8$ TeV*, JHEP **11** (2015) 018, arXiv:1508.07774 [hep-ex]. Cited on pages 218 and 221.

[322] ATLAS Collaboration, *Measurements of fiducial and differential cross-sections of $t\bar{t}$ production with additional heavy-flavour jets in proton–proton collisions at $\sqrt{s} = 13$ TeV with the ATLAS detector*, arXiv:1811.12113 [hep-ex]. Cited on page 224.

[323] ATLAS Collaboration, *Search for the standard model Higgs boson produced in association with top quarks and decaying into a $b\bar{b}$ pair in pp collisions at $\sqrt{s} = 13$ TeV with the ATLAS detector*, Phys. Rev. D **97** (2018) 072016, arXiv:1712.08895 [hep-ex]. Cited on page 224.

[324] ATLAS Collaboration, *Observation of Higgs boson production in association with a top quark pair at the LHC with the ATLAS detector*, Phys. Lett. B **784** (2018) 173, arXiv:1806.00425 [hep-ex]. Cited on page 224.

[325] CMS Collaboration, *Measurements of $t\bar{t}$ cross sections in association with b jets and inclusive jets and their ratio using dilepton final states in pp collisions at $\sqrt{s} = 13$ TeV*, Phys. Lett. B **776** (2018) 355, arXiv:1705.10141 [hep-ex]. Cited on page 224.

[326] CMS Collaboration, *Search for $t\bar{t}H$ production in the $H \to b\bar{b}$ decay channel with leptonic $t\bar{t}$ decays in proton–proton collisions at $\sqrt{s} = 13$ TeV*, JHEP **03** (2019) 026, arXiv:1804.03682 [hep-ex]. Cited on page 224.

[327] CMS Collaboration, *Observation of $t\bar{t}H$ Production*, Phys. Rev. Lett. **120** (2018) 231801, arXiv:1804.02610 [hep-ex]. Cited on page 224.

[328] F. Cascioli, P. Maierhöfer, N. Moretti, S. Pozzorini, and F. Siegert, *NLO matching for $t\bar{t}b\bar{b}$ production with massive b-quarks*, Phys. Lett. B **734** (2014) 210–214, arXiv:1309.5912 [hep-ph]. Cited on page 224.

[329] S. Hoeche, F. Krauss, P. Maierhoefer, S. Pozzorini, M. Schonherr, and F. Siegert, *Next-to-leading order QCD predictions for top-quark pair production with up to two jets merged with a parton shower*, Phys. Lett. **B**748 (2015) 74–78, arXiv:1402.6293 [hep-ph]. Cited on page 224.

[330] M. V. Garzelli, A. Kardos, and Z. Trócsányi, *Hadroproduction of $t\bar{t}b\bar{b}$ final states at LHC: predictions at NLO accuracy matched with Parton Shower*, JHEP **03** (2015) 083, arXiv:1408.0266 [hep-ph]. Cited on page 224.

[331] G. Bevilacqua, M. V. Garzelli, and A. Kardos, *$t\bar{t}b\bar{b}$ hadroproduction with massive bottom quarks with PowHel*, arXiv:1709.06915 [hep-ph]. Cited on page 224.

[332] T. Ježo, J. M. Lindert, N. Moretti, and S. Pozzorini, *New NLOPS predictions for $\boldsymbol{t\bar{t}+b}$ -jet production at the LHC*, Eur. Phys. J. **C**78 (2018) no. 6, 502, arXiv:1802.00426 [hep-ph]. Cited on page 224.

[333] ATLAS Collaboration, *Search for Supersymmetry at the high luminosity LHC with the ATLAS Detector*, ATL-PHYS-PUB-2014-010, 2014. `https://cds.cern.ch/record/1735031`. Cited on page 225.

[334] ATLAS Collaboration, *Search for squarks and gluinos in final states with jets and missing transverse momentum using $36\,fb^{-1}$ of $\sqrt{s} = 13$ TeV pp collision data with the ATLAS detector*, Phys. Rev. D **97** (2018) 112001, arXiv:1712.02332 [hep-ex]. Cited on page 225.

[335] ATLAS Collaboration, *ATLAS sensitivity to top squark pair production at the HL-LHC*, ATL-PHYS-PUB-2018-021, 2018. `https://cds.cern.ch/record/2644831`. Cited on page 225.

[336] ATLAS Collaboration, *Search for a scalar partner of the top quark in the jets plus missing transverse momentum final state at $\sqrt{s} = 13$ TeV with the ATLAS detector*, JHEP **12** (2017) 085, arXiv:1709.04183 [hep-ex]. Cited on pages 225, 226, and 227.

[337] ATLAS Collaboration, *Search for electroweak production of supersymmetric states in scenarios with compressed mass spectra at $\sqrt{s} = 13$ TeV with the ATLAS detector*, Phys. Rev. D **97** (2018) 052010, arXiv:1712.08119 [hep-ex]. Cited on page 225.

[338] G. Barenboim, E. J. Chun, S. Jung, and W. I. Park, *Implications of an axino LSP for naturalness*, Phys. Rev. **D**90 (2014) no. 3, 035020, arXiv:1407.1218 [hep-ph]. Cited on page 226.

[339] ATLAS Collaboration, *Search for supersymmetry in events with four or more leptons in $\sqrt{s} = 13$ TeV pp collisions with ATLAS*, Phys. Rev. D **98** (2018) 032009, arXiv:1804.03602 [hep-ex]. Cited on pages 227 and 253.

[340] Z. Marshall, B. A. Ovrut, A. Purves, and S. Spinner, *Spontaneous R-Parity Breaking, Stop LSP Decays and the Neutrino Mass Hierarchy*, Phys. Lett. **B**732 (2014) 325–329, arXiv:1401.7989 [hep-ph]. Cited on page 228.

[341] Z. Marshall, B. A. Ovrut, A. Purves, and S. Spinner, *LSP Squark Decays at the LHC and the Neutrino Mass Hierarchy*, Phys. Rev. **D**90 (2014) no. 1, 015034, arXiv:1402.5434 [hep-ph]. Cited on page 228.

[342] B. A. Ovrut, A. Purves, and S. Spinner, *A statistical analysis of the minimal SUSY B-L theory*, Mod. Phys. Lett. **A**30 (2015) no. 18, 1550085, arXiv:1412.6103 [hep-ph]. Cited on page 228.

[343] B. A. Ovrut, A. Purves, and S. Spinner, *The minimal SUSY $B - L$ model: from the unification scale to the LHC*, JHEP **06** (2015) 182, arXiv:1503.01473 [hep-ph]. Cited on pages 228 and 229.

[344] B. Fuks, M. Klasen, D. R. Lamprea, and M. Rothering, *Gaugino production in proton-proton collisions at a center-of-mass energy of 8 TeV*, JHEP **10** (2012) 081, arXiv:1207.2159 [hep-ph]. Cited on pages 242 and 246.

[345] B. Fuks, M. Klasen, D. R. Lamprea, and M. Rothering, *Precision predictions for electroweak superpartner production at hadron colliders with* RESUMMINO, Eur. Phys. J. C **7**3 (2013) 2480, arXiv:1304.0790 [hep-ph]. Cited on pages 242 and 246.

[346] DELPHES 3 Collaboration, J. de Favereau, C. Delaere, P. Demin, A. Giammanco, V. Lemaître, A. Mertens, and M. Selvaggi, *DELPHES 3, A modular framework for fast simulation of a generic collider experiment*, JHEP **02** (2014) 057, arXiv:1307.6346 [hep-ex]. Cited on page 246.